TECHNISCHE UNIVERSITÄT MÜNCHEN
Institut für Photogrammetrie und Kartographie
Lehrstuhl für Methodik der Fernerkundung

Derivation of mass balance and surface velocity of glaciers by means of high resolution synthetic aperture radar: application to the Patagonian Icefields and Antarctica

Wael Abdel Jaber

Vollständiger Abdruck der von der Ingenieurfakultät Bau Geo Umwelt
der Technischen Universität München zur Erlangung des akademischen Grades eines

Doktor-Ingenieurs (Dr.-Ing.)

genehmigten Dissertation.

Vorsitzender: Univ.-Prof. Dr.-Ing. Florian Seitz

Prüfer der Dissertation:

1. Univ.-Prof. Dr.-Ing. habil. Richard H.G. Bamler
2. Hon.-Prof. Dr. rer. nat. Michael Eineder
3. Ao. Univ. Prof. Helmut Rott
   Universität Innsbrück, Innsbrück, Österreich

Die Dissertation wurde am 05.07.2016 bei der Technischen Universität München eingereicht und durch die Ingenieurfakultät Bau Geo Umwelt am 30.07.2016 angenommen.

Abstract

The advent and the continuous development of airborne and spaceborne remote sensing has revolutionised traditional glaciology in the last decades by enabling the monitoring of hardly accessible regions at a much larger spatial and temporal scale than field surveys. Among the large variety of sensors, each having different benefits and drawbacks, synthetic aperture radar (SAR) is one of the most capable. SAR systems can produce high resolution, wide-coverage images under any illumination and weather condition and, particularly at longer wavelengths, have the ability to "perceive" features even in the sub-surface of dry ice and snow, which are otherwise invisible to optical systems.

Glaciers and ice sheets are fundamental components of the global climate system and are particularly sensitive to climate change. Significant and progressive ice mass loss has been registered worldwide in the last decades. To improve the currently uncertain global glacier loss projections and the related climate change models, a good understanding of the driving mechanisms governing mass balance and glacier flow is necessary. To this end, this dissertation aims at improving the estimation of both glacier mass balance and surface velocity by means of high resolution SAR data and simultaneously provide valuable results to the glaciological and climatological scientific communities.

Up-to-date and accurate mass balance estimates and temporal trends for a wide pool of glaciers is fundamental, but of difficult derivation. In the traditional input-output method models are often used to retrieve the surface mass balance, while the calving flux is estimated from ice flow velocity, a parameter derivable on a large scale only by remote sensing. Gravimetry offers good temporal resolution but coarse spatial resolution and necessitates models to isolate other sources of mass change leading to large uncertainties. In this thesis the high resolution Raw DEMs produced by the recent TanDEM-X mission were combined with the SRTM C-band DEM of year 2000. Together they constitute a powerful and reliable multitemporal dataset based on bistatic SAR interferometry (InSAR) for the retrieval of detailed elevation change maps of vast regions and the corresponding glacier mass balance thorough the geodetic method. Particular emphasis was set on the definition of a generalizable framework for the estimation of the uncertainty of the geodetic mass balance by quantifying all relevant sources of error. Among these, signal penetration into dry ice and snow can affect considerably radar elevation measurements. To this end the backscattering coefficient of the SAR acquisitions were analysed in order to evaluate the snow condition with respect to liquid water content.

The geodetic mass balance was derived for the Northern and Southern Patagonian icefields (NPI & SPI), the largest mid-latitude ice masses in the Southern Hemisphere with a surface of about 16700 km^2. The icefields are known to be very dynamic, displaying strong ice downwasting since the Little Ice Age maximum, causing the highest rate of isostatic rebound ever recorded worldwide. Total ice mass change rates of $-3.96 \pm 0.14\ Gt\,a^{-1}$ and $-13.14 \pm 0.42\ Gt\,a^{-1}$ have been obtained for NPI (2000 - 2014) and SPI (2000 - 2011/'12), respectively, these values do not include subaqueous changes which were separately estimated. These results appear to correct estimates obtained in the literature for similar observation periods with both the geodetic and the gravimetric methods, furthermore reducing their uncertainty. The Jorge Montt Glacier (SPI), featuring the highest thinning rate, was further analysed during the period 2011 - 2014 finding a mass change rate of $-2.59\ Gt\,a^{-1}$ (+50% with respect to the 2000 - 2011 period).

Glacier surface velocities are important in assessing the stability of icefields and ice sheets and their response to climate change. They are fundamental to the study of ice dynamics allowing to map ice transport from accumulation to ablation regions and to estimate strain rates and other geophysical parameters. SAR is particularly suited to the derivation of velocity maps: the high spatial resolution, good radiometric accuracy, short repeat cycle, left-looking capabilities and precise geolocalization of TerraSAR-X have been exploited in this thesis. A processing chain was developed for the derivation of detailed velocity maps by means of offset tracking based on incoherent cross-correlation. Several scientifically relevant glaciers worldwide have been monitored with particular focus on remote regions such as the interior of Antarctica where measurements are still scarce (e.g. Recovery, Thwaites and several Ross Ice Shelf glaciers).

Zusammenfassung

Das Aufkommen und die kontinuierliche Entwicklung der Satellitenfernerkundung hat die traditionelle Glaziologie in den letzten Jahrzehnten revolutioniert. Schwer zugängliche Regionen können jetzt mit viel besserer räumlicher und zeitlicher Auflösung, überwacht werden. Eine Vielfalt von Sensoren, jeder mit unterschiedlichen Vor- und Nachteilen, hat sich mittlerweile etabliert. Radar mit synthetischer Apertur (SAR) ist davon einer der Leistungsfähigsten. SAR-Systeme liefern Bilder mit höher Auflösung, großer Abdeckung und können die Eigenschaften der Erdoberfläche systematisch bei Tag und Nacht zu jeder Jahreszeit und Wetterlage erfassen. Dazu besitzen SAR-Sensoren bei längeren Wellenlängen die Eigenschaft, bis zu mehrere Meter in trockenen Schnee einzudringen und somit Beiträge aus dem Volumen und tiefer liegenden Grenzflächen, welche für optische Systeme unsichtbar sind, zu liefern.

Gletscher und die Eisschilde der Antarktis und Grönlands sind grundlegende Bestandteile des globalen Klimasystems und reagieren besonders empfindlich auf den Wandel des Klimas. Weltweit registrierte man in den letzten Jahrzehnten einen signifikanten und zunehmenden Eismassenverlust. Um die derzeit unsicheren Abschätzungen und Vorhersagen zum globalen Gletscherverlust und die damit verbundenen Modelle zum Klimawandel zu verbessern, ist ein gutes Verständnis der Mechanismen, welche die Massenbilanz und den Gletscherfluss beeinflussen, erforderlich. Die vorliegende Dissertation hat deshalb das Ziel, durch die Analyse hochauflösender SAR-Daten sowohl Massenbilanz und Oberflächengeschwindigkeit von Gletschern verbessert abzuschätzen. Die erzielten Ergebnisse sind sowohl für die glaziologische als auch die klimatologische Wissenschaftsgemeinde von besonderem Interesse.

Aktuelle und genaue Massenbilanzschätzungen sowie zeitliche Tendenzen für eine große Auswahl von Gletschern sind von grundlegender Bedeutung, aber aufwändig abzuleiten. Die traditionelle glaziologische (Input-Output)-Methode beruht auf Feldmessungen und Modellen, aus der sich Oberflächenmassenbilanzen ergeben. Um den Massenverlust durch Kalben abzuschätzen, sind weiterhin Messungen der Gletschergeschwindigkeit nötig, ein Parameter, der im großen Umfang nur durch Fernerkundung abzuleiten ist. Zwar erlaubt auch die Gravimetrie aus dem erdnahen Orbit die Bestimmung von Massenänderungen des Eises mit hohen zeitlichen Wiederholungsraten, jedoch nur mit grober räumlicher Auflösung. Außerdem benötigt sie Modelle, um andere Ursachen von Massenänderungen zu isolieren, was zu einer großen Unsicherheit führt. In dieser Dissertation wurden hochauflösende digitale Höhenmodelle (DHM) der aktuelle TanDEM-X Mission mit dem SRTM C-Band DHM aus dem Jahr 2000 kombiniert. Zusammen bilden sie einen leistungsfähigen und zuverlässigen multitemporalen, auf bistatischer SAR-Interferometrie (InSAR) basierenden Datensatz. Dieser dient der Erstellung von detaillierten Höhenänderungskarten über ausgedehnten Regionen und daraus abgeleitet, der entsprechenden Gletschermassenbilanz mittels des geodätischen Verfahrens. Besondere Beachtung fand die Schätzung der Unsicherheit der geodätischen Massenbilanzen durch die Quantifizierung aller relevanter Fehlerquellen. Insbesondere das Eindringen des Radarsignals in trockenen Schnee kann die Radarhöhenmessungen erheblich beeinflussen. Zu diesem Zweck wurde der Rückstreukoeffizient der SAR-Akquisitionen analysiert, um die Schneelage in Bezug auf ihren Wassergehalt zu untersuchen.

Die geodätische Massenbilanz der nördlichen und südlichen patagonischen Eisfelder (NPI & SPI) wurde abgeleitet. Mit einer Gesamtfläche von etwa 16700 km^2 repräsentieren sie die größten Eismassen in mittleren Breiten der südlichen Hemisphäre. Diese Eisfelder verhalten sich sehr dynamisch und zeigen starke Verluste seit dem Maximum der *Kleinen Eiszeit*, was die höchste Rate postglazialer Landhebung weltweit ausgelöste. Gesamte Eismassenänderungsraten von -3.96 ± 0.14 Gt a^{-1} und -13.14 ± 0.42 Gt a^{-1} wurden für NPI (Zeitraum 2000 - 2014) bzw. SPI (Zeitraum 2000 - 2011/2012) abgeleitet, jeweils ohne Berücksichtigung des Unterwasseranteils. Dieser wurde getrennt geschätzt. Die vorliegenden Ergebnisse korrigieren die publizierten Schätzungen basierend auf die geodätischen und gravimetrischen Methoden für ähnliche Beobachtungsperioden. Außerdem verringern sie deren Unsicherheit. Der Jorge Montt Gletscher (SPI) weist die höchste Ausdünnungsrate beider Eisfelder auf. Er wurde deshalb für den Zeitraum 2011 - 2014 eingehender analysiert. Diese Untersuchung führte zu einer Eismassenänderungsrate von -2.59 Gt a^{-1}, was einer 50%-igen Zunahme gegenüber dem Zeitraum 2000 - 2011 entspricht.

Die Kenntnis der Oberflächengeschwindigkeiten der Gletscher ist wichtig, um die Stabilität der

Eisfelder und des Inlandeises sowie ihre Reaktion auf den Klimawandel beurteilen zu können. Sie sind von grundlegender Bedeutung für Studien zur Eisdynamik. Damit wird die Kartierung des Eistransports vom Akkumulations- zum Ablationsgebiet, die Schätzung von Verformungsraten und anderer geophysikalischen Parameter ermöglicht. Weltraumgestützte SAR-Sensoren sind besonders geeignet für die Ableitung derartiger Geschwindigkeitskarten. Ihre hohe räumliche Auflösung, die gute radiometrische Genauigkeit, der kurze Wiederholungszyklus, die Aufnahmerichtung nach rechts und links der Satellitenbodenspur sowie die präzise Geolokalisierung von TerraSAR-X wurden in dieser Dissertation genutzt. Es wurde eine Verarbeitungskette zur Ableitung von detaillierten Fließgeschwindigkeitskarten mittels inkohärenter Kreuzkorrelationsverfahrens entwickelt. Mehrere wissenschaftlich relevante Gletscher wurden weltweit überwacht. Besonderes Augenmerk wurde dabei auf abgelegene Regionen wie das Innere der Antarktis gelegt, wo Messungen aufgrund ihrer Abgeschiedenheit nur selten möglich sind (beispielsweise die Gletscher *Recovery*, *Thwaites* sowie mehrere Ausflussgletscher des Ross-Schelfeises).

Contents

Chapter 1

Introduction

1.1 Scientific motivation

Snow and ice cover about a sixth of the Earth's surface in a multitude of forms: snow cover, glaciers, including ice caps and the ice sheets of Greenland and Antarctica, sea ice, lake and river ice, icebergs and permafrost. Together they form the *cryosphere* of our planet. The cryosphere and particularly glaciers and ice sheets play a fundamental role in the global climate system and are strongly influenced by changes in the system itself. Glaciers are furthermore a key component of the water cycle, and as such have a decisive impact on different ecological and societal aspects, among which: natural resource management, economic activities, agriculture, risk management, etc. Extending our knowledge of glaciers and ice sheets, understanding their properties, monitoring their temporal changes, modelling their role in the climate system and their response to its changes are matters of crucial scientific importance.

Traditional glaciology is based on *in situ* measurements obtained with different techniques such as ablation stakes, snow pits, ice cores, photography and geodetic surveys. Field campaigns are unique in enabling to describe the glacier surface and subsurface in great detail but their spatial and temporal coverage is very limited and costly, even more so because of the inaccessibility and the harsh weather of glaciated regions.

In the last decades remote sensing has revolutionised the spatial and temporal scale of cryospheric observations by means of airborne and spaceborne sensors offering insights even on previously inaccessible regions. The development of remote sensing sensors has been continuous and avails itself of different physical acquisition principles allowing to study different aspects of the cryosphere. These include: aerial photography, multispectral spaceborne optical sensors, passive microwave radiometers and active scatterometers, laser and radar altimeters, gravimeters, and synthetic aperture radar (SAR) imaging systems. Naturally, different sensors allow to measure different parameters but also have technical and intrinsic limitations and cannot substitute completely in situ measurements (Rees & Squire, 1989; Davis, 1991; Bindschadler, 1998). Optical observations are hindered in glaciated regions because of the long polar winters and the frequent cloud cover, they cannot offer any insight into the glacier subsurface and suffer from low contrast on smooth snow. Radiometers and scatterometers measure the emission and the backscatter at low resolution (~25 km) allowing to detect melting onset and distinguish glacier zones. Gravimetry can be used to measure mass changes at scales of hundreds of kilometres. Radar and laser altimetry allow to precisely measure the surface elevation and to track its changes. Laser altimeters (for instance on board the ICESat satellite) do not suffer from penetration of the microwave pulses into ice and snow and offer higher resolution compared to radar altimeters at the cost of a sparse spatial coverage.

Synthetic aperture radar represents one of the greatest advances in remote sensing, particularly for the cryosphere. SAR systems can acquire a two-dimensional complex representation of the backscattering of the scene by means of microwave pulses transmitted by a side-looking antenna. High resolution imaging is achieved by exploiting the platform motion to synthesize a larger "synthetic" antenna aperture in the along-track direction and by means of pulse compression in the across-track direction. Being it an active device emitting pulses in the microwave spectrum it can operate independ-

ently of solar illumination and nearly in any weather condition. Moreover it is sensitive to both surface and near-surface features, with penetration capabilities increasing with wavelength. The wavelengths commonly used for SAR range between between 3 cm and 75 cm. The retrieval of a high resolution backscattering image bearing amplitude and phase information allows to develop different techniques relevant to cryosphere monitoring: interferometry (InSAR) allows to produce precise digital elevation models, measure ice movement and small elevation changes with wavelength precision, polarimetry exploits the sensitivity of different electromagnetic polarizations to shape, orientation and dielectric properties of the surface and sub-surface scatterers.

Seasat was the first spaceborne SAR system, launched in 1978, it operated at L-band for a brief lifetime of about 110 days. The first glaciological studies based on SAR, and particularly on the analysis of its backscattering, have been published in the eighties (Rott, 1984; Bindschadler *et al.*, 1987; Rott & Mätzler, 1987). The SIR-C/X-SAR sensors flown in 1994 (L, C, X-band) with dedicated Shuttle missions provided the first polarimetric data from space (Mätzler *et al.*, 1997; Floricioiu & Rott, 2001). A significant impulse to SAR remote sensing was given by the launch of ESA's satellites ERS-1 (1991 - 2000, C-band) and ERS-2 (1995 - 2003, C-band), which also operated in tandem formation, and finally provided continuous temporal coverage. Other notable missions are the Canadian RADARSAT-1 (1995 - 2013, C-band), the ASAR on board of ENVISAT (2002 - 2012, C-band), JAXA's ALOS/PALSAR (2006 - 2011, L-band) and RADARSAT-2 (2007, C-band). Newer missions increased significantly the resolution and decreased the repeat pass time widening the applicability of interferometric techniques to the cryosphere by reducing the temporal decorrelation of the backscattered signal between acquisitions caused by precipitation, melting, refreezing and winds. These missions, operating in X-band, are DLR's TerraSAR-X and TanDEM-X (2007 and 2010) and ASI's COSMO-SkyMed (2007 to 2010) constellation of four satellites. ESA's newest satellite formation is composed by Sentinel-1A/B (2014/2016) with two possible additional satellites planned, all operating at C-band. JAXA's new ALOS-2 features an improved PALSAR-2 instrument working in L-band. Future missions like Tandem-L, operating at L-band with two satellites will further extend the range of scientific applications in the cryosphere by offering continuous and wide coverage at a frequency able to "look" for several meters below the ice and snow surface.

A warming trend of the climate system has been unequivocally observed during the last century, causing changes unprecedented over decades to millennia. Among these, global increase of average atmospheric and oceanic temperatures, widespread melting of permanent ice, average global sea level rise and increase of greenhouse gases concentration (IPCC, 2013). A progressive loss of land ice volume and mass was registered at a worldwide level during the last decades mostly with the use of satellite altimetry and gravimetry, for instance by Jacob *et al.* (2012); Gardner *et al.* (2013); Zemp *et al.* (2015). This trend was also reported in the fifth Assessment Report on Climate Change by the Intergovernmental Panel on Climate Change (IPCC) (Vaughan *et al.*, 2013). Figure 1.1 shows the global distributions of glaciers and their subdivision in macro regions according to the Randolph Glacier Inventory (RGI). The total area of glaciers is globally approximately $726 \cdot 10^3$ km^2, distributed among $168 \cdot 10^3$ basins according to the the RGI version 2.0 (Arendt *et al.*, 2012). The global percentage of area calving into tidewater is 38.5% (Gardner *et al.*, 2013).

Future global glacier volume loss projections for the 21st century are affected by a very large uncertainty, in the order of several tens of percentage points, caused by substantial variations linked to the model approach used to estimate surface mass balance, the dynamic response of glaciers, and ice/ocean interactions under current and future climate conditions (Giesen & Oerlemans, 2013). In order to produce realistic projections, an accurate knowledge of the processes governing ice-climate interactions is needed, achievable through understanding of the driving mechanisms governing glacier flow and mass balance. To this end precise measurements of key glacier parameters such as total net mass balance, surface velocity, accumulation, calving rates, ice thickness, subsurface and subglacial conditions and their evolution in time are fundamental.

Volume and mass changes and their temporal trends are essential for assessing the response of the glaciers to changing boundary conditions, identifying processes controlling the ice flux and estimating their current and future contributions to sea level rise (Barrand *et al.*, 2013; Rott *et al.*, 2014b). To calibrate and validate mass balance models driven by regional and global climate models it is fundamental

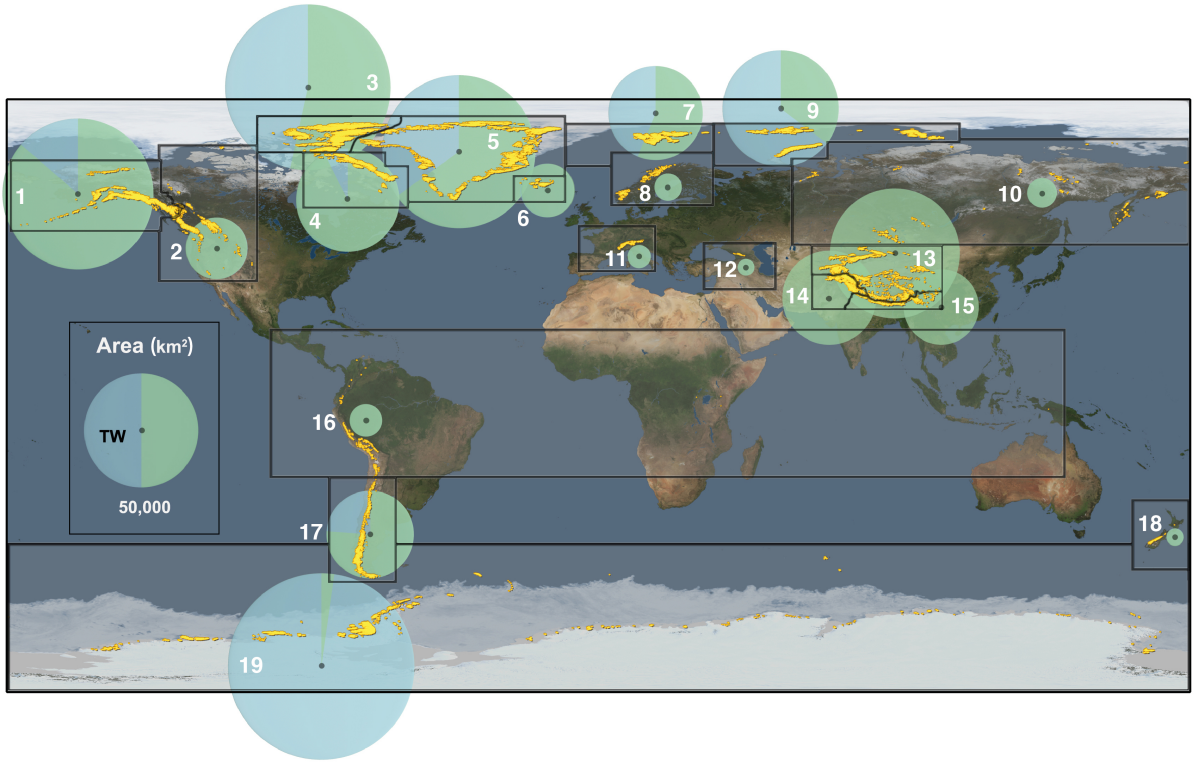

Figure 1.1 – Global distribution of glaciers (yellow, area increased for visibility) and area covered (diameter of the circle), subdivided into the 19 RGI regions. The fraction of the area belonging to tidewater glaciers is plotted in blue. Image from Vaughan *et al.* (2013). The glacier areas are derived from the RGI 2.0 (Arendt *et al.*, 2012) and the tidewater fraction is derived from Gardner *et al.* (2013). The RGI regions are the following: 1) Alaska, 2) Western Canada and USA, 3) Arctic Canada North, 4) Arctic Canada South, 5) Greenland, 6) Iceland, 7) Svalbard, 8) Scandinavia, 9) Russian Arctic, 10) North Asia, 11) Central Europe, 12) Caucasus, 13) Central Asia, 14) South Asia (West), 15) South Asia (East), 16) Low Latitudes, 17) Southern Andes, 18) New Zealand, 19) Antarctic and Sub-Antarctic.

to obtain spatially detailed information on the parameters involved in mass balance calculations, one of them being the surface elevation change. Further requirements include the widening of the currently limited pool of well-observed glaciers as well as repeated observations to track trends.

Another issue is the accuracy of the mass balance. Gardner *et al.* (2013) showed how estimates of global ice volume loss achieved by means of altimetry and GRACE gravimetry are significantly lower than extrapolations from in-situ measurements on a limited number of well-studied glaciers. Nevertheless gravimetric mass balance estimates remain affected by considerable uncertainty (10 - 20% globally) due to the coarse spatial resolution (about 300 km) and the difficulties of separating other mass change signals such as hydrological storage and glacial isostatic adjustment (Vaughan *et al.*, 2013; Jacob *et al.*, 2012; Gardner *et al.*, 2013).

The total net mass balance of glaciers can also be indirectly retrieved from repeated elevation observations, with the geodetic method. The geodetic mass balance is the variation of ice mass obtained integrating the surface elevation change over the glacier area and multiplying it by the ice density. This approach allows to isolate the ice volume change and to achieve better spatial detail compared to the gravimetric method. The main intrinsic uncertainty of this method is linked to the assumption of a certain snow density when not available from field measurements. The application of this method on a larger scale has been limited by the lack of spatially extended multitemporal elevation datasets with sufficient spatial resolution and accuracy. Geodetic mass balance studies have been mostly carried out on limited areas often by combining elevation datasets produced with different techniques: digitised cartographic maps (usually obtained from aerial photographs), airborne and spaceborne laser and radar altimetry, optical satellite DEMs (for instance from the ASTER mission), and the bistatic InSAR SRTM DEM acquired in February 2000. Moreover many geodetic mass balance results found

in the literature are characterized by relatively high errors. Cartographic maps suffer from low spatial resolution and accuracy, altimetry is precise but has limited coverage, optical images do not work on featureless smooth snow surface. Spaceborne InSAR in its bistatic configuration, allowing to eliminate temporal decorrelation and atmospheric disturbances, can produce DEMs with large spatial coverage and good accuracy particularly on glaciated terrain.

The TanDEM-X mission was initiated in 2010 by coupling two identical satellites in close formation with the objective of achieving a global DEM with the best accuracy to date by means of bistatic InSAR. The final global TanDEM-X DEM has not yet been released, and is of limited use on rapidly varying surfaces since it relies on averaging of acquisitions performed over a period of five years. However the single bistatic acquisitions can be processed in so-called "Raw DEMs" measuring the glacier height at a specific moment of the mission.

The combination of the SRTM C-band DEM and of TanDEM-X Raw DEMs leads to a powerful multi-temporal elevation dataset for the retrieval of the geodetic mass balance of large glaciated regions such as the Patagonian Icefields (NPI and SPI). The dataset offers extensive coverage: the SRTM is a final product obtained by mosaicking several ascending and descending acquisitions, these are particularly numerous at higher latitudes, contributing to reduce both relative and absolute error as well as voids. The 90 m posting of SRTM is relatively good for vast icefields such as the NPI and SPI, while the spatial resolution of the TanDEM-X is plentifully sufficient for this task. Both datasets are generated with single-pass bistatic InSAR at C and X-band, featuring the same basic advantages and suffering from the same problems, hence allowing for a better modelling of the error sources. Besides difficulties in unwrapping the interferometric phase on mountainous terrains, the main issue of InSAR DEMs on glaciated terrain is the signal penetration into dry snow and ice, inducing height biases in the DEMs. An analysis of the SAR backscattering of the active channel, recently released for all SRTM acquisitions and available for TanDEM-X acquisitions allows to detect dry and smooth snow areas susceptible to this issue, but a precise quantification of the elevation bias remains problematic. Finally the temporal baseline between the two datasets, approximately ranging from 11 to 15 years is particularly suited for the retrieval of the geodetic mass balance. It is large enough to allow to detect elevation change signals even on areas located at higher altitudes and characterized by smaller variations, at the same time providing a decent temporal resolution, fundamental to capture an up-to-date figure of thinning and mass loss given the accelerating trends previously discussed.

The error budget estimation of the geodetic mass balance often lacks a consistent approach in the literature, where even relevant error sources are sometimes ignored. A generalised framework applicable to different datasets is necessary to supply not only precise mass balance results but also reliable error budgets to the climate models.

The glacier surface velocity is a fundamental parameter for analyses and models in several glaciological, geological, hydrological and geophysical applications. This parameter plays a critical role in assessing the stability of icefields and ice sheets and their response to climate change. It allows to define the rates of ice transportation from regions of accumulation to regions of ablation and through which channels this occurs. Moreover it is important for computing the glacier mass balance with the input-output method allowing to estimate the calving flux. Remote sensing provides maps of ice flow velocity with wide spatial coverage, good spatial resolution and high accuracy. These are essential to ice dynamics. The flow of glaciers is a complicated process involving different driving and resisting forces. High resolution ice velocity fields allow to understand the balance of forces and ice mechanics processes. Monitoring glacier velocities with sufficient temporal resolution is also fundamental for safety and economic reasons is many regions of the Earth (for instance in the Himalayas) where glacial lake outbursts due to glacier stagnation (linked to reduced flow) pose a great danger for the population and the infrastructures (Luckman *et al.*, 2007). Furthermore melt water from glaciers represents often the main supply on which many inhabitants rely on and an energy source for hydroelectric power plants.

With the first available SAR instruments glacier surface velocities could be obtained by means of InSAR, offering very high precision, but relative measurements and limited robustness to temporal decorrelation of the phase signature. Offset tracking, was applied to both optical and SAR images, with SAR offering a much clearer signature and better localization properties. SAR coherent and

incoherent offset tracking tackles the limitations of InSAR at the cost of lower precision. The high spatial resolution, good radiometric properties, and short repeat pass cycle of newer SAR missions such as TerraSAR-X are particularly well suited for the retrieval of glacier surface velocities. At X-band the wavelength allows to generate a distinctive speckle pattern even on relatively smooth snow and firn which maintains good coherence even after several repeat pass cycles on stable regions such as the ice sheets. The high-resolution and the high geolocalization accuracy of TerraSAR-X allow tracking the speckle pattern and retrieving the relative displacements on the ground. For crevassed and fast glaciers, where speckle coherence is lost, the features of the surface can be tracked exploiting the spatial resolution of the sensor.

1.2 Research objectives

The research leading to this dissertation focused on the exploitation of large TerraSAR-X and TanDEM-X datasets and their combination with other remote sensing and in situ datasets for the retrieval of glacier parameters and for other glacier related applications. A major focus was set on the retrieval of the elevation change rates and the geodetic mass balance from SRTM and TanDEM-X data, with the following objectives.

- Take advantage of the unique multitemporal dataset constituted by the combination of two bi-static InSAR DEMs with a temporal baseline of 11 - 15 years, offering significant advantages in terms of accuracy compared to optical DEMs and in terms of coverage compared to laser altimetry.

- Develop a framework for the accuracy estimation of the geodetic mass balance by investigating and quantifying all possible error sources and criticalities with the goal of obtaining a more reliable error estimate compared to the studies found in the literature.

- Investigate the response of the backscattering coefficient of ice and snow with respect to liquid water content in order to assess possible signal penetration and consequent elevation biases, in turn affecting the volume change estimate.

- Derive detailed elevation change rate maps and the geodetic mass balance for the Northern and Southern Patagonian icefields with a low error and a reliable accuracy estimation. These icefields are the largest mid-latitude ice masses in the southern hemisphere. They are known to be very sensitive to climate changes, displaying highly dynamic processes and effects, such as strong ice downwasting since the Little Ice Age maximum, which triggered the highest rate of isostatic rebound ever recorded. A previous geodetic mass balance of the icefields was provided by Rignot *et al.* (2003) but it might be outdated (observation period 1968/'75 - 2000), it relied on cartographic maps obtained from aerial photography involving significant extrapolation on higher altitudes, hampering its reliability. A more recent result by Willis *et al.* (2012b,a) based on ASTER and SRTM DEMs corresponds to the observation period used in this thesis, but it appears to be overestimated.

A second relevant application consists in exploiting the advantageous properties of the TerraSAR-X sensor for the derivation of high resolution glacier surface velocity maps with the following objectives.

- Develop a processing chain to derive the glacier surface velocity from high resolution amplitude images by means of offset tracking based on the normalized cross-correlation function. The processing chain should allow for fast processing of a large number of data pairs with limited operator intervention and provide reliable results under different glacier scenarios.

- Obtain high resolution velocity maps for scientifically relevant glaciers, with wide coverage and multitemporal observations. Moreover interpret the obtained surface velocity results and derive additional parameters such as acceleration and strain rates.

1.3 Thesis outline

The investigation of glaciers by means of high resolution SAR products demands an interdisciplinary approach, requiring knowledge in the fields of glaciology, natural sciences, remote sensing, electromagnetism, signal processing, etc. The background necessary to the developed research, and a broad selection of references for further study are hence included in this dissertation for the sake of completeness. The rationale of the manuscript is to make the discussed aspects of SAR remote sensing of snow accessible by a multidisciplinary readership. The chapter structure gives readers the freedom to focus on the topics of greater interest and to skip those they are already familiar with.

Chapter 2 provides the basics of SAR and SAR interferometry, the radar equation and the backscattering coefficient are here defined, the latter playing a fundamental role in the interpretation of the surface conditions of glaciers. The working principle of across-track InSAR is provided here, as well as the concept of coherence and the sources of decorrelation.

A basic description of the main glaciological concepts of interest to the remote sensing of snow is given in Chapter 3. Starting from the physical properties of snow, which generates glaciers, the focus is moved to the physical parameters describing the surface of snow and glaciers at different scales. The glacier zones and the transformation process from snow to glacier ice are then described. A section is dedicated to the complex topic of glacier motion, explaining the driving and resisting forces. The definition of glacier mass balance and the different methods to estimate it are finally presented.

Chapter 4 outlines the basic theory of electromagnetic propagation and scattering within the ice volume and at the interface with air and ground. A broad section is dedicated to the dielectric properties of snow, models and experimental measurements from the literature are reported for ice, water, dry and wet snow. Particular focus is posed on the properties of the backscattering coefficient of snow with respect to different system and snow parameters, a collection of experimental results from the literature are here reported and commented. The main objective is the understanding of the behaviour of the backscattering coefficient at varying liquid water content and the effect of the latter on radar signal penetration in this medium, in order to evaluate possible elevation biases in the InSAR DEMs influencing the geodetic mass balance.

The investigated regions of the Northern and Southern Patagonian icefields are presented in Chapter 5. A wide selection of publications regarding all the multi-faceted aspects of the icefields and their temporal evolution, including in situ and remote sensing results, are here reported.

The data used to compute the elevation change maps and the geodetic mass balance is discussed in Chapter 6. The main focus in on SRTM and TanDEM-X DEM data, the chapter outlines the various aspects of the missions and the processing of the DEMs. Finally, larger space is given to the investigation of the accuracy of these datasets: the different aspects involved and the published studies are reported. The data used in thesis is listed, including additional data, such as glacier outlines.

The procedures followed for the derivation of the elevation change maps, and particularly the DEM coregistration and its accuracy, are described in Chapter 7. The obtained elevation change rate maps of NPI and SPI are reported here.

A critical aspect of the reliability of the InSAR DEMs for the retrieval of the geodetic mass balance is the possible penetration of the radar signal into the ice and snow surface leading to an elevation bias. To assess this error source the backscattering coefficient of the SAR data used have been analysed in Chapter 8. The recent availability of the SRTM C-band backscattering of all datatakes was exploited and meteorological data from a network of nearby station has been used to further support the analysis.

Chapter 9 deals with the geodetic mass balance. The state of the art of the method is firstly presented, the results relevant to the Patagonian icefields are reported and a wide part is dedicated to the various aspects of the error estimation and how it is performed in the literature. The method and the connected experiments used in this thesis to estimate the mass balance and its uncertainty are presented in detail. The estimation of the subaqueous ice loss is performed for completeness. Finally the mass balance results of NPI and SPI are presented and discussed also by comparing them to values and procedures found in the literature.

Chapter 10 reports briefly the elevation change rate and geodetic mass balance results obtained on the Jorge Montt Glacier, the most dynamic in Patagonia. Here an additional TanDEM-X DEM was

used to obtain a second more recent mass balance, giving insights on the accelerated thinning and ice volume and mass loss trend of this glacier.

Chapter 11 focuses on a different glaciological application of SAR: the retrieval of detailed glacier surface velocity fields using TerraSAR-X data. The state of the art of this application is briefly reported. The developed processing chain is described and the aspects affecting the accuracy are defined. Finally a selection of results restricted to the Patagonian Icefields and Antarctica are discussed.

The conclusion of the thesis discussing the scientific contributions to the field of SAR remote sensing of glaciers is given in Chapter 12, followed by an outlook containing recommendations for future developments and investigations.

Chapter 2

SAR and InSAR basics

The radar (RAdio Detection And Ranging) is an active system developed before and during World War II with the purpose of detecting military *targets*. In its simplest form, the antenna transmits pulses in the radiowave or microwave spectrum and receives the energy reflected by the target (allowing its *detection*). The distance to the target (*range*) is determined be the travelling time of the pulses. The Synthetic Aperture Radar (SAR) principle was first proposed by Wiley (1954) with the main purpose of improving the azimuth resolution. In the following decades many SAR airborne and spaceborne systems have been used for different remote sensing applications (Ulaby *et al.*, 1981). Being an active system operating in the microwave region (generally between P and Ku band) it provides its own illumination and can operate day and night and in almost any weather condition. This is particularly useful for cryosphere monitoring, as the study areas are affected by polar night and frequent cloud coverage. In Section 2.1 the SAR acquisition geometry and basic imaging principles, its spatial resolution and finally the backscattering coefficient are briefly presented. For a comprehensive discussion of the SAR system and the processing of its signal the reader is referred to Cumming & Wong (2005); Curlander & McDonough (1991). In Section 2.2 the basic principles of SAR interferometry are presented, the reader is referred to Bamler & Hartl (1998) for an extensive explanation of the topic.

2.1 Synthetic aperture radar

A monostatic SAR system transmits and receives pulses through the same antenna. It is mounted on a moving platform (aircraft or satellite) and operates in a side-looking geometry. Figure 2.1 depicts the SAR acquisition geometry. The platform moves along the *azimuth* or *along-track* direction. The antenna beam points to the ground perpendicular to the flight direction, along the so-called *range* or *across-track* direction.

The antenna beam defines on the ground a certain *footprint* illuminated by each pulse, its width along the ground range is defined *swath*. As the platform moves, pulses are transmitted with a certain *pulse repetition frequency* (PRF) and their echoes are received and recorded. These are processed to generate a two-dimensional SAR image of the scene reflectivity in the azimuth and slant-range plane. Because of the ranging principle, the third dimension, constituted by the topography, cannot be resolved by a single SAR antenna. At a fixed azimuth all points lying on the equi-range arc are projected on the same pixel of the SAR image.

The acquisition geometry causes some topography-related geometric effects in SAR images. *Foreshortening* defines the compression in the SAR image of terrain slopes tilted towards the SAR (slope $s < \theta_l$, otherwise in layover) and the stretching of slopes tilted away from the SAR ($s < 90° - \theta_l$, otherwise in shadow). *Layover* appears for slopes $s \geq \theta_l$ towards the sensor, in this case the projection becomes ambiguous, more than one point are mapped on the same pixel on the SAR image, higher points (e.g. a mountain peak) with a shorter range are mapped before lower points (e.g. a valley) with a longer range. These areas appear bright because of the overlay of different scattering contributions and because of the tilt, which increases backscattering. *Shadowing* affects areas which are not illuminated by the radar pulses because of an obstacle or a steep slope ($s > 90° - \theta_l$) away from the

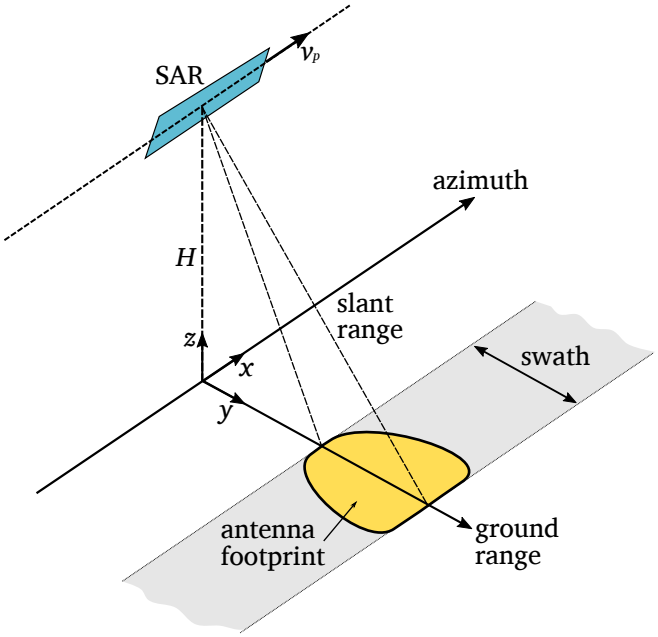

Figure 2.1 – SAR acquisition geometry.

sensor. These areas appear dark in the SAR image because of the lack of returned signal (Bamler & Hartl, 1998).

Two different scanning mechanisms are applied in range and in azimuth. In range the scanning happens through the transmitted pulses travelling at the speed of light c, its reflected energy is digitized by the receiver at a *range sampling frequency* f_{rg}. In azimuth the scene is scanned at the platform speed v_p and sampled at the PRF f_{PRF}. Across-track the range R of a target is proportional to the time delay Δt between transmission and reception of the pulse hitting the target, according to $\Delta t = 2R/c$. The resolution in slant range depends on the pulse duration τ and is given by $\rho_{\mathrm{rg}} = c\tau/2$. To improve the range resolution avoiding sending short pulses with very high transmit peak power, longer pulses with a linear (increasing or decreasing) frequency modulation (*chirps*) are used, thus increasing the pulse bandwidth B. The slant range resolution is given by:

$$\rho_{\mathrm{rg}} = \frac{c}{2B} \tag{2.1}$$

The received energy of the chirp is compressed again into a pulse by a cross-correlation operation with a replica of the chirp (range or pulse compression through a matched filter).

In azimuth the resolution is given by the width of the antenna footprint on the ground: $\rho_{\mathrm{az}} = \lambda R/L_{\mathrm{ant}}$, the physical length of the antenna L_{ant} must hence be increased to improve resolution with obvious limitations. The synthetic aperture concept exploits the fact that different targets falling within the antenna footprint display different Doppler frequency shifts. As the platform advances, each target is illuminated by many subsequent pulses within the same footprint: a much longer synthetic aperture can be generated by coherently combining the received pulses taking into account their Doppler history. The Doppler resolution depends on the "length" of the synthetic aperture which depends on the exposure time of each target and the platform velocity v_p. The azimuth resolution becomes hence:

$$\rho_{\mathrm{az}} = \frac{L_{\mathrm{ant}}}{2} \tag{2.2}$$

and does not depend on the range, the wavelength or the platform velocity, allowing to acquire very high spatial resolution SAR images even from space.

The pixel sizes in range and azimuth are given by:

$$\delta_{\mathrm{rg}} = \frac{c}{2f_{\mathrm{rg}}} \tag{2.3}$$

$$\delta_{\text{az}} = \frac{v_p}{f_{\text{PRF}}} \tag{2.4}$$

The pixel spacing is usually smaller than the resolution in order to avoid undersampling and aliasing, meaning that a certain degree of spatial correlation exists between nearby pixels.

2.1.1 Backscattering coefficient

The radar equation relates the characteristics of the radar, the target and the received signal. For a bistatic radar working in a lossless medium it can be written as (Ulaby *et al.*, 1982b):

$$P_r = \frac{P_t G_t A_r \sigma}{(4\pi)^2 R_t^2 R_r^2} \tag{2.5}$$

which for a monostatic radar can be simplified to:

$$P_r = \frac{P_t G_t A_r \sigma}{(4\pi)^2 R^4} = \frac{P_t G^2 \lambda^2 \sigma}{(4\pi)^3 R^4} = \frac{P_t A^2 \sigma}{4\pi \lambda^2 R^4} \tag{2.6}$$

where

- P_r is the received power and P_t is the transmitted power
- G is the antenna gain, for a monostatic system $G_t = G_r = G$
- A is the effective aperture of the antenna equal to $A = \frac{\lambda^2 G}{4\pi}$, for a monostatic system $A_t = A_r = A$
- R is the range between antenna and target, for a monostatic system $R_t = R_r = R$. The spreading loss is given by $\frac{1}{(4\pi)^2 R^4}$
- λ is the radar wavelength
- σ is the radar cross section of the target

It must be noted that for a synthetic aperture radar the received power is inversely proportional to the third power of the range due to the coherent integration on the synthetic aperture length, for the formula see Curlander & McDonough (1991).

The *radar cross section* (RCS) measures the capacity of the target to scatter the electromagnetic waves in the direction of the receiving antenna (Cumming & Wong, 2005). It depends on factors which are usually difficult to measure individually and it is a function of the frequency, polarization and directions of the incident and scattered waves, and of the shape, size and dielectric properties of the scatterer. The RCS is expressed in m^2 and corresponds to the projected cross sectional area of a perfectly conducting sphere returning an equal power to the radar as the target.

The RCS is suitable to describe *point targets*, but natural environments, particularly those linked to the cryosphere consist generally of *distributed targets*, areas containing many randomly distributed point targets among which no one dominates in amplitude. The received electric field is given by the coherent sum of the scattering contributions of each point target within a resolution cell. In order to extend the radar equation to distributed scatterers the *radar backscattering coefficient* σ^0 (also known as normalized radar cross section) is defined as the average value of the RCS per unit of area. (Ulaby *et al.*, 1982b):

$$\sigma^0 = \frac{\langle \sigma \rangle}{A_g} \tag{2.7}$$

where A_g defines a unit of area where P_t, G, R are nearly constant and which contains enough scattering centres to obtain a sensible average value. In the common definition of σ^0, the unit of area A_g is the illuminated area projected onto the ground. This area is normally assumed to be the pixel area, hence (Freeman, 1992; Van Zyl *et al.*, 1993):

$$A_g = \frac{\delta_{\text{az}} \delta_{\text{rg}}}{\sin \theta_{loc}} \tag{2.8}$$

where δ_{az} and δ_{rg} are the pixel spacings in azimuth and slant range, respectively, and θ_{loc} is the local incidence angle. It is worth noting that the unit of area is here defined by the sampling of the radar signals rather than the actual radar resolution, which is typically larger. The local incidence angle is the angle between the incident radar beam and the local surface normal. As suggested by Ulander (1996) assuming the actual local surface normal would lead to large σ^0 errors when a significant azimuthal surface tilt is present. For this reason the projection of the local surface normal on the zero-Doppler plane must be used, hence:

$$\theta_{loc} = \theta_i - \alpha_{loc}^{\text{zd}} \tag{2.9}$$

where θ_i is the radar incidence angle or look angle and α_{loc}^{zd} is the local slope in the range direction rather than along the aspect direction (direction of maximum slope).

Another useful measure often used when the local slope is not available or as natural intermediate measure is the *radar brightness* β^0 , defined as (Raney *et al.*, 1994):

$$\beta^0 = \frac{\langle \sigma \rangle}{\delta_{\text{az}} \delta_{\text{rg}}} \tag{2.10}$$

hence the relationship between *backscattering coefficient* σ^0 and *radar brightness* β^0 is:

$$\sigma^0 = \beta^0 \sin \theta_{loc} \tag{2.11}$$

Radiometric calibration is the process of relating the pixel value to the RCS σ of a point target or the backscattering coefficient σ^0 of a distributed target from the radar amplitude (Ulander, 1996). Internal calibration involves estimating the overall radar gain by means of pre-flight and in-flight measurements, and compensate it during processing in order to obtain the best estimate of σ or σ^0 (Freeman, 1992). This leads to the definition of two overall gain terms $K_s(x, y)$ and $K_n(x, y)$, of the signal and of the noise components, respectively. Besides the terms included in the radar equation (Eq. (2.6)), K_s includes the electronic gain at the receiver, loss terms due to the systems and the atmosphere and the compensation gain at the processor which should lead to $K_s = 1$ for a calibrated image. K_n is the processor gain in the presence of noise only. Noise sources are the microwave background radiation of the Earth, thermal noise of the the antenna and receiver, and quantization noise of the analogue to digital converter (ADC). External calibration allows to assess and complement internal calibration, it is performed by placing on ground different calibration devices of known RCS, for example a trihedral corner reflector, characterized by a peak RCS of $\sigma_{\text{tri}} = \frac{4\pi a^4}{3\lambda^2}$, where a is the leg length of the trihedral. The overall gain of the radar system can be obtained by measuring the energy of the point target of known RCS.

2.1.2 SAR images

The SAR is a coherent instrument, meaning that it records both the amplitude and the phase of the received signal. The SAR image is hence a 2D matrix composed of complex values, usually known as *single look complex* (SLC). For each resolution cell the total scattered field is the coherent sum of the contributions given by each elementary scatterer:

$$Ae^{j\varphi} = \sum_{k=1}^{N} A_k e^{j\varphi_k} \tag{2.12}$$

where A and φ represent the amplitude and the phase of a certain resolution cell (approximated by a pixel), A_k and φ_k are the amplitude and the phase of the individual elementary scatterers while N is the total number of elementary scatterers in the resolution cell.

The amplitude A is strictly related to the RCS in case of point targets. In case of distributed targets the N scatterers are randomly positioned within the resolution cell and their phase φ_k (which depends on the distance between the radar and the target) will be randomly distributed. Given the coherent sum, the amplitude A and phase φ will also feature a certain randomness which manifests itself as a

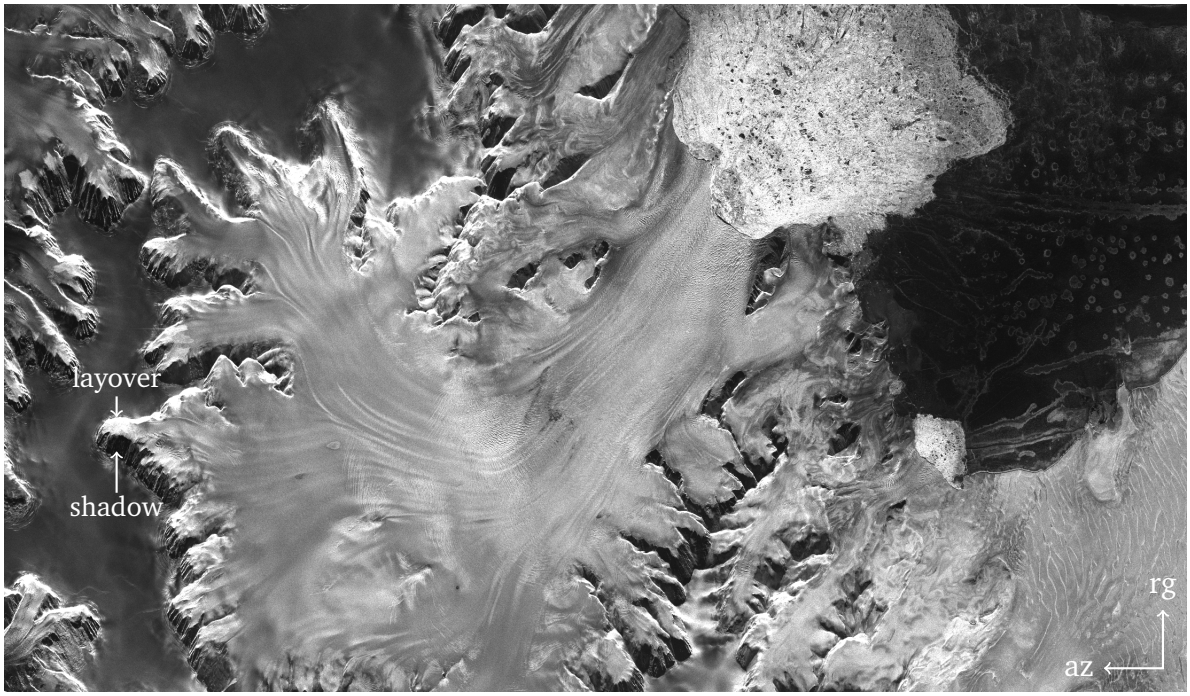

Figure 2.2 – Uncalibrated TerraSAR-X SSC amplitude image in radar geometry of the Drygalski Glacier (Antarctic Peninsula) acquired on 01.04.2008 in ascending right looking Stripmap mode (beam 10). Typical SAR effects of shadowing, foreshortening and layover are visible.

fast variability between neighbouring pixels, creating an effect known as *speckle*. Speckle is typical of coherent imaging operating at wavelengths smaller than the spatial resolution.

For a distributed target featuring a large number N of elementary scatterers the central limit theorem can be applied, according to which the recorded complex signal will have a real (in-phase) component $A\cos\varphi$ and an imaginary (quadrature) component $A\sin\varphi$ which are zero-mean, independent and identically Gaussian distributed. The corresponding SAR image will have an amplitude A featuring a Rayleigh distribution and a phase φ with uniform distribution over $[-\pi;\pi[$. The intensity or power image is obtained as $I = A^2$ and has a negative exponential distribution with equal standard deviation and mean.

Speckle is stable given the same acquisition and target configuration. This property is exploited in speckle tracking, where the movement of smooth slow glacier surface is estimated by means of coherent or incoherent cross-correlation. In fact within short observation periods the speckle pattern of the glacier surface remains stable displaying only very small shifts which allow retrieving a good level of coherence from a repeat pass image pair.

Nevertheless speckle is a multiplicative noise and can be limiting for certain applications, particularly when σ^0 must be estimated precisely. A common practice to reduce speckle consists in applying an averaging known as *multilooking*, at the cost of spatial resolution. It can be applied as spatial averaging of adjacent pixels or by splitting the synthetic aperture in segments (looks), generating separate images and averaging them into an L-look image. Averaging with L looks reduces the standard deviation by a factor $\sqrt{L}$ (Goodman, 1976). Since adjacent pixels are partially correlated the effective or equivalent number of looks L will be smaller than the number of averaged pixels N (nominal looks), their relationship is given by (Zebker *et al.*, 1994):

$$L = \frac{\delta_{\mathrm{rg}}\delta_{\mathrm{az}}}{\rho_{\mathrm{rg}}\rho_{\mathrm{az}}}N \tag{2.13}$$

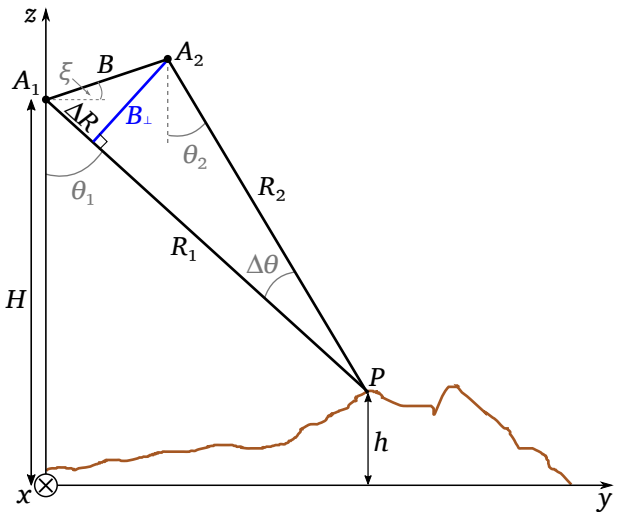

Figure 2.3 – InSAR acquisition geometry.

2.2 SAR interferometry

SAR interferometry (InSAR) includes all methods exploiting the phase of two or more complex-valued SAR images in order to derive additional information about a scene. The two images can be acquired in two ways: in *repeat-pass* the same antenna acquires the scene at different times; in *single-pass* two antennas are used, they can both transmit and receive independently within a short time (*monostatic*) or one can transmit and both receive (*bistatic*). In *across-track interferometry* the across-track separation (baseline) in the acquisition geometry of two images is exploited to retrieve a digital elevation model (DEM) (Zebker & Goldstein, 1986; Bamler & Hartl, 1998; Rosen *et al.*, 2000). Surface deformation in the line of sight can be retrieved through differential interferometry (D-InSAR). More advanced techniques based on stacking of many images allow extracting non-linear subsidence rates through permanent scatterer interferometry (PSI) (Ferretti *et al.*, 2000). In *along-track interferometry* (ATI) the along-track separation between the sensors flying on the same path is exploited to measure movement in the radar line of sight such as ocean currents (Goldstein & Zebker, 1987) and moving targets (Raney, 1971). This section focuses on across-track interferometry, with particular focus on the bistatic configuration, the one adopted to generate the SRTM and TanDEM-X DEMs used in this work.

2.2.1 Interferometric phase

The across-track acquisition geometry is depicted in Figure 2.3. The two antennas are separated by a baseline B, its perpendicular component, called effective baseline $B_\perp$, defines the sensitivity to height.

Following largely the notation of Bamler & Hartl (1998), let the single complex-valued SAR image be $u_i = |u_i| e^{j\phi_i}$, where $|u_i|$ is the amplitude, ϕ_i is the phase and the subscript i indicates the master ($i = 1$) or the slave channel ($i = 2$). The observed phase of a point scatterer is:

$$\phi_i = -\frac{2\pi R_{\text{tot},i}}{\lambda} + \phi_{\text{scat},i} + \phi_{N,i} \tag{2.14}$$

where λ is the radar wavelength, $R_{\text{tot},i}$ is the sum of the transmission and reception range distance (for a bistatic system $R_{\text{tot},1} = 2R_1$ and $R_{\text{tot},2} = R_1 + R_2$, for a monostatic system $R_{\text{tot},1} = 2R_1$ and $R_{\text{tot},2} = 2R_2$), $\phi_{\text{scat},i}$ is the *scattering phase* and $\phi_{N,i}$ is the noise phase. After coregistration of the two images the *interferogram* is formed by:

$$v = u_1 u_2^* = |u_1|\,|u_2|\, e^{j(\phi_1 - \phi_2)} = |u_1|\,|u_2|\, e^{j\phi} \tag{2.15}$$

where * indicates the complex conjugate operator. Assuming constant scattering phases due to the

small look angle difference, the *interferometric phase* $\phi = \phi_1 - \phi_2$ of a bistatic configuration becomes:

$$\phi = \frac{2\pi\Delta R}{\lambda} + \phi_N = \phi_T + \phi_N \tag{2.16}$$

with $\Delta R = R_2 - R_1$, ϕ_T is called *topographic phase* and the expression reported above must be doubled for a monostatic system. ϕ_N is an additive phase noise term assuming values in the range $[-\pi; \pi[$ (Just & Bamler, 1994). ϕ is the non-ambiguous absolute interferometric phase, which describes the slant range phase difference with accuracy of a fraction of a wavelength. Unfortunately given its nature only its modulo 2π principal value can be measured (i.e. in the interval $[-\pi; \pi[$). This is called *measured*, *observed* or *wrapped phase* ψ, which is ambiguous (its image displays the so-called *fringe* pattern). It can be hence defined as $\psi = W\{\phi\}$, where $W\{\cdot\}$ is an operator wrapping the phase in the range $[-\pi; \pi[$. To retrieve the absolute topographic phase, in a first step the relative phase between pixels are determined through a *phase unwrapping* procedure. This, when successful, allows to estimate the unwrapped phase:

$$\phi_{\text{unw}} = \psi + 2\pi k \tag{2.17}$$

where k is a spatially variable integer. Since the phase unwrapping algorithm determines k for the whole interferogram starting from a reference point to which it assigns $k = 0$, ϕ_{unw} is not yet absolute, a residual called *absolute phase offset* ϕ_{off} is missing to retrieve the absolute topographic phase:

$$\phi = \phi_{\text{unw}} + \phi_{\text{off}} = \phi_{\text{unw}} + 2\pi q + \phi_N \tag{2.18}$$

where q is an integer constant over the whole interferogram in the absence of phase unwrapping errors.

The phase unwrapping procedure is not trivial and will not be explained here, many different procedures have been developed as summarized in Bamler & Hartl (1998). A common approach is the Minimum Cost Flow (Costantini, 1998). A dual baseline phase unwrapping approach for the TanDEM-X mission is described in detail in Lachaise (2015), which also provides an up-to-date review of the state of the art. The absolute phase offset determination often relied on external height information sources, for the TanDEM-X mission a method not requiring any external a priori height information is used and described in Rossi *et al.* (2012).

The phase trend in range due to the flat earth is usually subtracted from the interferogram before further processing. The *height sensitivity* can be derived from the previous equations and for a bistatic system is equal to:

$$\frac{\delta\phi}{\delta h} = \frac{2\pi}{\lambda}\frac{B_\perp}{R_1 \sin\theta_1} = \frac{2\pi}{h_{\text{amb}}} \tag{2.19}$$

a monostatic system has double the sensitivity. The height of ambiguity h_{amb} is defined as the height resulting from a phase change of one fringe ($\delta\phi = 2\pi$), in other words one ambiguity cycle:

$$h_{\text{amb}} = \frac{\lambda R_1 \sin\theta_1}{B_\perp} \tag{2.20}$$

A larger baseline leads to fast phase variations hence higher precision but also higher unwrapping difficulty, smaller baseline leads to higher level of noise in the DEM but easier unwrapping.

2.2.2 Coherence

The *complex correlation coefficient* or *complex coherence* quantifies the similarity of the two SAR images and is given by (Bamler & Hartl, 1998):

$$\gamma = \frac{\mathrm{E}\{u_1 u_2^*\}}{\sqrt{\mathrm{E}\{|u_1|^2\} \cdot \mathrm{E}\{|u_2|^2\}}} = \frac{\mathrm{E}\{v\}}{\bar{I}} = |\gamma| \exp(j\phi_0) \tag{2.21}$$

where $\bar{I} = \sqrt{\mathrm{E}\{|u_1|^2\} \cdot \mathrm{E}\{|u_2|^2\}}$ is the geometric mean of the expectations of the two pixel intensities. The phase of γ is the expected interferometric phase ϕ_0 of the specific pixel and its amplitude $|\gamma|$, the *interferometric coherence*, is related to the phase noise term ϕ_N and quantifies disturbances. This

parameter varies between $|\gamma| = 1$ meaning total correlation and $|\gamma| = 0$ meaning total decorrelation of the two signals. There are different sources of signal decorrelation summarized by the following equation (Zebker & Villasenor, 1992; Just & Bamler, 1994):

$$|\gamma| = \gamma_{\text{thermal}} \cdot \gamma_{\text{geom}} \cdot \gamma_{\text{doppl}} \cdot \gamma_{\text{vol}} \cdot \gamma_{\text{temp}} \cdot \gamma_{\text{proc}} \tag{2.22}$$

- γ_{thermal} accounts for the thermal noise in the receiver affecting independently the master and the slave signals and hence not correlating. It is strictly related to the signal to noise ratio (SNR).
- γ_{geom} accounts for baseline and geometric decorrelation for flat surfaces due the spectral misalignment caused by different look angles. Decorrelation increases with baseline, reaching total decorrelation for a *critical baseline*. It can be reduced applying spectral shift filtering (Gatelli *et al.*, 1994).
- γ_{doppl} is caused by differences in the Doppler centroids of the two acquisitions.
- γ_{vol} is the volume decorrelation caused by different interactions within the scattering medium caused by distribution, orientation and material of the scatterers due to the different incidence angles. This term is particularly relevant for dry snow, forests and deserts.
- γ_{temp} is the temporal decorrelation due to temporal changes in the target properties and configuration, it is particularly critical for repeat-pass interferometry.
- γ_{proc} includes all decorrelation contributions due to the processing, particularly relevant is decorrelation arising from inaccurate coregistration of the two images.

In practice coherence is estimated by spatially averaging the considered pixel and its neighbours. The operation can be critical since enough pixels (looks) must be used in order to have a robust estimate but at the same time the spatial stationarity and ergodicity properties within the estimation window must not be be lost. Properties of the signal and the imaging system lead to a biased estimation of $|\gamma|$ particularly at lower $|\gamma|$ values and with small number of looks (Zebker & Chen, 2005; Touzi *et al.*, 1999).

2.2.3 Interferometric phase statistics

As reported in Section 2.1.2, many scatterers contribute coherently to the response of a resolution cell. A *distributed*, *Gaussian* or *Rayleigh scatterer* is composed of a sufficiently high number of random subscatterers of which no one dominates: the central theory limit can be applied allowing to model the pixel as a *zero-mean complex circular Gaussian* random variable (Goodman, 1963; Bamler & Hartl, 1998). For low and medium resolution SAR the assumption of Gaussian scattering holds for natural surfaces such as soil, forest, rocks, agricultural fields, glacier ice, snow and rough water. It does not necessarily hold for high resolution SAR systems and when few scatterers dominate, for instance for man-made objects and urban areas.

For distributed targets the processes u_1 and u_2 can be assumed to be jointly circular Gaussian, their joint probability density function (pdf) is (Just & Bamler, 1994; Lee *et al.*, 1994; Bamler & Hartl, 1998):

$$p(\mathbf{w}) = \frac{1}{\pi^2 |\mathbf{C}|} \exp\left\{-\mathbf{w}^{*T} \mathbf{C}^{-1} \mathbf{w}\right\} \tag{2.23}$$

where $\mathbf{w} = (u_1, u_2)^T$ and $|\mathbf{C}|$ is the determinant of the complex covariance matrix:

$$\mathbf{C} = \mathrm{E}\left\{\mathbf{w}\mathbf{w}^{*T}\right\} = \begin{pmatrix} \overline{I_1} & \gamma \bar{I} \\ \gamma^* \bar{I} & \overline{I_2} \end{pmatrix} \tag{2.24}$$

with $\bar{I} = \sqrt{\overline{I_1} + \overline{I_2}} = \sqrt{\mathrm{E}\{I_1\} + \mathrm{E}\{I_2\}} = \sqrt{\mathrm{E}\left\{|u_1|^2\right\} \cdot \mathrm{E}\left\{|u_2|^2\right\}}$.

The marginal probability density function of the interferometric phase ϕ can be derived from Eq. (2.23) and written as (Just & Bamler, 1994; Bamler & Hartl, 1998):

$$p(\phi) = \frac{1-|\gamma|^2}{2\pi} \frac{1}{1-|\gamma|^2 \cos^2(\phi-\phi_0)} \cdot \left\{ 1 + \frac{|\gamma| \cos(\phi-\phi_0) \arccos[-|\gamma| \cos(\phi-\phi_0)]}{\left[1-|\gamma|^2 \cos^2(\phi-\phi_0)\right]^{1/2}} \right\} \tag{2.25}$$

The two parameters characterizing the pdf are the noise-free phase ϕ_0 used for topographic reconstruction and the interferometric coherence $|\gamma|$ describing the phase noise. The support of the phase pdf is ambiguous, it is hence often referenced to the base interval $[\phi_0-\pi; \phi_0+\pi[$. By doing so and assuming ergodicity, the expectation and variance of the interferometric phase become (Just & Bamler, 1994; Bamler & Hartl, 1998):

$$\mathrm{E}\{\phi\} = \phi_0 = \arg\{\gamma\} \tag{2.26}$$

$$\sigma_\phi^2 = \mathrm{E}\left\{(\phi-\phi_0)^2\right\} = \int_{\phi_0-\pi}^{\phi_0+\pi} (\phi-\phi_0)^2 p(\phi)\, d\phi = \int_{-\pi}^{+\pi} \phi^2 p(\phi+\phi_0)\, d\phi \tag{2.27}$$

It follows from Eq. (2.25) that $p(\phi+\phi_0)$ is independent of ϕ_0. The pdf is uniform $p(\phi) = 1/(2\pi)$ for completely decorrelated signals (coherence $|\gamma| = 0$) and approaches a Dirac's delta for complete correlation ($|\gamma| = 1$).

Multilooking is usually applied to reduce noise and statistical variation, in this case the pdf $p(\phi)$ depends also on the number of independent looks L used, its shape becoming narrower as L increases. The expression is not reported here, it can be found in Eq. (18) of Lee *et al.* (1994).

The phase standard deviation σ_ϕ (or phase error) is an important parameter in InSAR since it defines the interferometric accuracy and consequently the height accuracy. σ_ϕ decreases with increasing interferometric coherence $|\gamma|$ and with increasing number of independent looks L, approaching the Cramer Rao Lower Bound (CRLB):

$$\sigma_{\phi,\mathrm{CRLB}} = \sqrt{\frac{1-|\gamma|^2}{2|\gamma|^2 L}} \tag{2.28}$$

By exploiting the height sensitivity in Eq. (2.19) the interferometric error for a pixel $\sigma_\phi(x,y)$ can be converted into a height error which for bistatic systems is equal to:

$$\varepsilon_h(x,y) = \sigma_\phi(x,y) \frac{|h_{\mathrm{amb}}|}{2\pi} \tag{2.29}$$

This error is annotated in the so-called height error map (HEM) usually provided along the digital elevation model (DEM).

Chapter 3

Glaciology basics

This chapter provides an overview of some glaciology basics useful to the microwave remote sensing of the cryosphere. The first three sections start by introducing the parameters describing a snowpack (Section 3.1), and its surface, from a small to a large scale (Section 3.2). The focus is then shifted to glaciers, their different zones are described as well as the transformation from fresh snow to glacier ice (Section 3.3). The movement of a glacier and the concept of grounding line are shortly presented in Section 3.4. Finally the glacier mass balance, its parameters and the methods used to derive it are described in Section 3.5.

3.1 Physical properties of snow

Snow is a two or three phase mixture of ice crystals, air and liquid water. A fundamental parameter describing a snowpack is its *density* ρ_s which generally lies between 200 and 600 $\mathrm{kg\,m^{-3}}$. Fresh (or new) snow has a density ranging from 50 to 100 $\mathrm{kg\,m^{-3}}$, increasing to 200 $\mathrm{kg\,m^{-3}}$ when damp. Snow density increases with time, for settled snow ρ_s ranges between 200 and 300 $\mathrm{kg\,m^{-3}}$ (Cuffey & Paterson, 2010). The main parameter describing the internal structure of the snowpack is the *grain size*, usually defined as the mean radius of the ice crystals. Typically grain size ranges from 0.1 to 3 mm, with values as low as 0.01 mm for fresh snow. The *porosity* of snow is the fraction of the total volume occupied by air (Rees, 2005).

When the snowpack temperature is below 0°C it does not contain water in liquid form, this condition is defined *dry snow*. If temperatures are at or above 0°C the snowpack incorporates liquid water. This is quantified by the *volumetric liquid water content* (LWC) which is the volume fraction of liquid water in the snowpack (V_w), sometimes expressed as volume percentage (cf. Section 4.3). Volumetric liquid water content m_v can range from 0 to 10%. A unit volume of wet snow contains a mass $V_w\rho_w$ of liquid water and a mass $\rho_s - V_w\rho_w$ of ice, where ρ_w is the density of water (Rees, 2005).

The total amount of water contained in a snowpack is quantified by the *snow water equivalent* (SWE), which is defined as the depth of the water that would be produced if all the ice in the snowpack were melted. It hence measures the mass of water contained per unit area in the snowpack and is computed as:

$$\mathrm{SWE} = \frac{1}{\rho_w}\int_0^d \rho_s dz \tag{3.1}$$

where z represents the vertical direction and d is the total depth of the snowpack (Rees, 2005). If the density is constant it simplifies to:

$$\mathrm{SWE} = \frac{\rho_s}{\rho_w} d \tag{3.2}$$

The electromagnetic properties of snow in the microwave region are described in detail in Chapter 4.

3.2 Surface characteristics

The surface of glaciers presents a vast variability of features and structures. For instance smooth surface is generally found on the accumulation area covered in newer snow and firn. On the ablation area, particularly where ice flows on steeper slopes, crevasses are a generally found. The geometry of the surface is particularly important for microwave remote sensing of the cryosphere as it plays a fundamental role in the electromagnetic interaction mechanism between signal and target and hence on the backscattering coefficient. In this regard the short scale surface properties (compared to the wavelength) are more relevant and are referred to as *surface roughness*. At larger scales the surface is characterized by its *topography*. The surface roughness is measured by the *root mean square (RMS) height deviation* σ_h (Rees, 2005):

$$\sigma_h^2 = \mathrm{E}\left\{[h(x,y) - \mathrm{E}\{h(x,y)\}]^2\right\} = \mathrm{E}\left\{[h(x,y)]^2\right\} - \mathrm{E}\{h(x,y)\}^2 \tag{3.3}$$

where $\mathrm{E}\{\bullet\}$ is the expected value, $h(x,y)$ is the snow surface height at the position (x,y). Typical values of σ_h measured on spatial scales of tens of centimetres to a meter range from 0.3 mm to 3 cm (Rott & Davis, 1993; Rott, 1984; Floricioiu & Rott, 2001; Rees, 2005; Cuffey & Paterson, 2010).

The horizontal scale of the surface variation is usually measured through the *autocorrelation function* (ACF), for a one-dimensional surface profile it is given by (Rees, 2005):

$$\rho_{\mathrm{surf}}(\xi) = \frac{1}{\sigma_h^2}\mathrm{E}\{[h(x+\xi) - \mathrm{E}\{h(x)\}][h(x) - \mathrm{E}\{h(x)\}]\} \tag{3.4}$$

where σ_h is the RMS height deviation of the surface height profile. The ACF is a measure of similarity between height on the profile points x and $x+\xi$. The ACF is usually modelled as a negative exponential or a Gaussian function. The 2-D ACF or more 1-D ACF on different directions can be used to detect anisotropies. The surface *correlation length* l_c is defined as the displacement ξ for which $\rho_{\mathrm{surf}}(\xi) = 1/e$ and defines the scale of the variation of the surface height. At distances greater than l_c, heights can be considered approximately statistically independent. Typical values range between 3 cm and 30 cm (Rott & Davis, 1993; Rott, 1984; Floricioiu & Rott, 2001; Rees, 2005).

The *slope* of a surface is another important topographic property (for all kinds of terrain). Its two dimensional vector is:

$$\mathbf{s} = \left(\frac{\partial h(x,y)}{\partial x}, \frac{\partial h(x,y)}{\partial y}\right)^{\mathrm{T}} \tag{3.5}$$

Often the term *slope* refers to the magnitude s of the vector $\mathbf{s}$ and the term *aspect* to its direction. Another useful way of characterizing the surface is through the *semivariogram*. This is defined in one dimension as:

$$\gamma(\xi) = \frac{1}{2}\mathrm{E}\left\{(h(x+\xi) - h(x))^2\right\} \tag{3.6}$$

and contains information about both the horizontal and vertical scale of surface variation. Where the ACF can be defined, it relates to the semivariogram according to:

$$\gamma(\xi) = \sigma_h^2(1 - \rho_{\mathrm{surf}}(\xi)) \tag{3.7}$$

Semivariograms are used in this study to measure correlation distances of DEM differences, their theory is described in detail in Section 9.1.1.2.

3.3 Glacier zones

A glacier is broadly defined as any ice body generated through the accumulation of snowfall. Among these are mountain glaciers and icefields, ice caps, continental ice sheets and floating ice shelves (Cuffey & Paterson, 2010). The ice mass constituting the glacier usually moves forward, mainly because of gravity. The surface of a glacier can be divided into different *zones*, or *facies*, which are illustrated in Figure 3.1. Zones do not typically show an abrupt transition and are categorized as follows (Cuffey & Paterson, 2010).

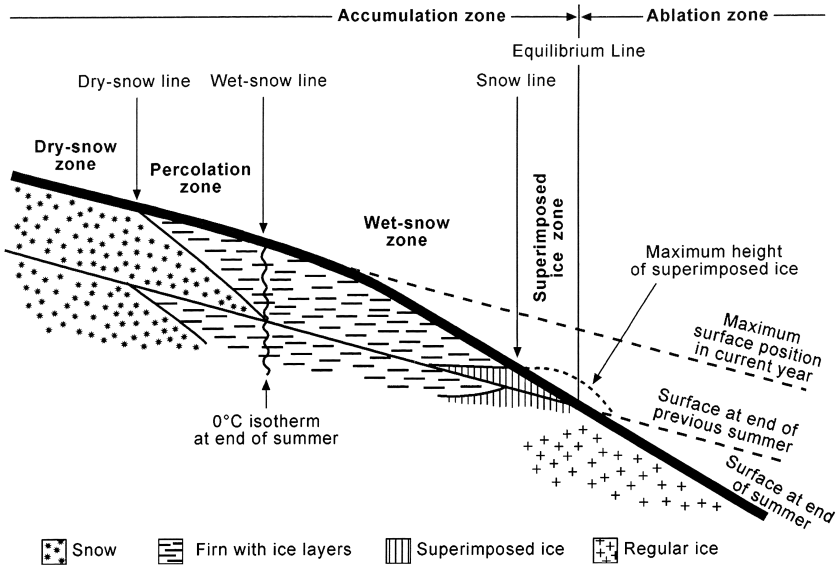

Figure 3.1 – Glacier zones. From Cuffey & Paterson (2010).

- *Dry snow zone*: where no melting occurs throughout the year, typically found only in the interior of Greenland and Antarctica (or on the highest mountain glaciers). The snowpack has low densities and small grain sizes.

- *Percolation zone*: localized melting occurs during summer with water percolating a certain distance into the snow and firn at temperatures below 0°C before refreezing. It may encounter impermeable layers and spread horizontally. This process forms subsurface *ice lenses* and *ice layers*. The vertical water channels also refreeze forming pipe-like structures known as *ice glands*. This zone is separated from the upper zone by the *dry snow line*.

- *Wet snow zone*: in summer it is subject to enough melt to saturate the entire snowpack with water, which might percolate into deeper layers deposited in previous years. Inclusions such as ice pipes and layers form. This zone is separated from the upper zone by the *wet snow line*.

- *Superimposed ice zone*: it occurs at lower elevations where considerable meltwater is produced on relatively flat areas where it refreezes forming a continuous thick ice layer, which might emerge from beneath the snow and firn and become exposed. Many superimposed layers with varying characteristics may form in different seasons. This zone is separated from the previous by the *snow line* (or the *firn line*).

- *Ablation zone*: the snow cover completely melts at the end of the summer leaving exposed underlying ice and forming ponds of water.

The lower boundary of the superimposed ice zone is called *equilibrium line*, above it is the *accumulation area*, where glacier has a net mass gain over the year, below it is the *ablation area*, where the glacier has a net mass loss over the year. The *equilibrium line altitude* (ELA) is the altitude of the equilibrium line spatially averaged over the entire glacier. The *snow line altitude* (SLA) is equivalently defined. The *accumulation area ratio* (AAR) is the ratio of accumulation area and total area of the glacier.

Not all the zones are always present. Only the coldest glaciers have a dry snow zone, in fact the whole sequence can be found in parts of Greenland and Antarctica. Antarctic ice shelves have only dry snow and percolation zones, hence all mass loss is due to calving and melting at the base. In *temperate glaciers* ice is at melting point throughout the year except on the surface layer (∼10 m) where it can fall below 0°C for parts of the year. In temperate glaciers the superimposed ice is usually limited or non existent, hence equilibrium line and snowline coincide in average (Cuffey & Paterson, 2010).

3.3.1 Snow to ice transformation and density variation with depth

Snow transforms into ice through different mechanisms. When snow is dry the sintering process is the dominant metamorphism mechanism at first: pressure and temperature tend to increase with depth causing particles to bond and grow larger, at the same time air space between them is reduced and density increases. Different processes prevail as density increases with depth. In the initial phases *settling* dominates: particles slide past one another, particularly as they get rounder, in fact changes of crystal size and shape also occur in the first stages. In a subsequent phase (with density of ~400 $\mathrm{kg\,m^{-3}}$) particles start to form bonds, particularly by sublimation. *Firn* starts to form at this point, it is still porous since it contains interconnected air channels. As the density increases porosity is reduced and the processes of recrystallization and deformation ("creep") dominate: both due to molecular diffusion and ice flow (where present, flow causes deformations due to stretching and compression, accelerating the densification). Once density reaches about 830 $\mathrm{kg\,m^{-3}}$ the air spaces between the grains close off completely, glacier ice is thus created in which air bubbles are still trapped. Glacier ice can reach a density up to 917 $\mathrm{kg\,m^{-3}}$. Grain size generally increase with depth, from 0.5 to 1 mm near the surface to a few millimetres at greater depths (Rees, 2005; Cuffey & Paterson, 2010).

A different transformation process of dry snow generates large faceted crystals in the shape of prisms and pyramids. This is the most coarse-grained firn and is called *hoar*. It forms by a combination of sublimation and vapour deposition in unconsolidated snow when a large temperature gradient exists. The average grain size of hoar layers (they can be in depth or on surface) ranges from 2 to 5 mm, with low density (100 to 300 $\mathrm{kg\,m^{-3}}$) and high porosity.

The presence of meltwater in the snowpack introduces additional transformation mechanisms. At the first stages melting accelerates the rounding of ice crystals and their movement (through lubrication) favouring the grain packing process, which can lead to a higher density compared to dry snow. Refreezing of meltwater accelerates the subsequent stages of transformation. Air spaces are rapidly filled this way. Refreezing rapidly produces ice layers and lenses. A superimposed ice zone represents the extreme case in which snow transforms into ice in a single summer. Melting and refreezing reduce the density of firn causing a certain reduction of the surface elevation (Cuffey & Paterson, 2010).

3.4 Glacier flow

A glacier can be broadly thought as a river of ice moving slowly downslope under the pull of gravity. The accumulation area presents a surplus of ice which is compensated by outflow to the ablation area, where it is then lost mainly through melting and calving. This transfer of ice should theoretically lead to a steady-state glacier profile: the *balance flux*. The corresponding velocity is the *balance velocity* and depends on mass balance and glacier geometry. Glacier flow responds with delay to fluctuations in mass balance, with response time depending on glacier type and size, meaning that measured velocities can be much lower or higher than balance velocities (Jiskoot, 2011). The velocity of glaciers depends on several factors, among which:

- ice geometry (thickness, surface slope),
- ice physical properties (temperature, impurities, density),
- shape of the valley (or lack of lateral walls for instance on ice sheets),
- conditions of the bed (frozen or thawed, hard bedrock or soft substrate, subglacial drainage),
- amount of floating ice at the terminus (for floating tongues or ice shelves)
- surface mass balance.

Most glaciers display seasonal velocity fluctuations, with faster flow in the early melt season. Some glaciers have quasi-periodic short surges of velocity (10 - 1000 times faster) interleaving longer periods of slower velocity (Jiskoot, 2011).

In response to the gravitational driving stress, glaciers move due to three possible independent flow mechanisms: (1) internal deformation (creep), (2) basal sliding, and (3) soft bed deformation. Internal deformation happens on all glaciers due to the fact that ice is polycrystalline and behaves like a visco-plastic material particularly in the lower layer where pressure is higher. When larger stresses are applied rapidly, ice can break in a brittle fashion opening *crevasses* in the upper layer.

Basal sliding is the mechanisms where the glacier slides on the underlying bed lubricated by the presence of water. This forms because ice melts at very high pressure. The mechanism is enhanced on rough glacier beds, as ice melts on the upstream side of bumps and freezes on their leeside (regelation), furthermore if the water pressure is high enough cavities can form on the leeside of obstacles leading to bed separation and drastically reducing friction. Basal sliding dominates in temperate and in polythermal glaciers.

Soft bed deformation happens when the bed features a layer of subglacial till: a mixture of unconsolidated sediments ranging in size from boulders to clay. The thickness of this layer ranges between 1 and 20 m. The finer sediments are not cohesive and almost frictionless, when filled with water at high pressure they deform under the gravitational driving stress (Jiskoot, 2011).

The mechanisms of sliding and bed deformation (together defining basal motion), where present, can contribute to more than 50% of the measured surface velocity of a glacier. Where internal deformation dominates, velocity decreases as a fourth order polynomial with depth, reaching almost zero at the base. For this type of glacier the transverse velocity profile has a parabolic shape, with higher velocity at the centre and lower velocity at the sides. Where basal motion prevails the transverse velocity profile is more flat, plug-like in extreme cases. Plug flow is common in tidewater and surging glaciers (Jiskoot, 2011).

Gravity pulls a glacier vertically causing a primarily horizontal flow because it generates a vertical pressure gradient in the glacier and, in some cases, because the glacier rests on a sloping bed. The gravitational driving stress τ_d depends on the gravitational acceleration g, the average ice density ρ_i, the ice thickness H and the surface slope α_s, according to:

$$\tau_d \approx \rho_i g H \alpha_s \tag{3.8}$$

for slopes below 20°, which is true for most of the glaciers (Cuffey & Paterson, 2010). This means that glaciers flow even on beds with slopes oriented in the direction opposite to the flow. Changes in surface mass balance can affect the thickness and surface slope influencing glacier flow. The gravitational driving stress is balanced by resistive stresses: the main component is the basal shear stress τ_b (basal drag), in absence of other resistive stresses it holds that

$$\tau_b \approx f \tau_d \tag{3.9}$$

where f is a dimensionless shape factor related to the glacier profile and valley shape (assumes values between 0 and 1 but ranges between 0.7 and 0.9 for valley glaciers). τ_b is ~100 kPa for valley glaciers and ~10 kPa for ice streams (Cuffey & Paterson, 2010).

Strain is the deformation in response to a stress (Van der Veen, 2013). The ice deformation rate (or shear strain rate) under a constant shear stress τ is high at the application point and it decreases to a constant value with distance (secondary strain rate $\dot{\varepsilon}$). The relationship between shear stress and secondary strain rate is expressed by the empirical *Glen's flow law*:

$$\dot{\varepsilon} = A\tau^n \tag{3.10}$$

where A is the ice softness parameter depending on ice temperature, crystal orientation, debris content and other factors, n is a constant depending on the applied stress ($n \sim 3$ for temperate glaciers).

Another resistive stress is the lateral drag τ_s at the valley walls or at the shear margins of ice streams. Its contribution to the resisting stress can range significantly according to the geometry of the glacier (Cuffey & Paterson, 2010).

Gradients of longitudinal stress τ_l may also act on the glacier, when present, they enhance or resist the basal shear stress, making Eq. (3.9) invalid. Ice acceleration creates extensional (tensile) stresses and deceleration creates compressional stresses (Jiskoot, 2011). Faster flow occurs over bumps on the

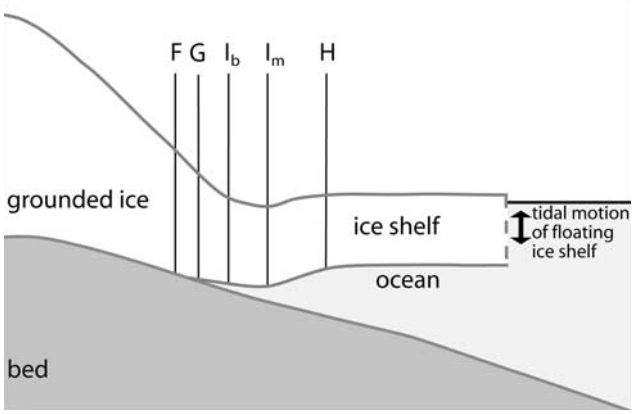

Figure 3.2 – Schematic representation of a grounding zone of an ice shelf. F: landward limit of tidal ice flexture , G: grounding line, I_b: break-in slope, I_m: local elevation minimum, H: seaward limit of ice flexture. From Fricker *et al.* (2009).

bed where ice is thinner, hence surface slope and driving stresses are higher, while slower flow occurs over bed depressions where ice is thicker. Thus on a mountain glacier long-wavelength variations of surface slope reflect variations of the bed slope. Differences in basal motion can also cause variations of velocity along a flow line.

Crevasses are fractures which open in the direction of maximum tension. In an idealized valley glacier the accumulation area is dominated by tensile stresses causing concave transverse crevasses to open and ice to thin. Downstream the flow lines tend to converge as the valley narrows, here the shear stress against the valley walls may cause marginal crevasses to open. In the ablation area compressive stress prevails causing ice thickening but lateral expansion may also be present at the terminus, inclined crevasses are hence formed. After formation crevasses are displaced, bent and rotated by the ice flow.

Other phenomena can nevertheless complicate such a scenario, particularly for calving and especially tidewater glaciers. In tidewater glaciers even small changes in mass balance can lead to very large self-sustaining retreat because of feedback processes regarding the balance of forces, the flow and the calving (Cuffey & Paterson, 2010). A phenomenon which is not yet completely understood is *dynamic thinning*. It consists in a strong and rapid thinning signal interesting the lower part of calving glaciers, often tidewater ones. The increased calving, possibly caused by increased water temperature, when not compensated by increased accumulation causes the glacier flow to accelerate and hence to thin, the strong longitudinal extension favours in turn fracturing which sustains large calving rates. Strong dynamic thinning with an accelerating trend was measured on the outlet glaciers of Greenland and Antarctica by Pritchard *et al.* (2009) between 2003 and 2007.

Dynamic thinning is often associated with retreat of the grounding line, which in turn reduces the resisting force from basal and side drags. The *grounding line* (GL), is the position where the glacier detaches from the ground (G in Figure 3.2). The ice thickness at the grounding line changes with its position influencing the ice flux through the gate: a fundamental parameter for the computation of the mass balance with the input-output method (cf. Section 3.5). The grounding line position is particularly important for the outlet glaciers of Antarctica terminating into ice shelves, where it influences ice sheet - ocean interactions. Particularly when ice shelves are present, a grounding zone, often more kilometres wide is usually defined between the point where ice starts to flex in response to tidal movements and the point where ice is floating freely (F and H in Figure 3.2, respectively). The grounding line is not directly observable and satellite data are used to derive its position through proxies using different techniques. Optical data are used to map the slope break (I_b), while D-InSAR maps the upper limit of the tidal flexure (F) (Rignot *et al.*, 2011b). Repeat track laser altimetry can detect H and F, from single profiles I_m and I_b can be determined (Fricker *et al.*, 2009; Bindschadler *et al.*, 2011).

3.5 Glacier mass balance

The mass of ice of an entire glacier can change through processes which transfer mass between the glacier and its surrounding or between ice and water within the glacier. The common mass exchanges are snowfall, avalanche deposition, melt, refreezing of water, sublimation, wind deposition and calving. *Calving* is the separation of ice blocks at the margins and occurs mostly at the front terminating in water, but can also have the form of ice avalanches on mountain slopes. The rates of these processes, summed over the glacier and over time, determine the glacier mass balance, which is the change in the total mass of ice (Cuffey & Paterson, 2010). The mass balance also depends on ice flow, directly, since it determines the calving rate and indirectly because it causes mass exchanges within the basin.

The *specific mass balance* (denoted with b) represents change of mass per unit of area in $\left[\mathrm{kg\,m^{-2}}\right]$ over a generic time period. It is traditionally computed over one hydrological year and denoted as *annual* (or *net) mass balance* (b_n). If this is not the case, it is conventionally expressed a as a *specific mass balance rate* $\dot{b}$, often expressed on a yearly basis in $\left[\mathrm{kg\,m^{-2}\,a^{-1}}\right]$. The specific mass balance at any point is given by:

$$b = b_a + b_c = \int_{t_1}^{t_2} \left(\dot{b}_a + \dot{b}_c\right) dt \tag{3.11}$$

where the subscripts a and c denote are the accumulation and ablation contributions. The first represents all processes adding mass, the second all processes removing mass. t_1 and t_2 denote the times of two successive surface elevation minima, they generally correspond to the end of the ablation season of successive years, hence including one entire hydrological cycle. The actual duration can vary from year to year, but for practical purposes the cycle is assumed to be as long as a solar year and the end of the ablation season is assumed to be on a fixed date (30 September in the Alps, 31 March in Patagonia). This convention, which is used in this work, is referred to as the *fixed-date system*, as opposed to the *stratigraphic system*, which uses the actual minima times of each year.

The surface balance of mountain glaciers often varies significantly over seasons. A typical idealized cycle over one balance year (t_1 to t_2) is shown in Figure 3.3. The mass added to the glacier surface generally increases over the winter reaching a maximum at t_m from mid-spring or early summer (defining the "end of winter"). During summer mass is lost leading to a minimum in late summer (t_2). The balance year can be divided into a winter season (t_1 to t_m) and a summer season (t_m to t_2) with their own specific mass balances b_w and b_s, hence the annual mass balance is equal to:

$$b_n = b_w + b_s \tag{3.12}$$

While the net mass balance is useful to observe long-term trends, the seasonal mass balances can give more insight on the causes of mass changes (e.g. variations in temperature or precipitation).

Another seasonal parameter is the *annual mass balance amplitude* or *turnover*. It is computed as the average of the absolute values of the two seasonal mass balances (Meier, 1984):

$$\alpha = \left(|b_w| + |b_s|\right)/2 \tag{3.13}$$

This parameter measures the flux of water through the glacier system and reflects the intensity of the hydrological cycle through that system. Large mass turnovers are typical of coastal maritime glaciers where accumulation is abundant and which often extend to lower elevation hence being subject to strong ablation as well. Glaciers located in a drier, more continental climate display lower mass turnover (Josberger *et al.*, 2007).

Integrating the specific mass balance or its rate over the total plan-view (projected on a horizontal plane) area of the glacier A gives the *glacier-wide mass balance* (sometimes defined as *cumulative* or just *glacier* mass balance) in [kg] and the *glacier-wide mass balance rate* in $\left[\mathrm{kg\,a^{-1}}\right]$ (Cuffey & Paterson, 2010):

$$B = \int_A b\,dA \;\text{ or }\; \dot{B} = \int_A \dot{b}\,dA \tag{3.14}$$

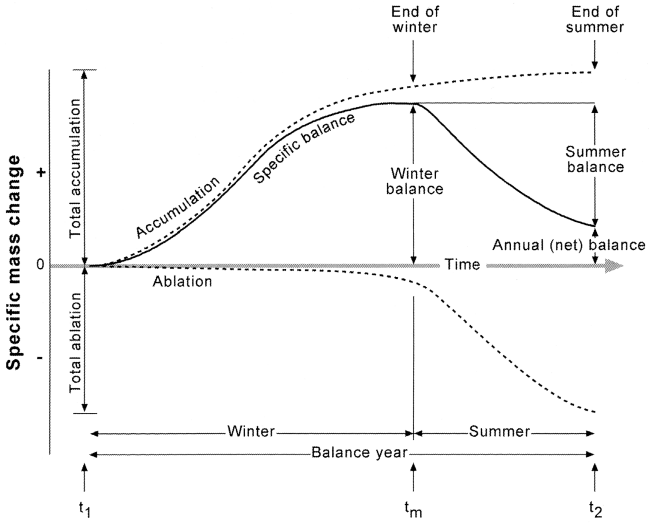

Figure 3.3 – Seasonal variation of specific mass balance over one hydrological year with accumulation and ablation contributions. From Cuffey & Paterson (2010).

The *average specific mass balance* (or its rate) is an important measure as it allows comparisons between glaciers of different sizes and is defined as:

$$\overline{b} = \frac{B}{A} \quad \text{or} \quad \overline{\dot{b}} = \frac{\dot{B}}{A} \tag{3.15}$$

The specific mass balance can be divided in its components along the vertical column as:

$$\dot{b} = \dot{b}_s + \dot{b}_e + \dot{b}_b \tag{3.16}$$

where $\dot{b}_b$ is the basal balance, $\dot{b}_e$ is the englacial (internal) balance and $\dot{b}_s$ is the surface balance. Usually this term dominates and it is assumed that $\dot{b} = \dot{b}_s$, thus the glacier mass balance rate is obtained as:

$$\dot{B} = \dot{B}_s - \dot{B}_{cv} = \int_A \dot{b}_s dA - \dot{B}_{cv} \tag{3.17}$$

where $\dot{B}_{cv}$ is the ice mass lost per unit of time by calving (or exported through the grounding line onto a floating ice shelf), which can be estimated as:

$$\dot{B}_{cv} = \rho_i \int_y v_{cv}(y) h(y) \, dy \tag{3.18}$$

where ρ_i is the ice density, y is the coordinate parallel to the calving front/grounding line, $v_{cv}(y)$ is the flow velocity normal to the calving front (an assumption is made regarding its variation with depth) and $h(y)$ is the ice thickness, both at position y.

The specific and the glacier-wide mass balances are often stated in *water equivalent* (w.e.). Often the water equivalent is used to express an (average) ice height change (ice equivalent) as the corresponding water height change, and indicated as [m w.e.]. In fact, the specific mass balance (or its average value) is almost always stated as a height change, either as ice equivalent in [m] or water equivalent in [m w.e.] (correspondingly for the rates) by dividing the value in $\left[\mathrm{kg\,m^{-2}}\right]$ by the density of ice ρ_i or the one of water ρ_w, respectively. It holds that 1 $\mathrm{kg\,m^{-2}}$ of ice is equal to 1 m w.e., the two units are hence often interchanged, but the latter is more common. Sometimes the glacier-wide mass change is stated as corresponding volume of water: 1 Gt of ice is equal to 1 $\mathrm{km^3}$ w.e. (correspondingly for the rates). To obtain the contribution to sea level change (SLC) or sea level rise (SLR), the glacier-wide mass balance in $\left[\mathrm{km^3\ w.e.}\right]$ is divided by minus the total area of the ocean of $362 \cdot 10^6$ $\mathrm{km^2}$ (correspondingly for the rates), and expressed in [mm] or [μm].

On most mountain glaciers the surface balance varies with altitude. The glacier-wide average thus depends on two important geographical variables: the variation of the specific balance with the altitude

and the distribution of glacier surface area as a function of altitude. The latter is called *area-elevation* (or *altitude*) *distribution* (AAD) or *hypsometry* and can be thought as a histogram of glacier area with respect to elevation. The behaviour of these two variables is usually represented in form of a plot. It is practice to divide the whole range of elevations of the glaciers in J bands (or elevation bins, with reference to histograms). Let b_j be the specific balance for bin j and A_j its area. The glacier-wide mass balance rate can be obtained as:

$$\dot{B} = \sum_{j=1}^{J} \dot{b}_j \cdot A_j \tag{3.19}$$

If the glacier calves, the corresponding rate $\dot{B}_{cv}$ must be subtracted from the right-hand side of the equation above.

The area and thickness of a glacier changes in time in reaction to climate and flow variations, leading to modification of the AAD. With the "traditional" glaciological method the annual glacier mass balance B_n is obtained at the end of the ablation season and the specific surface mass balance is computed punctually, the corresponding altitude (hence AAD) is obtained at the same time. According to Elsberg *et al.* (2001) this temporal correspondence defines the "conventional balance" which represents the actual change of a glacier over some specified time interval (not necessarily 1 year), often expressed as a rate. A time series of B_n will reflect both changes in AAD (A_j) and in the specific mass balances b_n with respect to elevation (b_{nj}). To isolate the variations of the latter, which are more strictly related to climate, Elsberg *et al.* (2001) introduces the "reference-surface balance", which is the mass balance that would have been observed if the glacier surface topography had not changed since a reference date. The *reference surface* can be for instance the one at the beginning of the observation program or the one with the best accuracy. The annual glacier balance rate is obtained in this case as $\dot{B}' = \sum_{j=1}^{J} \dot{b}_j \cdot A'_j$ where A'_j is the AAD of the reference surface. In this work the geodetic mass balance is obtained using as reference surface the one corresponding to the older DEM.

3.5.1 Methods to estimate the glacier mass balance

Diverse methods have been exploited to determine the mass balance. An overview given by Cuffey & Paterson (2010) is summarized here. The change of ice mass B of a glacier of area A in a time interval Δt can be written in three ways:

$$\underbrace{\int B}_{\text{term a}} = \underbrace{\Delta \int_A \overline{\rho}\,(h_{\text{surf}} - h_{\text{bed}})\,dA}_{\text{term b}} = \underbrace{\Delta t \cdot \left[\int_A \left(\dot{b}_s + \dot{b}_e + \dot{b}_b\right) dA - \dot{B}_{cv}\right]}_{\text{term c}} \tag{3.20}$$

where the mass at any coordinate is the product of the vertically averaged ice density $\overline{\rho}$ and the ice thickness $h = h_{\text{surf}} - h_{\text{bed}}$, where h_{surf} and h_{bed} indicate the elevations of the surface and bed, respectively. Let the three terms be defined (a), (b) and (c).

Glaciological method This is the classical approach where field measurements of annual snow accumulation (with snow pits) and surface wastage (with ablation stakes) are obtained at a network of points on the glacier. Spatial interpolation gives term (c) in Eq. (3.20) with the exception of the calving contribution $\dot{B}_{cv}$ which must be estimated separately. Internal and basal balances are generally neglected, except for refreezing of percolated water within near-surface firn (internal accumulation). The accuracy is difficult to assess and limited by the sampling, it can be affected by considerable systematic errors. Moreover this method is applicable to a few glaciers due the intensive fieldwork involved and the difficult accessibility.

Process-model method Regional atmospheric circulation models with special parametrization for surface-atmosphere exchange processes are used for the calculation of the single terms of surface mass exchanges: snowfall, melt, sublimation, allowing to reach an estimate for term (c) in Eq. (3.20) with the exception of the calving contribution $\dot{B}_{cv}$. Internal and basal balances are generally neglected,

except for refreezing in the snowpack. No reliable model for calving is available. The models can calibrated with in-situ data from the glacier for improved accuracy.

Hydrological method It computes mass balance from measured water inflow (precipitation, run-off from hillslopes) and outflow (runoff in the glacier foreland), independently of the surface mass balance. It implicitly includes surface, englacial and basal terms which is advantageous but it is now always reliable in obtaining the annual mass balance, because of the different timing of water storage and release.

Geological methods The past extent and height of the glacier surface are estimated through the geomorphological signature of ice-edge deposits and scours. These features can be dated with lichenometry, radiocarbon, etc. It is well suited to estimate long-term mass loss estimates, although detailed time series and ice advances cannot be reconstructed.

Input-output method (IOM) Also known as budgeting or flux-gate method. The ice flux flowing through a chosen cross-section of the glacier, generally at the grounding line, is measured and balanced with the surface mass balance. The ice flux is computed from measurements of surface velocity and ice thickness at the so called *flux gate*, along with an assumption about the velocity variation with depth. The surface velocity can be obtained reliably through remote sensing methods. Ice thickness measurement at the flux gate are critical for this method but are seldom available. The surface mass balance is generally obtained through the classical glaciological method or the process-model method. The input-output method allows understanding the link between glacier behaviour and external forcing parameters. On the other hand it requires different sources of information which are often estimated with significant uncertainty.

Gravimetric method This method allows to measure mass changes by means of small changes in the gravity vector provided as temporal solutions by the Gravity Recovery and Climate Experiments (GRACE)[1] tandem satellite mission, launched in 2002 and still operational. In order to isolate the ice mass change (term (a) in Eq. (3.20)), other sources of mass change, such as glacial isostatic adjustment (GIA), continental hydrology and tectonics must be estimated with models and subtracted. The gravity solutions and the models applied lead to significant uncertainty of the mass balance. Furthermore the spatial resolution is limited, in the order of hundreds of kilometres. An advantage is the good temporal resolutions in the order of months, allowing to investigate linear trends, seasonal signals and inter-annual changes.

Geodetic methods These methods measure changes in the glacier surface elevation h_{surf} over a time span in order to obtain term (b) in Eq. (3.20). Various techniques can be applied to obtain surface elevation, among which: InSAR, photogrammetry, ground surveys, airborne or spaceborne laser or radar altimetry. The multitemporal elevation information is used to compute an ice volume change which is then converted to a mass change. These methods are hence often referred to as altimetric or volumetric. A critical aspect is given by the term $\overline{\rho}$, this is usually unknown as many studies are based on remotely sensed data. On the accumulation area variation of firn density can occur during multiyear observation periods in response to changes of temperature and snowfall rate. This leads to uncertainty in the volume to mass conversion. Some authors correct this effect using a model of firn densification (Reeh, 2008; Helsen *et al.*, 2008). Other uncertainty sources are linked to the type of data used and the procedure applied, these are described in depth along with the approaches used to estimate them in the literature in Section 9.1. Over large time scales corrections for the variation of the bed elevation h_{bed}, for instance caused by isostatic adjustment or tectonic activity, are needed.

Time series of ICESat laser altimetric data were used by Pritchard *et al.* (2009) to detect strong dynamic thinning on the margins of Antarctica and Greenland. Thomas *et al.* (2001) and Krabill *et al.* (2004) obtain mass balance estimates in Greenland based on radar and laser altimetry. Similar

[1] A joint mission of NASA and DLR. A follow on mission is planned for launch in 2017.

results have been obtained over Antarctica by Davis *et al.* (2005) and Helsen *et al.* (2008) using radar altimetry. Discrepancies between results obtained with the glaciological and geodetic methods have been reported in the literature. A comparison of the two approaches, their uncertainties and their results on the same study area is given in Cogley (2009) and Zemp *et al.* (2010). An assessment of many mass balance results from gravimetry and IOM is given by Zwally & Giovinetto (2011) for Antarctica, where strong variability of results emerged. A review of the different methods with particular focus on Patagonia is found in Bamber & Rivera (2007). A formalization of the nomenclature and mathematical formulation pertaining the glacier mass balance was done in Cogley *et al.* (2011).

Chapter 4

Microwave properties of snow and ice

In this theoretical chapter the properties of snow and partially of ice in the microwave region are presented. Firstly the main concepts of electromagnetic wave propagation (Section 4.1) and scattering (Section 4.2) are provided. The dielectric properties of snow are described in Section 4.3 along with the main models and measurements found in the literature. The concept of extinction coefficient and penetration depth and their application to snow are provided in Section 4.4. Finally Section 4.5 deals with the backscattering of snow. Remote sensing applications, backscattering models and a large collection of experiential measurements from the literature are reported to describe the behaviour of σ^0 with respect to different snow and radar parameters. This section is particularly useful to interpret the backscattering of SAR data in order to assess the wetness of the snowpack and consequently the possibility of signal penetration.

4.1 Electromagnetic waves basics

The electromagnetic fields in a source-free region satisfy Maxwell's equations in the form (Ulaby *et al.*, 1981; Orfanidis, 1999):

$$\nabla \times \vec{E} = -\mu \frac{\partial \vec{H}}{\partial t} \tag{4.1}$$

$$\nabla \times \vec{H} = \sigma \vec{E} + \varepsilon \frac{\partial \vec{E}}{\partial t} \tag{4.2}$$

$$\nabla \cdot \vec{E} = 0 \tag{4.3}$$

$$\nabla \cdot \vec{H} = 0 \tag{4.4}$$

where the electromagnetic properties of the medium are described by its *permeability* μ, *permittivity* ε and *conductivity* σ. These quantities can be considered scalars for a medium which is linear, homogeneous and isotropic. From Maxwell's equations the *wave equation* is derived:

$$\nabla^2 \vec{E} = \mu\sigma \frac{\partial \vec{E}}{\partial t} + \mu\varepsilon \frac{\partial^2 \vec{E}}{\partial t^2} \tag{4.5}$$

A solution to Eq. (4.5) is obtained by assuming a monochromatic wave sinusoidal time dependence:

$$\vec{E}(\vec{r}, t) = \mathrm{Re}\left\{\vec{E}(\vec{r}) e^{j\omega t}\right\} \tag{4.6}$$

where $\omega = 2\pi f = 2\pi/T$ is the *angular frequency*, f is the *frequency* and T is the *time period* of the wave. Analogously in space $k = 2\pi/\lambda$ is the *wavenumber*, while λ is the space period or *wavelength*. Hence the *phasor* or *complex electric field* $\vec{E}(\vec{r})$ satisfies:

$$\nabla^2 \vec{E}(\vec{r}) = -\omega^2 \mu \left(\varepsilon - j\frac{\sigma}{\omega}\right) \vec{E}(\vec{r}) = -\omega^2 \mu \varepsilon_c \vec{E}(\vec{r}) = -k_c^2 \vec{E}(\vec{r}) \tag{4.7}$$

where ε_c is the *complex permittivity* or *dielectric constant*, defined as (Ulaby *et al.*, 1981):

$$\varepsilon_c = \varepsilon - j\frac{\sigma}{\omega} \hat{=} \varepsilon' - j\varepsilon'' \tag{4.8}$$

Permeability and permittivity are often expressed as dimensionless quantities relatively to their values in free-space: the *relative permeability* $\mu_r = \frac{\mu}{\mu_0}$ and the *relative dielectric constant* $\varepsilon_r = \frac{\varepsilon_c}{\varepsilon_0} = \varepsilon_r' - j\varepsilon_r''$, where $\mu_0 = 4\pi \cdot 10^{-7}$ Henry/m and $\varepsilon_0 = 8.854 \cdot 10^{-12}$ Farad/m. In the microwave region $\mu_r \cong 1$ for most materials found in nature (Ulaby *et al.*, 1981; Stiles & Ulaby, 1981). The term $k_c = \omega\sqrt{\mu\varepsilon_c}$ is called *complex wavenumber*. For a lossless medium $\sigma = 0$, hence $\varepsilon_c = \varepsilon'$ and $k_c = k = \omega\sqrt{\mu\varepsilon'}$ are the real valued permittivity and wavenumber.

A solution to Eq. (4.7) has the form:

$$\vec{E}(\vec{r}) = \vec{E}_0 e^{-j\vec{k}\cdot\vec{r}} \tag{4.9}$$

$\vec{E}_0$ is a constant complex vector, $\vec{r}$ is the displacement vector, $\vec{k} = k_c\widehat{\mathbf{k}}$ is the propagation vector, $\widehat{\mathbf{k}}$ is the unit vector defining the propagation direction of the wave.

For a lossy medium it is useful to express the complex wavenumber as $k_c = \omega\sqrt{\mu\varepsilon_c} = \beta - j\alpha$, where $\alpha = \mathrm{Im}\{k_c\}$ is the *attenuation constant* characterizing absorption in the medium and $\beta = \mathrm{Re}\{k_c\}$ is the *phase constant* which represents change in phase per unit length along the path travelled by the wave at any instant. Another commonly used notation is the *complex propagation constant* $\gamma = jk_c = \alpha + j\beta$. Since $k_c = k_0\sqrt{\mu_r\varepsilon_r}$, in a generic lossy medium, α and β can be expressed as:

$$\alpha = k_0\left|\mathrm{Im}\{\sqrt{\mu_r\varepsilon_r}\}\right| = k\left[\frac{1}{2}\sqrt{1+\left(\frac{\varepsilon''}{\varepsilon'}\right)^2} - 1\right]^{1/2} \tag{4.10}$$

$$\beta = k_0\left|\mathrm{Re}\{\sqrt{\mu_r\varepsilon_r}\}\right| = k\left[\frac{1}{2}\sqrt{1+\left(\frac{\varepsilon''}{\varepsilon'}\right)^2} + 1\right]^{1/2} \tag{4.11}$$

where $k_0 = \omega\sqrt{\mu_0\varepsilon_0}$ is the wavenumber in free space and $k = \omega\sqrt{\mu\varepsilon'} = k_0\sqrt{\mu_r\varepsilon_r'}$. A conducting or high loss medium is characterized by $\sigma \gg \omega\varepsilon$ ($\varepsilon'' \gg \varepsilon'$), in this case the former quantities approximate to $\beta \simeq \alpha \simeq \sqrt{\frac{\omega\mu\sigma}{2}}$. For a low loss medium characterized by $\sigma \ll \omega\varepsilon$ ($\varepsilon'' \ll \varepsilon'$) they approximate to $\beta \simeq \omega\sqrt{\mu\varepsilon'}$ and $\alpha \simeq \frac{1}{2}\sqrt{\frac{\mu}{\varepsilon'}}\sigma = \frac{1}{2}k\frac{\varepsilon''}{\varepsilon'}$.

By substituting (4.9) into (4.6) the electric field becomes:

$$\vec{E}(\vec{r}, t) = \vec{E}_0\cos\left(\omega t - \vec{k}\cdot\vec{r}\right) \tag{4.12}$$

which represents a wave propagating along the $\widehat{\mathbf{k}}$ direction with time phase ωt and space phase $\vec{k}\cdot\vec{r}$. For the case of a lossless medium a surface on which the phase of the electric field is constant is defined by:

$$\omega t - \vec{k}\cdot\vec{r} = \text{constant} \tag{4.13}$$

At any given time, this surface coincides with the plane orthogonal to $\widehat{\mathbf{k}}$ with $\vec{k}\cdot\vec{r} = \text{constant}$. For this reason (4.12) is said to represent a *plane wave*. In this case the plane of constant phase is also a plane of constant amplitude, (4.12) hence represents a *uniform plane wave*. The velocity of propagation of this constant phase plane, called *phase velocity* is:

$$v = \frac{\omega}{k} = \frac{1}{\sqrt{\mu\varepsilon'}} = \frac{c}{\sqrt{\mu_r\varepsilon_r'}} \tag{4.14}$$

where $c = 1/\sqrt{\mu_0\varepsilon_0}$ is the speed of light in vacuum. Plane waves are a useful and common simplification since they approximate well the wavefronts in the far-field of an antenna.

For a uniform plane wave the electric field vector lies on the plane orthogonal to the direction of propagation and it is a function of time for any fixed point in space. As the time changes the tip of the electric field vector designs a curve on the aforementioned plane. This curve defines the *wave polarization*. If the curve is a straight line the plane wave is linearly polarized, if it is a circle it is circularly polarized and if it is an ellipse it is elliptically polarized. The last two can be right-hand or left-hand polarized based on the rotation direction (Ulaby *et al.*, 1981).

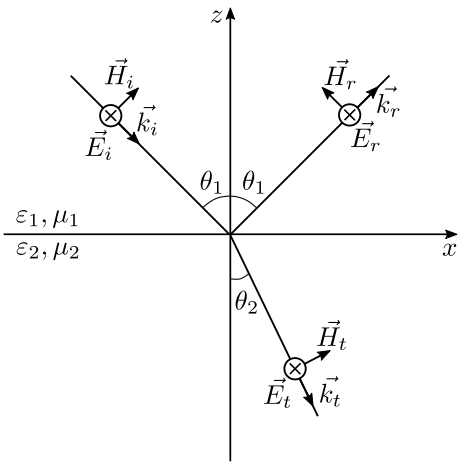

Figure 4.1 – Reflection and transmission scheme for a horizontally polarized wave.

4.2 Scattering

4.2.1 Reflection and transmission

A uniform plane wave hitting a plane interface (boundary) between two homogeneous media with different dielectric properties is divided into two waves: the reflected wave which propagates back into the first medium and a transmitted wave which propagates through the second medium. The plane of incidence is the one containing the normal vector to the interface and the propagation vector of the plane wave. When the incident $\vec{E}$ vector is perpendicular to the plane of incidence it is said to be perpendicularly or *horizontally polarized* (or a TE wave), when it is parallel to the plane of incidence it is said to be parallel or *vertically polarized* (or a TM wave). Both transmitted and reflected wave also lie on the plane of incidence. Reflection is a special case of scattering occurring when the boundary is smooth with respect to the wavelength, the angle of incidence is equal to the angle of reflection $\theta_i = \theta_r$. Refraction occurs at the transmitted wave, consisting in a change of the phase velocity and hence of the direction of propagation. The incident wave with incidence angle θ_1 will be refracted with an angle θ_2 according to Snell's law, reported here with all dependencies:

$$\frac{\sin\theta_1}{\sin\theta_2} = \frac{v_1}{v_2} = \frac{\lambda_1}{\lambda_2} = \frac{k_2}{k_1} = \frac{n_2}{n_1} \tag{4.15}$$

where $n = \frac{k_c}{k_0}$ is the *complex refractive index*. For a non-magnetic medium ($\mu_r = 1$) it holds that $n = \sqrt{\frac{\varepsilon_c}{\varepsilon_0}} = \sqrt{\varepsilon_r}$. Given that $v = \frac{\lambda}{T}$, the wavelength is equal to $\lambda = \frac{\lambda_0}{n}$, with λ_0 the wavelength in vacuum.

The *Fresnel equations* define the reflection and transmission coefficients for the horizontally polarized (R_h and T_h) and vertically polarized (R_v and T_v) wave, for non-magnetic media they can be expressed as:

$$R_h = \frac{n_1\cos\theta_1 - n_2\cos\theta_2}{n_1\cos\theta_1 + n_2\cos\theta_2} \qquad T_h = \frac{2n_1\cos\theta_1}{n_1\cos\theta_1 + n_2\cos\theta_2} \tag{4.16}$$

$$R_v = \frac{n_2\cos\theta_1 - n_1\cos\theta_2}{n_2\cos\theta_1 + n_1\cos\theta_2} \qquad T_v = \frac{2n_1\cos\theta_1}{n_2\cos\theta_1 + n_1\cos\theta_2} \tag{4.17}$$

from which it is possible to define the power reflection coefficient, or *reflectivity* Γ and the power transmission coefficient, or *transmissivity* Υ:

$$\Gamma_{h,v} = \left|R_{h,v}\right|^2 \qquad \Upsilon_h = \frac{\mathrm{Re}\{n_2\cos\theta_2\}}{\mathrm{Re}\{n_1\cos\theta_1\}}\left|T_h\right|^2 \qquad \Upsilon_v = \frac{\mathrm{Re}\{\cos\theta_2/n_2\}}{\mathrm{Re}\{\cos\theta_1/n_1\}}\left|T_v\right|^2 \tag{4.18}$$

It is worth noting that the field coefficients satisfy $T_h - R_h = 1$ and the power coefficients satisfy $\Gamma_h + \Upsilon_h = 1$.

4.2.2 Surface and volume scattering

The backscattering coefficient σ^0 of a distributed target depends on its dielectric properties. Another factor having a great impact on σ^0 is the surface roughness of the target. In fact a radar with a monostatic configuration would not be able to capture any of the energy reflected in the specular direction by a smooth interface, except for normal incidence. In practice natural surfaces are seldom perfectly smooth, causing the reflection mechanism to turn into scattering. In particular if the semiinfinite medium below the boundary is homogeneous the phenomenon is called *surface scattering* as it takes place exclusively at the surface boundary (Ulaby *et al.*, 1982b). A wave incident upon a rough surface boundary is reflected with two components: a coherent one in the specular direction and a diffuse or noncoherent one consisting of power scattered in all directions. As the roughness increases the power of the diffuse component increases while the coherent decreases, for very rough surfaces the radiation pattern approaches that of a Lambertian surface which consist of only diffuse scattering and σ^0 varies with $\cos^2\theta_i$. A monostatic radar captures the energy scattered in the backscattering direction, that of the receiving antenna (according to the antenna pattern). The degree of roughness is defined by statistical parameters which depend on the wavelength λ, namely the standard deviation of the surface height variation (RMS height) and the surface correlation length (see also Section 3.2) (Ulaby *et al.*, 1982b). A surface is considered smooth if the following criterion is true:

$$h < \frac{\lambda}{a \cos\theta_i} \tag{4.19}$$

where h is the vertical relief of the surface roughness and can be replaced with the RMS height. A general purpose criterion is known as *Rayleigh criterion*, obtained with $a = 8$. For natural surfaces in the microwave regions the stricter *Fraunhofer criterion,* obtained with $a = 32$ is considered more appropriate by Ulaby *et al.* (1982b). Contrary to smooth surfaces the scattering problem cannot be solved in closed form, however two main models are commonly used: the Kirchhoff scattering model for undulating surfaces and the small perturbation model for slightly rough surfaces.

If the medium below the main surface boundary is inhomogeneous a portion of the transmitted wave is scattered back by the inhomogeneities and may cross the boundary with the upper medium and be detected by the receiver. This phenomenon is known as *volume scattering*. In fact intuitively the transmitted wave hitting inhomogeneities which position is random (inclusions with different dielectric properties) scatters in multiple directions. The scattered wave may in turn hit other boundaries causing multiple scattering mechanisms. Hence modelling of volume scattering is not an easy task, typical approaches include the wave approach, the radiative transfer method (Ulaby *et al.*, 1986) or the discrete scatter approach.

4.3 Dielectric properties of snow

The dielectric properties of snow and firn have been well studied theoretically and experimentally by many authors with a peak activity in the mid eighties. Snow and firn are a heterogeneous mixture of air, ice and possibly liquid water. They are generally treated as homogeneous media, their electromagnetic behaviour is hence described by an effective, complex relative dielectric constant $\varepsilon_r = \varepsilon_r' - j\varepsilon_r''$, which is a weighted average of the dielectric constants of its constituents.

Air Air is generally be described by the dielectric constant in vacuum ε_0.

Liquid water Since the water molecule (H_2O) has a large dipole moment, the dielectric constant is dominated by the reorientation of the molecule. Liquid water and ice have a similar dielectric behaviour which follows the relaxation spectrum expressed by the Debye equation (Debye, 1929):

$$\varepsilon_r = \varepsilon_{r\infty} + \frac{\varepsilon_{rs} - \varepsilon_{r\infty}}{1 + j2\pi f\tau} \tag{4.20}$$

where $\varepsilon_{rs} = \lim_{f \to 0} \varepsilon_r$ is the static (low frequency) dielectric constant (around 90 at 0°C for both liquid water and ice) and $\varepsilon_{r\infty} = \lim_{f \to \infty} \varepsilon_r$ is the optical limit of the dielectric constant (approximately 4.9 for pure water), τ is the *relaxation time* of the material (around 18 psec for pure water). An electromagnetic field tends to align the dipole against the thermal forces which induce disorder, or "relaxation", and which depend on the temperature and viscosity of the material. The relaxation time is the average time required for the dielectric polarization to reach a new equilibrium in response to a change of the applied electromagnetic field. For liquid water (a high loss medium) the expression for τ derived by Debye for spherical polar molecules is a good approximation (Stiles & Ulaby, 1981): $\tau = \frac{4\pi\eta a^3}{kT}$, where η is the viscosity, a is the molecular radius, k is Boltzmann's constant and T is the temperature. For liquid water the relaxation frequency $f_0 = 1/2\pi\tau$ lies in the microwave region ($f_0 \approx 8.5$ - 10 GHz at $T = 0°C$) (Mätzler, 1987). ε_r'' has a symmetric behaviour with a maximum at $f = f_0$. ε_r' decreases with increasing frequency.

Ice The relaxation frequency of ice is located in the kilohertz region because of the higher viscosity compared to water, it hence has a weaker influence on the microwave spectrum (conventionally assumed to extend from around 0.3 to 300 GHz, or from 1 m to 1 mm wavelength). Ice is a low loss, non-magnetic medium, the real part of its dielectric constant for frquencies between 0.1 GHz - 1 THz falls in the range $\varepsilon_r' = \varepsilon_{r\infty} \in [3.14; 3.19]$ for pure ice according to several studies (Mätzler, 1987; Stiles & Ulaby, 1981). Slight variations are caused by impurities. The imaginary part of the relative dielectric constant, often referred to as *dielectric loss* because of its influence on the attenuation constant α (Eq. (4.10)), assumes very low and difficult to measure values in the microwave region. Here the loss is caused by the high frequency tail of the dipole relaxation spectrum (Stiles & Ulaby, 1981; Mätzler, 1987) and by the low frequency tail of the infrared absorption bands (Evans, 1965; Mätzler, 1987). This leads to a gentle minimum located between 1 and 3 GHz ($\varepsilon_r'' \approx 0.5 \cdot 10^{-3}$ at $T = -5°C$) and relatively linear behaviour outside this frequency range (Mätzler, 1987; Warren & Brandt, 2008). This behaviour is well approximated by $\varepsilon_r'' = A/f + Bf^C$, where A, B and C are empirical constants which depend on temperature and purity. Values in the literature are not always consistent. Mätzler (1987) reports that pure ice at $T = -5°C$ has $A = 6 \cdot 10^{-4}$ GHz, $B = 6.5 \cdot 10^{-5}$ GHz^{-1}, $C = 1.07$. ε_r'' increases when ionic impurities are present and decreases at lower temperatures. Tiuri *et al.* (1984) proposed a formula which includes the temperature dependency:

$$\varepsilon_r'' = 1.59 \cdot 10^6 \left(\frac{1}{f} + 1.23 \cdot 10^{-14} \sqrt{f} \right) e^{0.036T} \tag{4.21}$$

Snow A heterogeneous medium like snow is assumed to act electromagnetically like a homogeneous medium characterized by an effective dielectric constant described by mixing formulae encompassing the dielectric properties of its constituents (air, ice, liquid water). Different theoretical and empirical mixing formulae are present in the literature (Stiles & Ulaby, 1981; Hallikainen *et al.*, 1986; Mätzler, 1987). The complex dielectric constant of snow depends in general on frequency, temperature, volumetric water content, snow density, ice-particle shape and size and the shape of the water inclusions (Hallikainen *et al.*, 1986). While the first terms are strictly related to the dielectric properties of the constituents the last three are linked to the microstructure of snow. In this respect an important mechanism is represented by the metamorphism caused by melting and refreezing which causes the grains to become rounded and larger.

Dry snow Being a mixture of ice and air, dry snow has a ε_r' which, like ice, is independent of temperature and frequency in the microwave region (Evans, 1965) and is only dependent on the snow density. This varies between 0.2 and 0.5 g cm^{-3} for a natural snowpack, causing ε_r' to be roughly in the range 1.4 - 2 (Ulaby *et al.*, 1982b). No difference was found between different types of snow, such as old coarse grained snow or new fine grained snow. Some traditional models which describe well ε_r for dry snow are the Polder-Van Santen and the Tinga mixing formulae (not reported here). A generally used formula is

$$\varepsilon_r' = 1 + 1.7\rho_{ds} + c\rho_{ds}^2 \tag{4.22}$$

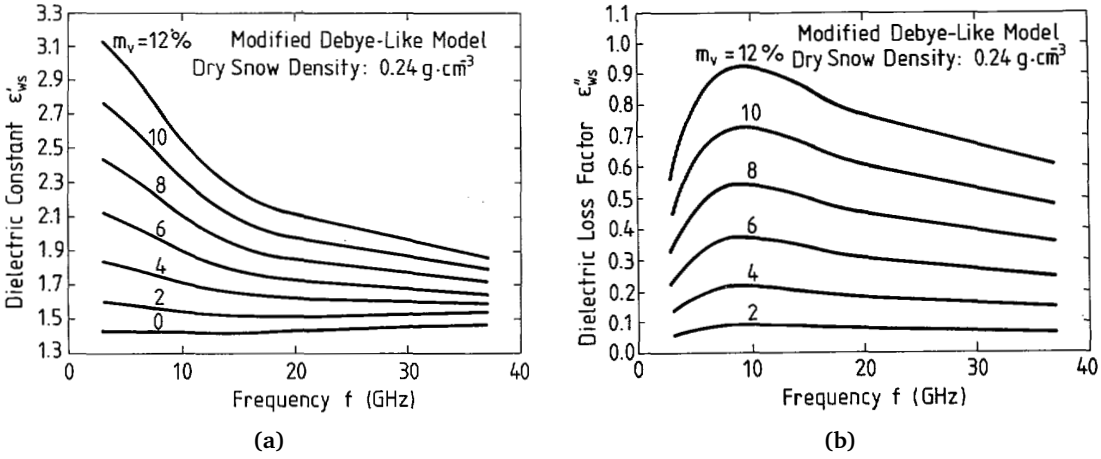

Figure 4.2 – Real ε'_{rws} (a) and imaginary ε''_{rws} (b) part of the relative dielectric constant of wet snow according to the Debye-like model as a function of frequency with liquid water content as a parameter. ε'_{rds} is also plotted in (a). An dry snow density $\rho_{ds} = 0.24$ g cm^{-3} was used in the model, corresponding to the average density value of the experimental samples when dry. From Hallikainen *et al.* (1986).

where ρ_{ds} is the relative density of dry snow (compared to water) with c equal to 0.7 for many authors (Tiuri *et al.*, 1984; Kovacs *et al.*, 1995; Kendra *et al.*, 1998). A practical approximation often used is the linear model $\varepsilon'_r = 1 + b\rho_{ds}$, with $b \approx 2$ for many studies (Tiuri *et al.*, 1984; Hallikainen *et al.*, 1986). The imaginary part of the dielectric constant of dry snow is, like ice, several degrees of magnitude smaller than the real part ($\varepsilon''_r/\varepsilon'_r \ll 1$) and depends on frequency, temperature and density of snow. Measurements present in the literature display a certain variability due to difficulty of measuring such small values in the microwave region. A formulation which includes temperature and fits relatively well to published data is given by Tiuri *et al.* (1984):

$$\varepsilon''_{rds} = \varepsilon''_{ri} \cdot (0.52\rho_{ds} + 0.62\rho_{ds}^2) \tag{4.23}$$

They obtain the best fit at varying snow density assuming ε''_{ri} at 2 GHz and −20°C to be $8 \cdot 10^{-4}$.

Wet snow According to the studies of Colbeck (1982), when the temperature approaches 0°C liquid water appears between the ice crystals which tend to become larger more rounded and with diameters of around 1 mm. The "wetness" of snow is measured by the *volumetric liquid water content* m_v, defined as the volume percentage of liquid water contained in a unit volume of snow. This parameter is occasionally expressed in the literature as the *volume fraction of water,* $V_w = m_v/100$. Wet snow has two regimes of liquid saturation: the *pendular regime* where air is continuous throughout the pore space and water inclusions are isolated, and the *funicular regime* where the liquid is continuous throughout the snow and air is present in distinct bubbles trapped in the pores. The transition between the two regimes is abrupt and occurs at a liquid saturation (i.e. the volumetric liquid content relative to the pore space between the ice grains) of 11 to 15%. In experimental results reported in Stiles & Ulaby (1981); Hallikainen *et al.* (1986), the transition happens when the m_v exceeds 3 to 6% depending on density of the snow sample. Typical values of m_v are between 0 and 10% by volume, only during rain higher values are expected (Mätzler, 1987). Plots of ε'_{rws} and ε''_{rws} based respectively on experimental measurements and model fitting found in Mätzler (1987) and Hallikainen *et al.* (1986) (Figure 4.2) present good agreement between each other. ε'_{rws} is not very sensitive to m_v with values rarely exceeding 4 and usually not exceeding 3. On the other hand ε''_{rws} is extremely sensitive to m_v, with the greatest relative change occurring as m_v passes from 0 to 0.5 (Ulaby *et al.*, 1982b). Many mixing formulae are reported for wet snow, Hallikainen *et al.* (1986) analyse six of them, finding the two-phase (dry snow + water) and the three phase (ice + air + water) Polder-van Santen models, as well as the Debye-like model to fit well to the empirical data with some discrepancies at frequencies above 15 GHz (the formulae are not reported here). A common procedure is to describe the real part of the dielectric constant of wet snow as that of dry snow (see above) plus an increment depending on liquid water

content (LWC): $\varepsilon'_{rws} = \varepsilon'_{rds} + \Delta\varepsilon'_{rws}$. The increment $\Delta\varepsilon'_{rws}$ appears to be almost linear with values between 0 and 1.6 as m_v ranges between 0 and 12%. Kendra *et al.* (1998) computes this incremental term as:

$$\Delta\varepsilon'_{rws} = 0.02 m_v^{1.015} + \frac{0.073 m_v^{1.31}}{1 + (f/f_0)^2} \tag{4.24}$$

where f_0 is the relaxation frequency of water (they use $f_0 \simeq 9.07$ GHz at 0°C). The loss factor ε''_{rws} of wet snow is dominated by the behaviour of water, hence no incremental term is necessary. According to experiments by Hallikainen *et al.* (1986) it has a nearly linear behaviour with values between 0 and 0.9 as m_v ranges between 0 and 12%. At varying frequency (see Figure 4.2b) it reaches a maximum around 9 - 10 GHz, the relaxation frequency of water at 0°C, the dynamic range is stronger as the liquid water content increases. As a general rule of thumb the dielectric loss of wet snow is 2 - 3 orders of magnitude higher than the dielectric loss of dry snow. Further modelling of the dielectric constant of wet snow, including its frequency dependence, is found in Tiuri *et al.* (1984); Sihvola *et al.* (1985). A review of several mixing formulae for dry and wet snow is given in Stiles & Ulaby (1981). Finally Mätzler (1987) proposes a simplified formula for the relative dielectric constant of wet snow for frequencies between 1 and 30 GHz:

$$\varepsilon'_{rws} = \varepsilon'_{rds} + \frac{23 V_w f_0^2}{f_0^2 + f^2} \tag{4.25}$$

$$\varepsilon''_{rws} = \varepsilon''_{rds} + \frac{23 V_w f_0 f}{f_0^2 + f^2} \tag{4.26}$$

4.4 Extinction coefficient and penetration depth

Volume scattering causes a redistribution of energy of the transmitted wave in other directions which results in losses. Naturally a wave propagating into a lossy medium is also subject to absorption (transformation in other forms of energy, for example as heat). The total loss due to both mechanisms is usually called extinction and its value per unit of length is the *extinction coefficient*:

$$\kappa_e = \kappa_a + \kappa_s \tag{4.27}$$

where κ_s is the *scattering coefficient* and κ_a is the power *absorption coefficient* defined as:

$$\kappa_a = 2\alpha \tag{4.28}$$

The attenuation constant α is defined in Eq. (4.10). For a low loss medium ($\varepsilon'' \ll \varepsilon'$) the approximated expression $\alpha \simeq \frac{1}{2}\sqrt{\frac{\mu}{\varepsilon'}}\sigma = \frac{1}{2}k\frac{\varepsilon''}{\varepsilon'}$ can be used, which assuming also $\mu_r = 1$, leads to (Stiles & Ulaby, 1981):

$$\kappa_a \cong \frac{2\pi\varepsilon''_r}{\lambda_0\sqrt{\varepsilon'_r}} \tag{4.29}$$

which is valid for ice, dry snow, and wet snow with liquid water content $m_v < 2\%$ (Stiles & Ulaby, 1981). κ_a is strongly frequency dependent with a rapid increase above 2 GHz for dry snow and ice. Naturally κ_a is strongly dependent on liquid water content, with the increase of the latter, absorption becomes rapidly the dominant extinction mechanism.

Scattering is due to inhomogeneities constituting a boundary with a variation of the dielectric constant. In firn and ice these are usually constituted by elements of different density such as lenses, pipes, air bubbles or layers of thicker ice which cause scattering even at lower frequencies. Snow is more homogeneous, with scattering elements constituted by ice crystals, and water inclusions in case of slightly wet snow in the pendular regime. Given the variability of the size of such inhomogeneities as well as their different dielectric properties the scattering coefficient is difficult to model. A common and simple approach is assuming Rayleigh scattering by modelling the snow crystals as uniformly distributed spheres of ice immersed in air.

The *penetration depth* δ_p is defined as the depth at which the average power of a wave travelling downward within a medium (the transmitted component of the wave incident on a boundary) attenuates to $1/e$ (37%) of the power at a point just below the surface. The penetration depth is related to the extinction coefficient by (Ulaby *et al.*, 1982b):

$$\delta_p = \frac{1}{\kappa_e} \tag{4.30}$$

For a wave travelling off nadir, as in the case of a synthetic aperture radar, the one-way vertical penetration depth also depends on the transmission angle θ_t according to the more general expression $\delta_p = \frac{\cos\theta_t}{\kappa_e}$. Accordingly, the two-way penetration depth, is defined as half the one way-penetration depth (Dall, 2007).

Absorption prevails at lower microwave frequencies, where snow particle size is much smaller than the wavelength. Scattering prevails at higher microwave frequencies and at mm wavelengths, where snow particle size is in the same order of magnitude of the wavelength. For instance for typical dry snow particles with diameter of 1 mm, scattering dominates for frequencies above 15 GHz according to the theory of Mie (Hallikainen, 1989).

Since the scattering coefficient is difficult to model, especially when the subsurface properties of the target are unknown, a rough approximation consists in assuming that $\kappa_s \simeq 0$ ($\kappa_e \simeq \kappa_a$). This approximation applies to wet snow in the microwave region under most conditions since absorption prevails. It also holds for dry, fine-grained snow at lower frequencies (below 5 GHz) since particles are significantly smaller than the wavelength. But above 10 GHz κ_a and κ_s may have comparable magnitude for large particle sizes (Stiles & Ulaby, 1981), besides the natural snowpack may have inclusions which enhance κ_s. For such cases the approximation $\delta_p = 1/\kappa_a$ represents an upper limit since the scattering losses are not accounted for. Dry snow and wet snow with $m_v < 2\%$ can be considered low loss media ($\varepsilon'' \ll \varepsilon'$) thus making Eq. (4.29) applicable.

A recent summary of extinction coefficient found in the literature, with both laboratory and in situ measurements is reported by Sharma (2010). Based on models presented in this section the behaviour of ε'_{rs} and ε''_{rs} and of the penetration depth δ_p with respect to LWC has been computed for different snow parameters and radar frequencies and is shown in Figure 8.1 and 8.2.

4.5 Microwave backscattering of snow

The power transmission coefficient Υ of the air-snow boundary depends on the relative permittivity of snow ε'_r, the angle of incidence θ_i and the polarization, as stated in Equation (4.18). Since for dry snow the relative permittivity ε'_r is less than 2 and for wet snow usually less than 3, significant transmission takes place across the boundary for a wide range of incidence angles for both linear polarizations. At nadir ($\theta_i = 0°$) transmissivity values of $\Upsilon \cong 0.98$ for dry snow with density $\rho_{ds} = 0.4\ \mathrm{g\,cm^{-3}}$ and $\Upsilon \cong 0.9$ for wet snow with liquid water content m_v of 5% are reported by Ulaby *et al.* (1982b).

For dry snow the backscattering can be determined by both surface and volume scattering mechanisms, the wavelength and the incidence angle play a role in the dominance of one over the other. Surface scattering is stronger near nadir (from the air-snow boundary and possibly from the ground), while volume scattering increases as the incidence angle increases. Volume scattering is primarily governed by the size of the ice particles relative to the wavelength (Ulaby *et al.*, 1986). As the liquid water content increases, absorption start to dominate over scattering as principal loss factor and δ_p decreases. When the snow is very wet, penetration and consequently volume scattering are negligible.

4.5.1 Remote sensing applications based on snow backscattering

Because the scattering mechanisms are dependent on different physical properties of snow and ice, many remote sensing applications have arisen based on measurements from both synthetic aperture radar and radar scatterometers. Much effort has been invested in the the retrieval of accumulation rates through the estimation of the snow water equivalent (SWE) of snowpacks, which is the the height of water which would result if the snow melted completely. Naturally these techniques are

only applicable to dry snow. Among others an empirical analysis of the relation between σ^0 and SWE is found in Ulaby & Stiles (1980), an algorithm for SWE estimation was developed by Shi & Dozier (2000a,b). Drinkwater *et al.* (2001) uses scatterometer and in situ data to derive empirical relations for SWE estimation. A satellite mission to monitor snow, including SWE was proposed in Rott *et al.* (2010), based on a dual frequency and dual polarisation SAR technique demonstrated in Rott *et al.* (2014a).

Another application consists in the classification of glacier zones or facies (see Section 3.3), which are areas characterized by different melting regimes which reflect in distinct backscattering signatures. Facies classification was performed among others by Drinkwater *et al.* (2001) and Schneider *et al.* (1997).

The detection of snowmelt is another application which exploits the strong sensitivity of σ^0 to the presence of liquid water. The results are relevant in hydrology as well as in glaciology since percolating water reaching the the bed of the glacier contributes to its acceleration due to a lubrication effect. Among others it was applied by Wismann (2000) and by Nagler & Rott (2000). Long term observation of backscattering from scatterometers in Antarctica have been presented by Bingham & Drinkwater (2000).

4.5.2 Models of backscattering coefficient

Although theoretical models of backscattering have been presented, they tend to be difficult to apply because of lack of knowledge of the statistical properties of the upper and lower snow boundaries and of the particle size, hence in Ulaby & Stiles (1981); Ulaby *et al.* (1984) an empirical model is proposed based on experiments with a single layer of snow over ground. As a first step the terms contributing to the backscattering coefficient are defined as: 1) the air-snow interface, 2) the snow volume, 3) the underlying ground. These terms contribute to σ^0 of a snowpack according to the following be expression:

$$\sigma^0(\theta_i) = \sigma^0_{sa}(\theta_i) + \Upsilon^2(\theta_i)\left[\sigma^0_s(\theta_t) + \frac{\sigma^0_g(\theta_t)}{L^2(\theta_t)}\right] \tag{4.31}$$

where $\sigma^0_{sa}(\theta_i)$ is the backscattering at the snow-air interface depending on snow surface roughness and dielectric properties of the snow surface layer. This can be neglected for dry snow (except at normal incidence) both because of the small dielectric mismatch ($\varepsilon'_r < 2$) causing $\Upsilon^2(\theta_i) \approx 1$ and because surface roughness has been proven to have no influence over a wide range of frequencies (1 - 35.6 GHz). On the other hand $\sigma^0_{sa}(\theta_i)$ must be considered for wet snow since the dielectric mismatch increases slightly ($\varepsilon'_r < 4$) and a strong dependence on surface roughness was empirically demonstrated (Ulaby *et al.*, 1982b). $\sigma^0_s(\theta_t)$ represents scattering from the snow volume and can be modelled as:

$$\sigma^0_s(\theta_t) = \frac{\sigma_v \cos\theta_t}{2\kappa_e}\left(1 - \frac{1}{L^2(\theta_t)}\right) \tag{4.32}$$

$$L(\theta_t) = \exp(\kappa_e d \sec\theta_t) \tag{4.33}$$

where σ_v is the volume scattering coefficient and d is the depth of the snow layer. The last term is $\sigma^0_g(\theta_t)$ which represents surface scattering from the underlying ground boundary, which influence decreases as d increases, up to the point where it can be neglected.

For wet snow σ^0_{sa} cannot be neglected, based on experimental observations Ulaby & Stiles (1981) included the liquid water content dependency using to the following model:

$$\sigma^0(W, m_v) = \sigma^0_{sa} + A_0 \exp(-a m_v) - \left[A_0 \exp(-a m_v) - \Upsilon^2 \sigma^0_g\right] \exp\left[-(C_0 + c m_v) W \sec\theta_t\right] \tag{4.34}$$

where a and c are constants at a given frequency and $\Upsilon^2 \approx 1$ can still be assumed. W is the snow water equivalent (SWE), see Section 3.1. Ulaby & Stiles (1981) determined the values of the constants involved in the previous equation using empirical observations. σ^0_g was measured directly (for both grass and asphalt). σ^0_{sa} is the most difficult to estimate, Ulaby & Stiles (1981) measured it with high m_v, when it dominates the backscattering and it its dependence on m_v becomes weaker. Still this term

might vary for different snow conditions, as its function of surface roughness and wetness. The values obtained at 8.6 GHz are $C_0 = 0.0344$, $c = 0.143$, $a = 0.802$, $A_0 = 0.63$, $\sigma^0_{sa} = 0.02$ with $\theta_i = 20°$ and $C_0 = 0.0198$, $c = 0.0932$, $a = 0.910$, $A_0 = 0.2$, $\sigma^0_{sa} = 0.002$ with $\theta_i = 50°$. The model fits very well the observations.

Ulaby *et al.* (1984) further shows how the impact of the ground on the total backscattering decreases rapidly with the snow depth. At 8.6 GHz (HH polarization) and $\theta_i = 50°$ when $m_v = 1\%$, as W exceeds 10 cm (ca. 25 cm for snow with typical density of $\rho_s = 0.4\ \mathrm{g\,cm^{-3}}$) the contribution from the ground becomes irrelevant and σ^0 saturates to -11 dB. When $m_v = 3\%$ $W = 3$ cm is enough to mask the ground contribution for concrete and asphalt (given their smoothness). For dry snow the ground starts to be irrelevant for $W > 60$ cm.

4.5.3 Experimental observations of backscattering

For this work the dependence of the backscattering coefficient on the wetness of the snowpack is of particular interest since it enables to assess the possibility of signal penetration into the snowpack, which would lead to an height bias in the InSAR DEM. In Chapter 8 the backscattering coefficient of the used acquisitions will be analysed and interpreted based on the theory reported in this chapter and on the experimental observations found in the literature and reported in this section.

A wide spectrum of experimental observations of backscattering of dry and wet snow and its dependence on different system and snow parameters are presented in Ulaby *et al.* (1986); Stiles & Ulaby (1980); Ulaby & Stiles (1981) and in Mätzler (1987), helping the validation of models and interpretation of real case scenarios.

Mätzler (1987) observed how the HH and VV polarizations show an almost identical angular pattern on dry snow, while the HV response is weaker. He further reports averaged observations at 10.4 GHz of snow-free soil, dry snow and wet snow at varying incidence angle showing a close behaviour in the first two cases (with slightly lower σ^0 for dry snow) and a significantly lower values of σ^0 for wet snow (up to 10 times lower). The difference ranges between 6 dB at $\theta_i = 80°$ and 8.6 dB between 30° and 50°, there is almost no difference at nadir. His measurements show also a large variability of wet snow σ^0 due to varying snow wetness and partially roughness, but even the higher bound (1-σ) is distinctively below the lower bound of dry snow, which variability is mainly linked to grain size. This confirms the applicability of the backscattering as a parameter for discerning between dry and wet snow.

The measured response of the backscattering of dry snow at varying incidence angle for different frequencies was measured by Ulaby *et al.* (1982b) and is shown in Figure 4.3. Ulaby & Stiles (1981) measured the angular response of dry and wet snow (early morning and afternoon) for a 27 cm deep snowpack at different frequencies, their plots are reported in Figure 4.4. The sensitivity to liquid water content for a relatively shallow snowpack is practically null at 2.6 GHz, because the underlying ground dominates the response. The different response is visible at higher frequencies, where the ground contribution is still present (to a lesser degree) when the snow is dry.

The spectral response extracted during experiments by Ulaby & Stiles (1981) is reported in Figure 4.5 and illustrates the effect of the frequency on the the sensitivity of σ^0 to liquid water. Even low levels of wetness (1.26%) cause the response to diverge significantly already at lower frequencies and much more at very high frequencies. A difference of around 4 dB is found between 5 and 12 GHz.

The response to snow wetness was extensively studied by Ulaby et al. using truck-mounted scatterometers between the end of the seventies and the beginning of the eighties. Some of their results are reported in Figure 4.6. They show that the sensitivity of σ^0 to m_v generally tends to increase with increasing frequency (Figure 4.5 and 4.6a). In Stiles & Ulaby (1980) for instance, a sensitivity of -2 dB/1% of m_v is found above 7 GHz, decreasing at lower frequencies ($\theta_i = 50°$). Relating directly σ^0 and m_v is difficult since σ^0 has contributions from the entire depth of the snowpack (which may have inhomogeneous wetness) and possibly from the underlying medium. Profiles of m_v with cm depth resolution would be needed at least for the top 10 - 20 cm layer (Stiles & Ulaby, 1980). The experiments in Figure 4.6 were preformed under different snow conditions and the measured values are often scarce, the results are hence not always matching, but the plots help building a general idea of

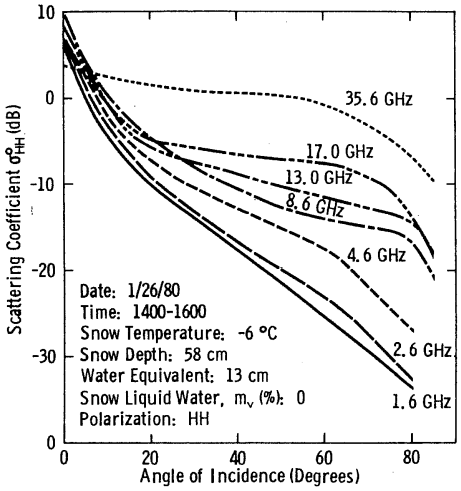

Figure 4.3 – Angular pattern of measured backscattering coefficient of dry snow for different frequencies. From Ulaby *et al.* (1982b).

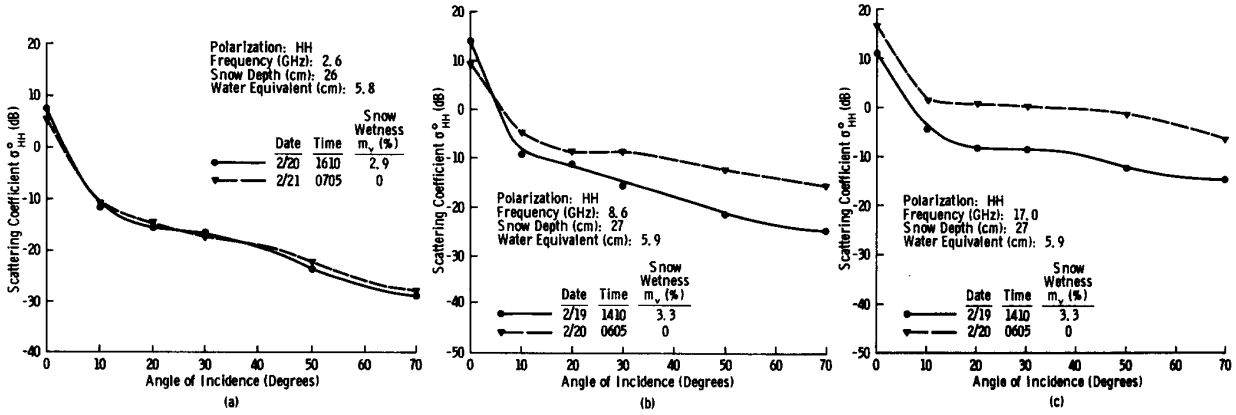

Figure 4.4 – Angular response of σ^0 for dry and wet snow at (a) 2.6 GHz, (b) 8.6 GHz, and (c) 17.0 GHz. The underlying soil has an impact on the σ^0 response given the shallow snow depth (26 - 27 cm). From Ulaby & Stiles (1981).

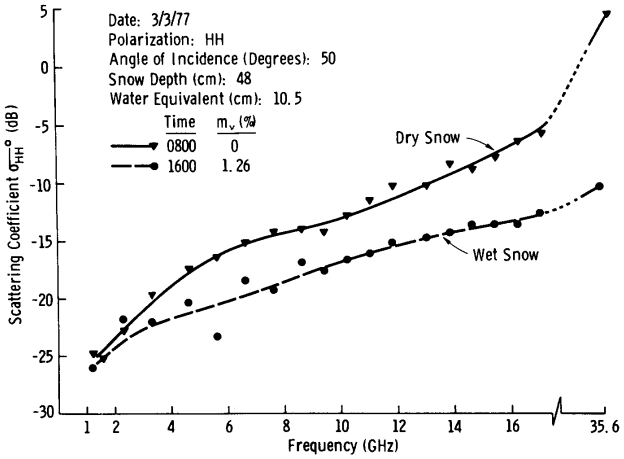

Figure 4.5 – Spectral response of σ^0 for dry and wet snow at $\theta_i = 50°$. From Ulaby & Stiles (1981).

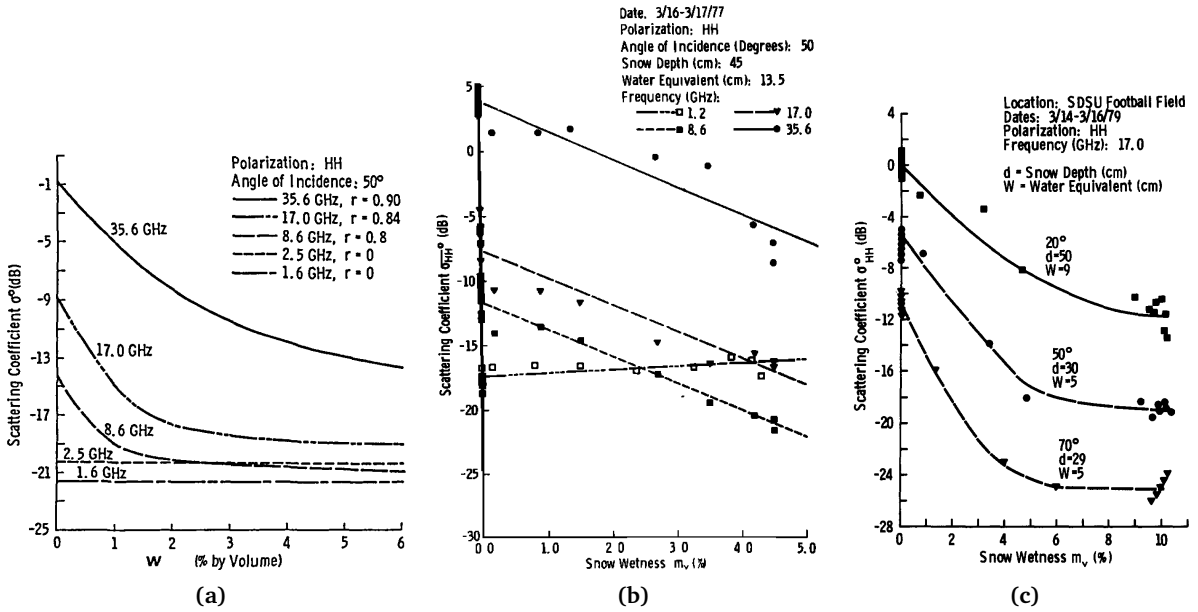

Figure 4.6 – Response of σ^0 to liquid water content for various experiments with truck-mounted scatterometer performed by Ulaby et al. in the winter seasons between 1977 and 1980. When available parameters are reported on the plot. (a) Curves fitted to 1980 data, r is the linear correlation between data and fit. From Ulaby *et al.* (1982a) as reported by Mätzler (1987). (b) Data from diurnal experiment, here the sensitivity is around −2 dB/1% m_v for frequencies above 7 GHz. From Stiles & Ulaby (1980). (c) Measurements at 17 GHz for different incidence angles showing nearly linear response up to a certain value of m_v after which sensitivity is lost, as expected particularly at higher frequencies. From Ulaby & Stiles (1981). For both results in (b) and (c) snow wetness refers unfortunately only to the upper 5 cm layer.

the expected relationship between backscattering and liquid water content at a typical incidence angle of 50°.

Further experiments involved prolonged observation over a 24-hour diurnal cycle (Figure 4.7). The response to a peak in liquid water content from 0 to 1.26% at (16:00) and back to 0% consisted in a dip of σ^0 for all frequencies. The magnitude of the dip becomes larger as the frequency increases, around 2 dB at 4.6 GHz, 4 dB at 8.6 GHz and 15 dB at 35.6 GHz. Seasonal variability was also monitored by Ulaby & Stiles (1981) at 8.6 GHz and $\theta_i = 50°$ at a test site in Colorado during 6 weeks in 1980. Results are reported in Figure 4.8 where snow water equivalent W, liquid water content m_v of the top 5 cm layer and backscattering coefficient σ^0 are plotted. It can be observed that increased wetness of the top layer reduces backscattering to an almost constant value σ^0_{min} of around −22 dB making it essentially independent of W. When the snow is dry σ^0 increases with increasing W causing the envelope marked as σ^0_{max} in the plot ranging between −15 dB and −9 dB in response to an increase in W of 7 cm (corresponding to a snow depth of 25 cm).

Mätzler (1987) performed several observations on natural snowpacks illustrating different possible snow conditions, these are important to consider when interpreting the backscattering of glaciers. In Section 4.8 of Mätzler (1987) he shows with experimental measurements (performed in the Swiss Alps) how the formation of a refrozen crust during summer affects the backscattering. In summer snow is usually older and metamorphism has created larger grains which are efficient scatterers. During daytime the melted water drives σ^0 down, but after sunset as temperature decrease the upper layer of snow refreezes (at higher elevations) causing an increase of σ^0. The peak of σ^0 is just before sunrise when the temperature is at its lowest, afterwards σ^0 plunges again. In this scenario possible penetration of the signal is limited to the upper crust, as the lower layer remains wet and suppresses any interaction from the snowpack and snow-ground interface. In Section 4.7 of Mätzler (1987) he details a typical spring scenario where the snowpack starts to become wet for a few hours during daytime and then refreezes completely. The effect of the wet layer is to attenuate or mask the signal

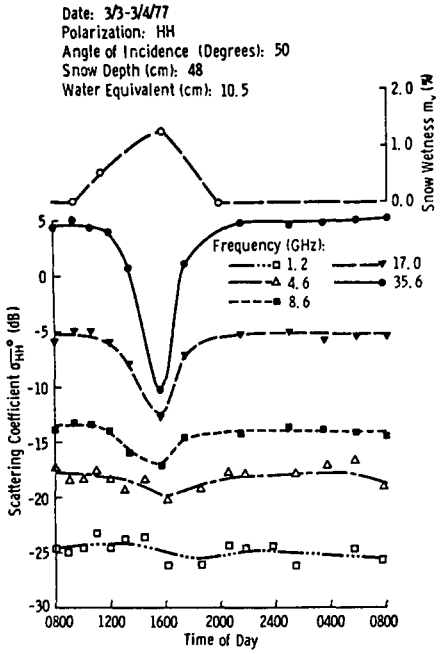

Figure 4.7 – Diurnal patterns of liquid water content (measured in the top 5 cm layer) and backscattering at different frequencies. From Stiles & Ulaby (1980).

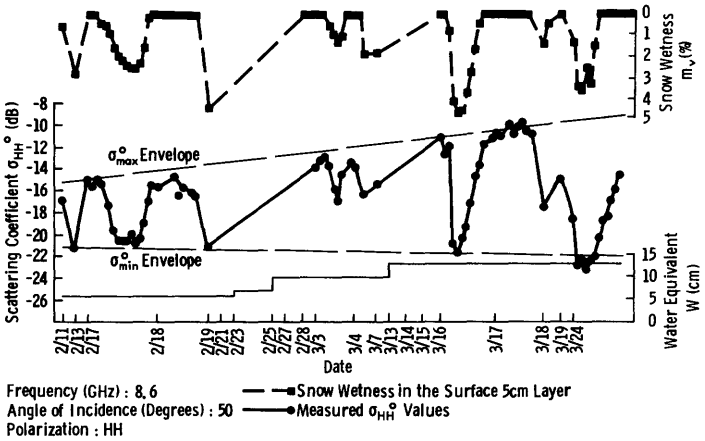

Figure 4.8 – Temporal variation of snow water equivalent W, liquid water content m_v of the top 5 cm layer and backscattering coefficient σ^0during the six week experiment at 8.6 GHz and $\theta_i = 50°$. From Ulaby & Stiles (1981).

from underlying snow and snow-ground interface leading to a decrease of σ^0. Furthermore, Mätzler (1987) shows how in some specific situations σ^0 can increase or at least remain stable although the temperature is rising. This can happen, especially during spring when only the superior layer of snow starts to melt. The liquid water does not percolate into the fine grained snow below which is still at subfreezing temperature, it refreezes instead forming a thin layer of ice at the interface between wet and dry snow which builds up surface scattering mechanisms.

A similar behaviour was found in one of the experiments performed by Kendra *et al.* (1998). They perform very well controlled experiments with artificial and natural snow together with ample ground truth in order to validate theoretical models. The first experiment concerns the measurement of the angular response of different depths of uniform artificial dry snow and of the underlying bare soil. In the second experiment depth profiles of liquid water content were recorded together with the backscattering at 40° during a diurnal cycle. Both co- and cross-polarized responses at C and X-band were recorded averaging 60 independent spatial measurements on a 18 × 30 m area. The co-polarized responses display a small dynamic range at varying incidence angle, σ^0_{VV} for 60 cm of snow ranges between −12 and −17 dB in C-band and between −11 and −14 dB in X-band for $\theta_i \in [20°; 60°]$. Plots for snow depth of 102 cm are similar, meaning a condition of half-space is reached. Cross-polarized σ^0_{VH} are between 14 and 11 dB lower for both frequencies. They argue that the existing models for dry snow fail to give reasonable predictions compared to the measured data. The second experiment was executed on two test sites with very different snow conditions with sub-freezing temperatures in the morning and late evening and warmer temperatures during the day (up to 6°C and 12°C at 15:00 respectively at the two test sites). The first test site was characterized by 90 cm of snow, of which the bottom layer was ice and the top layer fresh snow. Here wetness increased in the warmer hours in the upper 30 cm layer of snow up to 5%, while in the lower 30 cm reached values up to 12% at evening due to percolation. The backscattering reacted with a typical diurnal curve. Morning values of co-polarized σ^0 were around −14 dB for C-band and −6 dB for X-band, minima are reached around 16:00 (−21 dB in C-band, −19 dB in X-band), later backscattering increased as temperature and liquid water in the upper snow layer decreased. The second test site had only 20 cm of snow with low values of liquid water in the lower part throughout the day and higher values (up to 15%) in the upper layer

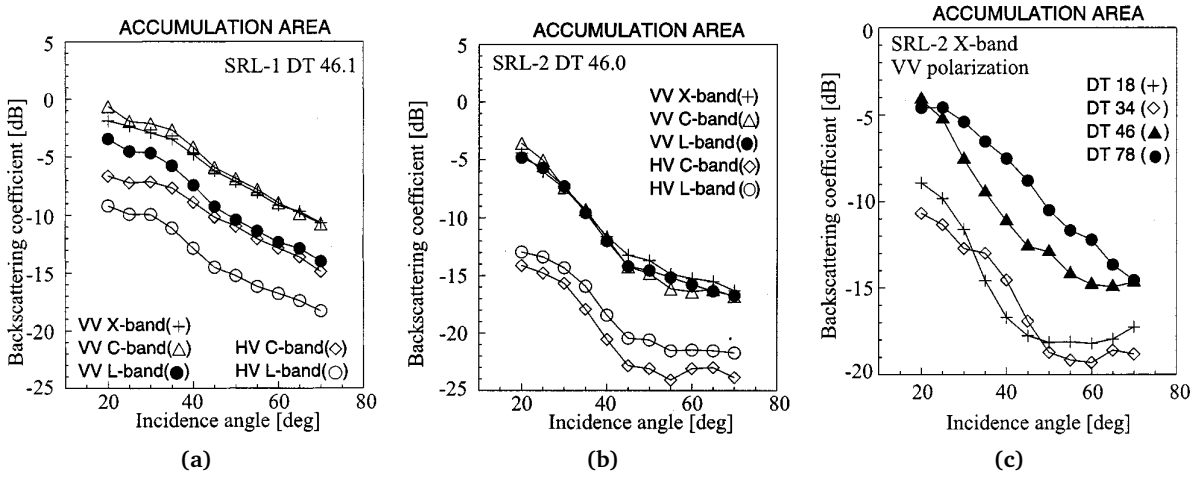

Figure 4.9 – Angular dependence of the mean backscattering coefficient computed on the accumulation areas. From Floricioiu & Rott (2001). Datatake acquisition times (CET=UTC+1h) were: 46.1: 12.4.1994 06:55; 46.0: 3.10.1994 07:02; 18: 1.10.1994 13:50; 34: 2.10.1994 13:32; 78: 5.10.1994 06:23. Snow conditions: 46.1: dry, 18, 34: wet; 46, 78: frozen top layer above wet firn.

after midday, because of an ice lens which impeded percolation. σ^0 decreased with values ranging between −18 dB and −24 dB in C-band and between −9 dB and −23 dB between 10:00 and 16:00. The presence of the lens caused a slight increase of σ^0 around midday because of an increase in surface scattering due to a higher dielectric constant, but it can be considered a very specific scenario. They use this extensive collection of data to validate the wetness inversion algorithm of Shi & Dozier (1995), finding a good agreement between model and measurements.

The algorithm by Shi & Dozier (1995) consists of a comprehensive polarimetric model for snow wetness retrieval from SAR (based on SIR-C/X-SAR data). The authors report an absolute accuracy of 2.5% at the 95% confidence level by comparison with ground measurements.

Arslan *et al.* (2005) present a two-phase backscattering model of volume scattering in wet snow. Wet snow is modelled as dry snow with asymmetrical water inclusions. The model provides a good fit to the experimental data, σ^0 at 8.6 GHz and $\theta_i = 50°$ is −14 dB at $m_v = 0.25\%$ and decreases to −22 dB for $m_v = 5.5\%$.

Floricioiu & Rott (2001) analyse SAR signatures (AIRSAR in C, L, P-band and SRL-1/2 in C, L, X-band) of glaciated areas in the Austrian Alps under different snow conditions and system parameters, such as frequency and incidence angle. Extensive field data regarding snow and ice parameters was concurrently collected, allowing to establish a link between signatures and conditions on the ground. The test site was located in Ötztal (46.7° N, 10.8° E) and the accumulation areas consist of relatively large plateaus with gentle topography with altitudes between 3000 m and 3400 m. Plots of the measured mean backscattering angular responses on the accumulation area are reported in Figure 4.9 for five SRL-1 and SRL-2 datatakes at different frequencies and polarizations. Backscattering mean values on glacier ice, bare rock and vegetation are also provided in the paper.

During the SRL-1 46.1 datatake (Figure 4.9a) the snow was completely dry, meaning that the main backscattering contributors are reflection from the snow-firn/ice interface and volume scattering from the firn and ice volume. During SRL-1 air temperature at 3000 m was below −10°C, and all the glaciers were covered with a smooth, dry, fine grained snow layer of 2 to 3 m of depth. On the Hintereisferner Glacier at 2900 m the upper 20 cm layer of snow was characterized by $\rho_s = 0.193$ g cm^{-3}, grain size $GS = 0.5$ mm and temperature $T_s = -4.4$°C. The lower layers were increasingly denser: $\rho_s = 0.350$ g cm^{-3} and $GS = 1.0$ mm up to 1 m of depth and $\rho_s = 0.435$ g cm^{-3} and $GS = 1.5$ mm from 1 to 3 m of depth. in Figure 4.9a σ^0_{VV} shows a similar angular response at X and C-band with values ranging between 0 and −10 dB. Lower values are recorded at L-band and for the HV polarization.

During SRL-2 (Figure 4.9b and 4.9c) meteorological and snow conditions were complex and variable. In September first heavy snowfalls and cold temperatures occurred, followed by a warm period at the end of the month, creating an intermediate layer of dry, frozen snow of 20 - 50 cm of depth.

During DT 18 and 34 air temperature was well above 0°C and concurrent field observations at about 3250 m revealed 130 - 200 cm of snow with density above 0.400 g cm^{-3} and m_v between 3 and 4% at 5 cm of depth. These snow conditions are reflected in the two lower σ^0_{VV} X-band signatures of Figure 4.9c. On the night of 2/3 October temperatures plunged below 0°C at 3000 m and 2 cm of dry snow fell. During DT 46.0 the top layer of the snowpack was frozen (at higher altitudes) while the old firn below was wet, leading to the backscattering angular responses in Figure 4.9b with similar behaviour of σ^0_{VV} at the L, C, and X-band. Comparable conditions with even lower temperatures (−6°C at 3000 m) were present during DT 78, causing the upper frozen crust to extend at lower altitudes and be thicker at higher altitudes, hence rising the mean σ^0_{VV} angular response in Figure 4.9c.

The glacier ice was snow free and wet during the whole SRL-2 mission, hence σ^0 depends on roughness and dielectric properties of the surface. An almost identical σ^0_{VV} signature is measured for all three frequencies as well as for all datatakes: a weaker angular dependence is highlighted compared to the accumulation area, ranging between −4 and −13 dB for $\theta_i \in [20°; 70°]$ (not shown). During the AIRSAR DT 270-1 (25.6.1991 10:30 CET) all glaciers were covered with recent snow, the upper 20 cm snow was wet with $m_v \in [4\%; 6\%]$, and air temperature was above 0°C at 3000 m. The C and L-band σ^0_{VV} angular responses are similar and range between −17 dB and −21 dB for $\theta_i \in [30°; 60°]$ (not shown).

Chapter 5

The Northern and Southern Patagonian icefields

This chapter discusses different aspects of the Northern and Southern Patagonian icefields, for which the geodetic mass balance is derived in this thesis. The chapter starts describing the geographical setting (Section 5.1), the structure of the icefields (Section 5.2) and the climate of the region (Section 5.3). The following sections report different glaciological studies investigating different aspects of the icefields. Areal and local ice thickness changes are discussed in Section 5.4 and 5.5, respectively. Section 5.6 deals with remote sensing studies focusing on the entire icefields. Other relevant studies are grouped in Section 5.7.

5.1 Geographical setting

The Northern and Southern Patagonian icefields (NPI and SPI) represent the largest mid-latitude ice masses in the Southern Hemisphere (see Figure 5.1). The NPI (Figure 5.2) extends north to south for approximately 120 km, between 46°25'S and 47°37'S, it is relatively compact in shape with an average width of approximately 45 km, located at an average longitude of 73°30'W. The SPI (Figure 5.3) is longer and irregular, with a north to south extension of 370 km between 48°15'S and 51°30'S and a width ranging between 85 km to 7 km around the mid longitude of 73°30'W.

The topography of the NPI and SPI, which are separated by a distance of approximately 90 km, is relatively similar. The accumulation area is mostly located on a relatively flat plateau, which is crossed longitudinally by mountain ranges. Elevation ranges from sea level to the 3607 m a.s.l. of the active Volcan Lautaro in SPI and to the 4058 m a.s.l. of Monte San Valentin in NPI. The topography and shape of the icefields and surrounding regions are qualitatively visible in the photographies in Figure 5.2 and 5.3 and the elevation is quantitatively described by the SRTM DEM reported in Figure 7.5 and 7.7 for NPI and SPI, respectively.

The glaciers of SPI, flowing from the Patagonian Andes are mostly calving into freshwater proglacial lakes on the eastern margin, and tidewater oceanic fjords on the western margin, only two terminate on land. The lakes are mostly large and split into different intricate and deep fjords into which the glaciers calve. The main lakes are Lago O'Higgins (San Martin), Lago Viedma, Lago Argentino (with its two branches periodically dammed by the Perito Moreno Glacier). On the other hand NPI has most of its glaciers terminating on land or calving into small and shallow proglacial lakes of newer formation. The only tidewater glacier is San Rafael (the one at the lowest latitude in the world) which calves into a well protected lagoon. A review of glaciological studies of this region was presented by Warren & Sugden (1993) and an updated review focusing on SPI by Casassa *et al.* (2002).

5.2 Glacier inventory

The first complete and detailed glacier inventory of the NPI was provided by Aniya (1988) who registered a total area of 4202 km^2 based on cartographic maps from 1974/'75, vertical aerial photo-

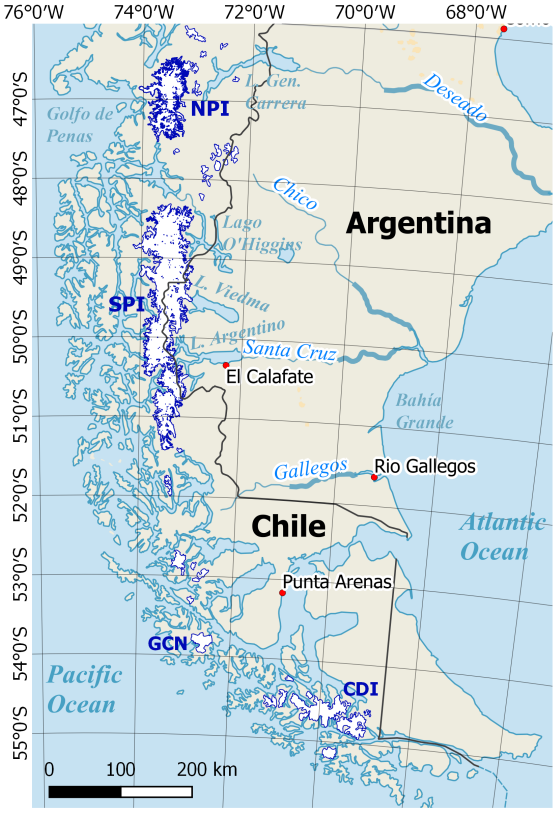

Figure 5.1 – Map of southern South America. The glaciated areas are shown in white with a blue outline.

graphs and additional oblique aerial photographs from 1986. A new inventory was provided by Rivera *et al.* (2007) using a Landsat ETM+ image of 2001. They found a total of 70 glaciers with a total area of 3953 km^2.

The first inventory of SPI was given by Aniya *et al.* (1996) based on Landsat TM images of 1986, they reported 48 major outlet glaciers and over 100 small cirque and valley glaciers, for a total ice area of 12772 km^2. A new inventory was compiled by Casassa *et al.* (2014) based on Landsat images of 1986 and for 2000, finding an area of 13003 km^2 and 12514 km^2, respectively.

The *equilibrium line altitude* (ELA) might vary significantly between glacier basins, ranging approximately between 900 m and 1350 m in NPI (1150 m a.s.l. in average) (Rivera *et al.*, 2007) and between 650 m and 1300 m in SPI (Aniya *et al.*, 1996). The average *accumulation area ratio* (AAR) in 2000 was 0.68 for NPI (Rivera *et al.*, 2007) and 0.71 for SPI (Casassa *et al.*, 2014). The hypsometry of the icefields in February 2000 is shown in Figure 9.16a and 9.17a, for NPI and SPI respectively.

5.3 Climate

The Patagonian icefields are strongly invested by mid-latitude westerlies and frontal (and cyclonic) systems all year round, leading to cloudy conditions during more than 77% of the year with precipitation on more than 290 days recorded at the northern end of SPI (Carrasco *et al.*, 2002). The overall annual behaviour indicated weaker SW winds during winter and stronger NNW winds during summer. Topography plays a very important role in the climatic regime of the region: the continuous winds coming from the ocean collide with the rapidly increasing western slopes of the Andes, generating a strong orographic effect which leads to a highly varying spatial distribution of precipitation. On the western side (windward) a high amount of annual precipitation is recorded, exceeding 7000 mm on the coast and 10000 mm on the icefield. Precipitation rapidly decreases on the eastern side (leeward) in the Argentinian Patagonia where average of 400 mm are recorded (Carrasco *et al.*, 2002; Ibarzabal y Donangelo *et al.*, 1996). The maritime climate on the western side and the drier climate on the

Figure 5.2 – Photography of the NPI from the west taken from the ISS (date unknown). Credits: NASA.

Figure 5.3 – Photography of the SPI from the east taken from the ISS on 13 February 2014. Credits: NASA.

eastern side (Warren & Sugden, 1993) also reflect on the vegetation coverage and type, as partially appreciable in Figure 5.3.

The mean annual temperature measured at stations nearby is around 7°C with higher seasonal variation on the eastern side. The ice is hence temperate on the ablation area and part of the accumulation area (Casassa *et al.*, 2002). A general warming trend between 1.3 and 2.0°C per century was recorded south of 45°S at meteorological stations near the icefields between 1933 and 1992 (Rosenblüth *et al.*, 1997), warming of 1.4°C per century was measured by Ibarzabal y Donangelo *et al.* (1996) at Rio Gallegos between 1938 and 1988. Villalba *et al.* (2003) also found a clear warming trend intensifying at higher latitudes. Rasmussen *et al.* (2007) used upper air conditions from the NCEP/NCAR[1] reanalysis data (Kalnay *et al.*, 1996) to derive variations in precipitation and temperature between 1960 and 1999. They found a non-definitive temperature increase of 0.5°C both in winter and in summer at 850 hPa, corresponding to an altitude level of ∼1400 m a.s.l, close to the average of the Patagonian icefields. If true, such an increase would lead to a shift from snow to rain of ∼5% of the precipitation (with small change of the total) and to an increase by ∼0.5 m w.e. in melt of the ablation areas.

Precipitation historical records are somehow scarce in the region and lead to uncertain conclusions. Nevertheless a negative trend has been measured during 1900 - 1990 particularly in northern Patagonia (41 - 47°S). On the other hand a positive trend has possibly been detected in southern Patagonia from the mid-80s at the Faro Evangelistas and Punta Arena stations (Carrasco *et al.*, 2002; Casassa *et al.*, 2014). Escobar (1992) derived annual precipitation of 6.7 m w.e. averaged on the plateau of NPI.

[1]National Centers for Environmental Prediction / National Center of Atmospheric Research

Seasonal variation is limited and snowfall events can occur all year round. A deeper overview of the climatic conditions of the Patagonian icefields is provided by Bippus (2007), where the climate sensitivity of three major glaciers of SPI is studied.

5.4 Areal changes

A huge Patagonian Ice Sheet with average thickness of 1130 m covered the southern Andes during the Last Glacial Maximum, approximately 20k years ago. In a recent study Boex *et al.* (2013) apply geomorphological mapping of moraines, trimlines and glacial surfaces along with cosmogenic isotope dating to map the extent and the thickness of the ice sheet. They report that the ice sheet started to retreat rapidly ∼19k years ago in response to climatic changes, and particularly to the migration of the Southern Westerlies towards the south, which caused reduced precipitation and increased temperatures. They hence sustain the high sensitivity to climate changes of the Patagonian Ice Sheet during the late Pleistocene.

Most of the glaciers of the Patagonian icefields underwent a general retreat from their maximum position held during the Little Ice Age (LIA), a period ranging loosely between AD 1600 and AD 1900. A general trend of areal loss might be detected from the end of the LIA (approximately AD 1870) until the 1940s, followed by an accelerated loss from then until the present days (Casassa *et al.*, 2014).

The first systematic mapping of the major glaciers was performed through aerial and satellite imagery in the period 1945 - 1985 by Aniya (1988) for NPI (updated to 1995 in Aniya (1999) and to 2005 in Aniya (2007)) and by Aniya *et al.* (1997) for SPI. On NPI they register an average annual retreat of 68 $\mathrm{m\,a^{-1}}$ between 1945 and 1985, with only two glaciers stable or slightly advancing (Reicher Glacier). The frontal recession was 64 $\mathrm{km^2}$ between 1945 and 1995. On SPI for the same period the authors found that 39 glaciers had retreated, 8 were mostly stable and Pio XI was advancing, stronger retreat rates were registered at the northern and eastern margins. The total area lost at the fronts was 200 $\mathrm{km^2}$. The volume loss due to frontal recession in NPI and SPI is estimated in Aniya (1999), while special focus on the behaviour of calving glaciers in the region is offered in Warren & Aniya (1999).

Glacier retreats for NPI, SPI and CDI have also been assessed through aerial photographs of 1945 and 2005 ASTER and Landsat images by Lopez *et al.* (2010). The strongest retreats affected the San Rafael Glacier in NPI (5.7 km) and the O'Higgins Glacier in SPI (12.2 km)

Using dendrochronology, lichenometry and aerial photographs, different periods of major retreat, interleaved by stability or advance periods, were identified around the 1870s, 1920s and 1960s for the San Rafael, S. Quintin, Gualas, Reicher, Colonia and Arco glaciers (NPI) (Winchester & Harrison, 1996; Harrison & Winchester, 1998, 2000).

Neoglacial advances until the LIA and subsequent retreat after AD 1870 were identified for the Ameghino Glacier by Aniya (1996). A retreat of 8 $\mathrm{m\,a^{-1}}$ occurred between 1928 and 1967 (Warren, 1994) and was followed by a fast retreat of 3.5 km (152 $\mathrm{m\,a^{-1}}$) until 1993, which formed a large proglacial lake, Laguna Ameghino. Aniya (1996) also measured at the snout a surface elevation decrease of roughly 100 m (−2.3 $\mathrm{m\,a^{-1}}$) between 1949 and 1993.

A very contrasting behaviour is found at the nearby Perito Moreno Glacier which was generally stable with periodic damming events recorded from the 1940s Naruse *et al.* (1995); Warren (1994); Aniya (1996, 1999).

Recent aerial variations were also analysed for the S. Rafael Glacier by Warren (1993), where fluctuating behaviour was found, often in contrast with the general trend of the NPI. A retreat of 3 km was recorded in the 1980s.

The Pio XI Glacier advanced at a rate of 1.45 $\mathrm{km^2\,a^{-1}}$ between 1945 and 1985 (Aniya *et al.*, 1997). Small frontal fluctuations were recorded between 1920s and 1945 when the glacier presented only one main front and did not dam the frontal fjord. After 1945 a very fast advance was recorded up to 1969, followed by slower advance (Warren & Sugden, 1993; Rivera *et al.*, 1997).

The strongest retreat until the mid-80s was registered at the O'Higgins Glacier and began in year ∼1896 from its LIA maximum, when it occupied the entire fjord up to the Isla Chica. A frontal retreat of ∼12 km occurred until 1986, major areal lossess were recorded between 1945 and 1975 (1.5 $\mathrm{km^2\,a^{-1}}$)

and between 1986 and 1995 (1.7 $km^2\,a^{-1}$). Approximate frontal thinning rates of −3.2 $m\,a^{-1}$ (1914 - 1933) and −6.7 $m\,a^{-1}$ (1933 - 1960) are reported (Aniya *et al.*, 1997; Casassa *et al.*, 1997).

Jorge Montt Glacier retreated a total of 18.5 km between 1898 (its maximum extent) and 2011 as documented by Rivera *et al.* (2012). Until 1945 a 6.7 km frontal retreat was recorded (146 $m\,a^{-1}$). The phenomenon accelerated abruptly and dramatically after 1990 making it the fastest retreating glacier of the Patagonian icefields: 6.6 km were lost until 1997 (943 $m\,a^{-1}$). Afterwards the retreat rates were 609 $m\,a^{-1}$ (1997 - 2000), 124 $m\,a^{-1}$ (2000 - 2008), finally a new phase of strong retreat has been recorded after 2008 with peak of 716 $m\,a^{-1}$ (2010 - 2011). Rivera *et al.* (2012) further measured the bathymetry of the 19.5 km fjord which was formed from the LIA maximum, presenting depths up to 390 m. These measurements are useful to assess subaqueous ice loss as described in Section 9.4.

The large Upsala Glacier underwent a significant retreat of about 5 km from 1980 to 2000, bathymetric surveys revealed a deep channel (up to 600 m) with the presence of bedrock rises which sustained the front between 1978 and 1990 slowing down its retreat. Afterwards the glacier front became floating and faster retreat rates were recorded until 1998 (Naruse & Skvarca, 2000). Relative frontal stability with seasonal fluctuations was observed until 2001 by Skvarca *et al.* (2002, 2003), who also provide new bathymetric data of Brazo Upsala of Lago Argentino along with calving rates and ice flow velocities of the glacier.

Glasser *et al.* (2011); Davies & Glasser (2012) use field determination of trimlines and terminal moraine location to derive the extent of the Patagonian icefields (NPI, SPI and Cordillera Darwin) at their LIA maximum, for the first time for all the former 640 glaciers (now 628). By comparing with recent Landsat multispectral images of years 1986, 2001 and 2011 they estimate the retreat rates for the last ∼140 years. The area reduction between 1870 and 2011 amounts to 660 km^2 (14.2%) for NPI and 1643 km^2 (11.4%) for SPI. Annual rates of area loss increased dramatically after 2001: −9.4 $km^2\,a^{-1}$ (−0.23%) for NPI and −20.5 $km^2\,a^{-1}$ (−0.15%) for SPI. Glasser *et al.* (2011) finally estimate a volume loss of 103 ± 20.7 km^3 in NPI from its Holocene peak extent in AD 1870 and 530 ± 101.1 km^3 in SPI from its Holocene peak in AD 1650. The corresponding sea level contributions are respectively 1.8 ± 0.4 $\mu m\,a^{-1}$ and 3.4 ± 0.7 $\mu m\,a^{-1}$.

5.5 Local ice thickness changes

Ice thickness change measurements have been mostly obtained through field studies usually limited to the ablation area of the most accessible glaciers and hence suffer from reduced coverage. Other techniques involved the use of cartographic maps, often generated from aerial photographs. The two methods are sometimes combined and historical data such as maps and photographs are often used for older periods. Unfortunately the accumulation areas remained mostly uncharted due to difficulty of access and lack of contrast on white smooth snow in aerial photographs (a problem still affecting optical DEMs). The increasing availability of optical satellite remote sensing data from the second half of the 80s allowed wide-scale measurements of glacier area, while large coverage elevation data started to be available in 2000 with the SRTM and ASTER missions.

A collection of elevation change field measurements found in the literature is given in Casassa *et al.* (2002). The most surveyed glacier with regards to thickness changes is probably Tyndall in SPI, where thinning of −2.0 $m\,a^{-1}$ in the period 1945 - 1993 is reported by Aniya *et al.* (1997). New field measurements of ice thickness from 1999 to 2002, including bathymetry of the Lago Geikie (in front of Tyndall Glacier) are reported by Raymond *et al.* (2005). They highlight an acceleration of the thinning trend and retreat of the main front of Tyndall Glacier. They relate this effect to a combination of climate and feedback processes, particularly melting due to lowering of the glacier surface (elevation feedback). Ice elevation changes from 1975 to 2003 on the glaciers of the Torres del Paine National Park (Tyndall, Grey, etc.) are provided by Rivera & Casassa (2004). Average thinning rates between −1.4 and −3.4 $m\,a^{-1}$ were detected on the ablation areas, while thinning rates on the accumulation areas were not reliable enough.

Thinning of the front of Upsala Glacier amounted to a rate of −3.6 $m\,a^{-1}$ between 1968 and 1990 (Aniya *et al.*, 1997). In a more recent study Sakakibara *et al.* (2013) offer a comprehensive study of the dynamics of this glacier from 2000 to 2011. They report a transition from a relatively stable phase to

a rapidly retreating and fast-flowing condition in 2008: frontal retreat of 2.9 km and velocity increase of 20 - 50% are measured between 2008 and 2011. An elevation change map for the period 2006 - 2010 was produced on the ablation area from DEMs obtained from ALOS panchromatic stereo pairs. They report change rates peaking at $-39.1\ \mathrm{m\,a^{-1}}$ at 1200 m from the 2010 front, while a much slower peak rate of $-12\ \mathrm{m\,a^{-1}}$ for the period 2000 - 2006 is derived using SRTM as elevation reference.

Elevation changes of Pio XI Glacier on a 5% surface fraction near the front was obtained by Rivera & Casassa (1999) from maps extracted from aerial photography from 1975 and 1995 where a thickening rate of $+2.2\ \mathrm{m\,a^{-1}}$ was found.

Elevation changes of Chico Glacier obtained through field data, aerial photography and an ASTER DEM amounted to a maximum of $-5.4 \pm 0.55\ \mathrm{m\,a^{-1}}$ at the front between 1975 - 1997. A thinning rate of $-1.9 \pm 0.14\ \mathrm{m\,a^{-1}}$ (1998 - 2001) in the accumulation area was inferred through GPS. A mass balance of $-0.29 \pm 0.1\ \mathrm{km^3\ w.e.\ a^{-1}}$ was finally derived for the period 1975 - 2001 (Rivera *et al.*, 2005).

5.6 Large-scale remote sensing studies

Due to the difficulty of , the higher altitude areas of the Patagonian icefields have been surveyed only by few field campaigns. Furthermore optical data on the plateau are often not reliable for elevation derivation due to lack of contrast and presence of clouds. Large-scale studies covering the entire icefields, with particular focus on elevation changes were initiated with the availability of remotely sensed data. Rivera *et al.* (2007) compared cartographic maps based on 1974/1975 aerial photographs with an ASTER DEM of 2001 over most of the NPI obtaining thinning rates up to $-4.0 \pm 0.97\ \mathrm{m\,a^{-1}}$. They updated the glacier outlines, particularly of the accumulation areas. Unfortunately significant parts of the smooth plateau could not be covered.

A geodetic mass balance of the NPI and SPI was first obtained by Rignot *et al.* (2003) by comparing the SRTM C-band DEM to cartography obtained with photogrammetry of the year 1968/1975 and 1995, although the elevation change maps are not reported. Recently the geodetic mass balance of NPI and SPI, along with the elevation change map, was derived using SRTM and ASTER DEMs by Willis *et al.* (2012b) and Willis *et al.* (2012a), respectively. These geodetic mass balance studies are presented in depth in Section 9.1. Their results are finally compared to those obtained in this study in Section 9.5.

Some gravimetric mass balances have been published for the Patagonian icefields. Jacob *et al.* (2012) obtained globally a mass loss rate of $-148 \pm 30\ \mathrm{Gt\,a^{-1}}$ excluding Greenland and Antarctica, contributing $0.41 \pm 0.08\ \mathrm{mm\,a^{-1}}$ to sea level rise. They report for Patagonia a mass loss rate of $-23 \pm 9\ \mathrm{Gt\,a^{-1}}$, although the exact geographical area included the estimate is not clear. This result is in good agreement with the $-25.1 \pm 9.9\ \mathrm{Gt\,a^{-1}}$ ($\sim -1.6\ \mathrm{m\,a^{-1}}$ average ice thinning) previously obtained on NPI+SPI for the period April 2001 - December 2006 by Chen *et al.* (2007) from GRACE data after corrections for postglacial rebound and hydrological effects. Similarly an ice loss of $-26 \pm 6\ \mathrm{Gt\,a^{-1}}$ was obtained for NPI+SPI between 2003 and 2009 by Ivins *et al.* (2011). Particular focus was put on the correction of the contribution of the solid Earth glacial isostatic adjustment (GIA) to LIA cryospheric loading, which are particularly strong in this region. Gardner *et al.* (2013) provide a global estimate of ice mass loss from gravimetry and altimetry measurements. Their main finding is that global extrapolations of local measurements (from field surveys) led to an overestimation of global melting rates. They report a global mass loss excluding Greenland and Antarctica of $-215 \pm 26\ \mathrm{Gt\,a^{-1}}$, The contribution of the southern Andes area of 29400 $\mathrm{km^2}$ is very significant with respect to its surface and amounts to $-29 \pm 10\ \mathrm{Gt\,a^{-1}}$ (from gravimetry).

The Patagonian icefields and particularly SPI are subject to the fastest present-day crustal uplift rates due to glacial isostatic adjustment as measured by Ivins & James (2004) and Dietrich *et al.* (2010) with GPS observations. This is due to the combination of rapid ice melting and a unique low viscosity of the underlying mantle caused by slab-window tectonics. Uplift rates up to $40\ \mathrm{mm\,a^{-1}}$ are measured near the plateau of SPI decreasing to $25\ \mathrm{mm\,a^{-1}}$ at a distance of approximately 120 km. These results are presented in more detail in Section 9.3.8.

Schaefer *et al.* (2013) and Schaefer *et al.* (2015) used a combined modelling approach based on NCEP/NCAR reanalysis data to simulate the annual surface mass balance of NPI and SPI, respectively.

The model was calibrated with geodetic mass balance data of three non-calving glaciers and point mass balance measurements preformed in NPI. They subtract geodetic mass balance results in order to derive the calving fluxes for the main glaciers finding a strong increase in the period ~2000 - 2010 compared to the period 1975 - 2000. They validate the model with a few punctual in situ measurements of mass balance finding there good agreement. Unfortunately the Patagonian icefields (particularly SPI) present strong spatial (horizontal and vertical) gradients of accumulation as well as significant annual variations, making unreliable the validation of the model based on a few punctual measurements of mass balance.

5.7 Other relevant studies

Ice thickness measurements were performed along some profiles on a few glaciers using radio-echo sounding and radar systems, their coverage is nevertheless limited. For instance an ice depth of up to 650 m was measured on the ablation area of Tyndall (Casassa *et al.*, 2002).

Ice velocity measurements have been carried out on the ablation area of some of the main glaciers with traditional surveying methods. With the availability of SAR images mainly from the SIR-C/X-SAR Shuttle Mission of 1994, the first flow velocity fields covering larger regions could be derived from interferometry and amplitude tracking. A collection of published ice flow velocity results until 2002 is reported by Casassa *et al.* (2002).

Rott *et al.* (1998); Stuefer (1999) initiated in 1995 a comprehensive field program supplemented by spaceborne radar data on the Perito Moreno Glacier in order to describe its accumulation, ablation, calving and flow dynamics. Ice velocity and ablation were measured using stakes at three profiles. Ice thickness of 440 m in average and up to 720 m was measured by seismic reflection along two of the profiles. The bathymetry of the lake in front of the glacier was surveyed. Field velocities were obtained from SIR-C/X-SAR images through InSAR and amplitude tracking supporting the derivation of the calving rate. Because of the difficulty of access, direct measurements of accumulation rates could not be done but were deduced from other measurements. A weather station was deployed close to the glacier front. An average annual net accumulation of 5.54 ± 0.5 m w.e. is one of the highest worldwide. Contrary to its neighbouring glaciers, the Perito Moreno is in a stable state thanks to the high calving flux to net accumulation ratio and the particular topography of the frontal peninsula and the bathymetry of the lake. The investigations were carried on during the seven successive years with further field measurements and with the estimation of the climate sensitivity of the mass balance derived using a degree-day model. This revealed comparable relevance of temperature and precipitation (Stuefer *et al.*, 2007). The derived net mass balances range from -18 m w.e. a^{-1} at the terminus to $+7.6$ m w.e. a^{-1} in the upper section of the accumulation area. Cumulative mass balance was slightly negative in the period 1988 - 1998, it then turned slightly positive, suggesting that the damming events in 2003/04 and 2005/06 were triggered by minor mass-balance fluctuations.

Koppes *et al.* (2011) analysed mass balance variations at the San Rafael Glacier over the period 1950 - 2005 using NCEP/NCAR reanalysis climate data together with local historical observations of climate, accumulation, ablation thinning, calving and retreat. The glacier underwent retreat and thinning since 1959 but not at the faster rates as other glaciers. The calving mechanisms and driving factors are well studied in this publication, suggesting that calving rates are inversely proportional to retreat rates and mainly controlled by terminus geometry.

Barcaza *et al.* (2009) derived oscillations of the equilibrium line altitude (ELA) of the entire NPI using Landsat images spanning from 1979 to 2003 and an ASTER DEM. The average ELA ranges between 870 m and 1529 m with lower altitudes on the western side.

A review of remote sensing based methods for glacier mass balance estimation, with particular focus on the Patagonian icefields is given by Bamber & Rivera (2007). They stress how remote sensing is the only viable approach to deriving wide area glacier mass balances and discuss the strengths and weaknesses of the different methods. Among those are: observation of elevation changes, estimation of ice flux, repeat measurements of areal changes, estimation of the snow line altitude and of the accumulation-ablation area ratio (AAR).

Observations of melting and refreezing timing of the glacier surfaces are possible using passive microwaves thanks to the high sensitivity to the smallest amounts of moisture of the brightness temperature T_b in the 18 - 19 and 36 - 37 Ghz bands (Ulaby *et al.*, 1986). The AMSR-E[2] sensor (Kawanishi *et al.*, 2003) features a 36.5 GHz vertically polarized channel with 8 × 14 km resolution. Mapping T_b with high temporal frequency, allows to determine the spatial and temporal extents characterized by frozen, wet, or transition-state snow. Such a mapping was performed on the entire SPI for the period 2002 - 2008 by Monahan & Ramage (2010). They determine the onset and the duration of the spring melt-refreeze period allowing to identify melt regimes and seasonal signals. They find that spring melt-refreeze period underwent a shortening rate between 10 and 16 $\mathrm{d\,a^{-1}}$ between 2002 and 2008. Willis *et al.* (2012b) use multiple daily observations from AMSR-E to extract surface melt parameters such as intra-day fluctuations and diurnal amplitude variations over NPI. These are used to interpret the ice elevation change and velocity results obtained from ASTER data. They confirm the temperate nature of the NPI with melting from October to March even at the highest altitudes (see Section 5.3). They report that the eastern margin has a continental climate with wet surface half of the summer days and frozen snow during 80% of winter days: the lower temperatures are due to the higher elevations and the lower precipitation is due to the orographic barrier. The western side has a maritime climate with wet snow half of the year, particularly in the southeastern margin where elevations are lower. The glaciers Acodado, Benito and HPN 1 are wet during the entire summer. They suggest a link between the wetness of the accumulation area and the acceleration of the glaciers, and indicate a possible cause in the rise of sub-glacial water pressure (originating from melt or rainwater on the surface and sub-surface) making its way to the glacier bed and reducing basal friction. During the 8 years of observation they did not detect a clear trend of surface wetness behaviour but observe how areas of strongest thinning also have the largest duration of wet surface.

First glacier elevation change maps based on TanDEM-X DEMs and older SRTM DEM were obtained over some glaciers of SPI (Abdel Jaber *et al.*, 2012) and NPI (Abdel Jaber *et al.*, 2014) along with glacier ice flow velocities through amplitude tracking applied to TerraSAR-X repeat pass images. The Upsala Glacier displayed strong thinning rates between 2000 and 2011. A significant frontal retreat was detected between January 2008 and October 2009 in conjunction with a very strong acceleration phase, with frontal velocities increasing from 4.7 $\mathrm{m\,d^{-1}}$ to 10 $\mathrm{m\,d^{-1}}$. The main front reached the Bertacchi tributary and underwent slight deceleration in October 2011 reaching 9 $\mathrm{m\,d^{-1}}$. The Perito Moreno Glacier confirmed its stable state with peak velocities of 6 $\mathrm{m\,d^{-1}}$ at the narrow upstream channels. The Ameghino Glacier displayed significant thinning at its terminus with velocities around 0.9 $\mathrm{m\,d^{-1}}$. A significant thinning signal was detected on the western side of NPI, particularly in the southwestern glacier termini (led by HPN 1 and Steffen Glacier) but also on the plateau. The San Rafael Glacier confirmed to be extremely fast (>15 $\mathrm{m\,d^{-1}}$ at the snout) while the S. Quintin Glacier moved at around 2 $\mathrm{m\,d^{-1}}$ at the main front and 2.5 $\mathrm{m\,d^{-1}}$ at the upstream bend. The ice elevation change of the entire SPI, published in this thesis was previously shown in Abdel Jaber *et al.* (2013).

[2]Advanced Microwave Scanning Radiometer for EOS on board of the Aqua satellite

Chapter 6

Elevation and other datasets

This chapter describes the remote sensing data used to compute the geodetic mass balance of NPI and SPI. The focus is set on the two remote sensing missions dedicated to the generation of a global DEM by means of bistatic InSAR: SRTM (Section 6.1) and TanDEM-X (Section 6.2). Different aspects of these complex mission are described in order to understand the main issues affecting the generated DEMs. Significant space is dedicated to the literature dealing with the DEM accuracy for both missions. Finally the data used in this work are summarized. In Section 6.3 the glacier outline defining the area of the icefields is described, with particular attention to its uncertainty. Supplementary remote sensing data exploited in this study are also listed in this section.

6.1 SRTM

The Shuttle Radar Topography Mission (SRTM) (Farr *et al.*, 2007; Rabus *et al.*, 2003) produced the most complete and highest resolution DEM of the Earth at its time. Such a dataset is fundamental for practically any geoscientific application. Up to this mission no global elevation dataset was available, instead many national datasets characterized by different accuracy, datums were available in most developed countries. Most of the remote regions of the Earth, such as Patagonia were covered by low quality elevation data. The objective of a global and consistent coverage with quantified accuracy could only be met by shifting the observation point to space and by relying on the relatively new InSAR technique allowing to surpass the insurmountable limitations of optical stereo mapping (cloud cover, matching on low contrast areas such as snow and poor positional control).

The SRTM was a joint project of NASA, DLR and ASI. It was flown on board of Space Shuttle Endeavour during the 11-day mission STS-99, with launch 11 February 2000 17:44 UTC and landing 22 February 2000, 23:22 UTC. Mapping operations took place during approximately 9 days (begin at MET 00/11:47 and at MET 09/18:10) (Seal & Rogez, 2000).

The mission built upon previous Space Shuttle radar imaging missions and particularly on the SRL-1 and SRL-2 (April and October 1994) which tested the SIR-C/X-SAR payload (Evans *et al.*, 1997), a fully polarimetric SAR system at L-band and C-band with electronic scanning capabilities coupled with an X-band single polarization VV mechanically steered radar developed by DLR and ASI.

The SRTM mission objective was to produce a DEM of all land between 60°N and 56°S (80% of the Earth's land surface) with 1×1 arcsec ($\sim 30 \times 30$ m) sampling, with linear vertical absolute height error of less than 16 m, linear vertical relative height error of less than 10 m, circular absolute geolocation error of less than 20 m, and circular relative geolocation error of less than 15 m. The relative height error of the X-band DEM was to be less than 6 m. All errors are quoted at 90% confidence level (Farr *et al.*, 2007).

The only viable way to achieve such accuracies, besides the global coverage within a short time span and automatic processing of large amounts of data, was to rely on single-pass bistatic interferometry as opposed to repeat-pass acquisitions. This is mainly for two reasons: (1) avoid variability of the target surface, leading to decorrelation, and of the atmospheric screen, causing phase delays; (2) to have a precise knowledge of the baseline and other systematic effects at all times.

The SRTM payload consisted of a radar system based on the SIR-C/X-SAR system, the JPL was responsible of the C-band subsystem while DLR for the X-band one, while the L-band was not activated. The antenna/mechanical system (AMS) had to be updated: most notably, to achieve the single-pass capabilities two receive-only C and X-band outboard antennas were mounted at the end of a retractable 60-m-long mast, constituting the baseline needed for interferometry. A newly developed attitude and orbit determination avionics (AODA) was included. The whole system architecture and parameters, including the flight and ground segments are well resumed by Shen *et al.* (2000).

The C-band radar system (5.6 cm wavelength) was the main mapping instrument. It was formed by a 12 m inboard antenna and an 8 m receive-only outboard antenna, both made of distributed active phased arrays with dual-pol. The ground swath of the SIR-C antenna was about 60 km wide, too narrow to meet the requirement of a global coverage within 10 days. To double the swath width, ScanSAR was used: halving the illumination time of a target allowed generating two electronically-steered 60-km beams, at the cost of resolution loss. A minimum of 50% time was required to meet noise performance requirements, limiting the ScanSAR to two beams. To double again the swath the polarimetric capabilities of SIR-C were exploited: one HH and one VV, independently-steered, beams were transmitted simultaneously. The combination of the two techniques allowed a 225 km swath. The look angle ranges from 30° to 56° (see Table 8.1). The coverage configuration of the four sub-swaths sequence (1: HH, 2: VV, 3: VV, 4: HH), along with other system parameters are represented by Figure 6.1.

The X-band radar (3.1 cm wavelength) operating only at VV polarization did not feature electronic steering. The main inboard antenna was 12 m long and the receive-only, outboard antenna 6 m long. It was included as an experimental demonstration, featuring higher resolution and better SNR than the C-system, allowing an independent quality control. It featured a 50 km swath which was steered mechanically to a look angle (at scene centre) of 54.5°, falling between sub-swaths 3 and 4 of the C-system (cf. Figure 6.1). The characteristics of this system and the DEM produced are well described by Rabus *et al.* (2003). In this work this dataset was not used and hence will not be discussed in detail.

The antenna/mechanical system (AMS) was updated from the SIR-C, mainly by removing some L-band panels to save weight and by adding the entire outboard antenna system (OASYS), attached to a 60 m deployable mast (stowed into a canister) through a mechanical alignment system. The mast had to be rigid in order to withstand dynamic loads of orbital adjustment manoeuvres and thermally inert to maintain alignment between the antennas at varying temperature. In mapping configuration the mast was to be 45° relative to the nadir vector in order to maintain the correct alignment between the antennas and hence the interferometric capability. To counteract gravity-torque a cold-gas thrust system was included at the tip of the mast to reduce orbital manoeuvres and spare propellant. Unfortunately this system failed, increasing the need of attitude control system firings, which triggered resonation and oscillations of the mast. These were relatively strong (maximum amplitude of 10 cm) because the passive damper at the root of the mast failed to function as well. Furthermore a quasi-static pointing bias was caused by gravity unloading, load shifts during launch and preflight assembly errors. Thermal deformation caused pointing errors with time constants of several minutes. The mast pointing errors had to be measured constantly by the AODA to be compensated by the radar and the ground processing system. The attitude adjustment manoeuvres (trim bursts), performed to maintain the correct orbit and pointing, were 8 in total spanning the duration of the mission (two were cancelled to save fuel in response to the cold-gas thruster failure), they were carefully planned to take place in quiet periods where almost no science acquisitions were planned, mostly over the Pacific Ocean, partially over Siberia (with no concurrent data recording). With respect to the study area, the trim bursts, happened to be very much apart from the beginning or ending of the acquisitions on SPI and NPI. Three of them were followed (approximately 20 - 30 minutes later) by acquisitions on the southernmost tip of the South America below 54°S (Seal & Rogez, 2000). An in-depth analysis of the stability and control of the system is given by Hamelin *et al.* (2002).

The attitude and orbit determination avionics (AODA) had to provide precise annotation of the interferometric baseline length, attitude and position with accuracies of 2 mm, 9 arcsec and 1 m, respectively (90% or 1.6 sigma confidence level). Furthermore it was used to ensure correct mast deployment and antenna alignment. This was fundamental to maximise the overlap of the antenna

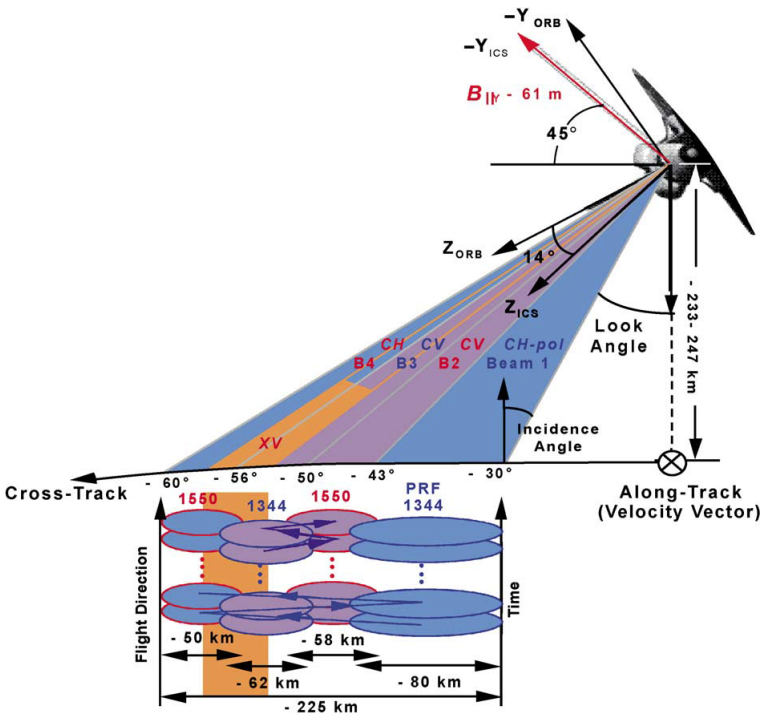

Figure 6.1 – SRTM beam geometry and acquisition configuration. C-band subswaths are shown in blue (1 and 4: HH-pol) and purple (2 and 3: VV-pol). The X-band swath, centred at 55°, is shown in orange. The ScanSAR illumination sequence is shown with blue and purple arrows. Image from Rabus *et al.* (2003).

patterns, the roll axis was less critical but the error about the yaw and pitch axes could not exceed 0.06°. The AODA consisted of many sensors, including a star tracker, an inertial reference unit, an optical target tracker and electronic distance meters. The first two measured the inertial platform attitude, while the last two measured the outboard antenna relative attitude and position (through targets located at the end of the mast). Finally, orbit (platform position and velocity) was determined to 1 m accuracy through differential GPS.

The nominal altitude was 233.1 km on a circular orbit with 57° inclination, leading to repeat cycle of 159 orbits in 9.8 days. During mapping the shuttle flew tail first with a left looking radar. The orbital separation of 218 km and the C-band swath of 225 km at the equator meant that a single 159 orbit cycle would be enough for the complete planned coverage. Actual mapping lasted 149 orbits achieving a coverage of 99.96% of the target surface (C-band), the 10 missing orbits leading to some unsurveyed patches in North America. The total raw data volume amounted to 12.3 TB. The X-band system achieved a coverage of 40% of the target surface.

The detailed data processing chain of the C-band SRTM data is fairly articulated and transcends the scope of this work, for a detailed description the reader is referred to Farr *et al.* (2007) and for more specific processing details to Hensley *et al.* (2000). The burst mode interferometric processing of the ScanSAR data is detailed in Holzner & Bamler (2002).

The extensive amount of data recorded by the AODA had to be reduced and blended but was fundamental to obtain the accuracy goals. Without this data a precise estimation of the baseline and its angle as well as of the position and height of the platform would have been impossible.

A priori elevation information was available and was used both for calibration and for validation (mutually exclusive). This included a 500-m-posting global DEM collected from different sources which was used to determine the approximate local height, together with a precise tidal model used to tie each datatake (which always started and ended on the ocean) to sea level. Furthermore ground control points distributed over the Earth were available.

The datatake was divided in bursts of approximately 1 km along-track and 60 km across-track originating from the four sub-swaths. For each burst the interferogram was obtained and combined into a larger patch interferogram. Filtering was applied to the patch interferograms with varying looks:

1 - 2 for beam 1 increasing to 2 - 4 for beam 4. Phase unwrapping was applied on a patch basis using a branch-cut algorithm (Goldstein *et al.*, 1988). Phase continuity between patches was assured and the phase as bootstrapped from one patch to the next, allowing unwrapping of an entire strip (ocean to ocean). The absolute phase was obtained by averaging the unwrapped phase to 500 m and comparing it to the low-resolution external DEM (particularly over the ocean), finding the multiple of 2π which minimized the standard deviation, thus resolving the phase ambiguity (Hensley *et al.*, 2000).

Heights of ambiguity ranged 125 m to 325 m. The original resolution was approximately 30 m but an adaptive variable-resolution smoothing inversely proportional to slope was applied, leading to a final product resolution of 45 to 60 m (Smith & Sandwell, 2003).

After several calibration steps involving different aspects of the system the mosaicking of the so-called strip data is performed on a continental basis. The most critical aspect was avoiding large-scale variations on a continental scale, key to ensuring this was the high degree of overlap of ascending and descending as well as neighbouring acquisitions. Tie points were generated from the overlapping regions through cross-correlation of topography, these were accumulated on the entire continent (in addition to GCPs) and used to adjust all strips relative to the others via a vast least-squares inversion. For each output $1° \times 1°$ cell all strip data were adjusted three-dimensionally according to the parameters estimated and then interpolated to the output grid. Final elevation pixels are obtained by an error-weighted average: weights are the inverse of the variances of the height error obtained from interferometric correlation. As a last step elevations are converted to the EGM96 geoid and quantized to 1 m (Farr *et al.*, 2007).

The processing was carried out at the Jet Propulsion Laboratory (JPL) and the DEM made available by the U.S. Geological Service (USGS) as an "unfinished" version 1.0. Data within the U.S were released with 1 arcsec posting while for the rest of the world with 3 arcsec posting. The DEM complied with the DTED-2[1] specification in its 1-arcsec version and with DTED-1 in its 3-arcsec version. The NGA (National Geospatial-intelligence Agency) post-processed the global DEM producing a "finished" version (Slater *et al.*, 2006) with editing, spike and pit removal, water body levelling and coastline definition, data were returned to NASA and distributed as version 2.0, here the 3 arcsec posting was obtained by sub-sampling. Version 2.1 by JPL/NASA recalculated the 3 arcsec DEM by averaging instead. Version 2.0 and 2.1 have voids where InSAR did not work (mostly due to phase unwrapping errors or lack of coherence), a subsequent void-filled version at 3 arcsec was produced by NGA based on license-restricted commercial data (Grohman *et al.*, 2006). With version 3.0 (known as SRTM Plus) the main goal of JPL/NASA was to eliminate voids in the 2.1 DEM with reliable elevation information, this was achieved mainly with ASTER GDEM2 and secondarily with the USGS GMTED2010 or NED elevation datasets. In 2015 version 3.0 was also gradually released in 1 arcsec posting for the entire globe, new 3-arcsec version are also available, both through averaging and sub-sampling.

6.1.1 SRTM validation and accuracy

A full report of the SRTM C-band DEM validation is given by Rodriguez *et al.* (2005) and an abridged version is published by Rodriguez *et al.* (2006). They summarize the main error sources affecting SRTM, which are reported below:

- Baseline roll angle error: which translates into a slope error in range with equal magnitude. The natural modes of oscillation of the mast, which constitute the main component of the baseline movement, can be modelled and removed. On the other hand the attitude manoeuvres of the Shuttle cause residual roll errors with wavelengths of thousands of kilometres and peak of approximately ±10 m (estimated over the ocean).

- Phase errors: they are caused by two sources: (1) thermal or differential speckle noise, (2) systematic phase variations due to antenna pattern mismatch or long term drifts of the electronics. Clearly the first source is random and with the shortest correlation lengths and cannot be compensated. The different antenna pattern along look angle cause a phase screen, which is estimated over the flat ocean surface and corrected. A very slow drift of the differential phase

[1] Digital Terrain Elevation Data

was probably caused by temperature variation of the instrument. The uncorrected phase errors are negligible compared to the residual roll angle errors.

- Beam differential errors: the four beams have systematic time-varying phase differences which induce height jumps between beams. The height difference on the beam overlap is used to compute an azimuth correction. This correction ensures consistency over the 225 km swath: the residual error is negligible (below 10 cm).

- Timing and position errors: they are caused by uncompensated delays or errors in the estimated baseline position and result in geolocation errors. They are corrected with GCPs, such as corner reflectors.

For the purpose of STRM DEM validation the NASA and the NGA collected an extensive ground truth dataset using kinematic GPS (KGPS) along radar-identifiable roads spanning all continents. 9.4 million samples were acquired with a general accuracy of 0.5 m (1 σ), unreliable points have been eliminated and data within a SRTM 30 m pixels averaged. Points were divided in two datasets, for the validation of the absolute height and of the geolocation accuracy. With these data Rodriguez *et al.* (2005, 2006) estimate a spatial error spectrum and absolute error estimates with high confidence which are valid on a continental basis even away from the KGPS tracks. The main drawback of the KGPS data is their confinement to regions of moderate topography and low vegetation, hence probably leading to optimistic results for high relief terrain, but some GCPs for such terrain over the Hindu Kush were also used.

The results show that the absolute vertical accuracy is better than 9 m, almost two times lower than the nominal value. Higher values are found on steep terrain (Himalayas, Andes) and smooth surfaces (Sahara). A spatial analysis of the error showed that it can be divided in three parts: (1) speckle noise decorrelating with distances of about one to two pixels, (2) random (medium to short wavelength) errors constituting the dominant error source and varying with surface brightness, slope and number of observations, (3) long wavelength error component caused mainly by residual roll errors with a magnitude of about 2 m and spatially non-stationary behaviour, this is uncorrelated with the random error.

Rodriguez *et al.* (2005, 2006) finally report continent-based summary of errors (expressed as 90%, 1.64 σ errors). For South America, they report an absolute geolocation error of 9.0 m, an absolute and relative height error of 6.2 m and 5.5 m, respectively and finally a long wavelength height error of 4.0 m. All figures improving significantly over the nominal values.

Brown *et al.* (2005) present results of an independent assessment of the SRTM DEM accuracy, realized by deploying an array of active and passive (trihedrals, tophats) calibration targets in south-eastern Michigan during four SRTM passes with both C-band and X-band coverage. They found that the SRTM DEM exceeds mission specifications for absolute and relative accuracies for these targets.

Carabajal & Harding (2006) compared on a global scale the SRTM C-band DEM to data from the Geoscience Laser Altimetry System (GLAS) on board the Ice, Cloud, and land Elevation Satellite (ICESat) with particular focus on vegetated areas to quantify the phase centre of SRTM. They found that in areas of low relief and sparse tree cover the difference of the ICESat centroid elevation minus the SRTM DEM varies between −3.9 m and 1.0 m (positive mean values are found only in Asia) with standard deviations between 3.0 and 3.7 m. Even at increasing roughness and tree cover the mean difference remains unbiased but standard deviations increase. For increasing roughness the variability increases significantly. The SRTM elevation on vegetated areas is in average approximately 40% of the top canopy height from the ground. Their results confirm the improvement over the 16 m nominal absolute elevation accuracy of SRTM particularly where topography is less rough.

Hoffmann & Walter (2006) evaluate the complementarity of the SRTM C-band and X-band DEM and propose a technique for the merging of the two datasets. They compare the resulting combined DEM and the original DEMs at 1 arcsec in four regions of the world (including the Andes) and also with an extensive network of 1125 GPS profiles (200k measurements with meter-level accuracy) in an alpine region in southern Germany. The global elevation difference map shows areas with significant offsets up to 10 m in magnitude, displaying high spatial correlation and slow variation in space. The largest

differences appear as a systematic bias at low spatial frequencies. They explain the inconsistencies as a possible difference in the block adjustment of the DEMs. They interpolated the elevations at the GPS points using a bilinear interpolation from the four nearest DEM grid points. Median (and mean) GPS—DEM differences are −73 cm (−26 cm) for the C-band and −55 cm (−17 cm) for the X-band, they are mostly due to higher DEM elevation on vegetated areas (agreeing with lower canopy penetration at X-band). 90% of the difference values were below 5 m from the GPS values, significantly better than the specifications. The histograms of the differences are very similar and follow closely a Gaussian distribution, with the exception of numerous outliers caused by phase unwrapping errors, particularity in the X-band DEM which did not have overlapping acquisitions (the C-band DEM had three). The standard deviation of the histograms are 3.9 and 4.0 m the C- and X-band DEMs. It is also noted that the X-band DEM has higher pixel-to-pixel noise than the C-band DEM, which was filtered and is obtained as average of many acquisitions. The X-band DEM on the other hand follows better fine scale detail which is lost in the C-band DEM. They also found that combining the two DEMs yields to a standard deviation of the difference histogram of 3.4 m and reduction in phase unwrapping errors.

Felbier (2009) compares globally the SRTM C-band and X-band to ICESat data using $1° \times 1°$ cells in order to detect long-wavelength height errors and correct them with a method based on spherical harmonics. Significant areas of error are generally found on all continents with magnitudes up to ±4 m and scales of variations in the order of hundreds to thousands of kilometres (Felbier, 2009; Huber *et al.*, 2009; Wendleder *et al.*, 2016). According to his results, the STRM C-band DEM of the South American continent seems to be affected by a vast zone of lower heights below the equator in rough correspondence to the Amazon rainforest (possibly influenced by signal penetration into the canopy), south of which a vast zone of higher elevations is detected particularly along the western coast between 12°S and 40°S. Some areas of higher elevations up to 3 m are also found along the central part of the continent. The rest of the continent, particularly in the north and the south seem to have no bias with ICESat. The area of NPI and SPI is relatively small compared to the scale of these errors, which, even if present would likely affect the region with a similar amplitude. Anyhow the entire southern tip of the continent (including SPI and NPI) seems not to be affected by such biases. Three isolated cells with higher values up to 4 m are found in correspondence of the western margin of SPI (48°S - 51°S; 73.5°W - 74.5°W), they do not fit the typical pattern shown by these errors and could be outliers or due to glacier thinning.

6.1.2 SRTM data used

The Patagonian icefields are located between 46.5°S and 51.5°S, with a width of about 50 km and a length of 150 km for NPI and 350 km for SPI. Given their high latitude, a large amount of datatakes was acquired in both ascending and descending orbit direction over these regions. The list of all 18 datatakes acquired over NPI and SPI and surrounding terrain is reported in Table 8.2. The high degree of overlap between the interwoven datatakes leads to increased accuracy due to averaging and to less voids (phase unwrapping or low coherence). On the other hand, the topography of the region is very rough, causing a higher error, but the terrain of interest for this work, namely the glaciated surface is relatively smooth and not too steep. At these latitudes the heading angle is very small meaning almost east - west acquisitions, which, given the geography of the continent, leads to very short datatakes (average 3 minutes) with ocean coverage before and after, likely improving the general calibration quality of each datatake.

The SRTM C-band DEM used in this work was extracted from the DLR - Earth Observation Centre (EOC) W42 database (Habermeyer *et al.*, 2009). It is version 2.1 of the DEM at 3 arcsec posting with heights referenced to the WGS84 ellipsoid and quantized to 1 m. For this region elevations are 14 to 21 m higher than orthometric (or geoid) heights. The sea level height on the western fjords is 16 m in the SRTM DEM.

Figure 6.2 – Artistic rendition of the TSX and TDX satellites flying in tandem formation and acquiring data in bistatic mode.

6.2 TanDEM-X

The TanDEM-X (TerraSAR-X add-on for Digital Elevation Measurement) mission (Krieger *et al.*, 2007) constitutes the first spaceborne single-pass SAR interferometer and was initiated in June 2010 with the launch of the TanDEM-X (TDX) satellite which was coupled in a tandem formation to the almost identical TerraSAR-X (TSX) satellite, launched in June 2007 (Figure 6.2). The main objective is the generation of a truly global high resolution DEM. The TanDEM-X mission is a public-private partnership between the German Aerospace Center (Deutsches Zentrum für Luft- und Raumfahrt - DLR), responsible of the mission planning and operations as well as the scientific data management, and Airbus Defence and Space (formerly EADS Astrium), responsible for the satellite construction and the commercial exploitation of the final DEM, the so-called WorldDEM™, through its subsidiary Infoterra.

6.2.1 The TanDEM-X mission

Objectives The primary objective of the mission is the generation of a truly global, consistent, high resolution and high precision DEM, a fundamental dataset for a wide range of scientific and commercial applications. The previous and sole similar effort was the SRTM mission, which lacked full coverage and complied with the DTED-2 specification and only with the DTED-1 for the publicly available (outside the USA until 2015) 3-arcsec DEM (cf. Section 6.1). The goal was to produce a final DEM complying with the HRTI-3 (High Resolution Terrain Information) specification. A comparison between the DTED-2 specifications to which the SRTM 1-arcsec DEM complies and the TanDEM-X final DEM nominal specifications is given in Table 6.1. A visual comparison between the SRTM 3 arcsec C-band DEM used for this work and a TanDEM-X Raw DEM, processed at 0.2 arcsec over the terminus of Pio XI Glacier (SPI) and surroundings is shown in Figure 6.3. Several secondary mission objectives are also foreseen, among these are along-track interferometry (ATI) applications such as road traffic monitoring and ocean currents measurement, single-pass polarimetric SAR interferometry, digital beamforming, etc.

Orbit and tandem formation The achievement of an interferometer for global mapping is strictly dependent on a precise flying formation. The TDX spacecraft normally maintains a distance between 200 and 500 m from TSX, which keeps its sun-synchronous dawn-dusk orbit with 11-day repeat cycle. This flying formation (shown in Figure 6.4), known as HELIX (Moreira *et al.*, 2004), consists of two

Table 6.1 – Specifications of the final TanDEM-X DEM and of the DTED-2 standard (complied by the SRTM C-band 1-arcsec DEM).

Requirement	Specification	DTED-2 (SRTM C-band)	TanDEM-X
Relative vertical accuracy	90% linear point-to-point error over a 1° × 1° cell	12 m (sl <20%) 15 m (sl >20%)	2 m (sl <20%) 4 m (sl >20%)
Absolute vertical accuracy	90% linear error	18 m	<10 m
Relative horizontal accuracy	90% circular error	15 m	3 m
Absolute horizontal accuracy	90% circular error	23 m	<10 m
Spatial Resolution	independent pixels	30 m (1 arcsec @ 0°N)	12 m (0.4 arcsec @ 0°N)

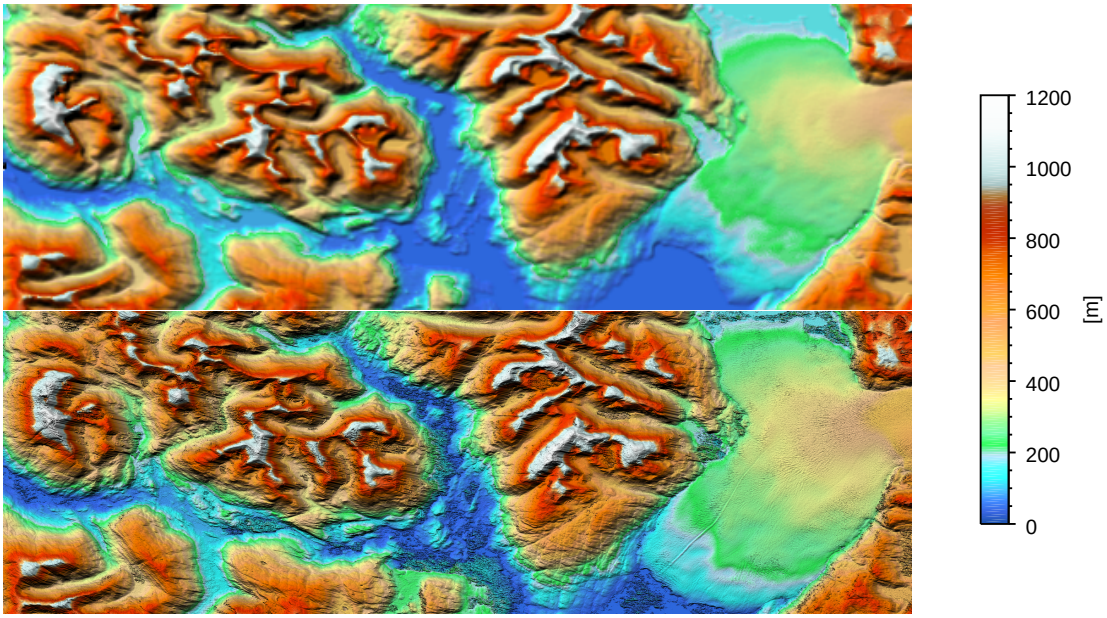

Figure 6.3 – Visual comparison of the SRTM C-band 3 arcsec DEM and a TanDEM-X Raw DEM (AID: 1057982 from 2012.02.16) processed at 0.2 arcsec over the terminus of Pio XI Glacier (SPI). The improvement in detail is appreciable in the TanDEM-X DEM, for example the crevasses pattern and longitudinal feature on the glacier terminus. The frontal advance and thickening of Pio XI is also noticeable in this comparison. Note that the blue colour shades do not necessarily indicate water here.

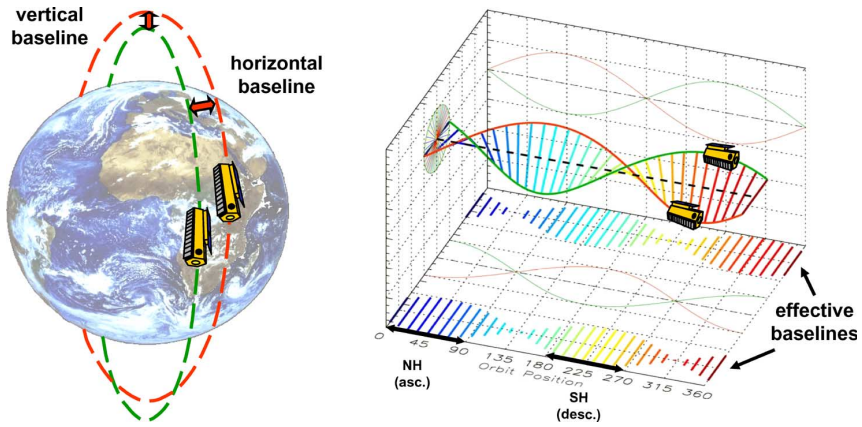

Figure 6.4 – HELIX satellite formation for TanDEM-X. Left: Orbital arrangement with horizontal (cross-track) and vertical (radial) baselines. Right: Cross-track baselines along one complete orbit cycle in Northern (NH) and Southern Hemisphere (SH). From (Krieger *et al.*, 2007).

orbits with slightly different ascending nodes, ensuring the maximum horizontal (cross-track) orbital displacement at the equator, and slightly different eccentricity, ensuring maximum vertical (radial) separation at the poles, and forming a relative helix-like movement of the satellites. Collisions are intrinsically avoided without the need of autonomous control as orbits do not cross. Furthermore this allows arbitrary shifts of the satellites along their orbit (baselines: 200 to 10 km across-track and 0 to 100 km along-track) adapting the acquisition configuration to different terrain or applications (e.g. ATI) (Krieger *et al.*, 2007).

Payload The TDX satellite is nearly a copy TSX, which was built itself with systems for tandem operation, such as X-band horn antennas for intersatellite phase synchronization, dual-frequency GPS for precise orbit determination, a SAR instrument with extremely stable phase, pulse repetition frequency (PRF) based on GPS as a common reference. The instrument on board of the two satellites is a high resolution SAR capable of operating in the standard Stripmap, Spotlight and ScanSAR with quad-pol capabilities. The central frequency is 9.65 GHz with a nominal chirp bandwidth of 100 MHz, increasable up to 300 MHz. The phased array antenna (aperture 4.8 m × 0.7 m) mounted on the spacecraft body is composed by 12 panels with 32 waveguide subarrays allowing flexible beam pointing and beam shaping.

Acquisition modes The satellites fly at an altitude of 514 km (at the equator), the swath width is approximately 30 km in Stripmap mode, which is used operationally during the mission. Several interferometric acquisition modes are possible. The operational mode is the bistatic one, where one of the two satellites transmits pulses illuminating a radar footprint and both receive the signal scattered by the Earth surface. This mode allows the elimination of temporal decorrelation and atmospheric perturbations in the interferometric phase. Both satellites can transmit and exclusion zones are foreseen along the orbit to avoid mutual illumination. The pursuit monostatic mode constitutes a classical repeat pass system with a temporal baseline of a few seconds. Finally, in the alternating bistatic mode the transmitter is switched on a pulse-to-pulse basis and the backscattered signal is received by both, generating two monostatic and two bistatic images within a single pass (Krieger *et al.*, 2007). The various products of the TanDEM-X mission are described by Fritz *et al.* (2012).

Bistatic synchronisation Having two satellites means that two interdependent ultra-stable oscillators (USO) are used to modulate and demodulate the radar pulses: small deviations in frequency and phase between the two would cause a residual modulation of the range and azimuth signal leading to significant errors in SAR focusing and interferometric phase if not compensated (Eineder, 2003; Krieger & Younis, 2006). To ensure knowledge of such deviations, the acquisition is periodically interrupted and radar pulses are transmitted to one of six dedicated horn antennas on the receiving

satellite which records them and transmits back a short sync pulse. The sync pulses are then processed on ground to correct the phase, a detailed explanation is given by Breit *et al.* (2011, 2012).

Acquisition plan The 5.5-years nominal lifetime of the satellites foresaw three years of joint operations leading to a very strict acquisition plan to achieve the mission goal. As reported by Krieger *et al.* (2007), in order to achieve the accuracy objectives, a height of ambiguity (HoA) of 30 to 40 m is necessary. Such small values would lead to frequent phase unwrapping problems. To overcome this issue two global mapping phases, lasting one year each, have been foreseen. The first one has larger HoA generally of 45 - 50 m (it thus has higher relative error but it is easier to unwrap), while the second one has smaller HoA of 30 - 35 m. The HoA ratio is approximately 0.7. The temporal separation is approximately one year to avoid seasonal changes. Furthermore, the swaths of the second coverage are shifted by half a swath's width with respect to the first coverage (Lachaise, 2015). This allows to partially compensate the performance decay at the swath margins caused by the antenna pattern and achieve a relatively constant relative height accuracy across the ground range. The Northern Hemisphere was imaged in ascending direction while the Southern in descending direction. To overcome shadow and layover effects, two acquisitions (with different baseline) in the opposite viewing geometry (crossing orbits) have been performed over mountainous terrain between September 2013 and April 2014 (Borla Tridon *et al.*, 2013). Adaptations to the acquisition plan were made during the mission, including new acquisitions with higher HoA over mountains and forests which proved to suffer from strong volume decorrelation (De Zan *et al.*, 2013). Dedicated coverage campaigns in Antarctica were performed in left-looking mode with large incidence angles during April to July, both in 2013 and 2014. These represent the first bistatic InSAR acquisition over this region, allowing the generation of a wide-coverage high-resolution DEM, lacking for this continent. Deserts which displayed low backscattering were also acquired again with steeper incidence angles. Operational acquisition for the global DEM ended in the second half of 2014. During the entire duration of the mission special acquisitions for the scientific community have been performed (Lachaise, 2015).

Ground segment and baseline calculation The TerraSAR-X and TanDEM-X missions utilize the same space and ground segment: this is formed by three main segments: the Mission Operations Segment (MOS), the Instrument Operations and Calibration Segment (IOCS) and the Payload Ground Segment (PGS). Those will not be described in depth, the reader is referred to Schättler *et al.* (2011) and Buckreuss & Schättler (2010) for a proper description. To comply with the strict accuracy budgets a precise knowledge of the spatial baseline between satellites is of paramount importance. This is extracted by ground processing of the data from the double differential GPS carrier phase measurements between the two satellites, allowing to eliminate ionospheric and other errors typical of the GPS. Baselines calculated by three different algorithms are combined achieving a precision in the order of 2 mm (Hueso González *et al.*, 2012; Antony *et al.*, 2013).

System calibration The absolute elevation is obtained without external sources using the absolute stereo-radargrammetric phase given by the different viewing geometry of the satellites, which causes different travelling times of the radar signal (see Section 6.2.2.2). It is hence very sensitive to differential instrument delays. All possible sources and their effects were analysed statistically from the processed data during the 11-month commissioning phase as well as during the operational phase. The following sources of uncompensated range delays were found, modelled and compensated in the processor (from Hueso González *et al.* (2012)):

- unbalanced global internal delays of both satellites;
- internal delays dependent on the chirp bandwidth and on the synchronization horn configuration;
- different internal delays of the instrument depending on the configuration of the attenuator elements (RxGain);

- relativistic effects on the time references of both satellites.

A further important calibration step is done operationally to estimate and compensate any bias in the baseline measurements, the procedure is described in Section 6.2.3.2.

DEM calibration and mosaicking The processing of the raw data is performed by the Integrated TanDEM-X Processor (ITP) which divides each datatake into scenes (usually 8 sec long corresponding to ~50 km along track), and generates a DEM for each scene, known as Raw DEM. The processor is described in more detail in Section 6.2.2. The following processing step consist in calibrating and mosaicking the Raw DEMs in order to generate the final global DEM, this task is performed by the Mosaicking and Calibration Processor (MCP). In this work the TanDEM-X data consists only of Raw DEMs processed specifically for the purpose: since the MCP and the final DEM were not used they will no be delved into. For a complete description the reader is referred to Gruber *et al.* (2012), nevertheless an overview is useful since a calibration procedure is also performed for this work (Section 7.2). Despite the intensive instrument calibration, the precise orbit and baseline determination and the compensation of all possible effects during processing, offsets and tilts in the order of some meters can still affect the Raw DEMs. These must be corrected to meet the specifications and to create a uniform DEM mosaic. The calibration step of MCP starts with the estimation of a height offset, a tilt in range and a slope in azimuth for each datatake. This is done by: (1) connecting tie-points on the overlap between adjacent Raw DEMs and measuring a relative height offset, (2) obtaining an absolute height offset with respect to the WGS-84 ellipsoid by using ICESat GLAS[2] data (Zwally *et al.*, 2002) as ground control points (GCPs). These GLAS measurements are properly filtered according to the number of peaks of the reflected signal (indicator of vegetation), the received energy and the signal width (indicator of terrain undulation). This leads to a standard deviation of 1.3 m obtained on a test site on flat bare land (Huber *et al.*, 2009). The points are compared to the TanDEM-X elevation (from which water, layover, shadow and outliers are removed) using the proper averaging function of the GLAS footprint. The tie-points consists in overlapping 1×1 km chips located at the centre of the overlapping region. For each chip the unsuited pixels (see before) are discarded and the histogram is computed, from which the median value is assigned to that chip. Furthermore the standard deviation of the difference chip is used as weighting information for the adjustment (Huber *et al.*, 2010). Finally the calibration is performed by estimating a polynomial correction for each datatake via a weighted least squares adjustment. The calibrated Raw DEMs are finally mosaicked averaging the elevations weighted by their height errors.

6.2.2 Integrated TanDEM-X Processor and Raw DEMs

The operational processing of the bistatic data into Raw DEMs is delegated to the Integrated TanDEM-X Processor (ITP) (Breit *et al.*, 2010a, 2012; Fritz *et al.*, 2011, 2012). It was newly developed for the mission within the DLR Remote Sensing Technology Institute (Institut für Methodik der Fernerkundung - IMF), based on the experience gained from the TerraSAR-X and SRTM X-band processors. High throughput was a requirement since it had to process in-line the data downlinked at the receiving stations and transferred at the processing and archiving facility in Oberpfaffenhofen. In fact the ITP is used for pre-screening of the downlinked data already at the receiving stations (Kiruna, Inuvik, O'Higgins, Chetumal) and to perform a deeper interferometric quality pre-check at the processing facility. Processing parameters are computed for the entire datatake, this is then divided in slightly overlapping scenes of approximately 50 km along-track (8 second scenes with 1 second overlap).

The processor is composed of single steps divided in two main blocks (from Breit *et al.* (2010a) and Breit *et al.* (2012)). The first block consists in the bistatic SAR processing, comprising:

- synchronization pulse analysis and evaluation resulting in timing and phase corrections to be applied to the SAR data (Eineder, 2003; Krieger & Younis, 2006; Balss *et al.*, 2010; Breit *et al.*, 2011);

[2]Geoscience Laser Altimeter System on board of the Ice, Cloud, and land Elevation Satellite

- generation of a bistatic focusing replica from calibration-pulses of both channels;
- calculation of the time variant bi-static acquisition geometry and focusing parameters (Bamler *et al.*, 2007);
- determination and analysis of common ground coverage and beam illumination overlap;
- mutual Doppler centroid deviation analysis;
- SAR data focusing by an enhanced version of the TerraSAR-X Multimode SAR Processor (TMSP) (Breit *et al.*, 2010b).

The second block performs the interferometric processing, specifically:

- filtering of both interferometric channels to common spectra (Yague-Martinez *et al.*, 2010a);
- high resolution slave image co-registration, based on a coherent and incoherent correlation approaches supported by geometrical predictions (Yague-Martinez *et al.*, 2010b) and subsequent resampling;
- single and dual baseline phase unwrapping (Lachaise *et al.*, 2012a,b; Lachaise, 2015);
- generation of the Raw DEM and supplementary geocoded quality maps (Rossi *et al.*, 2010, 2012).

6.2.2.1 Bistatic SAR processing

Compared to repeat pass interferometry, the requirements on instrument accuracy and calibration are much more strict with bistatic operations. Mainly, the two oscillators are independent and may drift (Eineder, 2003; Krieger & Younis, 2006), but many other issues have to be taken into account. For this reason an 11-month commissioning phase took place to investigate and compensate all instrument and physical effects of the bistatic system. Statistical exploitation of ITP processing parameters from thousands of scenes revealed several trends and offsets which could be then corrected operationally.

Phase and timing corrections Firstly the SAR data are corrected for instrument related effects. The USO frequencies might be slightly off and drift within a datatake leading to differences in radar frequency, PRF and RSF (Breit *et al.*, 2012) between the two channels (the active, used as reference, and the passive). Another issue is the π-ambiguity of the synchronization link phase caused by the combination of two 2π-ambiguous signals. The bistatic data has then an overall phase offset which is ambiguous by π (Fritz *et al.*, 2012). Further phase offset contributions arise because of the relative motion of the satellites and the limited speed of light during pulse exchange (relativistic effects) (Krieger & De Zan, 2014). Both SAR channels are first corrected for the effects already known from TerraSAR-X: electronic delays, antenna phase patterns, calibration network effects, etc. Afterwards the passive bistatic channel is corrected for (Breit *et al.*, 2012):

- pulse-by-pulse phase and range time corrections compensating frequency deviation and phase drifts of the oscillators (both corrections up to 2 cm);
- a range time offset due to the datatake start time difference (several hundred meters);
- differential range time offsets dependent of Rx-gain setting (correction up to 2 cm);
- synchronization horn delays (correction up to 2 cm).

The accuracy of the bistatic calibration was proven to be in the millimetre domain (Breit *et al.*, 2012).

Focusing Finally the focusing of both bistatic channels is performed. The moderate bistatic acquisition geometry of TanDEM-X permits the application of the TerraSAR-X chirp scaling focusing algorithm extended by a bistatic computation of an equivalent monostatic range history (Bamler *et al.*, 2007).

6.2.2.2 Interferometric processing

Spectral shift filtering Due to the different acquisition geometry of the two satellites, master and slave received spectra are composed of a coherent and a non-coherent band, both in range and azimuth. The non-coherent bands are eliminated in order to increase coherence, improving coregistration precision and reducing interferometric phase error. The overlapping spectrum in azimuth is derived from Doppler centroid estimates and azimuth processing bandwidth. In range the spectral displacement is obtained by simulating the phase of flat terrain using the average terrain height of the scene (Yague-Martinez *et al.*, 2010a).

Coregistration This is a fundamental step of the ITP interferometric chain, which results are used in different processing steps. It consists in estimating and adapting the grid of the slave image to the one of the master image, obtaining a precise geographical overlap. The rasters differ because of the parallax effect given by the different viewing geometry. An imprecise matching would cause loss of coherence, increasing relative height error. The first step is a "coarse" geometrical coregistration: the range and azimuth shifts are estimated on a regular grid (every 64 pixels) using an external DEM and precise orbit information. The second step is a precise coregistration based on the cross-correlation. The geometrical coregistration shifts are used as a-priori estimates to extract the patches (32×32 pixels) on the slave image maximising overlap. For each patch coherent cross-correlation is computed first, if coherence is too low the result is discarded and incoherent cross-correlation is applied. The position of the maximum of the cross-correlation function is obtained with sub-pixel accuracy by interpolation. Outliers are eliminated and replaced by bilinear interpolations (Yague-Martinez *et al.*, 2010b).

Accuracy of the coregistration The complex or coherent cross-correlation is the optimum (maximum likelihood) estimator (MLE) of mutual shifts of partially correlated stationary gaussian signals but is very sensitive to jumps of phase between the patches. The accuracy of the estimator is given by Bamler (2000); Bamler & Eineder (2005) for homogeneous patches (without image features) and represents the Cramér-Rao lower bound (CRLB):

$$\sigma_{\Delta\hat{x}_{ccc}} = \sqrt{\frac{3}{2N_s}} \frac{\sqrt{1-\gamma^2}}{\pi\gamma} \mathrm{OSF}^{3/2} \tag{6.1}$$

where $\sigma_{\Delta\hat{x}}$ is the standard deviation of the estimate $\Delta\hat{x}$ of a mutual shift Δx in units of samples, γ is the coherence, N_s is the number of samples in the estimation window and OSF is the oversampling factor of the data. The incoherent cross-correlation (or *speckle tracking*) is a suboptimum estimator but a more robust one, its accuracy for homogeneous patches is given by De Zan (2014) for intensity images:

$$\sigma_{\Delta\hat{x}_{icc}} = \sqrt{\frac{3}{10N_s}} \frac{\sqrt{2+5\gamma^2-7\gamma^4}}{\pi\gamma^2} \mathrm{OSF}^{3/2} \tag{6.2}$$

again in unit of samples. It must be noted that complex images must be oversampled by a factor of two before computing the intensity images, this factor is already included in the formula and OSF represents additional oversampling only.

Radargrammetric DEM The shifts computed during the coregistration step are also fundamental for the Raw DEM absolute calibration. In fact, since they are caused by the geometric parallax given by the different viewing geometry, they can be used to retrieve a *radargrammetric DEM*, which has a coarser resolution compared to the interferometric phase but has an absolute elevation. The absolute phase derived from the coregistration shifts, known as *stereo-radargrammetric phase* is used to determine the absolute phase offset, i.e. the absolute number of phase cycles (see below). Furthermore, the stereo-radargrammetric phase is also used during the dual-baseline phase unwrapping chain to support correction of unwrapping errors (Lachaise, 2015).

Interferogram formation The obtained shift matrices are used to resample the slave image to the grid of the master. The two coregistered images are a first by-product of the ITP generated for each scene and known as Co-registered Single look Slant range Complex (CoSSC): the operational processing stops here for experimental acquisitions not designed for global DEM generation, such as scientific acquisitions. For normal operational acquisitions the interferogram is generated computing the complex conjugate product of the CoSSCs. It is then multilooked and downsampled to the required ground resolution.

Single-baseline phase unwrapping For the first coverage the interferogram is unwrapped using the single baseline (1B-PU) Minimum Cost Flow (MCF) algorithm (Costantini, 1998) optimized for large interferograms (Eineder *et al.*, 1998), previously applied to the SRTM X-band DEM (Suchandt & Eineder, 2003). In the ITP implementation the cost functions are based on the topography-corrected coherence (Lachaise, 2015).

Absolute phase offset derivation The unwrapped phase has still a 2π-ambiguity and an additional π-ambiguity due to the synchronisation link. Rossi *et al.* (2012) show how the unwrapped phase ϕ^p_{unw} and the stereo-radargrammetric phase ϕ^p_{rdgr} measure the same quantity at each point, the absolute ranging, with the exception of a phase offset $\phi^p_{\text{off}} = \phi^p_{\text{unw}} - \phi^p_{\text{rdgr}}$ which can be estimated differencing the two quantities. The steps to determine a single value of phase offset for each scene are (Rossi *et al.*, 2012):

- downsampling of ϕ_{unw} to the raster of ϕ_{rdgr} and computation of the phase difference raster;
- noise reduction through median filtering to reject outliers caused by low coherence and layover/shadow areas, leading to a shrinking of the phase difference histogram;
- histogram search and detection of the peaks in the phase difference histogram. The peak of the main lobe is the absolute phase offset ϕ_{off}. Incoherent cross-correlation patches are not used for the histogram, unless coherent patches are less then 10% of the total (rarely the case).

Other possible smaller histogram lobes represent phase unwrapping errors: the pixels outside the main lobe are masked out in the so-called *radargrammetric control map* (example in Figure 7.1b), while correctly unwrapped pixels belonging to the main lobe are assigned an RGB colour where green corresponds to the peak ϕ_{off}. Given the lower resolution of ϕ_{rdgr}, smaller PU errors are not detected. From this classification the *phase unwrapping quality ratio* is derived as $q_{\text{ratio}} = (p_{\text{tot}} - p_{\text{out}})/p_{\text{tot}}$, where p_{out} is the number of pixels outside the main lobe and p_{tot} is the total number of pixels of the radargrammetric control map. In order to avoid jumps between subsequent scenes of the same datatake the integer (modulo 2π) of ϕ_{off} is taken as APO, while the fractional part is only annotated.

Absolute phase offset accuracy The accuracy of the absolute phase offset estimate depends on the accuracy of the coherent cross-correlation, given in Eq. (6.1). To resolve the absolute phase offset on a specific patch the shift estimation accuracy must be less than half a wavelength ($\lambda/2$ =1.55 cm) or expressed in units of resolution cells, less than $\lambda/2\rho_{\text{rg}} = B_{\text{rg}}/f_0$ (Bamler & Eineder, 2005). Where ρ_{rg} is the range resolution (~1.5 m), $f_0 = 9.65$ GHz is the carrier frequency and B_{rg} is the range (or chirp) bandwidth, equal to 100 MHz for nominal Stripmap acquisitions. Hence a $\sigma_{\Delta\hat{x}_{ccc}}$ below 1/100 of resolution cell is needed (1-σ), and below 1/300 to include 99% of the shifts in case of Gaussian distribution (3-σ). Typical ITP parameters are patch size $N_s = 32\times32$ pixels (which gives a good trade-off between accuracy and computation time) and range oversampling factor $\text{OSF}_{\text{rg}} = f_{\text{rg}}/B_{\text{rg}} = 1.1$, where f_{rg} is the range sampling frequency. With this parameters the 1-σ constraint to detect a PU error on a patch is achieved for $\gamma > 0.8$ and the 3-σ constraint for $\gamma > 0.95$. These are already strict constraints, furthermore the CRLB is a theoretical limit, valid for uniform patches where the topographic phase has been completely removed from the data: any residual artefact or non-Gaussian scattering degrades the accuracy. Fortunately, for the absolute phase offset estimation a considerable number of patches N_p is used (typically more than 10k), improving the accuracy by a factor $\sqrt{N_p}$ (Rossi *et al.*, 2012).

Absolute phase offset of difficult regions In regions of very low coherence or with limited land surface the radargrammetric approach is not usable to determine the absolute phase offset. For such regions ϕ_{off} is obtained by averaging the phase difference between the unwrapped phase and a simulated phase from reference DEM (SRTM C-band or GLOBE for high latitudes). It is less reliable since PU errors can bias the estimate and the reference DEM can be wrong or outdated. For every processing a map is generated from this phase difference, highlighting PU errors where the reference is reliable, but also elevation changes with respect to the reference DEM, as in the case of glaciers (example in Figure 7.1a).

Dual-baseline phase unwrapping correction The dual-baseline phase unwrapping processing chain is the topic of the PhD thesis by Lachaise (2015), as well as previous publications (Lachaise *et al.*, 2012a,b). The dual-baseline phase unwrapping correction (DB-PUC) is activated when some previously processed CoSSCs are available in the archives to support the current ITP processing. Operationally, this is the case for data starting from the second global coverage, or previously acquired data automatically flagged for reprocessing due to a low q_{ratio}. The interferometric data of the current processing are defined as *master* and those from the supporting CoSSCs are defined *slave*. The algorithm is actually a multi-baseline phase unwrapping as it can handle multiple CoSSCs in input (fundamental, as datatakes are shifted by half a swath during the second coverage), but each pair is processed separately, hence the nomenclature. The master and slave acquisitions must have the same acquisition geometry, enough overlap, and sufficiently different baseline (typical HoA ratio $h_{\text{amb}}^{2^{\text{nd}}}/h_{\text{amb}}^{1^{\text{st}}} \approx 0.7$). The main steps of the DB-PUC chain are:

- the slave CoSSC is coregistered on the master interferogram and cropped to the common part;
- the slave interferogram is obtained and unwrapped with 1B-PU (MCF);
- the phase unwrapping consistency of master and slave unwrapped phases is verified in the slant range height domain;
- if phase unwrapping is inconsistent, the differential interferogram in computed, which has larger HoA of both master and slave: it is easier to unwrap but has higher noise (adaptive filtering is hence applied). Its correctness is checked against the stereo-radargrammetric phase. The latter contains coarse absolute height information which, if necessary, is used to correct possible PU errors of the differential interferogram (by multiples of 2π);
- finally the differential phase is used to correct pixel-wise by integer multiples of 2π the discrepancies detected on the master unwrapped phase;
- if different corrected master unwrapped phases are available they are mosaicked together.

Particularly for time sensitive applications, such as the geodetic mass balance, it is important to emphasize that the elevation information comes from the master interferogram, supporting CoSSC are only used to correct phase unwrapping.

Geocoding Finally the unwrapped interferometric phase is geocoded, meaning that the absolute elevation information is converted from slant-range geometry to an Earth-related reference frame (Rossi *et al.*, 2010). The ITP algorithm is based on the method presented by Schwäbisch (1998). Atmospheric delay is taken into account. The ionospheric delay has a small impact on geolocation accuracy and is simply modelled as a constant of 5 TECU for the whole scene. The tropospheric delay, which is the dominant source of geolocation error, is modelled with a height-dependent model (Breit *et al.*, 2010b). In particular, as described by Breit *et al.* (2012), the differential tropospheric propagation is corrected, which is caused by the different local incidence angles of the two satellites. In a typical TanDEM-X acquisition scenario this leads to absolute height corrections between 0.7 and 2.0 meters.

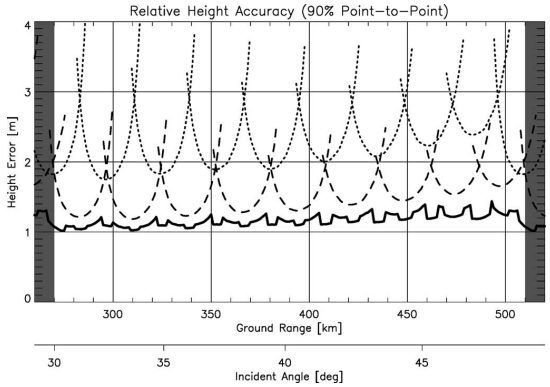

Figure 6.5 – Predicted relative height error (90% point-to-point) of TanDEM-X for HoA values of 45 m (dotted) and 30 m (dashed) and for the combination of multiple swaths (solid curve). From Krieger *et al.* (2007).

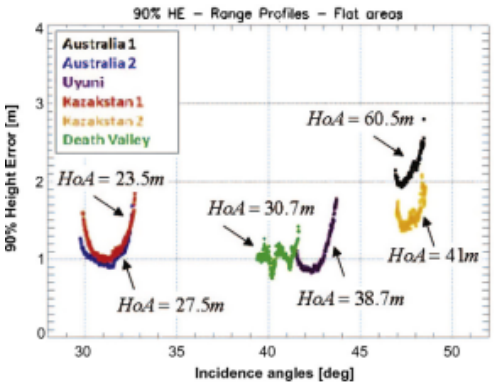

Figure 6.6 – Measured relative height error (90% point-to-point) for six acquisitions over soil and rocky terrain at varying incidence angle. From Rizzoli *et al.* (2012).

Raw DEM and quality maps The geocoded DEM represents the final product of the ITP, the Raw DEM, ready to be passed to the MCP. Furthermore, other output products are also generated by default by the ITP. First is the multilooked, detected amplitude (AMP) of the active channel geocoded with the newly generated Raw DEM. Second is the Height Error Map (HEM) representing, for each pixel, the standard error of its DEM value (Rossi *et al.*, 2010). The value is obtained directly from the coherence and geometrical considerations, as described in Section 2.2.3 and particularly according to Eq. (2.29). The third relevant output is the Flag Mask (FLM) annotating troublesome regions, in fact it gives for each pixel an indication about: shadow, layover, water, phase unwrapping residues and phase unwrapping branch-cuts (Rossi *et al.*, 2010).

6.2.3 TanDEM-X accuracy and validation

The interferometric performance is fundamentally described by the coherence γ. Error contributions affecting the coherence are: limited SNR, quantization, ambiguities, baseline decorrelation, relative shifts of the Doppler spectra, volume decorrelation and temporal decorrelation (see Section 2.2.2). The quantification of these contributions is assessed in Krieger *et al.* (2007), while a statistical evaluation of its behaviour in real acquisitions is given by Martone *et al.* (2012). As summarized in Section 2.2.3, the interferometric phase error can be computed from the coherence and the number of looks (as standard deviation or 90% point-to-point error) and converted to a relative height error (through Equation (2.29)). The predicted point-to-point errors of TanDEM-X DEM (at the 90% confidence level) are shown for HoA of 45 m and 30 m (typical of the first and second coverage) in Figure 6.5. The shifted beams allow to obtain a lower and almost constant relative height error when overlapping acquisitions from the first and second coverage, compensating the performance decay at the borders of the swaths.

To verify the actual performance of TanDEM-X, Rizzoli *et al.* (2012) computed the relative height error from the high-pass filtered DEM difference of subsequent acquisitions. Figure 6.6 shows the results obtained over six different scenes with soil and rocky flat terrain. The measured performance is in line with the predicted one.

The relative height error requirement (Table 6.1) is the most difficult to fulfil since, unlike the absolute height error, it cannot be corrected through a calibration phase. The global performance after the first coverage is shown in Martone *et al.* (2013), where for 25% of all Raw DEMs the predicted relative error is below 1.8 m, but there are also many areas of very low coherence such as forests, deserts and ice sheets. Slope is also very critical in the increase of this error term. Schulze *et al.* (2014) report that after the second coverage the relative error requirements are achieved with a confidence level of 96% and 97%, for slopes smaller and larger than 20%, respectively.

6.2.3.1 Systematic errors

Hueso González *et al.* (2010) analysed the systematic error sources affecting the TanDEM-X system during the development of the calibration concept, mostly based on simulations performed on the TerraSAR-X satellite. Main sources of height errors can be classified based on their variation rate within the typical datatake duration (50 - 200 sec). The main error source are interferometric phase errors and have a very fast variation rate. As seen previously, they are mostly described by the coherence and can partially be reduced by multilooking. This components are estimated to reach 1.8 m (90% point to point) in worst case scenarios, taking almost all of the relative height error budget of 2 m, and pushing for a stringent reduction of other errors, i.e. the systematic ones.

Among these are residual drifts and offsets in the phase determination within the radar instruments, which have a medium-fast to slow variation rate. The internal calibration takes care of slow phase and amplitude drifts by monitoring the temperature and compensating its effects. Residual errors display a systematic linear component in the order of 0.1 m (1-σ) every 100 sec with typical heights of ambiguity. Errors caused by temperature changes (ranging between −10°C and +50°C) in the internal bistatic calibration loop (medium-fast changing rate, up to 0.25 m) are compensated trough polynomials during processing. Residual drifts are present within the synchronisation link, these are compensated during processing but the accuracy of the temperature sensors on the amplifiers is limited. Mean height errors below 0.3 m (1-σ) have been simulated over a whole datatake of 300 sec.

Baseline determination errors have a much larger impact on the InSAR height accuracy. The baseline is determined by estimating the location of the SAR antenna phase centres, the spacecraft attitudes with star trackers and the relative satellite orbits with differential GPS. The last estimation is the only critical one, differential GPS measurements on the similar system of the GRACE mission have a residual low-frequency error of less than 1 mm with a main period of around one orbital revolution. Consequently for TanDEM-X a relative baseline accuracy of 1 - 2 mm is assumed, on top of which almost constant bias of 2 - 10 mm is cautiously added (Hueso González *et al.*, 2012).

Height errors due to interferometric phase errors (Eq. (2.29)) and due to baseline errors depend on h_{amb}, they hence present a temporal evolution as baseline and incidence angles change, a sort of low-frequency modulation of the DEM, affecting both relative and absolute errors (Krieger *et al.*, 2007).

The effects of a baseline error on the DEM are shown by Hueso González *et al.* (2010). Following their notation, B is the relative baseline, and $B_{\parallel}$ and $B_{\perp}$ its projection parallel and perpendicular to the LOS. The latter, also known as effective baseline, controls the height of ambiguity (Eq. (2.20)). Along-track baseline errors are resolved during coregistration and hence not critical. Baseline errors perpendicular to the LOS, $B_{\perp\text{err}}$, cause a bias in the phase-to-height scaling, resulting in a height error $h_{\text{err}} = h \cdot \frac{B_{\perp\text{err}}}{B_{\perp}}$, which is in the order of a few centimetres for typical acquisition parameters. Phase and baseline errors ($B_{\parallel\text{err}}$) parallel to the LOS cause a rotation of the DEM around the (master) flight trajectory and are the most critical ones. As a result the DEM will be vertically displaced by:

$$h_{\text{err}} = R \cdot \sin\theta_i \cdot \frac{B_{\parallel\text{err}}}{B_{\perp}} = \frac{h_{\text{amb}}}{\lambda} \cdot B_{\parallel\text{err}} \tag{6.3}$$

where R is the slant range distance to the target, θ_i is the incidence angle at the target position. Furthermore the DEM will be shifted in ground range by:

$$gr_{\text{err}} = R \cdot \cos\theta_i \cdot \frac{B_{\parallel\text{err}}}{B_{\perp}} \tag{6.4}$$

Since h_{amb} varies with θ_i the vertical displacement h_{err} also involves a tilt in ground range given by:

$$\varphi_{\text{tilt}} = \frac{h_{\text{err}}}{\Delta s} = \frac{B_{\parallel\text{err}}}{B_{\perp}} \tag{6.5}$$

where $\Delta s = R \cdot \sin\theta_i$ is the ground range distance from a properly selected reference point. For a typical $h_{\text{amb}} = 35$ m and $B_{\parallel\text{err}} = \pm 1$ mm (like the baseline relative error) the vertical displacement

is $h_{\text{err}} = \pm 1.1$ m and the $\varphi_{\text{tilt}} = 3.8$ mm/km for $\theta_i = 30°$. On the other hand even a small bias of $B_{\parallel\text{err}} = \pm 3$ mm causes h_{err} of several meters and $gr_{\text{err}} > 4$ m (depending on the HoA) which can be critical when mosaicking adjacent DTs, especially if they are shifted in opposite directions leading to more than 8 m of relative horizontal displacement and considerable slope dependent height difference (more in Section 7.2).

6.2.3.2 Baseline calibration

The processing of the TanDEM-X bistatic data can be performed with two types of baseline products: "precise" or "calibrated". The "precise" baseline product can lead to absolute elevation errors of several meters in the Raw DEMs. To meet the mission requirements (Table 6.1) further calibration of the Raw DEMs is needed. Fortunately baseline biases are (almost) constant and are relatively easy to detect and correct. The baseline calibration algorithm is described in Hueso González *et al.* (2010, 2012). If the bias in LOS is larger than 2 mm (critical threshold for the horizontal accuracy requirements) it can be considered the dominant systematic error source. The average height difference between a Raw DEM and a reliable elevation source (ICESat or STRM) is computed and $B_{\parallel\text{err}}$ is obtained with Eq. (6.3). Test sites are selected to be flat areas, in order to avoid coupling of ground range displacement with height errors, they are furthermore scarcely vegetated and distributed over the world in order to allow multiple measurements per day. To resolve the 2D baseline bias, acquisitions with different look angles are combined (Hueso González *et al.*, 2012). These measurements are then used to generate a "calibrated" baseline product which is then used by ITP to process the operational DEMs fed to the MCP.

The residual baseline error is (almost) only random and has been modelled with a sinusoidal function with period close to the orbit duration and 2 mm amplitude (1-σ). This component as well as residual offsets and tilts are then corrected by the MCP. The absolute elevation of the final product will in average be significantly lower than the requirement.

6.2.4 TanDEM-X dataset used

6.2.4.1 SPI data

In order to cover with a DEM a vast area such as the Southern Patagonian Icefield (SPI), different TanDEM-X datatakes and scenes had to be chosen, processed, evaluated and mosaicked. For this purpose TanDEM-X acquisitions available over the area at the time have been analysed using DLR's EOWEB catalogue and the IMF internal TanDEM-X processing monitoring tool. This tool allows searching through the operationally processed acquisitions using various parameters, and obtaining a kml file allowing to import the footprints of each scene in the Google Earth™ software, thus simplifying greatly the selection of the data. The selection and processing of the TanDEM-X scenes has been carried out in different phases in parallel to the TanDEM-X operational mission, progressively covering the whole of SPI as new acquisitions were made available and results proved to be encouraging. The number of acquisitions suitable to cover the SPI was limited at the time and not all of them produced DEMs of acceptable quality, the coverage increased as the mission entered its second and third year. For this reason some compromises had to be made in selecting the scenes, for example accepting scenes from different years and seasons. Only in the last phase as the second coverage of the globe started, it was possible to take advantage of the dual baseline phase unwrapping in order to obtain a sensible DEM over the regions characterized by the most difficult topography, where single baseline phase unwrapping failed to produce a usable DEM.

Table 6.2 summarizes all TanDEM-X scenes which were finally used for this study to cover the SPI. All scenes are acquired in bistatic configuration, mostly in operational mode and mostly in descending orbital direction (often orbit 126). Three of them are experimental scientific acquisitions (marked with * in Table 6.2), not part of the mission's operational acquisition plan, but instead requested by principal investigators for scientific purposes, two of these are acquired in ascending direction. Four more scenes were processed but resulted to be too heavily corrupted by phase unwrapping errors on the glacier surface and have since been discarded and substituted, thus not appearing in Table 6.2.

The first two columns of Table 6.2 specify the TanDEM-X datatake via its acquisition item ID (AID) and the scene number within the datatake. Among the accepted DEMs, 15 have been obtained using single baseline phase unwrapping (indicated by 1B) and four with dual-baseline phase unwrapping (2B), for these scenes, Table 6.2 reports both the master (2B M) and the supporting acquisitions (2B S). The supporting acquisitions were chosen among the relatively few available at the time, a single supporting acquisition per scene was used. The master and supporting acquisitions are maximum three months apart, thus minimizing glacier changes between them. Around half of the DEMs are based on acquisitions which span the year 2011 from March to October, unfortunately crossing different seasons. The other half was acquired in the first months of 2012, during the Austral summer. For some scenes the default length (8 seconds, ~50 km) of the processed section of datatake was extended in order to avoid adding a new separate scene or shortened to avoid coverage of non-relevant surface, thus reducing the risk of branch cuts during phase unwrapping in this region characterized by abundant water and steep slopes. Incidence angles reported in Table 6.2 refer to the centre of the swath and span between 33.7° and 44.6°. The effective baseline ($B_\perp$) and the height of ambiguity (HoA, h_{amb}) have a relatively large range, because the acquisitions span different mission phases and include non-operational datatakes. HoA ranges in absolute value between 43 m and 120 m, except for one experimental acquisition (S15) characterized by very small baseline and height of ambiguity of 256 m. Finally coherence values for master scenes range between 0.58 and 0.7. The last column in the table indicates the index which will be used to refer to each of the 19 processed TanDEM-X Raw DEMs.

The Integrated TanDEM-X Processor (ITP) was used to process satellite raw data obtaining 19 Raw DEMs. Calibrated baseline products were used. The Raw DEMs are projected in geographical coordinates, the elevations are represented in floating point and refer to the WGS84-G1150 datum (DLR-CAF, 2010). The TanDEM-X Raw DEMs were obtained with ITP's default posting (grid spacing): this is 0.2 arcsec (ca. 6.2 m) in latitude, while in longitude this is 0.2 arcsec for scenes located north of 50°S (corresponding to 4.3 m at 46.5°S of the upper NPI, down to 4.0 m at 50°S of the middle of SPI) and 0.3 arcsec for scenes located between 50°S and 60°S (ca. 6.0 m at 50°S and 5.8 m at the 51.5°S of the lowest margin of SPI). Furthermore ITP allows to extract the SRTM C-band DEM from the internal "W42" DEM database, matching the corner coordinates, posting and datum of the processed TanDEM-X scene. The upscaling is performed using bilinear interpolation with floating point output. The extracted SRTM DEM is useful as height reference to asses the quality of the processed Raw DEM.

Two main issues might affect the Raw DEM: (1) phase unwrapping (PU) errors, causing parts of the DEM to have a wrong absolute elevation and a horizontal shift in the range direction. (2) Wrong absolute phase offset (APO) estimation (cf. Section 6.2.2.2), causing a wrong absolute height, a shift and a tilt in ground range for the entire Raw DEM. A first comparison with the SRTM C-band, over relatively flat, ice-fee terrain, allows to detect obvious elevation offsets (larger than ca. 8 - 10 m) caused by a wrongly estimated absolute phase offset, often due to the π-ambiguity of the synchronization link (cf. Section 6.2.2.1). In three Raw DEM (S13, S15, S19) large elevation offsets were detected. In two cases (S13, S19) the measured height offset was nearly half of HoA meaning it was mainly due to a π-ambiguity which was corrected adding π to the original APO. For S15 the large HoA of 256 m caused the absolute elevation to be very sensitive to APO errors (according to Eq. (2.19)), a 16.5 m elevation offset was measured and the corresponding phase added to the original APO. The three scenes were geocoded again with the new APO value, obtaining an output which could be considered comparable for all of the 19 Raw DEMs. All of them still needed a finer calibration to correct residual APO errors and to achieve a good coregistration with the SRTM C-band DEM and between neighbouring TanDEM-X scenes. The calibration procedure is described in Section 7.2. The approach to deal with PU errors is described in Section 7.1.

6.2.4.2 NPI data

Given the scientific relevance of the results obtained in the SPI, the focus was shifted to the neighbouring Northern Patagonian Icefield (NPI). The idea was to apply the same technique in order to compute the glacier elevation changes and mass balance of this icefield to have a comprehensive understanding for the whole the Patagonian region. The advancement of the TanDEM-X mission was also

Table 6.2 – Processed TanDEM-X Raw DEMs over SPI.

DT AID	DT scene index	PU method	Acquisition date	Scene start time (UTC)	Scene length [sec.]	Rel. orbit / direction	Beam	Look angle [°]	Effective baseline [m]	HoA [m]	Average coherence	Posting (x/y) [arcsec]	Mosaic index
1012654	27	1B	2011.03.07	09:53:53.3	8.0	126 / D	A1 060	42.78	170.33	−43.14	0.62	0.2 / 0.2	S3
1012654	28	1B	2011.03.07	09:54:00.3	8.0	126 / D	A1 060	42.77	169.78	−43.44	0.61	0.2 / 0.2	S4
1012654	29	1B	2011.03.07	09:54:07.3	11.0	126 / D	A1 060	42.70	169.07	−43.63	0.59	0.2 / 0.2	S10
1021147	26	1B	2011.07.17	09:54:20.2	8.0	126 / D	A1 040	38.52	128.61	49.48	0.65	0.3 / 0.2	S13
1021147	27	1B	2011.07.17	09:54:27.2	8.0	126 / D	A1 040	38.48	128.49	49.75	0.68	0.3 / 0.2	S12
1027766*	01	1B	2011.05.09	23:45:31.3	7.8	89 / A	A1 020	33.71	44.53	120.98	0.67	0.2 / 0.2	S1
1027767*	01	1B	2011.04.22	23:53:28.9	8.6	165 / A	strip 012	40.94	27.16	256.05	0.65	0.3 / 0.2	S15
1027772*	01	1B	2011.05.01	09:53:58.8	12.1	126 / D	A2 055	41.28	144.81	48.42	0.68	0.2 / 0.2	S2
1042632	23	1B	2011.10.24	09:54:23.5	8.0	126 / D	A1 050	40.64	106.39	−64.88	0.63	0.3 / 0.2	S14
1042632	24	1B	2011.10.24	09:54:30.5	6.0	126 / D	A1 050	40.60	106.43	−64.83	0.65	0.3 / 0.2	S11
1055763	16	1B	2012.03.26	09:53:55.6	4.0	126 / D	A1 060	42.69	71.22	−105.52	0.66	0.2 / 0.2	S7
1056403 1041468	22 15	2B M 2B S	2012.03.15 2011.12.07	09:54:12.3 09:54:14.8	8.0 8.0	126 / D 126 / D	A1 050 A1 050	40.67 40.63	70.83 92.67	−98.85 −74.82	0.61 0.61	0.2 / 0.2	S17
1057982	19	1B	2012.02.16	10:02:17.0	12.0	35 / D	A1 030	36.22	67.64	−88.58	0.70	0.2 / 0.2	S9
1057982	20	1B	2012.02.16	10:02:28.0	8.0	35 / D	A1 030	36.19	67.89	−88.48	0.68	0.2 / 0.2	S5
1058255	8	1B	2012.02.11	09:53:46.8	12.0	126 / D	A1 070	44.57	70.53	112.98	0.60	0.2 / 0.2	S8
1058255	9	1B	2012.02.11	09:53:57.8	8.0	126 / D	A1 070	44.59	70.93	112.26	0.58	0.2 / 0.2	S6
1058255 1040740	10 18	2B M 2B S	2012.02.11 2012.01.09	09:54:04.4 09:54:05.8	8.0 8.0	126 / D 126 / D	A1 070 A1 070	44.53 44.53	71.25 91.82	111.81 −86.03	0.57 0.53	0.2 / 0.2	S16
1058868 1040940	3 14	2B M 2B S	2012.01.31 2011.12.29	09:54:19.3 09:54:19.6	8.0 8.0	126 / D 126 / D	A1 040 A1 040	38.46 38.54	69.18 90.78	−94.04 −70.81	0.67 0.64	0.3 / 0.2	S18
1058868 1040940	5 16	2B M 2B S	2012.01.31 2011.12.29	09:54:33.3 09:54:33.6	8.0 8.0	126 / D 126 / D	A1 040 A1 040	38.41 38.42	69.56 91.14	−93.46 −70.97	0.62 0.59	0.3 / 0.2	S19

Table 6.3 – Processed TanDEM-X Raw DEMs over NPI.

DT AID	DT scene index	PU method	Acquisition date	Scene start time (UTC)	Scene length [sec.]	Rel. orbit / direction	Beam	Look angle [°]	Effective baseline [m]	HoA [m]	Average coherence	Posting (x/y) [arcsec]	Mosaic index
1191233	10	2B M	2014.02.14	23:46:02.7	17.0	89 / A	A2 025	34.83	111.79	−50.45	0.60	0.4 / 0.4	N1
1170309	11	2B S	2013.12.21	23:46:18	8.0	89 / A	A2 025	34.77	82.81	68.17	0.73		
1149794	9	2B S	2013.09.02	23:46:05	8.0	89 / A	A1 030	36.21	92.25	64.40	0.64		
1149794	10	2B S	2013.09.02	23:46:12	8.0	89 / A	A1 030	36.19	92.29	64.45	0.63		
1153873	7	2B S	2014.01.31	13:02:51	8.0	89 / A	A1 020	36.13	92.16	64.46	0.66		
1153873	8	2B S	2014.01.31	13:26:23	8.0	89 / A	A1 020	36.16	92.21	64.49	0.60		
1149794	10	1B	2013.09.02	23:46:05.8	18.5	89 / A	A1 030	36.17	92.27	64.36	0.63	0.2 / 0.2	N5
1171117	9	1B	2014.01.01	23:46:03.98	19.0	89 / A	A2 035	37.19	89.53	68.58	0.59	0.2 / 0.2	N3
1171117	9	2B M	2014.01.01	23:46:03.98	19.0	89 / A	A2 035	37.19	89.53	68.58	0.55	0.4 / 0.4	N2
1132222*	3	2B S	2013.04.01	23:45:57.3	19.0	89 / A	A1 040	38.44	72.01	88.39	0.59		
1172605	7	2B M	2014.01.12	23:46:03.8	19.0	89 / A	A2 045	39.93	99.21	66.66	0.57	0.4 / 0.4	N4
1132222*	3	2B S	2013.04.01	23:45:57.3	19.0	89 / A	A1 040	38.44	72.01	88.39	0.59		
1152341	5	2B S	2013.10.16	23:46:07	8.0	89 / A	A1 050	40.60	83.67	−82.34	0.73		
1152341	6	2B S	2013.10.16	23:46:14	8.0	89 / A	A1 050	40.63	83.54.	−82.51	0.61		
1152341	7	2B S	2013.10.16	23:46:21	8.0	89 / A	A1 050	40.63	83.40	−82.67	0.62		

a major drive. The operational coverage (in descending orbit) over NPI after the second year of mission was still somehow scarce compared to the SPI and problematic due to the difficult topography and the seasonal differences between acquisitions. The operational coverages in opposite orbital direction (crossing orbits) performed over difficult terrain (cf. Section 6.2) proved to be ideal for the coverage of NPI in a short time span with dual-baseline data. During this mission phase, data were acquired in ascending orbital direction over NPI in two cycles during September and October 2013 and January and February 2014.

Table 6.3 summarizes all the TanDEM-X data used to cover the NPI in this study. Before reaching the final selection of data and processing configuration, various attempts were performed involving other data and different combinations of master and supporting scenes, but only the final configuration and data used appears in Table 6.3. Three summer acquisitions with different beam (A2 025, A2 035, A2 045) on the ascending orbit 89 were finally chosen in order to cover the entire icefield: datatakes 1191233, 1171117 and 1172605.

At this latitude snow is likely wet in summer, reducing the backscattering coefficient and accordingly increasing noise of the DEM. Nevertheless the choice was done for two reasons: (1) to minimize snow seasonal elevation variations since the acquisition period corresponds roughly to the one of the SRTM DEM and is close to the end of the hydrological year, (2) reduce the effect of radar signal penetration in ice and snow. Another advantage is the very short interval of 45 days between the acquisitions. An examination of the processed scenes revealed some areas affected by phase unwrapping errors. In order to improve the coverage a further beam was selected (A1 030), unfortunately no summer acquisition was available, so the datatake with AID 1149794, acquired in September 2013 was processed to be used as gap filling Raw DEM with limited coverage, accepting the fact that it might differ from the other scenes with regard to seasonal elevation changes and liquid water content of the snow.

The access to the ITP was exploited to manually define the portion of datatake to process, in order to have one single long scene per datatake, covering along-track the whole length of the icefield plus, where available, a portion of ice-free flat terrain to be used to validate and calibrate the Raw DEM. Doing so allows to reduce the number of Raw DEMs and the time and effort associated to the processing, calibration and mosaicking of each of them. It furthermore allows to have, at least for 3 of the 4 datatakes relatively large flat ice-free calibration areas (particularly north-west of NPI around Laguna San Rafael and south-east of NPI).

To increase the area with valid elevation with such a complicated topography, multibaseline phase unwrapping was employed for three of the five Raw DEMs. The supporting acquisitions were downloaded directly as CoSSC data (8 seconds length), except one which was experimental, and was processed with the ITP as a long scene before being used as supporting CoSSC. It must be noted that the ITP uses the supporting acquisitions in order to aid the phase unwrapping of the master scene, which interferometric phase is the one converted to elevation (see Section 6.2.2.2). Hence using supporting CoSSCs from different date and season, characterized by (limited) changes in snow and ice elevation, liquid water content, and other surface condition does not represent a limitation in this scenario. As Table 6.3 reports, master acquisitions display a small range of both incidence angles, between 34.8° and 40°, and of HoA, spanning from 50 m to 67 m. This is another small advantage since the height sensitivity to phase noise will be similar.

Finally 5 Raw DEMs were produced, identified by N1 to N5, with length in azimuth varying between 17 and 19 seconds (119 to 133 km along-track). Three of them (N1, N2, N4) are processed using multibaseline phase unwrapping with a vertical and horizontal posting of 0.4 arcsec in order to reduce file size. The phase unwrapping quality is relatively good especially on the icefield. No usable supporting acquisition was available for the western part of N2 (AID: 1171117), this led the ITP to assign a void value to this part, in fact producing a Raw DEM which is narrower across-track. For this reason the same acquisition was also processed with single baseline phase unwrapping into a separate Raw DEM. Unfortunately due to the lack of dual baseline processing some large phase unwrapping errors are present. In order to have a coverage of these icefield portions the winter acquisition 1149794 (N5) was also processed with single baseline PU, improving the mutual coverage of the icefield, at the cost of introducing data from winter. These two Raw DEMs were computed with a vertical and horizontal posting of 0.2 arcsec, since it provided better phase unwrapping results compared to the 0.4 arcsec

posting.

None of the DEMs displayed anomalous elevation offsets, hence no preliminary APO correction was performed in this case, leaving the task of fine tuning to the calibration phase (see Section 7.2).

6.3 Glacier outline and additional data

In order to compute the geodetic mass balance, besides the elevation change maps and the digital elevation model, a precise outline of the glaciated area is necessary. The main purpose is to define the pixels belonging to the glacier surface in order to compute the mean elevation change and to measure the area of the glacier which, a parameter needed to estimate the volume change. The glacier outline is also useful, together with water body outlines, to select ice-free, water-free pixels in order to estimate the uncertainty of the elevation difference.

Since up-to-date and historical glacier outlines are very important for many glaciological applications an inventory project known as GLIMS[3] (Global Land Ice Measurements from Space) is currently run by more than 60 institutions worldwide and hosted by the National Snow & Ice Data Center (NSIDC), Boulder, Colorado. This database of glacier outlines grows steadily as it gives the users the ability to submit their data, nevertheless it does not yet have a full global coverage. As a supplement to GLIMS, the Randolph Glacier Inventory (RGI)[4] (Pfeffer *et al.*, 2014) was created by more than 60 specialists of the field, and it owes its name to one of the meeting venues, Randolph (New Hampshire). This is a globally complete inventory of glacier outlines. It was motivated by the Fifth Assessment Report of the Intergovernmental Panel on Climate Change (IPCC AR5) with version 1.0 released in February 2012. The RGI database is also hosted at the NSIDC, the current version is 5.0 and was released in July 2015 (Arendt *et al.*, 2015). RGI is based on a combination of new and existing data, such as outlines already available in the GLIMS and previous glaciers inventories such as the World Glacier Inventory (WGI, 1989). In RGI the glaciers of the world are divided in 19 regions, the one of interest for the current work is region 17: southern Andes.

The original outline (v. 1.0) for region 17 was obtained from late-summer, cloud free Landsat 7 ETM+ (Enhanced Thematic Mapper Plus) imagery acquired prior to the 2003 Scan Line Corrector failure. In order to detect the glacier surface, the *normalized difference snow index* (NDSI) from the 30 m resolution ETM+ multispectral images was used:

$$\mathrm{NDSI} = \frac{b_2 - b_5}{b_2 + b_5} \tag{6.6}$$

where b_2 indicates spectral band 2 ($\lambda \in [0.52; 0.60]$ μm) and b_5 indicates band 5 ($\lambda \in [1.55; 1.75]$ μm). A threshold ranging between 0.5 and 0.65 is applied to the NDSI to identify debris-covered to bare ice and one ranging from 0.65 to 0.99 to detect snow-covered ice. The outline was largely improved in version 2.0. Version 3.0 included improvements in central Chile and in the mountains surrounding NPI and SPI (not of interest for this work). Only minor changes were applied afterwards in region 17.

For the current work version 2.0 of the RGI (Arendt *et al.*, 2012) was used to extract two separate glacier outlines for NPI and SPI[5]. To obtain a correct geodetic mass balance, a precise outline is needed particularly at the glacier front, where elevation changes display the strongest magnitude. In this work the outline was manually adapted to encompass the maximum glacier extent reached between the two observation epochs. This meant adapting the glacier outline to the extent of February 2000 for almost all glaciers, by using both the SRTM DEM and the elevation difference. The entire border of all glacier termini, not just their front, was checked and modified if needed. A detail of the glacier outline at the front of Jorge Montt Glacier is shown in Figure 9.15. Only four glaciers located on the western margin of SPI displayed surface thickening and area gain: Pio XI, Trinidad, Calvo and HPS 34. For these glaciers the TanDEM-X amplitude and the elevation change map were used to adapt the outline to the glacier extent of 2011/2012 corresponding an areal gain of approximately 13.1 km^2 between

[3] Available at: http://www.glims.org/
[4] Available at: http://www.glims.org/RGI/
[5] Shapefiles kindly provided by Matthias Reif, Enveo GmbH.

February 2000 and February 2012. With this procedure a total reference glacier plan-view area of 3867.0 km^2 and 12880.7 km^2 is obtained for NPI and SPI, respectively.

Some glacier inventories and outlines have been recently published in the literature. Rivera *et al.* (2007) computed the glacier outline of NPI from a Landsat ETM+ image of March 2001 (published in GLIMS) using the b_4/b_5 ratio. They obtain a total ice area of 3953 km^2. Casassa *et al.* (2014) published a glacier inventory of the SPI with areal changes between 1986 and 2000. They used Landsat TM images of January 1986 and ETM+ images of October 2000. Both indices were used: the NDSI to distinguish rock from snow and the b_4/b_5 ratio, to distinguish snow from ice. The authors further improved the outline manually using the 15 m pansharpened ETM+ image, finally obtaining for year 2000 a total glacier area of 12514 km^2, with an estimated error of 250 km^2 (2.0%).

The accuracy of the RGI, being it a compilation of different sources, is not given precisely for each outline. A rough statistical analysis of its error, produced by comparison with independent outlines is provided in Pfeffer *et al.* (2014), with particular focus on South America. They fit a power law to the obtained error data leading to the relation:

$$e(A) = ke_1 A^{0.7} \tag{6.7}$$

where e is the area error, A is the area, $e_1 = 0.039$ is the error for an area of 1 km^2, and k is an arbitrary factor ranging between 1 and 3. According to this model an error of 38.0 km^2 (1.0%) and 88.1 km^2 (0.7%) can be obtained for NPI and SPI, respectively.

Paul *et al.* (2013) discusses the topic of glacier outline accuracy in its various aspects and compares outlines obtained with low and high resolution multispectral images, as well as manual modifications performed by different human operators. They confirm previously published accuracy assessments, finding typical accuracies between 2% and 5%. Larger values are found as glacier size decreases.

Based on the previous error assessments, the glacier areas obtained in this work are assigned an arbitrarily defined error of 2%, equal to 77 km^2 and 258 km^2, for NPI and SPI, respectively.

Another dataset used in this work is the water outline. It was used to avoid selecting water samples when computing the statistics of bare rock pixels for the purpose of accuracy assessment and visualization. The water outline used here comes from the SRTM Water Body Data (SWBD) product (Farr *et al.*, 2007). The outlines reflect the glacier frontal position at the time of the SRTM acquisition and are hence well suited for this work (except for the few advancing glaciers). A general visual inspection confirmed the acceptable quality of the water outlines for the purpose of this work.

Chapter 7

Ice elevation change maps

This chapter describes the methodology applied to generate the ice elevation change maps and the obtained results. Section 7.1 reports the procedure followed to deal with phase unwrapping errors in the TanDEM-X Raw DEMs. Section 7.2 focuses on the vertical and horizontal coregistration of the TanDEM-X Raw DEMs to the SRTM DEM assumed as reference. This is a particularly important aspect: the procedure, the correction values and the accuracy of the calibration are reported here. The steps adopted to produce the maps (Section 7.3) and the results are finally presented and discussed (Section 7.4).

7.1 Dealing with phase unwrapping errors

A major problem affecting the Raw DEMs are phase unwrapping errors. These are areas where the phase unwrapping algorithm (PU) did not manage to unwrap the interferometric phase consistently with the rest of the scene, failing to follow the phase fringes pattern. This often happens because of loss of coherence especially in areas of steep topography affected by layover and shadow as well as for water bodies which tend to loose coherence even in bistatic acquisitions. PU errors can be limited to an area of low coherence such as a lake or a slope but often tend to extend to very large areas. This is because once a phase jump is introduced the fringes unwrapped afterwards will also be affected and further phase jumps can occur as well. Areas affected by PU errors are assigned a wrong number of 2π phase cycles, corresponding to an elevation error (positive or negative) which is multiple of the height of ambiguity (Eq. (2.19)) and a horizontal shift and tilt in range (towards or away from the sensor).

The Patagonian icefields are located in a region of extremely harsh and varied topography (see Section 5.1). They are set in a very rough mountainous area and feature a large plateau crossed by snow covered mountain ranges. At its margins ice is discharged through larger gentler glaciers, but also narrow steep glaciers. The icefields (particularly SPI) are surrounded by an intricate net of lakes, sea fjords and water streams.

Steep slopes result in layover and shadow as well as very dense fringe patterns with small values of HoA, which the PU algorithm cannot always follow. Finally, low coherence water bodies, including narrow rivers act as an obstacle to the fringe tracking algorithm, leading often to large PU errors. Almost all of the processed TanDEM-X Raw DEMs display large phase unwrapping error areas mostly located at the scene borders and various smaller areas within the scene, particularly over lakes and steep slopes. Glaciers are generally well unwrapped having gentler slopes, but they may fall within a large PU error. Four of the processed Raw DEMs had to be discarded because very limited usable ice surface was included. For certain regions more overlapping Raw DEMs had to be processed in order to achieve a good coverage by filling the mutual wrong areas. Using the dual-baseline PU correction reduced significantly PU errors and allowed to achieve usable elevations even for very critical regions. Nevertheless PU errors cannot be completely avoided.

Particular attention was paid to locating and masking out PU errors, since they would influence the results of the elevation comparison (on-glacier) as well as the calibration of the DEM (off-glacier). The masked areas can subsequently be filled with elevation data from overlapping Raw DEMs where

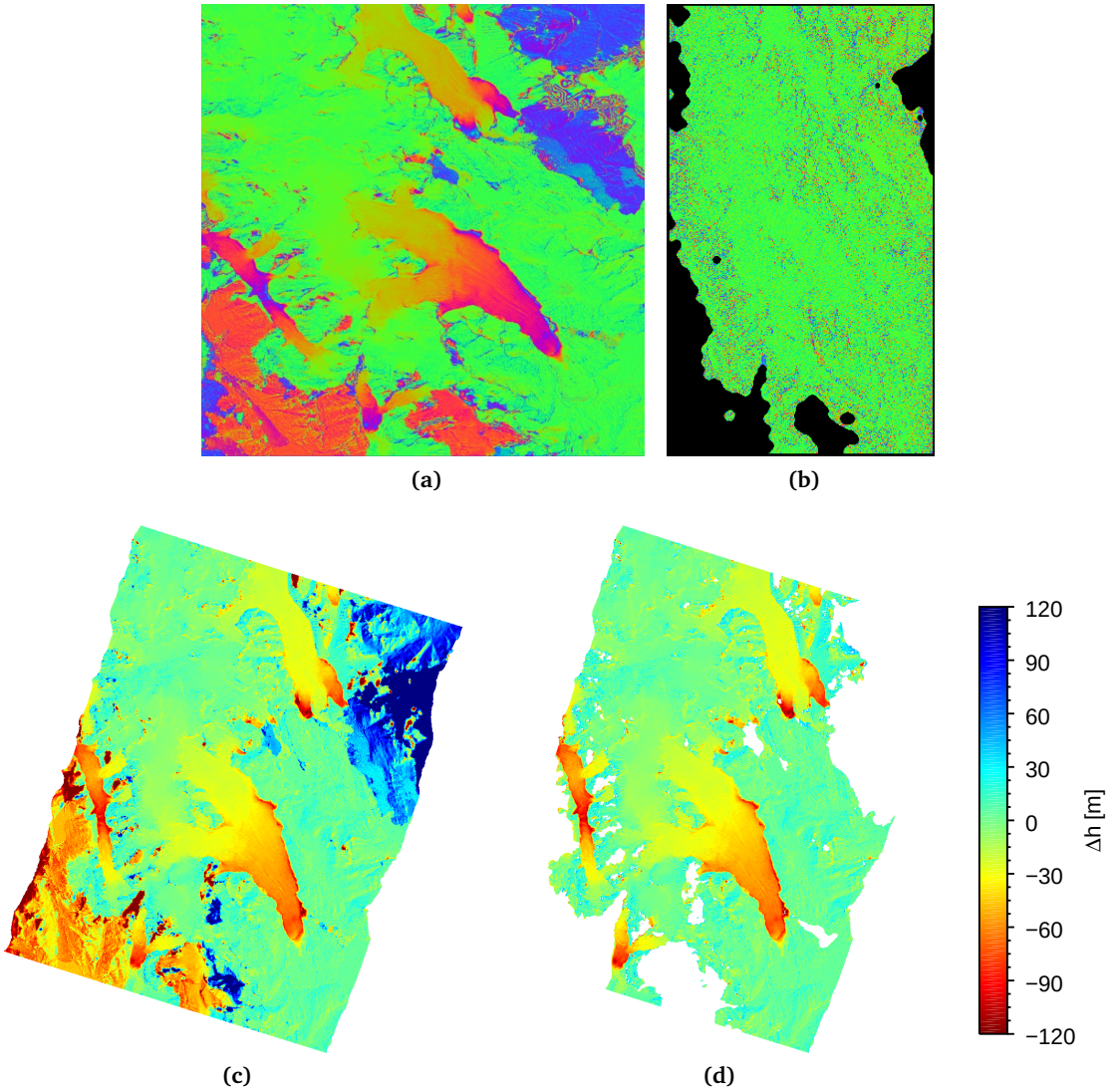

Figure 7.1 – Masking of phase unwrapping error areas for scene S12. (a) Interferometric phase difference with SRTM. (b) Radargrammetric control map. (c) Elevation difference $\Delta h = h_{\mathrm{TDM}} - h_{\mathrm{SRTM}}$ displaying several phase unwrapping errors, as well as ice thinning with similar order of magnitude and residual misregistration. (d) Elevation difference after masking the phase unwrapping errors.

available. In order to detect and mask such areas each Raw DEM and the matching SRTM C-band DEM, extracted through ITP, are subtracted obtaining a first difference image $\Delta h = h_{\mathrm{TDM}} - h_{\mathrm{SRTM}}$, which values display elevation differences due to ice surface changes, PU errors (theoretically in both DEMs, but mainly in the TanDEM-X Raw DEM) and a residual absolute elevation offset between the two DEMs.

This difference image was mainly used to locate phase unwrapping error areas in each Raw DEM scene. Furthermore ITP provides two useful images in radar geometry which can be used as a visual aid: the interferometric phase difference with SRTM and the radargrammetric control map. Those are shown for a Raw DEM over Grey and Tyndall glaciers in Figure 7.1a and 7.1b, respectively. In the interferometric phase difference areas of agreement are displayed in green, while areas of discrepancy with a phase jump of $\pm 2\pi$ or multiples (typically due to PU errors) are marked in magenta-red ($+2\pi$) and purple-blue (-2π). Intermediate phase changes, for instance due to glacier thinning assume intermediate colour shades. The radargrammetric control map displays very roughly in black the largest PU error areas detected by comparison with the stereo-radargrammetric phase (see Section 6.2.2.2).

Phase unwrapping errors were detected separately on each Raw DEM according to the following procedure: after a first visual check of the quality of the PU on the main glaciers using the interferometric phase difference image, the minimum and maximum actual ice elevation change was measured on

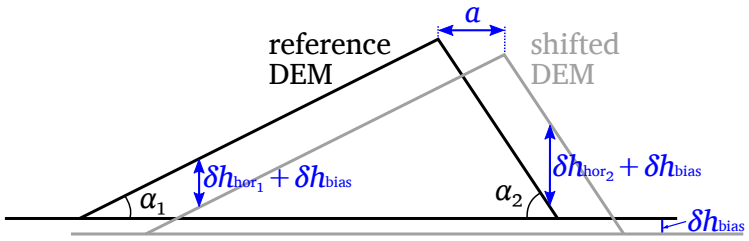

Figure 7.2 – DEM misregistration scheme showing the effect of (1) a constant elevation bias δh_{bias} and (2) a horizontal shift a in slope direction ($b = \psi$) causing elevation difference error δh_{hor}.

the DEM difference image for glaciers which were correctly unwrapped. Such changes often amounted to several tens of meters. These values plus a reasonable margin were used as positive and negative Δh thresholds to roughly isolate areas with phase unwrapping errors. A second step involved a thorough visual and manual selection: undetected PU errors having elevations below the thresholds were manually added and the borders of the thresholded areas were refined. The obtained mask was filtered with a 9×9 median filter to eliminate isolated pixels caused by noise in the TanDEM-X Raw DEMs. The filtered mask was used to assign to the PU errors areas an invalid value of -32767.0, which during the mosaicking allows to discard such areas and use valid values from overlapping Raw DEMs, if available. As an example, the elevation difference image for scene S12 (Grey and Tyndall glaciers) is shown in Figure 7.1 along with the corresponding ITP control images. Large errors are visible particularly in the north-east and south-west of the scene. The elevation difference obtained after masking out the PU errors is shown in Figure 7.1d.

7.2 Vertical and horizontal coregistration of the DEMs

In order to obtain an accurate elevation change map and consequently use it to derive a mass balance through the geodetic method, a precise vertical and horizontal coregistration of the SRTM and TanDEM-X DEMs must be achieved. A precise relative calibration is the main priority for this application, while a precise absolute calibration, i.e. the fit of the DEM to the chosen datum, is desirable but not strictly critical.

The effects of a DEM misregistration are depicted in Figure 7.2. One of the DEMs is assumed to be "correct", i.e. corresponding to the actual topography, and used as reference. With respect to the reference the second DEM might suffer from an elevation bias δh_{bias}, which can be constant or have slow variation in space (e.g. a tilt) or with elevation. The second DEM might furthermore be affected by a horizontal shift of magnitude a in direction b, this will cause an elevation difference error δh_{hor} when the terrain has a slope α with an aspect ψ non-orthogonal to b (ψ and b are 0° towards the north and increase clockwise). The sign and magnitude of δh_{hor} depends on these parameters according to (Nuth & Kääb, 2011):

$$\delta h_{\text{hor}} = a \cdot \cos(b - \psi) \cdot \tan\alpha \tag{7.1}$$

Because of these dependencies, an elevation difference image between two shifted DEMs appears like a hillshade image, which is in fact obtained by shifting two copies of a single DEM. δh_{bias} can hence be measured on flat areas, while on slopes it will be coupled with δh_{hor}.

Nuth & Kääb (2011) propose a universal method for assessing and coregistering DEMs to derive glacier elevation changes and their geodetic mass balance. The authors fit a cosine function $a \cdot \cos(b - \psi) + c$ to all the $\delta h / \tan\alpha$ samples obtained on stable terrain. The parameters a, b and $c = \frac{\delta h_{\text{bias}}}{\tan\alpha}$ are then obtained by an iterative least squares minimization and used to coregister the second DEM to the reference DEM.

The procedure proposed by Nuth & Kääb (2011) is generic and well suited for classic scenarios where two DEMs are available as finished products, meaning that no access to the processing of the DEMs is available. It involves a parameter estimation which is strongly dependent on the stable (ice-free) pixels of the DEMs. The terrain surrounding glaciers is generally mountainous and hence critical under many aspects, particularly in InSAR DEMs. Here the accuracy achieved is generally lower on

slopes, furthermore layover and shadow areas do not have valid elevation data: they are either void or filled with a ramp. Furthermore phase unwrapping errors can render unusable large portions of terrain. These factors limit the availability and the quality of the ice-free points used to estimate the correction parameters and hence the quality of the fit.

In this work a great advantage with respect to DEM coregistration arises from the self-processing of the the TanDEM-X Raw DEMs through the operational processor (ITP), and the possibility to tweak some of the processing parameters, particularly in the interferometric part (cf. Section 6.2.2.2). This allows to restrict the generic DEM registration problem to the issues strictly linked to the InSAR geometry and DEM generation (Section 2.2.1).

The SRTM C-band DEM (Section 6.1) is naturally chosen as reference elevation for several reasons. It is a final product obtained by calibration and mosaicking of overlapping datatakes (Section 6.1.1), particularly numerous in this region, leading to better accuracy and no voids. The product underwent several internal and external accuracy assessments which proved it to exceed the nominal absolute and relative accuracy requirements. In particular long wavelength elevation biases were not detected in this region (cf. Section 6.1.1).

The TanDEM-X Raw DEMs processed through the ITP with calibrated baseline product are still affected by absolute elevation and positioning errors. Those are corrected operationally during the mosaicking phase by the MCP (cf. Section 6.2.1). Sources of systematic errors are described in more detail in Section 6.2.3.1, where the baseline error is identified as the main contributor and its effects are described. Phase errors and baseline errors parallel to the line of sight will impact the estimation of the absolute phase offset (term ϕ_{off} in Eq. (2.18)), which in the ITP is based on the stereo-radargrammetric phase (cf. Section 6.2.2.2). The Raw DEM is hence affected by a height offset (Eq. (6.3)), an across-track shift (Eq. (6.4)) and a tilt around the master flight trajectory (Eq. (6.5)). Furthermore APO errors can arise during its estimation, particularly on difficult topography. For instance because of (generally small) undetected PU errors, or because of a large fractional part after integer rounding.

The three systematic effects can be corrected by adjusting the estimated APO of each Raw DEM. This can be done by extracting a relative height offset between the Raw DEM and the reference DEM, corresponding to a constant δh_{bias} (Figure (7.2)). Eq. (2.19) is used to convert the measured relative height offset δh_{bias} into a phase offset $\delta\phi_{\text{bias}}$ which is added to the previous APO $\phi_{\text{off}_{\text{old}}}$, obtaining an updated value of the APO $\phi_{\text{off}_{\text{new}}} = \phi_{\text{off}_{\text{old}}} + \delta\phi_{\text{bias}}$. The geocoding module of the ITP is run again with this updated value of APO, obtaining a new Raw DEM which fits the reference DEM. Not only the height offset is corrected but also the across-track horizontal shift and tilt. A precise vertical and horizontal DEM coregistration is hence is obtained without any manipulation of the DEMs.

7.2.1 Determination of the Raw DEM height offset and its accuracy

An appropriate strategy must then be set for the determination of a single value of δh_{bias} for each Raw DEM. It must be first noted that the Raw DEMs were previously pre-screened for possible large APO errors, for instance due to the synchronization link π-ambiguity (cf. Section 6.2.2.1), those were corrected by adding an appropriate multiple of π to $\phi_{\text{off}_{\text{old}}}$ and obtaining a new Raw DEM (see Section 6.2.4). This implies that the residual δh_{bias} will be relatively small (below ~8 m) and almost constant as the tilt will be negligible. The horizontal shift will also be small, reducing the effect of δh_{hor} for low slopes.

To estimate a value of δh_{bias} for each Raw DEM, "calibration regions" (CRs) were visually identified and manually selected over delimited off-ice terrain. They were chosen to be as flat and vegetation-free as possible and as spatially distributed over the Raw DEM as possible, to account for possible spatial trends of $\delta\phi_{\text{bias}}$ (e.g. a residual tilt). Slopes (particularly those parallel to the across-track direction) cause coupling of δh_{hor} with δh_{bias}, biasing the estimate of the latter. Vegetation is not desirable as C and X band have varying penetration into the canopy, leading to different position of the scattering phase centre (the difference with these frequencies is nevertheless limited). The largest difference happens when comparing canopy elevation between winter and summer. The presence and type of vegetation (i.e. its height and density) has been assessed on optical imagery with the commercial software Google Earth™, the spatial resolution and quality is mostly sufficient for the purpose except

for older Landsat imagery. Given the difficult topography it was not always possible to fulfil both criteria (especially in SPI) and some compromises had to be accepted.

The availability of suitable CRs is strongly varying between Raw DEMs and generally limited. This is due, in the first place, to the extreme topography surrounding the icefields, which often does not offer flat ice-free areas. The availability is furthermore reduced by the presence of large phase unwrapping errors on this kind of terrain.

The situation is worse for the **SPI** because its surroundings are geographically rougher then NPI: the icefield is completely surrounded by mountains and water bodies, flat plains are not present in the vicinity of the icefield. Furthermore phase unwrapping errors are more frequent because single baseline phase unwrapping was used for most of the scenes. Finally being SPI much longer than NPI some scenes cover almost exclusively glaciated terrain. For this reason on SPI the effort was made to identify as many CRs as possible, even if small, to achieve a better statistical representation. A total of 74 non-adjacent CRs have been identified in SPI and are summarized in Table 7.1. The number of CRs per TanDEM-X Raw DEM is rather variable, but at least one CR was selected on each of them and at least three CRs on each datatake in order to increase the robustness of the coregistration procedure against possible outliers. Subsequent scenes belonging to the same datatake displayed generally small or negligible elevation offset between each other on the overlapping area (both on and off-glacier). This is somehow expected as the APO estimation should lead to similar results on subsequent scenes covering similar topography. This fact is also generally confirmed by the mean elevation difference displayed on the CRs of the same datatake (see Table 7.1). Because of the scarceness of CRs for some scenes (which have limited off-glacier terrain) it was decided to use all the CRs belonging to the same DT together and derive a single common height offset for all the scenes belonging to the DT. An exception are scenes S18 and S19 which are treated separately although belonging to the same datatake, because they are not subsequent.

The availability of suitable terrain is better in **NPI**. A large plain is present on the north-west of the icefield at the terminus of S. Quintin and S. Rafael glaciers, and other smaller flat regions are located at the southeastern margin (see Figure 7.5). The scene length of the Raw DEMs was changed to include these regions. The central datatakes either do not cover such regions or suffer from phase unwrapping errors at their location, hence smaller regions had to be used. The dual baseline phase unwrapping correction proved to be advantageous in NPI where performed, correctly unwrapping larger parts of ice-free terrain compared to the single baseline approach. The CRs identified in the NPI data are reported in Table 7.2. Scenes N2 and N3 have been processed from the same raw data once with multi baseline (N2) and once with single baseline (N3) phase unwrapping. They display exactly the same elevation on overlapping areas and thus require for coregistration a single height offset value obtained from a common set of CRs. Unfortunately for these scenes the flat terrain north of Laguna S. Rafael was affected by a large phase unwrapping error which rendered arduous the selection of CRs, restraining the selection to small and not too flat regions. For the whole NPI a total of 21 CRs has been identified, some extremely flat and large (up to 112 km^2). As shown in Table 7.2, some of the CRs in NPI are common to different adjacent datatakes allowing not only an estimate of the elevation offset against SRTM but also between TanDEM-X Raw DEMs. This procedure helped validating the estimated elevation offsets, although the quantitative results of this check are not reported here.

For each CR the mean and standard deviation of the corresponding TanDEM-X Raw DEM and of the DEM difference $\Delta h = h_{\mathrm{TDM}} - h_{\mathrm{SRTM}}$ have been extracted and are reported in Table 7.1 and 7.2, for SPI and NPI respectively. The standard deviation of the DEM is an indicator of flatness (and DEM noise) on the CR. The mean of Δh on CR r is denoted μ_r^{reg} and represents a local estimate of δh_{bias}, its values will be used to derive a single height offset for each DT. The standard deviation of Δh on r is denoted σ_r^{reg} and describes the spread of Δh within the CR, its values will be used to define the uncertainty of the obtained height offset for each DT. The distribution of Δh samples within the CR is not shown but it generally close to Gaussian. The uncertainty of the spatial mean μ_r^{reg} on CR r, can be defined by the standard error of the mean:

$$\mathrm{SE}_r^{\mathrm{reg}} = \frac{\sigma_r^{\mathrm{reg}}}{\sqrt{N_r}} \tag{7.2}$$

Table 7.1 – Calibration regions for SPI. The table reports for each CR their geographic position, area, mean and standard deviation of the TanDEM-X Raw DEM and of the $\Delta h = h_{\mathrm{TDM}} - h_{\mathrm{SRTM}}$ difference image, as well as the vegetation condition on the CR.

			TanDEM-X		Mos.			TanDEM-X DEM		Δh = (TDM - SRTM)			
CR ID	CR Name	CR Coordinates	DT AID	Sc.	IDX	Acq. date	Area [km²]	Mean [m]	Stdev [m]	Mean [m]	Stdev [m]	Std. Err. [m]	Vegetation
RS1	W_of_Chico	48°59'55.80"S, 73°5'18.15"W	1012654	27	S3	2011-03-07	1.5399	545.136	25.250	1.946	2.589	0.34855	No
RS2	W_of_Chico_2	48°59'40.65"S, 73°6'41.41"W	1012654	27	S3	2011-03-07	0.9709	546.411	38.883	2.015	2.974	0.50375	No
RS3	W_of_HPS13	49°41'33.32"S, 73°40'53.50"W	1012654	28	S4	2011-03-07	0.3024	535.980	18.427	2.382	5.078	1.50104	No, rock
RS4	S_of_Guilardi	50°26'56.17"S, 73°59'16.70"W	1012654	29	S10	2011-03-07	1.7095	22.997	3.403	-1.058	2.371	0.30301	Yes, not tall
RS5	south_front_Guilardi	50°23'10.04"S, 73°54'50.08"W	1012654	29	S10	2011-03-07	1.5982	194.827	48.596	0.089	3.761	0.49706	No, sparse
RS6	front_of_U27	50°11'18.96"S, 73°55'19.34"W	1012654	29	S10	2011-03-07	0.3631	143.746	30.140	1.565	3.817	1.03859	Yes, not tall
RS7	between_Penguin_and_Europa	50°9'18.94"S, 73°53'46.29"W	1012654	29	S10	2011-03-07	0.5557	372.031	37.848	1.374	4.805	1.06998	No, bare rock
RS8	front_of_Ameghino	50°24'12.29"S, 73°7'48.38"W	1021147	26	S13	2011-07-17	0.5658	225.348	3.619	2.863	1.046	0.23097	No, sand
RS9	SE_of_Tyndall	51°16'42.07"S, 73°10'39.62"W	1021147	27	S12	2011-07-17	7.1820	42.158	5.651	3.031	1.527	0.09523	No
RS10	SW_of_Grey	51°3'42.24"S, 73°16'49.38"W	1021147	27	S12	2011-07-17	3.5925	184.675	4.481	2.806	1.667	0.14701	Partial
RS11	between_Snowy_and_HPS41	51°19'13.06"S, 73°31'4.30"W	1021147	27	S12	2011-07-17	0.9461	58.310	3.237	3.191	1.760	0.30200	Likely sparse (Landsat)
RS12	S_of_Grey	51°7'39.77"S, 73°6'34.47"W	1021147	27	S12	2011-07-17	1.9613	82.577	18.268	3.167	1.632	0.19472	Partial
RS13	W_of_JorgeMontt	48°15'27.36"S, 73°36'6.83"W	1027766	1	S1	2011-05-09	1.0551	17.133	1.919	-1.451	1.716	0.27894	Likely not tall (Landsat)
RS14	NW_of_JorgeMontt_2	48°15'1.09"S, 73°30'4.30"W	1027766	1	S1	2011-05-09	0.9269	33.774	12.808	-1.394	2.529	0.43845	Likely not tall (Landsat)
RS15	N_of_JorgeMontt	48°10'36.88"S, 73°24'10.25"W	1027766	1	S1	2011-05-09	1.7325	68.077	10.876	-1.573	3.481	0.44185	Likely not tall (Landsat)
RS16	NW_of_JorgeMontt_4	48°13'58.68"S, 73°33'9.38"W	1027766	1	S1	2011-05-09	3.6734	21.227	5.206	-1.357	2.258	0.19690	No, grass
RS17	W_of_Mayo	50°21'40.99"S, 73°22'25.95"W	1027767	1	S15	2011-04-22	0.5722	209.078	5.638	1.399	3.998	0.87778	No
RS18	W_shore_L_Argentino	50°39'51.93"S, 73°0'1.15"W	1027767	1	S15	2011-04-22	2.1297	208.586	6.350	1.145	4.245	0.48609	No
RS19	S_of_PMoreno	50°34'24.74"S, 73°3'21.62"W	1027767	1	S15	2011-04-22	2.0623	601.400	10.310	1.182	4.859	0.56544	Partial, mostly grass
RS20	W_of_Frias	50°43'40.82"S, 73°3'29.75"W	1027767	1	S15	2011-04-22	1.0410	255.059	10.859	1.234	4.390	0.71845	No
RS21	S_of_Viedma	49°35'6.22"S, 73°10'11.09"W	1027772	1	S2	2011-05-01	0.1720	634.941	5.211	4.089	2.002	0.75031	No
RS22	S_of_Viedma_2	49°33'51.48"S, 73°10'14.88"W	1027772	1	S2	2011-05-01	0.2146	613.647	5.709	4.306	2.470	0.84648	Yes
RS23	N_of_viedma	49°23'7.07"S, 73°3'20.32"W	1027772	1	S2	2011-05-01	0.2918	685.777	3.806	2.871	3.590	1.07810	No
RS24	front_of_Upsala_E	49°52'37.92"S, 73°11'48.21"W	1027772	1	S2	2011-05-01	0.6735	453.939	56.406	4.155	4.882	0.99025	No, rock
RS25	N_of_Viedma_2	49°28'10.46"S, 73°3'17.26"W	1027772	1	S2	2011-05-01	1.9553	827.601	27.594	4.107	4.858	0.58054	No, rock
RS26	NW_of_HPS31	50°35'29.85"S, 73°40'44.04"W	1042632	23	S14	2011-10-24	1.2149	25.730	3.563	1.900	2.179	0.33019	Yes
RS27	between_HPS29_and_HPS31	50°30'18.33"S, 73°36'2.85"W	1042632	23	S14	2011-10-24	1.0690	219.649	66.537	2.257	6.061	0.97887	Yes
RS28	W_of_HPS34	50°39'26.06"S, 73°42'26.92"W	1042632	23	S14	2011-10-24	0.2882	27.275	4.339	2.359	2.554	0.77132	No, sparse
RS29	SW_of_HPS38	51°8'5.79"S, 73°40'56.36"W	1042632	24	S11	2011-10-24	1.6623	25.786	4.227	2.011	1.500	0.19440	No, sparse and low
RS30	W_of_HPS38	51°5'13.05"S, 73°45'4.92"W	1042632	24	S11	2011-10-24	3.1447	29.345	3.905	3.295	1.220	0.11494	No, sparse and low
RS31	W_of_Amalia	50°58'20.05"S, 73°46'14.46"W	1042632	24	S11	2011-10-24	1.4236	29.790	6.747	2.694	1.561	0.21858	No
RS32	W_of_HPS38_2	51°0'11.77"S, 73°59'13.98"W	1042632	24	S11	2011-10-24	4.7251	41.209	5.201	2.159	1.410	0.10837	No, sparse and low
RS33	front_HPS38	51°1'50.17"S, 73°48'52.68"W	1042632	24	S11	2011-10-24	1.5343	83.683	29.559	2.210	3.178	0.42861	No, grass
RS34	front_of_Chico	48°54'44.82"S, 72°57'58.95"W	1055763	16	S7	2012-03-26	0.9827	280.254	7.178	4.470	2.541	0.42797	No
RS35	N_of_OHiggins	48°48'51.78"S, 73°2'0.79"W	1055763	16	S7	2012-03-26	0.2782	526.005	32.207	4.030	2.915	0.89391	No, sparse
RS36	E_of_Chico	49°4'9.63"S, 72°57'21.13"W	1055763	16	S7	2012-03-26	0.9950	714.059	26.535	4.364	4.665	0.78070	No
RS37	E_of_Upsala	49°57'35.97"S, 73°7'31.62"W	1056403	22	S17	2012-03-15	2.8681	204.950	4.284	2.044	1.999	0.19722	No, sparse and low
RS38	S_of_Upsala	50°0'40.19"S, 73°9'51.18"W	1056403	22	S17	2012-03-15	0.3107	204.369	4.546	1.679	3.029	0.88447	No, sparse and low
RS39	SE_of_Upsala	50°0'45.22"S, 73°12'27.27"W	1056403	22	S17	2012-03-15	3.0394	203.881	4.100	1.401	1.671	0.16013	No
RS40	SW_of_Upsala	49°58'30.07"S, 73°20'40.33"W	1056403	22	S17	2012-03-15	0.9921	455.961	25.922	3.269	2.708	0.45383	No
RS41	E_of_Agassiz_Onelli	50°6'16.82"S, 73°17'29.05"W	1056403	22	S17	2012-03-15	0.7400	213.629	3.794	3.061	2.253	0.43651	Yes
RS42	W_of_Spegazzini	50°12'54.71"S, 73°9'17.98"W	1056403	22	S17	2012-03-15	1.4318	924.123	30.904	2.532	4.078	0.56940	Partial
RS43	SW_of_Upsala_2	49°58'55.20"S, 73°19'23.64"W	1056403	22	S17	2012-03-15	0.5088	302.302	22.922	2.383	4.329	1.00561	No
RS44	front_of_Tempano	48°40'2.59"S, 73°57'25.35"W	1057982	19	S9	2012-02-16	1.9910	124.446	3.005	3.257	1.573	0.18631	Likely not tall (Landsat)
RS45	front_of_Bernardo	48°35'29.32"S, 73°54'3.97"W	1057982	19	S9	2012-02-16	3.3144	24.005	3.296	2.860	1.591	0.14602	No, sparse and low
RS46	front_of_Ofhidro	48°23'59.80"S, 73°49'43.55"W	1057982	19	S9	2012-02-16	1.2655	25.491	4.299	3.347	1.837	0.27279	Yes (Landsat image)
RS47	SW_of_JorgeMontt	48°24'12.69"S, 73°43'1.96"W	1057982	19	S9	2012-02-16	0.7299	82.728	7.175	2.351	2.322	0.45286	Yes (Landsat image)
RS48	W_of_JorgeMontt_2	48°17'37.31"S, 73°37'33.56"W	1057982	19	S9	2012-02-16	0.8479	34.987	4.054	1.868	1.870	0.33883	Likely sparse (Landsat)
RS49	NW_of_JorgeMontt	48°14'26.25"S, 73°48'45.87"W	1057982	19	S9	2012-02-16	0.5778	450.051	18.503	3.161	3.754	0.82034	Likely sparse (Landsat)
RS50	between_Tempano_and_Bernardo	48°41'40.87"S, 73°51'25.21"W	1057982	19	S9	2012-02-16	0.3591	667.530	10.974	3.348	4.090	1.11872	No
RS51	W_of_Pio	49°9'32.92"S, 74°7'27.25"W	1057982	20	S5	2012-02-16	0.5989	76.350	16.218	3.427	4.034	0.86639	Partial
RS52	W_of_Pio_2	49°11'3.44"S, 74°15'33.75"W	1057982	20	S5	2012-02-16	1.1890	86.349	5.710	1.724	2.999	0.45942	No, sparse
RS53	front_of_Occidental_3	48°51'52.10"S, 74°9'51.96"W	1057982	20	S5	2012-02-16	0.4179	129.774	5.786	2.063	4.055	1.03386	No, sparse
RS54	front_of_Occidental_2	48°51'52.10"S, 74°9'51.96"W	1057982	20	S5	2012-02-16	1.2503	87.603	13.824	2.881	4.616	0.68959	No
RS55	front_of_Occidental	48°51'46.85"S, 74°12'46.30"W	1057982	20	S5	2012-02-16	2.7189	45.656	6.106	3.399	2.673	0.27085	Likely not tall (Landsat)
RS56	extreme_north	48°13'13.46"S, 73°19'24.74"W	1058255	8	S8	2012-02-11	2.4170	17.147	2.626	-2.555	1.959	0.21054	No, low (Landsat)
RS57	N_of_Lucia_Pascua	48°16'33.39"S, 73°10'38.05"W	1058255	8	S8	2012-02-11	3.0669	66.524	8.020	-2.755	2.044	0.19508	Partial
RS58	E_of_Bravo	48°39'5.74"S, 73°7'42.33"W	1058255	8	S8	2012-02-11	2.4997	286.113	14.045	-2.805	3.830	0.40478	No
RS59	N_of_Lucia_2	48°13'52.82"S, 73°17'1.90"W	1058255	8	S8	2012-02-11	0.9654	17.993	1.898	-2.574	1.937	0.32911	No, sparse and low
RS60	N_of_Oriental	48°25'3.50"S, 73°0'11.61"W	1058255	8	S8	2012-02-11	2.7487	279.749	7.001	-1.762	2.729	0.27511	No, sparse and low
RS61	S_front_HPS_9	49°4'44.61"S, 73°45'0.57"W	1058255	9	S6	2012-02-11	0.7592	181.016	4.746	-2.214	3.426	0.65532	No, rock
RS62	S_of_HPS9	49°5'50.99"S, 73°41'34.73"W	1058255	9	S6	2012-02-11	0.2207	208.902	6.031	-2.990	2.817	0.95427	No, sparse and low
RS63	between_pio_and_HPS10	49°18'51.21"S, 73°46'7.85"W	1058255	9	S6	2012-02-11	0.3870	104.934	9.354	-3.166	5.797	1.53168	Partial
RS64	front_of_HPS10	49°32'16.85"S, 73°49'41.51"W	1058255	10	S16	2012-02-11	2.4445	32.695	12.294	-2.558	2.610	0.27898	Partial
RS65	W_of_HPS12	49°39'16.17"S, 74°1'15.71"W	1058255	10	S16	2012-02-11	1.5307	22.014	2.552	-2.877	1.910	0.25794	Yes
RS66	S_of_Pio	49°20'49.93"S, 73°51'10.71"W	1058255	10	S16	2012-02-11	0.4576	21.736	3.434	-2.739	2.099	0.51280	No, sparse
RS67	S_of_Pio_2	49°21'54.12"S, 73°51'17.64"W	1058255	10	S16	2012-02-11	0.2428	36.456	7.476	-3.328	2.529	0.82283	No, sparse
RS68	front_of_Ameghino_2	50°23'43.17"S, 73°6'49.75"W	1058868	3	S18	2012-01-31	0.3238	207.380	3.344	1.910	1.867	0.53533	No, sand
RS69	E_shore_L_Argentino	50°39'23.54"S, 72°56'42.18"W	1058868	3	S18	2012-01-31	0.5940	209.222	3.519	2.257	2.301	0.49610	No
RS70	W_of_Lago_Dickson	50°51'41.46"S, 73°2'41.15"W	1058868	3	S18	2012-01-31	2.2173	202.702	6.154	1.030	2.482	0.27851	No, sparse
RS71	shore_front_PMoreno	50°29'23.50"S, 73°2'16.85"W	1058868	3	S18	2012-01-31	0.4262	236.129	14.001	1.082	5.454	1.37783	Yes
RS72	SW_of_HPS41	51°18'31.06"S, 73°37'50.60"W	1058868	5	S19	2012-01-31	3.5628	27.286	5.005	2.486	2.361	0.20902	Paritial
RS73	SW_of_HPS41_2	51°17'20.31"S, 73°38'30.91"W	1058868	5	S19	2012-01-31	1.2544	27.729	5.397	2.564	2.929	0.43684	Partial
RS74	S_of_Snowy_2	51°24'40.77"S, 73°33'21.25"W	1058868	5	S19	2012-01-31	0.8153	49.149	8.590	3.139	1.512	0.27917	No, low

Table 7.2 – Calibration regions for NPI. See caption of Table 7.1.

CR ID	CR Name	CR Coordinates	TanDEM-X DT AID	Sc.	Mos. IDX	Acq. date	Area [km²]	TanDEM-X DEM Mean [m]	Stdev [m]	Δh = (TDM - SRTM) Mean [m]	Stdev [m]	Std. Err. [m]	Vegetation
RN1	Calib_01_1191233	46°46'58.38"S, 74°9'13.61"W	1191233	10	N1	2014-02-14	112.1090	17.009	1.637	-3.070	0.931	0.01469	Small portion
RN2	Calib_02_1191233_1149794	46°45'0.38"S, 74°1'40.01"W	1191233	10	N1	2014-02-14	57.6636	19.683	1.972	-2.846	0.166	0.00366	No
RN3	Calib_03_1191233	46°53'53.97"S, 74°6'54.01"W	1191233	10	N1	2014-02-14	29.8608	18.456	1.806	-2.638	1.238	0.03785	Small portion
RN4	Calib_04_1191233	46°38'43.98"S, 74°10'8.81"W	1191233	10	N1	2014-02-14	19.0592	42.029	5.362	-3.292	1.093	0.04185	Low
RN5	Calib_05_1191233_1149794	47°0'38.77"S, 73°56'25.62"W	1191233	10	N1	2014-02-14	17.5675	25.581	5.113	-2.577	0.469	0.01870	Partially, not dense
RN6	Calib_06_1191233	46°40'4.78"S, 74°17'0.80"W	1191233	10	N1	2014-02-14	17.2154	26.507	3.610	-3.437	1.464	0.05896	Partially
RN7	Calib_07_1191233_1149794	46°48'56.38"S, 74°0'44.81"W	1191233	10	N1	2014-02-14	12.9846	34.298	4.632	-2.753	0.915	0.04245	No
RN8	Calib_08_1191233_1149794	46°32'17.19"S, 74°8'5.61"W	1191233	10	N1	2014-02-14	10.4430	50.165	3.876	-4.016	1.085	0.05613	No
RN9	Calib_09_1191233	47°0'27.57"S, 74°7'20.81"W	1191233	10	N1	2014-02-14	5.2342	51.712	6.249	-3.729	1.214	0.08866	Yes
RN2	Calib_02_1191233_1149794	46°45'0.38"S, 74°1'40.01"W	1149794	10	N5	2013-09-02	57.6636	18.678	2.421	-3.851	1.594	0.03508	No
RN5	Calib_05_1191233_1149794	47°0'38.77"S, 73°56'25.62"W	1149794	10	N5	2013-09-02	17.5675	24.388	5.367	-3.770	2.133	0.08503	Partially, not dense
RN7	Calib_07_1191233_1149794	46°48'56.38"S, 74°0'44.81"W	1149794	10	N5	2013-09-02	12.9846	33.452	4.794	-3.599	1.457	0.06756	No
RN8	Calib_08_1191233_1149794	46°32'17.19"S, 74°8'5.61"W	1149794	10	N5	2013-09-02	10.4430	49.268	4.056	-4.913	1.513	0.07826	No
RN10	Calib_10_1171117	47°8'38.37"S, 73°20'25.24"W	1171117	9	N2, N3	2014-01-01	8.9088	1018.102	104.330	-5.313	10.363	0.58022	Partial
RN11	Calib_11_1171117	47°5'31.97"S, 73°16'54.84"W	1171117	9	N2, N3	2014-01-01	7.7091	813.891	115.333	-4.463	6.458	0.38869	No
RN12	Calib_12_1171117	47°10'17.16"S, 73°16'38.44"W	1171117	9	N2, N3	2014-01-01	6.5870	606.420	101.970	-5.552	5.162	0.33609	No
RN13	Calib_13_1171117	47°19'18.36"S, 73°14'14.44"W	1171117	9	N2, N3	2014-01-01	6.2279	721.765	64.942	-7.007	5.284	0.35385	No
RN14	Calib_14_1171117	46°31'6.79"S, 73°41'49.63"W	1171117	9	N2, N3	2014-01-01	3.2942	29.830	8.668	-5.331	1.273	0.11717	Very sparse
RN15	Calib_15_1171117	47°28'19.15"S, 73°20'11.64"W	1171117	9	N2, N3	2014-01-01	2.5695	365.786	59.023	-4.979	5.476	0.57089	Sparse
RN16	Calib_16_1172605	46°21'34.79"S, 73°19'27.64"W	1172605	7	N4	2014-01-12	25.1067	35.669	10.666	-4.567	2.864	0.09551	Partially
RN17	Calib_17_1172605	47°19'19.16"S, 72°57'52.05"W	1172605	7	N4	2014-01-12	11.4043	110.551	8.458	-4.737	1.443	0.07142	No
RN18	Calib_18_1172605	47°7'10.37"S, 72°54'0.45"W	1172605	7	N4	2014-01-12	10.5681	226.048	5.678	-4.954	1.646	0.08460	No
RN19	Calib_19_1172605	46°27'27.99"S, 73°12'28.04"W	1172605	7	N4	2014-01-12	8.8693	73.759	13.131	-5.066	2.861	0.16055	Small portion
RN20	Calib_20_1172605	46°43'23.18"S, 73°3'48.05"W	1172605	7	N4	2014-01-12	6.2680	287.695	12.292	-5.371	2.606	0.17394	Sparse
RN21	Calib_21_1172605	46°18'23.60"S, 73°25'50.84"W	1172605	7	N4	2014-01-12	5.5346	15.141	0.635	-4.701	0.856	0.06081	No

where N_r indicates the number of spatially uncorrelated samples on CR r and is obtained according to Equation (9.30) as explained in 9.3.4, which simplifies to:

$$N_r = \frac{9}{2}\frac{A_r}{A_{\text{cor}}} \tag{7.3}$$

if $A_r \gg A_{\text{cor}}$, where A_r is the total area of the CR and A_{cor} is the correlation area, i.e. the area within which elevation difference measurements are spatially correlated. The correlation area is defined from the correlation distance d_{cor}, which is estimated empirically on the $\Delta h = h_{\text{TDM}} - h_{\text{SRTM}}$ using semivariograms and represents the distance beyond which spatial correlation approaches zero. The spatial statistics theory behind semivariograms is explained in Section 9.1.1.1, while the quantitative derivation of the correlation distance used here can be found in Section 9.3.4. The correlation distance for relatively flat areas such as those characterizing the calibration regions has been estimated to be $d_{\text{cor}} = 200$ m. The correlation area is obtained as the area of a circle with radius d_{cor}, i.e. $A_{\text{cor}} = \pi d_{\text{cor}}^2 = 0.12566\ \text{km}^2$.

To obtain a single heigh offset for the entire datatake (which is an estimate of δh_{bias}), the weighted mean of the μ_r^{reg} for all $r \in d$ is computed. CRs are considered to be statistically independent as they are geographically distant and scattered on the entire datatake. The weights used are the squared inverse of the standard errors of the mean SE_r^{reg}, i.e. $w_r = \frac{1}{\left(\text{SE}_r^{\text{reg}}\right)^2} = \frac{N_r}{\left(\sigma_r^{\text{reg}}\right)^2}$. The higher the weight, the more accurate the spatial mean μ_r^{reg}. The weight is linearly proportional to the area A_r of the CR (through N_r) and inversely proportional to the variance of the elevation difference pixels $\left(\sigma_r^{\text{reg}}\right)^2$. The height offset for datatake d is computed as the following weighted mean:

$$\mu_d^{\text{reg}} = \frac{\sum_r w_r \mu_r^{\text{reg}}}{\sum_r w_r} = \frac{\sum_r \frac{\mu_r^{\text{reg}}}{\left(\text{SE}_r^{\text{reg}}\right)^2}}{\sum_r \frac{1}{\left(\text{SE}_r^{\text{reg}}\right)^2}} \tag{7.4}$$

and its standard error is obtained as:

$$\text{SE}_d^{\text{reg}} = \frac{\sqrt{\sum_r \left(w_r \cdot \text{SE}_r^{\text{reg}}\right)^2}}{\sum_r w_r} = \frac{1}{\sqrt{\sum_r \frac{1}{\left(\text{SE}_r^{\text{reg}}\right)^2}}} \tag{7.5}$$

SE_d^{reg} expresses the uncertainty of the derived height offset and hence the accuracy of the calibration procedure for datatake d. This term will be included in the mass balance error budget as a systematic error affecting all elevation difference pixels equally, as described in Section 9.3.6.

Table 7.3 – Estimated height offsets and the corresponding accuracy along with the elevation correction applied to the TanDEM-X Raw DEM scenes of the SPI.

AID	Scene	Index	Date	μ_d^{reg} [m]	SE_d^{reg} [m]	δh_{bias} correction [m]
1012654	27, 28, 29	S3, S4, S10	2011.03.07	0.563	0.18457	−0.6
1021147	26, 27	S13, S12	2011.07.17	2.993	0.06858	−3.0
1027766	1	S1	2011.05.09	−1.408	0.14290	+1.4
1027767	1	S15	2011.04.22	1.203	0.30722	−1.2
1027772	1	S2	2011.05.01	4.011	0.35313	−4.0
1042632	23, 24	S14, S11	2011.10.24	2.565	0.06658	−2.6
1055763	16	S7	2012.03.26	4.386	0.34602	−4.4
1056403	22	S17	2012.03.15	1.889	0.11169	−1.9
1057982	19, 20	S9, S5	2012.02.16	2.936	0.08847	−2.9
1058255	8, 9, 10	S8, S6, S16	2012.02.11	−2.583	0.09350	+2.6
1058868	3	S18	2012.01.31	1.415	0.21837	−1.4
1058868	5	S19	2012.01.31	2.700	0.15625	−2.7

Table 7.4 – Estimated height offsets and the corresponding accuracy along with the elevation correction applied to the TanDEM-X Raw DEM scenes of the NPI.

AID	Scene	Index	Date	μ_d^{reg} [m]	SE_d^{reg} [m]	δh_{bias} correction [m]
1191233	10	N1	2014.02.14	−2.858	0.00343	+2.9
1149794	10	N5	2013.09.02	−3.931	0.02739	+3.9
1171117	9	N2, N3	2014.01.01	−5.414	0.09885	+5.4
1172605	7	N4	2014.01.12	−4.782	0.03563	+4.8

The values of μ_d^{reg} and SE_d^{reg} are reported in Table 7.3 for SPI and in Table 7.4 for NPI. The obtained values of μ_d^{reg} are relatively small (maximum of −5.414 m for N2/N3), this reflects also in small horizontal shifts in ground range. Datatakes where larger CRs could be selected (particularly N1, N4, N5) result in a low error SE_d^{reg} (minimum 0.00343 m on N1). Other datatakes, with CRs characterized by small area and larger standard deviation σ_r^{reg} due to the slope and roughness, have larger error SE_d^{reg} (maximum 0.35313 m on S2).

For each scene s of DT d the estimated elevation offsets μ_d^{reg} (a positive value means that the TanDEM-X Raw DEM is higher than the SRTM DEM) have been rounded to the first decimal and used as an estimate of the relative height offset δh_{bias} between the Raw DEM and the SRTM DEM. This was used (with opposite sign) to coregister vertically and horizontally the Raw DEM to the reference SRTM DEM according to the procedure described before.

The newly calibrated Raw DEMs have been assessed against each other on overlapping terrain, including ice covered surface. Here for acquisitions from the same year and season the mean elevation was extracted and compared on overlapping areas characterized by similar radar backscattering. The corrected elevations displayed good agreement. The horizontal coregistration with respect to the SRTM appears to be achieved as well: the difference images do not display a hillshade effect (see Figure 7.9) and the method of Nuth & Kääb (2011) confirmed the validity of the correction. The quality of the coregistration was furthermore confirmed by comparing on stable terrain (ice-free) the corrected TanDEM-X Raw DEMs and the SRTM C-band DEM to several ICESat GLAS altimetry tracks acquired between 2003 and 2009. Nevertheless a certain amount of residual horizontal misregistration can be expected, given the uncertainty linked to the height offset estimation. Its contribution will be accounted in the mass balance error budget.

Some issues concerning the coregistration procedure are now discussed. Variability of the μ_r^{reg} extracted on different CR r within the datatake d (evident on scene S10, Table 7.1) can be due to different reasons. Slopes on a CR (marked by higher elevation standard deviation) will introduce a δh_{hor} component which affects the extracted Δh statistics. TanDEM-X winter scenes might have snow cover on the CR which, especially if wet, would lead to a higher scattering phase centre compared

to the ground measured by the summer SRTM. A similar effect would happen on the few CR with dense, tall vegetation, particularly with acquisitions in different seasons. Variability among CRs of the same datatake might also be due to relative error of both DEMs, especially SRTM. As discussed in 6.1.1, the major problem would be caused by long wavelength height errors, but given their nature they would be almost constant across the study area and thus be compensated by the coregistration procedure, besides this region proved not to be affected by such a problem (cf. Section 6.1.1). The SRTM DEM might still have some residual unmasked PU errors but they would mostly affect layover and shadow areas rather than flat terrain. These are unlikely in this region given the abundance of overlapping acquisitions, in fact height jumps in the order of the SRTM HoA (125 - 325 m) were not observed. The interpolation to fill small gaps performed during editing of the SRTM DEM, or some residual mosaicking "jumps" between datatakes could also lead to less reliable local elevations. All these problems are somehow counteracted by the use of a weighted average of different CRs scattered spatially. An elevation dependent bias as reported by some authors in the literature was not observed over flat terrain (see 9.1.1.7 and 9.3.1) and should not affect the coregistration. Dietrich *et al.* (2010) measured very strong crustal uplift rates due to glacial isostatic adjustment up to 40 mm a^{-1} on SPI (lower values are expected on NPI). The relative coregistration presented here based on CRs located in the vicinity of the icefield allows to compensate most of the crustal uplift. This issue is discussed in more detail in 9.3.8.

7.3 Elevation change maps derivation

After calibration, elevation difference images were obtained for each scene by subtracting the SRTM DEM (bi-linearly oversampled) from each coregistered TanDEM-X Raw DEM, obtaining the elevation difference image $\Delta h = h_{\mathrm{TDM}} - h_{\mathrm{SRTM}}$. A corresponding elevation difference rate image $\frac{\Delta h}{\Delta t}$ was obtained dividing all pixels by the time span Δt in years between the TanDEM-X acquisition and a time reference for the SRTM DEM (17.02.2000 was used). All images are in geographic coordinates up to this point.

The calibrated TanDEM-X Raw DEMs h_{TDM}, the elevation difference Δh and elevation difference rate images $\frac{\Delta h}{\Delta t}$ were mosaicked for each icefield. UTM projection was used (zone 18 south) for the mosaics, with a pixel spacing of 10 m (in easing and northing) for SPI, where Raw DEMs have a 0.2/0.3 arcsec posting and 12 m for NPI, where Raw DEMs where either processed at 0.4 arcsec or subsequently converted to this posting. The overlapping SRTM DEM for SPI and NPI was also obtained with the same coverage, projection and pixel spacing.

The mosaics are composed of 19 scenes in SPI and 5 scenes in NPI. These are assigned an index as reported in Table 7.5 and 7.6 and stacked according to the order of the index (lower index in foreground, higher index in background). Invalid values of each scene are filled by valid values of underlying scenes, where available. The tables also report some useful parameters of each TanDEM-X scene (referring to the master acquisition when dual baseline PU was used), including the Δt with SRTM and the glacier surface covered in the mosaic. The spatial coverage of the scenes is shown in Figure 7.3 for NPI an Figure 7.4 for SPI.

7.4 Results and discussion

The elevation change rate maps obtained are shown in Figure 7.6 for NPI and 7.8 for SPI. The SRTM C-band DEM, which has no voids, is also shown in Figure 7.5 and 7.7 to aid interpretation. The glacier outline (cf. Section 6.3), represents the maximum extent during the observation period. The total glacier area A^{GL}, amounts to 12880.7 km^2 for SPI and 3867.0 km^2 for NPI. The unsurveyed areas due to phase unwrapping errors in the TanDEM-X Raw DEMs are marked in white in Figure 7.6 and 7.8. The total unsurveyed area A^{EX} amounts to 497.8 km^2 (12.9% of A^{GL}) and 921.1 km^2 (7.2% of A^{GL}) for NPI and SPI, respectively. For NPI most of the unsurveyed areas are located in the north-east margin where the higher altitudes are reached, mostly within scene N4. As expected other PU error are located along the mountain ranges crossing the plateau, where steeper slopes are found. This generally applies to SPI as well, although here some flat areas are also affected due to the use of single baseline PU for

Table 7.5 – SPI mosaic scenes and relevant characteristics (master DT). Experimental datatakes are marked with *.

IDX	Main glaciers covered	Acquisition date	Acq. time (UTC)	Look ang. [°]	HoA [m]	AID	Δt [a]	Glac. area [km^2]
S1	Jorge Montt, Lucia	2011.05.09	23:46	33.71	120.98	1027766*	11.230	988.7
S2	Upsala, Viedma, Cono, Bertacchi	2011.05.01	09:54	41.28	48.42	1027772*	11.208	1180.6
S3	Viedma (upstream), Chico	2011.03.07	09:54	42.78	−43.14	1012654	11.058	1115.9
S4	Upsala (upstream), Viedma (upstream), Cono, Bertacchi	2011.03.07	09:54	42.77	−43.44	1012654	11.058	936.4
S5	Pio XI (terminus), Occidental, Greve, HPS 8	2012.02.16	10:02	36.19	−88.48	1057982	12.005	419.9
S6	Pio accumulation, HPS 9	2012.02.11	09:54	44.59	112.26	1058255	11.992	1104.3
S7	O' Higgins, Gaea, Chico (terminus)	2012.03.26	09:54	42.69	−105.52	1055763	12.112	255.9
S8	Jorge Montt (part), Lucia, Pascua, Bravo, Melizo Sur, Oriental	2012.02.11	09:54	44.57	112.98	1058255	11.992	946.5
S9	Jorge Montt (fraction), Tempano, Bernardo, Ofhidro	2012.02.16	10:02	36.22	−88.58	1057982	12.005	513.2
S10	HPS 19, Penguin, Europa, Guilardi	2011.03.07	09:54	42.70	−43.63	1012654	11.058	1335.5
S11	Asia/Burjo, Amalia, HPS 38	2011.10.24	09:54	40.60	−64.83	1042632	11.690	523.5
S12	Grey, Tyndall, Olvidado, Pingo, HPS 38, HPS 41	2011.07.17	09:54	38.48	49.75	1021147	11.419	678.0
S13	Perito Moreno, Grey (upstream)	2011.07.17	09:54	38.52	49.48	1021147	11.419	591.6
S14	Ameghino, HPS 31, HPS 34, Fernando	2011.10.24	09:54	40.64	−64.88	1042632	11.690	459.5
S15	Perito Moreno, Ameghino, Frias HPS, Mayo, HPS 28, Cubo	2011.04.22	23:53	40.94	256.05	1027767*	11.184	289.1
S16	HPS 10, Trinidad	2012.02.11	09:54	44.53	111.81	1058255	11.992	252.5
S17	Spegazzini, Onelli, Bolados, Agassiz, Bretacchi	2012.03.15	09:54	40.67	−98.85	1056403	12.082	207.8
S18	Ameghino, Perito Moreno, Frias HPS, Calvo, Dickson, Olvidado	2012.01.31	09:54	38.46	−94.04	1058868	11.962	40.1
S19	Balmaceda, Snowy, HPS 41 (terminus)	2012.01.31	09:54	38.41	−93.46	1058868	11.962	120.5

Table 7.6 – NPI mosaic scenes and relevant characteristics (master DT).

IDX	Main glaciers covered	Acquisition date	Acq. time (UTC)	Look ang. [°]	HoA [m]	AID	Δt [a]	Glac. area [km^2]
N1	S. Quintin, Benito, HPN 1, Acodado, Steffen	2014.02.14	23:46	34.83	−50.45	1191233	14.0	875.1
N2	Gualas, S. Rafael, S. Quintin, Pared Norte, Colonia	2014.01.01	23:46	37.19	68.58	1171117 2B	13.9	1440.5
N3	Gualas, S. Rafael, S. Quintin, Pared Norte, Colonia	2014.01.01	23:46	37.19	68.58	1171117 1B	13.9	416.2
N4	Grosse, Exploradores, Fiero, Nef	2014.01.12	23:46	39.93	66.66	1172605	13.9	357.4
N5	S. Rafael, S. Quintin, Benito, HPN 1, Acodado, Steffen	2013.09.02	23:46	36.17	64.36	1149794	13.6	280.1

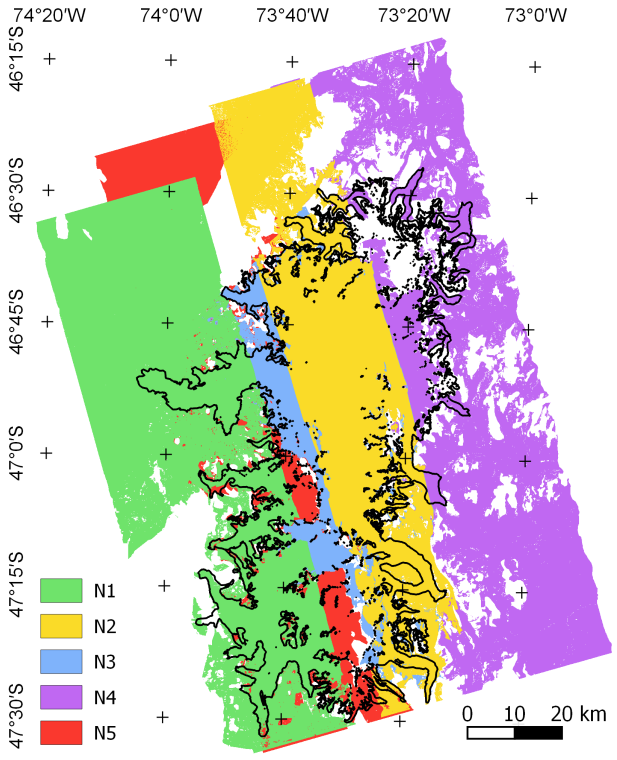

Figure 7.3 – NPI Raw DEM coverage.

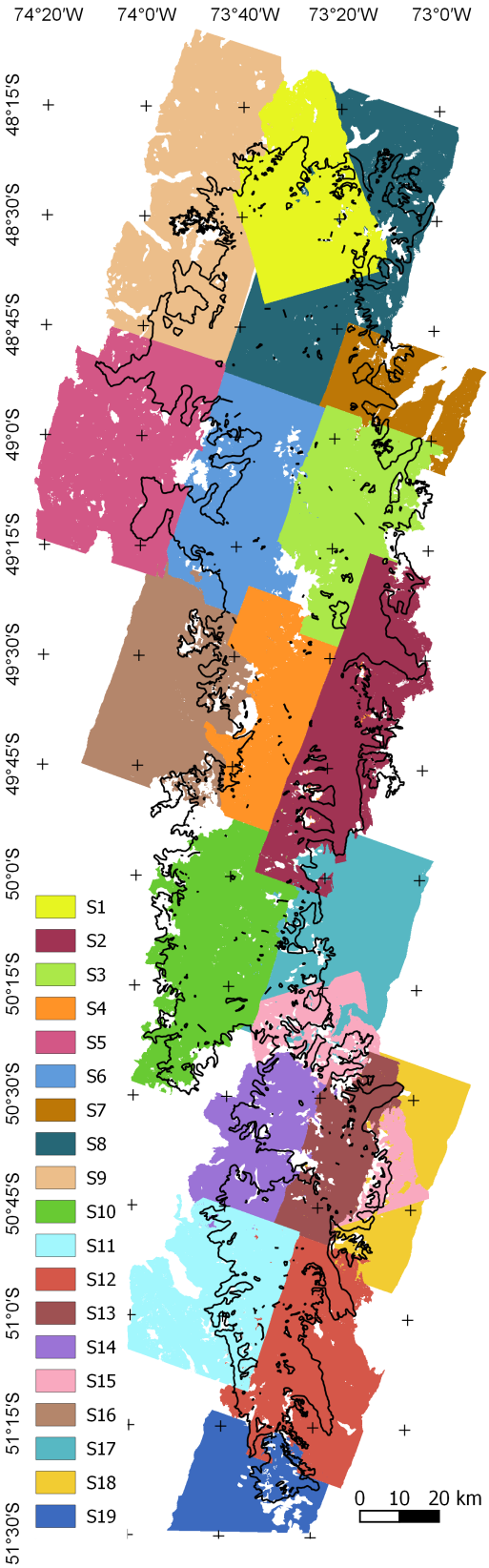

Figure 7.4 – SPI Raw DEM coverage.

most of the Raw DEMs.

The **NPI** elevation change rate observed between February 2000 and early 2014 does not feature any thickening trend. Instead most of the outlet glaciers display thinning and in rare cases a stable behaviour. The strongest thinning trends are found on the glacier termini located in the south-west of the icefield. The elevation change rate reaches its peak of $-9\,\mathrm{m\,a^{-1}}$ at the front of HPN 1 Glacier, while the nearby Benito, Acodado and Steffen glaciers lost up to $-8\,\mathrm{m\,a^{-1}}$ of ice thickness. The latter two are characterized by a significant thinning trend extending up to the plateau until approximately 1800 m of altitude. A similar behaviour is shared by the calving S. Rafael Glacier, which is the second largest glacier with an area of 720 $\mathrm{km^2}$ and is characterized by an extremely fast ice flow up to $15\,\mathrm{m\,d^{-1}}$. The other glaciers display strong thinning on their termini but have a more limited ice loss within their basins on the plateau, up to $1.5\,\mathrm{m\,a^{-1}}$. The largest glacier is the S. Quintin (790 $\mathrm{km^2}$), here strong thinning is detected at the termini, while a relatively constant thinning of approximately $1.3\,\mathrm{m\,a^{-1}}$ characterizes the plateau. The divide between its basin and that of the nearby S. Rafael Glacier is clearly visible in Figure 7.6. The glaciers on the eastern margin have a more limited thinning mostly constrained to their termini, the maximum elevation loss is found at the Colonia glacier ($-7\,\mathrm{m\,a^{-1}}$). At higher altitudes, above 2000 m, the thinning signal is reduced. The large unsurveyed area surrounding Monte San Valentin (4058 m a.s.l.) is expected to have a stable behaviour given its altitude and by observing the small measured patches in its surroundings. Most of the glaciers of NPI are non-calving, or calve into relatively constrained lakes. The lack of the calving ice loss phenomenon may be one of the explanations for the slower thinning rates compared to those of SPI.

The **SPI** is characterized by a vast extent and different climatological dynamics on its western and eastern margins, which are separated by a mountain range crossing the plateau approximately north to south from west of Grey Glacier up to north-east of Pio XI Glacier (see Figure 7.7). These features make the icefield a complex system displaying a variable dynamic behaviour which reflects in the ice elevation changes measured by this study in the observation period 2000 - 2011/2012 and shown in Figure 7.8.

The southern sector of SPI displays significant thinning at all of its termini in the eastern and western margin, including the two large glaciers Grey (255 $\mathrm{km^2}$) and Tyndall (315 $\mathrm{km^2}$). This sector displays modest altitudes up to 2000 m and is not divided longitudinally by the mountain range crossing the plateau starting just above the Grey Glacier basin.

The mid-southern sector up to Upsala Glacier displays a generally stable behaviour on both margins. The two largest glacier basins are those of the Europa Glacier (390 $\mathrm{km^2}$) and Perito Moreno Glacier (255 $\mathrm{km^2}$) which proved to be in a balanced state. The Calvo Glacier (95 $\mathrm{km^2}$) which flows in a very deep and constrained valley shows a light thickening trend up to $+3\,\mathrm{m\,a^{-1}}$ at the front with almost negligible frontal advance. Other smaller glaciers display thinning at the the termini, this is particularly strong for the Ameghino Glacier (65 $\mathrm{km^2}$) and the Onelli and Bolados glaciers. On the plateau varying behaviour is recorded, from stable to slight thinning (ca. $-0.3\,\mathrm{m\,a^{-1}}$).

The northern half of SPI hosts the largest glacier termini and basins and features the strongest change patterns. On the eastern margin the huge Viedma (1040 $\mathrm{km^2}$) and Upsala (750 $\mathrm{km^2}$) glaciers thinned at very fast rates on the entire basin. The Upsala Glacier displays rates up to $-2\,\mathrm{m\,a^{-1}}$ at 1650 m and up to $-18\,\mathrm{m\,a^{-1}}$ at its main front (Figure 7.9b) which underwent a strong frontal retreat of 3.5 km. Increasing frontal flow velocities from $4\,\mathrm{m\,d^{-1}}$ to $10\,\mathrm{m\,d^{-1}}$ were measured from January 2008 to October 2009 with feature tracking applied to TerraSAR-X data (see Section 11.5.1). As a consequence, dynamic thinning (cf. Section 3.4) may explain the high elevation change of the terminus.

The Pio XI (or Brüggen) Glacier is the largest of the SPI (1220 $\mathrm{km^2}$), its catchment basin, partially discharging in the smaller Trinidad Glacier, appears to be well confined by an arching mountain range which includes the peaks of Cordon Moreno (3490 m a.s.l.) and Volcan Lautaro (3607 m a.s.l.). These two glaciers display a significant thickening trend mostly on the terminal part, with average of around $+3.5\,\mathrm{m\,a^{-1}}$ and a peak of $+10\,\mathrm{m\,a^{-1}}$ at the main front of Pio XI, a peak of $+15\,\mathrm{m\,a^{-1}}$ at the smaller north front of Pio XI and $+9\,\mathrm{m\,a^{-1}}$ at the front of Trinidad Glacier. A detailed unsaturated view of the elevation change rate at the terminus of Pio XI is shown in Figure 7.9c. On the plateau, weak positive elevation rates are measured on the western margin and turn into null or slightly negative values towards the east.

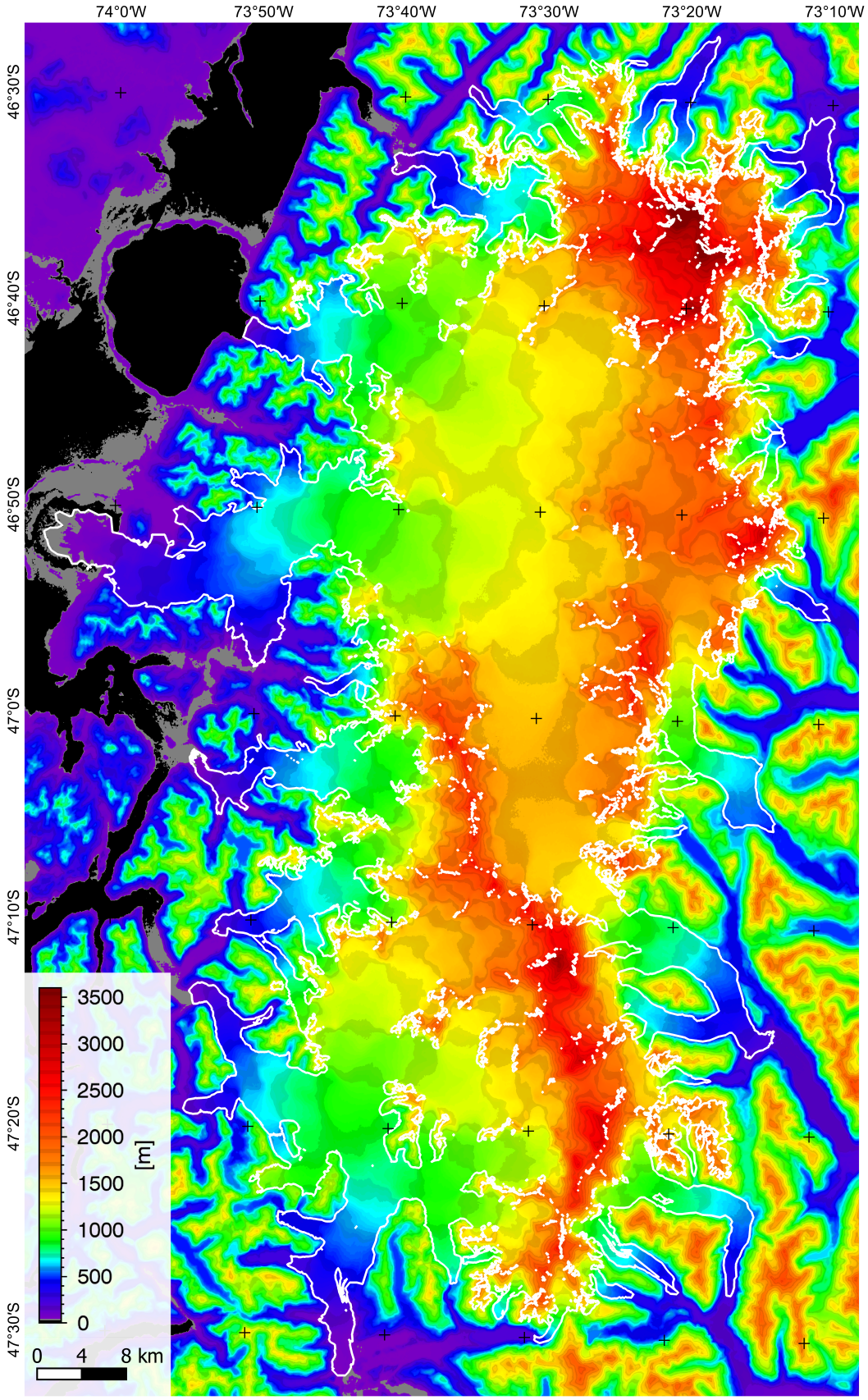

Figure 7.5 – SRTM C-band DEM of the NPI region. The icefield is outlined in white.

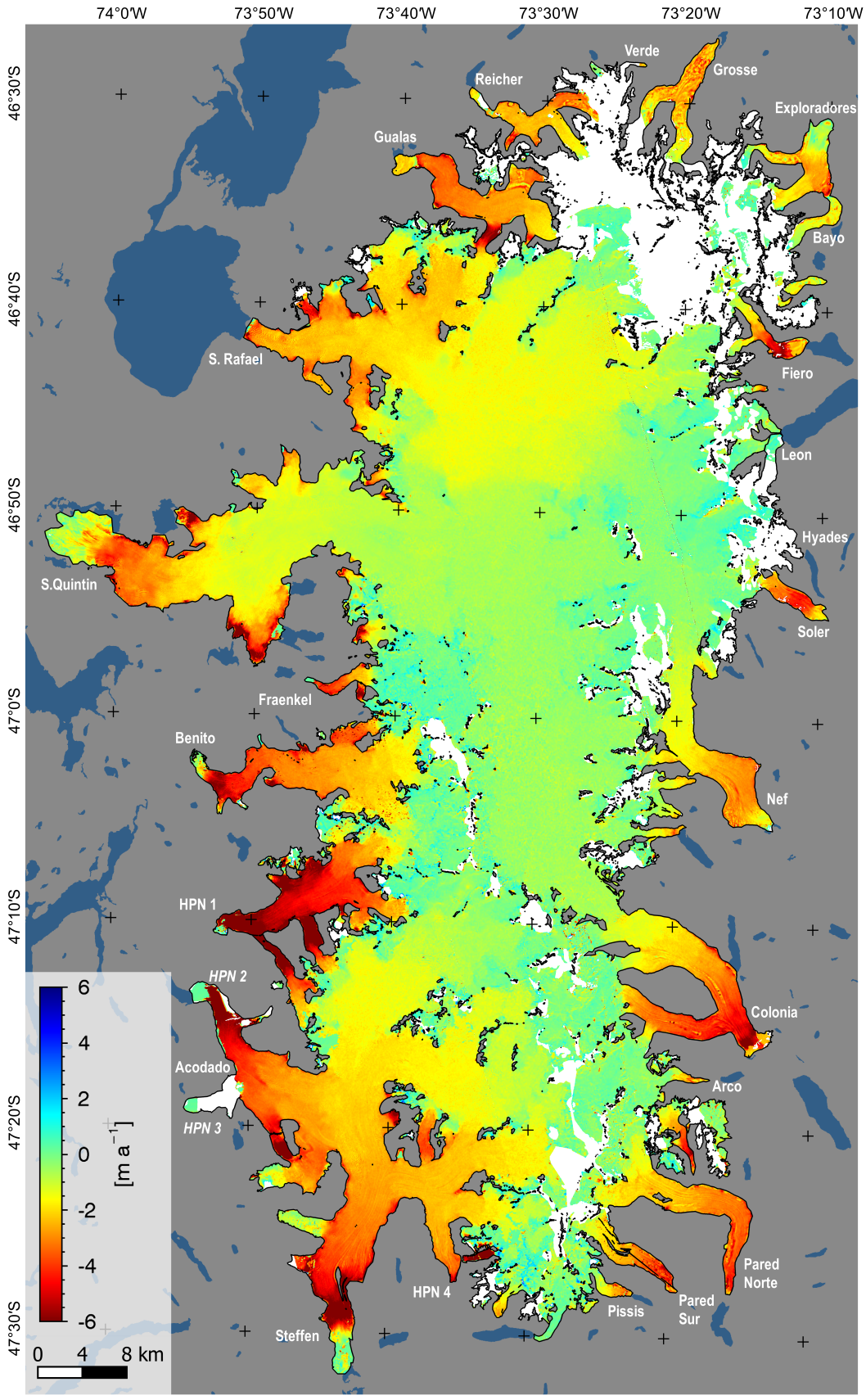

Figure 7.6 – Elevation change rate map of NPI. The icefield is outlined in black. White areas represent icefield missing data due to phase unwrapping errors in the TanDEM-X Raw DEMs. Land surface is filled in grey and water bodies in blue.

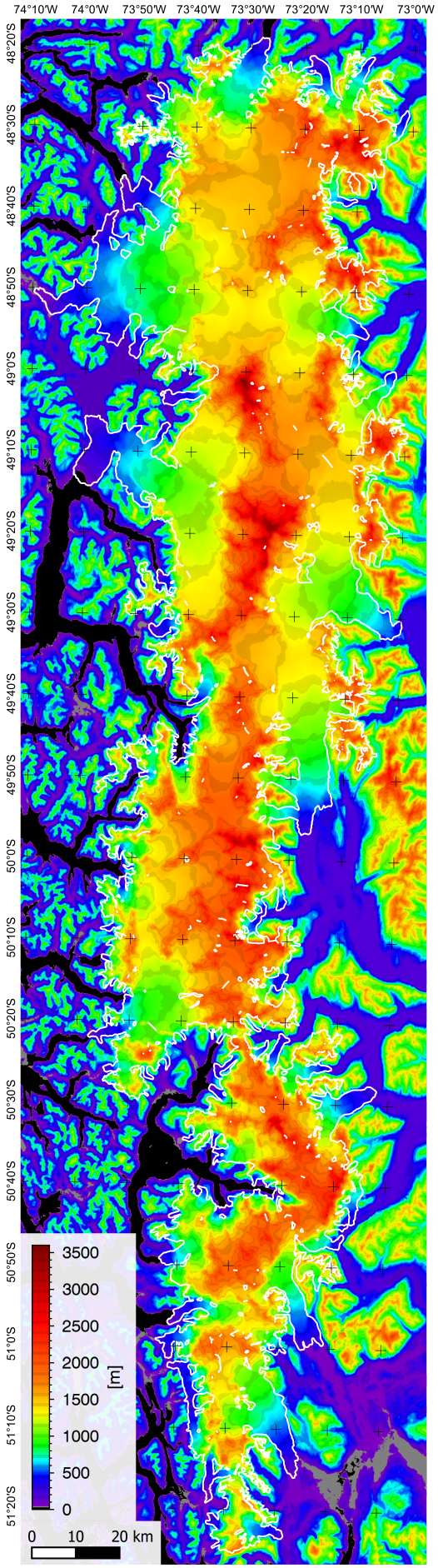

Figure 7.7 – SRTM C-band DEM of SPI.

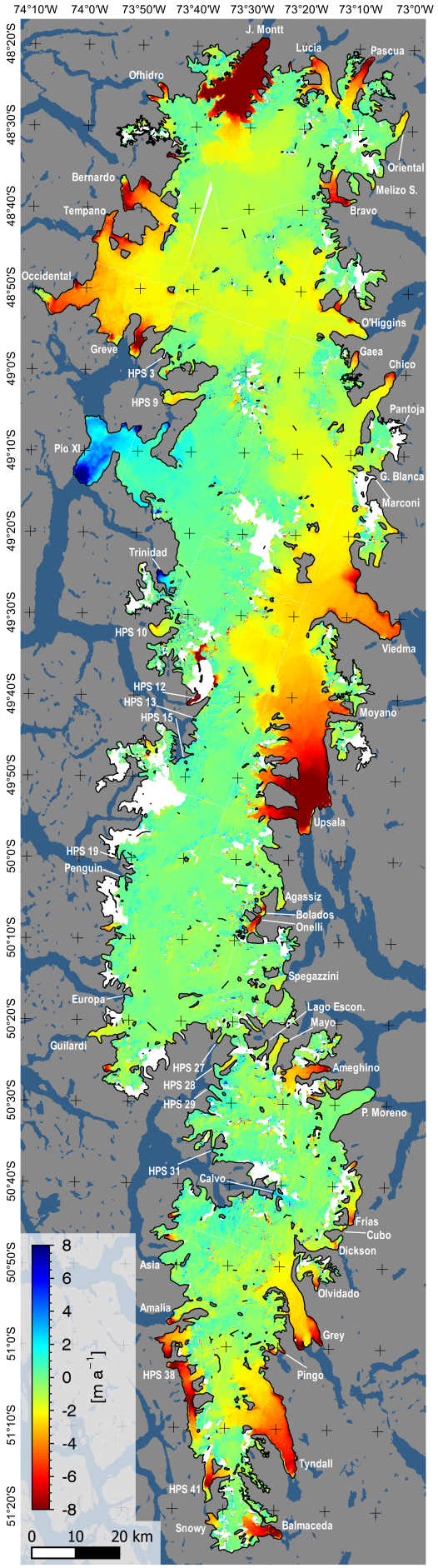

Figure 7.8 – Elevation change rate of SPI.

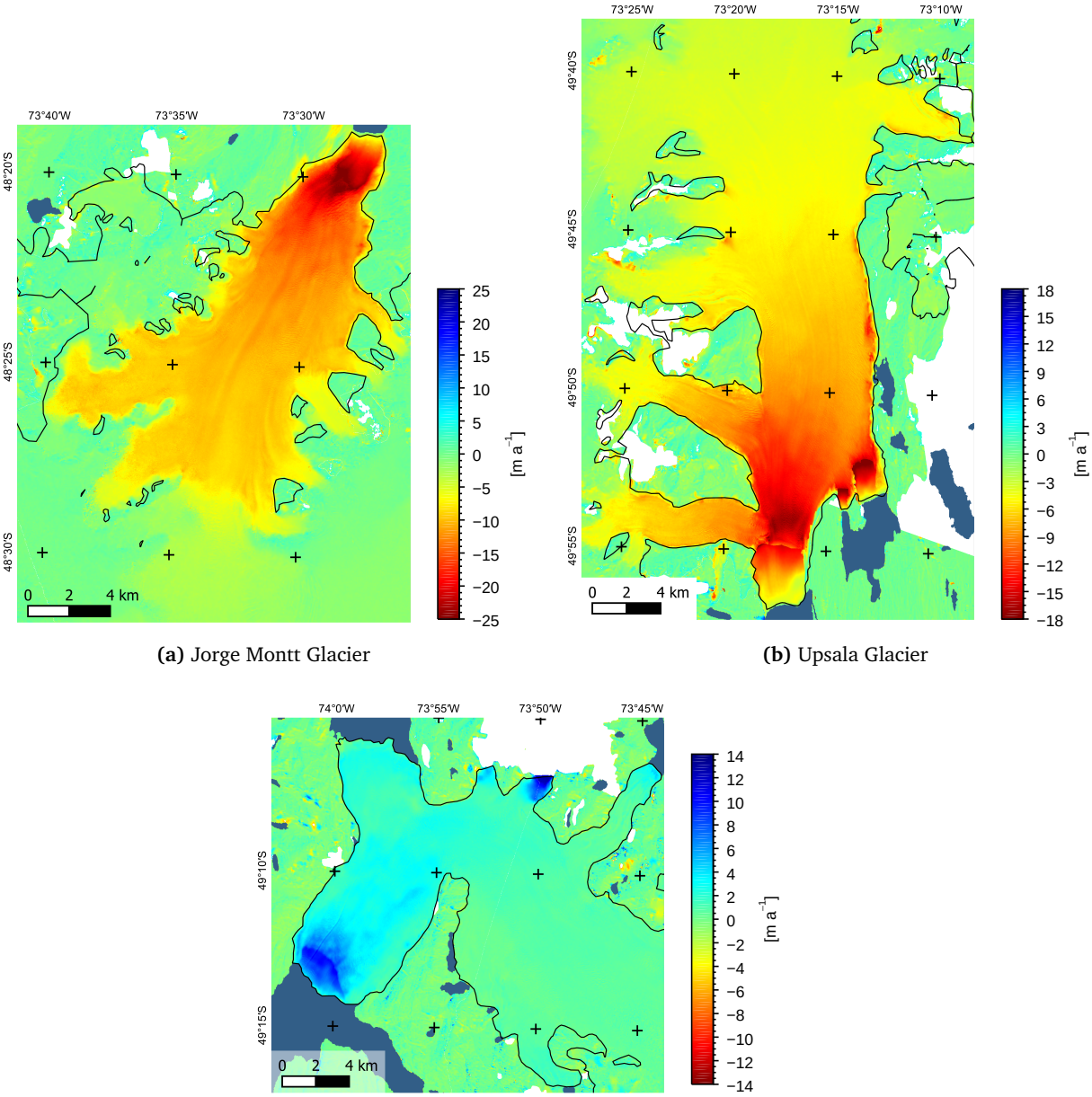

(a) Jorge Montt Glacier

(b) Upsala Glacier

(c) Pio XI Glacier

Figure 7.9 – Elevation change rate for three main glaciers of SPI displaying the strongest elevation changes, causing colourscale saturation in Figure 7.8. White areas indicate missing data due to phase unwrapping errors in the TanDEM- X Raw DEMs.

The O'Higgins Glacier (790 km^2) appears to have a relatively constant thinning rate around −1.6 $m\,a^{-1}$ across its basin including its terminus.

The glacier complex formed by Greve (495 km^2), Occidental (176 km^2), Tempano (285 km^2) and Bernardo (540 km^2) forms the largest catchment basin of SPI. It displays significant thinning on the plateau up to 1500 m, and increasingly high losses on the termini.

The Jorge Montt Glacier (490 km^2) is probably the most interesting and impressing case of the Patagonian icefields. It is located at the northern margin of SPI and calves into a tidewater fjord. Ice thinning rates ranging from −1.5 $m\,a^{-1}$ at 1550 m to −3.1 $m\,a^{-1}$ at 1200 m are measured on the plateau. As soon the glacier starts to flow within a confined and steep basin at altitude below 1000 m, the ice thinning rate drops abruptly to approximately −10 $m\,a^{-1}$ on the main flow channel and on the tributary channels. Since the colourscale in Figure 7.8 is saturated, the elevation change map of Jorge Montt is shown in greater detail in Figure 7.9a. Along the terminus the thinning rate decreases slowly but steadily up to −25 $m\,a^{-1}$ near the front of May 2011. To put it into prospective, this figure corresponds to approximately 280 m of elevation loss during the observation period of 11.2 years, during which the glacier underwent a marked frontal retreat of 2.5 km. Since Jorge Montt is the most dynamic glacier of the Patagonian icefields, its thinning behaviour was investigated on a recent observation period by computing the elevation change rate between the TanDEM-X Raw DEM of 2011 and a new Raw DEM of 2014. This result and the multitemporal geodetic mass balance for the 2000 - 2011 and the 2011 - 2014 observation periods are presented in Chapter 10. The availability of a recent elevation change map allows to detect a strong thinning acceleration trend. The recent elevation change rate map shows that the glacier thins at rate of up to 33 $m\,a^{-1}$ at its snout (see Figure 10.1).

In Figure 7.9 the off-glacier terrain has not been masked in order to show the good degree of horizontal and vertical coregistration achieved according to the procedure described in Section 7.2. Some features due to the different resolution of the DEMs can be noticed. The possible light residual misregistration is well described by the errors obtained in Section 7.2, which will contribute to the final error budget of the mass balance.

The TanDEM-X DEM mosaic and the SRTM C-band DEM were compared to several ICESat GLAS altimetry tracks acquired between 2003 and 2009 on the icefield surface of the main glaciers (Grey, Perito Moreno, Ameghino, Pio XI, Upsala, Jorge Montt) in order to measure punctually the variations in the elevation change trend. The thinning trend, where detected, proved to be accelerating. The corresponding plots are not reported here.

Chapter 8

SAR Backscattering and penetration depth

This chapter tackles the issue of the InSAR elevation bias caused by radar signal penetration in ice and snow from a practical point of view for the datasets used in this work. Specifically, the backscattering of the SAR acquisitions will be analysed in order to understand the snow condition with respect to liquid water content, allowing to evaluate if such a bias affects the used DEMs. The effects of liquid water on the microwave properties of snow are shown in Section 8.1, where the possible snow conditions and their effects on the backscattering are also discussed. The backscattering analysis is performed for the SRTM data (Section 8.2), exploiting the recently released brightness products, and for the TanDEM-X data (Section 8.3). To complement the interpretation of the backscattering, concurrent meteorological data from nearby stations are also used. In Section 8.4 the results of a multitemporal experiment are reported. Two overlapping TanDEM-X DEMs (one from winter and one from summer) and their backscattering are compared in order to estimate the InSAR elevation bias due to radar penetration, but also to quantify the seasonal elevation change caused by melting and firn compaction within four months.

8.1 Backscattering analysis of snow

The penetration depth is linked to the dielectric properties of the snowpack, which are in turn strongly dependent on the presence of liquid water. This element causes a strong increase in absorption leading to a fall in penetration depth. In order to establish a liquid water content (LWC) threshold for which the effect of signal penetration into ice and snow can be neglected, the models for the dielectric properties of snow introduced in Section 4.3 and the electromagnetic theory leading to the penetration depth expression explained in Section 4.4 have been applied to obtain the plots of the relative dielectric constant of snow in Figure 8.1 and the vertical penetration depth shown in Figure 8.2. The real part ε_r' was computed according to Equation (4.22) (Tiuri *et al.*, 1984; Kendra *et al.*, 1998) for dry snow (for two typical values of ρ_{ds}) and by adding the increment of Equation (4.24) (Kendra *et al.*, 1998) for wet snow. The imaginary part ε_r'' was obtained for dry snow according to the model of Tiuri *et al.* (1984) in Equation (4.23), where the ε_{ri}'' of ice was obtained using Eq. (4.21). For wet snow the simplified model by Mätzler (1987) of Eq. (4.26) was applied. Snow density ρ_s was assumed to be 0.4 $\mathrm{g \cdot cm^{-3}}$ with $T = -1$°C to simulate older compact snow and $\rho_s = 0.2$ $\mathrm{g \cdot cm^{-3}}$ with $T = -10$°C to simulate fresh snow. The snow density affects noticeably only ε_r'. The other plots show only calculations with $\rho_s = 0.4$ $\mathrm{g \cdot cm^{-3}}$. The temperature of the ice has an effect only on ε_{rds}'', which is very small and difficult to model, meaning that for dry snow the penetration depth cannot be computed precisely and will depend on volume scattering properties (snow microstructure). The relaxation frequency of water was assumed to be $f_0 \simeq 9$ GHz. The signal frequencies were 1.3 GHz for L-band, 5.3 GHz for C-band and 9.6 GHz for X-band, the latter two corresponding to the operating frequencies of SRTM and TanDEM-X, respectively. ε_{rds}' and ε_{rws}' were also compared to other models by Mätzler (1987) highlighting good convergence.

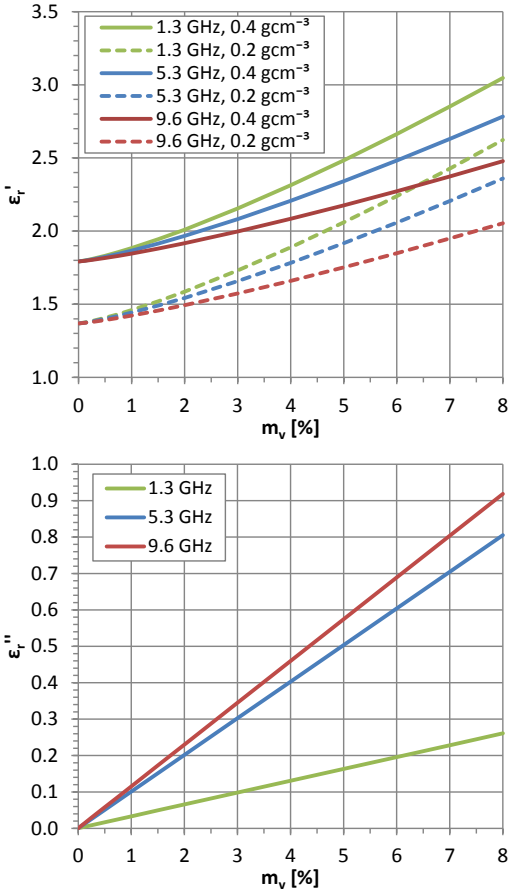

Figure 8.1 – Relative dielectric constant of snow for varying liquid water content m_v at L-band, C-band and X-band. The real part ε'_r is shown for two different snow densities.

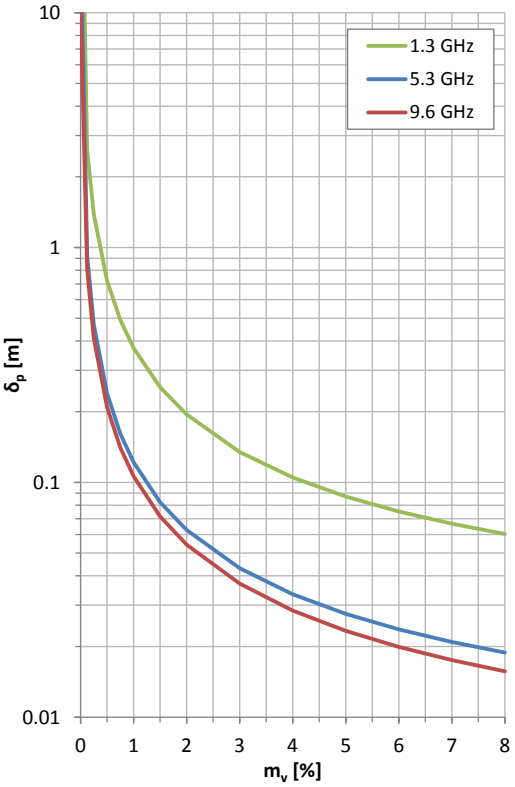

Figure 8.2 – Vertical penetration depth δ_p for varying liquid water content m_v at L-band, C-band and X-band.

The plot in Figure 8.2 shows how even a low quantity of liquid water in the snowpack leads to an abrupt drop in the vertical penetration depth. Furthermore for off nadir signals such that of a SAR, the actual penetration depth on a horizontal surface will be reduced by a factor $\cos\theta_t$, where θ_t is the transmission angle, which can be computed according to Snell's law in Equation (4.15). The factor $\cos\theta_t$ increases with wetness and density of the snowpack. For dry or lightly wet snow with $\rho_s = 0.2\ \mathrm{g\cdot cm^{-3}}$, $\cos\theta_t$ is around 0.65 for an incidence angle $\theta_i = 60°$ and around 0.9 at $\theta_i = 30°$. The elevation bias in the InSAR DEM will be at its maximum equal to half the actual penetration depth (see Section 9.1.1.6).

The backscattering coefficient σ^0 (cf. Section 2.1.1) can be used to distinguish wet and dry snow. The behaviour of σ^0 of ice and snow with respect to different parameters and particularly liquid water content has been extensively covered in Section 4.5. The experimental results from the literature reported there will be used in this chapter for the interpretation of the SAR backscattering images of SRTM and TanDEM-X. This is not straightforward as σ^0 depends on SAR imaging parameters as well as surface and volume physical properties. The focus of the investigation is restricted to the smoother surface typical of the plateau, mainly occupied by the accumulation area of the glaciers. This is because the termini flowing into steeper beds at lower elevations (~0 - 1000 m a.s.l) feature very rough ice surfaces which lead to very strong backscattering. The transmissivity is hence small and penetration depths are negligible. Four main conditions of the snow and firn of the accumulation area of a temperate climate icefield can be profiled as reported below (see also Section 4.5).

- **Dry snow** Typical of the cold season, often featuring an upper layer of younger fresh snow with small grain size and low density. Such a layer would be practically transparent to the radar especially at longer wavelengths. The lower layers which underwent metamorphism through

compression and melt-refreeze cycles have larger grain sizes and isolated elements such as lenses and pipes enhancing strongly volume scattering and driving up σ^0. In this situation the scattering phase centre might be located several meters below the actual surface at C and X-band (δ_p can be in the order of several hundred times the wavelength). An estimation of δ_p is difficult in this case. Fresh snow could decrease σ^0 slightly.

- **Wet snowpack** Typical of warmer seasons. Melting starts to occur as temperature rises above 0°C. Water starts to percolate down the snowpack soaking it more and more in depth. In this scenario surface scattering prevails and penetration depth is small due to the strong absorption, this scenario reflects in low values of σ^0. The scattering phase centre can be assumed to be on the actual surface.

- **Temporarily wet upper layer** Typical in spring. The upper layer starts to become wet in the warmer hours/days and refreezes as temperature declines. The lower layer remains dry. σ^0 starts to decrease as LWC increases and surface scattering prevails. Under certain circumstances the water might refreeze some centimetres below the surface creating a frozen layer which causes σ^0 to rise slightly or remain stable. The scattering phase centre at C and X-band is near the surface in this case.

- **Refrozen upper layer** Typical of warmer seasons. When temperatures decline below zero, often during night time or colder days, the upper layer of the wet snow starts to refreeze forming a crust below which the snow remains wet. σ^0 increases slowly but steadily as the frozen crust becomes more compact and thicker, only to drop again as temperatures rise, usually after sunrise on a sunny day. The scattering phase centre is located below the refrozen crust, thus not much deeper as the actual surface (5 - 30 cm).

A general knowledge of the climatological conditions of the region is useful to interpret the backscattering. These are described in more detail in Section 5.3. SPI and NPI feature a maritime climate on their western side, characterized by strong winds and advection from the Pacific Ocean with very high precipitation rates. The icefields display a dryer more continental climate on the eastern side. Annual temperatures do not exhibit a large dynamic, on the plateau they can temporarily go below zero even in summer. Rain can occur at all seasons at lower altitudes and similarly snowfall at higher altitudes. Altitude gradients of rain, wet snowfall and dry snowfall can occur, even in summer. Winter snowfall can generally be very abundant except at the lower termini where rain may be dominant all year round.

8.2 Surface condition during SRTM

8.2.1 Processing the SRTM backscattering

The SRTM mission and dataset is discussed in Section 6.1. NASA and the USGS released at the beginning of 2015 the SRTM C-band Swath Image Dataset[1] (SRTMIMGR) (Farr *et al.*, 2007) under the MEaSUREs initiative. This dataset consists of all the amplitude images of the mission divided in $1° \times 1°$ tiles. They are provided as orthorectified and terrain corrected radar image brightness images for each of the four sub-swaths, with a resolution of 1 arcsecond. Each image is complemented by a local incidence angle mask, computed on a 3×3 window of the DEM and resampled back to 1 arcsecond. According to Farr *et al.* (2007) the SRTM goals for absolute and relative radiometric calibration were 3 dB and 1 dB, respectively. The C-band (5.3 GHz) antenna acquired 4 sub-swaths in ScanSAR mode with two polarizations, the look angle ranges from 30° to 56° as summarized in Table 8.1.

The SRTMIMGR file contains radar brightness β^0 which was corrected for flat earth using only the look angle and no topographic information[2]. The provided local incidence angle map has been used to obtain a σ^0 estimate by applying $\sigma^0 = \beta^0 \cdot \sin\theta_{loc}$ (see Section 2.1.1). A precise retrieval of the

[1] DOI: 10.5067/MEaSUREs/SRTM/SRTMIMGR.003
[2] Personal communication with USGS User Services

Table 8.1 – SRTM C-band antenna sub-swath characteristics.

Sub-swath	Polarization	Look angle
1	HH	30° - 42°
2	VV	41° - 48°
3	VV	47° - 53°
4	HH	52° - 59°

Table 8.2 – All SRTM C-band datatakes covering the entire SPI and NPI and used for the DEM generation. The table reports orbit number, datatake index, orbital direction and the sub-swaths used to compute $\bar{\sigma}^0$. The acquisition time refers to the start of the datatake.

Orbit n.	DT	Orb. dir.	Used sub-swaths	Acq. time (UTC—4h)
10	200	D	4	12/02/2000 04:04
28	230	A	4	13/02/2000 06:56
41	190	D	1	14/02/2000 02:04
44	230	A	3,4	14/02/2000 06:42
57	190	D	1,2	15/02/2000 01:50
60	230	A	2,3,4	15/02/2000 06:29
73	190	D	1,2,3,4	16/02/2000 01:37
76	230	A	1,2,3,4	16/02/2000 06:16
89	190	D	1,2,4	17/02/2000 01:24
92	230	A	1,2,3,4	17/02/2000 06:02
105	200	D	2,3,4	18/02/2000 01:10
108	230	A	2,4	18/02/2000 05:49
121	200	D	1,3,4	19/02/2000 00:57
124	230	A	1,2,3,4	19/02/2000 05:35
137	200	D	1,2,3,4	20/02/2000 00:43
140	230	A	1,2	20/02/2000 05:22
153	200	D	3,4	21/02/2000 00:30
156	240	A	1	21/02/2000 05:09

uncorrected β^0 from the data was not possible since the platform orbital parameters are not provided. The look angle correction has been thus compensated using the mid-range look angle for the entire sub-swath, introducing an error up to ±0.6 dB for sub-swath 1, ±0.3 dB for sub-swath 2, ±0.2 dB for sub-swaths 3 and 4. These are acceptable values given the nominal accuracies for the product and the subsequent averaging of multiple sub-swaths from different ascending and descending passes.

The backscattering coefficient σ^0 of the icefield can be used to determine if elevation biases due to signal penetration affect the SRTM C-band DEM. As explained in Section 6.1, the SRTM DEM is obtained by mosaicking, within an $1° \times 1°$ tile, all the InSAR DEMs from each sub-swath acquired during 9 days (12.2 - 21.2.2000). Given the high latitudes (especially for SPI) a large number of ascending and descending acquisitions contributed to the final DEM, increasing its accuracy and reliability in this region. The list of all SRTM C-band datatakes acquired on the Patagonian icefields and surroundings is reported in Table 8.2.

In order to have a single representation of the backscattering to relate to the final DEM an average $\bar{\sigma}^0$ of the σ^0 images of all sub-swaths covering the plateau of NPI and SPI has been computed, these are indicated in the third column of Table 8.2. Sub-swaths covering only glacier termini or bare-rock have been ignored in the averaging process. The acquisition time (Seal & Rogez, 2000) refers to the start of the datatakes (which are in average 3 minutes long in this region) and is reported in local solar time (UTC—4h)[3]. The time of day is useful to interpret the backscattering coefficient with respect to liquid water content. A total of 54 files were selected across six $1° \times 1°$ tiles from 46°S to 52°S. The

[3]Note: DST was in effect in Chile and Argentina in February 2000 making the official time UTC—3h

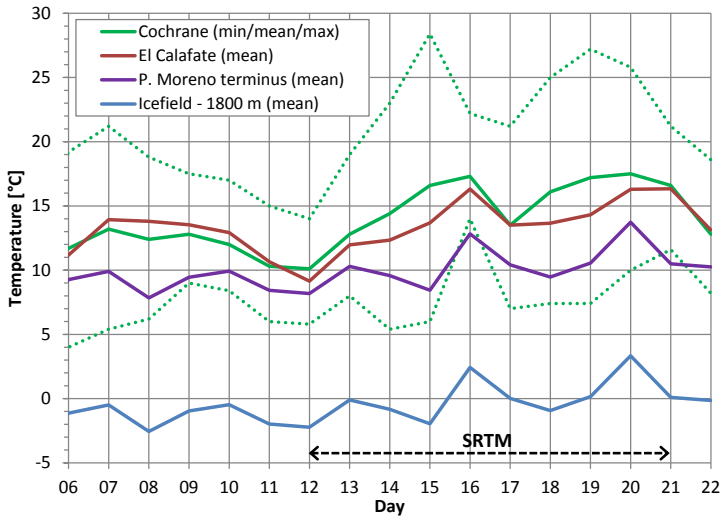

Figure 8.3 – Air temperature trends during February 2000 at Cochrane airfield, El Calafate airfield and Perito Moreno terminus. By applying to the latter a lapse rate of −0.65°C/100 m the mean temperature on the icefield was estimated. The black arrow highlights the days of SRTM acquisition.

number of overlapping acquisitions selected on the plateau range generally between 4 and 7, only between 49°50'S and 50°S some sectors are covered with only 2 to 5 overlapping acquisitions.

The SRTM acquisitions have a large range of look angles between 30° and 60° corresponding to a variation of σ^0 of several dB (around 7 dB at 4.6 GHz for dry snow in the experimental results from Ulaby *et al.* (1982b) shown in Figure 4.3). On the areas with overlapping sub-swaths characterized by different look angles the $\bar{\sigma}^0$ estimate will have an increased spread, making interpretation less reliable. Another possible source of σ^0 spread is temporal variation of liquid water content (Section 4.5), caused by temperature changes and possibly by rain. The backscattering signature is very similar for the HH and VV polarizations, the differences are below the nominal radiometric accuracy. Averaging the two polarizations is hence not problematic.

8.2.2 Meteorological conditions during SRTM

In this region sunrise occurs around 6:00 (UTC−4h) and sunset around 20:10 in mid-February, with solar noon around 14:00. All datatakes were acquired either after midnight or shortly after sunrise (cf. Table 8.2). Since these are the coldest hours of the day, the risk of strong temporal variations in liquid water content due to diurnal temperature cycles is reduced.

Air temperature data on the plateaus would be useful to infer the wetness of the snow and possible nocturnal refreezing but unfortunately direct measurements are not available. Daily mean air temperatures from a meteorological station installed and operated by the University of Innsbruck in SPI were made available. The station was located 500 m south of the terminus of Perito Moreno Glacier (198 m a.s.l., 50°29'23"S, 73°03'48"W) on the shore of Lago Argentino (southern arm). The values recorded during part of February 2000, including the days of the SRTM mission, are shown in Figure 8.3. Average daily temperatures were 9.4°C in February, 10.5°C in January and 9.8°C in November and December 1999. In order to roughly estimate the mean temperature on the icefield a lapse rate of −0.65°C/100 m (Bippus, 2007) was applied. At 1800 m a.s.l. the extrapolated daily mean air temperature was around 0°C during the SRTM with a slight increasing trend (Figure 8.3). This implies that at this altitude freezing may occur during the night (usually reaching a peak before sunrise) and melting occurs during daytime. According to the applied lapse rate, altitudes with temperatures constantly below zero during February 2000 are likely located above 2500 - 2600 m, hence including only the higher sections of the mountain ranges crossing the plateau. A similar behaviour is to be expected in NPI, possibly with a slightly increased mean temperature due to the lower latitude.

Daily mean air temperatures recorded by the Argentinian Meteorological Service[4] at the meteor-

[4]Temperature records at P. Moreno and El Calafate have been kindly provided by Dr. Gabriele Bippus, ENVEO IT GmbH.

ological station located at the Lago Argentino Airfield (ca. 220 m a.s.l., approx. 50°20'S; 72°15'W) near the town of El Calafate, circa 60 km east of the Perito Moreno terminus are also shown in Figure 8.3. Despite the similar altitude and latitude, a difference in temperature with the Perito Moreno temperature is noticeable.

Meteorological records are also available on the Chilean Meteorological Division website for a station located at the Cochrane Airfield (196 m a.s.l, 47°14'40"S; 72°35'11"W), approximately 50 km east of the terminus of Colonia Glacier (NPI). Minimum, maximum and average daily temperatures are shown in Figure 8.3. Mean values are close to those recorded at El Calafate. Minimum peaks were reached between 3:45 and 6:30, maximum peaks between 13:30 and 17:30. At this station, located on the east of NPI, recorded precipitation levels were close to zero during the SRTM acquisition period and the preceding days.

8.2.3 Interpretation of the SRTM backscattering

The average backscattering coefficient $\bar{\sigma}^0$ obtained as explained in Section 8.2.1 is shown in Figure 8.4 for NPI and in Figure 8.5 for SPI. The standard deviation image is also shown as it supports the interpretation as a measure of spread and hence reliability. The backscattering average and standard deviation were analysed in parallel with the DEM and optical images where available.

The plateau of SPI ranges altitudes between roughly 1100 m and 2400 m, with some mountain ranges exceeding these elevations and characterized by a very high σ^0 due to roughness and steep slopes causing layover (see DEM in Figure 7.7). NPI has similar altitude ranges with the exception of the northeastern (46°38'S, 73°21'W) mountain complex south of Monte San Valentin (4058 m) where a higher plateau with relatively gentle slopes and elevations between 2300 and 3200 m is present (see DEM in Figure 7.5).

Backscattering at the glacier termini High mean backscattering $\bar{\sigma}^0$ was measured by SRTM at C-band on the glacier termini. This is due to the high sensitivity of the backscattering at 5.6 cm wavelength to the rough ice found in this part of the glacier (due to features from centimetre to meter scale up to large crevasses). A representative example is the S. Quintin Glacier (NPI). On the heavily crevassed terminus local mean values of $\bar{\sigma}^0$ up to -6.5 dB are measured. Upstream at the beginning of the plateau (46°51'S, 73°40'W) $\bar{\sigma}^0$ is $-19/-18$ dB at the flanks of the glacier, where small-scale surface features are present, but it is lower (-24 to -22 dB) along the mid line where a tongue of very smooth surface is found (see Figure 8.4), at both locations the low $\bar{\sigma}^0$ values are likely an indicator of wet snow and firn. Very high $\bar{\sigma}^0$ is measured on ice strongly covered by debris such as in the north-east of NPI (especially Grosse Glacier) and the southern flank of Nef Glacier (47°04'S, 73°15'W). Standard deviation values on the glaciers are also generally low between 1.5 and 3 dB indicating stability against acquisition geometry. On the glacier termini the backscattering is dominated by the surface scattering mechanism and has limited sensitivity to liquid water content. The penetration depth of the radar in the ice volume is thus negligible.

Backscattering on the icefield plateau The interpretation of $\bar{\sigma}^0$ on the smooth icefield plateau with respect to snow wetness, and hence signal penetration depth is not straightforward, because of the relatively high spread and because it is not easy to establish a precise $\bar{\sigma}^0$ threshold between dry and wet snow since many parameters are involved. The theory and experimental results summarized in Section 4.5 are used as reference for a coarse assessment of the dryness/wetness of the snow cover. Based on such results a rough σ^0 threshold below which the presence of liquid water in the upper layer is likely can be assumed to lay around -17 dB at 5.3 GHz for $\theta_i = 45°$ (which is the mid look angle for SRTM) for smooth snow surface. Higher σ^0 can be expected on wet snow with slightly rough surface. An angular variation of circa 2.5 dB/10° is expected. Given the temperature behaviour at 1800 m (Section 8.2.2) and since the acquisitions are made during the coldest time of day, an increase of backscattering (up to circa -14 dB) would probably be a consequence of nocturnal freezing of the upper snow layer, rather than the presence of deep layers of dry snow. The presence of an upper crust of frozen snow (10 to 30 cm deep) would not have a drastic impact on the InSAR elevation as the scattering phase centre

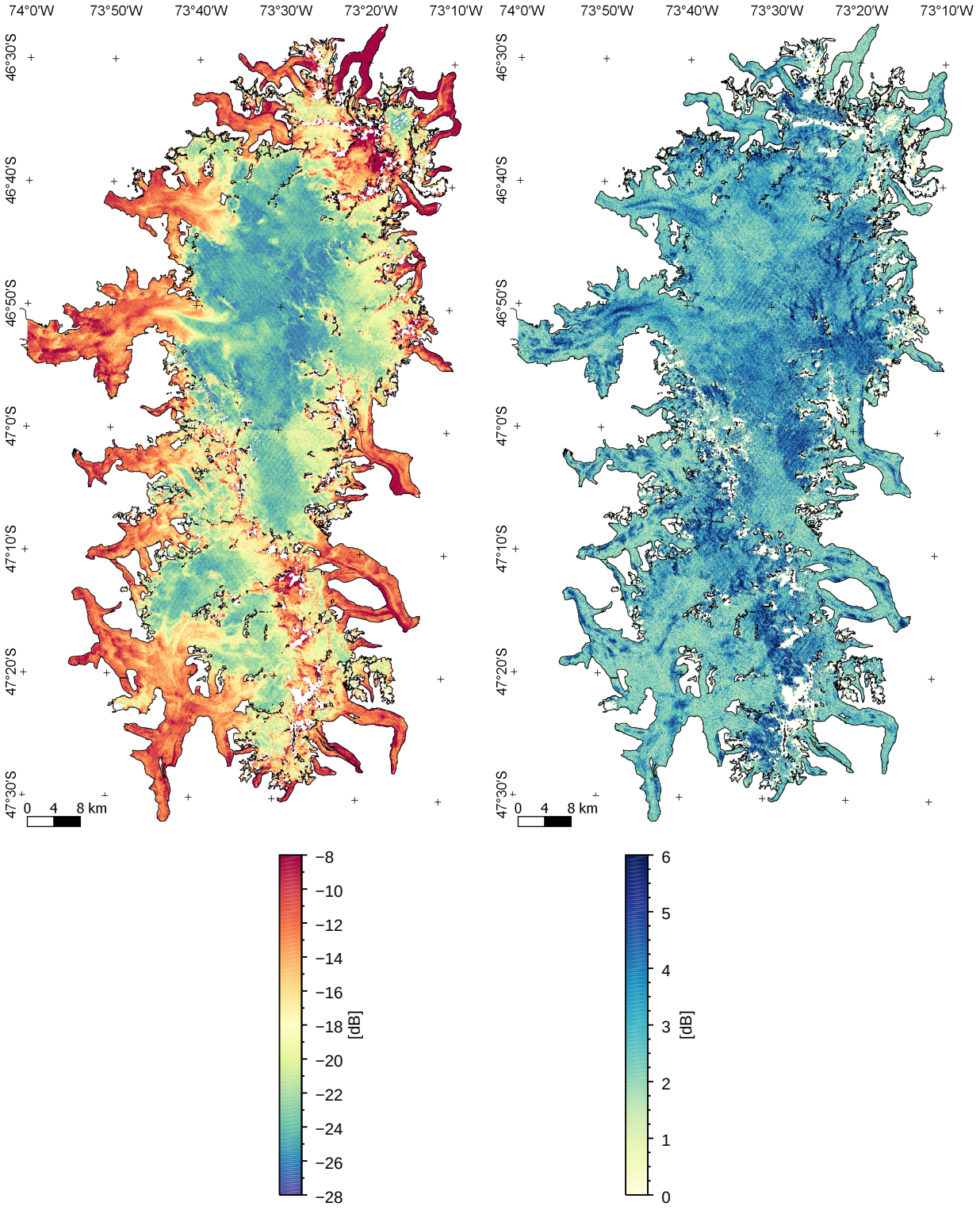

Figure 8.4 – Mean (left) and standard deviation (right) of the SRTM C-band σ^0 of NPI.

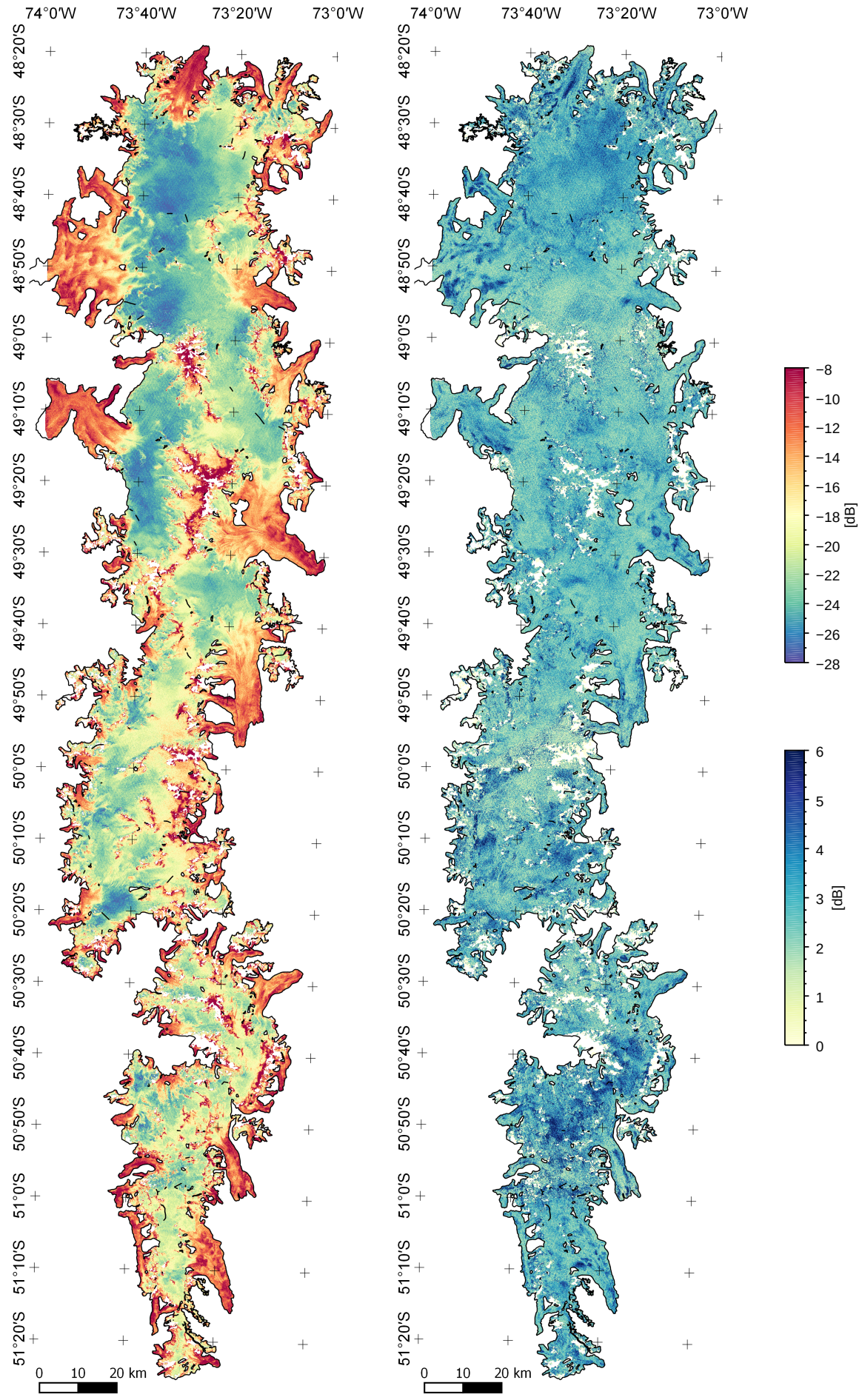

Figure 8.5 – Mean (left) and standard deviation (right) of the SRTM C-band σ^0 of SPI.

would lie slightly below the surface. Fresh snow precipitation at higher altitudes cannot be completely excluded even in summer, this would lower the signature of a frozen snowpack by some dB. Finally, $\bar{\sigma}^0$ values above −14 dB coupled with high altitudes, where temperatures stay almost all day below 0°C, might be a sign of frozen snowpack with the possibility of tangible penetration depth.

Status of the NPI plateau In NPI (Figure 8.4) where the plateau is extended and flat, very low values of $\bar{\sigma}^0$ are found, up to −26 dB in certain parts. Slightly higher values are encountered on the eastern and southern margins of the plateau (up to −19 dB) with higher standard deviations (for example the accumulation basin of Nef Glacier). On the the gentler slopes of the mountain ranges, $\bar{\sigma}^0$ is higher and shows dependence on elevation. Values up to −18 dB are found in the 1800 - 1900 m range and up to −16 dB on the limited areas up to circa 2300 m. The limited areas above 2300 m characterized by slopes gentle enough not to be affected by layover (for example around Cerro Pared Norte in the south and Monte San Valentin in the north) display $\bar{\sigma}^0$ ranging from −15 dB to −13 dB with peaks reaching −11 dB.

Status of the SPI plateau SPI (Figure 8.5) exhibits a more heterogeneous scenario given its extension in latitude and the complexity of the geographical scenario, characterized by oceanic fjords on the west, lakes on the east and a mountain range along the central and southern sections of the plateau. The standard deviation values are generally lower than for NPI, but very high values are found in correspondence of the southern mountains (50°50'S), caused by topography and differences in acquisition geometry. The northern section of the plateau exhibits very low $\bar{\sigma}^0$; an east to west gradient with lower values on the western margin is visible. Where altitude increases (generally above 1900 - 2000 m) $\bar{\sigma}^0$ values of −18 dB are measured, this is particularly true on the central and southern section (particularly on the eastern margin) of the SPI where topography is more pronounced. Values are rarely above −16 dB even up to 2300 m. Above this threshold, on the the few small isolated regions with gentler slopes, $\bar{\sigma}^0$ can climb up to −13 dB. South of 50°20' S $\bar{\sigma}^0$ ranges between −24 and −19 dB below 2000 m of elevation.

Conclusion From the analysis of the mean backscattering coefficient of SRTM it can be concluded that most of the plateau of both NPI and SPI displays a signature typical of wet snow. Sections of the plateau with $\bar{\sigma}^0$ around 15 dB might be due to wet snow with rough surface. Another possibility, corroborated by the time of SRTM overflights (night) and by the temperature estimated on the plateau, is the presence of a refrozen top crust which increases backscattering but does not lead to a deep scattering phase centre. Values of $\bar{\sigma}^0$ above −15 dB are found as elevation increases on gentler slopes, these most likely fall under the refrozen snow scenario. Only at altitudes above 2500 - 2600 m, where air temperature were constantly below 0°C before and during the acquisitions, the snow layer might be completely dry. Most of these areas are generally steep and do not cover a significant surface of the icefields. In conclusion, the likelihood of an elevation bias due to signal penetration affecting the SRTM C-band DEM of NPI and SPI is very low.

8.3 Surface condition during TanDEM-X acquisitions

8.3.1 Processing the TanDEM-X backscattering

The backscattering coefficient σ^0 of the TerraSAR-X and TanDEM-X acquisitions can be computed using the following expression (DLR-CAF, 2013) :

$$\sigma^0 = \beta^0 \sin\theta_i = \left(k_s\,|\mathrm{DN}|^2 - \mathrm{NEBN}\right)\sin\theta_i \tag{8.1}$$

where k_s is the calibration and processing scaling factor (annotated), θ_i is the local incidence angle, DN represents the digital number of the CoSSC product, obtained from the real and imaginary part of the complex signal as $\mathrm{DN} = \sqrt{\mathrm{I}^2 + \mathrm{Q}^2}$. For TanDEM-X bistatic data the image acquired by the active channel must be used. NEBN is the noise equivalent beta nought representing the β^0 produced

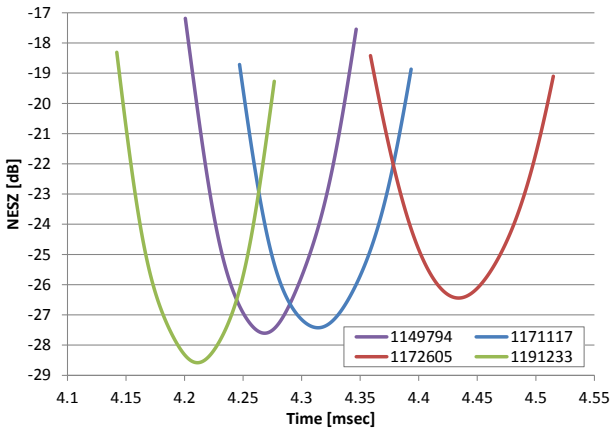

Figure 8.6 – NESZ plots in range at one azimuth position for the four TanDEM-X datatakes over NPI. Flat topography was assumed in order to compare different datatakes. The time offset has not been removed avoid overlap.

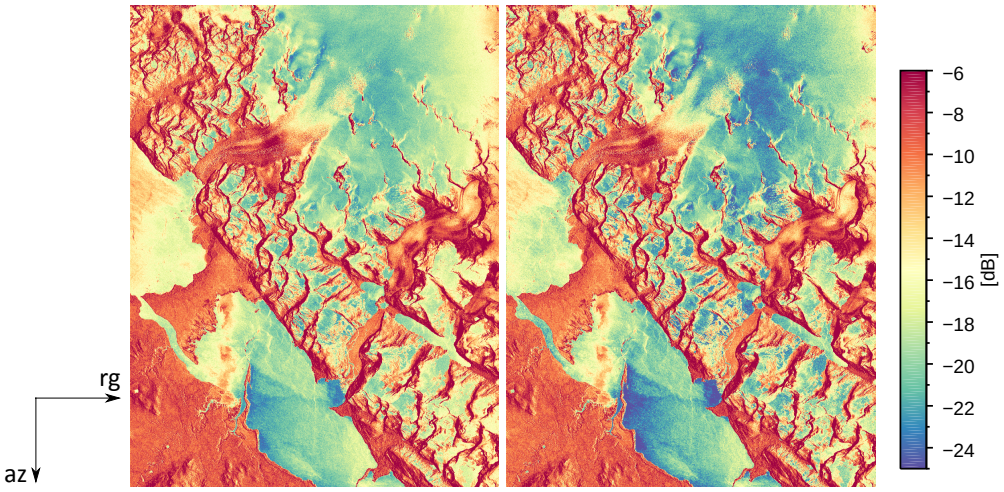

Figure 8.7 – Backscattering coefficient of a crop from DT 1171117 in radar geometry without (left) and with (right) the NESZ contribution.

by different noise contributions of the system and $\mathrm{NESZ} = \mathrm{NEBN} \cdot \sin\theta_i$ is the corresponding noise equivalent sigma zero. The radiometric accuracy of the SAR sensor onboard these satellites is very high. The absolute accuracy represents the RMS error between the measured and the true radar cross section at different locations within one scene and over time. During the commissioning phase and subsequent recalibration campaigns of the TerraSAR-X mission, an absolute radiometric accuracy of 0.6 dB was measured. The relative accuracy is the standard deviation of the radiometric error of known targets within one datatake and was measured to be 0.3 dB for the TerraSAR-X stripmap mode (DLR-CAF, 2013).

The noise affecting the acquisition depends on many factors, among which the antenna pattern, the power of the transmitted pulse, the quantization, the receiver noise and the bandwidth. The expected NEBN variation over range can be obtained from polynomial coefficients annotated at regular intervals along the azimuth direction (every 2 seconds). For the TerraSAR-X mission average values of NESZ ranging between −19 dB and −26 dB for different beams (DLR-CAF, 2013) were measured. A strong variability in range is due to the antenna pattern, while the variability in azimuth is very slow. The influence of NESZ is hence negligible for strong scatterers but weaker ones, such as roads, water, wet snow have a σ^0 comparable to the noise level (especially in near and far range), thus the NESZ must be considered for a precise estimation of σ^0.

For the NPI the backscattering coefficient images of all four used TanDEM-X datatakes (Table 7.6) have been obtained according to Equation (8.1). The local incidence angle was obtained computing the slope along the line of sight from the SRTM DEM. The plots of the NESZ in range for one azimuth

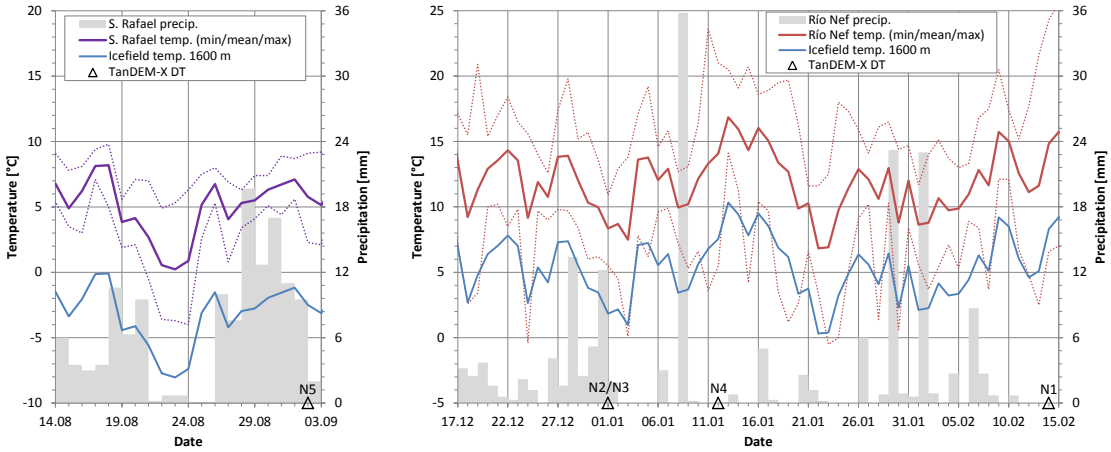

Figure 8.8 – Air temperature and precipitation data recorded at two stations on the margins of NPI for the period preceding TanDEM-X acquisitions and air temperature extrapolated at 1600 m. Time range: 14.8.2013 - 3.9.2013 for the S. Rafael station (a) and 17.12.2013 - 15.2.2014 for the Río Nef station (b).

position are shown in Figure 8.6 for the four datatakes used over NPI. Only one plot per datatake is depicted as they proved to be very similar along azimuth: the standard deviation of the 11 azimuth records of DT 1171117 ranged from 0.08 dB (mid-range) to 0.5 dB (far range). To generate the plots flat topography was simulated for all four datatakes, in order to simplify the comparison. For instance, the NESZ contribution for DT 1171117 ranges between 0.2 dB and 1.5 dB for $\sigma^0 = -15$ dB and between 0.5 dB and 2.5 dB for $\sigma^0 = -18$ dB and even higher for weaker scatterers. For snow applications it is hence important to consider the NESZ contribution of σ^0 or, if not possible, to keep in mind that the backscattering estimated from the image data might be some dB lower, particularly at near and far range. The effects of the NESZ correction on σ^0 are visualized in Figure 8.7 for a crop of DT 1171117 in radar geometry covering different types of surface: snow, glacier ice, terrain (possibly vegetated) and water. The NESZ correction leads to a significant decrease of the backscattering for weak targets such as wet snow or calm water at all ranges and even of intermediate scatterers in near and far range. Very strong scatterers such as terrain and crevassed ice (or layover areas) are unaffected by the correction.

The NESZ corrected σ^0 images of NPI have then been geocoded and the areas affected by PU errors in the Raw DEMs have been masked. The images were finally mosaicked (Figure 8.9) with the same order as the DEM mosaic so to have a pixelwise equivalence between the two. The same mosaic was not obtained for SPI because of time constraints, the backscattering will be nevertheless evaluated on relevant areas.

8.3.2 Meteorological conditions in NPI during TanDEM-X acquisitions

To support the interpretation of the backscattering, meteorological data were recovered from the website of the Chilean General Water Directorate[5] which operates a vast network of water quality stations. Records are available online starting with 2012. Minimum, maximum and average daily air temperatures, as well as daily precipitation for the periods preceding the four TanDEM-X NPI acquisitions (Table 7.6) measured at two nearby stations are reported in Figure 8.8. Data until November 2013 are available for the S. Rafael station (8 m a.s.l., 46°38'35"S, 73°51'28"W, ID: 11440000-9) located on the shore of Laguna San Rafael, 5 km west of the terminus of the glacier. The western margin of the NPI where the station is located is subject to maritime weather and high precipitation rates (cf. Section 5.3). Meteorological data for January - February 2014 are available at the Rio Nef meteorological station (281 m a.s.l., 47°08'17"S, 73°05'13"W, ID: 11532000-9), located approximately 11 km east of

[5]http://www.dga.cl/

the terminus of Nef Glacier, on the dryer eastern margin of NPI. The air temperature on the plateau at 1600 m is extrapolated by applying a lapse rate of −0.65°C/100 m to the average daily temperatures measured at the meteorological stations.

As Figure 8.8 shows, scenes N1 (DT 1191233) and N4 (DT 1172605) were acquired during warm and dry 3 day periods, characterized by maximum temperatures above 21°C at the Rio Nef station, where a daily mean value of incident solar radiation (south-west) above 265 W/m^2 was measured, indication of sunny summer days. Scene N2/N3 (DT 1171117) was acquired during a cold summer day (1.1.2014) with a maximum air temperature of 11°C, which extrapolates to negative average daily air temperature above 1600 m of altitude. Rain was recorded during the previous six days, possibly snow at high elevations. A mean solar radiation of 195 W/m^2 was detected on that day. As a reference the wettest day of that summer (8.1.2014) was characterized by 36 mm of water and a mean solar radiation of 18 W/m^2. Finally the only winter scene N5 (DT 1149794), which has a very limited coverage of the icefield (7.2%), was acquired during a sunny, not too cold winter day (2.9.2014), with minimum temperatures above zero and period peak in solar radiation of 138 W/m^2 measured at the S. Rafael station. Nevertheless on the plateau, sub-zero temperatures during daytime can be expected above 1300 - 1400 m. Noticeable precipitation was recorded during the previous days, while on the acquisition day it decreased to 1.5 mm.

8.3.3 Interpretation of the TanDEM-X backscattering of NPI

As summarized by Table 7.6, all four acquisitions were performed at 19:46 (UTC−4h): approximately an hour before sunset in January, shortly before sunset in February and 1h30 after sunset for the winter scene N5 (DT 1149794). Mid look angles lay between 34.8° and 39.4°, a variation of approximately ±1.5° from the mid value is expected at near and far range.

Based on the theory and experimental results presented in Section 4.5, a coarse σ^0 threshold above which snow is very likely dry (even for low SWE) lies around −11/−12 dB in X-band at $\theta_i = 37°$ which is the average look angle of the four TanDEM-X acquisitions (Table 7.6). The look angle varies approximately between 34° and 39° on the plateau, therefore this threshold is considered valid for the whole mosaic. A light presence of liquid water (below 1%) would decrease σ^0 by 2 - 3 dB but some degree of signal penetration could persist, particularly on winter snow (less dense and with small particle size).

The backscattering mosaic in Figure 8.9 highlights that on the smooth firn plateau σ^0 presents relatively low values linked to wet snow, mostly below −15 dB. Extremely low values below −20 dB are recorded on large areas of the NPI plateau, particularly at lower elevations such as on the accumulation basin of S. Rafael Glacier (up to 1400 m). $\sigma^0 < -23$ dB can also be found at 1600 m in scene N2 and up to 1900 m in N4 which was acquired on a warm day (e.g. at 46°50'S, 73°20'W).

In the north-east of the icefields an obvious change of σ^0 between scenes N2 and N4 can probably be imputed to the lower temperatures recorded for N2/N3 (daily average air temperature was 5°C lower at the Rio Nef station). In fact on scenes N2/N3 large areas with σ^0 values around −15 dB (with peaks up to −13 dB) are measured above 1550 m. According to Figure 8.8 for N2/N3 an average daily air temperature around 0°C is extrapolated at 1600 m, but preceding days featured higher temperatures and precipitation. These higher σ^0 values are likely linked to a lower LWC or possibly to partially refrozen upper layer, particularly above 1700 m. A bias due to signal penetration is hence unlikely or negligible in this area.

The mountain range crossing diagonally the southern part of NPI presents in scene N2/N3 σ^0 values up to −14 dB for elevations up to 2200 m (and sometimes up to 2400 m). Above this altitude higher σ^0 values typical of dry snow (up to −8 dB at 2600 m) can be found only on specific spots which cannot be considered critical due to their small areas.

The winter scene N5 has a very limited coverage of the icefield within the mosaic (7.2%), which σ^0 at elevations up to 1400 m are comparable with the neighbouring summer acquisition N1. At higher altitudes along the south-east front of the mountain range (around 47°15'S, 73°30'W) there are small areas with dry snow signature, for instance −9.5 dB around 1550 m. Snowfall is likely at these elevations in the days preceding the acquisition (Figure 8.8).

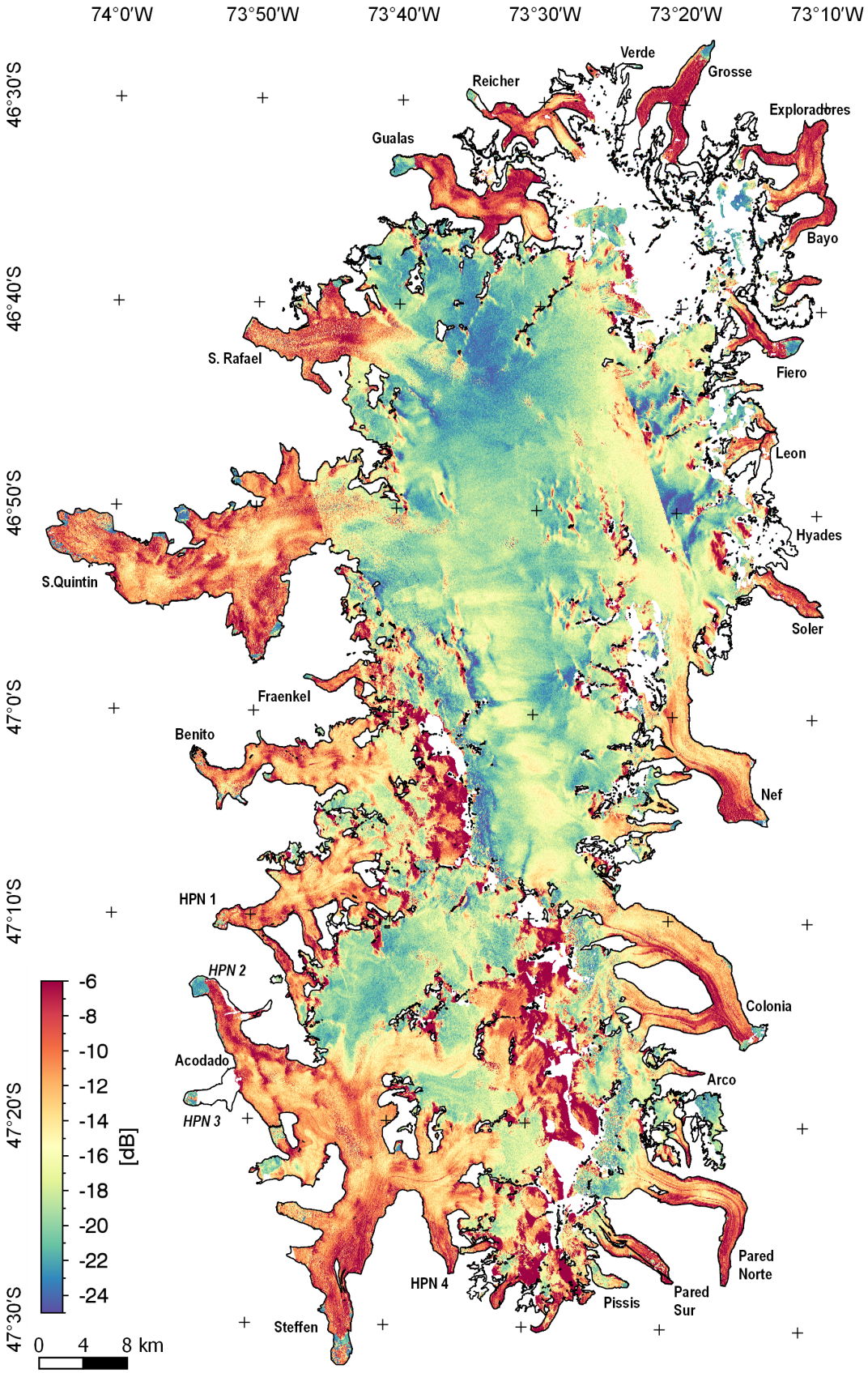

Figure 8.9 – TanDEM-X σ^0 mosaic of NPI.

In conclusion the NPI TanDEM-X DEM mosaic should not be be affected by a height offsets due to signal penetration in ice and snow, except possibly on very small areas at high elevations covered by scene N5 and N2/N3.

8.3.4 Analysis of the TanDEM-X backscattering of SPI

For the SPI the backscattering coefficient was not computed punctually in the form of calibrated and geocoded images but as mean value on rectangular regions of interest (ROIs). The computation is based on Equation (8.1). The calibration constant k_s of the TanDEM-X active channel is annotated. The local incidence angle θ_i is obtained from annotated values of the SRTM DEM which are interpolated, making it less precise in regions with rapidly changing topography, which is rarely the case on the icefield plateau. The NEBN is not taken into account, meaning that the actual σ^0 is lower than the reported one particularly for weak scatterers at near and far range. Considering typical values of NESZ (Figure 8.6) the error becomes significant (greater than 1 dB) for reported σ^0 values below −19 dB at mid range and below −12 dB at near and far range. Reported σ^0 values must hence be interpreted as upper bounds. Figure 8.10 is a mosaic on uncalibrated active channel amplitudes. Intensities can hence only be compared within each scene for flat regions and a colourbar is hence omitted. The position of the ROIs is also marked on the map, while Table 8.3 contains the measured mean σ^0 values, along with other parameters useful for the interpretation, such as mid look angle of the scene, altitude and local acquisition time. Table 8.4 reports multitemporal mean σ^0 values for some ROIs where overlapping acquisitions are available. These are reported as a means of comparison and to broaden the current analysis. Nevertheless the only σ^0 values relevant for the interpretation to the DEM mosaic are those of Table 8.3, which are marked as “used” in Table 8.4.

Meteorological data of three station operated by the Chilean General Water Directorate near the termini of Tempano, Dickson and O’Higgins Glacier are available online. Since they do not cover the TanDEM-X acquisitions of autumn and winter 2011 a plot is not reported here, but they have been used to better understand the snowcover state during the 2012 datatakes.

Table 8.3 contains σ^0 measurements only for the 13 scenes covering the plateau. The remaining 6 scenes covering rough ice or with negligible fractions of the plateau were excluded. The scene names and relevant data are summarized in Table 7.5. The only ascending scene was acquired approximately at sunset, the descending scenes are acquired at 5:54 local time (except S9, which was acquired few minutes later, being not an operational acquisition). This is approximately sunrise time in February and 3 hours before sunrise in July. These are generally the coldest hours of the day, although it must be noted that the plateau of NPI and SPI often displays limited daily variations of temperature due to the dense clouds and strong precipitation occurring most of the year. The backscattering observed on the ROIs and the uncalibrated amplitude images were analysed separately for each datatake. The conclusions are the following.

- S1 (DT 1027766): this is the only ascending scene, it was acquired approximately at sunset in autumn. For this steep look angle (33.7°), σ^0 below −15 dB is typical for wet snow even at 1600 m. On ROIs 2, 3 and 4 typical dry snow signatures between −5 dB and −8 dB were observed in winter 2010 at the same time of the day on a separate TerraSAR-X Stripmap monostatic acquisition (Table 8.4).

- S9 (DT 1057982): typical wet snow σ^0 values are observed on the plateau sections covered by this summer scene, which reach 1400 m of altitude. Daily mean air temperatures recorded at the nearby Tempano Glacier (covered by the scene) were around 7°C during the three previous days.

- S6, S8 (DT 1058255): low backscattering is found over the whole plateau surface even up to 2200 m. In fact this was one of the warmest days of the year with minimum air temperature above 15°C at the Dickson Glacier station located at 200 m of altitude. The previous two days were also warm and without precipitation.

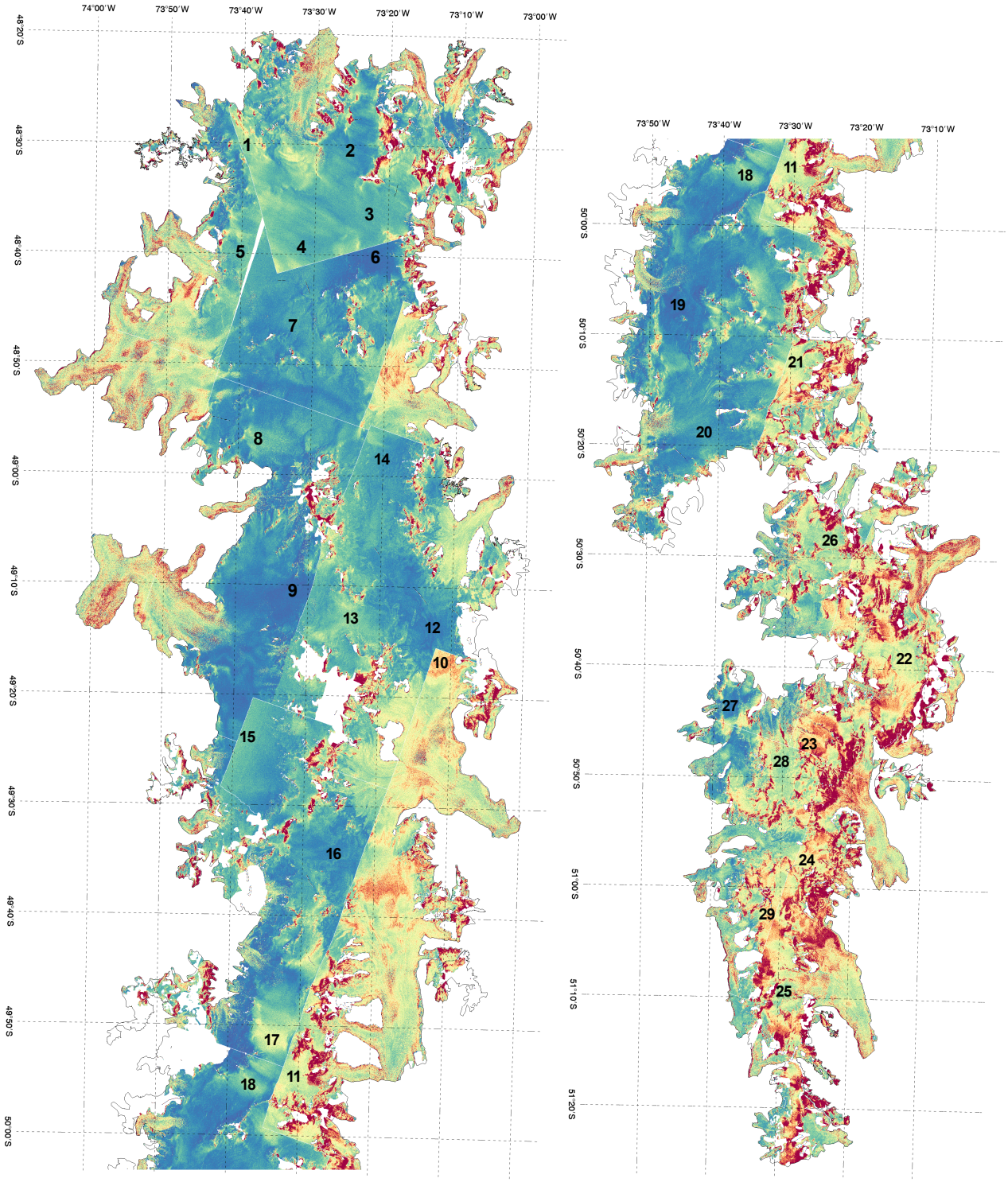

Figure 8.10 – TanDEM-X uncalibrated amplitude mosaic for SPI. The numbers mark the position of the ROIs over which the average σ^0 was computed, which values are reported in Table 8.3 and 8.4. A colourbar is not present since consistency between scenes is not assured.

Table 8.3 – Average values of σ^0 estimated over ROIs for the TanDEM-X scenes covering the plateau of the SPI.

ROI ID	Lat.	Lon.	Area [km²]	Elev. [m]	σ^0 [dB]	θ [°]	Season	Acquisition time (UTC-4)		Mos. scene
1	-48.503	-73.659	0.64	1330	**-14.52**	33.71	Autumn	2011-05-09	19:45:31	S1
2	-48.510	-73.428	4.17	1625	**-17.62**					
3	-48.600	-73.380	7.62	1605	**-16.60**					
4	-48.648	-73.527	9.95	1495	**-16.76**					
5	-48.663	-73.667	1.26	1385	**-16.15**	36.22	Summer	2012-02-16	06:02:17	S9
6	-48.668	-73.367	7.35	1755	**-21.73**	44.57	Summer	2012-02-11	05:53:46	S8
7	-48.770	-73.544	7.89	1385	**-17.56**					
8	-48.947	-73.618	5.66	1400	**-15.42**	44.59	Summer	2012-02-11	05:53:57	S6
9	-49.178	-73.541	11.54	1280	**-21.56**					
10	-49.277	-73.188	2.44	1350	**-7.79**	41.28	Autumn	2011-05-01	05:53:58	S2
11	-49.913	-73.516	2.51	1890	**-11.74**					
12	-49.222	-73.212	8.32	1430	**-20.08**	42.78	Summer	2011-03-07	05:53:53	S3
13	-49.214	-73.401	6.07	1740	**-14.01**					
14	-48.975	-73.337	6.56	1315	**-17.92**					
15	-49.394	-73.635	4.82	1250	**-15.44**	42.77	Summer	2011-03-07	05:54:00	S4
16	-49.568	-73.431	5.30	1480	**-19.29**					
17	-49.852	-73.562	4.56	1850	**-10.89**					
18	-49.919	-73.610	4.66	1825	**-14.15**	42.70	Summer	2011-03-07	05:54:07	S10
19	-50.115	-73.772	8.57	1320	**-20.90**					
20	-50.315	-73.691	7.03	1055	**-18.17**					
21	-50.208	-73.486	7.60	1935	**-16.47**	40.67	Summer	2012-03-15	05:54:12	S17
22	-50.654	-73.214	4.90	1995	**-11.10**	38.52	Winter	2011-07-17	05:54:20	S13
23	-50.779	-73.425	3.82	1900	**-7.62**					
24	-50.957	-73.438	2.08	1350	**-8.94**	38.48	Winter	2011-07-17	05:54:27	S12
25	-51.156	-73.488	2.53	1010	**-13.02**					
26	-50.472	-73.407	4.21	1780	**-12.77**	40.64	Spring	2011-10-24	05:54:23	S14
27	-50.726	-73.625	3.14	1035	**-19.88**					
28	-50.810	-73.499	4.55	1730	**-13.43**	40.60	Spring	2011-10-24	05:54:30	S11
29	-51.044	-73.528	3.14	1410	**-8.49**					

Table 8.4 – Multitemporal values of average σ^0 computed on the same ROIs on overlapping scenes.

ROI ID	Lat.	Lon.	Area [km²]	Elev. [m]	σ^0 [dB]	θ [°]	Season	Acquisition time (UTC-4)		Used - scene
2	-48.510	-73.428	4.17	1625	**-19.43**	44.57	Summer	2012-02-11	05:53:46	No - S8
					-17.62	33.71	Autumn	2011-05-09	19:45:31	Yes - S1
					-8.18	33.30	Winter	2010-07-05	19:45:29	No - //
3	-48.600	-73.380	7.62	1605	**-15.70**	44.57	Summer	2012-02-11	05:53:46	No - S8
					-16.60	33.71	Autumn	2011-05-09	19:45:31	Yes - S1
					-4.86	33.30	Winter	2010-07-05	19:45:29	No - //
4	-48.648	-73.527	9.95	1495	**-17.30**	44.57	Summer	2012-02-11	05:53:46	No - S8
					-16.76	33.71	Autumn	2011-05-09	19:45:31	Yes - S1
					-8.44	33.30	Winter	2010-07-05	19:45:29	No - //
10	-49.277	-73.188	2.44	1350	**-18.75**	42.78	Summer	2011-03-07	05:53:53	No - S3
					-7.79	41.28	Autumn	2011-05-01	05:53:58	Yes - S2
11	-49.913	-73.516	2.51	1890	**-15.80**	42.70	Summer	2011-03-07	05:54:07	No - S10
					-11.74	41.28	Autumn	2011-05-01	05:53:58	Yes - S2
15	-49.394	-73.635	4.82	1250	**-15.44**	42.77	Summer	2011-03-07	05:54:00	Yes - S4
					-18.97	44.59	Summer	2012-02-11	05:53:57	No - S6
22	-50.654	-73.214	4.90	1995	**-13.47**	38.46	Summer	2012-01-31	05:54:19	No - S18
					-13.20	40.94	Autumn	2011-04-22	19:53:28	No - S15
					-11.10	38.52	Winter	2011-07-17	05:54:20	Yes - S13
28	-50.810	-73.499	4.55	1730	**-13.63**	38.46	Summer	2012-01-31	05:54:19	No - S18
					-13.43	40.60	Spring	2011-10-24	05:54:30	Yes - S11
					-9.22	38.52	Winter	2011-07-17	05:54:20	No - S13

- S2 (DT 1027772): this autumn scene covers the termini of the Viedma and Upsala glaciers and a plateau portion with smooth snow and firn between 1900 and 2100 m, on which a variable σ^0 is found. For some regions high values are observed (ROI 10, 11), which could be explained by the formation of a refrozen upper layer under which liquid water persists. This might be the case since the acquisition was performed in autumn around the coldest time of the day. Nevertheless the possibility of dry snow cannot be excluded, and a definitive interpretation results difficult. The plateau surface interested by σ^0 above −14 dB is approximately 356 km^2. On the same ROIs much lower values were measured 2 months earlier in summer (Table 8.4).

- S3, S4, S10 (DT 1012654): a very low σ^0 is observed on most of the three summer scenes. Some isolated regions of higher backscattering are found only at high elevations (for instance −11 dB of ROI 17 at 1850 m). This is likely due to refrozen upper crust just before sunrise. The scattering phase centre would hence be located 10 - 30 cm below the actual surface not causing a significant elevation bias in the InSAR DEM.

- S17 (DT 1056403): a small portion of plateau above 1700 m is included in this summer scene. ROI 21 points to wet snow even at 1900 m. Warm air temperatures with average values above 11°C at the Dickson station, along with absent precipitation, were registered in the 2 days preceding the acquisition.

- S12, S13 (DT 1021147): regions above 1100 m display σ^0 above −12 dB, increasing with elevation. Since acquisitions are in the middle of winter and at the coldest hours it is safe to assume frozen firn, likely covered by recent dry snow featuring lower density and small particle size. In such a scenario the scattering phase centre might be up to some meters below the air-snow interface. Some mountain ranges south of Perito Moreno Glacier are also covered by these two scenes, leading to high backscattering caused by increased SWE but also strong reflection due to roughness and layover. The area of the plateau featuring backscattering above −14 dB and likely affected by signal penetration is approximately 272 km^2 on S12 and 385 km^2 on S13.

- S11, S14 (DT 1042632): variable signature is observed on this spring datatake, σ^0 is below −13 dB on most of the plateau even at 1800 m. Values around −15/−13 dB with a look angle of 40° and acquired at the coldest time of day might be linked to a very low LWC which could still allow a certain amount of signal penetration. A partially refrozen upper layer could also be a possibility given the weak backscattering values found at lower altitudes. A definitive interpretation is difficult. At ROI 28, $\sigma^0 = -13$ dB was measured, a similar value as in summer, while in winter −9 dB are observed (Table 8.4). Extremely weak backscattering (for instance ROI 27) is registered in lower western regions, indicating wet snow. Especially on S11 some isolated zones with higher σ^0 (maximum −8.5 dB at ROI 29) are found, here dry snow is likely but the interested area is very limited. The plateau surface featuring backscattering above −14 dB is approximately 216 km^2 on S11 and 161 km^2 on S14. Given the lower average σ^0 less or no penetration depth is expected compared to the winter scenes S12 and S13.

The SPI TanDEM-X mosaic might suffer from possible signal penetration on the smooth firn and snow of the plateau covered by the winter scenes S12 and S13. Some areas with higher backscattering within the autumn scene S2, and the spring scenes S11 and S14 might be either affected by some degree of signal penetration, or by none according to the scattering mechanism which is difficult to interpret for intermediate values of σ^0. The amount of penetration is spatially variable and difficult to estimate, possibly in the order of some meters.

8.4 Seasonal comparison of σ^0 and surface elevation

A multitemporal experiment was carried out on the NPI with the goal of quantifying empirically the InSAR elevation bias due to signal penetration in ice and snow and possibly to measure seasonal elevation changes of the icefield. The TanDEM-X datatakes selected and processed over NPI (Table 7.6) were acquired in summer (cf. Section 6.2.4.2). Due to some phase unwrapping errors on the

mountain range crossing the plateau a winter scene was included in the DEM mosaic as background to fill the gaps. Since the datatakes belong to neighbouring beams a large overlap is present between N3 (DT 1171117 1B) and N5 (DT 1149794) and the look angle is very similar (37.2° and 36.2°, respectively). N5 was acquired towards the end of winter on 2.9.2013, while N3 was acquired four months later (1.1.2014) at the beginning of summer of the same hydrological year, both at 19:46 local time (UTC−4h). Observations about the meteorological conditions are reported in Section 8.3.2, while the state of the snow has been discussed in Section 8.3.3.

The difference $\Delta h = h_w - h_s$ between the winter and the summer DEM is shown in Figure 8.11 along with the backscattering coefficient of both acquisitions and the DEM from the summer acquisition as elevation reference. For clarity only the common icefield coverage is shown. Phase unwrapping errors (a single baseline procedure was employed for these two scenes) affected some large areas particularly in the southern sector in correspondence of the mountain range crossing the plateau.

In winter (Figure 8.11a) a high σ^0_w exceeding −10 dB is measured on N5 on the southern part of the plateau with values increasing with elevation. Above approximately 1350 m the strong backscattering is due to dry firn and snow, furthermore strong precipitation was recorded in the previous days at the nearby S. Rafael station (Figure 8.3.2). Moreover, the freezing elevation estimated by extrapolation of the daily average air temperature (with a lapse rate of of −0.65°C/100 m) is approximately 1350 m. The transition to lower σ^0 values (below −17 dB) is abrupt for elevations below this threshold (both to the north and to the south-west). Wet snow can be expected even in winter at the end of a sunny and relatively warm day, at least up to a certain elevation. When the snow is dry σ^0 depends mainly on its microstructure, in fact a spatial variability of σ^0 is observable on the plateau.

In summer, σ^0_s of the plateau (Figure 8.11b) on N3 appears more uniform. σ^0 is equal or below −18 dB for most part of the plateau with areas with σ^0 as low as −24 dB at lower elevations (for instance upstream of S. Rafael Glacier). These values indicate a wet snowpack before sunset when acquisition took place. Areas of higher σ^0_s up to −15 dB are found mostly above 1200 m. The acquisition day was not warm, negative daily average air temperatures are estimated above 1600 - 1700 m. The acquisition day was preceded by a warmer period with some precipitation detected at the Rio Nef meteorological station (Figure 8.3.2). An upper layer of re-frozen snow is likely to form in this scenario as air temperatures go below 0°C driving up σ^0 but not affecting heavily the penetration depth, as wet snow is found below. Deep layers of dry snow appear unlikely in this acquisition.

The $\Delta h = h_w - h_s$ elevation difference image (Figure 8.11d) shows relatively uniform positive values below the approximate 1350 m altitude threshold, indicating a decrease in elevation from winter to summer, due to melting of snow and firn compaction. Here signal penetration is not expected to affect neither N3 nor N5, given the low values of σ^0. On the same plateau at altitudes above 1350 m a drop of Δh is found in correspondence with the areas of high σ^0_w. This drop is likely due to signal penetration in the dry winter snow and firn of N5, the scattering phase centre might be located in correspondence of a subsurface refrozen layer. The transition from positive to negative Δh is relatively abrupt and well correlated with the increase of σ^0_w.

In order to quantify the elevation difference in the X-band InSAR DEMs caused by radar signal penetration, three regions of interest (ROIs) were delimited on the plateau (Figure 8.11). The obtained mean values $\overline{h_s}$, $\overline{\sigma^0_w}$, $\overline{\sigma^0_s}$, and $\overline{\Delta h}$ are reported in Table 8.5 for the three ROIs A, B and C. The standard error of $\overline{\Delta h}$ is negligible since the average is performed on very large areas. $\overline{\Delta h}$ is affected by systematic errors due to the precision of the vertical registration, according to Table 7.4 these are 0.1 m and 0.03 m for N3 and N5 respectively, their squared root sum gives an error on $\overline{\Delta h}$ of 0.1 m.

ROIs A and B have been selected to be approximately adjacent to each other on the plateau (excluding the transition zone) and to include a limited range of elevations and a uniform behaviour of Δh within the same ROI. On ROI B the same value of σ^0 is found in winter and summer and $\overline{\Delta h} = +1.8$ m is registered. On the other hand, ROI A displays a large backscattering coefficient difference (8.4 dB) with $\overline{\Delta h} = -1.9$ m.

The elevation variation on ROI B is due to seasonal change. On ROI A two causes of elevation variations are coupled: actual seasonal change and spurious variation due to signal penetration. In order to isolate and quantify the latter, the seasonal height change estimated on ROI B is assumed to be valid also on ROI A. With this assumption an elevation offset due to signal penetration of approximately

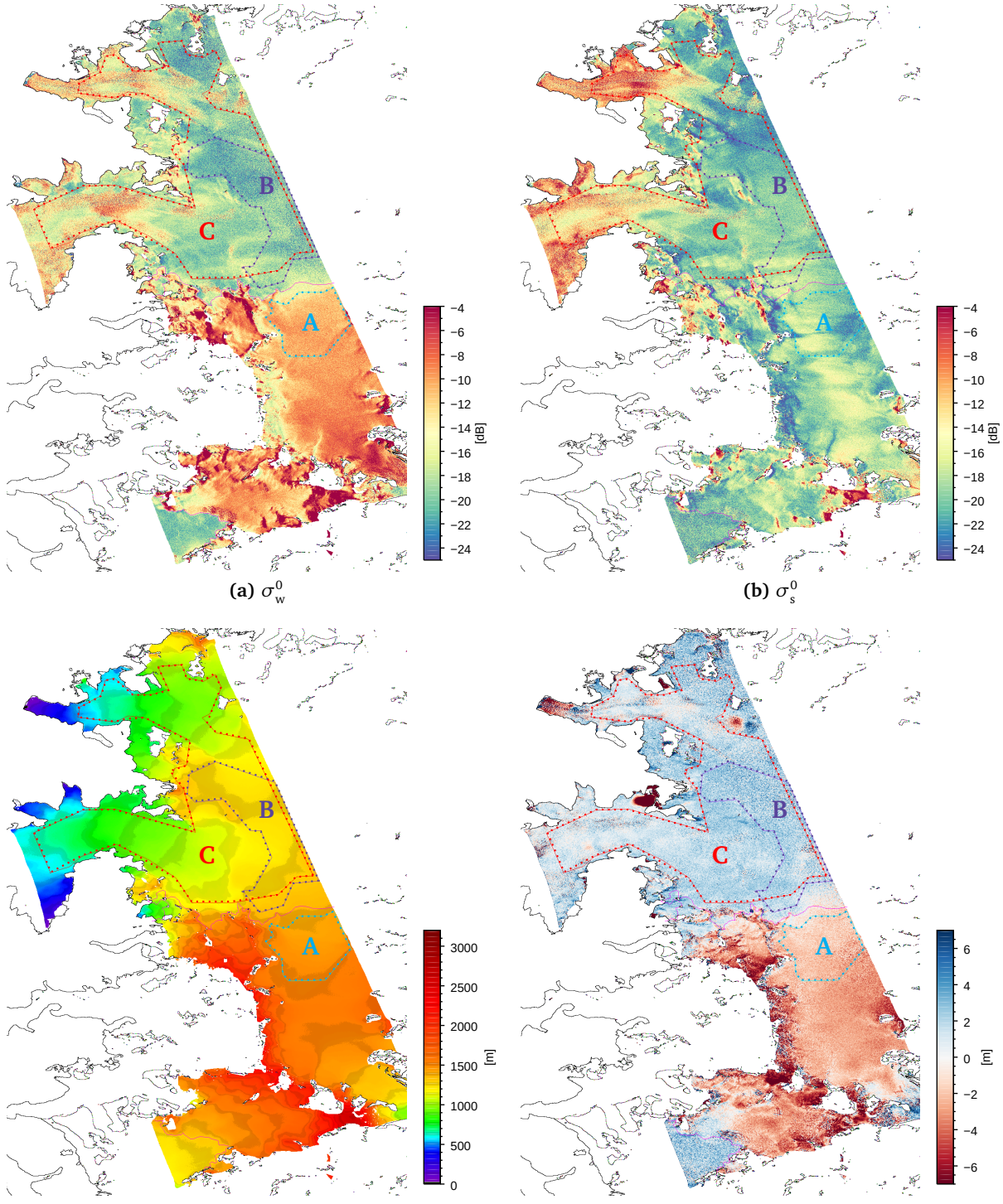

(a) σ^0_w **(b)** σ^0_s

(c) h_s **(d)** $\Delta h = h_w - h_s$

Figure 8.11 – Seasonal comparison of backscattering coefficient and elevation over a large section of NPI. σ^0_w of the winter (a) and σ^0_s of the summer (b) acquisitions. Summer DEM h_s, not affected by signal penetration in ice and snow (c). Elevation difference $\Delta h = h_w - h_s$ (d). The polygons indicate the ROIs used to compute the statistics.

Table 8.5 – Statistics computed on the ROIs marked in Figure 8.11.

ROI	Area [km^2]	$\overline{h_s}$ [m]	$\overline{\sigma^0_w}$ [dB]	$\overline{\sigma^0_s}$ [dB]	$\overline{\Delta h}$ [m]
A	106.28	1462.54	−10.50	−18.86	−1.90
B	106.64	1260.37	−19.77	−19.46	+1.85
C	342.89	1049.89	−17.70	−17.69	+1.57

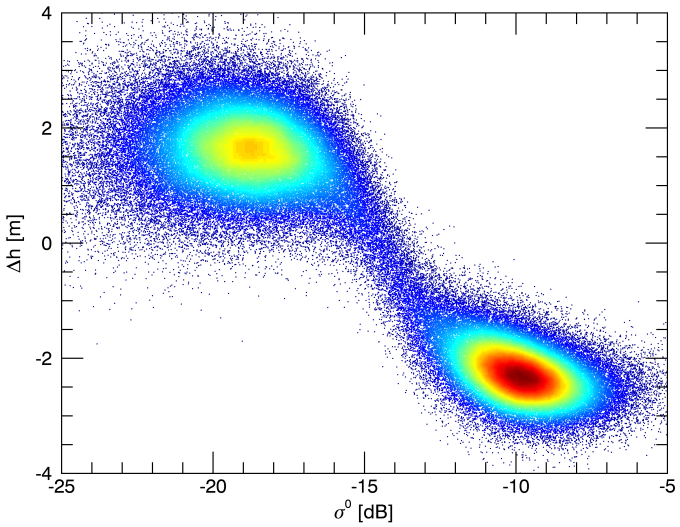

Figure 8.12 – Scatterplot of $\Delta h = h_w - h_s$ with σ^0_w for plateau elevations between 1150 and 1550 m.

3.8 m is estimated on ROI A. The assumption might overestimate melting and compaction because of the 200 m difference in mean altitude between ROI B and ROI A. Nevertheless the obtained value is a coarse empirical estimate of elevation bias due to signal penetration in snow and firn, a figure which is rarely found in the literature. It must be stressed that the estimate is strictly linked to the system parameters and to the geophysical characteristics of the target during the two acquisitions, in particular the density and the particle size of the dry winter snow of N5.

To understand the behaviour of Δh (due to both seasonal changes and signal penetration bias) at varying σ^0_w, a scatterplot (Figure 8.12) has been extracted on a single ROI corresponding approximately to ROI A, ROI B and the transition zone between them, and covering altitudes between 1150 m and 1550 m. The scatterplot displays a cluster for σ^0_w between −23 dB and −17 dB with a mean Δh of ∼+1.6 m and a large spread corresponding approximately to the points of ROI B. This height offset is due to seasonal elevation change. Δh starts to decrease at −14/−15 dB with a linear trend saturating approximately at −11 dB, presumably caused by a gradual decrease of liquid water content in the winter snow cover as elevation increases and temperature decreases. In this transition interval of σ^0_w, the effect of seasonal changes and signal penetration balance themselves. Another cluster is found for σ^0_w between −12 dB and −6 dB corresponding approximately to the points of ROI A.

Assuming again that the seasonal change measured at low σ^0_w is uniform on the entire investigation area and subtracting a Δh offset of 1.6 m from the scatterplot allows to isolate roughly the behaviour of the InSAR elevation bias due to signal penetration at varying backscattering coefficient for this data. Empirical results linking backscattering and elevation bias is rarely found in the literature for SAR data. A mean elevation bias of −1 m is measured at −15 dB, −2 m at −14 dB, −3 m at −12 dB, saturating to −4 m above approximately −9 dB. The large variability of Δh at low σ^0_w and the unproven assumption about the uniformity of the seasonal changes introduce a not quantifiable uncertainty.

Finally, in order to obtain a rough estimate of seasonal elevation change occurring in the period 2.9.2013 - 1.1.4014 ROI C was selected to include a wide range of altitudes (above and below the equilibrium line) with both ice and snow coverage exclusively where no signal penetration is expected. As Table 8.5 reports, a mean elevation change $\overline{\Delta h} = 1.6$ m was measured on ROI C. This approach would be more valuable if the whole time span of the ablation season (30.9 - 30.3) was available since it would have represent an estimate of the summer mass balance b_s (cf. Section 3.5).

Chapter 9

Geodetic mass balance

This chapter deals with the glacier mass balance obtained through the geodetic method. In Section 9.1 the state of the art is given. Results obtained on the Patagonian icefields are firstly presented, followed by an extensive literature review focusing on the different aspects of the error budget of the method (Section 9.1.1). The procedure and the notation used in this work are reported in Section 9.2. Section 9.3 presents in detail the approach undertaken to estimate the error budget of the geodetic mass balance of NPI and SPI and the obtained error values. The estimation of subaqueous ice mass loss at the front of calving glaciers is presented in Section 9.4. Finally the results of the geodetic mass balance of NPI and SPI are discussed and compared to values found in the literature in Section 9.5.

9.1 Geodetic mass balance state of the art

In this section the state of the art of the net mass balance derivation through the geodetic method will be presented. The focus will be set mainly on the error budget estimation being this the most challenging methodological aspect. In Section 9.1.1 the main issues and uncertainty sources will be outlined along with the approaches taken by different authors. This section serves also as a general outline to the error estimation performed in the current study, described later in Section 9.3. For this reason a subsection dealing with geostatistics (Section 9.1.1.2) and semivariograms is also included. Before reviewing the error estimation state of the art, some publications concerning the general approach to the geodetic mass balance and its comparison with traditional mass balance estimation methods will be given. Deeper detail, including data used, method description and obtained results will be dedicated to publications studying the Patagonian icefields.

Bamber & Rivera (2007) present a detailed literature review of different remote-sensing-based methods used to determine the glacier mass balance with their strengths and weaknesses, particularly those applied to the Patagonian icefields. They also list glaciological (field based) mass balance results of the largest Patagonian glaciers, which are mainly limited to the ablation areas. Zemp *et al.* (2010) compare glaciological mass balance results to geodetic mass balance results obtained from photogrammetry applied to aerial vertical photographies of the Storglaciären Glacier (Sweden). The uncertainties affecting both methods are exposed. Cogley (2009) presents a framework for the comparison of geodetic and glaciological mass balance, which have proven to be often divergent. He assembles and compares data from hundreds of sources and proposes a statistical approach for the adaptation of multi-annual geodetic measurements to the annual glaciological methods.

Rivera *et al.* (2007) derived ice elevation and areal changes between 1975 and 2001 over NPI using a DEM obtained from cartographic maps and an ASTER DEM. Based on a Landsat ETM image of 2001 they report a total icefield area of 3953 km^2, including adjacent small ice surfaces. They measure on the icefield local thinning rates up to $-4.0 \pm 0.97\ m\,a^{-1}$, but they do not compute the mass balance. A similar approach and data were applied to the Chico Glacier in SPI by Rivera *et al.* (2005). They estimate a mean net volume balance of $-0.29 \pm 0.097\ km^3\ w.e.\ a^{-1}$ between 1975 and 2001.

Möller *et al.* (2007) and Möller & Schneider (2010) obtain the geodetic mass balance of the 190 km^2 wide Gran Campo Nevado (GCN) Icefield in Patagonia by comparing a DEM from aerial pho-

tographs of 1984 with the C-band SRTM DEM. They report a mean annual elevation change rate of -0.37 ± 0.14 m w.e. a^{-1}.

Rignot *et al.* (2003) compare the SRTM C-band DEM with cartographic maps of 1968/1975 obtained from aerial photography in order to estimate the volume change of the largest 63 glaciers of SPI and NPI. The photogrammetry failed to produce reliable contour lines for 75% of the accumulation area above 1200 m. They hence extrapolate elevation changes for these areas by fitting a polynomial to the measured values at lower elevations. They report for 24 glaciers of NPI a volume change rate of -2.63 ± 0.4 km^3 a^{-1} over an area of 3481 km^2 (with an additional frontal change of -0.2 km^3 a^{-1}, presumably not including subaqueous changes), they scale this value over the entire icefield (area: 4200 km^2) obtaining a volume change rate of -3.2 ± 0.4 km^3 a^{-1}. On SPI they measure a loss of -7.2 ± 0.5 km^3 a^{-1} over an area of 8167 km^2 (with an additional frontal change of -1.3 km^3 a^{-1}), they scale this value over the entire icefield (area: 13000 km^2) obtaining a volume change rate of -13.5 ± 0.8 km^3 a^{-1}. The corresponding contribution of both icefields to sea level change is 0.042 ± 0.002 mm a^{-1}. For some glaciers of SPI they further compare SRTM to 1995 cartography. On glaciers covered both in 1975 and in 1995 they detect strong increase in thinning rates, resulting in a volume change rate of -14.3 ± 1.9 km^3 a^{-1} over an area of 5642 km^2. They scale this value over the entire icefield assuming a constant frontal loss of -1.3 km^3 a^{-1}, obtaining a volume change rate of -38.7 ± 4.4 km^3 a^{-1} for the period 1995 - 2000.

Willis *et al.* (2012b) derive ice loss rates over the entire NPI by using the SRTM C-band DEM as reference and a series of 55 ASTER optical DEMs acquired during the subsequent 11 years. These DEMs are obtained from two simultaneously acquired nadir and backward pointing images (bands 3N and 3B, λ=0.76 - 0.86 μm). The vertical accuracy is approximately 7 - 15 m on rough terrain. Horizontal coregistration between each ASTER DEM and the SRTM is obtained by cross-correlation between ASTER's band 3N image and a pansharpened band 8 Landsat image, which was previously orthorectified and registered to the SRTM with an accuracy of better than 50 m. The obtained tie points are used to guide a solid body translation and rotation of the ASTER image. This process is repeated iteratively and the transformation parameters applied to the ASTER DEM. Finally the 30 m ASTER DEM is resampled to the 90 m posting of SRTM. They perform vertical coregistration in order to correct long wavelength errors due to the lack of ground control points, orbital artefacts and clouds. This is done by fitting a plane to the difference samples over bedrock relative to the STRM DEM and removing it from the whole ASTER DEM. The sum of the mean and the standard deviation of the bedrock offsets is used as uncertainty of each elevation pixel of that specific ASTER DEM. The SRTM pixels are assigned a fixed uncertainty of 5 m. The elevation change rate is computed by fitting a least-squares linear trend to the time series of elevation samples of each icefield pixel, using the inverse of the uncertainty of each sample as weight. The 1-σ uncertainty associated to the elevation change rate of each pixel is obtained from the model covariance matrix of the weighted linear regression. Willis *et al.* (2012b) report for the entire NPI (area[1]: 3871 km^2) a volumetric ice change rate of -4.06 ± 0.11 km^3 a^{-1} (not including volume loss due to frontal retreat and subaqueous melting). They derive the mass change rate by using a density of 917 kg m^{-3} below the ELA and 550 kg m^{-3} for the firn above the ELA, the latter value is taken from published results of upper layer ice density from cores drilled on the accumulation area of the San Rafael and Nef glaciers.

Following the same procedure, Willis *et al.* (2012a) obtain the mass balance of SPI based on 156 ASTER DEMs and the SRTM DEM. In order to assess possible radar signal penetration, they compare the SRTM C-band and X-band DEM, after correcting the elevation difference for a curvature dependent bias. They obtain a mean offset of 2 m which they assume to be caused by signal penetration in the lower frequency C-band DEM, and correct it. For the 12118 km^2 icefield (excluding 432 km^2 of exposed bedrock) they estimate an average volume change rate of -21.2 ± 0.5 km^3 a^{-1} between 2000 and 2012. They report an additional subaqueous ice loss of -1.0 ± 0.8 km^3 a^{-1}, although the estimation procedure is not reported. They also revise the volume loss of NPI by applying the +2 m radar penetration correction leading to a volume change rate of -4.9 ± 0.3 km^3 a^{-1} (subaqueous loss not included). They use an ice density of 900 kg m^{-3} for the entire icefields to obtain the mass change.

Melkonian *et al.* (2012) apply the same procedure to the smaller Cordillera Darwin Icefield (CDI)

[1]Derived as sum of all glaciers in Table 1 of Willis *et al.* (2012b)

using 36 ASTER DEMs. The 2 m elevation bias due to signal penetration in the SRTM C-band DEM is also assumed. For the 2605 km^2 CDI, they estimate a volume change rate of -4.2 ± 1.7 $km^3\,a^{-1}$ and an additional subaqueous volume loss rate of -0.12 ± 0.06 $km^3\,a^{-1}$. An ice density of 900 $kg\,m^{-3}$ is assumed in order to obtain the total ice mass change rate.

9.1.1 Error budget: general approach and state of the art

The error estimation of glacier elevation differences and geodetic mass balances is often treated in a fragmented way in the literature: different approaches are undertaken and different error sources are considered or ignored. This is because the applied procedure as well as the input data may vary significantly (optical or InSAR DEMs, digitized cartography, radar or optical altimetry, etc.), making an approach more suitable than the other. An attempt at finding and describing the common grounds to most of the proposed approaches, as well as their differences, is done in this section.

Various error sources might come into play when computing the geodetic mass balance, these may differ according to the data used and to the specific procedure applied. The absolute height errors of the two elevation datasets play a minor role, as they express the accuracy of the elevation relative to a certain datum, the relative elevation accuracies are more relevant in this context. A fundamental component of the error is the uncertainty of the elevation difference, which includes different error sources: from the uncertainties of the input data to errors linked to the procedure used to obtain the elevation difference. Another error source common to the geodetic approach is related to the assumption of a certain density of the changed volume of ice and snow. The vertical profile of ice and snow density is unknown unless field measurement are performed and might also vary within the glacier basin. Other error sources are dependent on the sensor used to measure the surface elevation. In the case of microwave data the signal might penetrate in ice and snow causing the scattering phase centre, to which the recorded elevation refers, to be below the actual surface. In the case of photogrammetrical elevation data, the lack of contrast over smooth ice and snow and the presence of clouds might lead to missing data. Uncertainty might be associated to the glacier outlines obtained with automatic procedures from multispectral data, particularly over debris-covered ice displaying unexpected reflectance. DEMs obtained from old topographic maps are affected by other issues linked to the accuracy of the original contour maps and to the digitization process.

As Nuth & Kääb (2011) point out, the physical determination or modelling of the errors based upon the original transformation equations, processing and acquisition methods and parameters is very difficult or impossible. This is because this information is often not provided along the distributed data, which, especially in the case of DEMs, undergoes various steps of post processing and merging. The approach preferred in the literature and in the present study is therefore the statistical error modelling, which, as stated by Nuth & Kääb (2011) has the advantage of being widely applicable to data from different sensor systems and is independent of the processing methods, since it is based on the empirical analysis of the actual elevation data used.

9.1.1.1 Uncertainty of the elevation difference sample

The uncertainty of an individual statistically independent sample (pixel or point) of elevation difference is defined as ε, two main approaches can be applied to quantify this parameter. The first one is to derive it as $\varepsilon = \sqrt{\sigma_1^2 + \sigma_2^2}$ where σ_1 and σ_2 represent the random elevation errors of the first and second elevation dataset. Ideally σ_1 and σ_2 should be calculated empirically comparing a pool of elevation samples of the glacier surface with an elevation source of much higher accuracy (such as laser altimetry or GPS) acquired within a short time span in order to avoid physical variations of the ice surface. A similar approach is taken by Larsen *et al.* (2007) where the SRTM C-band DEM from February 2000 is compared to airborne laser altimeter data of August 2000 to estimate σ_1. They find a slight linear trend with elevation to σ_1, which they attribute to seasonal variations and radar signal penetration and correct this trend before comparing the SRTM elevations to the other DEM, produced from aerial photography acquired in the summer season (from 1948 and 1987). The standard deviation around the mean, amounting to ±5 m is assumed as uncertainty of the SRTM DEM σ_1 by Larsen

et al. (2007). Unfortunately an independent elevation dataset over glaciers acquired at the same epoch of the DEM is rarely available. To obviate, a common approach is obtaining σ_1 and σ_2 from empirical analyses published by others for the same dataset. Doing so means that σ_1 and σ_2 are not extracted directly from the used elevation data, but from acquisitions in other geographical areas, with different terrain coverage and possibly under changed acquisition parameters. The resulting ε is hence less representative of the actual uncertainty of the elevation difference sample, also because it would not include errors linked to the differencing procedure, for example due to residual misregistration.

The second, more common, approach uses the elevation difference samples over ice-free areas (off-glacier), here defined with Δz, where no physical elevation changes are expected, as statistical pool to estimate the uncertainty of the elevation difference ε. This uncertainty is assumed to be valid also for the glacier elevation difference sample Δh. This is generally defined as the "standard deviation about the mean" of the off-glacier elevation difference samples, i.e. $\varepsilon = \sigma_{\Delta z}$. It is statistically inferred from the same data used to compute the mass balance, thus taking into account the characteristics and issues related to the acquisition and the processing of the used datasets. For instance, in the case of this study, each bistatic TanDEM-X acquisition is characterized by a specific height of ambiguity, linearly influencing the relative elevation error of the DEM due to the interferometric noise (Section 2.2.3). Furthermore each TanDEM-X datatake is separately coregistered to the SRTM DEM used as reference (see Section 7.2). This operation is rather delicate given the complex topography of the territory and might result in a small degree for horizontal misregistration. This translates into a height difference error δh_{coreg} affecting differently each pixel since it depends on the magnitude and direction of the horizontal shift as well as on the local slope and the aspect of the terrain as quantified by Eq. (7.1) (Nuth & Kääb, 2011). Estimating the uncertainty over the off-glacier elevation difference allows taking into account those and other data and processing issues leading to a more representative error estimate.

With this approach an issue to be considered is the validity of the uncertainty determined off-glacier when extended to the on-glacier elevation difference. The issue is generally briefly handled in the literature, except by Rolstad *et al.* (2009) with focus on photogrammetry. Naturally there are differences between the glacier surface and the surrounding non-glaciated terrain.

The first, and probably main issue, concerns the different topography. Typically glaciers flow in basins confined into valleys and characterized by moderate slopes, especially in the case of larger glaciers. These are often outlets of icefields, which typically feature plateaus characterized by high elevations and relatively flat surfaces in the central part and discharge ice through glaciers with higher slopes on the margins. The aspect angle distribution of glaciated areas might have a prevailing component. On the other hand the terrain surrounding the icefields is generally mountainous, with peaks and ridges following one another; there might be some flat areas further away from the glacier termini as well as lakes and fjords. The surfaces off-glacier can hence display much higher slopes compared to the glaciated areas and an aspect distribution which is more uniform. According to Equation (7.1) a residual horizontal coregistration error will lead to larger elevation difference errors δh_{coreg} over the steeper off-glacier terrain, causing an overestimation of the on-glacier uncertainty computed as $\varepsilon = \sigma_{\Delta z}$. To alleviate this effect the off-glacier pixels are often filtered according to their local slope before computing $\sigma_{\Delta z}$ by imposing a threshold which is more representative of the slope of the studied glaciers. Nuth *et al.* (2007) use a threshold of 20°, Nuth *et al.* (2010) of 15° (both in Svalbard), Rolstad *et al.* (2009) of 30° (on the Svartisen Ice Cap, Norway). It must be noted that the actual distribution of the slope on and off-glacier is what influences the difference in the δh_{coreg} error component. Since the distribution of glacier pixels generally displays a peak at lower slopes, while the terrain pixels might be more uniformly distributed (cf. Figure 9.5), imposing a threshold would still not avoid an overestimation of δh_{coreg}, but it represents a simple way of mitigating this effect. Nevertheless it is useful to compare the slope distributions in order to choose an appropriate threshold; such a comparison has not been found in the literature and will be shown in Section 9.3.2. In the case of InSAR DEMs, the mountainous off-ice terrain might be affected by layover and shadow effects which render the elevation pixels untrustworthy as strong interpolation is involved. A surface is in layover as soon as its slope exceeds the look angle when its aspect is facing the line of sight. As acquisition geometries (orbit direction and incidence angle) might be totally different between the first and the second DEMs the

elevation difference might not be equal to zero for these regions. Using off-glacier pixels affected by layover would overestimate $\varepsilon = \sigma_{\Delta z}$, filtering steeper terrain is thus necessary.

Another possible issue in this respect resides in the different physical properties of ice and snow as compared to non-glaciated terrain, the latter generally consisting of bare rock especially at higher altitudes or vegetated terrain at lower altitudes. These differences may affect the quality of the elevation data, according to the type of sensor and acquisition geometry. As acknowledged by Rolstad *et al.* (2009) in case of optical DEMs the image contrast and thus the DEM quality is very different for snow, crevassed ice, bare rock or vegetated areas, besides the fact that all areas may have a different degree of sun and shadow. The lack of contrast typical of white snow areas is a well known problem of photogrammetry and leads to failure of the correlation algorithm. Elevation inferred from SAR bistatic interferometry are more robust to different types of coverage and terrain, the quality of the elevation values and the noise associated to them are strictly related to the complex correlation coefficient (or coherence) (Bamler & Hartl, 1998). The coherence of the bistatic acquisition depends on the physical properties of the distributed scatterer (see Section 2.2.2). The estimation of the elevation difference uncertainty as $\varepsilon = \sigma_{\Delta z}$ could be affected by differences in the properties of the off-glacier surface compared to the icefield (which has varying properties within itself). This could lead to an underestimation of the error, especially for optical data, but might have an impact on InSAR data as well if the icefield surface has very low coherence.

A last issue that might affect the validity of the off-glacier statistics is the difference in resolution between the two DEMs. Basically the DEM with lower resolution does not have the same capacity of following the slope gradients typical of the rough mountainous ice-free terrain, overestimating elevation for gorges and underestimating it for peaks. This might lead to a bias in the off-glacier elevation differences which would reflect in an overestimation of $\varepsilon = \sigma_{\Delta z}$, while the smoother glacier surfaces are certainly less affected by this problem. This issue is tackled in more detail in Section 9.3.1.

The previously reported approaches are found in the literature for the estimation of ε. The first one, in which the random elevation errors of each dataset are propagated to the difference using $\varepsilon = \sqrt{\sigma_1^2 + \sigma_2^2}$, is adopted by Larsen *et al.* (2007), as previously mentioned. The random error of the older DEM, which is based on aerial photography, is deduced from previously published studies (Arendt *et al.*, 2002, 2006) as the nominal accuracy of the contour placement on the topographic map, and it is increased (doubled or tripled) on the accumulation area where the contrast is lower and the elevations are harder to be identified by the cartographers. The authors take also into account systematic errors which are typical when dealing with elevation acquired from topographic maps, although more difficult to estimate. Nuth *et al.* (2010); Nuth & Kääb (2011) use a similar approach to determine ε by comparing off-glacier the SRTM DEM and ASTER GDEM to the much more accurate lidar ICESat elevation points (Zwally *et al.*, 2002), in order to estimate the random error of the DEMs. They use a σ obtained empirically from the literature for the ICESat points. Rott *et al.* (2014b) compare multitemporal TanDEM-X DEMs and assign to each of them an uncertainty according to those estimated empirically by Rizzoli *et al.* (2012) as a function to the height of ambiguity of the TanDEM-X acquisition. In other pubblications many authors, for instance Etzelmüller (2000), apply the first approach by simply propagating the nominal relative error of each DEM to the elevation difference samples using $\varepsilon = \sqrt{\sigma_1^2 + \sigma_2^2}$.

The second approach, in which the elevation uncertainty is estimated directly as the off-glacier spread of the elevation difference $\varepsilon = \sigma_{\Delta z}$, is adopted in Nuth *et al.* (2007); Schiefer *et al.* (2007); Howat *et al.* (2008); Rolstad *et al.* (2009); Haug *et al.* (2009); Nuth *et al.* (2010); Bolch *et al.* (2011); Zemp *et al.* (2013). A slightly different method, also based on the off-glacier statistics, is applied by Willis *et al.* (2012a,b); Melkonian *et al.* (2012). They quantify the mass loss respectively in SPI, NPI and Cordillera Darwin Icefield (CDI), by using the SRTM DEM and a time series of ASTER DEMs acquired between 2001 and 2011. After coregistering the ASTER DEMs to the SRTM, a weighted least-squares linear trend is used to calculate an elevation change rate for each glacier pixel. Each elevation pixel is weighted by the inverse of its uncertainty. The uncertainty of each ASTER elevation sample is obtained as the sum of the mean and the standard deviation of the bedrock offsets between the corresponding ASTER DEM and the SRTM DEM used as reference. The uncertainty of all SRTM elevation pixels is set arbitrary to 5 m. The uncertainty associated with the elevation change rate of each pixel is obtained

from the model covariance matrix, which accounts for the uncertainties on the elevations incorporated into the regression (Melkonian *et al.*, 2012).

Koblet *et al.* (2010) explore both approaches. For the first one they compute the statistic and random error of each DEM by comparing them to 26 differential GPS points and propagate the error to the elevation difference. For the second one they obtain the uncertainty from the standard deviation of the off-glacier elevation difference pixels. They also statistically test the significance of the ice properties changes with respect to the uncertainty and the dependence of errors on slopes. In their case the second approach generally led to larger systematic errors and slightly lower random errors of the elevation difference.

9.1.1.2 Geostatistics and semivariograms

The previous section dealt with the estimation of the uncertainty of an individual statistically independent sample (pixel or point). When studying large-scale geophysical phenomena, for instance in the mass balance of glaciers, spatial averaging of data is usually performed. It is hence necessary to obtain the uncertainty of the average. This differs from the uncertainty of the single samples included in the averaging process since usually a certain degree of spatial correlation exists between samples. To determine the degree of spatial correlation geostatistical methods can be used.

The field of geostatistics (or spatial statistics) saw the light in the 1950s when significant financial resources where invested in research by the mining industry with the objective of predicting the grade of gold and other metals in ore bodies from a limited number of scattered samples. The empirical work undertaken in South Africa, particularly by mining engineer Danie Gerhardus Krige, was then formalized by the French mathematician Georges Matheron in his work "The Theory of Regionalized Variables" (Matheron, 1971). The principal objective, pertaining the field of geology and mining, was obtaining the best estimate of an unknown variable at a certain spatial location: this is known as kriging or gaussian process regression. The interpolated values are modelled by a gaussian process governed by prior covariances, when these fulfil suitable assumptions kriging gives the best linear unbiased prediction of the intermediate values. The innovation of geostatistics compared to the classical estimation consisted in the mathematical quantification of spatial correlation and its use for the prediction. Geostatistics have since expanded their scope to diverse fields of science where spatial information is included, such as environmental and earth sciences (Webster & Oliver, 2007), meteorology and remote sensing. In the following the theoretical basics of spatial statistics which will be needed for the determination of the correlation distance are introduced, based mainly on Matheron (1971) and partially on Clark (1979), these citations will thus not be repeated.

At the core of spatial statistics is the variogram, which consists in a function describing the degree of spatial correlation of a spatial random field. A spatial random field $Z(x)$ is a random vector in space (a vector of generally non-independent random variables), as the elements of the vector become infinite $Z(x)$ is defined as a random function. x defines a point in the n-dimensional space $\mathbb{R}^n$, which in this study case will be the two dimensional image space. To every support point x_0 in space corresponds a random variable $Z(x_0)$. A realization of each random variable $Z(x_0)$ will be a particular numerical value $z(x_0)$, while a realization of random vector will be a vector of values, and consequently a realization of a random function $Z(x)$ will be a numerical function $z(x)$. The latter can always be considered a regionalized variable, and vice versa, a regionalized variable can always be regarded as a realization of a certain random function. Naturally, statistical inference of $Z(x)$ is not possible having a single realization $z(x)$, unless some supplementary hypotheses about $Z(x)$ are introduced.

A first possible hypothesis is the stationarity of the random function $Z(x)$, that is, its law is invariant under translation, in other words the random variable $Z(x_0)$ will have the same distribution as $Z(x_0+h)$, where h is any vector in space (often called lag vector) characterized by a modulus r and a direction α. Under this assumption the expectation of $Z(x_0)$, defined as $m(x_0) = E[Z(x_0)]$ is equal to $m(x_0+h)$ and hence is a constant $m = E[Z(x)]$ independent of x_0. It is generally assumed that $m = 0$ (even by replacing $Z(x)$ with $Z(x)-m$).

If two random variables $Z(x_0)$ and $Z(x_0+h)$ have finite variances, they also have a covariance $C(x_0,h)$ (often referred to as auto covariance in spatial statistics), which under the assumption of

stationarity (and $m = 0$) will be independent of x_0 and can be written as:

$$C(h) = E[Z(x) \cdot Z(x+h)] \tag{9.1}$$

For $h = 0$ $C(0) = E\left[Z(x)^2\right]$, this is the variance of the stationary random function $Z(x)$.

A weaker hypothesis is the second order stationarity of $Z(x)$, according to which $Z(x_0)$ has an expectation independent of the support point x_0 and for every vector h a covariance which exists and is also independent of x_0, writeable as:

$$C(h) = E[Z(x_0) \cdot Z(x_0+h)] - m^2 \tag{9.2}$$

This hypothesis is sufficient for the theory of the regionalized variables, but it supposes, as the previous one, a finite a priori variance $C(0)$ of the random function $Z(x)$ in order for the covariance function $C(h)$ to exist. Unfortunately many phenomena have an almost unlimited capacity of dispersion and cannot be properly described by a finite a priori variance. Besides, the assumption of stationarity (both in its stricter and weaker form) cannot always be assumed, for instance in the original problem of estimating the grade of a metal in a large deposit: this is generally described by a smooth unknown variation (trend) around which there is a random variation (possibly stationary).

Hence an even weaker hypothesis must be assumed: the *intrinsic hypothesis*. Even when the a priori variance $C(0)$ does not exist (i.e. is infinite), it is possible that the increments $[Z(x_0+h) - Z(x_0)]$ have a finite variance. If these, for any vector h, have an expectation and a variance which are independent of the support point x_0 (but depend on h), the random function $Z(x)$ fulfils the intrinsic hypothesis (which can be seen as the second order stationarity of the increment), it can be hence written that:

$$m(h) = E[Z(x+h) - Z(x)] \tag{9.3}$$

$$2\gamma(h) = \mathrm{var}[Z(x+h) - Z(x)] \tag{9.4}$$

The function $m(h)$ is the *linear drift* and it is linear in h, it can be assumed that it is equal to zero, even by replacing $Z(x)$ with $Z(x) - m(x)$. The function

$$\gamma(h) = \frac{1}{2} E\left\{[Z(x+h) - Z(x)]^2\right\} \tag{9.5}$$

is defined *semivariogram* or *intrinsic function*. The semivariogram, thanks to the intrinsic hypothesis, can be defined even when the covariance function does not exist, making it a more useful tool for analysing the spatial dependencies between points. The semivariogram allows to describe the degree of correlation between a sample and its neighbours, determining how fast this decreases and up to which distance the influence exists. Here follow some properties of the covariance and the semivariogram:

- They are both symmetric functions: $C(h) = C(-h)$ and $\gamma(h) = \gamma(-h)$
- The covariance satisfies the Schwarz inequality: $|C(h)| \leq C(0)$
- The semivariogram is non negative $\gamma(h) \geq 0$ and always $\gamma(0) = 0$
- The covariance function must be positive definite and a semivariogram function must be conditionally negative definite, this poses conditions on the linear combinations which can be used to describe a semivariogram, especially in the case of infinite a priori variance.
- If $Z(x)$ is second order stationary it must have a finite a priori variance equal to $C(0)$ and it also fulfils the intrinsic hypothesis, in this case it is true that $\gamma(h) = C(0) - C(h)$. Under this hypothesis it holds evidently that $|C(h)| \leq C(0)$ and $\gamma(h) \leq C(0)$: the semivariogram is then bounded, that is $\lim_{h\to\infty} \gamma(h) = C(0)$ is its limiting value $\gamma(\infty)$, often referred to as the *sill*. The *range* $a(\alpha)$ is the distance (lag) beyond which, in the direction α, $Z(x)$ and $Z(x+h)$ are no longer correlated (or have a negligible correlation). For $|h| > a(\alpha)$ $C(h) = 0$ and $\gamma(h) = \gamma(\infty) = C(0)$. A random function satisfying only the intrinsic hypothesis with an unbounded semivariogram does not have a finite range or sill.

- The structure of the spatial correlation is isotropic if it is equal in all directions, in this case the semivariogram and the covariance function (if it exists) depend only on r, the magnitude of the lag vector h, i.e. $\gamma(h) = \gamma(r)$. This is often the case for many applications, but for others, such as geology, the autocorrelation structure can change with direction and an anisotropic semivariogram model $\gamma(h)$ must be used. A common and simple model is the geometric anisotropy where the semivariogram reaches the same sill in all directions but at different ranges. In this case a simple linear transformation of the coordinates is sufficient to restore isotropy.
- The continuity and the regularity in space of the random function $Z(x)$ are expressed by the behaviour of $\gamma(h)$ near the origin:
  - Parabolic trend: $\gamma(h)$ is twice differentiable in $h = 0$. $Z(x)$ is itself differentiable (in the mean square) and has thus a high degree of regularity.
  - Linear behaviour: $\gamma(h)$ is continuous but not differentiable in $h = 0$. $Z(x)$ is continuous (in the mean square) but not differentiable and thus less regular.
  - Nugget effect: $\gamma(h)$ does not tend to 0 as h tends to 0, the value it tends to is known as *nugget*. $Z(x)$ is not continuous in the mean square, thus highly irregular.
  - Pure nugget effect: $\gamma(h)$ is a constant for $h > 0$. This is a limit case in which $Z(x)$ displays no correlation between any of its points (white noise).

  $Z(x)$ is continuous in the mean square if $E\left\{[Z(x+h)-Z(x)]^2\right\} \to 0$ when $|h| \to 0$. In a one-dimensional space $Z(x)$ has a derivative in the mean square sense $Z'(x)$ if $E\left\{\left[\frac{Z(x+h)-Z(x)}{h} - Z'(x)\right]^2\right\} \to 0$ when $|h| \to 0$ (similar definitions for n-dimensional spaces), this is satisfied if and only if $\gamma(h)$ is twice differentiable in $h = 0$.

The *empirical semivariogram* $\hat{\gamma}(h)$ is defined (Cressie, 1993) for observations $z(x_i)$ at locations x_i as:

$$\hat{\gamma}(h) = \frac{1}{2\,|N(h)|} \sum_{(i,h)\in N(h)} \left|z(x_i) - z(x_j)\right|^2 \tag{9.6}$$

where $N(h)$ denotes the set of pairs of observations such that $(x_j - x_i) = h$ and $|N(h)|$ is the number of observations in the set. Often h is implemented with a tolerance interval around its module r and around its direction α if anisotropy is assumed. Cressie (1993) asserts that for observations $z(x_i)$ of the random variables $Z(x_i)$ from the stationary random field $Z(x)$, the empirical semivariogram (with lag tolerance set to 0) is an unbiased estimator of the theoretical semivariogram, due to:

$$E\left[\hat{\gamma}(h)\right] = \frac{1}{2\,|N(h)|} \sum_{(i,h)\in N(h)} E\left[\left|Z(x_i) - Z(x_j)\right|^2\right] = \frac{1}{2\,|N(h)|} \sum_{(i,h)\in N(h)} 2\gamma(x_j - x_i) = \frac{2\,|N(h)|}{2\,|N(h)|}\gamma(h) \tag{9.7}$$

The empirical semivariogram is generally used to estimate a valid theoretical semivariogram which is needed for many geostatistical methods such as kriging interpolation.

The theoretical semivariogram is obtained by fitting a model function to the values of the empirical semivariogram. The most commonly used semivariogram models, for all of which holds that $\gamma(0) = 0$, are the following:

- Pure nugget effect:

$$\gamma(h) = n \tag{9.8}$$

- Spherical model:

$$\gamma(h) = \begin{cases} n + s\left[\frac{3}{2}\frac{h}{a} - \frac{1}{2}\left(\frac{h}{a}\right)^3\right] & 0 < h < a \\ n + s & h \geq a \end{cases} \tag{9.9}$$

- Exponential model:

$$\gamma(h) = n + s\left[1 - \exp(-3h/a)\right] \tag{9.10}$$

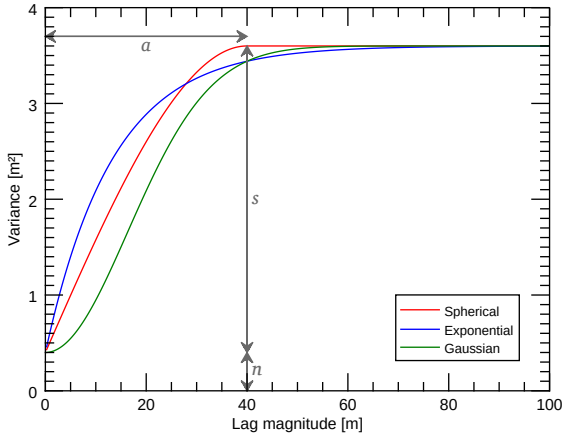

Figure 9.1 – Three commonly used semivariogram models and the three variables characterizing them: sill s, nugget n and range a.

- Gaussian model:

$$\gamma(h) = n + s\left[1 - \exp(-3h^2/a^2)\right] \tag{9.11}$$

- Power model (including linear model):

$$\gamma(h) = n + ph^{\omega} \tag{9.12}$$

  where p is a constant and $0 \leq \omega < 2$.

- De Wijs model:

$$\gamma(h) = n + 3\omega \ln(h) \tag{9.13}$$

In the above model functions the notation n indicates the nugget, s is the sill and a is the range, as defined before. Figure 9.1 shows these parameters and the first three models which are often used. Rolstad *et al.* (2009) explain very clearly the significance of such parameters: the nugget variance n was introduced in mining applications to represent small scale discontinuities introduced by solid "nuggets" of minerals. In other spatial applications such as the present study, it describes unresolved scales of variance, such as variance on scales smaller than the sampling interval, and it represents the spatially uncorrelated variance. The sill s is the maximum spatially correlated variance. The sum $n+s$ represents the total variance $C(0)$ of the random field. The term sill is sometimes used for refer to $s+n$, instead than just s. The range a is the distance within which some degree of spatial correlation exists between spatially separated points.

The pure nugget model represents a $Z(x)$ with no spatial correlation (purely random). The spherical model reaches its maximum $n+s$ at a range a. The exponential and Gaussian models approach their theoretical maximum $n+s$ only asymptotically. In this case a is defined as a "practical range", conventionally set as the distance where the semivariance reaches 95% of $n+s$. The power model and the De Wijs model describe an unbounded semivariogram, the corresponding random function $Z(x)$ does not satisfy the second order stationarity and has infinite a priori variance. The Gaussian model displays a parabolic behaviour near the origin, as seen before, this corresponds to a smoothly varying random function $Z(x)$. The spherical and exponential model are linear near the origin, meaning that $Z(x)$ exhibits a higher level of short range variability. In practice empirical semivariograms are often described by a combination of these models, a very common one is given by two spherical semivariograms one at shorter range and one at larger range (Clark, 1979; Rolstad *et al.*, 2009).

9.1.1.3 Uncertainty of the spatially averaged elevation difference

Once ε, the uncertainty of an individual, statistically independent sample (pixel or point) of elevation difference, is calculated, it becomes important to define the accuracy of a spatial average of the el-

evation difference, i.e. computed over a larger number of samples included in a certain area A (also known as "integrated uncertainty"). This area could be the total surface of a glacier or the icefield area included in a certain elevation range (elevation bin). This is often defined as the "standard error of the mean":

$$\mathrm{SE} = \frac{\varepsilon}{\sqrt{N}} \tag{9.14}$$

where N represents the number of uncorrelated samples involved in the spatial average carried out on area A. In the best case scenario all the samples involved will be uncorrelated, hence $N = n$, with n the actual number of samples. In reality there will always be a certain degree of spatial correlation which must be considered, making $N < n$ and worsening thus the uncertainty. Finally if all samples are correlated, then $N = 1$, implying that no improvement in accuracy is brought by the averaging process since no amount of new information is supplied by averaging different correlated samples. There can be several orders of magnitude of error difference between the cases of totally correlated and totally uncorrelated samples (Rolstad *et al.*, 2009). Few approaches in the literature assume the errors to be totally correlated, but generally a common agreement exists in considering the spatial correlation according to Equation (9.14). Geostatistics can be used to quantify N. In fact the range a of the semivariogram can be used as *correlation distance* d_{cor}, i.e. the distance from a sample beyond which spatial correlation becomes negligible. The correlation distance defines a *correlation area* A_{cor}, from which N is usually obtained in the literature as $N = \frac{A}{A_{\mathrm{cor}}}$. This approach is a valid approximation, but a theoretically sounder approach to obtaining the integrated uncertainty, strongly based on spatial statistics, is taken by Rolstad *et al.* (2009) and will be exposed later in this section.

A review of how the literature approached spatial correlation for the error budget of the geodetic mass balance will be now outlined. A common approach is computing the empirical semivariogram of the elevation difference on stable terrain to determine the correlation distance d_{cor} as the range a of the semivariogram. Details on this approach are usually quite scarce in the literature, just the final correlation distance is reported. One of the first semivariogram analysis of the DEM on glaciers was done by Etzelmüller (2000) but the results were not directly used for error estimation. Nuth *et al.* (2007) acknowledge the importance of the spatial correlation in the elevation differences and their impact on the error of spatial integration. They report a correlation distance of 500 m using elevation obtained from topographic maps (in turn obtained from an oblique aerial survey performed in 1936) and a DEM obtained from vertical aerial photographs in 1990. Koblet *et al.* (2010) use $d_{\mathrm{cor}} = 100$ m for a study based on 5 m resolution orthophotos, Kääb (2008) uses $d_{\mathrm{cor}} = 1$ km with an ASTER DEM and ICESat laser elevation points. Howat *et al.* (2008) compare ASTER and ICESat elevations and assume $d_{\mathrm{cor}} = 200$ m. Bolch *et al.* (2011) apply a correlation distance of 600 m using ASTER DEMs with an effective spatial resolution of 30 m. Willis *et al.* (2012b) report elevation change rates in the Northern Patagonian Icefield based on SRTM and a time series of ASTER DEMs. They find a correlation distance ranging between 630 m and 930 m and conservatively assume the latter, but they fail to convert the distance to a correlation area, obtaining this way a higher N which leads to a consistent underestimation of the error. Melkonian *et al.* (2012) do not seem to rely on the semivariogram, they plot instead the off-glacier elevation difference variance for patches of increasing size in the Cordillera Darwin Icefield finding a correlation area of 1.8 by 1.8 km.

Most of these publications define the correlation area as square, i.e. $A_{\mathrm{cor}} = d_{\mathrm{cor}}^2$ (sometimes A_{cor} is increased arbitrary as a conservative measure) and obtain the number of uncorrelated samples as $N = \frac{A}{A_{\mathrm{cor}}}$ before applying Equation (9.14). This approach is an approximation as it does not account for the shape of the semivariogram, instead only using its range. It would imply a semivariogram with a step function shape (totally correlated below d_{cor} totally uncorrelated above it), when instead the spatial correlation decreases gradually with distance. The approximation affects particularly the standard error of the mean computed over integration areas which are smaller or comparable to the correlation area (defined according to the theory as $A_{\mathrm{cor}} = \pi d_{\mathrm{cor}}^2$), but is accepted as if often leads to overestimation.

The theoretically correct integration of the spatial statistics for the estimation of the uncertainty of the spatially averaged ice elevation change is done by Rolstad *et al.* (2009). They compute the mass balance of the Svaritisen Ice Cap (Norway) from a DEM obtained from contour maps of August 1968

(in turn extracted from vertical aerial photography) and from two DEMs computed with digital photogrammetry using vertical aerial photography from August 1985 and August 2002. They also acquired airborne laser scanning data in August 2002 and used them to interpolate a DEM with a grid of 5 m, which was proved to be in perfect agreement with almost 5000 differential GPS points. They estimate the uncertainty of the individual pixel of elevation difference Δz as the standard deviation over bedrock $\sigma_{\Delta z}$. Their goal is to obtain the uncertainty of the spatial average of the elevation difference, which they relate to the spatial covariance with the following expression:

$$\sigma_A^2 = \mathrm{var}\{E[\Delta z(x)]\} = E\{\mathrm{cov}[\Delta z(x)]\} \tag{9.15}$$

They assume first and second order stationarity, which for the current application implies that the mean $\mu_{\Delta z}$ and the variance $\sigma^2_{\Delta z}$ of the elevation difference are constant in space, practically this requires no large-scale trends in the data and no significant changes of variance in space. The assumptions allow to define the semivariogram as: $\gamma(h) = C(0) - C(h)$ where $C(0) = \sigma^2_{\Delta z} = E\left[(\Delta z(x) - \mu)^2\right]$. The variance of the spatially averaged elevation difference is then:

$$\sigma_A^2 = E[C(h)] = E\left[\sigma^2_{\Delta z} - \gamma(h)\right] = \frac{1}{A}\int\int_A \left[\sigma^2_{\Delta z} - \gamma(h)\right] dx dy \tag{9.16}$$

which can be converted to polar coordinates assuming a circular area $A = \pi L^2$ of radius L, as:

$$\sigma_A^2 = \frac{2}{L^2}\int_0^L h\left[\sigma^2_{\Delta z} - \gamma(h)\right] dh \tag{9.17}$$

They compute the empirical semivariogram from the available off-glacier elevation difference points and fit to them an analytical semivariogram model. They fit the isotropic spherical model (Equation (9.9)), which is then used to solve the integral. In the current application the total variance of the elevation difference $\sigma^2_{\Delta z}$ can be expressed as the sum of the spatially uncorrelated variance (nugget) and the maximum spatially correlated variance (sill), i.e. $n + s = \sigma^2_{\Delta z}$. Solving the integral leads to the following expression of the variance of the spatially averaged elevation difference:

$$\sigma_A^2 = \begin{cases} n + s & L \leq \Delta h \\ n\left(\frac{\Delta h}{L}\right)^2 + s\left[1 - \frac{L}{a} + \frac{1}{5}\left(\frac{L}{a}\right)^3\right] & \Delta h < L < a \\ n\left(\frac{\Delta h}{L}\right)^2 + s\frac{1}{5}\left(\frac{L}{a}\right)^2 & L > a \end{cases} \tag{9.18}$$

where Δh is the sampling distance in polar coordinates. In order to apply this formula to the gridded data, Rolstad *et al.* (2009) impose the equivalence between the sampling grid area Δx^2 (pixel area) and the integrated area from 0 to Δh (i.e. $\pi \Delta h^2$), leading to $\Delta h = \frac{\Delta x}{\sqrt{\pi}}$. In the case of pure nugget effect equivalent to a field with no spatial correlation, Equation (9.18) leads to the expected $\sigma_A^2 = \frac{\sigma^2_{\Delta z}}{n}$. Intuitively, a larger range a leads to a higher uncertainty for a given averaging area, while an increased nugget fraction of the total variance $n + s = \sigma^2_{\Delta z}$ leads to decreasing uncertainty for a given area. The integration area is for many applications often larger than the correlation area ($L > a$), in this case given a spherical model with no nugget, the uncertainty simplifies to:

$$\sigma_A^2 = \sigma^2_{\Delta z}\frac{1}{5}\frac{A_{\mathrm{cor}}}{A} \tag{9.19}$$

where $A_{\mathrm{cor}} = \pi a^2$ is the area of a circle of radius equal to the range a of the semivariogram. Rolstad *et al.* (2009) remind that the assumption of stationarity, linked to a bounded semivariogram (such as the spherical model), should be verified on the real data. In fact a presence of a spatial trend would lead to a continuously increasing variance in the semivariogram, in which case they suggest to remove any large scale spatial trend as a preliminary step. They do this using a polynomial detrending function fitted to the bedrock areas using least square and applied to both bedrock and glacier.

Rolstad *et al.* (2009) applied the previously outlined theoretical formulation to the geodetic mass balances from the 1968 - '85 and the 1985 - 2002 elevation difference data. For both elevation differences, in order to capture different scales of spatial correlation, they extrapolated semivariograms

from bedrock with 25 m lag bin for scales up to 1 km and with 200 m bins for scales up to 20 km, and fitted individual spherical models using non linear optimization for all three parameters. They obtained ranges $a_1 = 430$ m and $a_2 = 3100$ m for the 1968 - '85 dataset and $a_1 = 260$ m and $a_2 = 17000$ m for the 1985 - 2002 dataset. They attributed the very large scale range to poor georeferencing of parts of the 2002 DEM caused by the lack of visible GCPs and the less pronounced (i.e. a smaller sill) intermediate 3 km range to a small residue of trend. They obtained σ_A^2 in closed form applying the method outlined in the previous paragraph, using a semivariogram model composed of the sum of two spherical models (with just one nugget parameter) applying the fitted semivariogram parameters a, s and n. They could hence plot the integrated uncertainty σ_A^2 as a function of integration area. Furthermore they used the difference between the August 2002 photogrammetric DEM and the highly accurate laser DEM in order to assess whether the spatial statistics (and $\sigma_{\Delta z}$) of the bedrock are also representative for glaciated areas (at least for optical DEMs). For this purpose they computed empirical semivariograms and fitted an individual spherical model for three types of surface (bedrock, flat blue ice, steep blue ice and snow) as the quality of the optical DEM is strongly varying among these categories of surface. They found that the bedrock has the largest $\sigma_{\Delta z}$ due to the higher slope and less accurate photogrammetric matching, it is followed by snow where the matching algorithm fails and strong interpolation is applied, while on blue ice higher standard deviations are found on steeper slopes. Correlation scales are also varying, bedrock displays a short range of 140 m, steep blue ice 260 m and snow and flat ice have larger ranges around 800 m, as flatter and more homogeneous regions are correlated over larger ranges (Rolstad *et al.*, 2009). However the bedrock and blue-ice have a larger nugget component relative to the sill indicating a significant amount of uncorrelated variance. These results highlight the strong dependency of the variance of the elevation difference and of the semivariogram on the slope, which demands attention when extending off-glacier elevation difference uncertainties to glacier elevation differences.

9.1.1.4 Ice density profile uncertainty

In order to convert the computed geodetic ice volume loss to ice mass loss the density profile of the lost ice must be known. This is rarely the case as this knowledge would require expensive field campaigns in remote and hardly accessible regions. It is then necessary to rely on assumptions or models for the vertical ice density profile. Huss (2013) analyses extensively this issue and introduces the problem with a simple mathematical formulation. The temporal change in mass is given by $\frac{\partial M}{\partial t} = \frac{\partial(\rho V)}{\partial t}$ which integrated in time gives $\Delta M = \Delta\rho V + \Delta V\rho$ where ρ is the bulk density of the glacier including its firn part and $\Delta\rho$ is the change in the average glacier density over the time interval considered. He writes the previous equation as $\Delta M = f_{\Delta V} \cdot \Delta V$ where the term $f_{\Delta V} = \frac{\Delta\rho V}{\Delta V} + \rho$ is the one to be modelled in time and space in order to have an accurate mass conversion, but unfortunately the exact quantification of $\Delta\rho$, ρ and V is impossible.

Most past and recent studies computing the geodetic mass balance rely on Sorge's law (Bader, 1954) which assumes that no changes in the vertical firn density profile have occur during the observation period, meaning $\Delta\rho = 0$ and $f_{\Delta V} = \rho$. In this scenario a single ρ is assumed as equal to the generic density of ice, i.e. $\rho = 900$ (or 917) kg m^{-3}. This approach is undertaken among others in Cox & March (2004); Paul & Haeberli (2008); Rignot *et al.* (2003); Berthier *et al.* (2010); Bolch *et al.* (2011); Nuth *et al.* (2010); Haug *et al.* (2009); Kääb (2008); Willis *et al.* (2012a); Melkonian *et al.* (2012). In some cases an uncertainty interval is assumed (although it is often arbitrarily defined). Huss (2013) is sceptical about this assumption and notes how a significant change in volume would cause a shift in the firn line over time thus contradicting Sorge's law. Gardner *et al.* (2012) use a constant density $\rho = 900 \pm 17$ kg m^{-3}, but recognize the partial invalidity of Sorge's law for the short-term observations due to proven changes in the firn density profile and thus assign an additional uncertainty of 4 kg m^{-3} a^{-1} to areas above the equilibrium line for studies spanning less than 20 years. Haug *et al.* (2009) estimate the uncertainty linked to the constant density assumption and due to both changes in the equilibrium line altitude and changes in the density of the firn. They compare results of the geodetic mass balance with those of the traditional glaciological mass balance, consisting of accumulation and ablation measurements with drilled stakes on representative points on the glacier, and snow

density profile observed with snow pits or snow cores.

Other authors assume variable densities according to the glacier zone, generally distinguishing accumulation and ablation area (Schiefer *et al.*, 2007; Moholdt *et al.*, 2010; Kääb *et al.*, 2012; Melkonian *et al.*, 2012; Shepherd *et al.*, 2012; Willis *et al.*, 2012b). A common practice is comparing the two assumptions: the assumption of $\rho = 900\ \mathrm{kg\,m^{-3}}$ for the entire glacier and the assumption of different densities according to the zone: $\rho = 900\ \mathrm{kg\,m^{-3}}$ for the ablation area and lower density (between 500 and 600 $\mathrm{kg\,m^{-3}}$) for the firn zone. The two scenarios are evaluated and sometimes averaged together (Kääb *et al.*, 2012). Moholdt *et al.* (2010) recognize that the assumption of Sorge's law has little impact on decadal mass balances but might not be applicable over short time spans, as the effects of firn pack changes could be significant. For the reported 5 year mass balance of Svalbard they apply three different conversion schemes to the elevation change curves: (1) applying Sorge's law by assuming constant firn density in time ($\rho_{\mathrm{ice}} = 900\ \mathrm{kg\,m^{-3}}$), (2) assuming that all thinning consists of ice while all thickening consists of firn ($\rho_{\mathrm{firn}} \sim 500\ \mathrm{kg\,m^{-3}}$), (3) assuming ρ_{ice} for the lowermost 1/3 of elevation bins, ρ_{firn} for the uppermost 1/3 and a linearly decreasing density from ρ_{ice} to ρ_{firn} for the middle 1/3 of elevation bins.

Bolch *et al.* (2013) emphasize that snow, firn and ice densities as well as firn compaction should be taken into account. They calculate the firn density based on an empirical relationship between snow density and mean firn temperature at 10 m depth (in turn estimated from the mean annual air temperature), obtaining for glaciers and ice caps in the Arctic values ranging between 530 and 800 $\mathrm{kg\,m^{-3}}$. They apply these values above the equilibrium line which they approximate as the median elevation of the glacier and assume a conservative total uncertainty of the firn density of 150 $\mathrm{kg\,m^{-3}}$. They furthermore model the firn compaction, which ranges between $-0.22 \pm 0.02\ \mathrm{m\,a^{-1}}$ in the warmer and wetter southeastern sector and $+0.09 \pm 0.01\ \mathrm{m\,a^{-1}}$ (expansion) in the colder and drier northern sector.

Another common approach is to compute an average density for the entire glacier surface based on ice and firn densities. This possibility was first explored by Sapiano *et al.* (1998), where an average density $\rho = 850 \pm 60\ \mathrm{kg\,m^{-3}}$ was assumed. Zemp *et al.* (2010) use an average between two scenarios: (1) $\rho = 917\ \mathrm{kg\,m^{-3}}$ for the entire glacier and (2) a spatial average of 800 $\mathrm{kg\,m^{-3}}$ obtained assuming $\rho = 700\ \mathrm{kg\,m^{-3}}$ for the firn area and $\rho = 917\ \mathrm{kg\,m^{-3}}$ for the accumulation area; for the studied Swedish glacier this leads to a value of $\rho = 860 \pm 60\ \mathrm{kg\,m^{-3}}$. Huss (2013) attempts to investigate the value and temporal robustness of the conversion factor $f_{\Delta V}$ by taking into account an empirical firn densification model coupled to idealized surface mass balance forcing applied to simplified synthetic glacier geometries. He applies the classical firn densification model by Herron & Langway Jr (1980) modified for temperate and polythermal firn of mountain glaciers which allows to calculate the density of the firn layer deposited at a specific moment in the past after a span of years. The average density of firn is averaged from values reported in a series of studies over different mountain glaciers in the world and equals 490 $\mathrm{kg\,m^{-3}}$. Densification due to refreezing of melt water is also accounted for using a generic end of winter firn temperature profile. Four experiments of idealized changes in surface mass balance (each with positive and negative shift in equilibrium line) are used to force the firn compaction model for the simplified non-calving glacier geometries and analysed over a span of 50 years. He finds that after a shift in ELA, $f_{\Delta V}$ converges to 900 $\mathrm{kg\,m^{-3}}$ after some decades. Hence, after the firn density profile is given sufficient time to adapt, the cumulative volume loss in the ablation area (with ice density $\rho = 900\ \mathrm{kg\,m^{-3}}$) tends to dominate over the changes in the firn area. According to his results, for periods shorter than 15 years $f_{\Delta V}$ could be lower (between 700 and 800 $\mathrm{kg\,m^{-3}}$). He computes an average $f_{\Delta V}$ for the six more relevant scenarios for time intervals ranging between 5 and 50 years and obtains $f_{\Delta V} = 850\ \mathrm{kg\,m^{-3}}$ to which he assigns an uncertainty of $\pm 60\ \mathrm{kg\,m^{-3}}$ and recommends this value for geodetic mass balances when a specific analysis of changes in firn volume and density is not performed. He warns however that this generic value might not be applicable for (i) periods shorter than 5 years, (ii) significant changes in the mass balance gradients, (iii) small overall volume changes or (iv) an insignificant firn area. He also varies the glacier geometry model and finds that the area elevation distribution has a small influence on $f_{\Delta V}$.

9.1.1.5 Extrapolation to unsurveyed areas

The DEMs used to compute the elevation difference over glaciated terrain might not always have a full coverage of the site of interest, especially for very large icefields. This might be due to the availability of suitable data or to voids within the DEM, typically caused by phase unwrapping errors in SAR interferometry and by the presence of clouds as well as lack of contrast in photogrammetry. Nevertheless it is usually important to obtain a mass balance for an entire glacier basin or an icefield. For this purpose it is common to extrapolate the mean elevation change rate of a specific elevation bin (i.e. range) to the uncovered regions of the same elevation bin, simply by multiplying its value by the total area of the bin. The issue when taking this course resides in the representativeness of the mean elevation difference for the uncovered regions. In the case of icefields composed of various glaciers, the extrapolation is more precise when done separately for each glacier basin, where the melting/thickening trend is generally consistent implying limited variability of mean elevation difference within each elevation bin. On the other hand the mean elevation change could be significantly less representative if the mean is computed over the entire icefield when the individual glaciers display different elevation change behaviour. The larger the glacier and the stronger its influence on the mean elevation change rate. This effect is more relevant at lower elevations where the behaviour of the glaciers tends to diverge according to several factors (size, slope, temperature, accumulation rates in the basin, precipitation, exposure, calving, basal and side friction etc.) and less relevant at higher altitudes as elevation changes are less marked and different basins tend to behave more similarly. In this respect an important role is also played by the percentage of uncovered area within each elevation bin and how well it is distributed among different glacier basins.

Arendt *et al.* (2002) compare laser altimetry tracks on the centreline of Alaskan glaciers with DEMs derived from old contour maps. They assume the obtained thickness change is valid over the entire elevation bin for each glacier. For each glacier an area averaged elevation change is obtained dividing the total volume change by the average of the old and the new glacier area. They cover this way only 20% of the total glacier surface of Alaska. To have an estimate for the whole Alaska, they extrapolate the elevation change of each Alaskan region to the unmeasured parts of the same region. Each region is composed by different glaciers and a single elevation change curve is obtained. This is then integrated separately over the area elevation distribution (hypsometry) of the covered and uncovered areas obtaining two volume curves which are added to give the total volume change. To quantify the uncertainty linked to the extrapolation procedure they consider three factors: (1) the total random error of the measured glaciers (quadrature sum of the random errors of each glacier), (2) the scatter of the measured elevation changes about their mean value for each elevation bin, which when propagated across the hypsometry of unmeasured glaciers gives an estimate of the error in the extrapolated volume change, (3) the difference between the total volume change calculated from an area weighted average elevation change and that calculated from an unweighed average. The three errors are assumed independent and combined (quadrature sum) and amount for the totality of Alaska to 7 $km^3\,a^{-1}$ for the mid-1950s - mid-1990s period (with 20% of unmeasured glaciated area) and 28 $km^3\,a^{-1}$ for the mid 1990s - 2001 period. Berthier *et al.* (2010) apply the same extrapolation procedure on the Alaskan glaciers but account for the uncertainty in a much simpler manner: by doubling the measurement error of the surveyed areas for the unsurveyed areas (27% of total glaciated surface). Similarly Rott *et al.* (2014b) account for the extrapolation error due to the representativeness of the mean elevation change rate (of each altitude bin) for the void areas of each bin by increasing the uncertainty of the mean elevation change rate by a 30% for the uncovered surface. Contrary to the previous studies, they extrapolate the elevation changes separately for each glacier basin within 50 m elevation bins, assuring a better representativeness.

9.1.1.6 Dealing with radar signal penetration in ice and snow

If one or more radar based elevation datasets are used, the issue of radar signal penetration in ice and snow should be considered, since the signal scattering phase centre might be located below the actual surface introducing an error in the elevation difference. Both theory and experimental observations concerning this issue have been outlined in Chapter 4. The penetration depth is difficult to estimate and

depends strongly on various parameters, among those system parameters such as the radar frequency and the incidence angle and physical parameters of the ice and snow layers, such as internal structure and density, crystal size, liquid water content, wetness of the surface, roughness of the surface, etc. The penetration depth magnitude is thus normally unknown and characterized by a strong spatial and temporal variability. Available DEM products, such as the SRTM or the future TanDEM-X WorldDEM, are provided as an edited mosaic of different acquisitions performed over time spans ranging from weeks to years and with different system parameters (orbit direction, look angle, polarization, height of ambiguity, etc.). Furthermore, amplitude products, which through calibration would allow to estimate the backscattering coefficient σ^0 and thus permit to make assumptions about state of the ice, firn and snow, are often not provided. There are few experimental studies which measured the actual microwave penetration in ice and snow. Given the dependence of this effect on many variables it is rarely possible to use generic values without a thorough analysis of the actual conditions of the firn and snow at the time of acquisition. It is hence hard to model this error source in the budget estimation of the geodetic mass balance. This section reports how this uncertainty has been treated in the literature. Geodetic mass balance studies based on interferometric DEMs often refer to Rignot *et al.* (2001) for estimates of penetration depth. Here the authors compare InSAR and laser altimetry finding a penetration depth of $d_p^C = 9 \pm 2$ m at C-band $d_p^L = 14 \pm 4$ m at L-band on the cold polar firn in Greenland, $d_p^C = 1 \pm 2$ m and $d_p^L = 3 \pm 3$ m on the exposed Jakobshavan Isbrae Glacier, and d_p^L reaching 60 to 120 m on the colder marginal ice of northeastern Greenland. On temperate Alaskan glaciers they report d_p^C varying from 0 ± 3 m to 4 ± 3 m and $d_p^L = 7 \pm 4$ m. It must be noted that InSAR and laser acquisitions are not simultaneous and a mean ice thinning rate from multitemporal laser altimetry was used to compare the data.

Dall *et al.* (2001) compared airborne laser altimeter measurements to a C-band airborne InSAR DEM acquired in summer on the Geikie Ice Cap in East Greenland. They report no height bias and σ^0 around -20 dB for areas below 1900 m covered by older wet snow and firn (soaked zone). From 1900 m to 2300 m the bias increases up to 13 m while σ^0 increases up to almost 0 dB. The elevation bias is due to an increasing penetration depth of the radar signal as liquid water content decreases and fresh dry snow covers the plateau (percolation zone). The very strong backscattering in the percolation zone is due to the domination of volume scattering and the abundance of subsurface ice lenses and pipes generated by melt and refreeze cycles in the percolation zone.

Dall (2007) formalizes how a specific penetration depth (defined in Eq. (4.30)) relates to the elevation bias Δh of an InSAR measurement in infinitely deep uniform volumes, such as ice and dry snow. The depth can be considered infinite if it is 2 to 5 times larger than the penetration depth and surface scattering from the top and bottom of the volume are negligible. The elevation bias is defined as the the difference between the measured InSAR elevation and the actual surface. Δh is approximately equal to the two way penetration depth $\frac{\cos\theta_t}{2\kappa_e}$ if the latter is much smaller than the height of ambiguity in the volume h^v_{amb}, defined in Dall (2007). On the other hand it tends to $h^v_{\text{amb}}/4$ a for penetration depths which are much larger than the height of ambiguity h^v_{amb}. He further relates the elevation bias directly to the interferometric coherence magnitude allowing its estimation:

$$\Delta h = -\frac{\left|h^v_{\text{amb}}\right|}{2\pi} \arctan\left(\sqrt{|\gamma|^{-2} - 1}\right) \tag{9.20}$$

The quality of the estimate will depend on the accuracy of the coherence estimate and will be affected by other decorrelation sources.

Similarly Weber Hoen & Zebker (2000) pioneered the glaciological exploitation of the interferometric decorrelation caused by volume scattering and modelled it in order to estimate the penetration depth of the radar signal. They apply their algorithm on the Greenland Ice Sheet using ERS C-band data. They find a one-way penetration depth of around 27 m in the dry snow zone and 23 m in the percolation zone, indicating a large degree of volume scattering despite the internal structure. They report minimal penetration in the coastal areas. Their estimates are associated to significant uncertainty mainly due to other sources of decorrelation but the method allows wide coverage penetration depth estimation.

Müller (2011) in his PhD thesis investigates the position of the ground penetrating radar phase

centre z_Φ in snow, firn and ice on the East Antarctic Plateau and on Svalbard and relates these results to SAR and InSAR observations. He reports z_Φ exceeding 40 m on dry firn in east Antarctica at 1.75 GHz (L-band), and z_Φ exceeding 5 m on coastal Antarctica and Svalbard at C-band. Davis *et al.* (1993) also analysed GPR tracks over the east Antarctic firn in order to estimate the penetration depth at X-band. They report minimal values of one-way penetration depth of 4.7 m on the inner plateau (73.3°S at 3420 m), characterized by extremely cold and dry conditions. They measure 2.1 m at 87.0°S at an elevation of 930 m where surface temperatures and recrystallization rates are higher leading to larger particles and stronger scattering. Surazakov & Aizen (2006) correct the on-glacier elevation difference by a constant 1 m to counteract the deeper scattering phase centre in the SRTM C-band DEM.

Gardelle *et al.* (2012) compare the SRTM 90 m C-band DEM and the 30 m X-band DEM over the Karakoram region, characterized by one of the most difficult topographies on earth with mountain peaks above 6000 m. They first find a bias due to different original resolution which depends on the terrain maximum curvature and correct for this effect both on and off glaciers (cf. Section 9.1.1.7). After this correction they report a bias between the two DEMs on snow and ice which they interpret as differential penetration between the two frequencies. For snow covered glacier the bias is 2 m and relatively constant while it increases up to 7 m between 5000 and 6000 m of elevation. They arbitrary assume that the X-band penetration is approximately zero and attribute the bias to the C-band penetration depth. This is not plausible, under similar snow conditions a certain degree of penetration is to be expected at both frequencies.

Larsen *et al.* (2007) compare the SRTM C-band DEM to laser altimetry points over glaciers in Alaska. They find a slight trend with elevation which they attribute to ice and snow seasonal changes and possible signal penetration. They correct the trend without discerning the two phenomena. Other studies (Schiefer *et al.*, 2007; Nuth & Kääb, 2011) acknowledge the possibility of some degree of penetration in C-band DEM, but due to the impossibility of its estimation they do not apply any correction and often do not include this source of uncertainty in the error budget. Kääb *et al.* (2012) use ICESat altimetry and SRTM C-band DEM in order to investigate glacier mass changes in the Hindu Kush - Karakoram - Himalaya region. They extrapolate the ICESat glacier elevation changes to the acquisition date of SRTM in order to investigate radar signal penetration in ice, firn and snow. After correcting the SRTM for suspected low frequency biases subtracting the median off-glacier offset with ICESat they find $d_p^C = 2.1 \pm 0.4$ m in average over the entire region, with significant differences among areas and type of glacier coverage: $d_p^C = 4.3 \pm 0.5$ m on firn and snow, $d_p^C = 1.2 \pm 0.6$ m on clean ice and $d_p^C = -0.6 \pm 0.9$ m on debris-covered ice.

Willis *et al.* (2012a) follow the method proposed by Gardelle *et al.* (2012) comparing SRTM C and X-band DEMs on the Southern Patagonian Icefield. After horizontal and vertical coregistration and removal of the curvature dependent bias they find that ice surfaces are 2 m higher in the X-band DEM compared to the C-band DEM at all elevations. They attribute this difference entirely to the C-band signal since the ice surface was wet during the late austral summer. They correct the detected 2 m constant offset on the glacier surface of the C-band DEM. The same estimation is used to correct SRTM ice and snow elevations over the Cordillera Darwin Icefield in (Melkonian *et al.*, 2012) and to revise the mass balance of the Northern Patagonian Icefield since signal penetration was not considered initially in (Willis *et al.*, 2012b). This conclusion is arguable. The condition of the snow and firn affecting signal penetration is strongly variable at higher elevations even days apart and between day and night time. An analysis of the actual backscattering signatures is required in order to draw any conclusions on the state of the snow and on possible signal penetration. Such an analysis for the same region (SPI and NPI) is presented in this work in Chapter 8. Furthermore, under similar conditions (the STRM C- and X-band were acquired simultaneously during a 10 days span) if snow was wet (which is more likely in summer) signal penetration should be negligible at both frequencies, a difference of 2 meters is hardly expectable even with a scarce liquid water content of 0.5% (cf. theory in Section 4.4).

Rott *et al.* (2014b) obtain mass changes of outlet glaciers in the northern Antarctic Peninsula by comparing four pairs of TanDEM-X DEMs of June/July 2011 and March/April 2013 (except for one scene acquired in July 2013). They include possible variations of the scattering phase centre in the vertical registration uncertainty as it is based on statistics from stable terrain covered by ice and snow. Since the comparison involves two InSAR datasets at the same frequency the error is given by the

difference of scattering phase positions between the two acquisitions and not by the penetration phenomenon itself. To reduce this difference they select both acquisitions during the same season and particularly during the cold season, when the conditions of the snow firn and ice are more stable. Nevertheless they estimate the position of the scattering phase centre z_Φ at X-band based on the backscattering coefficient σ^0. For wet snow, z_Φ this is located at the surface or a few centimetres below (Mätzler, 1987). For dry firn and snow it depends on the scattering efficiency and is half the one way penetration depth d_p^X. They invert the X-band, HH polarization TanDEM-X σ_0 using a semi-empirical radiative transfer model. They find a relatively high mean backscattering coefficient $\sigma^0 = -4.5$ dB in the percolation zone due to the large size of the scattering elements (refrozen firn) which leads to $d_p^X = 2$ m and $z_\Phi = 1$ m. For more typical backscattering of dry fine-grained winter snow they obtain $d_p^X = 12$ m.

9.1.1.7 Bias due to different resolution of the DEMs

Berthier *et al.* (2006) compare the SRTM C-band DEM with a SPOT5 optical DEM with 20 m resolution and with a DEM from aerial photographs of 1979, on the rough topography of the French Alps. By computing the mean difference off-glacier fitting a linear trend they report that SRTM displays an elevation dependent bias of about −7 m per 1000 m of elevation compared to both other DEMs, the bias is positive below 1700 m of altitude and negative above. They do not explain the bias but acknowledge the underestimation of elevation on sharp mountain tops and overestimation of narrow valley elevations reported by Rodriguez *et al.* (2005). In Berthier *et al.* (2007), they follow the same procedure with SRTM and SPOT5 DEMs in the Western Himalayas, finding a similar elevation dependent bias, which they attribute to SRTM and correct on the whole DEM, including the glaciated surfaces. Surazakov & Aizen (2006) compare SRTM and a DEM generated from topographic maps of 1977 over the Akshiirak glaciers (Tien Shan, central Asia) and report that systematic and random errors increase with slope on glacier-free areas. The systematic component of error ranges from 0.1 m in the 0° - 5° slope bin up to −7.6 m in the 40° - 78° slope bin, negative values indicating lower SRTM elevations. They correct the measured slope dependent systematic errors on the glacier surface. Larsen *et al.* (2007) do not find such trends comparing the SRTM DEM with laser altimeter data acquired in late August 2000 on the glacier surface in Alaska, characterized by gentler slopes and elevations up to 1600 m. A very weak linear trend with elevation is attributed to seasonal surface variability and possible radar signal penetration in ice and snow. Schiefer *et al.* (2007), comparing SRTM to a 25 m DEM based on aerial photography in British Columbia, report an elevation dependent bias in excess of −12 m per 1000 m of elevation starting at 1250 m, which they correct on the glacier elevation differences, they do not detect a similar bias with respect to varying slope and aspect. Paul (2008) analyses specifically the issue of the SRTM elevation dependent bias based on data and results published in another paper (Paul & Haeberli, 2008). They compute elevation changes in the Swiss Alps differencing the SRTM C-band DEM and a Swisstopo DEM from 1985 with a resolution of 25 m finding similar bias to that reported by Berthier *et al.* (2006). To investigate the effect of DEM spatial resolution on DEM elevations, Paul (2008) performed an experiment using only the high resolution Swisstopo DEM, averaging it to a 100 m posting and then resampling it bilinearly to a 25 m posting and finally subtracting the original 25 m DEM from its “coarser” version. The elevation difference is averaged per elevation bin, and an elevation dependent bias similar to the one found in SRTM is found off-glacier, a weaker bias is also found on glaciers but only above 3500 m. The bias is due to the increasing occurrence of steep ridges and mountain crests as the altitude increases, their height is smoothed in coarser DEMs leading to lower average elevation. On the other hand occurrence of steep gorges increases at lower altitudes and their elevation is overestimated at coarser resolution. Paul (2008) relates the amplitude of this effect to slope (first derivative of elevation), the bias of 2 m for slopes of 40° on-glacier is explained by the increase of steeper glaciated regions at higher elevations. He does not recommend any correction of the bias on-glacier, especially using the trend extracted off-glacier, as the smoother, gentler surface is not affected by the same magnitude of bias. In fact he shows in Paul & Haeberli (2008) that applying such a correction would lead to mass gains in the accumulation region which would not be explicable for the studied area and time period. Möller *et al.* (2007) assume that the bias found in the elevation

difference between SRTM and a 10 m DEM from aerial topography in Gran Campo Nevado (GCN), Patagonia, is inherent to the SRTM DEM, and hence corrected it following Berthier *et al.* (2006). The same authors in Möller & Schneider (2010) completely revise their mass balance by eliminating any elevation dependent correction, as they attribute the bias to different resolution and an estimation done over non-glacier terrain is not suitable for glacier terrain because of the different morphology. In fact the icefield of GCN is situated on a plateau characterized by gentler slopes at higher elevations and steeper slopes at lower elevations, the inverse situation compared to the surrounding off-glacier terrain. Gardelle *et al.* (2012) build on the findings of Paul (2008) to analyse possible elevation biases caused by different DEM resolution. They subtract from the original 90 m C-band SRTM DEM the same DEM oversampled to 40 m and then again undersampled to 90 m. It must be objected that oversampling a low resolution DEM does not "create" the spatial detail of a higher resolution DEM, and that the experiment should have been performed by worsening the resolution of the available 30 m X-band SRTM DEM or of the 40 m SPOT5 DEM. Nevertheless they report an elevation dependent bias similar to Paul (2008), but with higher values off-glacier. The bias is not evident at increasing of slope (only slightly on glaciers), instead they found a linear trend with maximum curvature with very similar behaviour both on and off-glacier. They find also good correlation with "planform curvature" but worse than with maximum curvature. They thus correct the bias on the SPOT5—SRTM elevation difference over Karakoram both on and off-glacier according to the maximum curvature (measured on the higher resolution DEM) using the trend obtained off-glacier where no changes are expected. Small corrections (up to 2 m) have been applied between 2000 m and 5000 m, while large biases up to 12 m have been corrected between 5000 and 6000 m of altitude.

In fact the bias caused by different DEM resolution on mountainous topography must be physically linked to curvature, the second derivative of elevation, which describes how fast the slope changes. The relation with elevation and its first derivative, the slope, is then indirect. This is due to typically increased mean curvature (in absolute value) and of slope at higher elevations in mountainous terrain. The phenomenon will be analysed empirically in Section 9.3.1.

9.1.1.8 Other sources of uncertainty

Other possible sources of error impacting the geodetic mass balance of glaciers are listed here in no particular order:

Subaqueous ice volume changes In order to have a precise mass balance the mass of ice lost below water should be considered for tidewater glaciers. In order to compute this contribution reliably the bathymetry at the glacier terminus must be known, otherwise only very coarse estimations can be performed. Ice is about 10% less dense than water ($\rho_{\text{ice}} = 900\,\text{kg}\,\text{m}^{-3}$) and thus has 10% more volume (Arendt *et al.*, 2006). For a retreating tidewater glacier the contribution to sea level rise of the portion below water is hence negative. The total sea level rise contribution of the glacier is overestimated by 10% of the volume lost underwater. This term, besides being difficult to estimate without bathymetric data, is generally small compared to the volume lost over the whole glacier basin and can generally be neglected. Berthier *et al.* (2010) admits the impossibility of a correct estimation of this term for the lack of bathymetric data but claims that this error is small for Alaskan glaciers. Arendt *et al.* (2006) estimate it for Columbia Glacier (Alaska), which is characterized by a very large calving terminus, where bathymetric data was available and reduce the total contribution to sea level rise of the glacier by 2.4%.

Seasonal elevation changes The ideal acquisition period of ice elevation data for the geodetic mass balance is theoretically the end of the ablation season when the yearly accumulation-ablation cycle comes to its end and the glacier surface is at its annual minimum. Comparing elevations measured in different seasons might lead to some systematic elevation change error due to the seasonal variation of surface elevation caused by the accumulation-ablation cycle. Berthier *et al.* (2010) estimate this uncertainty computing the absolute temporal departure of each DEM from the end of the ablation season (seasonal origin), assumed to be the 15 September in Alaska. They compute the area-weighted

average time departure over the whole glacier surface and multiply it by a recent mass balance annual amplitude (or turnover, see Eq. (3.13)) found in the literature (based on GRACE gravimetric data) obtaining an estimate of the systematic error on the total mass change of 17.2 Gt (0.19 m w.e. per unit of area when divided by the total area of the Alaskan glaciers). They then divide it by the mean time separation of 44 years between the two DEM sets to obtain a very low systematic error on the mass change rate (0.4 Gt a^{-1}). Howat *et al.* (2008) also consider this issue but find its effect small probably because the inter-annual dynamic thinning rates on the outlet glaciers of southeastern Greenland are large compared to seasonal variability. Arendt *et al.* (2006) and Echelmeyer *et al.* (1996) estimate ablation correction from the summer mass balance of a nearby glacier and use this estimate as an uncertainty due to seasonal changes. Cox & March (2004) estimate ablation adjustment on the Gulkana Glacier (Alaska) using a degree-day model based on summer precipitation and temperature obtained from a nearby weather station. They also estimate this term to be the major source of error of their study, equal to 0.2 m w.e. per unit of area, similarly to what Berthier *et al.* (2010) obtained. Haug *et al.* (2009) also perform ablation correction estimating the melt rate on a single glacier (Engabreen) and extend it on the mass balance of the whole of western Svartisen. Since the difference in positive degree-days is small, the error due to the extension is small. They finally assume an error of 0.3 m w.e.

Glacier bed erosion Elevation changes attributed to thinning might have a component due to this phenomenon. Berthier *et al.* (2010) neglect this contribution for the relatively short (from a geological point of view) observation period of 44 years. Kääb *et al.* (2012) do not quantify bed erosion but claim that it might "play a significant role in part of the Hindu Kush - Karakoram - Himalaya region" reaching the same order of magnitude of crustal uplift (see following paragraph) thus partially contrasting it.

Tectonics Glacial isostatic adjustment (GIA) to ice wastage since the end of the little ice age causes crustal uplift which leads to a systematic error in the ice elevation changes which magnitude increases with the observation period. Berthier *et al.* (2010) acknowledge this error but do not account for it as the uplift is not well documented for the whole Alaskan glaciers. Kääb *et al.* (2012) do not correct for this effect for the same reason and because it counteracts the effect of sub-glacial erosion (see above). Dietrich *et al.* (2010) report for the Patagonian icefields regionally variable crustal uplifts as high as 39 mm a^{-1}. Willis *et al.* (2012b) acknowledge this finding, but consider this amount negligible compared to the magnitude of ice elevation change and the associated uncertainties. Gardner *et al.* (2012) account for glacial isostatic adjustment by adding 6 mm a^{-1} to the uncorrelated uncertainty of elevation changes based solely on altimetry data, while for DEM based elevation changes, the isostatic adjustment is compensated during the vertical adjustment on ice-free terrain.

Errors due to vegetation Berthier *et al.* (2010) report that change in the canopy elevation over 40 - 50 years influences the vertical adjustment of their map based DEM to ICESat data, but lack data to quantify this effect. In case of InSAR based DEMs, the vertical adjustment would be likewise influenced by a different penetration rate of the radar signal into the canopy depending on the microwave frequency and on the seasonal differences in the canopy.

Accuracy of the glacier outline and changes in the glacier area Glacier outlines are often obtained by manual or semi-automatic methods based on orthophotos or satellite multispectral imagery. The presence of debris on top of ice might lead to underestimation while the presence of snow on bedrock at the margins of the glacier might lead to overestimation of the area (Haug *et al.*, 2009; Kääb *et al.*, 2012; Arendt *et al.*, 2006). Changes in glacier surface through time are accounted for by Gardner *et al.* (2012) by assigning a ±10% uncertainty interval on the volume change rate.

9.2 Mass balance derivation

The dataset used in this work to obtain the geodetic mass balance represents a particularly advantageous configuration compared to other elevation data over glaciers used in the literature (Section 9.1). Some of the main advantages of using SRTM and TanDEM-X DEMs are:

- The availability of two raster digital elevation models with (almost) full coverage of the icefields. No interpolation is needed as with methods based on punctual elevation measurements such as laser and lidar altimeters. The SRTM C-band DEM is a final edited product with filled gaps. The TanDEM-X mosaics present some gaps on regions of harsh topography which proved to be challenging for phase unwrapping (particularly for the single baseline PU method).

- Both DEMs are obtained by bistatic single-pass SAR interferometry. This is likely the most reliable technique for elevation retrieval with large coverage for ice and snow, taking advantage of the high precision provided by the phase of the radar signal. The single-pass configuration allows to overcome the main problems affecting InSAR on this type of terrain, like temporal decorrelation caused by changes on the ground and variations of the ionospheric screen. The main problem linked to radar elevations is the possible signal penetration in ice and snow. The reliance on the same technique for both datasets (with the main difference being the radar frequency) offers some advantages particularly for the error modelling. Compared to bistatic InSAR DEMs, optical DEMs based on matching suffer from gaps due to the lack of contrast on the snow cover or presence of clouds, and generally from lower accuracy. Even worst, the digitalising of cartographic maps, which is often used to obtain older elevations, is prone to significant systematic errors.

- The temporal span of each DEM used is relatively short, reducing temporal variations of surface height and other physical properties of the natural surfaces. The SRTM DEM is a mosaic of several acquisitions performed within a 9 days campaign in February 2000. The TanDEM-X mosaic of NPI is mostly acquired within 2 months. The SPI mosaic spans approximately one year. The observation epoch of 11 to 14 years is long enough to detect glaciological changes even on the plateau areas of SPI and NPI. The acquisition season is generally well suited, being close to the end of the hydrological cycle (end of summer) which is the correct time for the derivation of the mass balance and reduces risk of radar signal penetration in ice and snow. The austral summer acquisition criterion is satisfied by the SRTM DEM and the TanDEM-X mosaic of NPI, but could not be fulfilled for all scenes of the SPI TanDEM-X mosaic due to data unavailability at the time of processing.

The advantageous configuration of the data allowed to reduce the complexity of the geodetic mass balance derivation approach, which will be described in this section. Nevertheless efforts were done in order to compute a precise and complete error budget as reported in Section 9.3, defining an approach which can be adopted also for other datasets. The obtained mass balance results with their low uncertainty presented in Section 9.5 are a consequence of the DEMs in input and of the procedure used to obtain the elevation change maps, both described in Chapter 7.

The input data for the derivation of the geodetic mass balance of NPI and SPI consists of:

- the $\Delta h/\Delta t$ elevation change rate map obtained in Chapter 7. This is a mosaic of the $(\Delta h/\Delta t)_s = (h_{\mathrm{TDM}} - h_{\mathrm{SRTM}})/\Delta t_s$ image obtained for each TanDEM-X scene. Due to phase unwrapping errors, the coverage of the TanDEM-X DEM and consequently of the $\Delta h/\Delta t$ map presents some gaps. The most affected areas are the mountain ranges within the plateau at higher elevations. The resulting maps are shown in Section 7.4.

- A glacier binary mask indicating which samples belong to the icefield (described in Section 6.3). In order to include all possible glaciated surface the mask covers the maximum extent of glaciers during the observation period. In this study it is generally correspondent to the glacier extent in February 2000, except for a couple of glaciers on the western margin of SPI which have an advancing trend.

- A digital elevation model of the icefield. This is used to link elevation change rate and surface distribution to a fundamental parameter such as altitude. This allows to derive the surface variation with respect to elevation as well as reduce mass balance uncertainty linked to the unsurveyed areas. The SRTM DEM h_{SRTM} was chosen as reference surface for the derivation of the geodetic mass balance (cf. Section 3.5) because of its completeness on the icefields. The altitude refers hence to the surface status in year 2000 and might differ by tens of meters at the glacier termini compared to the TanDEM-X altitude.

The SRTM DEM is used to extract the *hypsometry*, or *area-elevation distribution* of the icefield. This is a common plot in glaciological studies and represents the area of the icefield (defined by the glacier mask) falling within a certain elevation bin (interval) A_b^{GL}, computed over the entire elevation range. It can be thought as a histogram of the icefield altitude. Different bin sizes have been used: from 20 m to a single bin covering the entire elevation range: 0 to 3600 m for SPI, 0 to 4000 m for NPI. The sum over the bins gives the entire icefield area: $A^{\mathrm{GL}} = \sum_{b=1}^{B} A_b^{\mathrm{GL}}$. The hypsometry of both icefields is shown in Section 9.5 (Figure 9.16a and 9.17a). Using the SRTM DEM is advantageous because, besides having full coverage, presents a smoother glacier surface than the TanDEM-X Raw DEM mosaic, leading to smoother bin spatial boundaries. Since all maps are in UTM projection, the area of each bin b is obtained as $A_b^{\mathrm{GL}} = n_b^{\mathrm{GL}} \cdot ps^2$, where n_b^{GL} is the number of samples included in b and ps is the pixel spacing in both easting and northing, equal to 10 m for the SPI raster and 12 m for the NPI raster.

The elevation change rate map is used to obtain a mean value $\mu_b^{\frac{\Delta h}{\Delta t}}$ for each elevation bin b. Only the valid $\Delta h/\Delta t$ samples are used, their number is denoted as n_b^{AV} and their area A_b^{AV}, where the superscript "AV" indicates samples used for the averaging operation. Because of the incomplete TanDEM-X coverage it holds that $A_b^{\mathrm{AV}} \leq A_b^{\mathrm{GL}}$. Each elevation bin includes $\Delta h/\Delta t$ samples from different TanDEM-X datatakes and scenes, which are averaged together. The $\mu_b^{\frac{\Delta h}{\Delta t}}$ distribution with respect to altitude are shown in Figure 9.16b and 9.17b, for NPI and SPI, respectively.

The mean ice volume change rate for each altitude bin b is obtained according to:

$$\mu_b^{\frac{\Delta V}{\Delta t}} = \mu_b^{\frac{\Delta h}{\Delta t}} \cdot A_b^{\mathrm{GL}} = \mu_b^{\frac{\Delta h}{\Delta t}} \cdot \left(A_b^{\mathrm{AV}} + A_b^{\mathrm{EX}}\right) \tag{9.21}$$

doing so the value of $\mu_b^{\frac{\Delta h}{\Delta t}}$, derived on A_b^{AV}, is extrapolated to the unsurveyed area of the bin $A_b^{\mathrm{EX}} = A_b^{\mathrm{GL}} - A_b^{\mathrm{AV}}$. This inevitably introduces an error which cannot be estimated precisely, particularly on lower altitudes, where the behaviour of different glaciers can vary significantly. Fortunately the percentage of unsurveyed area per bin is small and mostly located at higher elevations where surface is scarce. The area-elevation distribution with its surveyed (A_b^{GL} in blue) and unsurveyed (A_b^{EX} in red) components is shown in Figure 9.16a and 9.17a, for NPI and SPI, respectively. The obtained $\mu_b^{\frac{\Delta V}{\Delta t}}$ plots are shown in Figure 9.16c and 9.17c, for NPI and SPI respectively. The error linked to the extrapolation is discussed in Section 9.3.9. The total $A^{\mathrm{EX}} = \sum_{b=1}^{B} A_b^{\mathrm{EX}}$ amounts to 493.6 km^2 (12.8% of A^{GL}) and 917.7 km^2 (7.1% of A^{GL}) for NPI and SPI, respectively.

The volume change rate for the entire icefield is derived as:

$$\mu^{\frac{\Delta V}{\Delta t}} = \sum_{b=1}^{B} \mu_b^{\frac{\Delta V}{\Delta t}} \tag{9.22}$$

The mass change rate for each bin is obtained by assuming the validity of Sorge's Law (Bader, 1954), which implies stability of the vertical firn density profile between the acquisitions, according to the following equation:

$$\mu_b^{\frac{\Delta M}{\Delta t}} = \mu_b^{\frac{\Delta V}{\Delta t}} \cdot \rho \tag{9.23}$$

A single value of ice density equal to $\rho \pm \delta\rho = 900 \pm 17$ kg m^{-3} is used for all altitudes, without distinguishing accumulation and ablation areas. The $\mu_b^{\frac{\Delta M}{\Delta t}}$ plots for NPI and SPI are shown in Figure 9.16c and 9.17c, respectively. The mass change rate for the entire icefield is derived as:

$$\mu^{\frac{\Delta M}{\Delta t}} = \sum_{b=1}^{B} \mu_b^{\frac{\Delta M}{\Delta t}} \tag{9.24}$$

$\mu^{\frac{\Delta M}{\Delta t}}$ is the glacier-wide mass balance rate of the icefield, corresponding to $\dot{B}$ according to the traditional notation used in Section 3.5. It is reported either in $\left[\mathrm{Gt\,a^{-1}}\right]$ or in equivalent volume of water $\left[\mathrm{km^3\,w.e.\,a^{-1}}\right]$.

A very common way of reporting the mass balance is the average specific mass balance rate ($\overline{\dot{b}}$ in Eq. (3.15)), this is useful to compare the mass balance of different glaciers, independently of their area. This quantity is either expressed as ice equivalent or water equivalent. In the first case it corresponds to the average elevation change rate (hence the notation adopted here). It is obtained as:

$$\begin{aligned} \mu^{\frac{\Delta h}{\Delta t}} &= \frac{\mu^{\frac{\Delta M}{\Delta t}}}{A^{\mathrm{GL}}\rho_i} = \frac{\mu^{\frac{\Delta V}{\Delta t}}}{A^{\mathrm{GL}}} \quad \left[\mathrm{m\,a^{-1}}\right] \\ \mu^{\frac{\Delta h}{\Delta t}} &= \frac{\mu^{\frac{\Delta M}{\Delta t}}}{A^{\mathrm{GL}}\rho_w} = \frac{\mu^{\frac{\Delta V}{\Delta t}}}{A^{\mathrm{GL}}}\frac{\rho_i}{\rho_w} \quad \left[\mathrm{m\,w.e.\,a^{-1}}\right] \end{aligned} \tag{9.25}$$

The contribution to sea level rise (SLR) of the icefield is obtained by dividing the total mass change rate $\mu^{\frac{\Delta M}{\Delta t}}$ expressed in equivalent volume of water $\left[\mathrm{km^3\,w.e.\,a^{-1}}\right]$ by minus the global ocean area ($362\cdot10^6$ $\mathrm{km^2}$) and expressed in $\left[\mu\mathrm{m\,a^{-1}}\right]$. The values of $\mu^{\frac{\Delta V}{\Delta t}}$, $\mu^{\frac{\Delta M}{\Delta t}}$, $\mu^{\frac{\Delta h}{\Delta t}}$ and SLR obtained in this work for NPI and SPI are summarized in Table 9.7.

9.3 Mass balance uncertainty estimation

A general description of the main error sources and the various procedures and adaptations found in the literature has been presented in Section 9.1.1. This section details how the various error sources were modelled in this study in order to achieve a complete uncertainty estimation of the mass balance derived in Section 9.2. The defined framework can be generalized to other types of data in input. Different aspects affecting the accuracy are tackled in each subsection, finally coming to the combination of all error sources in Section 9.3.9. The numerical results are given in Section 9.3.10.

9.3.1 Influence of the different resolution of the DEMs

Many studies on geodetic mass balance have tackled the issue of a possible elevation dependent bias, finally attributed to the different resolution of the DEMs, and whether to correct it. In this work the experiment proposed by Paul (2008) is developed in order to assess the influence of the different DEM resolution on the data, particularly on the TanDEM-X DEM. As seen in Section 9.1.1.7 this bias is due to the different ability of a high and low resolution DEM in describing high frequency variations of topography. The lower resolution DEM will result in underestimation of the elevation of thin ridges and peaks and overestimation of the elevation of narrow gorges and valleys compared to the high resolution DEM. When differencing the two DEMs a bias arises. This should be likely correlated with the second derivative of the topography, the surface curvature, which indicates how fast the slope changes and describes the convexity or concavity of the terrain. Given a surface $z = z(x, y)$, the slope is defined as $\mathrm{SL} = \sqrt{p^2 + q^2}$ and expressed in degrees as $\mathrm{SLD} = \arctan\left(\sqrt{p^2 + q^2}\right)$, where $p = \frac{\partial z}{\partial x}$ and $q = \frac{\partial z}{\partial y}$. The aspect $\mathrm{AS} = \arctan(q/p)$ indicates the direction of the slope on the XY plane. Different curvature definitions can be made according to which plane is intersected to the surface, the most common are (Shary *et al.*, 2002; Shary, 1995; Romstad & Etzelmüller, 2012):

- profile (or vertical) curvature: describes the rate of change of slope along the flow line, with negative values indicating upward convexity. It relates to acceleration or deceleration of flow on the surface.
- planform curvature: describes the rate of change of aspect, with positive values indicating sidewards concavity. It relates to the convergence or divergence of flow on the surface.
- horizontal curvature: the curvature in an inclined plane perpendicular to the direction of flow and to the surface.

- minimum curvature: the minimum curvature value for any normal section at a given point on a surface. Negative values indicate concavities.
- maximum curvature: the maximum curvature value for any normal section at a given point on a surface. Negative values indicate concavities.
- mean curvature: the average curvature of any two mutually perpendicular normal sections at a given point on a surface, it can be hence obtained as the average of vertical and horizontal curvature or minimum and maximum curvature (Shary, 1995). It can be computed as as $\mathrm{MC} = -\left[\left(1+q^2\right)r - 2pqs + (1+p^2)t\right] / \left[2\left(1+p^2+q^2\right)^{3/2}\right]$ where $r = \frac{\partial^2 z}{\partial x^2}$, $s = \frac{\partial^2 z}{\partial x \partial y}$ and $t = \frac{\partial^2 z}{\partial y^2}$ (Shary *et al.*, 2002). Negative values indicate concavities.

In the present work the mean curvature was chosen to describe the terrain convexity and concavity and to explore their relationship with the elevation differences between two DEMs with different resolution. This parameter has been often used in geomorphology studies.

An experiment was performed in order to quantify the effects of the different resolution between the 90 m STRM C-band DEM and the 10/12 m TanDEM-X DEM mosaic on the elevation change values obtained as $h_{\mathrm{TDM}} - h_{\mathrm{SRTM}}$. For this experiment a large crop (rectangular tile) was extracted from the TanDEM-X DEM mosaic in the south of SPI. The DEM has a posting of 10 m in easting and northing. The selected area is well representative of the topographical characteristics of both NPI and SPI. It comprises $16.77 \cdot 10^6$ valid pixels off-glacier and $15.33 \cdot 10^6$ valid pixels on-glacier, covering the whole width of SPI from 50°44'S to 51°23'S, including a large section of the plateau and wide glaciers such as Balmaceda, Tyndall, HPS38 and Grey. Elevation data originate from TanDEM-X scenes: S11, S12, S13, S14, S15, S18, S19 (Table 7.5). The slope, the minimum and maximum curvature images were extracted from this DEM. The mean curvature image was obtained as the average of minimum and maximum curvature images. The DEM was then block averaged by a factor of 8 to simulate a low resolution DEM. This was then oversampled bilinearly to a 10 m posting and subtracted from the original high resolution DEM obtaining the difference image $\Delta h = h_{\mathrm{HR}} - h_{\mathrm{LR}}$.

To perform a statistical analysis the pixels were classified as off-glacier when having a valid value not belonging neither to the glacier mask nor to the water mask. The glacier mask applied is the same used for the mass balance, which corresponds to the glacier extent of year 2000 but with frontal positions adapted to the TanDEM-X acquisition (cf. Section 6.3). Because of the general glacier melting it has a slightly larger extent on the glacier sides with respect to the glaciated surface of year 2011. Some bare rock pixels will tickle into the on-glacier statistics especially at lower elevations where the glacier retreat is more pronounced. The same effect is also caused by the inaccuracies of the glacier mask in defining rocky outcrops on the plateau, when they are covered by snow in the multispectral image. Nevertheless, given the large glacier surface analysed, the errors of the glacier mask should not affect the statistics.

The visual analysis of the difference image shows that higher absolute values, with a positive and negative pattern are present on the mountainous terrain surrounding the glaciers (for instance on the terminus of Grey Glacier in Figure 9.2). On flat off-glacier terrain the difference is approximately null. On the glacier ice the difference is also null but patterns due to crevasses and other surface features are visible where present. Some higher elevation differences are found on the mountainous parts of the plateau included in the glacier mask.

The difference $\Delta h = h_{\mathrm{HR}} - h_{\mathrm{LR}}$ has an off-glacier mean of 0.13 m and a standard deviation of 5.9 m, the on-glacier mean is −0.2 m and the standard deviation is 3.6 m. Mean values of the DEM difference $\Delta h = h_{\mathrm{HR}} - h_{\mathrm{LR}}$ were extracted with respect to elevation (using 20 m bins), slope (1° bins) and mean curvature (0.1 m^{-1} bins) to understand the relation between the bias and this properties of topography. Mean values obtained using less than 7000 samples were discarded since considered statistically unreliable for the elevation ans slope plots. A threshold of 1000 samples was used in the case of mean curvature, since the mean Δh appeared to be more robust against this parameter.

Figure 9.3a shows Δh with respect to elevation (and the histogram of elevation). The elevation histogram shows that, on-glacier, altitudes with significant area (>0.25% of total area) range from around 40 to 2100 m. In this interval the on-glacier Δh displays some peaks up to −1 m below 300

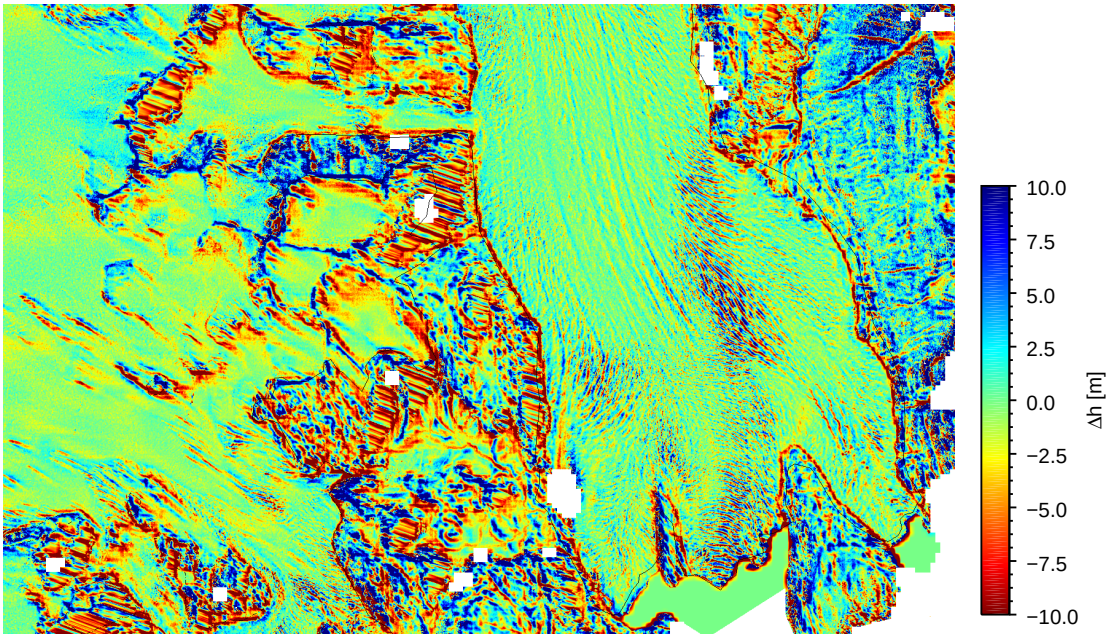

Figure 9.2 – Detail of the $\Delta h = h_{\mathrm{HR}} - h_{\mathrm{LR}}$ difference image over the terminus of Grey Glacier (SPI; 50°58'S, 73°14'W). Elevation differences due to the inability to follow fast changes in topography in the low resolution DEM are strong on the mountainous terrain surrounding the glaciers but are also present in correspondence of the ice features (crevasses, etc.) on the glacier surface. The black line indicates the glacier outline, invalid values are shown in white.

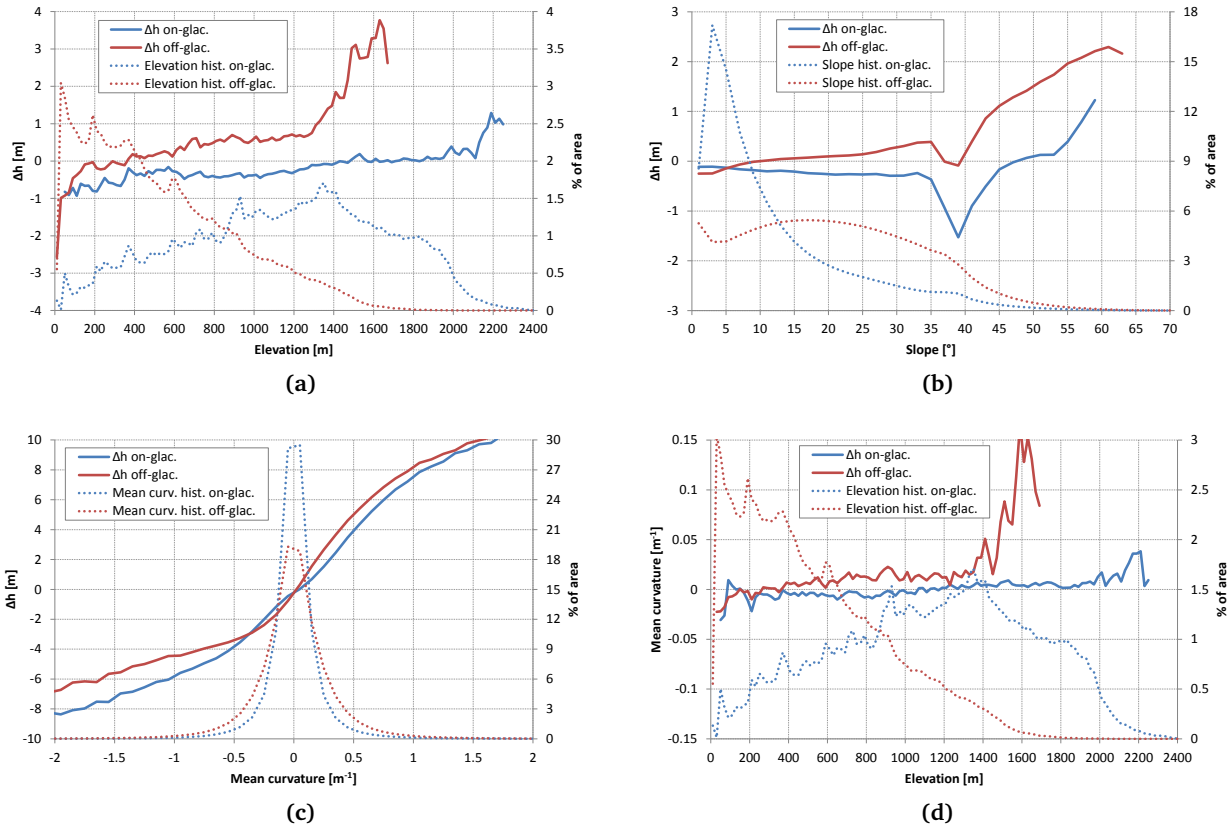

Figure 9.3 – Analysis of the DEM difference due to different resolution, $\Delta h = h_{\mathrm{HR}} - h_{\mathrm{LR}}$. Average Δh on and off-glacier at varying elevation (a), slope (b) and mean curvature (c), the histograms of these parameters are included. (d) Mean curvature at varying elevation on and off-glacier and elevation histogram. The plots above were obtained for the southern sector of SPI, between 50°44'S to 51°23'S.

m, it then oscillates around 0.4 m up to 1200 m before stabilizing at 0, for higher elevations found on the ice-covered mountain ranges Δh increases. Off-glacier an elevation dependent trend is more evident. Excluding the fist bin, Δh increases steadily from -1 m to 1 m at 1300 m, after which Δh climbs rapidly.

Figure 9.3b shows Δh with respect to slope (and the histogram of slope), it displays a light decrease on-glacier and a light increase off-glacier up to 35°. Afterwards a drop and a fast increase is present both on and off-glacier. For slopes up to 40° the average Δh is -0.2 m on-glacier and 0.08 m off-glacier.

Figure 9.3c shows Δh with respect to mean curvature (and the histogram of the mean curvature). The plot displays a strong, nearly linear, dependence of Δh with curvature, both on and off-glacier. In the low resolution DEM elevations are overestimated for concavities (MC < 0) and underestimated for convexities (MC > 0). The distribution of curvature is symmetrical with a high peak around 0.

To understand the impact of the curvature dependent bias at varying elevations the average mean curvature was plotted for 20 m elevations bins in Figure 9.3d. The glaciers are in average slightly concave up to 1200 m, and slightly convex above (up to 2100 m where significant area is present), explaining the behaviour of Δh with respect to elevation observed in Figure 9.3a. On ice-free areas, mean curvature is in average negative at low altitudes below 350 m. Above this threshold mean curvature displays a lightly increasing trend up to 1400 m. At higher altitudes increasing values are obtained as expected but fewer samples were used making the average less reliable. This behaviour is again reflected in the trend of Δh with elevation, and is explainable by the higher frequency of valleys and gorges at low elevations and the higher occurrence of peaks and ridges at higher altitudes. The Δh trend at varying slope does not allows to assume a direct dependence of the bias with slope, but rather an indirect one based on the distribution of curvature at varying slope (plot not shown here), similarly to elevation.

The on-glacier elevation difference due to different resolution of the DEMs obtained in this experiment has a mean of -0.2 m, ranges between -0.5 m and -0.8 m up to 1200 m and is approximately null above this altitude (Figure 9.3a). These values are small compared to the elevation changes due to ice loss or gain measured at the corresponding altitudes (see maps in Section 7.4 and elevation change rate plots in Section 9.5). For this reason no correction is applied. The same choice was done by different authors as outlined in Section 9.1.1.7. An error term for this effects was also not included in the error budget because of the uncertain modelling and the strong dependence on the surface characteristics.

9.3.2 Estimation of the uncertainty of the elevation difference sample

As introduced in Section 9.1.1.1 the estimation of the uncertainty of each elevation difference sample is based on the elevation difference Δz of ice-free pixels, where no physical changes are expected. Ideally, its mean $\mu^{\Delta z}$ is zero as the two DEMs have been coregistered vertically and horizontally. The standard deviation $\sigma^{\Delta z}$ describes the spread of the elevation difference Δz around the mean and can be used as estimate of the uncertainty of the off-glacier elevation difference sample. This uncertainty, under specific conditions, is extended to the glacier elevation difference samples ε, i.e. $\varepsilon = \sigma^{\Delta z}$, which contributes to the mass balance error budget. Following the notation introduced in Section 9.1.1.1, Δz indicates the elevation difference off-glacier (and off-water) and Δh the elevation difference on-glacier. Both are obtained from the same $\Delta h = h_{\mathrm{TDM}} - h_{\mathrm{SRTM}}$ elevation difference raster. The issues encountered in the present dataset are here exposed along with the proposed solutions and the obtained results. Instead of considering all off-glacier pixels indiscriminately, it was decided to compute the mean $\mu_d^{\Delta z}$ and the standard deviation $\sigma_d^{\Delta z}$ for each datatake d separately. This is because different datatakes are characterized by different acquisition parameters, among others: (1) height of ambiguity, with larger values leading to higher interferometric noise, (2) multilooking factor, which might vary between different scenes, with higher number of looks leading to decreased interferometric noise, (3) incidence angle, affecting the backscattering and the slope above which layover occurs in the line of sight, leading to erroneous elevations. But more importantly, the absolute elevation of each datatake has been calibrated separately, by estimating, and correcting, the elevation offset with respect to the SRTM DEM over flat ice-free terrain (cf. Section 7.2). The determination of the elevation

offset is subject to errors, hence some residual misregistration (along the line of sight direction) might still affect the DEMs, this translates into an elevation error which is strongly dependent on slope and aspect, as quantified in Equation (7.1). It is therefore likely that the off-glacier elevation difference statistics differ between datatakes. Since the distribution of glacier area among the various datatakes is not reflected by the distribution of bare terrain, a single estimation using all datatakes indiscriminately might be biased by a datatake with larger off-glacier surface. The statistics obtained for a specific datatake are considered valid for all its scenes, i.e. $\mu_s^{\Delta z} = \mu_d^{\Delta z}$ and $\sigma_s^{\Delta z} = \sigma_d^{\Delta z}$ $\forall s \in d$.

For the selection of the glacier pixels a glacier mask corresponding to the maximum extent of ice between the two acquisition epochs was used. In the present study this requisite is already fulfilled by the SRTM glacier mask (described in Section 6.3) except for the advancing Pio XI Glacier (and neighbouring glaciers), to which the mask was adapted. The off-glacier pixels are selected outside the glacier and water mask where valid elevation difference data is available, meaning that both SRTM and TanDEM-X have coverage and the TanDEM-X samples were not discarded because of phase unwrapping errors (see Section 7.1). Furthermore, to avoid extreme elevation difference outliers, such as residual unmasked phase unwrapping errors, a relaxed range of $[-45; 45]$ m was used to select Δz points.

The current procedure allows to obtain an estimate of the actual elevation difference uncertainty when no other elevation dataset of much higher accuracy (such as a lidar DEM) is available. It offers the advantage of providing an empirical measure based on the actual data used for the geodetic mass balance. This is an objective uncertainty estimate compared to the use of a generic value of accuracy for the two DEMs (cf. Section 9.1.1.1).

A possible issue consists in the fact that the elevation error can be affected by the different surface characteristics off and on-glacier. For instance the interferometric coherence for the snow and firn on the plateau might be lower than the one of bare rock, leading to higher interferometric error. This aspect is tackled in Section 9.3.3. It is concluded that no significant difference in interferometric elevation error is present between the two surface types, meaning that the standard deviation $\sigma_d^{\Delta z}$ estimated off-glacier is representative for the on-glacier samples Δh.

Another aspect has been tackled in Section 9.3.1, the difference in resolution of the TanDEM-X and SRTM DEMs causes spurious elevation differences, which depend on the surface curvature (Figure 9.3c). The experiment, performed on a representative sector of SPI, highlighted that the bias is smaller (slightly negative up to 1200 m) on-glacier particularly above 1300 m (Figure 9.3a). For all elevations and for slopes below 40°, the average of $\Delta h = h_{\mathrm{HR}} - h_{\mathrm{LR}}$ is -0.2 m on-glacier and 0.07 m off-glacier, its standard deviation is equal to 3.5 m on-glacier and 5.7 m off-glacier. Given the small impact of this effect on-glacier no correction will be performed. The effects of the different resolution might lead to a light overestimation of the uncertainty of the on-glacier elevation change sample. This is accepted as it tends towards a more conservative error budget.

An important issue concerning the representativeness of the off-ice standard deviation for the glacier surface is the slope dependence of the elevation errors. The nominal accuracy of the DEMs is worse on steeper terrain. Furthermore residual horizontal miseregistration cause elevation errors which are strongly slope dependent according to Equation (7.1) (cf. Section 7.2). Furthermore, layover and shadow are strictly linked to slope. The difference in slope distribution, with gentler surfaces on glaciers and steeper surfaces on the surrounding mountainous terrain will likely lead to an overestimation of the on-glacier uncertainty. In order to investigate this issue, the slope image was obtained from the oversampled SRTM DEM by computing the maximum slope using a 5×5 pixel window (equal to 50×50 m for SPI and 60×60 m for NPI). Furthermore the aspect image was extracted with the same window size. The SRTM DEM was chosen because of the lack of gaps and because it provided a much smoother result given its lower resolution and being a final edited mosaic of many acquisitions. Small-scale slopes are not of interest for this purpose.

The effects of slope over the elevation difference were analysed through scatterplots of the off-ice absolute elevation difference $|\Delta z|$ at varying slope, for both SPI and NPI (Figure 9.4a and 9.4b). The scatterplots have been smoothed with a sliding window of size 200 to highlight the trend. All available off-glacier points were considered at the same time with no datatake distinction. No slope threshold was applied. Around $96.8 \cdot 10^6$ points were extracted on SPI and $36.5 \cdot 10^6$ points on NPI. Both plots highlight the dependence on slope of the $|\Delta z|$, with a trend increasing mostly linearly from around

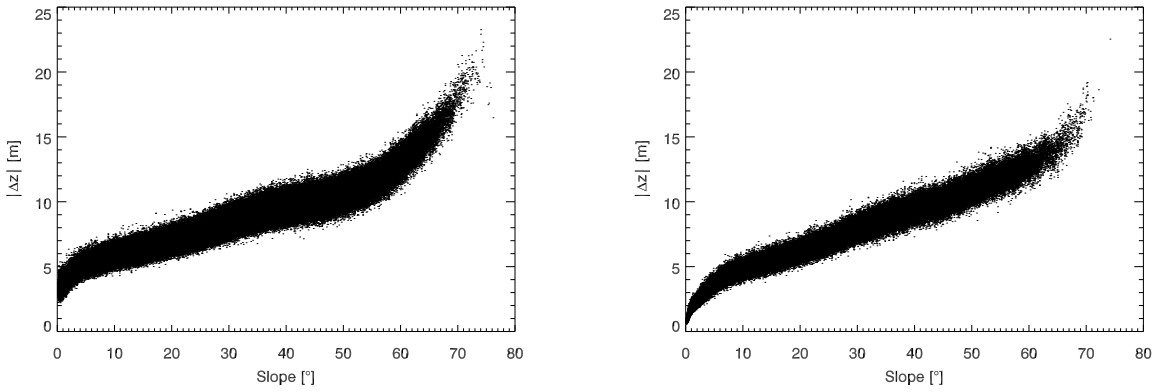

(a) SPI **(b)** NPI

Figure 9.4 – Scatterplot of the off-glacier elevation difference $|\Delta z|$ versus terrain slope for SPI (a) and NPI (b). The scatterplot has been smoothed with a 200 points wide sliding window to highlight the trend, which displays a consistent increase with slope.

5 m at 10° up to around 12 m at 60° of slope (slightly higher for SPI). The increase of $|\Delta z|$ is more pronounced at slopes greater than 60°, especially for SPI. The behaviour at gentler slopes displays some differences between the two icefields and their respective datasets. As detailed in Section 7.2 the vertical and horizontal registration could be performed with a better accuracy in NPI thanks to the presence of some large nearly flat ice-free areas, this drives the scatterplot down, particularly between 0° and 10° compared to SPI. The scatterplots highlight the strong dependence of $|\Delta z|$ on slope and hence the importance of this parameter when extending the off-glacier statistics as uncertainty of the glacier surface.

The histograms of the on-glacier and off-glacier slope are compared in Figure 9.5a and 9.5c, respectively for SPI and NPI. The distribution of slope on-glacier is relatively similar for both icefields: it displays a strong peak at low slopes as expected on the vast relatively flat glacier and plateau surface. Mountain ranges cross the plateau both in SPI and NPI explaining the occurrence of higher slopes. The cumulative distributions (Figures 9.5b and 9.5d) show how 80% of the glacier surface has a slope of less than 23° on SPI and less than 15° on NPI. The off-glacier distributions of slope below 10° displays for NPI a peak of flat terrain due to the large plains located in the north-west and south-east of the icefield, which have been included in the TanDEM-X scenes for calibration purposes. This feature is not present in the SPI which is surrounded by rough topography constituted by mountains, fjords and lakes. After 10° the distribution is similar: for the SPI it slowly increases and decreases with a maximum around 30°, for the NPI it has a more uniform behaviour decreasing at 60°. The comparison between off and on-glacier slope histograms highlights a very different distribution (particularly marked for SPI) as expected: strongly skewed towards lower slopes on-glacier and more spread between 5° and 55° off-glacier. Considering the increasing trend of $|\Delta z|$ with slope shown previously, it is evident how the statistics of Δz are strongly influenced by the difference in slope distribution. The mean $\mu^{\Delta z}$ computed off-glacier cannot be assigned to the glacier elevation differences and interpreted as a systematic error. Nevertheless a small value of $|\mu^{\Delta z}|$ (at least compared to the values of $|\Delta z|$ found in Figure 9.4) would be an indicator of a successful vertical coregistration. The off-glacier standard deviation $\sigma^{\Delta z}$ will display higher values as it would on-glacier because of the different slope distribution (peak at low values vs. spread over a large range of slopes). This leads to an overestimation of the uncertainty of the glacier elevation difference sample. In order to mitigate the effect of the different slope distribution and the consequent error overestimation, an upper bound on slope is imposed when computing the off-glacier statistics. The idea is to limit the samples to slope values which are more typical of the icefields in order to obtain a more reliable estimate of uncertainty, nevertheless the difference in slope distribution up to the threshold still plays a role in overestimating the uncertainty. The overestimation is nevertheless accepted as it tends towards a more conservative error budget.

The next step consists in choosing an appropriate value for the slope upper bound. In order to

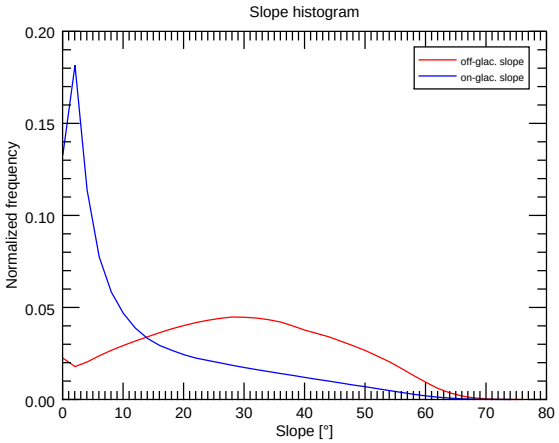

(a) SPI

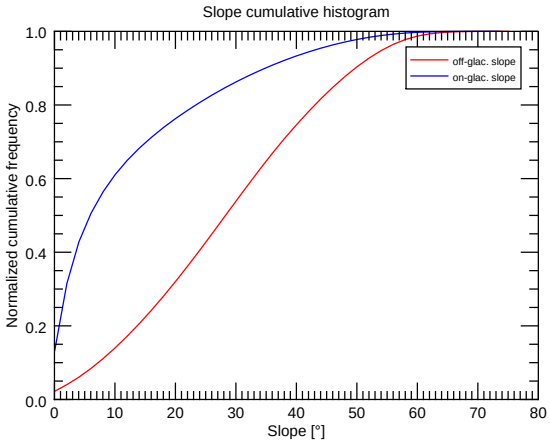

(b) SPI

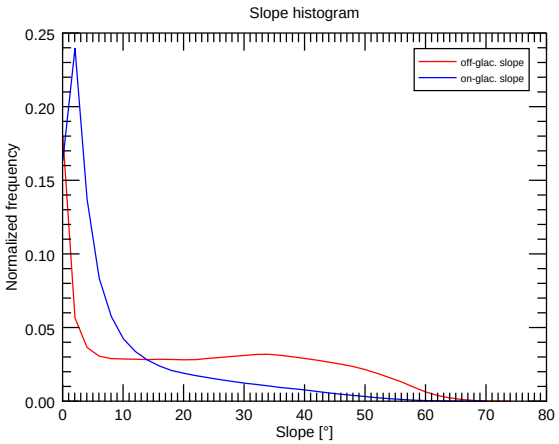

(c) NPI

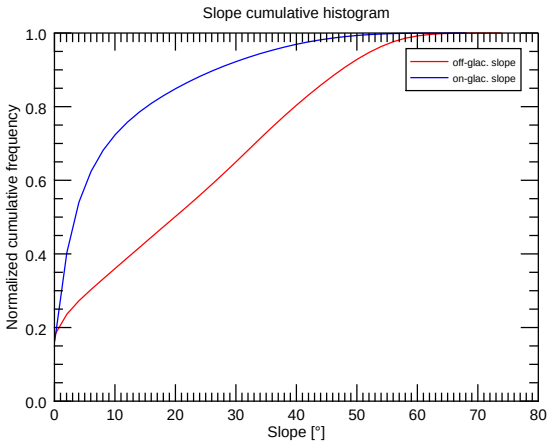

(d) NPI

Figure 9.5 – Histograms of slope off-glacier and on-glacier for SPI (a) and NPI (c). Cumulative histograms of slope off-glacier and on-glacier for SPI (b) and NPI (d).

understand the effect of the thresholding on the statistics off-glacier, the values of $\mu^{\Delta z}$ and $\sigma^{\Delta z}$ at varying slope threshold are shown in Figure 9.6. They are computed off-glacier without any datatake discrimination. Analysing the plot from right to left, i.e. increasing the strictness of the slope threshold, it can be noticed that $\sigma^{\Delta z}$ remains practically unchanged up to 60° since no significant amount of samples is present at higher slopes. $\sigma^{\Delta z}$ starts to decrease at 60° almost linearly with decreasing slope threshold, with a faster trend for NPI. As expected $\sigma^{\Delta z}$ is higher on SPI, ranging between 7 and 11.2 m, while for NPI it ranges between 2.8 m and 9.5 m. The steady decrease of $\sigma^{\Delta z}$ confirms the previous analysis. The histogram of Δz (not shown, but similar to those in Figure 9.7) has a Gaussian-like unimodal shape, the "peak" is more pronounced compared to the normal distribution, especially for NPI. Imposing a stricter threshold on the slope reduces the shoulders of the distribution and increases its "peakedness" (which is quantified by the excess kurtosis), hence lowering the standard deviation.

The behaviour of $\mu^{\Delta z}$ is more difficult to predict and not strictly relevant, it is very specific to the off-glacier topography and cannot be directly extrapolated to the glacier topography. Nevertheless it can be very useful as an assessment of the quality of the vertical coregistration between the two DEMs. The following point can be observed: (1) $|\mu^{\Delta z}|$ despite the variability with slope does never exceed 1.1 m at varying slope thresholds, a value which can be considered small when compared to the scatterplots of $|\Delta z|$ and the nominal accuracies of the DEMs, as well as the values of $\sigma^{\Delta z}$. (2) The trend of $\mu^{\Delta z}$ for flat terrain only (slope threshold of 1°) reaches a value of 0.2 m for SPI and −0.3 m

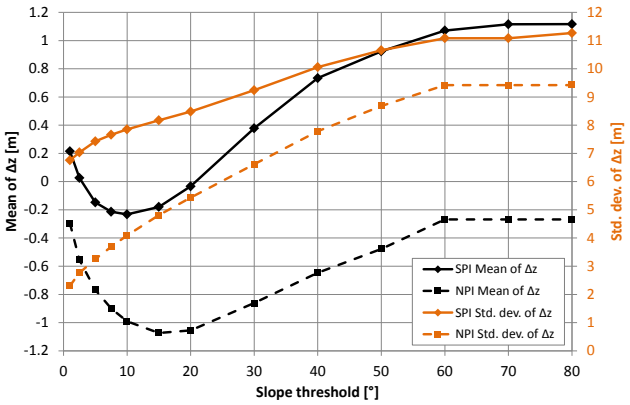

Figure 9.6 – Off-glacier mean $\mu^{\Delta z}$ and standard deviation $\sigma^{\Delta z}$ values for SPI and NPI at varying slope upper bound. The statistics are computed on the valid off-glacier pixels for all datatakes.

for NPI. This small values, obtained indiscriminately using all off-glacier flat terrain are an indicator of the reliability of the coregistration procedure, which was based on the mean Δz obtained on several manually selected calibration regions with relatively flat terrain (see Section 7.2).

A slope upper bound of 40° was finally selected in order to include most of the glacier slope range, even if it implies an overestimation of the of the uncertainty, caused by the different on-glacier and off-glacier slope distribution. According to the cumulative histograms in Figure 9.5b and 9.5d this threshold includes 97% of the glacier surface in NPI and 94% in SPI. Figure 9.6 shows how this filtering criterion reduces $\sigma^{\Delta z}$ from 11 m to 10 m (−9%) for SPI and from 9.5 m to 7.8 m (−18%) for NPI.

The uncertainty estimate for the elevation difference sample was computed for each datatake separately, using the off-glacier elevation difference pixels within the range [−45; 45] m and with a slope of less than 40°. For each datatake d, mean $\mu_d^{\Delta z}$, standard deviation $\sigma_d^{\Delta z}$, skewness $\gamma_{1d}^{\Delta z}$, excess kurtosis $\gamma_{2d}^{\Delta z}$, median and interquartile range $\mathrm{IQR}_d^{\Delta z}$ have been computed, the results are summarized in Table 9.1a for SPI and Table 9.1b for NPI. The tables also report the area used to compute the statistics and the glacier area covered by each datatake, indicating the impact of each datatake to the total glacier uncertainty. In order to have a better understanding of the Δz statistics and their significance it is important to evaluate the statistics together with their distributions, shown in Figure 9.7.

Two parameters can be used to describe the spread of Δz, defining the uncertainty of the sample elevation difference: the standard deviation and the interquartile range. The interquartile range is a robust measure of spread, for a Gaussian distribution it covers 50% of the population and is equal to 1.349σ. The standard deviation is an appropriate spread measure for the Gaussian distribution but tends to overestimate the spread if the probability density function is more "peaked" ($\gamma_{2d}^{\Delta z} > 0$), in which case the IQR might give a better representation of spread.

Evaluating the statistics reported in Table 9.1 together with the histograms of Figure 9.7 shows that the Δz distributions are unimodal with a mean very close to 0 (maximum mean: $\mu_d^{\Delta z} = -1.56$ m for DT 1171117), the median is also close to 0 (not reported in Table 9.1). The distributions display good symmetry as expressed by their low skewness $\gamma_{1d}^{\Delta z}$. The distributions have generally a Gaussian-like shape with stronger "peakedness", expressed quantitatively by the positive excess kurtosis $\gamma_{2d}^{\Delta z}$. Low spread and pronounced peaks translate into lower uncertainty. In this regard the best cases are found in NPI where DT 1191233 and 1149794 have an excess kurtosis higher than 10.0, diverging from the normal distribution. Oppositely the distributions with the larger spread are those of DT 1027772 and 1055763, which are the closest to being Gaussian. These two datatakes are those where the 1-σ standard deviation can be most sensibly used as spread measure, with a slight overestimation compared to the real Gaussian distribution. In this case the IQR exceeds noticeably the standard deviation. For DT 1191233 and 1149794 the standard deviation is significantly larger compared to the IQR and tends to overestimate significantly the spread. The 1-σ is nevertheless chosen for all datatakes as a measure of spread in order to maintain consistency.

The values of $\sigma_d^{\Delta z}$ for each datatake d are extended as uncertainty of the elevation difference sample on-glacier. Since the glacier elevation changes are expressed as annual rates, their uncertainty

Table 9.1 – Statistics of Δz per datatake for SPI (a) and NPI (b) computed with a slope upper bound of 40°. Mean $\mu_d^{\Delta z}$, standard deviation $\sigma_d^{\Delta z}$, skewness $\gamma_{1d}^{\Delta z}$, excess kurtosis $\gamma_{2d}^{\Delta z}$ and interquartile range $\mathrm{IQR}_d^{\Delta z}$ are reported. The off-glacier pixels and area used to compute the statistics and the glacier area covered by each datatake are given in order understand the impact of each datatake to the total uncertainty.

(a) SPI

DT AID	Scenes	# pixels	Off-glac. area [km²]	$\mu_d^{\Delta z}$ [m]	$\sigma_d^{\Delta z}$ [m]	$\gamma_{1d}^{\Delta z}$	$\gamma_{2d}^{\Delta z}$	$\mathrm{IQR}_d^{\Delta z}$ [m]	Glac. area [km²]
1012654	S3 S4 S10	2259904	225.99	0.4017	11.0363	0.1911	1.1697	12.2317	3387.84
1021147	S12 S13	5806199	580.62	−0.8392	9.9077	−0.1251	2.2240	9.9165	1269.63
1027766	S1	2721760	272.18	0.1592	10.1694	0.4492	1.6039	11.1777	988.66
1027767	S15	2697467	269.75	0.1207	10.7902	0.2255	1.4920	11.5499	289.10
1027772	S2	2388385	238.84	1.0932	12.1219	0.1719	0.7054	14.4484	1180.63
1042632	S11 S14	6872487	687.25	1.0978	10.0264	−0.0211	1.5468	10.9391	983.04
1055763	S7	2489448	248.95	0.8815	11.3666	0.1517	0.7116	14.5974	255.93
1056403	S17	5063425	506.34	0.2970	8.2111	−0.1819	4.0598	7.9441	207.80
1057982	S5 S9	19150195	1915.02	1.2575	10.3001	0.0580	1.6693	11.5159	933.12
1058255	S6 S8 S16	12251739	1225.17	1.0350	9.6851	0.0368	3.0439	9.3924	2303.29
1058868_3	S18	3483158	348.32	0.2127	8.6287	−0.0081	3.7424	8.3104	40.10
1058868_5	S19	3383468	338.35	0.6496	10.8628	−0.2049	1.5430	11.9360	120.50

(b) NPI

DT AID	Scenes	# pixels	Off-glac. area [km²]	$\mu_d^{\Delta z}$ [m]	$\sigma_d^{\Delta z}$ [m]	$\gamma_{1d}^{\Delta z}$	$\gamma_{2d}^{\Delta z}$	$\mathrm{IQR}_d^{\Delta z}$ [m]	Glac. area [km²]
1191233	N1	12340571	1777.04	−0.4375	5.9342	−0.4503	10.1658	3.5003	875.07
1171117	N2 N3	3094292	445.58	−1.5563	10.7055	−0.5677	2.4384	9.9157	1856.66
1172605	N4	10554608	1519.86	−0.5218	9.1943	−0.5475	2.8772	9.0780	357.41
1149794	N5	2300568	331.28	−1.1199	7.3222	1.1551	11.8414	4.6794	280.11

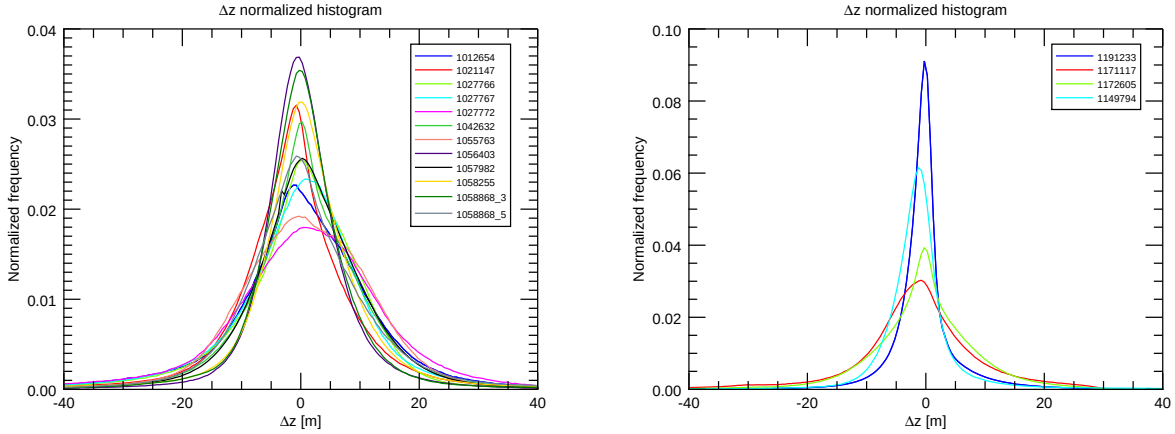

(a) SPI **(b)** NPI

Figure 9.7 – Histograms of the Δz samples used to compute the off-glacier datatake statistics for SPI (a) and NPI (b). The distributions exhibit mostly Gaussian-like shape with a pronounced "peakedness".

Table 9.2 – Summary of uncertainties of the elevation difference sample per datatake. These are assigned to the glacier changes and converted to annual rates.

(a) SPI

DT AID	Scenes	Δt_d [a]	$\sigma_d^{\Delta z}$ [m]	$\sigma_d^{\frac{\Delta h}{\Delta t}}$ [m a^{-1}]	Glac. area [km^2]
1012654	S3 S4 S10	11.058	11.0363	0.998083	3387.84
1021147	S12 S13	11.419	9.9077	0.867639	1269.63
1027766	S1	11.230	10.1694	0.905545	988.66
1027767	S15	11.184	10.7902	0.964827	289.10
1027772	S2	11.208	12.1219	1.081520	1180.63
1042632	S11 S14	11.690	10.0264	0.857658	983.04
1055763	S7	12.112	11.3666	0.938435	255.93
1056403	S17	12.082	8.2111	0.679603	207.80
1057982	S5 S9	12.005	10.3001	0.857953	933.12
1058255	S6 S8 S16	11.992	9.6851	0.807649	2303.29
1058868_3	S18	11.962	8.6287	0.721366	40.10
1058868_5	S19	11.962	10.8628	0.908136	120.50

(b) NPI

DT AID	Scenes	Δt_d [a]	$\sigma_d^{\Delta z}$ [m]	$\sigma_d^{\frac{\Delta h}{\Delta t}}$ [m a^{-1}]	Glac. area [km^2]
1191233	N1	14.0	5.9342	0.423874	875.07
1171117	N2 N3	13.9	10.7055	0.770181	1856.66
1172605	N4	13.9	9.1943	0.661464	357.41
1149794	N5	13.6	7.3222	0.538396	280.11

is obtained as $\sigma_d^{\frac{\Delta h}{\Delta t}} = \frac{\sigma_d^{\Delta z}}{\Delta t_d}$ and expressed in $\left[\mathrm{m\,a^{-1}}\right]$. Δt_d is the temporal interval between the SRTM acquisition and the acquisition of the TanDEM-X datatake d (Table 9.2). The estimated uncertainties $\sigma_d^{\frac{\Delta h}{\Delta t}}$ represent the random component of the error associated to the measured sample of $\frac{\Delta h}{\Delta t}$ within datatake d.

9.3.3 Interferometric uncertainty: surface type comparison

As reported in Section 9.3.2, the standard deviation $\sigma_d^{\Delta z}$ computed for each datatake d on the off-glacier samples Δz, where no physical changes are expected, is extended to the glacier surface and used as the random error of the elevation difference samples Δh. In this section, the representativeness of $\sigma_d^{\Delta z}$ for the glacier samples is investigated. Since both DEMs are achieved with (bistatic) interferometry, the accuracy of the interferometric phase, which translates into an elevation accuracy, is relevant in this context, and particularly the differences of accuracy between the glacier surface and the off-glacier surface.

Both off-glacier and on-glacier the terrain is assumed to be characterized by distributed scatterers in the Rayleigh regime, which reflectivity can be modelled as a complex, circular, stationary Gaussian process. The probability density function and the standard deviation of the phase σ_ϕ for this type of scatterer are reported in Section 2.2.3, in Eq. (2.25) and (2.27), respectively. σ_ϕ which describes the uncertainty of the phase is strictly dependent on the interferometric coherence $|\gamma|$ (cf. Section 2.2.2) and the number of independent looks L, decreasing as these parameter increase (Just & Bamler, 1994; Bamler & Hartl, 1998). The interferometric error for a pixel $\sigma_\phi(x, y)$ can be converted into an elevation error according to Eq. (2.29). This error is annotated in the height error map (HEM) produced by the ITP along with the Raw DEM (cf. Section 6.2.2.2). It must be stressed that this term includes only the error intrinsic to the interferometry and not errors linked to the entire system (such

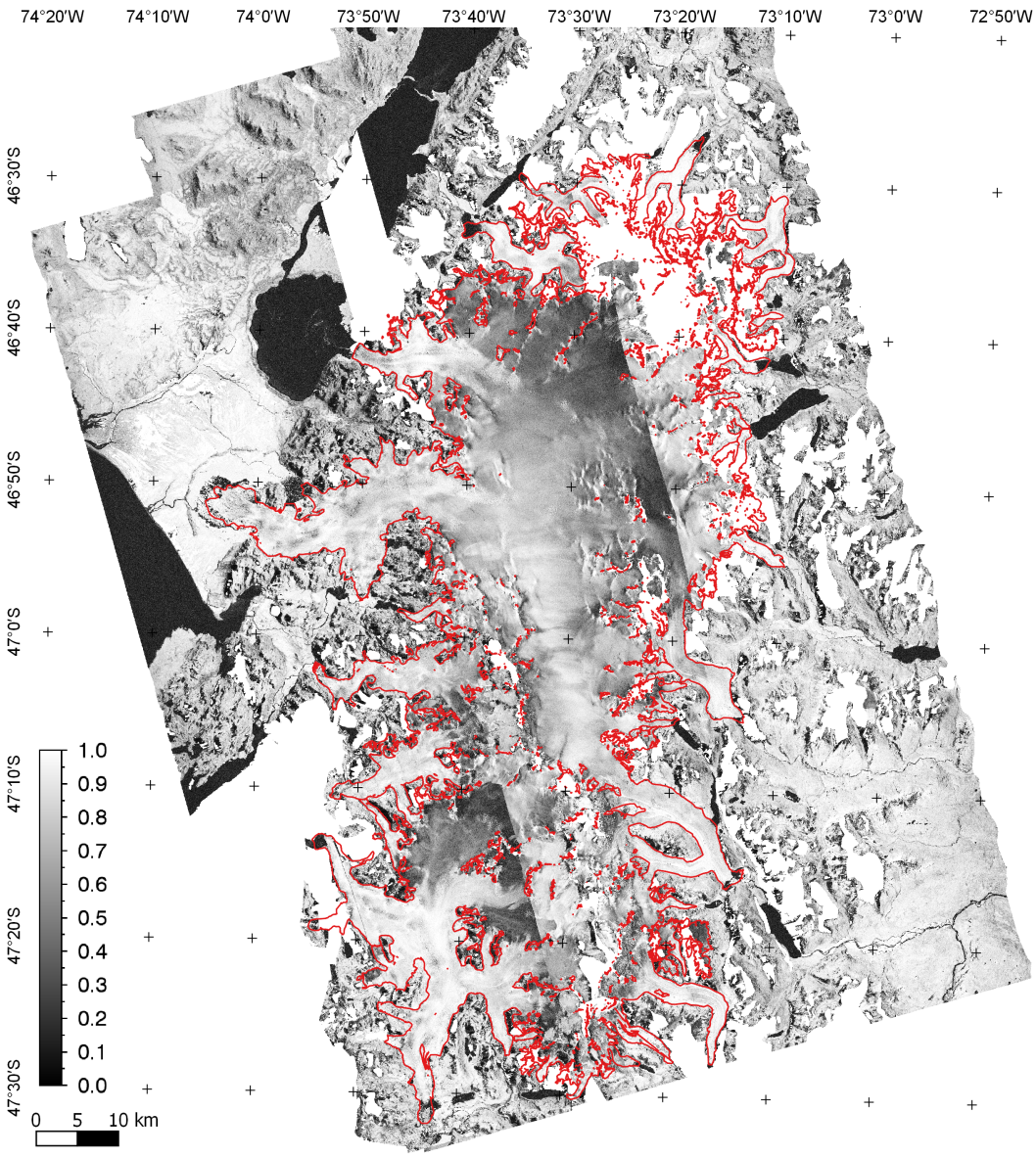

Figure 9.8 – TanDEM-X coherence mosaic of NPI.

as orbit inaccuracies, clock drifts, etc.), nor phase unwrapping errors or inaccuracies linked to the absolute elevation determination.

The TanDEM-X coherence mosaic is shown in Figure 9.8 (phase unwrapping errors are masked). Possible causes of lower coherence on glacier terrain, particularly on snow and firn, can be volume decorrelation in case of dry snow or low backscattering coefficient reducing the SNR in case of wet smooth surface. On the plateau varying behaviour is found. Low values (0.3 - 0.5) are found south-west on N1. N2/N3 displays higher values around 0.8 in the middle of the plateau and low values (0.3 - 0.5) in the north-east, in correspondence of areas with both low (−18 dB) and higher (−14 dB) backscattering coefficient σ^0 (cf. Figure 8.9). Higher values are found on the north-east margin covered by N4 where also lower σ^0 is present, creating an evident jump in coherence with respect to N2/N3. On the glacier termini high coherence values (0.8 - 0.9) are recorded.

In order to understand the representativeness of the off-glacier standard deviation $\sigma_d^{\Delta z}$ for the glacier surface, the average values of the coherence $|\gamma|$ and the height error ε_h have been compared on the two terrain types: off-glacier on the pixels used to compute $\sigma_d^{\Delta z}$ and on-glacier on the pixels used to obtain Δh. The comparison was performed on the TanDEM-X data of NPI. Table 9.3 summarizes the results of this comparison. The coherence is in average generally comparable or slightly higher off-glacier. For instance, over the whole dataset ("All" row) values of $\overline{\gamma^{\mathrm{OFF}}} = 0.718$ and $\overline{\gamma^{\mathrm{GL}}} = 0.660$

Table 9.3 – Comparison of coherence γ and interferometric height error ε_h off and on-glacier for each scene and without scene distinction (last row). L is the number of equivalent looks. Standard deviation values are not reported in this table: they range between 0.2 and 0.28 for γ and between 1.4 m and 2.9 m for ε_h (except N3 which has 4.8 m off-glacier). $\overline{\Delta\varepsilon_h} = \overline{\varepsilon_h^{\mathrm{OFF}}} - \overline{\varepsilon_h^{\mathrm{GL}}}$.

Sc.	h_{amb} [m]	Posting ["]	L	A^{OFF}[km²]	$\overline{\gamma^{\mathrm{OFF}}}$	$\overline{\varepsilon_h^{\mathrm{OFF}}}$ [m]	A^{GL} [km²]	$\overline{\gamma^{\mathrm{GL}}}$	$\overline{\varepsilon_h^{\mathrm{GL}}}$ [m]	$\overline{\Delta\varepsilon_h}$ [m]
N1	−50.45	0.4	98.08	1777.04	0.735	0.869	875.07	0.688	1.000	−0.131
N2	68.58	0.4	90.70	395.12	0.658	1.652	1440.45	0.635	1.331	0.321
N3	68.58	0.2	18.74	50.46	0.544	5.146	416.21	0.641	3.139	2.007
N4	66.66	0.4	96.82	1519.86	0.728	1.140	357.41	0.728	0.944	0.196
N5	64.36	0.2	24.34	331.28	0.688	2.255	280.11	0.645	2.685	−0.430
All	—	—	—	4073.76	0.718	1.212	3369.25	0.660	1.539	−0.327

are measured. An exception is N3, but this may be due to the limited coverage of ice-free surface. The interferometric height error ε_h depends inversely also on the number of equivalent looks L, which increases with the posting used to process the DEM. $\overline{\varepsilon_h}$ has similar values off and on-glacier. The difference $\overline{\Delta\varepsilon_h} = \overline{\varepsilon_h^{\mathrm{OFF}}} - \overline{\varepsilon_h^{\mathrm{GL}}}$ ranges between −0.43 and 0.32 m (except for N3). For all scenes together it is equal to −0.33 m. A higher $\overline{\varepsilon_h}$ difference of 2 m is found on N3, which also has higher standard deviation values of 2.9 m on-glacier and 4.8 m off-glacier (not reported in Table 9.3), where a smaller number of samples was available ($\sim 352 \cdot 10^3$).

There is no trend across scenes indicating a significant difference in interferometric accuracy on and off-glacier for this dataset. Some scenes display lower $\overline{\varepsilon_h}$ off-glacier and vice versa. Furthermore, the absolute value of the $\overline{\varepsilon_h}$ difference is small, particularly compared with the random errors $\sigma_d^{\Delta z}$ estimated off-glacier (Table 9.1b) which range between 5.9 m and 10.7 m. While this holds in average it must be noted that specific areas of low coherence and higher interferometric error ε_h can be found on the smooth snow on the plateau.

This experiment was conducted on NPI only, but similar conclusions are expected for SPI. Similar behaviour is expected from the SRTM DEM which was acquired in the same season as most of the NPI TanDEM-X datatakes, the difference might be even lower due to the fact that the SRTM DEM is a final product obtained mosaicking many datatakes.

In conclusion no significant difference in interferometric accuracy is found in average between off-glacier and on-glacier elevation samples, meaning that the off-glacier estimated $\sigma_d^{\Delta z}$ can be considered well representative for the on-glacier Δh samples of the same datatake, with regard to the interferometric error.

9.3.4 Spatial correlation analysis

The theory of spatial statistics presented in Section 9.1.1.3 was applied in order to estimate the spatial correlation, and in particular the correlation distance, present in the data. The correlation distance d_{cor} can be obtained as the range a of the semivariogram of the elevation difference Δz, i.e. $d_{\mathrm{cor}} \simeq a$. The correlation distance d_{cor} and the relative correlation area $A_{\mathrm{cor}} = \pi d_{\mathrm{cor}}^2$ are used to obtain the number of uncorrelated samples N which in turn is used to define the standard error of the mean $\mathrm{SE} = \frac{\sigma}{\sqrt{N}}$. An estimation of the correlation area on the actual elevation difference dataset is needed in this study for the computation of the standard error of the spatial mean: (a) for the mean of the elevation difference over calibration regions of stable terrain for the purpose of DEM coregistration, (b) for the mean elevation difference over elevation bins on the glacier. Ideally the correlation distance should be estimated on the same regions on which the spatial average is carried out. This computation applied to each calibration region is time consuming, besides many of this regions are too small to extract relevant spatial statistics. The estimation of the correlation distance on each elevation bin of glaciated terrain is not possible because the elevation difference is affected by changes in ice thickness. For this reason the correlation distance is estimated from the empirical semivariogram on two test regions. Both test regions were chosen in order to have a topography, and particularly a slope distribution, as similar as possible to the one over which the spatial mean is carried out. The slope dependence of Δz

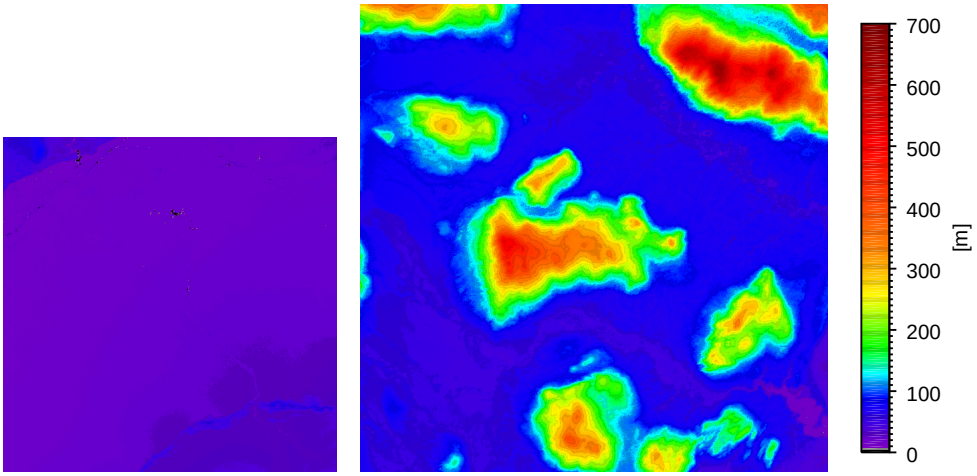

Figure 9.9 – TanDEM-X DEM of the crop A (a) and B (b) which Δz values were used to compute the empirical semivariograms.

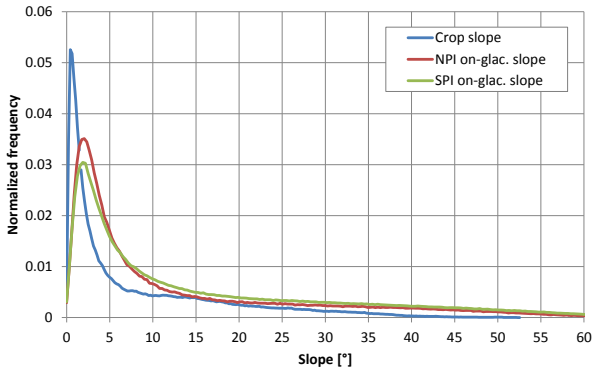

Figure 9.10 – Slope distribution of crop B compared to the one of NPI and SPI.

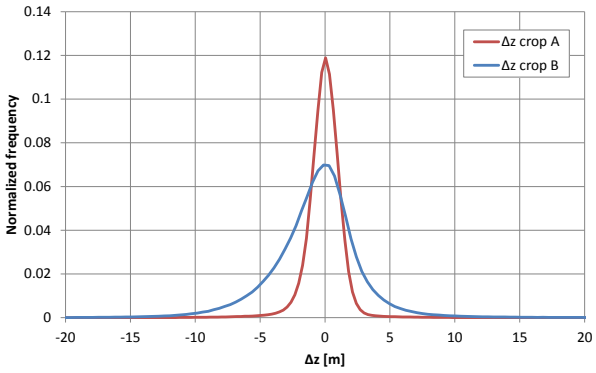

Figure 9.11 – Histograms of Δz for crop A and crop B.

affects its standard deviation and semivariogram (cf. Section 9.3.2, Figures 9.4 and 9.6). Consequently the semivariograms were computed on two ice-free crops (i.e. data windows) of elevation difference $\Delta z = h_{\mathrm{TDM}} - h_{\mathrm{SRTM}}$ in the NPI data, where larger sections of ice-free terrain are present. The TanDEM-X DEM for the two crops is shown in Figure 9.9: crop A has a size of 1000×1000 pixels (12×12 km^2), is located north-west of the S. Quintin Glacier terminus (upper left corner coordinate: 46°42'44.54"S, 74°9'50.30"W) and has flat topography, well representing the calibration regions used to coregister the DEMs (see Section 7.2). Crop B has a size of 1400×1400 pixels (16.8×16.8 km^2) and is located north-west of S. Rafael Glacier (upper left corner coordinate: 46°25'34.39"S, 74°10'6.09"W) and features a topography which resembles the one of the icefields, with a stronger presence of low slopes and decreasing occurrence of higher slopes. The slope histogram of crop B is compared to those of the SPI and NPI in Figure 9.10. The slope distribution of crop B displays a narrower peak at slightly lower slopes compared to those of the icefields, making it possibly a better scenario than the icefields but has the same distribution at higher slopes, which are the more critical with respect to increasing spread of Δz.

Crop A falls completely into TanDEM-X scene N1, the sample mean and standard deviation of Δz are respectively $\mu^{\Delta z} = 0.081$ m and $\sigma^{\Delta z} = 1.555$ m, its histogram is depicted in Figure 9.11. This flat region is characterized by a peaked elevation distribution (mean of 24 m, standard deviation of 6.6 m, not shown), and a slope close to 0° (mean of 0.6°, standard deviation of 1.23°). The topography is similar to the calibration regions, but it represents a best case scenario since many calibration regions have generally a higher mean slope (see Tables 7.1 and 7.2).

Crop B falls between scenes N1 and N5 (52% and 48% of area, respectively). The Δz histogram

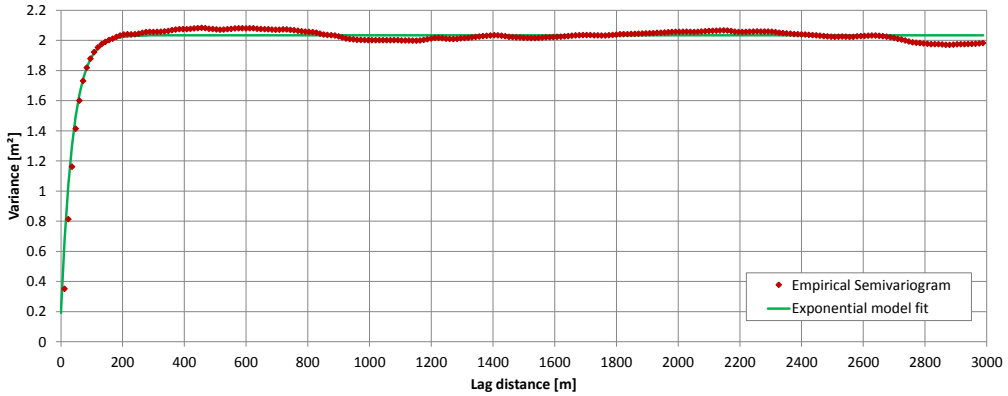

(a)

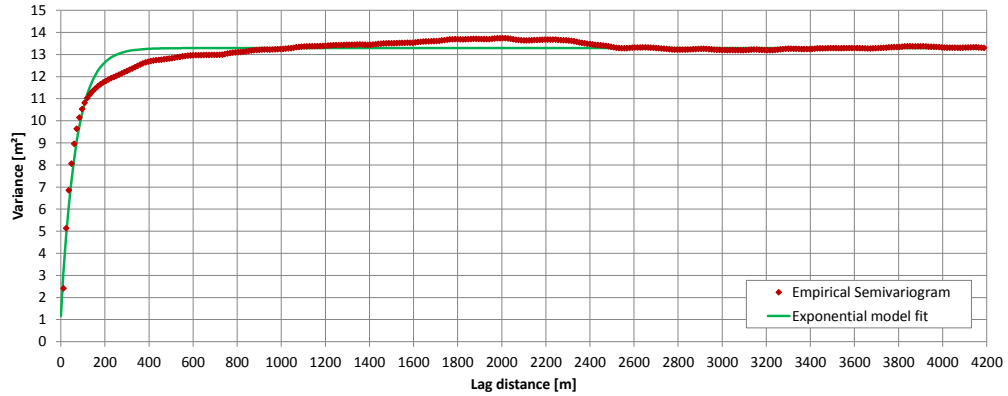

(b)

Figure 9.12 – Empirical semivariogram (red) for crop A (a) and B (b). The non-linear least square fit of an exponential model function is shown in green. A perfect fit is obtained for crop A. The fit is less accurate but acceptable for crop B. characterized by a more complex topography.

(Figure 9.11) is characterized by mean $\mu^{\Delta z} = -0.466$ m (-0.578 m on N1 and -0.345 m on N5) and standard deviation $\sigma^{\Delta z} = 3.668$ m (3.252 m on N1 and 4.066 m on N5). The slope distribution (Figure 9.10) has a mean of 8.4° and standard deviation of 9.7° and is similar to the one of the icefields. The elevation distribution of crop B (mean of 125.8 m, standard deviation of 99.1 m) does not correspond to the one of the icefields, but this should not affect the semivariogram.

The empirical semivariograms were obtained for the elevation difference $\Delta z = h_{\mathrm{TDM}} - h_{\mathrm{SRTM}}$ of crop A and B using the commercial software "ENVI Classic 5.2" and are plotted in red in Figure 9.12. The built-in algorithm computes the omnidirectional semivariogram subtracting each pixel to its neighbours at lag distances increasing by steps of 1 pixel. The spherical and exponential models (Equations (9.9) and (9.10)) were fitted to the empirical semivariogram, a non-linear least square fit was applied to determine the best values of range a, nugget n and sill s. The fitting is based on the Levenberg-Marquardt algorithm which combines the steepest descent and inverse-Hessian function fitting methods (Press *et al.*, 1992). The exponential model resulted in a better fit than the spherical model for both crops. For crop A (Figure 9.12a) the fit is very good leading to the following estimations: $a = 116.910 \pm 4.746$ m, $s = 1.842 \pm 0.061$ m^2, $n = 0.192 \pm 0.062$ m^2, where the uncertainties are expressed as 1-σ. The sum $n+s = 2.034$ m^2, which according to the theory represents the variance of the random field (cf. Section 9.1.1.2), is close to the sample variance of Δz, $\left(\sigma^{\Delta z}\right)^2 = 2.419$ m^2. Since the exponential model approaches its theoretical maximum $n+s$ asymptotically, it is common practice to obtain the range a of the semivariogram as a "practical range" equal to the distance for which the empirical semivariogram reaches 95% of $n+s$. For crop A this distance is equal to 120 m and very close to the fitted value of a, because of the good fit.

The fit of the exponential function to the semivariogram of crop B was less precise, particularly on the bend (Figure 9.12b), where the empirical semivariogram increases more slowly than the model.

Besides for lag distances ranging between 1200 and 2400 m the empirical semivariogram very slightly exceeds the estimated value of $n+s$. The estimated values are: $a = 204.139 \pm 6.876$ m, $s = 12.126 \pm 0.311$ m^2 and $n = 1.166 \pm 0.312$ m^2. The value of $n+s = 13.292$ m^2 is close to the sample variance of Δz on the crop equal to $\left(\sigma^{\Delta z}\right)^2 = 13.454$ m^2. The "practical range" for crop B is equal to 384 m, hence higher than the fitted value of a because of the suboptimal fit on the bend.

The theory of spatial statistics, as distilled in Rolstad *et al.* (2009) (see Section 9.1.1.3), is followed in order to obtain the variance of the spatial average, and hence its standard deviation (referred to as standard error since it derives from the sample standard deviation of Δz). In order to compute the variance of the mean the following integral in polar coordinates is applied (Equation (9.17)):

$$\mathrm{SE}^2 = \frac{2}{L^2}\int_0^L h\left[\sigma^2 - \gamma(h)\right]dh \tag{9.26}$$

where L is the radius of the the integration area $A = \pi L^2$ and σ is the sample standard deviation of the data: in the present work it could be the one characterizing each calibration region σ_r^{reg} or the one obtained for each elevation bin $\sigma_b^{\frac{\Delta h}{\Delta t}}$. Assuming the exponential semivariogram model and describing the variance of the data as $\sigma^2 = n+s$, the integral resolves into the following equation:

$$\mathrm{SE}^2 = \begin{cases} n+s & L \leq \Delta h \\ -\frac{2a^2}{9L^2}s\left(\frac{3L}{a}e^{-\frac{3L}{a}} + e^{-\frac{3L}{a}} - 1\right) & L > \Delta h \end{cases} \tag{9.27}$$

where Δh is the sampling distance in polar coordinates and is defined as the radius of a circle with area equivalent to the pixel area Δx^2, i.e. $\Delta h = \Delta x/\sqrt{\pi}$.

If $L = \sqrt{A/\pi} \gg a$ (practically $L \gtrsim 2a$), meaning that the integration area A is much larger than the correlation area A_{cor} (which is often the case), the expression above simplifies to:

$$\mathrm{SE}^2 = \frac{2}{9}\frac{a^2}{L^2}s \tag{9.28}$$

The correlation distance d_{cor} can be generalized using an estimate of the range a computed over similar terrain ($d_{\mathrm{cor}} \simeq a$), but the actual variance $\sigma^2 = n+s$ of Δz must be used. The possible nugget n within σ^2, representing the uncorrelated component of the variance for the applied sampling interval, cannot be discerned but is generally small. Therefore the approximation $\sigma^2 \simeq s$ is used in the present work, leading to a slightly higher standard error (conservative approximation):

$$\mathrm{SE} \cong \frac{\sqrt{2}}{3}\frac{d_{\mathrm{cor}}}{L}\sigma = \frac{\sqrt{2}}{3}\sqrt{\frac{A_{\mathrm{cor}}}{A}}\sigma \tag{9.29}$$

This expression is very close to the one obtained by Rolstad *et al.* (2009) using the spherical semivariogram model under the same assumptions ($L > a$ and negligible or zero nugget), i.e. $\mathrm{SE} = \frac{1}{\sqrt{5}}\sqrt{\frac{A_{\mathrm{cor}}}{A}}\sigma$. It is equal to 83.6% of the expression commonly used by other authors in the literature who do not integrate the semivariogram function and simply use a square correlation area with side d_c, i.e. $\mathrm{SE} = \sqrt{\frac{d_c^2}{A}}\sigma$. Their approach does not take into account the shape of the semivariogram, practically reducing it to a step function where all samples are correlated below d_{cor} and totally uncorrelated above it. It is acceptable when integration areas are usually larger than correlation areas.

The standard error obtained in Equation (9.27) can be re-written in the common form $\mathrm{SE} = \frac{\sigma}{\sqrt{N}}$ by defining

$$N = \left[-\frac{2d_{\mathrm{cor}}^2}{9L^2}\left(\frac{3L}{d_{\mathrm{cor}}}e^{-\frac{3L}{d_{\mathrm{cor}}}} + e^{-\frac{3L}{d_{\mathrm{cor}}}} - 1\right)\right]^{-1} = \left[-\frac{2}{9}\frac{A_{\mathrm{cor}}}{A}\left(3\sqrt{\frac{A}{A_{\mathrm{cor}}}}e^{-3\sqrt{\frac{A}{A_{\mathrm{cor}}}}} + e^{-3\sqrt{\frac{A}{A_{\mathrm{cor}}}}} - 1\right)\right]^{-1} \tag{9.30}$$

For $L \gg d_{\mathrm{cor}}$, i.e. $A \gg A_{\mathrm{cor}}$, which is fulfilled for almost all spatial averages found in the present error budget, with some exceptions for the smallest calibration regions of SPI (where still holds that $A > A_{\mathrm{cor}}$, see Table 7.1), the expression for N simplifies to:

$$N = \frac{9}{2}\frac{A}{A_{\text{cor}}} \tag{9.31}$$

For $L \gg d_{\text{cor}}$ the standard error is linearly dependent on the correlation distance d_{cor}, hence an increase of the latter by a certain factor leads to the same increase on the standard error.

In the present error budget, the correlation distance used for the calibration regions is set to $d_{\text{cor}} = 200$ m ($A_{\text{cor}} = 125.66 \cdot 10^{-3}$ km^2) by arbitrarily increasing the fitted range a (or the similar "practical range") obtained on crop A (by a factor 1.7). This leads to a more conservative estimate of the standard error of the mean which takes into account the higher slopes found on some calibration regions. The correlation distance used for the glaciated terrain is set by arbitrarily increasing the "practical range" obtained on crop B (by a factor 1.3) to $d_{\text{cor}} = 500$ m ($A_{\text{cor}} = 785.398 \cdot 10^{-3}$ km^2). The "practical range" of 384 m is chosen instead of the fitted value of $a = 204$ m in order to account for the slower increase of the semivariogram at the bend compared the exponential fit. The arbitrary increase is done to take into account the slightly higher slopes of the icefields compared to those found on crop B (Figure 9.10). Increasing d_{cor} leads to to a more conservative error budget.

9.3.5 Standard error of the spatial average

In Section 9.3.2 an estimate of the 1-σ random error $\sigma_d^{\frac{\Delta h}{\Delta t}}$ affecting each elevation change rate sample has been obtained for each datatake d. In Section 9.3.4 an analytical procedure to estimate the number of uncorrelated samples has been presented, allowing to compute the standard error of a spatial average. Here the empirical values and the theory introduced by both sections are applied to obtain the standard error $\text{SE}_b^{\frac{\Delta h}{\Delta t}}$ of the spatial average of $\frac{\Delta h}{\Delta t}$ performed over each elevation bin b, that is of:

$$\mu_b^{\frac{\Delta h}{\Delta t}} = \frac{\sum_{i \in b} (\Delta h/\Delta t)_i}{n_b^{\text{AV}}} = \frac{\sum_d \sum_{i \in b,d} (\Delta h/\Delta t)_i}{n_b^{\text{AV}}} = \frac{\sum_d \mu_{bd}^{\frac{\Delta h}{\Delta t}} n_{bd}^{\text{AV}}}{n_b^{\text{AV}}} \tag{9.32}$$

As illustrated by Table 9.2 each datatake covers a strongly variable area of icefield, and is characterized by a variable uncertainty of the elevation difference sample $\sigma_d^{\frac{\Delta h}{\Delta t}}$. The surface corresponding to an elevation bin can cross several datatakes within the TanDEM-X mosaic and be hence affected by different values of random error $\sigma_d^{\frac{\Delta h}{\Delta t}}$.

As a first step the standard error associated to $\mu_{bd}^{\frac{\Delta h}{\Delta t}}$, the spatial average Δh within each bin and each datatake, is computed as:

$$\text{SE}_{bd}^{\frac{\Delta h}{\Delta t}} = \frac{\sigma_d^{\frac{\Delta h}{\Delta t}}}{\sqrt{N_{bd}}} \tag{9.33}$$

where N_{bd} is the number of uncorrelated samples used to compute the spatial average and is defined by Equation (9.30), where the integration area A is in this case A_{bd}^{AV}, i.e. the area of bin b belonging to datatake d and used to compute the average elevation change rate (valid pixels). N_{bd} could be also obtained in this context with the simplified Equation (9.31), since it easily holds that $A_{bd}^{\text{AV}} \gg A_{\text{cor}}$. For the elevation difference of the icefield Δh, a correlation distance $d_{\text{cor}} = 500$ m and a corresponding correlation area $A_{\text{cor}} = \pi d_{\text{cor}}^2 = 785.398 \cdot 10^{-3}$ km^2 were found empirically in Section 9.3.4.

Based on the last form in Equation (9.32), since datatakes are independent the total standard error of $\mu_b^{\frac{\Delta h}{\Delta t}}$ is obtained summing in quadrature:

$$\text{SE}_b^{\frac{\Delta h}{\Delta t}} = \frac{\sqrt{\sum_d \left(\text{SE}_{bd}^{\frac{\Delta h}{\Delta t}}\right)^2 \left(n_{bd}^{\text{AV}}\right)^2}}{n_b^{\text{AV}}} \tag{9.34}$$

To clarify the notation: n_{bd}^{AV} represents the actual number of Δh samples included in bin b and belonging to datatake d and $n_b^{\text{AV}} = \sum_d n_{bd}^{\text{AV}}$ those included in bin b. They correspond to an area A_{bd}^{AV}

and A_b^{AV}, respectively. These are the samples used to perform the spatial average of $\frac{\Delta h}{\Delta t}$, and are hence marked by the superscript AV. A_b^{AV} is smaller (or equal) than the actual glacier area within a bin A_b^{GL} (number of samples n_b^{GL}) because of the incomplete coverage of the TanDEM-X DEM mosaic.

9.3.6 Uncertainty of the DEM registration procedure

As described in Section 7.2 each TanDEM-X scene has been coregistered vertically and horizontally to the SRTM DEM by deriving the elevation offset between the two datasets. This was obtained on calibration regions on relatively flat and vegetation free off-glacier terrain distributed around the icefields. A single elevation offset μ_d^{reg} for each datatake d is obtained through a weighted mean (Equation (7.4)) and its standard error $\mathrm{SE}_d^{\mathrm{reg}}$ is obtained through Equation (7.5). The values of $\mathrm{SE}_d^{\mathrm{reg}}$ indicate the accuracy of the calibration procedure and are reported in Tables 7.3 and 7.4 for SPI and NPI, respectively. This accuracy is treated in the error budget as a systematic error affecting each $\frac{\Delta h}{\Delta t}$ sample of datatake d:

$$\varepsilon_d^{\mathrm{reg}} = \frac{\mathrm{SE}_d^{\mathrm{reg}}}{\Delta t_d} \tag{9.35}$$

where the superscript $\frac{\Delta h}{\Delta t}$ is omitted for clarity of notation. Given its systematic nature, this error does not decrease when more pixels are averaged spatially. The same error $\varepsilon_d^{\mathrm{reg}}$ affects the single sample of $\frac{\Delta h}{\Delta t}$ and the average $\mu_{bd}^{\frac{\Delta h}{\Delta t}}$ obtained with Equation (9.32). Given the independence between datatakes, due to their separate calibration (cf. Section 7.2), the calibration error affecting the average $\mu_b^{\frac{\Delta h}{\Delta t}}$ is computed summing in quadrature the contributions from each datatake, according to:

$$\varepsilon_b^{\mathrm{reg}} = \frac{\sqrt{\sum_d \left(\varepsilon_d^{\mathrm{reg}}\right)^2 \left(n_{bd}^{\mathrm{AV}}\right)^2}}{n_b^{\mathrm{AV}}} \tag{9.36}$$

9.3.7 Error due to seasonal elevation changes and signal penetration

In order to minimize the effects of seasonal elevation variations of snow and ice coverage in the geodetic mass balance, the two elevation datasets should be acquired at the same time of year. Ideally this should correspond with the end of the hydrological cycle, corresponding to the end of the ablation season, when the surface elevation reaches its minimum because of melting and firn compaction. The end of the hydrological year is assumed conventionally to be the 31 March in the Southern Hemisphere. Similarly to Berthier *et al.* (2010) the absolute temporal departure (in days) from the end of the nearest ablation season $|\delta t^{\mathrm{seas}}|$, was computed for each TanDEM-X datatake and for the SRTM mission (for which 17.2.2000 was considered as acquisition time). The seasonal elevation offset is obtained as:

$$\delta h^{\mathrm{seas}} = \frac{h_\alpha}{182} |\delta t^{\mathrm{seas}}|$$

where h_α is the annual spatially averaged elevation (ice equivalent) amplitude obtained from the annual mass balance amplitude (or turnover) α, defined in Eq. (3.13). It must be noted that the turnover might change significantly according to the region and the specific year considered.

Unfortunately a measured value of α for SPI and NPI for the acquisition years is not available. In Section 8.4 an average seasonal variation of 1.6 m during the four months from September 2013 to January 2014 was obtained for a fraction of NPI. This figure underestimates b_{winter} temporally since approximately 2.5 months are missing to the end of the ablation season, but overestimates it geographically since most of the ROI is located above the equilibrium line of the S. Quintin and S. Rafael glaciers. To obtain α precisely an estimate of b_{summer} is also missing (for which a third DEM would be necessary). Nevertheless, for lack of a better figure, here $h_\alpha = 1.6$ m is assumed. As a comparison, Berthier *et al.* (2010) and Cox & March (2004) used a value of 1.4 m for the Alaskan glaciers. The differential elevation between each TanDEM-X scene and the STRM DEM is computed as $\delta h_d^{\mathrm{seas}} - \delta h_{\mathrm{SRTM}}^{\mathrm{seas}}$. This estimate is too unreliable to perform ablation correction, therefore its is treated as a source of systematic error affecting differently each datatake d.

Table 9.4 – Computed values of the systematic error $\varepsilon_d^{\mathrm{sp}}$ due to the seasonal and the penetration elevation biases. The seasonal elevation offset for SRTM is $\delta h_{\mathrm{SRTM}}^{\mathrm{seas}} = 0.290$ m.

(a) SPI

DT AID	Scenes	Date	Δt_d [a]	$\delta h_d^{\mathrm{seas}}$ [m]	$\delta h_d^{\mathrm{pen}}$ [m]	A_d^{pen} [km²]	A_d^{GL} [km²]	$\varepsilon_d^{\mathrm{sp}}$ [m a^{-1}]
1012654	S3 S4 S10	2011.03.07	11.058	0.123	0	0	3387.84	$-1.511 \cdot 10^{-2}$
1021147	S12 S13	2011.07.17	11.419	1.037	−3.8	657	1269.63	$-1.068 \cdot 10^{-1}$
1027766	S1	2011.05.09	11.230	0.431	0	0	988.66	$1.253 \cdot 10^{-2}$
1027767	S15	2011.04.22	11.184	0.281	0	0	289.10	$-7.861 \cdot 10^{-4}$
1027772	S2	2011.05.01	11.208	0.360	−2.0	356	1180.63	$-4.753 \cdot 10^{-2}$
1042632	S11 S14	2011.10.24	11.690	1.310	−2.0	378	983.04	$2.145 \cdot 10^{-2}$
1055763	S7	2012.03.26	12.112	0.044	0	0	255.93	$-2.032 \cdot 10^{-2}$
1056403	S17	2012.03.15	12.082	0.053	0	0	207.80	$-1.965 \cdot 10^{-2}$
1057982	S5 S9	2012.02.16	12.005	0.299	0	0	933.12	$7.323 \cdot 10^{-4}$
1058255	S6 S8 S16	2012.02.11	11.992	0.343	0	0	2303.29	$4.399 \cdot 10^{-3}$
1058868_3	S18	2012.01.31	11.962	0.440	0	0	40.10	$1.249 \cdot 10^{-2}$
1058868_5	S19	2012.01.31	11.962	0.440	0	0	120.50	$1.249 \cdot 10^{-2}$

(b) NPI

DT AID	Scenes	Date	Δt_d [a]	$\delta h_d^{\mathrm{seas}}$ [m]	$\delta h_d^{\mathrm{pen}}$ [m]	A_d^{pen} [km²]	A_d^{GL} [km²]	$\varepsilon_d^{\mathrm{sp}}$ [m a^{-1}]
1191233	N1	2014.02.14	14.0	0.308	0	0	875.07	$1.256 \cdot 10^{-3}$
1171117	N2 N3	2013.09.02	13.9	0.695	0	0	1856.66	$2.909 \cdot 10^{-2}$
1172605	N4	2014.01.01	13.9	0.598	0	0	357.41	$2.214 \cdot 10^{-2}$
1149794	N5	2014.01.12	13.6	1.451	0	0	280.11	$8.533 \cdot 10^{-2}$

In Chapter 8 the backscattering coefficient of the SRTM and TanDEM-X dataset was analysed together with meteorological data in order to assess the possibility of signal penetration in ice and snow. It is concluded that the SRTM dataset acquired during mid-summer is likely not affected by signal penetration. Similar conclusions are found for the NPI TanDEM-X dataset, except possibly some negligible areas at very high elevations. The TanDEM-X dataset over SPI suffers from signal penetration on the winter scenes S12 and S13 (DT 1021147) on the plateau where the snow and firn are smooth. The autumn scene S2 (DT 1027772) and the spring scenes S11 and S14 (DT 1042632), have in average a lower backscattering than the winter ones. Their interpretation is uncertain: the snow and firn on the plateau might be dry or slightly wet (below ∼1% of LWC) and hence suffer by a certain degree of signal penetration, possibly lower than the winter scenes. Another possibility is the presence of a frozen upper layer below which liquid water is present, in this case signal penetration is very shallow.

As shown in Section 8.4 the elevation bias due to signal penetration, when present, counteracts the effects of seasonal changes. The actual elevation bias cannot be estimated precisely making a correction unreliable, it is hence treated as a source of systematic error. The multiseasonal experiment in Section 8.4, and particularly the behaviour expressed by Figure 8.12, were used to obtain rough estimates of the elevation bias affecting the plateau during winter with respect to the backscattering coefficient σ^0. In accordance with the backscattering and meteorological observations presented in Chapter 8, an elevation bias of $\delta h_d^{\mathrm{pen}} = -3.8$ m is assumed for S12 and S13 where the plateau has very high σ^0 typical of winter dry snow. For S2, S11 and S14, which have slightly lower average σ^0, an elevation bias $\delta h_d^{\mathrm{pen}} = -2.0$ m is assumed according to Figure 8.12, even if it is not clear whether actual dry snow or frozen upper layer affect these scenes. In both scenarios this likely implies an overestimation of the error. This elevation bias affects only the smooth snow on the plateau, hence to obtain a single contribution its value is averaged over the whole glacier area.

The seasonal and the penetration elevation bias estimates are summed for each TanDEM-X scene and an estimate of systematic error caused by these two effects is obtained and assigned to the elevation

change rate of each datatake d according to:

$$\varepsilon_d^{\mathrm{sp}} = \frac{1}{\Delta t_d}\left[\delta h_d^{\mathrm{seas}} - \delta h_{\mathrm{SRTM}}^{\mathrm{seas}} + \left(\delta h_d^{\mathrm{pen}} \cdot \frac{A_d^{\mathrm{pen}}}{A_d^{\mathrm{GL}}}\right)\right] \tag{9.37}$$

where A_d^{pen} is the area suspected to be affected by signal penetration in datatake d and was obtained in Section 8.3.4. The computed values for each datatake d are reported in Table 9.4.

The contribution of $\varepsilon_b^{\mathrm{sp}}$ to the mean elevation change rate $\mu_b^{\frac{\Delta h}{\Delta t}}$ of each elevation bin is obtained in similar fashion to the previous error sources by summing in quadrature across the datatakes, given their independence:

$$\varepsilon_b^{\mathrm{sp}} = \frac{\sqrt{\sum_d \left(\varepsilon_d^{\mathrm{sp}}\right)^2 \left(n_{bd}^{\mathrm{AV}}\right)^2}}{n_b^{\mathrm{AV}}} \tag{9.38}$$

9.3.8 Crustal uplift due to glacial isostatic adjustment

Dietrich *et al.* (2010) deployed four GPS stations between 2003 and 2006 on a virtual line departing from the northeastern edge of the SPI and stretching 160 km in NNE direction in order to quantify and model the glacial isostatic adjustment of this region. They report measured vertical crustal uplift of 39 mm a^{-1} and 32 mm a^{-1}, respectively upstream of Chico Glacier and at its terminus, 25 mm a^{-1} at Villa O'Higgins (located at 66 km from the icefield) and 23 mm a^{-1} 27 km further away. These are the largest isostatic rates ever recorded. Dietrich *et al.* (2010) attribute such rates to the combination of rapid ice meting in SPI and the relative low viscosity of the underlying mantle due to unique regional slab-window tectonics. They develop a model resulting in a smooth gradient reaching a peak vertical uplift to 41 mm a^{-1} at the centre of SPI. Measurements for NPI were not performed but the lower mass loss rate will lead to a lower vertical uplift.

The high uplift rates of the Patagonian icefields would lead to a non negligible systematic error over long observation periods, such as the time between the SRTM and TanDEM-X acquisitions. The calibration procedure applied to these two datasets and described in Section 7.2 relies on off-glacier calibration regions (CR) located around the icefield, often at the ice margin, and thus affected by similar values of crustal uplift as the icefield. The local crustal uplift is hence corrected during the calibration procedure performed separately on each TanDEM-X datatake. Particularly on SPI, many geographically scattered CR were used, counter-acting the effects of the slow gradient of the crustal uplift. Differences in crustal uplift (which are likely below 5 mm a^{-1} within a datatake) are hence already well included in the calibration error (Section 9.3.6) which is treated as a systematic error of the obtained ice elevation change values. No additional error is needed to take into account for glacial isostatic adjustment.

9.3.9 Other error sources and combination of uncertainties

In this section the combination of different sources of error is discussed, which allows to obtain the final error assigned to the mean elevation, volume and mass change rates of each elevation bin, as well as the total error of the mass balance.

Elevation change rate error. Every elevation change rate sample $(\Delta h/\Delta t)_i$ belonging to a single datatake can be thought of as a measure obtained by a calibrated instrument, characterized by a random error $\sigma_d^{\frac{\Delta h}{\Delta t}}$ and a systematic error $\varepsilon_d^{\mathrm{reg}}$ given by the accuracy of its calibration procedure. The latter error affects each sample and does not decrease by averaging more measurements, while the first one does. The corresponding errors affecting the mean elevation change rate $\mu_b^{\frac{\Delta h}{\Delta t}}$ of bin b are obtained in the preceding sections: in Section 9.3.5 the standard error of the spatial average $\mathrm{SE}_b^{\frac{\Delta h}{\Delta t}}$ and in Section 9.3.6 the systematic error due to the coregistration $\varepsilon_b^{\mathrm{reg}}$. Another systematic error $\varepsilon_b^{\mathrm{sp}}$ due to seasonal elevation changes and signal penetration in ice and snow is obtained in Section 9.3.7.

These three error sources, obtained respectively according to Equations (9.34), (9.36) and (9.38), are independent and can be hence summed in quadrature leading to the total error of $\mu_b^{\frac{\Delta h}{\Delta t}}$:

$$E_b^{\frac{\Delta h}{\Delta t}} = \sqrt{\left(\mathrm{SE}_b^{\frac{\Delta h}{\Delta t}}\right)^2 + \left(\varepsilon_b^{\mathrm{reg}}\right)^2 + \left(\varepsilon_b^{\mathrm{sp}}\right)^2} \tag{9.39}$$

Volume change rate error (glacier area and extrapolation errors). The volume change rate is obtained according to:

$$\mu_b^{\frac{\Delta V}{\Delta t}} = \mu_b^{\frac{\Delta h}{\Delta t}} \cdot A_b^{\mathrm{GL}} = \mu_b^{\frac{\Delta h}{\Delta t}} \cdot \left(A_b^{\mathrm{AV}} + A_b^{\mathrm{EX}}\right) \tag{9.40}$$

where A_b^{EX} is the glacier area not covered by TanDEM-X DEM within bin b, for which the value of $\mu_b^{\frac{\Delta h}{\Delta t}}$ computed on the rest of the icefield area A_b^{AV} must be extrapolated. The total A^{EX} amounts to approximately 12.8% and 7.1% of A^{GL} for NPI and SPI, respectively. The A^{EX} altitude distributions (red in Figure 9.16a and 9.17a, for NPI and SPI respectively) show increasing occurrences at higher altitudes, due to the phase unwrapping errors involving mountainous ice-covered terrain. Extrapolating $\mu_b^{\frac{\Delta h}{\Delta t}}$ computed on A_b^{AV} to the entire A_b^{GL} introduces an error, particularly at lower altitude bins where the termini of the glaciers display a higher $\frac{\Delta h}{\Delta t}$ variation, and even opposite sign (for instance Pio XI glacier). The extrapolation introduces a systematic error on $\mu_b^{\frac{\Delta V}{\Delta t}}$ (and hence on the total volume change) which varies with the altitude bin size and depends on the distribution of A_b^{EX} and the behaviour of $\mu_b^{\frac{\Delta h}{\Delta t}}$ along elevation. The use of a single large bin (or very few bins) to compute directly the entire mass balance would be too strongly affected by a systematic error due to the non-uniform distribution of A^{EX} in altitude. In this case the total volume loss would be overestimated by assigning to most of extrapolated areas (located at high elevations) a mean $\mu_b^{\frac{\Delta h}{\Delta t}}$ which is too high (in absolute value), being driven by the strong losses happening at low elevations. This systematic error is reduced by using narrow altitude bins, thus assigning to each A_b^{EX} a better estimate of $\mu_b^{\frac{\Delta h}{\Delta t}}$. It was observed that the total volume change of the icefield computed with decreasing bin size converges already at a bin size of 400 m. Nevertheless, some degree of error remains due to the missing elevation change samples and the extrapolation procedure. To account for this uncertainty the total elevation error $E_b^{\frac{\Delta h}{\Delta t}}$ is increased by an arbitrary factor $F^{\mathrm{EX}} = 2$ when extrapolated to A_b^{EX}. The total error linked to the volume change rate $\mu_b^{\frac{\Delta V}{\Delta t}}$ is hence obtained as:

$$E_b^{\frac{\Delta V}{\Delta t}} = E_b^{\frac{\Delta h}{\Delta t}} \cdot A_b^{\mathrm{AV}} + E_b^{\frac{\Delta h}{\Delta t}} \cdot A_b^{\mathrm{EX}} \cdot F^{\mathrm{EX}} \tag{9.41}$$

The area of the glacier A^{GL} is defined by the glacier outline, described in detail in Section 6.3. The uncertainty of this term is not given and cannot be estimated without an independent dataset. Nevertheless this error represents a multiplicative independent contribution and should not be completely neglected as often happens in literature studies. An error of 2% is assigned to the glacier area as discussed in Section 6.3, and included in Eq. (9.41) as a multiplicative independent uncertainty source (standard error propagation rule, formula not shown).

Mass change rate error. The mass change rate for each bin is obtained as $\mu_b^{\frac{\Delta M}{\Delta t}} = \mu_b^{\frac{\Delta V}{\Delta t}} \cdot \rho$, where ρ is the ice density. As custom in geodetic mass balances (cf. Section 9.1.1.4), Sorge's Law (Bader, 1954) is assumed, implying that the vertical firn density profile is unchanged between the acquisitions. Uncertainties linked to this assumption can arise from both changes of the equilibrium line altitude or in the firn layer density (Haug *et al.*, 2009). Due to the lack of in-situ data it is not possible to establish the validity of Sorge's law, nor to estimate the uncertainties linked to its assumption. An ice density value of $\rho \pm \delta\rho = 900 \pm 17\ \mathrm{kg\,m^{-3}}$ is assumed here for all elevation bins, without distinction of accumulation and ablation area. The error linked to ice density is an independent error, and the

standard error propagation rules apply:

$$E_b^{\frac{\Delta M}{\Delta t}} = \left|\mu_b^{\frac{\Delta M}{\Delta t}}\right| \cdot \sqrt{\left(\frac{E_b^{\frac{\Delta V}{\Delta t}}}{\mu_b^{\frac{\Delta V}{\Delta t}}}\right)^2 + \left(\frac{\delta\rho}{\rho}\right)^2} \tag{9.42}$$

Total volume and mass change rate error. As described in Section 9.2, the total volume and mass change rates are obtained by summing the contributions of all elevation bins: $\mu^{\frac{\Delta V}{\Delta t}} = \sum_{b=1}^{B} \mu_b^{\frac{\Delta V}{\Delta t}}$ and $\mu^{\frac{\Delta M}{\Delta t}} = \sum_{b=1}^{B} \mu_b^{\frac{\Delta M}{\Delta t}}$. The bins means being summed are neither independent nor totally correlated between each other. The most straightforward way to compute the errors of the total volume and mass change rates of the icefield is by using a single elevation bin (only for the error) avoiding any covariance calculation. In this case Equations (9.41) and (9.42) lose their dependence on the bin and give directly the error $E^{\frac{\Delta V}{\Delta t}}$ of $\mu^{\frac{\Delta V}{\Delta t}}$ and the error $E^{\frac{\Delta M}{\Delta t}}$ of $\mu^{\frac{\Delta M}{\Delta t}}$.

9.3.10 Mass balance error budget for NPI and SPI

In this subsection the results of the uncertainty estimation for the elevation, volume and mass change rates are reported. The behaviour with respect to elevation of $E_b^{\frac{\Delta h}{\Delta t}}$, the error of $\mu_b^{\frac{\Delta h}{\Delta t}}$ obtained with Eq. (9.39), is shown in Figure 9.13a for both NPI and SPI. Here, with a small bin of 20 m, the trend is dominated by the standard error of the spatial average $\mathrm{SE}_b^{\frac{\Delta h}{\Delta t}}$ (Eq. (9.34)) which is strictly dependent on the bin area. The average of $\mathrm{SE}_b^{\frac{\Delta h}{\Delta t}}$ across all bins is 0.137 $\mathrm{m\,a^{-1}}$ for NPI and 0.144 $\mathrm{m\,a^{-1}}$ for SPI. The error due to seasonal elevation and signal penetration $\varepsilon_b^{\mathrm{sp}}$ is in average almost one order of magnitude smaller than $\mathrm{SE}_b^{\frac{\Delta h}{\Delta t}}$: the average of $\varepsilon_b^{\mathrm{sp}}$ across all bins is 0.016 $\mathrm{m\,a^{-1}}$ for NPI and 0.013 $\mathrm{m\,a^{-1}}$ for SPI. The two errors are comparable where area elevation distribution is higher: between 500 - 2000 m of altitude according to Figure 9.16a and 9.17a, for NPI and SPI respectively. The coregistration error $\varepsilon_b^{\mathrm{reg}}$ is in average approximately two orders of magnitude smaller than $\mathrm{SE}_b^{\frac{\Delta h}{\Delta t}}$. The average $\varepsilon_b^{\mathrm{reg}}$ across all bins is 0.004 $\mathrm{m\,a^{-1}}$ for NPI and 0.007 $\mathrm{m\,a^{-1}}$ for SPI.

The volume change rate error $E_b^{\frac{\Delta V}{\Delta t}}$, which includes the extrapolation and glacier mask error contributions is shown in Figure 9.13b. The mass change rate error $E_b^{\frac{\Delta M}{\Delta t}}$ behaves similarly and includes the small error assigned to the ice density $\rho = 900 \pm 17$ $\mathrm{kg\,m^{-3}}$ (plot not shown).

The uncertainties assigned to the total mass balance of the icefield have been computed using a single elevation bin covering the entire elevation range and hence the entire surface. This leads to a strong drop of $\mathrm{SE}_b^{\frac{\Delta h}{\Delta t}}$ while the systematic errors $\varepsilon_b^{\mathrm{reg}}$ and $\varepsilon_b^{\mathrm{sp}}$ maintain approximately the mean values reported above for the 20 m bins. For a comparison the three components are reported in Table 9.5. According to the table, the error linked to seasonal changes and signal penetration $\varepsilon^{\mathrm{sp}}$ is the largest component of $E^{\frac{\Delta h}{\Delta t}}$. It is hence advisable not to neglect these two sources of uncertainty as well as any kind of systematic error since they do not decrease by averaging with increasing samples. $\mathrm{SE}^{\frac{\Delta h}{\Delta t}}$ and $\varepsilon^{\mathrm{reg}}$ have the same order of magnitude, the latter is much larger on SPI compared to NPI, as expected given the more precise calibration preformed on the NPI dataset (cf. Section 7.2). Despite the lower off-glacier standard deviation $\sigma_d^{\Delta z}$ (cf. Section 9.3.2) the standard error $\mathrm{SE}^{\frac{\Delta h}{\Delta t}}$ tends to be slightly larger in NPI because of its much smaller surface (approximately one third). $\varepsilon^{\mathrm{sp}}$ resulted similar on both icefields. The combination of the three terms leads to a higher error assigned to $\mu^{\frac{\Delta h}{\Delta t}}$ in NPI compared to SPI. As expected the volume and mass change rate errors are approximately three times larger for SPI compared to NPI.

9.4 Frontal and subaqueous ice changes

The mass balance estimation over the very final part of the glacier terminus needs to be treated in more detail, because of the highest elevation change rates are found here and because the ending

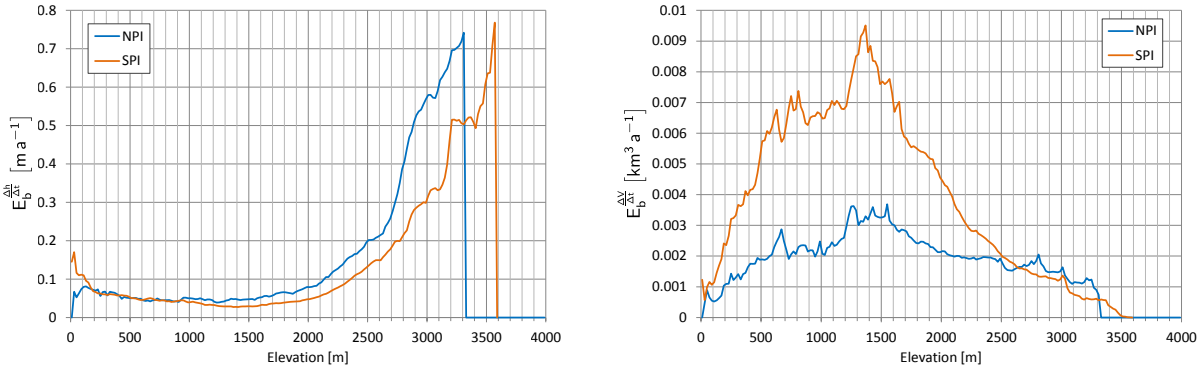

(a) (b)

Figure 9.13 – Errors of the elevation change rate (a) and volume change rate (b) with respect to elevation binned at 20 m.

Table 9.5 – Error budget of the geodetic mass balance of NPI and SPI.

Region	$\mathrm{SE}^{\frac{\Delta h}{\Delta t}}\ [\mathrm{m\,a^{-1}}]$	$\varepsilon^{\mathrm{reg}}\ [\mathrm{m\,a^{-1}}]$	$\varepsilon^{\mathrm{sp}}\ [\mathrm{m\,a^{-1}}]$	$E^{\frac{\Delta h}{\Delta t}}\ [\mathrm{m\,a^{-1}}]$	$E^{\frac{\Delta V}{\Delta t}}\ [\mathrm{km^3\,a^{-1}}]$	$E^{\frac{\Delta M}{\Delta t}}\ [\mathrm{Gt\,a^{-1}}]$
NPI	$4.802 \cdot 10^{-3}$	$3.935 \cdot 10^{-3}$	$1.769 \cdot 10^{-2}$	$1.875 \cdot 10^{-2}$	$1.290 \cdot 10^{-1}$	$1.381 \cdot 10^{-1}$
SPI	$3.519 \cdot 10^{-3}$	$6.100 \cdot 10^{-3}$	$1.319 \cdot 10^{-2}$	$1.495 \cdot 10^{-2}$	$3.746 \cdot 10^{-1}$	$4.186 \cdot 10^{-1}$

into water requires a different approach. Most of the Patagonian (particularly in SPI) glaciers are calving: terminating into tidewater ocean fjords, freshwater lakes or smaller shallower proglacial lakes of geologically recent formation. Less glaciers (mostly in NPI) terminate on land. In the observation period, most of the glaciers of Patagonia presented thinning at the front (cf. Figure 7.6 and 7.8), often linked to frontal retreat. Exceptions are some stable glaciers (Perito Moreno is the largest one) and the two neighbouring Pio XI and Trinidad glaciers which show frontal thickening and advance.

Figure 9.14 exemplifies the glacier mass changes at a calving glacier terminus between two times t_1 and t_2. The longitudinal section at the central flowline is shown for two scenarios: floating front (Figure 9.14a) and grounded front (Figure 9.14b). The first scenario is typical of deeper and usually wider water basins, while the second applies to shallower and usually narrower water basins. Figure 9.14c is a transversal section of the glacier front of a grounded glacier.

The elevation change maps (results in Section 7.4) allow a precise estimation of the volume and mass changes above water and the derivation of the total net mass balance according to Section 9.2. In fact at a calving glacier front the DEM difference $\Delta h = h_{\mathrm{TDM}} - h_{\mathrm{SRTM}}$ will represent the difference between the glacier surface height at t_1 and the water height at t_2 (or the bedrock height at the sides the glacier front). The chronological order of t_1 and t_2 depends on the retreat or advance of the glacier. This change is included in the mass balance by using a glacier mask covering the maximum glacier extent between t_1 and t_2. This scenario is depicted in Figure 9.15, which shows the two DEMs h_{SRTM} and h_{TDM} along with their difference $\Delta h = h_{\mathrm{TDM}} - h_{\mathrm{SRTM}}$ at the front of Jorge Montt Glacier, which has the strongest thinning and frontal retreat rates of both Patagonian icefields.

Measuring the water surface elevation with TanDEM-X is problematic due to the very low interferometric coherence, leading to strong noise in the differential interferogram and hence in the DEM, besides water bodies are often affected by phase unwrapping errors. Higher coherence is nevertheless found sometimes, thanks to floating small icebergs in front of the termini. Erroneous water elevations in the TanDEM-X DEM were manually substituted with the elevation obtained from nearby coherent regions or by arbitrary assigning the STRM elevation for that lake. The edited SRTM DEM used here has flat water heights obtained by setting the sea surfaces to 0 m a.s.l. and by flattening lakes wider than 600 m (Farr *et al.*, 2007). Lakes heights from SRTM probably have a relatively high error, besides the fact that water levels may be subject to changes. For oceanic fjords water elevation is influenced by tides which may also affect the elevations of floating glacier fronts. For the relatively narrow Patagonian tidewater glaciers termini small elevation variations are expected, hence ocean tides are not

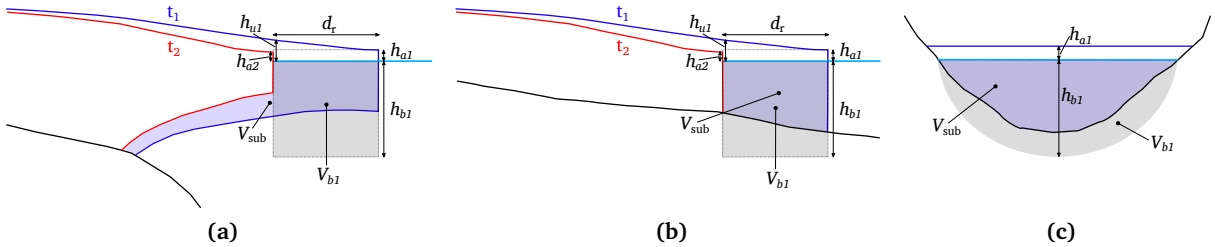

Figure 9.14 – Ice volume changes scheme at the front of a calving glacier. Longitudinal section along the central flowline of (a) a floating and a (b) grounded glacier; (c) transversal section of a grounded glacier.

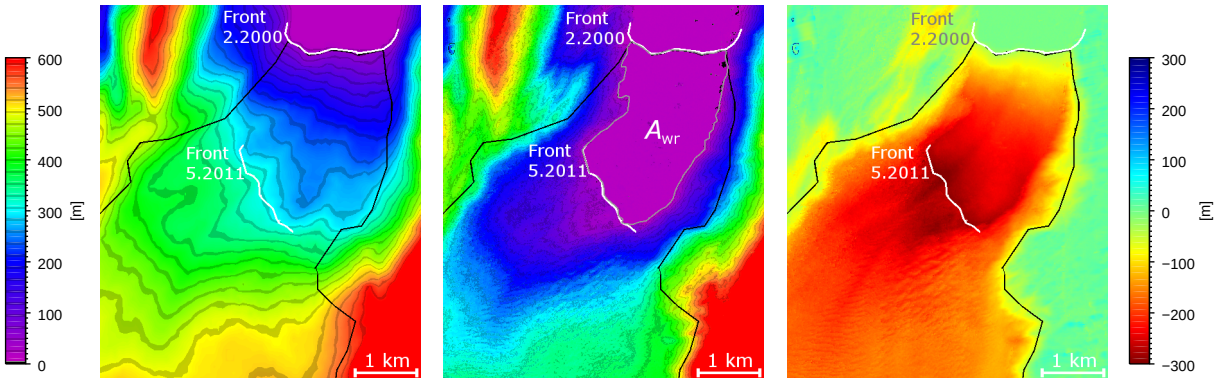

Figure 9.15 – (a) SRTM DEM, (b) TanDEM-X DEM at the front of Jorge Montt Glacier (SPI). White line: front position during STRM (February 2000) and TanDEM-X acquisition (9.5.2011). Black line: glacier outline used to compute the mass balance (February 2000). Grey line: the water area below the retreated front A_{wr}.

taken into account here. The volumetric ice change above water can thus be measured with relatively good accuracy.

The subaqueous ice volume changes are on the other hand not directly measurable. This component is not particularly critical as its sea level contribution is minimal compared to the one of the icefield, being the ice already submerged. The only contribution is a negative one, due to the decrease of 10% in volume when water passes from a solid to a liquid state, since $V_w = \frac{\rho_i}{\rho_w} V_i = 0.9 V_i$. For a precise estimation the bathymetry below the changing front is needed, an information rarely available. Nevertheless it is useful to have a rough estimate of the subaqueous volume changes to better quantify the total volume change of the icefield.

In order to attempt an estimate of V_{sub}, the available DEMs were used to extract the following parameters of the glacier front, visualized in Figure 9.14:

- h_{a1} and h_{a2}: the mean frontal central elevation at t_1 and t_2,
- h_{u1}: the mean central elevation at t_1 at the frontal position of t_2,
- the retreat distance d_{r} at the central flowline,
- the water area A_{wr} below the retreated front.

The measured values are reported in Table 9.6 for the SPI glaciers with a significant frontal volume change.

The present rough estimation of V_{sub} is based only on h_{a1} and A_{wr}. The frontal height h_{a1} was assumed to be floating freely and the ice height below water corresponding to a floating iceberg with

Table 9.6 – SPI glaciers with most significant frontal changes. Measured front parameters (Figure 9.14) and estimated subaqueous ice height h_{b1} (Eq. (9.43)) and volume changes V_{b1} (Eq. (9.44)). Arbitrary multiplicative factors applied to h_{b1} before computing V_{b1} are also reported. The values of V_{b1} marked with * were obtained using bathymetric information.

Glacier	d_r [km]	A_{wr} [km^2]	h_{a2}[m]	h_{u1}[m]	h_{a1}[m]	h_{b1}[m]	V_{b1}[km^3]
Upsala W fr.	3.45	9.78	41	175	34	309	−2.800*
Occidental	2.2	5.35	22	34	18	160	−0.671
HPS8	2.9	5.32	22	66	16	142	−0.595
Pio XI S fr.	1.89	5.22	52	161	77	557	2.283
HPS9	1.13	4.42	23	32	20	178	−0.618
Greve	1.13	4.31	33	69	27	240	−0.813
HPS41	1.85	4.24	16	97	18	162	−0.539
Upsala E fr.	2.4 / 1.3	4.24	58	223	23	204×0.5	−0.339
HPS12	3	3.80	n/a	526	38	275×0.8	−0.655
Jorge Montt	2.36	3.76	31	303	60	435	−0.680*
Amalia	0.6	2.58	61	120	38	273	−0.552
Dickson	2.33	2.33	31	81	8	71	−0.130
Balmaceda	1.48	2.18	24	146	35	317×0.8	−0.434
HPS38	1.37	2.02	42	165	29	265	−0.168
Tyndall	1.3	2.00	37	95	29	263	−0.590*
Pio XI N fr.	0.53	1.91	15	50	27	246	0.369
Onelli & Bolados	2	1.85	31	135	34	305×0.6	−0.267
Grey	0.7 / 0 / 0.7	1.43	28	89	29	260	−0.292
Bernardo W fr.	0.7	1.37	14	29	16	146×0.5	−0.079
Ofhidro S fr.	1.38	1.21	39	110	21	191×0.3	−0.054
Lucia	1	1.14	35	92	20	184×0.8	−0.132
Ofhidro N fr.	0.7	1.07	28	120	31	280×0.3	−0.071
Ameghino	0.85	0.97	25	102	25	221	−0.050*
Viedma	0.82	0.80	56	107	49	445	−0.279
O'Higgins	0.3	0.59	50	54	42	378	−0.174

constant area A_{wr} was obtained applying Archimede's principle:

$$h_{b1} = h_{a1} \frac{\rho_i/\rho_w}{1-\rho_i/\rho_w} \tag{9.43}$$

with ice density $\rho_i = 900$ kg m^{-3} and water density $\rho_w = 1000$ kg m^{-3} for freshwater fronts and $\rho_w = 1025$ kg m^{-3} for tidewater fronts. The transversal section was assumed to be a semi-ellipse with minor axis h_{b1}, the estimated volume below water is obtained as:

$$V_{b1} = \frac{\pi}{4} \cdot h_{b1} \cdot A_{wr} \tag{9.44}$$

V_{b1}, depicted as a filled grey polygon in Figure 9.14, can be quite different from the real volume change V_{sub}, which cannot be estimated without knowledge of the bathymetry.

The previous main assumption of a completely free floating front at h_{a1} is not totally valid: the shorter the floating part and the less valid it is and in case of a completely grounded glacier it does not apply at all (Figure 9.14). Furthermore the front is never floating on the sides. This assumption implies a 1 to 9 ratio between h_{a1} and h_{b1} (Eq. (9.43)) thus likely leading to an overestimation of V_{sub}. If the glacier is floating, this overestimation compensates to an unknown amount the volume change below the glacier front at t_2 (Figure 9.14a) which cannot be estimated. If the glacier is grounded the real change is strictly dependent on the bed topography and cannot be directly linked to the frontal height above water h_{a1} (Figure 9.14b).

In this region only wide glaciers which flow into large, and hence likely deep, lakes are possibly floating. Most of the glaciers are instead relatively narrow and often terminate in small proglacial lakes: here a grounded condition is almost surely the case. For such glaciers the lake shape and size and the surrounding topography was evaluated and extrapolated to the bed. Where the estimated h_{b1} appeared to be too high it was reduced by a multiplicative factor arbitrary deduced from the topography and annotated in Table 9.6.

For some glaciers bathymetric data found in the literature was used to verify the grounding condition and to derive the subaqueous volume loss more precisely.

Upsala Glacier Naruse & Skvarca (2000) and Skvarca *et al.* (2002) published bathymetric profiles of the Brazo Upsala of Lago Argentino acquired in December 1998 and 1999 with an echo sounder. They reveal a very deep channel (up to 700 m) extending along the central part of Brazo Upsala. The channel of the western terminus of Upsala Glacier is approximately 3 km wide and more than 600 m deep at the position corresponding to the front in year 2000. The height above buoyancy, or ice thickness in excess of flotation is defined as $F = \left(h_f + h_w\right) - h_w \frac{\rho_w}{\rho_i}$ (Naruse & Skvarca, 2000), where h_f is the height above water of the front and h_w is the water depth. A negative value of F indicates likely floating at the central section of the terminus. For the year 2000 by taking $h_f = h_{a1} = 34$ m and $h_w = 630$ m a negative value of F is obtained meaning that the floating condition is very likely. Even for the year 2011, after a severe frontal retreat, taking $h_f = h_{a2} = 41$ m means that the floating condition is likely for water depths greater than $h_w = 400$ m, which is safe to assume true. In this case the estimated h_{b1} is used as subaqueous maximum thickness and the volume loss is estimated by using the actual bathymetry for the grounded margins, instead of a generic ellipse. A total volume change of -2.8 km^3 is derived.

Jorge Montt Glacier Rivera *et al.* (2012) performed extensive bathymetric mapping at the Baker fjord in front of Jorge Montt Glacier in February 2010, including a transversal profile at 100 m from the terminal ice cliff. The approximately 1.6 km wide, 3.45 km long stretch of channel underlying the 2000 - 2011 frontal retreat presents steep flanks and is quite deep, exceeding 300 m of water depth at the 2000 front, decreasing to 280 m upstream (2004 front) and reaching a minimum of 390 m at the 2010 front. Rivera *et al.* (2012) report that the terminus underwent the strongest retreat of approximately 6.5 km between 1990 and 1997. In this stretch the channel has the deepest average bathymetry (up to 370 m) and coincides with the timing of the most rapid ice acceleration and thinning. By computing the excess floatation at the 2010 front they report that the front is approaching (without reaching) its floating point because of the depth of the channel. For the current study the terminus is hence considered to be always grounded, particularly given the narrow fjord. By integrating the bathymetry published by Rivera *et al.* (2012) a subaqueous volume change of -0.68 km^3 is derived between February 2010 and May 2011 for a retreat distance of $d_r = 3.45$ km. The frontal positions and the ice loss above water are depicted in Figure 9.15.

Tyndall and Ameghino glaciers The subaqueous volume loss of the Tyndall and the Ameghino glaciers were obtained similarly, by using bathymetric profiles published by Raymond *et al.* (2000) and Stuefer (1999), respectively. The bathymetry of Lago Geikie reveals depths up to 330 m at the 2000 front, while Lago Ameghino displays a v-shaped bathymetric profile with depths up to 160 m at the 2000 front. They were considered both fully grounded on account of their (slightly) positive excess floatation. The derived volume changes are -0.59 km^3 for Tyndall and -0.05 km^3 for Ameghino.

All termini of SPI have been analysed, but only those with a significant areal or elevation change were included in Table 9.6. The estimated total subaqueous volume change of SPI amounts to -8.3 km^3, the volume change rate is equal to -0.73 km^3 a^{-1}. Given the very rough estimation these figures have a very high uncertainty, chosen arbitrary to be equal to ±30%. The estimated subaqueous ice volume change rate of -0.73 ± 0.22 km^3 a^{-1} leads to a negative sea level rise (SLR) contribution of -0.20 ± 0.06 μm a^{-1} having water approximately 10% less volume than ice. As a comparison, Willis *et al.* (2012a) estimated for SPI a total subaqueous volume loss rate of -1.0 ± 0.8 km^3 a^{-1}, although the estimation method is not explained.

The glaciers of NPI mostly terminate either on land or in very small and shallow proglacial lakes of recent formation. Only two glaciers have substantial calving: San Rafael, which is the only tidewater glacier and Leon (Harrison *et al.*, 2008), which terminates on a relatively deep lake. The contribution of subaqueous losses of this icefield is hence very limited. For this reason time was not invested to perform a similar estimation of the subaqueous volume loss in NPI.

9.5 Mass balance results

This section reports the results of the geodetic net mass balance of NPI and SPI obtained according to the procedure outlined in Section 9.2 along with the relative uncertainties described in Section 9.3. The DEMs and the elevation change maps used to compute the mass balance have been described in Chapter 7 and are useful to interpret the results. In particular the SRTM DEM is shown in Figure 7.5 and 7.7 and the elevation change rate map is shown in Figure 7.6 and 7.8, for NPI and SPI respectively. Figure 9.16 and 9.17 show the behaviour with respect to elevation (h_{SRTM}) of the main derived parameters: the hypsometry and the mean elevation, volume and mass change rates.

The hypsometry (or area-elevation distribution) is a general characteristic of a glacier or icefield (see Section 3.5), even if not a result describing temporal changes it is presented here for the entire NPI and SPI as it represents an important parameter for the mass balance derivation through the geodetic method. It is shown in Figure 9.16a and 9.17a, for NPI and SPI. It was derived from the SRTM DEM h_{SRTM}, which was chosen as reference surface for the mass balance, it hence reflects the status at February 2000 and elevations refer to the WGS84 ellipsoid (sea level corresponds approximately to 16 m in this region). The total glacier area A^{GL}, derived from the glacier mask discussed in Section 6.3, amounts to 12880.7 km^2 for SPI and 3867.0 km^2 for NPI. It represents the maximum glacial extension, corresponding to the status in February 2000 (at the time of the SRTM acquisition), with the exception of Pio XI, Trinidad, Calvo and HPS 34 glaciers in SPI which advanced in complex approximately 13.1 km^2 between February 2000 and February 2012. In the plots the portions of $A^{\mathrm{GL}}_b = A^{\mathrm{AV}}_b + A^{\mathrm{EX}}_b$ for each elevation bin b (20 m bins) which were surveyed (A^{AV}_b) and not surveyed (A^{EX}_b) with TanDEM-X data are marked in blue and red, respectively. The total unsurveyed area A^{EX} amounts to 497.8 km^2 (12.9% of A^{GL}) and 921.1 km^2 (7.2% of A^{GL}) for NPI and SPI, respectively. The spatial distribution of A^{EX} is depicted in white in Figure 7.6 and 7.8, for NPI and SPI respectively.

The two icefields have a similar area-elevation distribution, the largest part of the surface is occupied by the plateau located approximately above 1000 - 1100 m. In SPI most of the plateau is located below 2300 - 2400 m of altitude but the topography presents mountain ridges crossing the plateau north to south with elevations up to 3500 m. NPI presents higher mountains particularly in the north-west around Monte San Valentin (4058 m a.s.l). This region in particular and mountainous complexes in general proved to be difficult to unwrap (even with dual baseline PU) on both icefields driving up A^{EX}_b between 1500 and 4000 m. The topography of the icefields is better described in Section 5.1 and Section 5.2.

The elevation change rate $\mu_b^{\frac{\Delta h}{\Delta t}}$ with respect to the h_{SRTM} altitude is plotted for NPI and SPI in Figure 9.16b and 9.17b along with the bin area A^{GL}_b. The estimated error $E_b^{\frac{\Delta h}{\Delta t}}$ of $\mu_b^{\frac{\Delta h}{\Delta t}}$ is plotted for both icefields in Figure 9.13a. The lower elevation bins are dominated by the fronts of the tidewater glaciers of the western icefield margin. Between 0 and 20 m (first bin, $b = 1$) there is no coverage on NPI and a small area of 5.6 km^2 on SPI where $\mu_1^{\frac{\Delta h}{\Delta t}} = 8.04\ \mathrm{m\,a^{-1}}$ (out of the ordinate range in Figure 9.17b) reflects the elevation gain due to the frontal advance into the sea of Pio XI (mainly) and Calvo Glacier. With increasing altitude up to ~900 - 1000 m, $\mu_b^{\frac{\Delta h}{\Delta t}}$ becomes suddenly strongly negative because these elevation bins include the strong depletion of most of the glacier termini. Above 1000 m on the plateau $\mu_b^{\frac{\Delta h}{\Delta t}}$ are still negative ($-1.7\ \mathrm{m\,a^{-1}}$ on NPI, $-1.3\ \mathrm{m\,a^{-1}}$ on SPI at 1000 m) with slowly increasing trend indicating significant thinning on the bins featuring the largest areas A^{GL}_b. $\mu_b^{\frac{\Delta h}{\Delta t}}$ reaches zero at 2000 m for NPI and at 2500 m for SPI.

Above 2500 m estimates of $\mu_b^{\frac{\Delta h}{\Delta t}}$ are less reliable (particularly in NPI), as reflected by the error $E_b^{\frac{\Delta h}{\Delta t}}$ shown in Figure 9.13a, due to the relatively low number of samples n_b^{AV} they are based on (less than

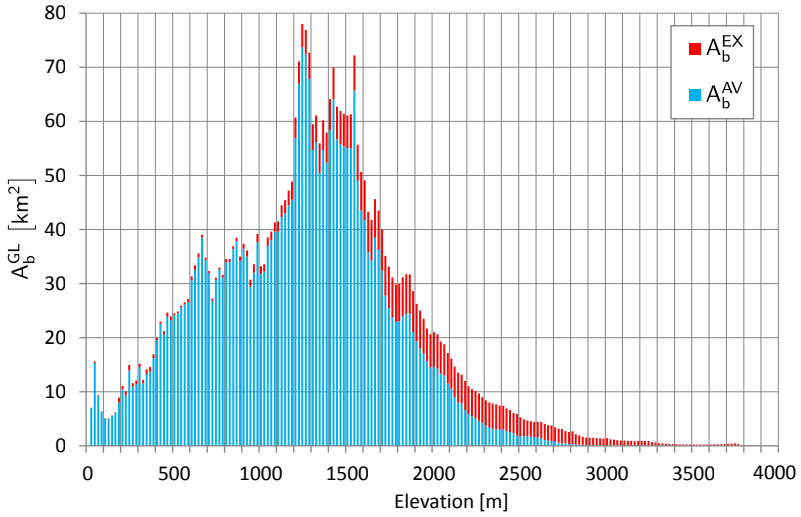

(a)

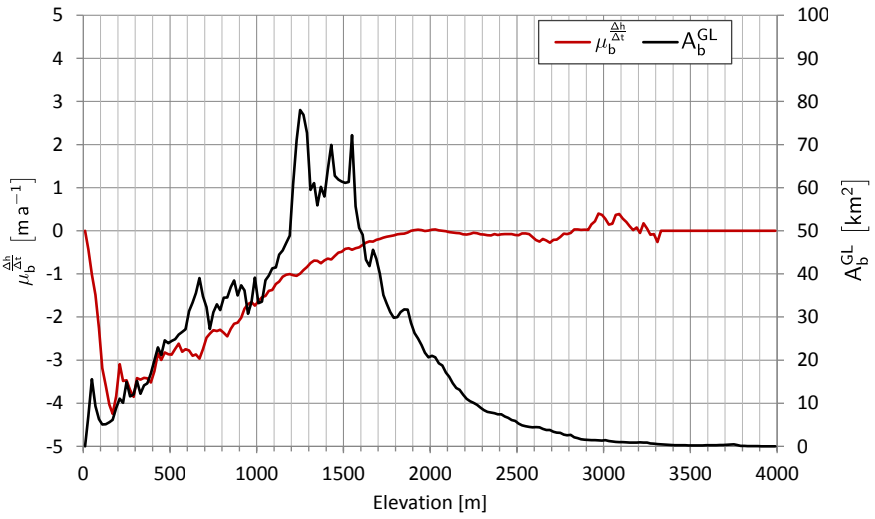

(b)

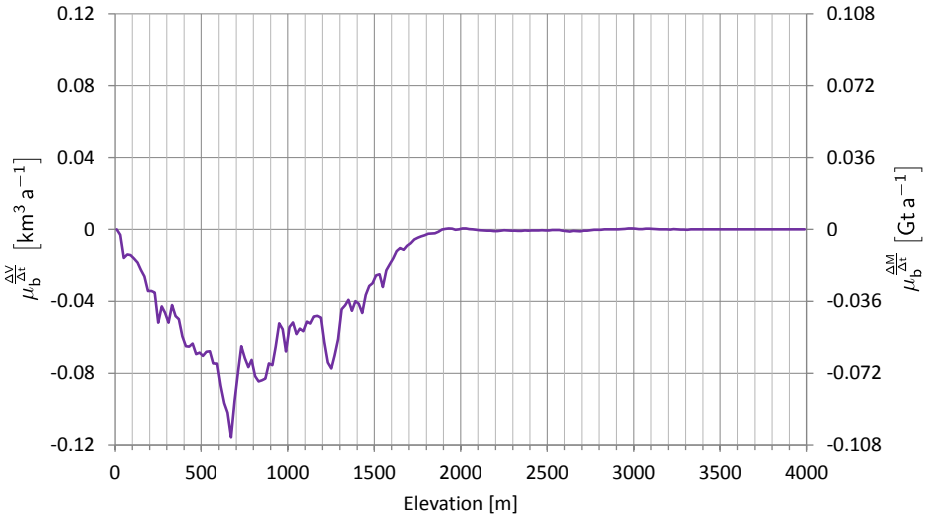

(c)

Figure 9.16 – NPI: estimated mass balance parameters with respect to elevation (height above ellipsoid), binned at at 20 m. (a) Hypsometry $A_b^{GL} = A_b^{AV} + A_b^{EX}$, distinguishing surveyed and unsurveyed area. (b) Hypsometry A_b^{GL} (black) and mean elevation change rate $\mu_b^{\frac{\Delta h}{\Delta t}}$ (red). (c) Mean volume change rate $\mu_b^{\frac{\Delta V}{\Delta t}}$ and mass change rate $\mu_b^{\frac{\Delta M}{\Delta t}}$.

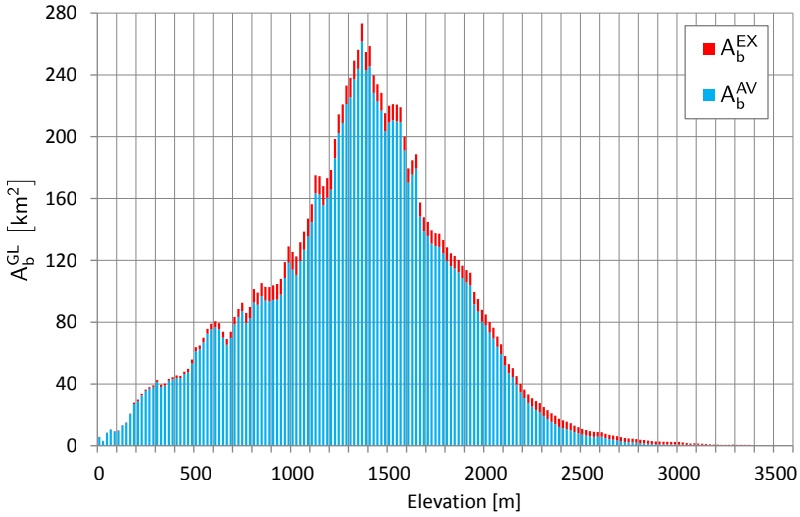

(a)

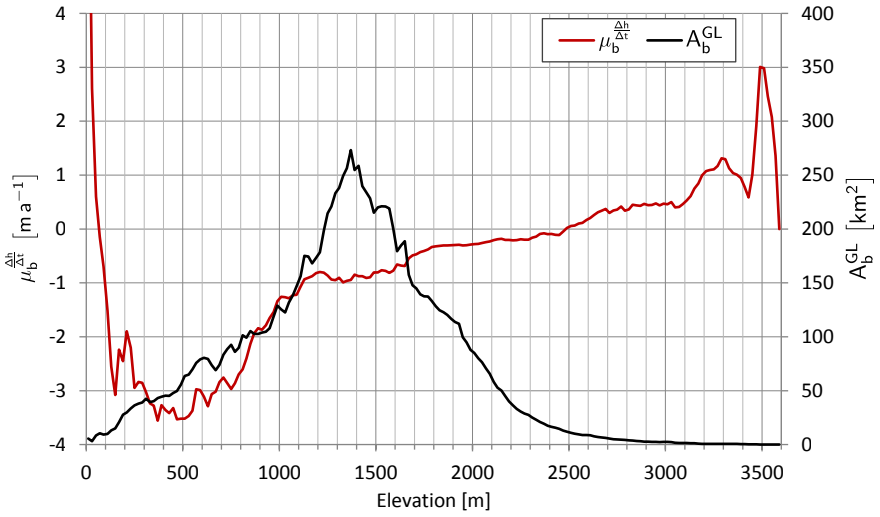

(b)

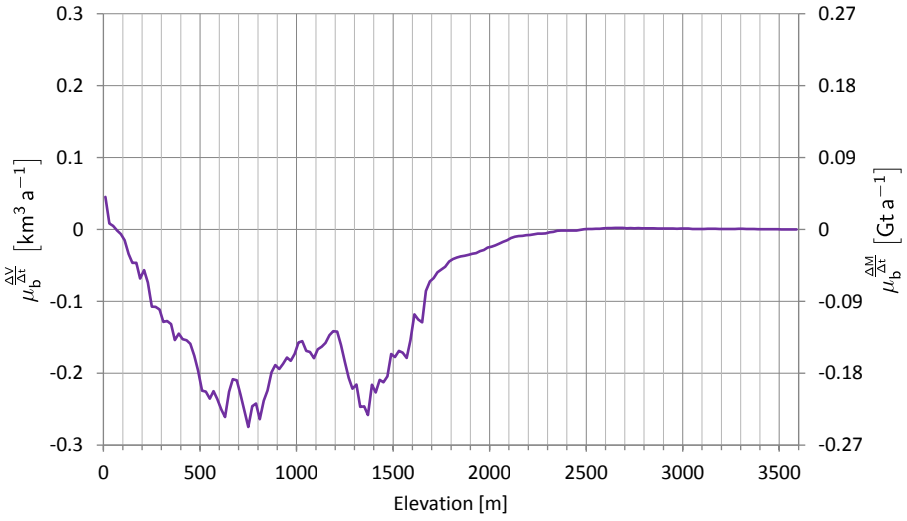

(c)

Figure 9.17 – SPI: estimated mass balance parameters with respect to elevation (height above ellipsoid), binned at 20 m. (a) Hypsometry $A_b^{GL} = A_b^{AV} + A_b^{EX}$, distinguishing surveyed and unsurveyed area, (b) Hypsometry A_b^{GL} (black) and mean elevation change rate $\mu_b^{\frac{\Delta h}{\Delta t}}$ (red), here $\mu_1^{\frac{\Delta h}{\Delta t}} = 8.04\ \mathrm{m\,a^{-1}}$ is out of the ordinate range. (c) Mean volume change rate $\mu_b^{\frac{\Delta V}{\Delta t}}$ and mass change rate $\mu_b^{\frac{\Delta M}{\Delta t}}$.

Table 9.7 – Geodetic mass balance results for NPI (2000 - 2014), SPI (2000 - 2011/'12) and the sum of both icefields. The values do not include subaqueous ice volume losses.

Region	$A^{\mathrm{GL}}\,[\mathrm{km}^2]$	$\mu^{\frac{\Delta V}{\Delta t}}\,[\mathrm{km}^3\,\mathrm{a}^{-1}]$	$\mu^{\frac{\Delta M}{\Delta t}}\,[\mathrm{Gt\,a}^{-1}]$ / $[\mathrm{km}^3\,\mathrm{w.e.\,a}^{-1}]$	$\mu^{\frac{\Delta h}{\Delta t}}\,[\mathrm{m\,a}^{-1}]$ and $[\mathrm{m\,w.e.\,a}^{-1}]$	SLR $[\mu\mathrm{m\,a}^{-1}]$
NPI	3867.0	-4.4008 ± 0.1290	-3.9607 ± 0.1381	-1.1380 ± 0.0334 -1.0242 ± 0.0357	10.9412 ± 0.3815
SPI	12880.7	-14.5949 ± 0.3746	-13.1354 ± 0.4186	-1.1331 ± 0.0291 -1.0198 ± 0.0325	36.2857 ± 1.1564
NPI+SPI	16747.7	-18.9957 ± 0.3962	-17.0961 ± 0.4408	-1.1342 ± 0.0237 -1.0208 ± 0.0263	47.2269 ± 1.2177

$11 \cdot 10^3$ for NPI and less than $60 \cdot 10^3$ for SPI). Given the small bin area their impact on the mass balance is negligible. The positive values of $\mu_b^{\frac{\Delta h}{\Delta t}}$ measured on SPI above 2500 m (on the mountain ranges) are likely biased by the different resolution of the DEMs. As shown in Section 9.3.1, $h_{\mathrm{TDM}} > h_{\mathrm{SRTM}}$ over mountain peaks, a bias which is not included in the estimated uncertainty $E_b^{\frac{\Delta h}{\Delta t}}$.

The volume change rate $\mu_b^{\frac{\Delta V}{\Delta t}}$ trend along altitude is obtained according to Eq. (9.21) by multiplying $\mu_b^{\frac{\Delta h}{\Delta t}}$ and A_b^{GL}. The mass change rate $\mu_b^{\frac{\Delta M}{\Delta t}}$ is obtained by multiplying $\mu_b^{\frac{\Delta V}{\Delta t}}$ by a constant ice density $\rho = 900\,\mathrm{kg\,m}^{-3}$ according to Eq. (9.23). $\mu_b^{\frac{\Delta V}{\Delta t}}$ and $\mu_b^{\frac{\Delta M}{\Delta t}}$ have thus the same behaviour and are shown in Figure 9.16c and 9.17c, for NPI and SPI respectively. Fast variations in these curves (particularly in NPI) are mainly driven by the shape of the hypsometry A_b^{GL}, acting as a weight of each value of the generally smoother $\mu_b^{\frac{\Delta h}{\Delta t}}$.

Between 0 m and 60 m $\mu_b^{\frac{\Delta V}{\Delta t}}$ and $\mu_b^{\frac{\Delta M}{\Delta t}}$ show positive values ($+0.05\,\mathrm{km}^3\,\mathrm{a}^{-1}$) in SPI dominated by the gains of Pio XI and other smaller glaciers and subsequently turn negative, this is not the case in NPI which has no positive values. Ice volume change rate drops quickly with increasing elevation reaching a local minimum around 700 m of altitude. On NPI it then shows an increasing trend and reaches the balanced state at 1900 m. On SPI it increases between 800 m and 1200 m, dropping again at 1400 m where A_b^{GL} reaches its maximum and $\mu_b^{\frac{\Delta h}{\Delta t}}$ is relatively stable, finally reaching a balanced state at 2400 m. The elevation interval featuring thinning and volume loss extends approximately 500 m more in SPI compared to NPI.

The results of the geodetic mass balance of NPI and SPI are shown in Table 9.7. The total volume change rate ($\mu^{\frac{\Delta V}{\Delta t}}$) and mass change rate ($\mu^{\frac{\Delta M}{\Delta t}}$) for each icefield are obtained by summing the contributions of all altitude bins (using 20 m bins). Their errors have been reported in Table 9.5. $\mu^{\frac{\Delta M}{\Delta t}}$ is the so-called glacier-wide mass balance rate $\dot{B}$ stated in $[\mathrm{Gt\,a}^{-1}]$ or $[\mathrm{km}^3\,\mathrm{w.e.\,a}^{-1}]$ (Section 3.5). The average elevation change rate is obtained as $\mu^{\frac{\Delta h}{\Delta t}} = \mu^{\frac{\Delta V}{\Delta t}} / A^{\mathrm{GL}}$, it corresponds to the average specific mass balance rate $\overline{\dot{b}}$ and is stated in both ice equivalent $[\mathrm{m\,a}^{-1}]$ and water equivalent height $[\mathrm{m\,w.e.\,a}^{-1}]$. The sea level rise (SLR) contribution is also reported. Their error intervals are obtained from those of the preceding terms.

As shown in Table 9.7, the volume and mass change rates of the two largest Patagonian icefields indicate a very strong downwasting trend, with a total volume change rate of $-19.0 \pm 0.40\,\mathrm{km}^3\,\mathrm{a}^{-1}$, and a mass change rate of $-17.1 \pm 0.44\,\mathrm{Gt\,a}^{-1}$. Interestingly both icefields underwent approximately the same average thinning rate of $-1.13\,\mathrm{m\,a}^{-1}$ ($-1.02\,\mathrm{m\,w.e.\,a}^{-1}$), this is not unexpected as it suggests similar melting driving factors and climatological conditions. It must be noted that the observation period is longer for NPI, likely inflating its results compared to SPI, given the accelerating thinning trend of the Patagonian icefields generally reported in the literature. In Section 9.4 a subaqueous ice volume change rate of $-0.73 \pm 0.22\,\mathrm{km}^3\,\mathrm{a}^{-1}$ was estimated for SPI, leading to a negative SLR contribution of $-0.20 \pm 0.06\,\mu\mathrm{m\,a}^{-1}$. The subaqueous loss is reported separately because of the high uncertainty and for ease of comparison with NPI (where this contribution is limited and was not estimated) and with results published in the literature.

Table 9.8 – Published geodetic mass balance results for NPI and SPI, subaqueous losses are not included. Only the volume change rate $\mu^{\frac{\Delta V}{\Delta t}}$ is reported since the ice density assumption can vary. The area-averaged thinning rates $\mu^{\frac{\Delta h}{\Delta t}}$ in $\left[\mathrm{m\,a^{-1}}\right]$ is computed dividing $\mu^{\frac{\Delta V}{\Delta t}}$ by the glacier area A^{GL}. Its variation with respect to the results obtained in the current study (Table 9.7) is provided in the last column. (*) NPI area derived as sum of all glaciers in Table 1 of Willis *et al.* (2012b).

Reference	Region	Observ. period	$A^{\mathrm{GL}}\left[\mathrm{km^2}\right]$	$\mu^{\frac{\Delta V}{\Delta t}}\left[\mathrm{km^3\,a^{-1}}\right]$	$\mu^{\frac{\Delta h}{\Delta t}}\left[\mathrm{m\,a^{-1}}\right]$	$\mu^{\frac{\Delta h}{\Delta t}}$ variat.
Rignot *et al.* (2003)	NPI	1968/'75 - 2000	4200	-3.2 ± 0.4	-0.76 ± 0.10	−33.0%
Rignot *et al.* (2003)	SPI	1968/'75 - 2000	13000	-13.5 ± 0.8	-1.04 ± 0.06	−8.3%
Rignot *et al.* (2003)	SPI	1995 - 2000	13000	-38.7 ± 4.4	-2.98 ± 0.34	+162.7%
Willis *et al.* (2012b)	NPI	2000 - 2011	3871*	-4.06 ± 0.11	-1.05 ± 0.03	−7.8%
Willis *et al.* (2012a)	NPI	2000 - 2011	3871*	-4.9 ± 0.3	-1.27 ± 0.08	+11.2%
Willis *et al.* (2012a)	SPI	2000 - 2012	12118	-21.2 ± 0.5	-1.75 ± 0.04	+54.4%

It must be noted that due to time constraints, the disjoint mass balance of each glacier basin has not been computed here. Nevertheless the data are available and the procedure for mass balance and error estimation defined in this chapter can be applied without changes just by using a specific glacier outline. As an example the geodetic mass balance of Jorge Montt Glacier, the most dynamic of both Patagonian icefields was derived from the available data (observation period 2000 - 2011) and additionally for a recent observation period: 2011 - 2014. The results are reported in Chapter 10. A significant acceleration in the mass loss rate has been detected between the two observation periods (see Figure 10.2 and Table 10.2).

It is useful to compare the geodetic mass balance results of NPI and SPI obtained here with those of other authors found in the literature, those have been presented in Section 9.1 and are summarized in Table 9.8. Here the volume change rate $\mu^{\frac{\Delta V}{\Delta t}}$ and the area-averaged thinning rate $\mu^{\frac{\Delta h}{\Delta t}}$ are reported, the latter being more useful for a comparison since it does not depend on the area used, which can vary. The variation in average thinning rate $\mu^{\frac{\Delta h}{\Delta t}}$ with respect to the results obtained in this work (Table 9.7) is reported in the last column as percentage. The mass change rate is omitted since the ice density assumed may vary (particularly in Willis *et al.* (2012b)). It must be noted that the literature studies reported here do not assign an error contribution neither to the glacier area nor to the ice density, contrary to the results obtained in this work, where a 2% error was assigned to the glacier area and a 1.9% error to the ice density.

The 1968/'75 - 2000 mass balance of Rignot *et al.* (2003) (see also Section 9.1) is not really directly comparable with the observation period of this work, it is nevertheless useful to understand if a possible trend can be found. Their estimates are slightly lower than those achieved here, in fact an increasing trend is to be expected. The results of Rignot *et al.* (2003) involve heavy extrapolation on SPI where the unsurveyed area A^{EX} amounts to 37% of the reported total area. The additional results of Rignot *et al.* (2003) for the period 1995 - 2000 have a closer observation period to that of the current work. Unfortunately their $\mu^{\frac{\Delta V}{\Delta t}}$ of $-38.7 \pm 4.4\ \mathrm{km^3\,a^{-1}}$ appears to be strongly overestimated even at the lower bound of its error interval. Simply comparing it to the 1968/'75 - 2000 estimate found in the same publication makes this figure unlikely large. Their result for 1995 - 2000, which is often referenced in the literature (for instance corroborating gravimetric mass balances, see below) is hence considered not reliable.

The first NPI mass balance published by Willis *et al.* (2012b) obtained from DEMs acquired from 2000 to 2011 is slightly lower than the result found in this study (−7.8% on the average elevation change rate $\mu^{\frac{\Delta h}{\Delta t}}$), the less recent observation period might explain the lower value. The glacier area they used is also similar to the one used in this work. They revise this result in Willis *et al.* (2012a) by applying a +2 m correction to the SRTM C-band DEM to account for signal penetration (they also apply a new spatial averaging and a new ice density of $900\ \mathrm{kg\,m^{-3}}$, see Section 9.1), leading to an increase in volume change rate of 20.7%. The revised average elevation change rate $\mu^{\frac{\Delta h}{\Delta t}}$ is 11.2% higher than the one achieved in the this study (Table 9.8).

The constant correction for signal penetration applied by Willis *et al.* (2012a) on the entire icefields

does not seem very reliable. Firstly, on the rough glacier termini no significant radar signal penetration is to be expected in any season because of the prevalence of surface scattering. Secondly, the snow and firn on the smoother plateau has a good probability of being wet in summer in this region, at least up to a certain elevation, excluding the risk of signal penetration. Despite this likelihood, in this work the backscattering coefficient of both SRTM C-band acquisitions and the TanDEM-X acquisitions were analysed along with concurrent meteorological data to assess the condition of the snow and the possibility of signal penetration (Chapter 8). It was concluded that no signal penetration is likely in the SRTM DEM even on the plateau. According to Willis *et al.* (2012a), their +2 m correction contributes to approximately 10% of their thinning rate for the period 2000 - 2012. Reducing their volume change rate by a 10% would give a result very similar to the one obtained in this study for NPI.

But Willis *et al.* (2012a) focus mainly on the mass balance of SPI, here they apply the same +2 m correction for radar signal penetration. They obtain a final volume change rate of -21.2 ± 0.5 km^3 a^{-1} (excluding subaqueous ice changes which they estimate to be -1.0 ± 0.8 km^3 a^{-1}), a much larger figure than the one derived in this work for the same observation period. In fact their area-averaged elevation change rate is 54.4% higher (see Table 9.8). Even removing a 10% contribution due to the radar signal penetration correction from their results the volume change rate is still high: -19.1 km^3 a^{-1} (+30.9% compared to this study) and the area-averaged elevation change rate becomes -1.57 m a^{-1} (+38.6% compared to this study). Besides the erroneous correction for the SRTM signal penetration bias, a clear explanation for the significantly higher SPI mass balance by Willis *et al.* (2012a) is difficult to conceive, since the same procedure on the NPI led to results which are more in line to those obtained in this study. In conclusion the SPI mass balance provided by Willis *et al.* (2012a) is considered too high.

The combined NPI+SPI ice mass loss rate of -23.5 ± 0.5 Gt a^{-1} (excluding subaqueous ice losses) presented by Willis *et al.* (2012a) is on the other hand closer to GRACE results found in the literature and summarized in Section 5.6. Chen *et al.* (2007) report a loss rate of -25.1 ± 9.9 Gt a^{-1} (2001 - 2006) and Ivins *et al.* (2011) -26 ± 6 Gt a^{-1} (2003 - 2009) for NPI+SPI. More recently Jacob *et al.* (2012) reported a loss rate -23 ± 9 Gt a^{-1} (2003 - 2010) for Patagonia (although the geographical coverage is not clearly stated). All these gravimetric results are much larger (+35 - +53%) than the mass loss rate obtained in this work, which amounts to -17.1 ± 0.44 Gt a^{-1} (plus -0.66 ± 0.20 Gt a^{-1} of subaqueous contribution for SPI), but at least two of the GRACE results cover this value with their stated uncertainty interval.

GRACE measurements are affected indiscriminately by mass changes of superficial ice/snow/water, ground-stored water and changes of the solid Earth (see Section 3.5.1). To derive the mass balance, as Jacob *et al.* (2012) reports, models must be applied to estimate and remove mass change contributions due to: (a) hydrology, (b) glacial isostatic adjustment, (c) ongoing solid Earth deformation from the Little Ice Age loading. Jacob *et al.* (2012) report for Patagonia a mass loss trend measured by GRACE of -13 ± 7 Gt a^{-1} to which they add the following corrections: (a) 0 ± 3 Gt a^{-1} , (b) -2 ± 1 Gt a^{-1} and (c) -9 ± 5 Gt a^{-1}. The LIA loading correction is particularly high for this region because of the viscosity of the mantel and was modelled by Ivins & James (2004) (cf. Section 5.6).

As evident from these figures, the uncertainty associated to the GRACE inversion and to the model-based corrections is quite large. Some biases might affect the correction models leading to overestimation. Furthermore the spatial resolution of GRACE is limited, the icefields are isolated using very coarse user-defined regions (known as “mascons”) but mass changes from areas surrounding the actual icefields may also be also included (“leakage”). The problems linked to the gravimetric mass balance are discussed by Zwally & Giovinetto (2011) in the case of Antarctica, where strong variability between different mass balance studies has emerged.

In conclusion, the geodetic net mass balance derived in this study for NPI and SPI is often in disagreement with results presented in the literature for the same region for overlapping or adjacent observation periods. Gravimetry results are proved to overestimate significantly ice mass losses in Patagonia, the results are generally more sensible at the lower end of the stated error range. Since these methods have been applied to quantify mass losses at a global scale (Jacob *et al.*, 2012; Gardner *et al.*, 2013), caution is suggested when using and interpreting these results, for instance for climatological research.

The comparison of the obtained mass balance with other geodetic results led to diversified conclusions. The smaller NPI tends have better agreement, although some significant overestimation can be caused by wrong systematic correction of non-existent biases. The vast SPI is subject to a much larger variability of the results. Literature results tend to overestimate the mass balance, even significantly. The 1968 - 2000 result of Rignot *et al.* (2003) is reasonable but a possibility of overestimation cannot be excluded when compared to the results obtained here. Their results for 1995 - 2000 are overestimated beyond any physical or logical explanation. The SPI mass balance of Willis *et al.* (2012a) has been proved to be highly overestimated.

The results presented here will hopefully provide an accurate estimate of a fundamental parameter such as the mass balance for this climate-sensitive region, often used within global climatological studies. Furthermore the results will help reassess estimates found in the literature allowing an improvement of the methods for geodetic mass balance derivation. The results will also contribute to the assessment and tuning of the gravimetry inversions and allow to improve the correction models involved.

Chapter 10

Multitemporal geodetic mass balance of the Jorge Montt Glacier

This short chapter reports in a concise manner the results of a multitemporal geodetic mass balance computation performed on the Jorge Montt glacier, the most rapidly thinning glacier of the Patagonian icefields. The applied procedure is the one described extensively in Chapter 7 and 9. Three bistatic interferometric DEMs were available:

- SRTM C-band at 1 arcsec (∼30 m) with reference date: 17.02.2000. In contrast to the DEM used for the entire icefields which was the 3 arcsec version (Section 6.1.2) the recently available full-resolution SRTM C-band DEM version 3[1] was used (cell: S49E074). The original DEM values have been converted to the WGS84 ellipsoidal height and oversampled to 0.2 arcsec in x and y to fit the TanDEM-X Raw DEMs. This elevation source is here referred to as h_{2000}.
- TanDEM-X Raw DEM of 9.5.2011. This experimental acquisition was also used to cover the Jorge Montt Glacier in the SPI mosaic (Table 7.5). The raw data was processed again with the newest ITP release obtaining a new version of the Raw DEM at 0.2 arcsec, its parameters are summarized in Table 10.1. This elevation source is here referred to as h_{2011}.
- TanDEM-X Raw DEM of 21.4.2014. A new experimental acquisition processed with the newest ITP release obtaining a Raw DEM at 0.2 arcsec, its parameters are summarized in Table 10.1. This elevation source is here referred to as h_{2014}.

The two TanDEM-X acquisitions were processed with single baseline phase unwrapping which gave good results on most of the glacier surface and on surrounding off-glacier regions. Although it was not strictly necessary, dual baseline phase unwrapping was tested, but it encountered problems on the glacier snout because the strong thinning between the master and the supporting acquisition. The single baseline version of both Raw DEMs was hence chosen and the phase unwrapping errors were masked out following the procedure described in Section 7.1. A small sector in the south-western part of the glacier basin is not covered by the two TanDEM-X Raw DEMs (see Figure 10.1a and 10.1b). In order to have a reference elevation for year 2011 to obtain the hypsometry of the glacier, the voids were filled with the calibrated SPI TanDEM-X mosaic (Table 7.5) which relies on additional Raw DEMs in this region.

A careful DEM calibration phase was conducted according to the procedure described in Section 7.2 by using the SRTM DEM as reference to coregister vertically and horizontally the two TanDEM-X Raw DEMs. Eight calibration regions (CRs) were selected on the three DEMs with a total area of 9.55 km^2. Four further CRs with a total area of 7.87 km^2 were selected on the SRTM and the 2014 Raw DEM only, since they were affected by phase unwrapping errors in the 2011 Raw DEM. The statistics extracted on each CR are not reported here for brevity, the final correction δh_{bias} amounted to −1.2 m for the 2011 Raw DEM (confirming the correction found in Table 7.3) and +2.7 m for the 2014 Raw DEM.

[1] DOI: 10.5067/MEaSUREs/SRTM/SRTMGL1.003

Table 10.1 – Newly processed TanDEM-X Raw DEMs over Jorge Montt Glacier.

DT AID	1203015*	1027766*
DT scene index	01	01
PU method	1B	1B
Acquisition date	2014.04.21	2011.05.09
Scene start time (UTC)	23:45:46.3	23:45:31.3
Scene length [sec.]	8.4	7.8
Rel. orbit / direction	89 / A	89 / A
Beam	A1 020	A1 020
Look angle [°]	33.81	33.71
Effective baseline [m]	78.60	44.33
HoA [m]	-69.64	121.93
Average coherence	0.69	0.67
Posting (x/y) [arcsec]	0.2 / 0.2	0.2 / 0.2

All three possible combinations of elevation change maps were derived and the corresponding mass balances computed. For the sake of brevity only the subsequent differences $\Delta h_{2011-2000} = h_{2011} - h_{2000}$ and $\Delta h_{2014-2011} = h_{2014} - h_{2011}$ are discussed here in order to appreciate the trends of thinning and mass loss. The corresponding elevation change rate maps $\Delta h/\Delta t$ were obtained using Δt of 11.2 and 3.0 years, respectively, and are shown in Figure 10.1.

A much higher thinning rate can be observed in the $(\Delta h/\Delta t)_{2014-2011}$ map compared to the $(\Delta h/\Delta t)_{2011-2000}$ map on the terminus of Jorge Montt Glacier and on its lateral branches indicating a clear acceleration in thinning between the two epochs. Thinning appears to be accelerating even in the upper part of the glacier basin in a wide channel between approximately 600 m and 1500 m. To aid the interpretation of the elevation difference maps a longitudinal profile of $\Delta h/\Delta t$ is plotted in Figure 10.1c along the footprints shown in Figure 10.1a and 10.1b. The acceleration on the thinning between the two observation periods is clear, a difference of $\sim$7 m a^{-1} is found on the entire main terminus between the two profiles, the trend is less pronounced but still significant at higher altitudes on the plateau.

The glacier outlines were adapted manually to the maximum glacier extension for each of the two epochs (corresponding to year 2000 and 2011). For year 2000 the total glacier area A^{GL} amounts to 489.6 km^2 of which the surveyed area A^{AV} amounts to 463.6 (94.69% of A^{GL}). For year 2011 the total glacier area A^{GL} amounts to 470.9 km^2 of which the surveyed area A^{AV} amounts to 435.3 (92.44% of A^{GL}). A frontal retreat of 2.6 km (surface loss 5.8 km^2) was registered between February 2000 and May 2011 and of 1.1 km (surface loss 1.9 km^2) between May 2011 and April 2014.

The mass balance of the glacier was derived following the procedure described in Section 9.2. The reference surface was chosen to correspond to the older of the two DEMs within each observation period (cf. Section 3.5), the derived hypsometry plots A_b^{GL} are shown in Figure 10.2a. A shift in the area elevation distribution towards lower altitudes is noticeable between the A_b^{GL} of 2000 and A_b^{GL} of 2011. The elevation change rate $\mu_b^{\frac{\Delta h}{\Delta t}}$ behaviour with respect to altitude is also shown in Figure 10.2a for both observation periods. A very high increase in thinning can be noticed al all elevations. The resulting volume change rate $\mu_b^{\frac{\Delta V}{\Delta t}}$ and mass change rate $\mu_b^{\frac{\Delta M}{\Delta t}}$ behaviour with respect to altitude are shown in Figure 10.2b. An increased ice loss is measured in the 2011 - 2014 period with respect to the 2000 - 2011 period. The volume loss at altitudes ranging between 730 m and 1060 m is higher in the 2000 - 2011 observation period because the reference surface is not the same, h_{2011} shifted significantly towards lower elevations in 11 years because of the thinning phenomenon.

The results of the geodetic mass balance of Jorge Montt glacier for all three observation periods are reported in Table 10.2. In the 2011 - 2014 observation period a mass balance of -2.6 Gt a^{-1} is found, with an extreme increase of about 50% compared to the 2000 - 2011 period. The error budget of these mass balances is not reported here, nevertheless the increased accuracy of the DEM coregistration step allows to reduce the related systematic error $\mathrm{SE}_d^{\mathrm{reg}}$ with respect to the scene S1 of the mass balance

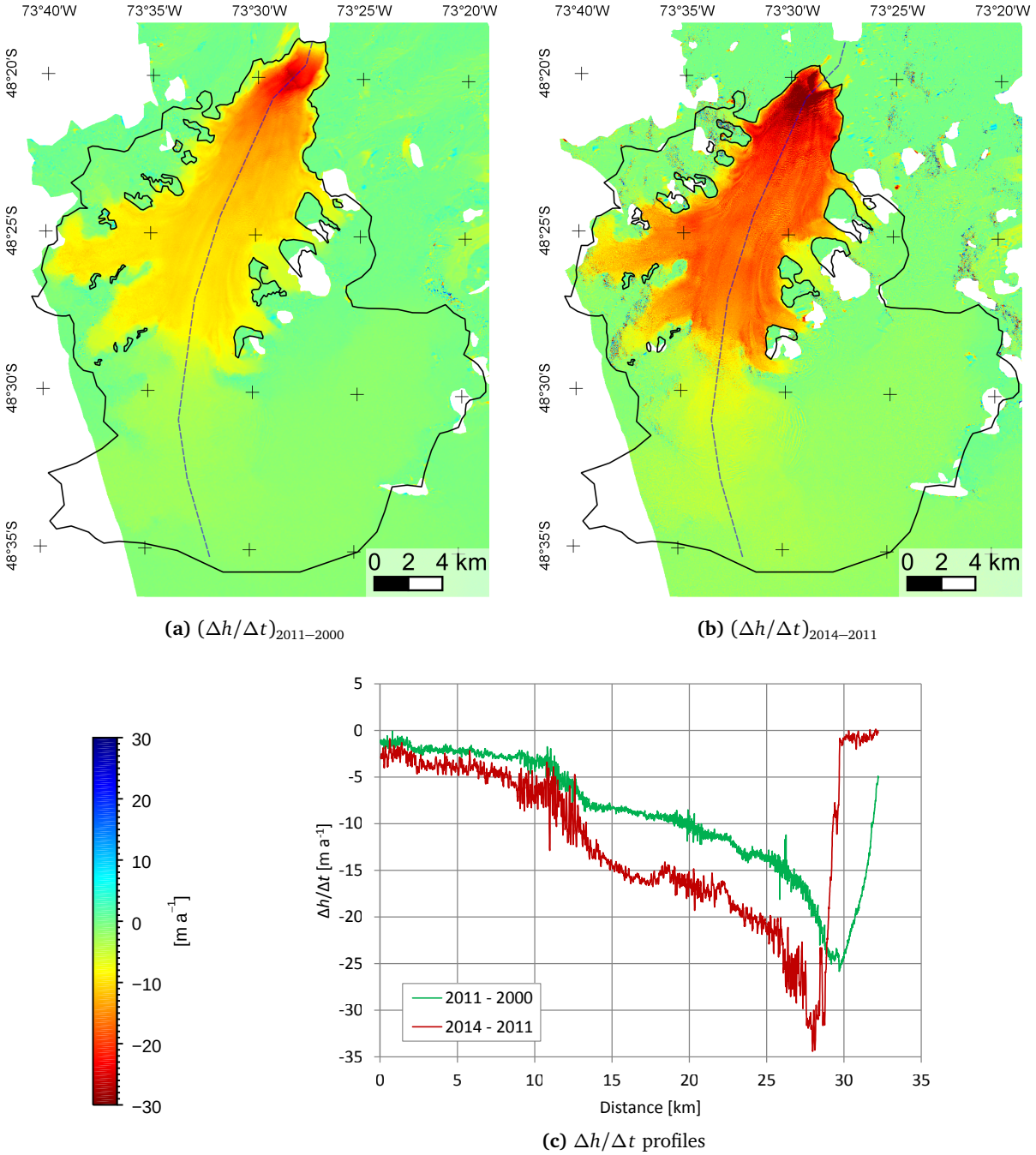

(a) $(\Delta h/\Delta t)_{2011-2000}$

(b) $(\Delta h/\Delta t)_{2014-2011}$

(c) $\Delta h/\Delta t$ profiles

Figure 10.1 – Multitemporal elevation change rate maps of Jorge Montt Glacier (SPI) and extracted longitudinal profile.

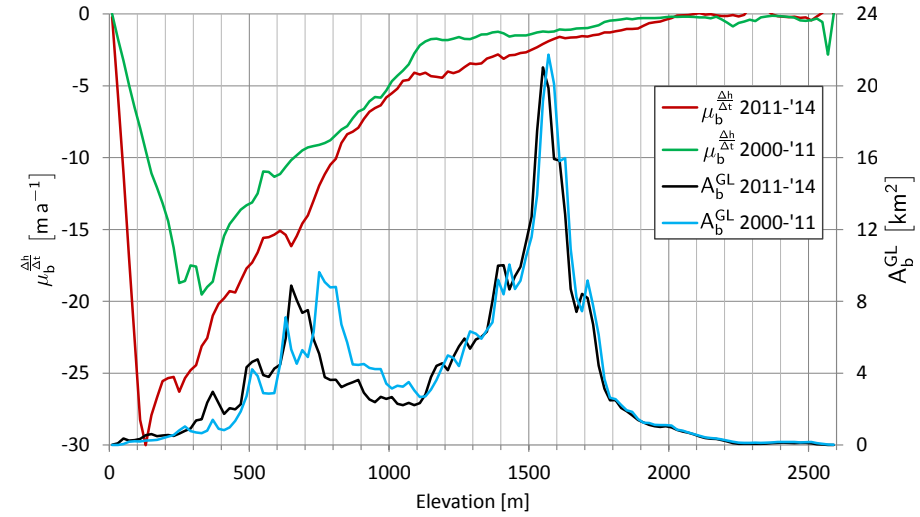

(a)

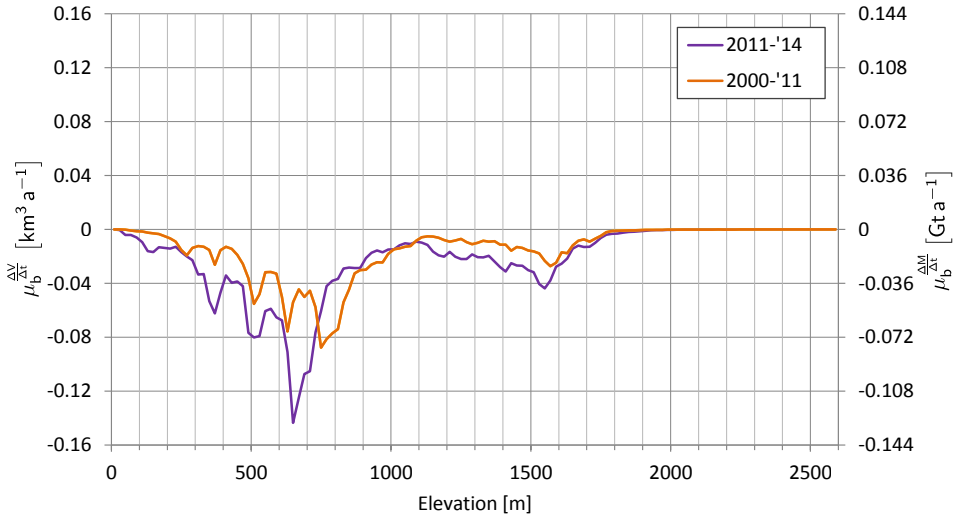

(b)

Figure 10.2 – Jorge Montt Glacier (SPI): estimated mass balance parameters with respect to elevation (height above ellipsoid), binned at at 20 m for two observation periods: 2000 - 2011 and 2011 - 2014. (a) Hypsometry $A_b^{\mathrm{GL}} = A_b^{\mathrm{AV}} + A_b^{\mathrm{EX}}$ and mean elevation change rate $\mu_b^{\frac{\Delta h}{\Delta t}}$. (b) Mean volume change rate $\mu_b^{\frac{\Delta V}{\Delta t}}$ and mass change rate $\mu_b^{\frac{\Delta M}{\Delta t}}$.

Table 10.2 – Geodetic mass balance results for Jorge Montt Glacier for three observation periods: 2000 - 2011, 2011 - 2014 and 2000 - 2014. The values do not include subaqueous ice volume losses.

Period	A^{GL} $[\mathrm{km}^2]$	$\mu^{\frac{\Delta V}{\Delta t}}$ $[\mathrm{km}^3\,\mathrm{a}^{-1}]$	$\mu^{\frac{\Delta M}{\Delta t}}$ $[\mathrm{Gt\,a}^{-1}]$ / $[\mathrm{km}^3\,\mathrm{w.e.\,a}^{-1}]$	$\mu^{\frac{\Delta h}{\Delta t}}$ $[\mathrm{m\,a}^{-1}]$ and $[\mathrm{m\,w.e.\,a}^{-1}]$	SLR $[\mu\mathrm{m\,a}^{-1}]$
2000 - 2011	489.59	−1.9140	−1.7226	−3.9094 −3.5185	4.7586
2011 - 2014	470.90	−2.8766	−2.5889	−6.1087 −5.4978	7.1517
2000 - 2014	489.59	−2.0925	−1.8833	−4.2741 −3.8467	5.2025

of SPI (Table 7.3). This is particularly true for the 2011 - 2014 period because of the higher spatial resolution and relative height accuracy of the TanDEM-X DEMs. However for this period all Δh errors are divided by a Δt of 3.0 years instead of 11.2 years. The analysis of the backscattering coefficient for all three DEMs appears do discard the possibility of radar signal penetration and consequent height bias. Thus the other systematic error $\varepsilon_d^{\mathrm{sp}}$, describing seasonal variations and signal penetration is the same given for S1 in Table 9.4 for the 2000 - 2011 period. For the 2011 - 2014 period it must be scaled to $\Delta t = 3.0$ years.

A comparison with the geodetic mass balance results of the entire Patagonian icefields (Table 9.7) highlights the tremendous contribution of the Jorge Montt Glacier (Table 10.2) to the mass balance of SPI (13.1%) for the same observation period (2000 - 2011). The estimated mass change rate of this glacier alone was equal to 47.5% of that of the entire NPI (which is eight times larger) for the same observation period (2000 - 2014).

The availability of two recently acquired TanDEM-X DEMs allows to derive an up-to-date mass balance and to derive a temporal trend. This information is crucial for the study of such a dynamic glacier and of the Patagonian icefields. The mass balance of Jorge Montt Glacier for the period 2011 - 2014 shows how fast can the thinning trend vary and renders obsolete the 2000 - 2011 mass balance values. It must be pointed out that the Jorge Montt Glacier represents a particularly extreme case, displaying already in the period 2000 - 2011 much higher thinning rates than the other glaciers of SPI and NPI (Section 7.4). Its accelerating frontal retreat has also been recently documented by Rivera *et al.* (2012). The thinning and mass balance trends found here for Jorge Montt Glacier cannot certainly be extrapolated to other glaciers of the Patagonian icefields, nevertheless they suggests that an acceleration of the elevation change rates in recent years is possible and even on other glaciers. The results unequivocally highlight the need for repeated and updated observations of dynamic glaciers.

Chapter 11

Glacier surface velocity

This chapter describes the processing chain set up at DLR IMF to compute glacier surface velocities from a large amount of high resolution TerraSAR-X repeat pass images allowing to cover wide regions or long time series of acquisitions. Section 11.1 presents the literature concerning the derivation of surface velocities with remote sensing data, with particular focus on SAR data. Section 11.2 outlines the objectives of the processing chain, describes the different TerraSAR-X acquisition modes and datasets and offers an evaluation of their suitability for the objective at hand. In Section 11.3 the processing chain is described. Section 11.4 deals with the criticalities and the accuracy of the estimated surface velocity. Finally surface velocity maps are presented in Section 11.5, with scope restricted to the Patagonian icefields and Antarctica where most of the investigations were conducted.

11.1 State of the art

Over the last two decades repeat pass SAR interferometry (InSAR) has provided spatially extensive measurement of glacier flow velocity. The principles of InSAR are discussed in Section 2.2: this technique allows to retrieve the displacement in the radar line of sight with very high accuracy using the phase of the signal. To separate the topographic phase from the phase due to the displacement an external DEM can be used.

Some limitations affect the repeat pass InSAR technique for glacier flow velocity estimation. (1) The measurements have a relative nature, a reference point with known displacement must be used as reference. (2) Only the displacement in the line of sight (slant range) is measured, to obtain a bi-dimensional flow field interferograms from crossing orbits must be combined. (3) The interferogram phase is affected by secondary phenomena which couple with the ice motion, for instance ice floatation on water or atmospheric perturbations. (4) The measurements are sensitive to temporal decorrelation of the interferometric phase (cf. Section 2.2.2), which can be caused by changes on the ground between acquisitions leading to a redistribution of the elementary scatterers within the resolution cell. Volumetric decorrelation in dry ice and snow is also possible.

The InSAR technique has been applied extensively to measure glacier flow velocities in different regions and with data from different sensors at varying wavelengths, among others by Goldstein *et al.* (1993); Joughin *et al.* (1995); Kwok & Fahnestock (1996); Rignot & Macayeal (1998); Lang *et al.* (2004); Rignot (2008). It has been applied to some glaciers of the NPI and SPI using data from the Spaceborne Imaging radar C (SIR-C) at both C-band and L-band by Rignot *et al.* (1996); Rott *et al.* (1998); Michel & Rignot (1999); Forster *et al.* (1999) .

The combination of more interferograms from ascending and descending orbits allows the retrieval of the two-dimensional motion field which can be projected on the surface of a DEM to obtain an estimate of the 3D velocity, as has been shown by Mohr *et al.* (1998); Joughin *et al.* (1998); Mattar *et al.* (1998). This estimate can be erroneous in case of dynamic instabilities, at least three observations with different line of sight are needed for a true 3D motion field. High resolution SAR data, from sensors such as TerraSAR-X and the airborne Experimental SAR (E-SAR), have also recently been used, among others by Vasile *et al.* (2008); Prats *et al.* (2009). Stacking of interferograms for the reduction

of rapidly varying signals such as tides, atmosphere and noise has been explored by McMillan *et al.* (2012), leading to an uncertainty on the velocity estimate of ~6 cm d^{-1}.

In order to overcome the stringent InSAR limitation of measuring only the movement parallel to the line of sight a technique developed for interferometric coregistration (Scheiber & Moreira, 2000) can be used, this is known as spectral diversity, split-bandwidth interferometry, delta-k or multiple aperture interferometry (MAI). This technique allows to retrieve the shifts in azimuth and range directions by comparing interferograms generated with different sub-bands (looks). It can hence substitute the usual cross-correlation-based coregistration, being generally more accurate and computationally efficient (Bamler & Eineder, 2005) since it does not require interpolation. Like InSAR it requires high coherence of the signal. It is less accurate than InSAR, being the uncertainty linked to the resolution of the sensor and not to the wavelength. Since the flow field is measured in two directions it is possible to estimate a three-dimensional displacement field using a single pair of SAR images and a parallel flow assumption (using an external DEM) or retrieve a true 3D velocity using two pairs of images from different geometries (Bechor & Zebker, 2006; Jung *et al.*, 2009; Erten *et al.*, 2010). Multiple aperture interferometry has been applied for the estimation of glacier surface velocity among others by Gourmelen *et al.* (2011).

The offset tracking technique allows to obtain the two dimensional displacements from a pair of SAR or optical images by computing the cross-correlation function between patches on the master and slave images. For SAR data, the offset tracking method can be based on the coherent cross-correlation (often defined speckle tracking), which offers higher accuracy but higher sensitivity to decorrelation or on the incoherent cross-correlation, which ignores the phase, leading to lower accuracy but increased robustness (Bamler & Eineder, 2005). In this case this technique is also known as amplitude or intensity tracking or feature tracking. The incoherent speckle pattern in the amplitude image can also be tracked with this technique allowing to measure 2D absolute shifts even where speckle coherence is not preserved (for instance because of flow, snowfall, wind-induced snow redistribution), at the cost of lower accuracy (especially for incoherent cross-correlation) compared to multiple aperture interferometry, and clearly to InSAR. The new generation of SAR sensors (such as TerraSAR-X, COSMO-SkyMed) offering high spatial resolution and operating at small wavelength with short repeat pass cycles augmented the applicability of the offset tracking method to slow moving glaciers particularly on the ice sheets where the speckle pattern remains stable between two acquisitions. Nevertheless for slow moving glaciers and short temporal baselines the uncertainty of the incoherent cross-correlation, which depends on the samples used, might be in the order of the estimated velocity.

The offset tracking method was initially applied to optical satellite images from different sensors, for instance Landsat, SPOT and ASTER. The definition of the method and further developments, the accuracy assessment and results on different glaciers can be found, among others, in Scambos *et al.* (1992); Berthier *et al.* (2005); Scherler *et al.* (2008); Stearns & Hamilton (2005); Stearns *et al.* (2008). The feature tracking method was applied on time-lapse fixed camera images by Evans (2000).

Offset tracking was applied to SAR data later than InSAR, when the spatial resolution of the new sensors started to increase. Gray *et al.* (2001) applied the method to RADARSAT data on the Filchner Ice Shelf and its tributaries, including Recovery Glacier on the grounding zone. A formalization of the method and some accuracy assessments can be found in de Lange *et al.* (2007); Strozzi *et al.* (2002, 2008); Erten *et al.* (2007); Gray *et al.* (1999); Werner *et al.* (2005). The method has been widely applied on several glaciers and with several sensors, among others by: Luckman *et al.* (2003); Giles *et al.* (2009).

A comparison of offset tracking with InSAR on the Himalayan glaciers is given by Luckman *et al.* (2007), while a combination of the results obtained with the two methods is explored by Joughin (2002); Liu *et al.* (2007, 2008). The velocity of Perito Moreno Glacier (SPI) was obtained from a time series of high resolution COSMO-SkyMed images at time intervals of 8 and 16 days by Ciappa *et al.* (2010). The speckle tracking technique, partially combined InSAR (Mouginot *et al.*, 2012), was used to derive the surface velocity of the entire Antarctica and Greenland from data acquired by different SAR missions (mainly RADARSAT-2, ENVISAT, ALOS PALSAR, RADARSAT-1), within the International Polar Year initiative between 2007 and 2009. The results are reported in Rignot *et al.* (2011a) and in Rignot & Mouginot (2012) for Antarctica and Greenland, respectively. The procedure was also applied

by Mouginot & Rignot (2015) to the Northern and Southern Patagonian icefields using SIR-C, ERS-1/2, RADARSAT-1, ALOS PALSAR and feature tracking on optical Landsat images. Nagler *et al.* (2015) applied the offset tracking method to ~900 SAR scenes acquired in interferometric wide swath mode by Sentinel-1a obtaining a comprehensive velocity mosaic of Greenland.

Other approaches to offset tracking have been explored in the literature, for instance for the conventional image registration problem (Brown, 1992; Zitova & Flusser, 2003). The normalized cross-correlation (NCC) has the advantage of being insensitive to changes in brightness and contrast, but on the other hand it is not optimum for feature tracking since it is not invariant with respect to scaling, rotation and distortions of the image patch (Lewis, 1995). These issues might affect fast moving glaciers particularly when matching images with large temporal baseline and low resolution. In Schubert *et al.* (2013) a matching algorithm based on complex wavelet decomposition was compared to the traditional cross-correlation-based method, but the latter was found preferable. Erten *et al.* (2009) proposed an intensity tracking algorithm based on maximum likelihood estimation. Tested on ENVISAT ASAR data, it proved to be more accurate and more robust to speckle decorrelation than the classical intensity tracking.

The least squares matching (LSM) method minimizes the sum of the squares of the pixel value differences between the master and slave images. The geometric mapping between the coordinates of the master and the slave is carried out through a transformation model (e.g. affine transformation). LSM can determine not only the magnitude and direction of the ice surface displacements (like the amplitude cross-correlation technique) but also rotation and shearing, and moreover can assess the magnitude of the error (McGlone, 2013). Debella-Gilo & Kääb (2012) apply least squares matching to optical remote sensing images of glaciers. The method allows to include models for geometric and radiometric distortions and determine their parameters using a least squares adjustment, allowing to achieve matching with sub-pixel accuracy.

Erten (2013) proposed a polarimetric tracking method based on mutual information, the statistical dependence between images is measured and used to determine the best match and the corresponding shift with subpixel accuracy (without oversampling). The method is tested on fully polarimetric L-band E-SAR data and single-polarization ENVISAR ASAR C-band data. Maksymiuk *et al.* (2016) recently proposed a workflow for the extraction of glacier surfaces and their velocity. The initial estimation is based on intensity tracking of SAR image pairs, these results are corrected with a spatial regularization based on a fluid mechanics model. The surface velocity is approximated by the two-dimensional Navier-Stokes equation for incompressible fluids. Their method is sensor independent, they tested it on the Taku Glacier in the Juneau Icefield (Alaska) using TerraSAR-X geocoded images.

11.2 Objectives and data

The high resolution SAR images produced by the TerraSAR-X mission are particularly well suited for the retrieval of glacier surface velocities. Radar imaging is independent of night and weather conditions, an important advantage in glaciated regions. SAR images offer a distinctive speckle pattern even on smooth snow surfaces where no contrast is found in optical images. Even on very rough surfaces, such as crevassed areas, the contrast is much stronger than in optical images because of the radar cross section of such features and the scattering mechanisms involved (cf. Section 2.1). A big advantage is given by the recent high spatial resolution SAR sensors. High resolution images allow having within each tracking window (patch) a distinct backscattering pattern (due to surface features or speckle). These features are well suited for the estimation of surface velocities through amplitude tracking, which allows to measure two-dimensional absolute shifts from two repeat pass acquisitions.

A processing chain for the retrieval of glacier surface velocity from TerraSAR-X high resolution data over glaciers was set up at DLR IMF. Shift estimation is performed by applying offset tracking on SAR backscattering images: the normalized incoherent cross-correlation is computed between pairs of repeat pass TerraSAR-X geocoded images. The system fulfils the following objectives:

- full processing chain: visualization-ready results are obtained automatically from a generic pool of L1b products;

- reliability and adaptability: results are obtained in most cases without operator interaction and parameter selection. For difficult scenarios and fine tuning of the results, full control of the processing parameters is granted through parameter files;

- speed: a large number of high resolution repeat pass pairs can be processed within reasonably short time and mosaicked to achieve large spatial coverage.

11.2.1 TerraSAR-X data

The TerraSAR-X mission is composed of two identical SAR instruments on board of the TSX-1 and TDX-1 satellites. Some of the common features of these satellites were presented in Section 6.2.1, while their radiometric performance was discussed in Section 8.3.1. Their nominal orbit is set at 514 km of altitude at the equator with an 11 day repeat pass cycle. The 4.8 m long phased array antenna operates at 9.65 GHz (X-band) in all four linear polarizations. The satellites can be turned in order to look to the left, this capability is necessary to image areas at high southern latitudes (below ~80°S).

The TerraSAR-X system is capable of acquiring images in different operational imaging modes: Stripmap (SM), ScanSAR (SC), Spotlight (SL), High Resolution Spotlight (HS) and Staring Spotlight (ST) described in detail in DLR-CAF (2013). For the estimation of glacier surface velocities the basic Stripmap mode was chosen since it provides high resolution and a relatively good coverage of 30 × 50 km in single polarization. The antenna can be electronically steered to acquire 12 different full performance beams (27 in total) with incidence angle ranging from 19.7° to 45.5° (look angle: 18.2° - 41.3°) (DLR-CAF, 2013). The TerraSAR-X Multi Mode SAR Processor (TMSP) (Breit *et al.*, 2010a), developed at DLR IMF, is responsible of processing the SAR raw data into various L1b products with different geometric and radiometric resolution and different geometric projections (DLR-CAF, 2013).

The theoretical maximum slant range resolution in single polarization is 0.89 m with a range bandwidth of 150 MHz. Both the range and azimuth spectrum are weighted with a Hamming window (α coefficient of 0.6) to suppress the side lobes of the point target response (PTR) to less than −0.25 dB (DLR-CAF, 2013). This reduces the slant range resolution to 1.2 m, which scales to ground range by $1/\sin\theta_i$, where θ_i is the incidence angle. Far range beams ($\theta_i >\sim 40.5°$) are operated with a reduced range bandwidth of 100 MHz. Typical SSC ground range resolutions are hence 3.5 m at $\theta_i = 20°$ and 2.4 m at $\theta_i = 45°$. The Stripmap SSC azimuth resolution, after bandwidth reduction and spectral shaping, is equal to 3.3 m and 6.6 m in single and dual polarization, respectively. The radiometric accuracy is discussed in Section 8.3.1. Two variants of detected products can be generated by the TMSP:

1. Spatially Enhanced (SE) products maximise spatial resolution, the largest value of ground range and azimuth resolution is fixed and the smaller one is adjusted to it. The corresponding reduction of bandwidth is used for speckle reduction.

2. Radiometrically Enhanced (RE) products optimize radiometry by averaging 5 to 7 looks in order to reduce speckle, obtaining a radiometric resolution of 1.5 dB (compared to the ~3 dB of SE products).

The TMSP provides four different product types in terms of geometric projection (DLR-CAF, 2013):

- Single Look Slant Range Complex (SSC): the basic (zero-Doppler) focused radar signal in azimuth - slant range geometry. Pixel spacing is determined by the PRF and range sampling frequency (cf. Section 2.1).

- Multi Look Ground Range Detected (MGD): detected (real valued) multilooked amplitude-only SAR image in azimuth - ground range projection. This is achieved through a simple polynomial slant to ground range projection to the WGS84 ellipsoid using a constant terrain height. Square ground resolution cells and pixel spacing are achieved through multilooking. Interpolation artefacts caused by rotation are avoided but pixel localization is less accurate than geocoded products.

- Geocoded Ellipsoid Corrected (GEC): the detected multi look image is projected and resampled to the WGS84 reference ellipsoid using an average terrain height. Since terrain is not corrected pixel location varies with topography. SAR distortions are not corrected leading to high spatial error especially in areas of strong relief and with steep incidence angles.

- Enhanced Ellipsoid Corrected (EEC): the detected multi look image is projected and resampled to the WGS84 reference ellipsoid. The SAR distortions are corrected using an external DEM, therefore the pixel localization is highly accurate. This still depends on the terrain type, on the DEM quality and resolution and on the incidence angle. The DEM used is compiled from different sources among which: SRTM X-band, SRTM C-band, ERS-tandem, DTED-1 and DTED-2 height data. Remaining gaps, including the Antarctic continent are filled with the GLOBE[1] DEM. A geocoded local incidence angle map (GIM) is optionally provided.

Both geocoded products (GEC and EEC) use WGS84 as geodetic datum. The UTM and UPS map projections are chosen in order to preserve angular relations (conformal). The UPS projection is used for polar regions between 84°N and 90°N and between 80°S and 90°S. Horizontally the products refer to the WGS84 ellipsoid, and grid formats are UTM or UPS. The pixel spacing of detected products is dynamically adjusted to satisfy the Nyquist sampling criterion to multiples of 25 cm. The MGD, GEC and EEC SE products feature a pixel spacing of 1.25 m in easting and northing for most of the incidence angle range and 1.5 m at very steep incidence angles.

11.2.2 Approach

Given the available data types, two main approaches can be undertaken for the retrieval of the two-dimensional glacier surface movement from a pair of repeat pass SAR acquisitions. (1) Use the SSC amplitude images to retrieve the relative displacement in radar geometry (after proper coregistration) and subsequently geocode the obtained shift matrix to a certain map projection using an external DEM. (2) Use the precisely geocoded EEC SE products to retrieve the horizontal shifts directly in map coordinates (east - north). Both approaches have their advantages and drawbacks.

In order to meet the objectives of the glacier motion processing chain, the second approach was undertaken. The EEC products allow to simplify significantly the processing steps. The SAR image is already map projected, an interferometric pair is hence intrinsically coregistered with an accuracy which proved to be very high for TerraSAR-X products. This is due to the accurate orbit determination and to the precise processing performed by the TMSP. By using EEC products the coregistration and the subsequent geocoding phases are avoided. The estimated shifts obtained through the normalized cross-correlation function are already map projected and can be directly used. Furthermore the map projected images simplify coverage selection and image combination and visualization.

The Spatially Enhanced (SE) product is the natural choice as it features higher spatial resolution and smaller pixel spacing. This is particularly relevant when tracking speckle on featureless slow-moving glacier surface since the strong multilooking applied on RE products would reduce the speckle signature. The light degree of multilooking applied on SE products allows to improve the tracking of physical glacier features but also provided good results with speckle.

The advantage of using SSC products is the higher degree of flexibility at the cost of an increased system complexity. This approach allows a direct access to the SAR signal and to the acquisition and processing parameters. Since no multilooking is applied, higher resolution is available and the full speckle spectrum is preserved. The radar geometry avoids any interpolation distortions and artefacts possibly caused by the rotation of the image and terrain correction during geocoding. It furthermore simplifies the error estimation. The availability of the full complex signal allows attempting coherent cross-correlation. Finally, full control is given over the geocoding of the displacements, allowing the choice of the DEM. This aspect was not yet critical when the processing chain was set up but became more relevant with the increasing availability of TanDEM-X Raw DEMs (cf. Section 6.2).

[1] Global Land One-km Base Elevation Project

11.3 Methodology

In this section the main steps of the glacier surface velocity processing chain will be described with focus on the algorithm and the theory behind it. The practical use of the processing chain has been detailed in a user manual. The processing parameters can be easily changed through a parameter pool in the form of an ASCII file. The system has been tested extensively with TerraSAR-X geocoded products over glaciers of different size, velocity and surface type. The knowledge gained allowed to determine the default values of the processing parameters, which tend to to provide good results under most common circumstances.

11.3.1 Data selection and cropping

The input to the chain is a folder containing TerraSAR-X geocoded products. The system works with EEC and GEC, both SE and RE variants, but EEC SE was used in most cases. The Stripmap mode was usually used, but ScanSAR was tested as well. The available repeat pass scenes forming an interferometric pair are selected according to their temporal baseline Δt. Good surface velocity results have been obtained with one TerraSAR-X repeat cycle Δt of 11 days, but also with 22 and 33 days over slow-moving glaciers, when the features and the speckle pattern are preserved. Some geometrical parameters of the interferometric pair, in particular the effective baseline $B_\perp$ and the height of ambiguity h_{amb} are computed as well. The user is prompted to select the pairs to be processed.

For each selected interferometric pair the coordinates of the overlapping surface are determined and used to crop the master (older) and slave (newer) TerraSAR-X images to the same coverage. The precise pixel localization provided by the geocoding allows to avoid any further coregistration step. The TerraSAR-X original product images are provided in a 16 bit geotiff file while the cropped images are saved in the Sun Raster File (SRF) format. Parallel to cropping an option to downscale the image by averaging is implemented for feature tracking of heavily crevassed glaciers: the noise is reduced at the cost of spatial resolution, which is acceptable for large features. This option has been tested but seldom used, as the full resolution images generally lead to better results. Different classical speckle reduction filters (Shi & Fung, 1994) were also tested for feature-rich glacier surfaces.

11.3.2 Shift estimation through incoherent cross-correlation

Given two stationary random processes $X(t)$ and $Y(t)$, their statistical cross-correlation function is given by:

$$R_{xy}(\tau) = \mathrm{E}[X^*(t)\,Y(t+\tau)] \tag{11.1}$$

where $\mathrm{E}[\cdot]$ denotes the statistical average and * the complex conjugate. τ is called lag or delay. The autocorrelation function $R_{xx}(\tau)$ of $X(t)$ is defined by substituting Y with X in Eq. (11.1). Assuming the two stationary random processes are ergodic in the first and second moments (mean and autocorrelation function) the statistical cross-correlation (and auto-correlations) can be estimated from two single realizations $x(t)$ and $y(t)$ of the processes through the time-average cross-correlation function (CFF) $r_{xy}(\tau)$:

$$R_{xy}(\tau) = \lim_{T_0\to\infty} r_{xy}(\tau) = \lim_{T_0\to\infty} \frac{1}{2T_0}\int_{-T_0}^{T_0} x^*(t)\,y(t+\tau)\,dt \tag{11.2}$$

where $2T_0$ is the observation interval. In the discrete domain, assuming the two realizations are sampled respecting the Nyquist criterion, two finite-duration sequences $x(n)$ and $y(n)$, with $0 \le n \le N-1$ can be obtained. Their time-average cross-correlation sequence (and equivalently the two autocorrelation functions) can be obtained as the following estimate (Proakis & Manolakis, 2007):

$$\hat{r}_{xy}(m) = \frac{1}{N-m}\sum_{n=0}^{N-m-1} x^*(n)\,y(n+m), \quad m = 0,1,...,N-1 \tag{11.3}$$

with $\hat{r}_{xy}(m) = \left[\hat{r}_{xy}(-m)\right]^*$ for negative values of m. This estimate is unbiased since its mean value is equal to the true statistical cross-correlation sequence $\mathrm{E}\left[\hat{r}_{xy}(m)\right] = R_{xy}(m)$ of $x(n)$ and $y(n)$. The

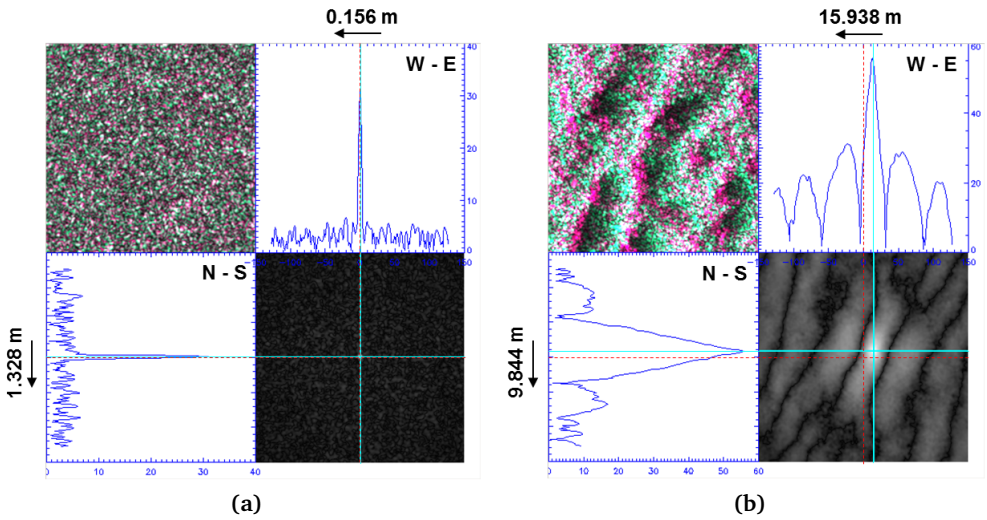

Figure 11.1 – Cross-correlation function for a 256×256 patch of (a) a smooth slow section and (b) of a faster and rough section of Nimrod Glacier (Antarctica). The upper left inset is an RGB composition of the master and slave images (Red: m, Green: s, Blue: (m+s)/2). The lower right inset represents $\sqrt{|\mathrm{CCF}|}$ in 2D. Upper right and lower left: the CCF profiles in correspondence of the peak along the easting and northing directions, respectively.

variance of $\hat{r}_{xy}(n)$ tends to zero as N tends to infinity (making the estimate consistent), but it tends to be large for large values of the lag m. An alternative estimate characterized by smaller variance is the following:

$$\tilde{r}_{xy}(m) = \begin{cases} \frac{1}{N}\sum_{n=0}^{N-m-1} x^*(n)\, y(n+m), & m = 0, 1, ..., N-1 \\ \frac{1}{N}\sum_{n=|m|}^{N-1} x^*(n)\, y(n+m), & m = -1, -2, ..., 1-N \end{cases} \tag{11.4}$$

This estimate is still consistent but biased since its mean value is $\mathrm{E}\left[\tilde{r}_{xy}(m)\right] = \frac{N-|m|}{N} R_{xy}(m)$, the bias is equal to $\frac{|m|}{N} R_{xy}(m)$. In practice since scaling is unimportant, the autocorrelation and cross-correlation functions are normalized between -1 and 1 as:

$$R_{xx_{\mathrm{norm}}}(\tau) = \frac{R_{xx}(\tau)}{R_{xx}(0)} \tag{11.5}$$

$$R_{xy_{\mathrm{norm}}}(\tau) = \frac{R_{xy}(\tau)}{\sqrt{R_{xx}(0) R_{yy}(0)}} \tag{11.6}$$

The lag $\hat{\tau}$ for which the cross-correlation $r_{xy}(\tau)$ is maximum represents the differential shift between the two realizations $x(t)$ and $y(t)$:

$$\hat{\tau} = \arg\max_{\tau} \left\{ r_{xy}(\tau) \right\} \tag{11.7}$$

The shifts in the east and north directions between the master and the slave are estimated on a regular grid of patches covering the entire common area. The process is done for all the selected pairs. For each patch the 2D incoherent normalized cross-correlation function (CCF) of the master and slave patch is computed. The shift (from 0) of the peak of the CCF in each direction corresponds to the displacement in that direction. The CCF of a smooth featureless patch presents a well defined peak as shown in Figure 11.1a. On the other hand for a rough surface the CCF presents a shape resembling the features of the surface, the main peak is wide and secondary peaks are present (Figure 11.1b).

The computation of the displacements is performed using a modified version of the coregistration module of ITP (see Section 6.2.2.2) optimized for fast multithread processing. The C++ code was modified to accept geocoded images as input: for instance the coherent cross-correlation step is skipped and only the incoherent one is performed. The normalized CCF is obtained by implementing the 2D

unbiased CFF estimate of Eq. (11.3) in the frequency domain. A test on the amplitude of the normalized CCF is performed: if the difference between the peak and average is below a certain threshold the patch is discarded. The threshold can be specified in the parameter pool and is kept loose (usually between 0.02 and 0.05) in order to accommodate CCFs with large secondary peaks when performing feature tracking (Figure 11.1b) and because an outlier rejection step is performed afterwards. The CCF around the peak is oversampled and interpolated in order to determine the position of the peak with sub-pixel precision (Yague-Martinez *et al.*, 2010b). The correlation coefficient (or coherence, cf. Section 2.2.2) is also computed. The ITP coregistration module foresees the possibility of having in input coarse shifts in order to extract the patch from the slave image on a different position than on the master, improving the overlap of the signal between master and slave and hence coherence and accuracy.

The main output of this module are two matrices containing the displacements in the east and north directions. Since both spatial resolution and pixel spacing are equal in east and north, square patches with customizable size are used. The distance between patches in east and north can also be selected. In order to increase the robustness of the system against outliers, an overlap between patches is often used, generally corresponding to half the patch size, thus doubling the number of patches in each direction.

The patch size is a particularly critical parameter for the derivation of the displacement matrices. Larger patches increase the accuracy of the shift estimation (cf. Section 11.4) but decrease the spatial resolution of the estimated shifts since displacement gradients within the patches are smoothed out. Glacier velocities do not usually change abruptly, except at the margins of the glacier. The high spatial resolution of TerraSAR-X thus generally allows to have patches with limited or no velocity variation and similar surface pattern. With this respect only for small mountain glaciers the patch size must be reduced. Increasing the degree of overlap between patches allows to improve the tracking of glacier velocity variations even if the information used is partially redundant. Patches of 64, 128, 256 and 512 pixels per side have been tested (corresponding to 80, 160, 320 and 640 m in the EEC SE products with 1.25 m pixel spacing). Patch sizes of 128 and 256 pixels proved to be the most suitable for most scenarios. Patches of 64 pixels per side are generally too small to obtain a reasonable cross-correlation function estimate, while patches of 512 pixels per side are usable on wide glaciers (e.g. ice streams and ice shelves) where less resolution is needed to track variations of velocity but are too large for many outlet glaciers. Furthermore larger patches have a significant impact on computational time: patches of 512 pixel lead to long processing times even on performing machines.

When the tracked feature pattern moves considerably during the observation period (this is generally not an issue with speckle) large patches are needed in order to increase the overlapping portion of the signal between the stacked master and slave patches, and hence the accuracy. In order to improve accuracy and keep a reasonable patch size, a-priori coarse shifts can be provided in input to the coregistration module. The displacement estimation step is run iteratively (generally two times) and the displacement matrices of the first run (usually obtained with larger patch size) are provided in input as coarse shifts to the second run. Alternatively for the final termini of extremely very fast glaciers where no clear CCF peak is found even with large patches a synthetic coarse shift map can be provided as input. The latter approach proved to be unnecessary even on fast flowing glaciers, like the Jakobshavn Isbræ Glacier in Greenland, known to be the fastest non-surging glacier in the world with velocities up to 35 $\mathrm{m\,d^{-1}}$ at its front, although here patches of 512 pixels were necessary. The computationally costly match search step performed by traditional methods was avoided in this processing chain.

Some secondary output files produced in this step are the following.

- Matrices containing the position of the patches in image and map coordinates.
- Matrices containing the correlation coefficient, the maximum and mean value of the CCF, and the ratio between the two, which is used as a signal to clutter index.
- The east and north velocity matrices in $\mathrm{m\,d^{-1}}$.
- The matrices containing the absolute velocity (v) in $\mathrm{m\,d^{-1}}$ and its direction (α).

- A "shift estimation annotation mask" bearing a code for each patch: (0) patch not computed (e.g. borders), (1) incoherent cross-correlation shift computed, (2) reserved code, (3) peak test not passed (discarded patch), (4) reserved code.

11.3.3 Outliers rejection and interpolation

The displacement matrices can be affected by outliers. To obtain more accurate surface velocity maps an outlier rejection step was developed. This precedes an interpolation step over small areas with missing or discarded data.

The outlier rejection step evaluates sequentially all patches of the measurement matrices obtained in the previous stage according to a series of rejection criteria, composed by one or more rules. The patches discarded are annotated in an "outlier mask" according to the rule which triggered their rejection. The outlier mask is initialized as the shift estimation annotation mask and its values are sequentially updated when a patch is discarded by a certain criterion. Rules of the same criterion are evaluated in parallel. After extensive testing, the following criteria were implemented and are applied in the following order:

- Patches with a very high absolute velocity v are discarded, according to $v > k_{v_{\max}} \cdot v_{\max}$. Where $v_{\max}$ is a generic maximum expected velocity set by the user and $k_{v_{\max}} > 1$ a tolerance parameter. Discarded patches are annotated with value 5 in the outlier mask.

- Patches with low correlation coefficient are discarded if $\rho < \rho_{\text{th}}$, where ρ_{th} is a threshold set by the user. Discarded patches are annotated with value 6 in the outlier mask.

- Taking advantage of the relatively slow variation of glacier velocity and direction, a first neighbourhood criterion evaluates each valid patch with respect to the n_1 patches in its square neighbourhood of patches. The neighbourhood size can be set according to the patch distance, the patch size and the variability of the velocity (n_1 was often set to 9 or 25). If the number of valid patches in the neighbourhood satisfies $n_{\text{valid}} \geq k_1 \cdot n_1$, with k_1 a constant between 0 and 1 (usually between 0.2 and 0.4), statistics are computed among its valid members and used to evaluate the following rules:

  - the patch is discarded if $v \notin]\tilde{v}_1 - v_{\text{th}}; \tilde{v}_1 + v_{\text{th}}[$. Where $\tilde{v}_1$ is the median velocity of the n_{valid} valid patches in the neighbourhood and v_{th} defines a velocity range and is obtained as $v_{\text{th}} = k_v \cdot \tilde{v}_1$, with k_v a tolerance parameter set by the user (often 0.5). Discarded patches are annotated with value 7 in the outlier mask.
  - the patch is discarded if $\alpha \notin]\bar{\alpha}_1 - \alpha_{\text{th}}; \bar{\alpha}_1 + \alpha_{\text{th}}[$. Where $\bar{\alpha}_1$ is the mean direction of the n_{valid} valid patches in the neighbourhood and α_{th} defines a direction interval (α_{th} is often set to 30°). This rule eliminates shifts which diverge too much in direction compared to the neighbouring ones. It often eliminates also patches on stable terrain which have $v \approx 0$ and relatively random α. Discarded patches are annotated with value 8 in the outlier mask.
  - the patch is discarded if $n_{\text{valid}} < k_1 \cdot n_1$, whether it is reliable or not. Discarded patches are annotated with value 9 in the outlier mask.

- A second neighbourhood criteria is implemented to further clean the results by discarding isolated patches. For each patch the remaining valid patches n_{valid} in its square neighbourhood of size n_2 are counted, where n_2 is thought to be larger, or equal to n_1 (and often set to 49). If $n_{\text{valid}} < k_2 \cdot n_2$, with k_2 a constant between 0 and 1 (usually between 0.1 and 0.4), the patch (if still valid) is discarded (whether it is reliable or not) and annotated with value 10 in the outlier mask. All patches meeting the criterion are furthermore annotated (with code 3) in an "interpolation mask".

The neighbourhood rules (optionally) discard isolated patches (whether they are reliable or not) to avoid them disrupting the interpolation procedure and to provide cleaner results. The patches which remained after outlier rejection are used to drive the interpolation of the discarded patches, they are

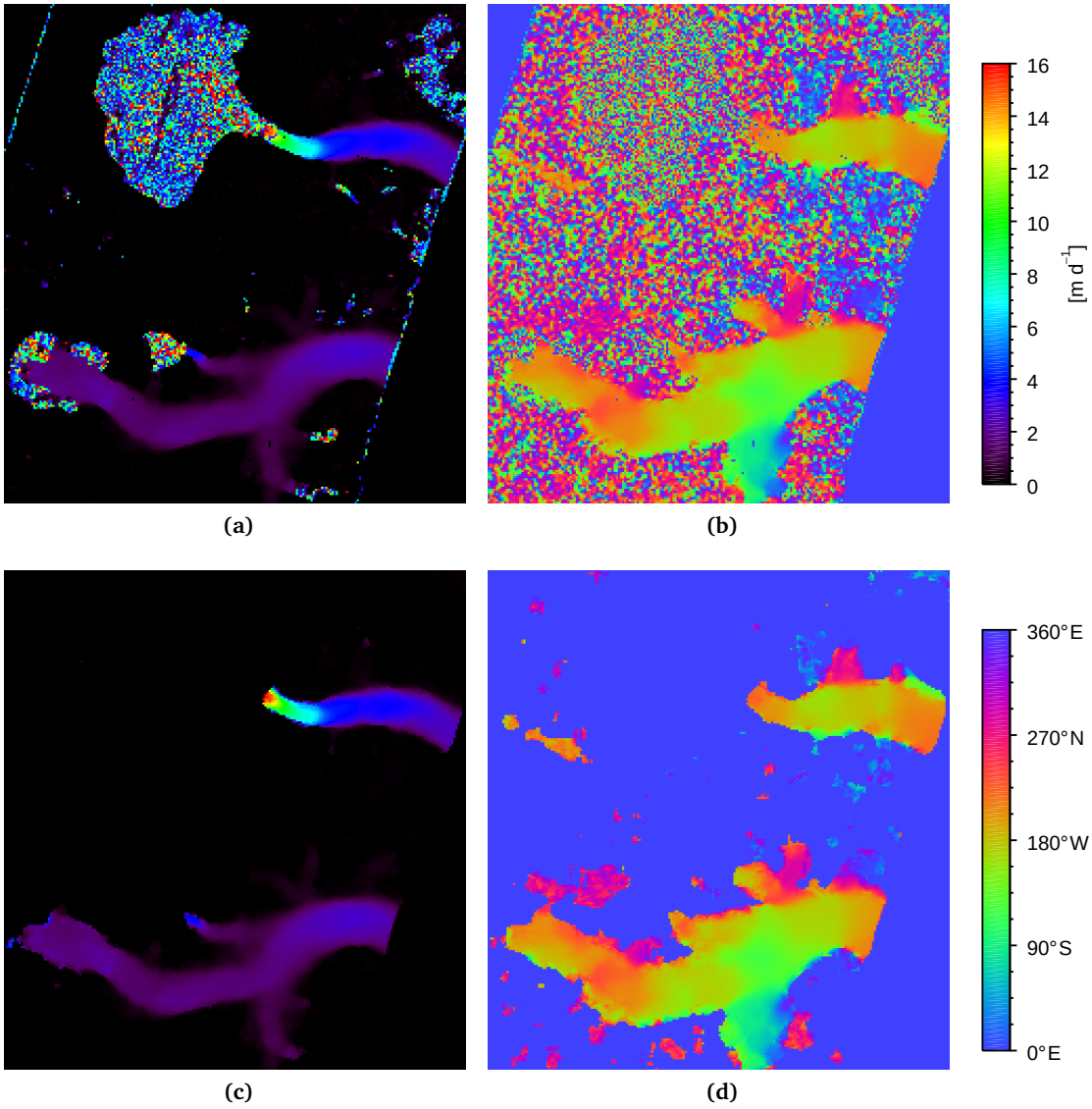

Figure 11.2 – Glacier velocity magnitude (a, c) and direction (b, d) matrices before and after outlier rejection. Patch size: 256 × 256 pixels. Patch distance: 128 pixels. Region: S. Rafael and S. Quintin glaciers (Northern Patagonian Icefield).

marked with code 1 in the interpolation mask and their value remains unchanged after interpolation. Bilinear interpolation is used to obtain the shifts in the east and north directions. All patches meeting the last criterion (whether previously valid or not) are (optionally) masked out since they belong to large outlier-rich areas where shifts are likely not desired (ice-free surface or large glacier area with unreliable results). The interpolated patches which are not masked out have code 2 in the interpolation mask. Interpolation can optionally be avoided and only remaining patches are used to generate the results.

The parameters affecting the criteria are fully customizable by the user in the parameter pool, allowing to tune or disable each rule. Being the outlier elimination, interpolation and visualization steps built as a separate module, they can be run independently of the computationally heavy shift estimation allowing to improve the final results by adjusting different parameters linked to these procedures. Nevertheless the procedure was tested on different types of glaciers leading to the definition of a default parameter set which lead to good results in the majority of cases. Figure 11.2 shows the effects of the outlier rejection procedure on the absolute velocity and direction matrices.

Finally graphical files visualizing the obtained surface velocities in different styles are generated. The preferences can be set by the user in the parameter pool. A header file containing geographic

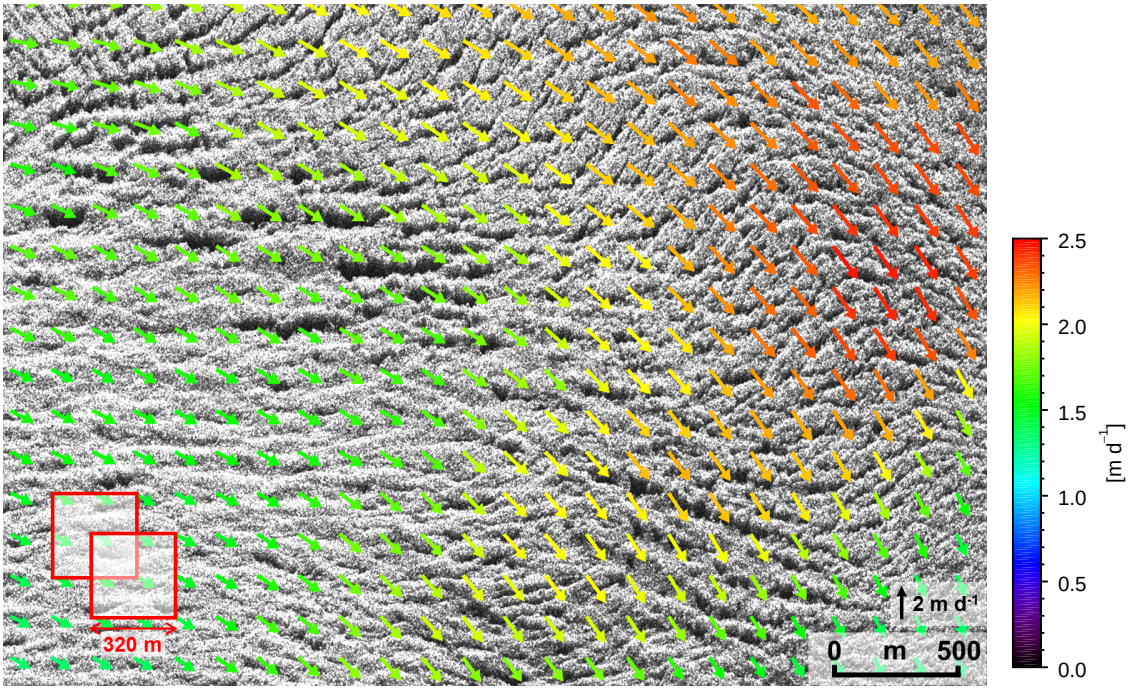

Figure 11.3 – Surface velocity field of a section of the Nimrod Glacier (Antarctica). The patch size of 256 × 256 pixels and the overlap between neighbouring patches is highlighted in red.

annotations is generated for the various images allowing them to be opened by the remote sensing software ENVI™ and by common GIS software such as QGIS™. As an example, the velocity field for a section of the Nimrod Glacier is shown in Figure 11.3, where the patch size and overlap are appreciable with respect to the dimension of the surface features.

11.4 Accuracy

11.4.1 Accuracy of the differential shift estimation through cross-correlation

The lag $\hat{\tau}$ (Eq. (11.7)) corresponding to the maximum of the cross-correlation function is the objective of the estimation. Thus in $\hat{\tau}$ the first derivative $r'_{xy}(\tau)$ of the CCF is equal to zero. A zero mean noise contribution affecting $r'_{xy}(\hat{\tau})$ and characterized by a certain variance $\mathrm{Var}\left\{r'_{xy}(\hat{\tau})\right\}$ causes a shift of the zero-crossing position of $r'_{xy}(\tau)$ which scales with the average slope (first derivative) of $r'_{xy}(\tau)$ at $\hat{\tau}$. This is the curvature of the cross-correlation peak. The resulting uncertainty of the estimated $\hat{\tau}$, is hence given by the variance of the zero-crossing position of $r'_{xy}(\tau)$ (Bamler, 2000; De Zan, 2014):

$$\sigma^2_{\hat{\tau}} = \mathrm{Var}\{\hat{\tau}\} = \frac{\mathrm{Var}\left\{r'_{xy}(\hat{\tau})\right\}}{\mathrm{E}\left\{r''_{xy}(\hat{\tau})\right\}^2} \tag{11.8}$$

This equation represents a generic expression strictly related to the cross-correlation function and is applicable to both complex and real valued processes characterized by different distributions.

The optimum estimator (MLE) of mutual shifts of partially correlated stationary circular Gaussian signals (such as smooth featureless surfaces) is the coherent cross-correlation. Nevertheless this estimator loses quickly robustness as the coherence drops. To maintain high values of coherence (Eq. (2.21)), temporal decorrelation (Eq. (2.22)) must be minimized between acquisitions: hence only very small shifts must be present in order to maintain the phase of each resolution cell. The accuracy achievable by the coherent cross-correlation represents the Cramér-Rao lower bound and was obtained in analytical form by Bamler (2000) by deriving the terms of Eq. (11.8) and is reported in Equation (6.1).

As described in Section 11.2, the present method for glacier surface velocity estimation is based on the incoherent cross-correlation applied to geocoded SAR amplitude images. In the case of featureless surface, the samples of the homogeneous patches of fully-developed speckle can be modelled as independent and circular Gaussian. For this type of signals the accuracy of the differential shift estimation was obtained analytically by De Zan (2014) for intensity images and large number of samples and is given by (also in Eq. (6.2)):

$$\sigma_{\hat{\tau}_{\mathrm{ST}}} = \sqrt{\frac{3}{10N_s}} \frac{\sqrt{2+5\gamma^2-7\gamma^4}}{\pi\gamma^2} \tag{11.9}$$

where $\sigma_{\hat{\tau}_{\mathrm{ST}}}$ is normalized to the resolution element, the number of independent samples N_s refers to the original complex signals. It must be noted that the complex images must be oversampled by a factor of two before computing the intensities. De Zan (2014) further shows that the analytical expression of Eq. (11.9) matches very well with simulations. Furthermore the simulated cross-correlation of amplitude signals has worse performance compared to intensity signals at low coherence (within 1 dB with $\gamma = 0.3$), converging as γ increases and becoming almost indistinguishable for $\gamma > 0.6$. According to the simulations, performances within 1 dB from Eq. (11.9) can be obtained with approximately 1000 samples for $\gamma = 0.3$, 200 samples for $\gamma = 0.5$, and 50 samples for $\gamma = 0.7$. The homogeneity hypothesis might lose validity for larger patches, making Eq. (11.9) invalid.

A coarse computation assuming a heading angle $\psi = 30°$ (angle between the north and the ground track) and azimuth and range resolutions of ~3.0 m will lead to a map projected resolution element of ~4.0 m in east and north. The number of independent samples are roughly equal to $N_s = A_{\mathrm{patch}}/A_{\mathrm{res.elem.}}$: approximately 6400 with patches of 256^2 pixels, 1600 with patches of 128^2 pixels, and 400 with patches of 64^2 pixels. Typical values of correlation coefficient range with speckle tracking range between ~0.2 and ~0.6. Patches of 64^2 pixels are usually avoided to increase accuracy for areas of lower coherence, in fact Eq. (11.9) would not be valid in this scenario. Assuming a typical patch of 256^2 pixels, Eq. (11.9) gives a differential shift accuracy in east and north of 0.33 m for $\gamma = 0.2$, 0.09 m for $\gamma = 0.4$, and 0.04 m for $\gamma = 0.6$. Since amplitude signals are used, the actual accuracies are larger for $\gamma < 0.6$ but an analytical quantification is not possible. Based on the simulated amplitude results of De Zan (2014), the previously given accuracies become 0.45 m for $\gamma = 0.2$[2], 0.11 m for $\gamma = 0.4$, and 0.04 m for $\gamma = 0.6$. The accuracy of the velocity estimate is obtained dividing the standard deviation by the time interval Δt.

The lower parts of the glaciers are usually characterized by pronounced surface structure, for instance crevasses (cf. Section 3.4), furthermore these areas generally move more rapidly compared to upstream regions. In this case signal coherence is generally lost: the speckle pattern is no longer correlated but the differential shifts can be nevertheless retrieved by tracking the features of the amplitude images where present, similarly to optical images (feature tracking). The accuracy of feature tracking is not computable analytically and Eq. (11.8) is difficult to estimate empirically. The accuracy depends on the autocorrelation function of the texture, the sharper the feature and the more accurate is the shift estimation (Eineder *et al.*, 2011b). Based on Monte Carlo simulations applied to synthesized data Villano & Papathanassiou (2011) confirm that the standard deviation still depends on $1/\sqrt{N_s}$ assuming homogeneous shifts within the patch. It must be noted that this assumption might not be applicable in the shear zones of fast flowing glaciers where significant gradients can be present within the tracking patch.

11.4.2 Pixel localization accuracy

The pixel localization (or geolocation) accuracy defines how well can a pixel be positioned with respect to a reference system. For SSC the definition of such an accuracy is more straightforward as no projection is performed and only system errors are relevant. Geocoded images, such as the EEC products are further subject to errors caused by the geocoding procedure, and particularly to the quality of the DEM used. In this application the relative (differential) shifts between two images are retrieved, these are affected by differences in the geolocation errors affecting the master and slave images.

[2]Amplitude simulated accuracy for $\gamma = 0.2$ communicated personally by De Zan.

The localization accuracy of an image is affected in the first place by the accuracy with which the position of the satellite is known. In TerraSAR-X the orbit determination is performed with the on-board dual-frequency GPS receiver and subsequent processing, leading to a very high accuracy. The science (SCIE) orbit product specification states a nominal 1-σ accuracy of 20 cm in 3D, with aim to 10 cm. In fact the achieved orbit accuracies are often better: the rapid (RAPD) orbit product, rated at a nominal 1-σ accuracy of 2 m in 3D is often found to be below 20 cm (DLR-CAF, 2013), while the science product has an accuracy of better than 10 cm, and it can reach up to 3 cm with low solar activity (Yoon *et al.*, 2009). Orbital auxiliary data are operationally available within less than 10 hours from acquisition as RAPD product and within 5 days as SCIE product (Breit *et al.*, 2010a). For the processing of the L1b EEC SE data used for the estimation of the glacier surface velocities the SCIE orbit product was selected.

Residual azimuth timing errors are still present after the correction of the stop-and-go approximation during processing. Furthermore an instrument time tagging delay is annotated and must be corrected. Finally the quantization of the SAR instrument corresponds to an azimuth position accuracy of 6.5 cm (Breit *et al.*, 2010a).

A major contribution to the localization accuracy is caused by unaccounted delays along the signal paths due to the different refractive index of the atmosphere compared to vacuum, leading to a 2 - 4 m error in slant range. The signal path is corrected in the TerraSAR-X products using basic models with constant values applied to the entire image, reducing the error to 0.5 m, representing half of the total specified accuracy of 1 m (DLR-CAF, 2013). This error source is discussed in Section 11.4.2.1.

The specified absolute pixel localization accuracy, determined during the commissioning phase is 1 m for nominal imaging modes with science orbits, and includes all residual uncertainties on the signal path and azimuth errors. This makes repeat pass images intrinsically coregistered at a sub pixel level (DLR-CAF, 2013). This value does not include localization errors in geocoded products caused by errors in the DEM, which are discussed in Section 11.4.2.2.

Eineder *et al.* (2011b) and Cong *et al.* (2012) assessed the geolocation potential of TerraSAR-X by precisely compensating shifts due to atmospheric delays, earth deformation and continental drift between GPS reference systems for a series of images containing a corner reflector with well known coordinates. They obtain an absolute pixel localization accuracy of 3.8 cm in range and 5.5 cm in azimuth. For the residual offset affecting all images, they find a mean value equal to 28.2 cm in range and 7.9 cm in azimuth. Similarly Schubert *et al.* (2012) obtain a mean range error of +13.0 cm with a standard deviation of 3.3 cm and a mean azimuth error of −8.3 cm with a standard deviation of 4.4 cm. The range offset in the order of 30 cm is caused by a residual electronic delay, mainly due to the original instrument calibration constants. These were determined during the commissioning phase using simplified models for the atmospheric signal path delay and therefore still contain atmospheric information. Corrected calibration constants allow to eliminate this offset (Balss *et al.*, 2014b). Corrections of the timing system proposed by Balss *et al.* (2014a) allow to further reduce the offset and the accuracy in azimuth and the offset in range. In particular a technique is presented for the estimation of the deviation of the true ADC sampling rate from the nominal value and for the mitigation of the quantization error of the instrument fine time (IFT). The main improvement of the first correction is an offset reduction of approximately 7 cm in range, while the second correction eliminates the residual azimuth offset and halves the azimuth standard deviation. With the described corrections, Balss *et al.* (2014b,a) report pixel location accuracies of 0 ± 15 mm in azimuth and 0 ± 12 mm in range based on 52 HS datatakes at a 1.5 m trihedral corner reflector located in Wettzell (Germany). Values of -7 ± 19 mm in azimuth and -9 ± 13 mm in range were obtained from 19 HS datatakes at a 1.5 m trihedral corner reflector located in Metsähovi (Finland).

11.4.2.1 Error due to the propagation in the atmosphere

The atmosphere, through which the radar signal travels for a range between 550 km and 730 km, is composed by a mixture of gases which cause the signal to propagate slower than in vacuum, causing refraction (cf. Section 4.2.1). The increase in travel time in the atmosphere compared to the vacuum is defined *path delay*. The effects of the different layers of the atmosphere on the SAR signal propagation

are discussed below.

The **ionosphere** ranges between 60 km and 1000 km of altitude, here the atmosphere is ionized by the solar radiation. It acts like a dispersive (frequency dependent) medium causing a group delay which depends on the VTEC, the total number of electrons in a vertical cylinder (measured in TECU, i.e. units of 10^6 electrons per square meter). The slant range delay in meters is given by (Breit *et al.*, 2010b; Eineder *et al.*, 2011b):

$$\delta_{\text{iono}} = \frac{40.28 \cdot \text{VTEC}}{f^2 \cdot \cos\theta} \tag{11.10}$$

where f is the carrier frequency. Typical VTEC values are 5 - 10 TECU with values up to 100 TECU during strong solar activity. Equation (11.10) assumes that the signals travel through the complete atmosphere, but the TSX-1 and TDX-1 satellites orbit the Earth at a nominal altitude of 514 km, making the actual delay lower. According to Eq. (11.10) the *zenith path delay* (i.e. the path delay at an incidence angle of 0°, abbreviated ZPD) due to ionosphere is equal to 2.16 cm at X-band ($f = 9.65$ GHz) with a moderate value of VTEC = 5 TECU. The constant value $\delta_{\text{iono}}^{\text{TSX}} = \frac{2.16 \cdot 10^{-2}}{\cos\theta}$ is assumed for all TerraSAR-X scenes, it is simply annotated in SSC products and corrected in geocoded products. Actual VTEC values for a given time and location can be derived from ground-based GNSS networks or from space-based radio occultation measurements, a method for operational correction of this delay is proposed in Gomba *et al.* (2016). The typical ionospheric path delay δ_{iono} is lower than the orbit accuracy, temporal variations between acquisitions from the corrected values can generally be neglected at X-band.

The **troposphere** is the lowest layer of the atmosphere, with thickness between 7 km at the poles and 17 km at the equator. The weather develops in this layer which contains about 3/4 of the atmospheric mass, it hence has a strong rapidly varying effect on the signal propagation time which cannot be neglected. The troposphere imposes a non-dispersive path delay which can be divided in the following three main components (Eineder *et al.*, 2011b; Cong *et al.*, 2012).

- The hydrostatic (dry) component, caused by dry gases, is the the largest contribution (around 2.3 m at sea level, with standard deviation of a few centimetres over one year) and can be modelled precisely (within ~1 mm) by knowing the altitude and the surface pressure.
- The wet component depends on the precipitable water vapour content and hence is weather dependent and can amount up to 40 cm or more. Absolute values are larger as latitude decreases.
- The liquid component is due to the droplets of liquid water within clouds and its effect is negligible compared to the other components.

Tropospheric path delay values are higher at lower latitudes and during summer. They decrease with altitude because of the decreased pressure. In the TerraSAR-X products a simple model of tropospheric path delay is assumed (Breit *et al.*, 2010b):

$$\delta_{\text{tropo}}^{\text{TSX}} = \frac{\text{ZPD}}{\cos\theta} \cdot \mathrm{e}^{-\frac{h}{h_0}} \tag{11.11}$$

where h_0 is a reference height of 6000 m and where a constant ZPD = 2.3 m, and a single average height value h for the entire scene are used. The resulting tropospheric value for the scene is only annotated in SSC products and corrected in geocoded products. This simple model is often not accurate enough, as it does not consider wet delay variations, besides assuming a single height may lead to errors where variations of topography are present.

A precise estimate of the actual tropospheric path delay can be obtained via GNSS measurements. Unfortunately the coverage of the GNSS network remains too sparse. In Cong *et al.* (2012); Cong (2014) a method for the estimation of the tropospheric path delay based on the integration of numerical weather model data is presented. This technique allows to estimate the tropospheric delay with global coverage with a spatial resolution below 10 km and an accuracy of 3.2 cm, compared to the 3.8 cm of the GNSS measurements (Cong *et al.*, 2012).

Figure 11.4 shows one year sequences of tropospheric zenith path delay measured at three stations of the IGS[3] permanent network:

[3] International GNSS Service

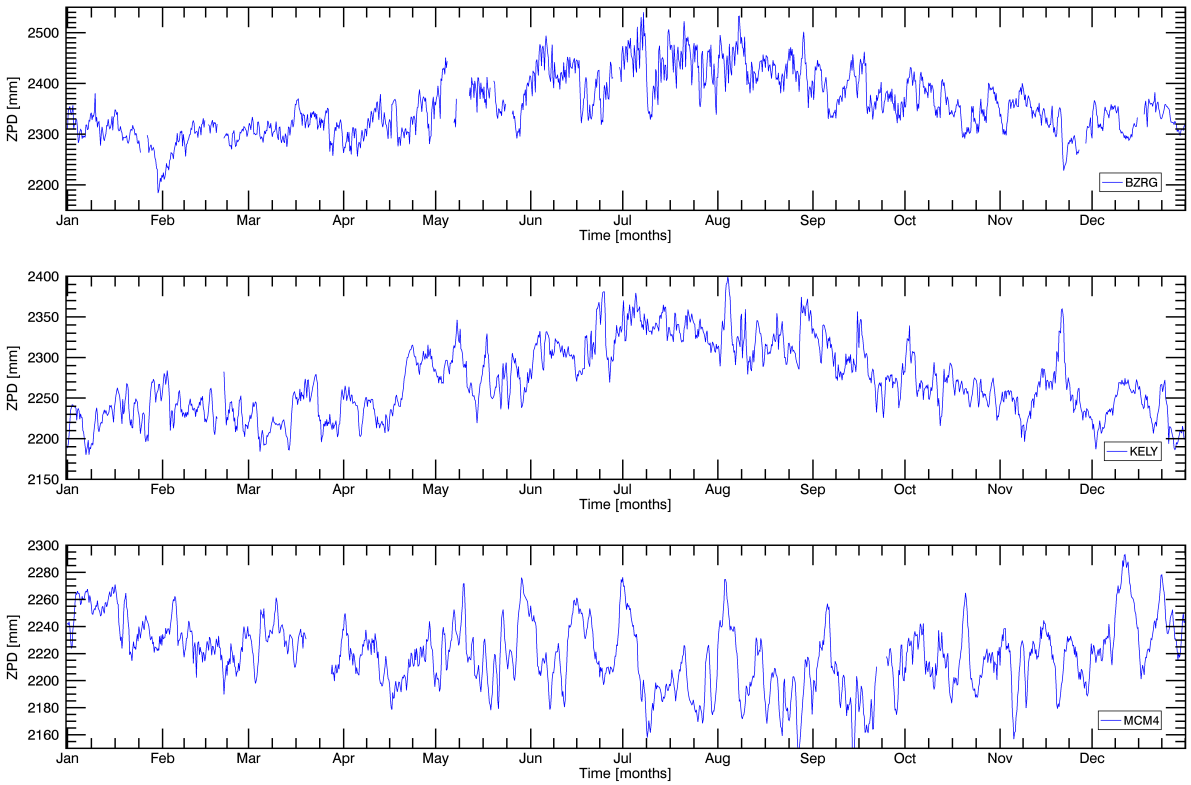

Figure 11.4 – Tropospheric ZPD of year 2015 measured at three IGS GNSS stations: BZRG (Alps), KELY (Greenland), MCM4 (Antarctica). Plotted values are 6 hour averages of the original measurements reported every 300 seconds. Standard deviations (not shown) are between 1.2 mm and 4.5 mm for BZRG, between 1.0 mm and 4.0 mm for KELY, and between 0.9 mm and 3.5 mm for MCM4.

- BZRG (46°30'N, 11°20'E) located near the Alps in the city of Bolzano Bozen (Italy) at an elevation of 328 m.
- KELY (66°59'N, 50°56'W) located in Kangerlussuaq, western Greenland at an elevation of 229 m.
- MCM4 (77°50'S, 166°40'E) located at the McMurdo U.S. station on the Ross Island in Antarctica at an elevation of 98 m.

As shown in Figure 11.4, tropospheric zenith path delay variations up to 20 cm can occur within days. Much faster (even hourly) variations occur at lower latitudes, mostly caused by the wet component (see BZRG) which reaches here up to 40 cm in summer. On the other hand in Antarctica (MCM4) variations are slower (days) and mainly linked to the dry component, while the wet component is practically null all year round. Greenland (KELY) represents an intermediate scenario with wet component up to 15 cm in summer and almost null in winter.

A variation of the actual path delay, with respect to the corrected value (Eq. (11.10) for the ionospheric part and Eq. (11.11) for the tropospheric part) represents an unaccounted path delay in slant range and causes a localization shift in ground range in the geocoded image. The relative localization error between the master and the slave represents an offset in ground range in the cross-correlation shifts, given by:

$$\Delta gr_{\text{atmo}} = \frac{\left(\delta_{\text{tropo}_1} - \delta^{\text{TSX}}_{\text{tropo}}\right) + \left(\delta_{\text{iono}_1} - \delta^{\text{TSX}}_{\text{iono}}\right)}{\sin\theta_1} - \frac{\left(\delta_{\text{tropo}_2} - \delta^{\text{TSX}}_{\text{tropo}}\right) + \left(\delta_{\text{iono}_2} - \delta^{\text{TSX}}_{\text{iono}}\right)}{\sin\theta_2} \tag{11.12}$$

where $\delta_{\text{tropo}} = \frac{\text{ZPD}}{\cos\theta}$ is the actual tropospheric path delay in slant range and δ_{iono} is the actual ionospheric path delay in slant range. The subscripts 1 and 2 indicate master and slave acquisitions, respectively. The ionospheric correction can be generally neglected at X-band, since it is usually small

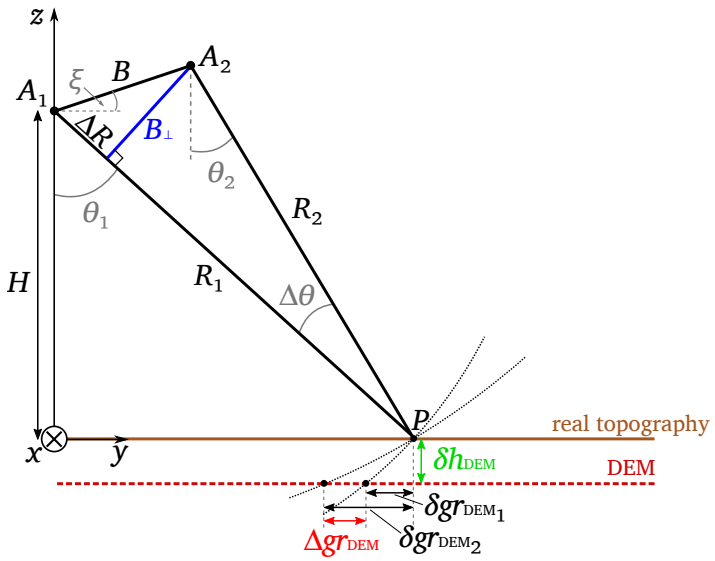

Figure 11.5 – Pixel localization errors ($\delta gr_{\mathrm{DEM}_{1,2}}$) and shift error ($\Delta gr_{\mathrm{DEM}}$) in geocoded images due to a DEM error.

and the corrected value $\delta^{\mathrm{TSX}}_{\mathrm{iono}}$ is good enough. Nevertheless its must be taken into account for lower radar frequencies and periods of strong solar activity. This relative localization offset must be projected on the east and north directions, and divided by Δt to obtain the error on the velocity.

11.4.2.2 Error due to geocoding

The main contribution to the pixel localization accuracy of a geocoded image is linked to the height accuracy of the DEM used for geocoding. A DEM error could be represented by a lack of resolution, hence the inability to follow rapid variations of topography, interpolation errors, residual phase-unwrapping errors in case of an InSAR DEM, mosaicking inconsistencies, and obsolescence due to changes of the topography in time, a relevant issue for glaciers as discussed in this thesis. The TerraSAR-X EEC products are mainly geocoded with the following DEMs in the areas of interest to this thesis:

1. STRM X-band DEM (1 arcsec posting) and C-band DEM (3 arcsec posting) between 60°N and 56°S. The absolute and relative vertical accuracies are approximately 16 m and 8 m (although it might be higher on steeper terrain), respectively (DLR-CAF, 2013). The accuracy of the SRTM DEM is discussed in detail in Section 6.1.1.

2. GLOBE DEM for the rest of the planet. It features a 30 arcsec posting and poor quality, with relative and absolute accuracies varying between tens and hundreds of meters (DLR-CAF, 2013).

As depicted by the scheme in Figure 11.5, a local DEM error δh_{DEM} causes in the geocoded image a pixel localization error in ground range equal to:

$$\delta gr_{\mathrm{DEM}} = \delta h_{\mathrm{DEM}} \cdot \cot\theta_i \tag{11.13}$$

steeper incidence angles θ_i are hence more strongly affected by a DEM error. δh_{DEM} is assumed to be positive when the DEM is higher than the real terrain elevation, leading to a positive δgr_{DEM} away from the sensor.

Although repeat pass images are acquired from the same orbit and using the same beam, a certain baseline B might be present between the satellite positions in subsequent passes. This introduces a small difference in incidence angle which leads to a different pixel localization error δgr_{DEM} in the master and the slave images. The differential shift estimation will hence be locally affected by a spurious shift given by the difference:

$$\Delta gr_{\mathrm{DEM}} = \delta gr_{\mathrm{DEM}_1} - \delta gr_{\mathrm{DEM}_2} = \delta h_{\mathrm{DEM}} \left(\cot\theta_1 - \cot\theta_2\right) \tag{11.14}$$

by applying simple trigonometry and $B_\perp = R_2 \sin\Delta\theta$ (with $\Delta\theta = \theta_1 - \theta_2$) and $\sin\theta_1 \approx \sin\theta_2$ in a repeat pass configuration, one can obtain that:

$$\Delta gr_{\mathrm{DEM}} = \delta h_{\mathrm{DEM}} \frac{-\sin\Delta\theta}{\sin\theta_1 \sin\theta_2} = -\delta h_{\mathrm{DEM}} \frac{B_\perp}{R_2 \sin\theta_1 \sin\theta_2} \approx \frac{-\delta h_{\mathrm{DEM}} B_\perp}{R_2 (\sin\theta_2)^2} \tag{11.15}$$

where Δgr_{DEM} is positive away from the sensor. Typical values of $B_\perp$ for TerraSAR-X repeat pass pairs range between 0 and 300 m, and full performance incidence angles lie between 19.7° and 45.5°, corresponding to ranges between ~550 and ~730 km. For instance the shift error in ground range for $B_\perp = 50$ m, $\theta_i = 35°$, will be approximately $-0.24 \cdot \delta h_{\mathrm{DEM}}$. This error must be projected on the east and north directions and divided by Δt to obtain the error on the velocity. This error can be corrected if a more accurate DEM is available.

The SRTM DEM generally represents a reliable elevation source, but may be affected by significant elevation error at the termini of the glaciers as shown in Chapter 7. The GLOBE DEM (Hastings & Dunbar, 1999), used in polar regions, has very poor quality. Antarctica is of particular interest for this thesis since many glacier velocity results were obtained in this continent. The GLOBE DEM for Antarctica is based on topographic contour maps from eleven nations digitized and collected in the Antarctic Digital Database (ADD) by the Scientific Committee on Antarctic Research (SCAR) and published in 1993 (Hastings & Dunbar, 1999).

For Antarctica a more reliable DEM with 1 km posting was obtained using ICESat GLAS laser altimeter data and satellite radar altimetry from ERS-1 by Bamber *et al.* (2009); Griggs & Bamber (2009). Recently an improved dataset containing ice bed and surface height for Antarctica and called Bedmap2 has been released based on multiple sources (Fretwell *et al.*, 2013). In order to roughly map the accuracy of the GLOBE DEM and highlight the most critical areas, the Bedmap2 surface elevation was taken as reference to compute the difference $\Delta h = h_{\mathrm{GLOBE}} - h_{\mathrm{Bedmap2}}$, shown in Figure 11.6. Numerous large areas particularly at the margins of the continent are characterized by strong elevation differences, in the interior a better agreement is found.

The TanDEM-X mission (cf. Section 6.2) covered operationally Antarctica in left looking mode with two dedicated campaigns during the Austral winter of 2013 and 2014. At the time of writing the final DEM of Antarctica was not yet finalized. In order to coarsely assess the quality of the GLOBE DEM, 5 TanDEM-X Raw DEMs of approximately 20 seconds of length covering a section of Recovery Glacier (81°S; 26°W, black outline in Figure 11.6) were processed using the ITP. The absolute calibration of the DEMs is particularly challenging in this region due to variable signal penetration of the radar signal in ice and snow, making the comparison with optical altimetric data less reliable. Nevertheless a manual calibration was performed using ATM laser altimetry data acquired within NASA's Operation IceBridge over stable terrain, with an expected absolute elevation accuracy within ±3 m. The TanDEM-X and corresponding GLOBE DEMs are shown in Figure 11.7 along with the difference image $\Delta h = h_{\mathrm{GLOBE}} - h_{\mathrm{TDM}}$. Large offsets exceeding 250 m, already observable in Figure 11.6, affect vast parts of the Recovery Glacier in the GLOBE DEM. The mountainous area to the north appears also problematic. Furthermore the GLOBE DEM suffers from interpolation artefacts (see Figure 11.7a at 81°20'S between 24°W and 26°W), scaling artefacts (scalloping effect, not visible in the image) and mosaicking artefacts.

11.4.3 Error due to the deformation of the Earth

The solid Earth is not static, it deforms as an elastic body under the effect of external forces and loading effects, each characterized by different orders of magnitude and time scales. For a specific location the difference in horizontal and vertical Earth shift between the master and the slave acquisition couple with the glacier surface movements affecting the shift measurements, although by relatively small magnitudes. These geodynamic effects can be modelled with high accuracy according to the International Earth Rotation Service (IERS) conventions. The main deformation contributions are the following (Eineder *et al.*, 2011b).

- The main contribution comes from the solid Earth tides: deformations due to gravitational pull exercised by the Sun and the Moon. The radial (vertical) component can reach up to ~40 cm peak-to-peak, the east and north components up to ~12 cm peak-to-peak. The period is

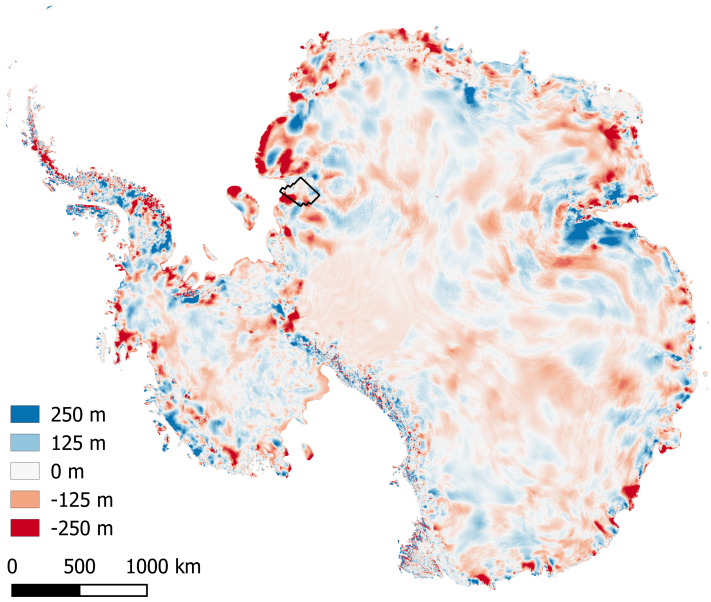

Figure 11.6 – DEM difference $\Delta h = h_{\text{GLOBE}} - h_{\text{Bedmap2}}$. The area of the comparison with the TanDEM-X DEM of Figure 11.7 is marked in black.

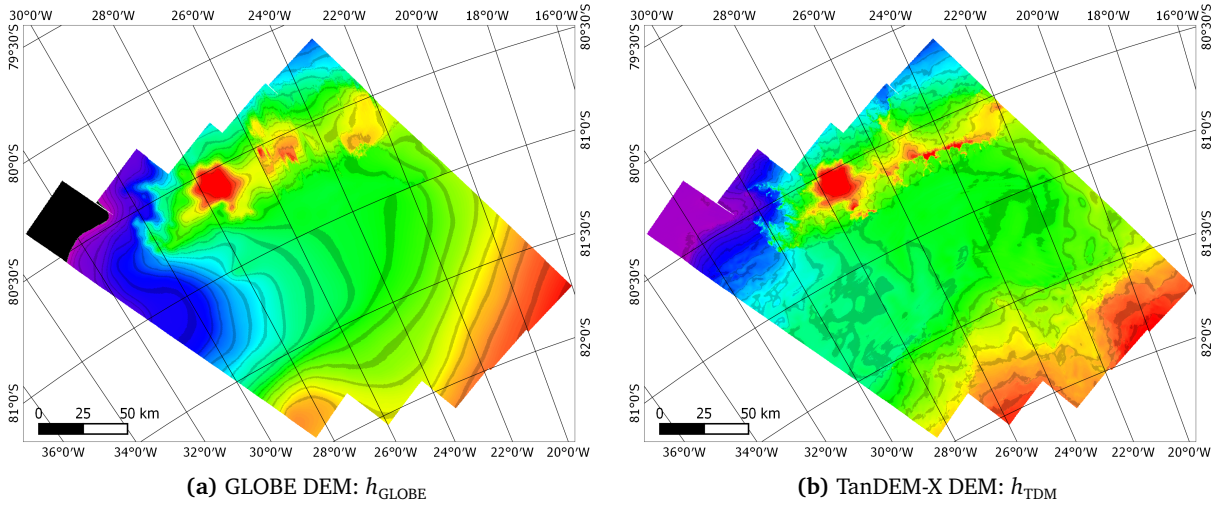

(a) GLOBE DEM: h_{GLOBE}

(b) TanDEM-X DEM: h_{TDM}

(c) $\Delta h = h_{\text{GLOBE}} - h_{\text{TDM}}$

Figure 11.7 – Comparison of GLOBE and TanDEM-X DEMs over a section of the Recovery Glacier marked in black in Figure 11.6.

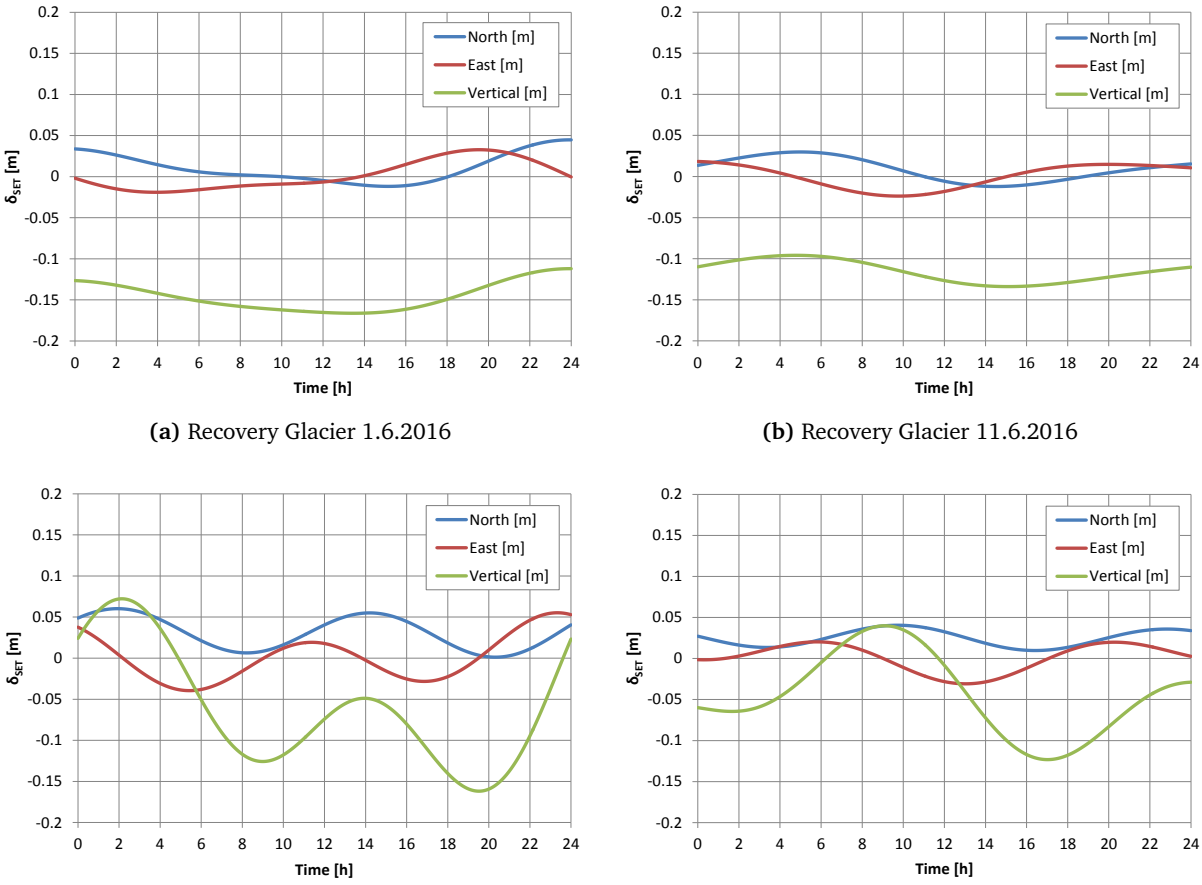

(a) Recovery Glacier 1.6.2016

(b) Recovery Glacier 11.6.2016

(c) SPI 1.6.2016

(d) SPI 11.6.2016

Figure 11.8 – Solid earth tides for the Recovery Glacier (81°S; 26°W) in Antarctica and for the Southern Patagonian Icefield (50°S; 73°W) on 1.6.2016 and 11.6.2016.

approximately 12 hours. A sample deformation for two locations of interest and two dates is shown in Figure 11.8.

- The polar tides are deformations of the Earth induced by changes in the Earth's rotational axis caused by polar motion. They reach 25 mm in the radial and 7 mm in the horizontal components.
- The oceanic tidal loading causes deformations of the earth near the coast and in areas with large tidal range, here several centimetres of radial displacement can happen, while it is less than 1 cm for continental sites.
- Atmospheric pressure loading is the reaction of the Earth to changes of the weight of the atmosphere column due to variations of pressure. These deformations are in the order of 10 mm peak-to-peak in the vertical component (but can reach up to 40 mm in some regions) and 0.5 mm in the horizontal component. They are higher on continental regions distant from the oceans.
- Hydrological loading has usually a peak-to-peak contribution of 3-10 mm vertically (but can reach 30 mm) and only a few millimetres horizontally. It is usually very seasonal and most significant in South America, Southern Africa and Asia. This effect cannot be modelled, but estimated through GNSS measurements. Given the small contributions and the large time scale of the variations this issue does not affect the glacier surface shift measurements.

The horizontal component of the described Earth deformations is strongly dominated by the solid Earth tides, but their contribution remains small. The vertical component is also dominated by the solid Earth tides, oceanic loading can nevertheless contribute up to some centimetres. A vertical shift of the earth surface δv_{Earth} with respect to the reference surface will contribute in a single geocoded

image to a shift in ground range of $\delta gr_{\text{Earth}} = \delta v_{\text{Earth}} \cdot \cot\theta_i$, similarly to the DEM induced geolocation error computed in Eq. (11.13). The corresponding shift in ground range between a target in the master and slave image is given by:

$$\Delta gr_{\text{Earth}} = \delta gr_{\text{Earth}_1} - \delta gr_{\text{Earth}_2} \approx \left(\delta v_{\text{Earth}_1} - \delta v_{\text{Earth}_2}\right) \cdot \cot\theta_2 \tag{11.16}$$

Assuming a worst case scenario with a vertical earth displacement difference of 20 cm between repeat pass acquisitions, Δgr_{Earth} will amount to 0.54 m at $\theta_i = 20°$ and 0.2 m at $\theta_i = 45°$. This offset must be projected on the east and north directions, summed to the horizontal Earth deformation components (δe_{Earth} and δn_{Earth}) and divided by Δt to obtain the error on the velocity.

11.5 Results

This section provides an overview of the most relevant surface velocity results obtained with the processing chain described in Section 11.3. The description is kept short and the investigated regions reported here are restricted to the Patagonian icefields and Antarctica, although glaciers in other regions have been monitored. For each investigated glacier, a table reporting the main acquisition and processing parameters and a figure with the derived glacier surface velocity fields are given. The latter reports the colour coded velocity overlapped on the amplitude image of the master acquisition as obtained in output to the processing chain (only annotations are added manually), the direction of the flow is omitted to avoid overloading the representation.

11.5.1 NPI and SPI

The Northern and Southern Patagonian icefields have been investigated extensively in this thesis. A comprehensive description of this region is given in Chapter 5. The strong glacier surface thinning affecting the icefields is quantified in Chapter 7 while the geodetic mass balance is derived in Chapter 9. The outlet glaciers of SPI and NPI have also been monitored with respect to their surface velocity.

The Perito Moreno and Ameghino glaciers have been monitored with a sequence of 6 image pairs acquired in different seasons between 2008 and 2011 (cf. Table 11.1). The surface velocity measured in January 2008 is shown in Figure 11.9. The velocity of these glaciers proved to be relatively stable during the observation period (Abdel Jaber *et al.*, 2012), small seasonal variability was observed, but annual average values proved to be in agreement with measurements from GPS and D-InSAR applied to L-band SIR-C data from October 1994 reported in Stuefer *et al.* (2007).

The surface velocity of the terminus of Pio XI Glacier, characterized by the largest basin in SPI, was derived from one data pair acquired in October 2010 (cf. Table 11.2) and is shown in Figure 11.10. A fast moving area with velocity up to $\sim$5 m d^{-1} is found on the bend.

The results in Figure 11.9 and 11.10 highlight a criticality of the velocity derivation by means of offset tracking for temperate glaciers. As discussed in Section 5.3, the weather conditions on the icefields are extremely variable: snowfalls can occur even in summer and rapid changes of temperature are possible. This leads to variations of the smooth snow and firn surface of the plateau and consequent loss of coherence. The reliance on the speckle pattern, due to the absent texture, makes the method unreliable due to fast flow, abundant snowfall or variations in the liquid water content. The latter aspect is discussed in Chapter 4, while an analysis of the backscattering of the NPI and SPI, including seasonal variations is reported in Chapter 8.

The velocity field of the S. Rafael and S. Quintin glaciers (NPI) has been derived from a pair of Stripmap TerraSAR-X images acquired in May 2012 (Table 11.3) and is shown in Figure 11.11 (see also Abdel Jaber *et al.* (2014)). The S. Rafael Glacier is the lowest latitude tidewater glacier of the Earth and is characterized by a narrow terminus featuring glacier flow up to 16 m d^{-1} at the snout, making it the fastest glacier in Patagonia. It is hence a challenging test site for the processing chain, and the resulting flow field confirms the robustness of the algorithm. The S. Quintin to the south has a larger terminus and is much slower (different colour scales are used in Figure 11.11) with maximum speed of 2.7 m d^{-1} at the bend.

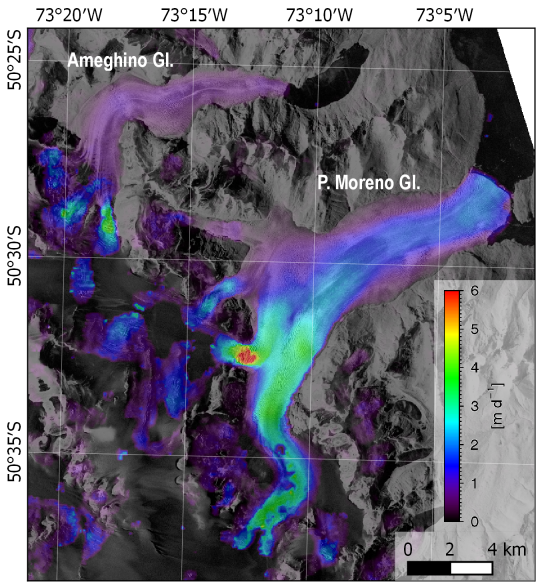

Figure 11.9 – Surface velocity of Perito Moreno and Ameghino glaciers (SPI).

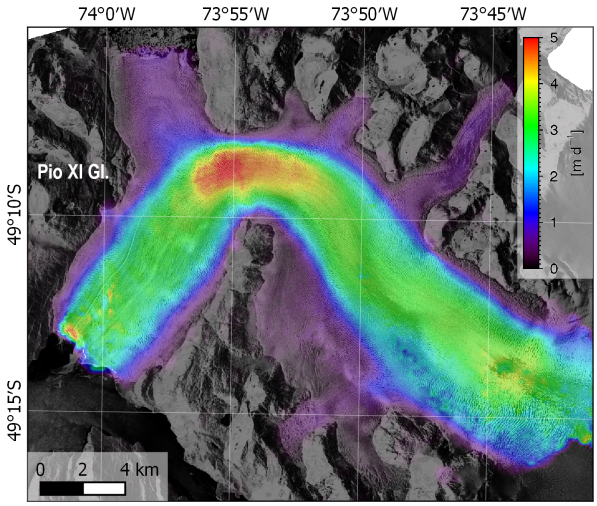

Figure 11.10 – Surface velocity of Pio XI Glacier (SPI).

Table 11.1 – Processing parameters for Perito Moreno and Ameghino glaciers (SPI).

No. of image pairs	6 (time series)
Acquisition date range (master)	20.01.2008 - 03.05.2011
Δt [days]	11
Beam	strip_012
Orbit / look direction	ascending / right
Polarization	HH
Patch size / overlap [m] (side)	320 / 160
$B_\perp$ [m]	27.83 - 270.83

Table 11.2 – Processing parameters for Pio XI Glacier (SPI).

No. of image pairs	1
Acquisition date (master)	05.07.2010
Δt [days]	11
Beam	strip_006
Orbit / look direction	ascending / right
Polarization	HH
Patch size / overlap [m] (side)	320 / 160
$B_\perp$ [m]	96.78

The Upsala Glacier (SPI) was monitored with a time series of 10 TerraSAR-X image pairs between December 2007 and October 2011 (Table 11.4). Eight of the obtained surface velocity fields are shown in Figure 11.12. The terminus of Upsala Glacier has undergone strong velocity changes and surface loss during the 4 year observation period. Its main terminus accelerated near the glacier front from around 5 $\mathrm{m\,d^{-1}}$ in 2008 to 10 $\mathrm{m\,d^{-1}}$ in October 2009. The glacier maintained its velocity at least till mid-2010 along with strong calving rates, it then underwent a deceleration phase with the front stabilizing at the level of the Bertacchi Glacier. The main front retreated 2.1 km between January 2008 and October 2011. The accelerated flow might trigger dynamic thinning (cf. Section 3.4) and explain the elevation change at the terminus reported in Section 7.4 and specifically in Figure 7.9b.

11.5.2 Antarctica

Great effort was put in the processing of large datasets in the Antarctic continent allowing to retrieve high resolution velocity results of glaciers which are scarcely imaged by appropriate sensors. The stability of the weather conditions in the interior of the continent provides high reliability of the offset tracking method, particularly for slow moving parts where speckle coherence is preserved even after three repeat pass cycles (33 days). In the figures below, where no TerraSAR-X coverage is available, the background is the RADARSAT-1 amplitude mosaic acquired during the RADARSAT Antarctic Mapping Project (RAMP) of 1997, when the Continent was mapped in high resolution for the first time. The grounding line (marked in pink) originates from the Antarctic Surface Accumulation and Ice Discharge

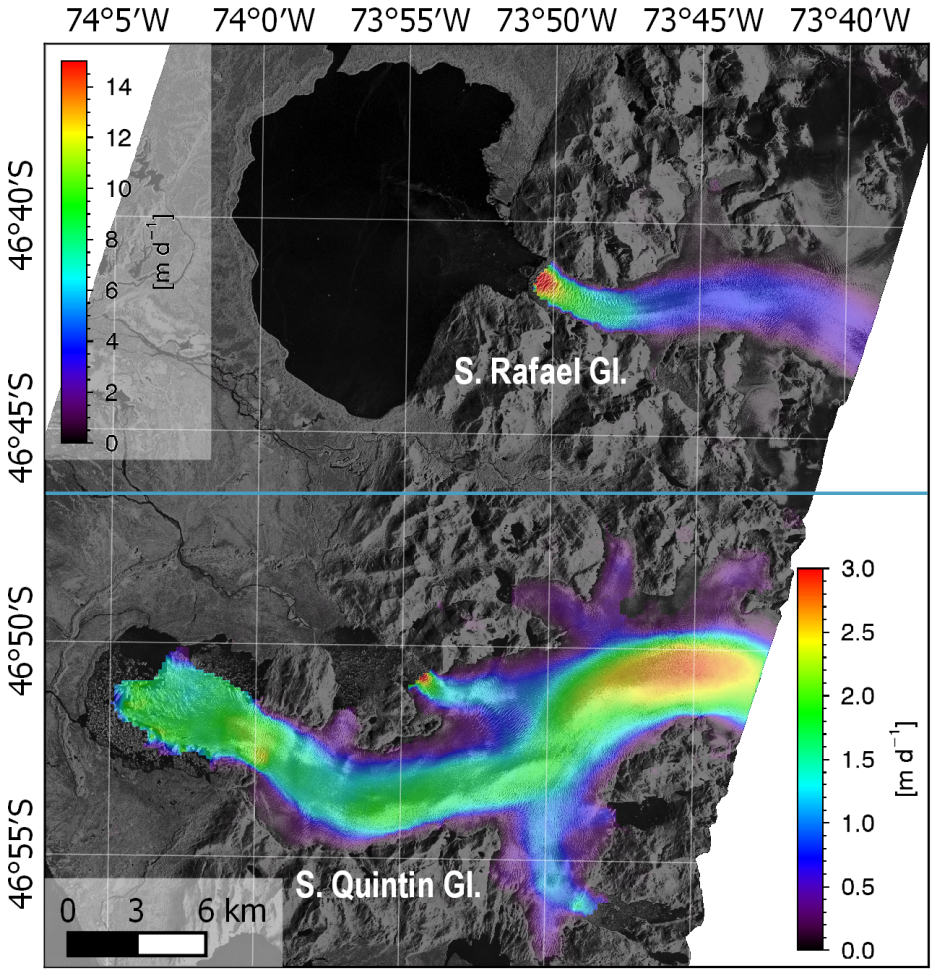

Figure 11.11 – Surface velocity of S. Rafael and S. Quintin glaciers (NPI).

Table 11.3 – Processing parameters for S. Rafael and S. Quintin glaciers (NPI).

No. of image pairs	1
Acquisition date (master)	14.05.2012
Δt [days]	11
Beam	strip_012
Orbit / look direction	descending / right
Polarization	HH
Patch size / overlap [m] (side)	320 / 160
$B_\perp$ [m]	55.74

Table 11.4 – Processing parameters for Upsala Glacier (SPI).

No. of image pairs	10 (time series)
Acquisition date range (master)	27.12.2007 - 04.10.2011
Δt [days]	11
Beam	strip_012 d., 013 a.
Orbit / look direction	asc. (3) + desc. (7) / right
Polarization	HH
Patch size / overlap [m] (side)	320 / 80
$B_\perp$ [m]	16.37 - 152.94

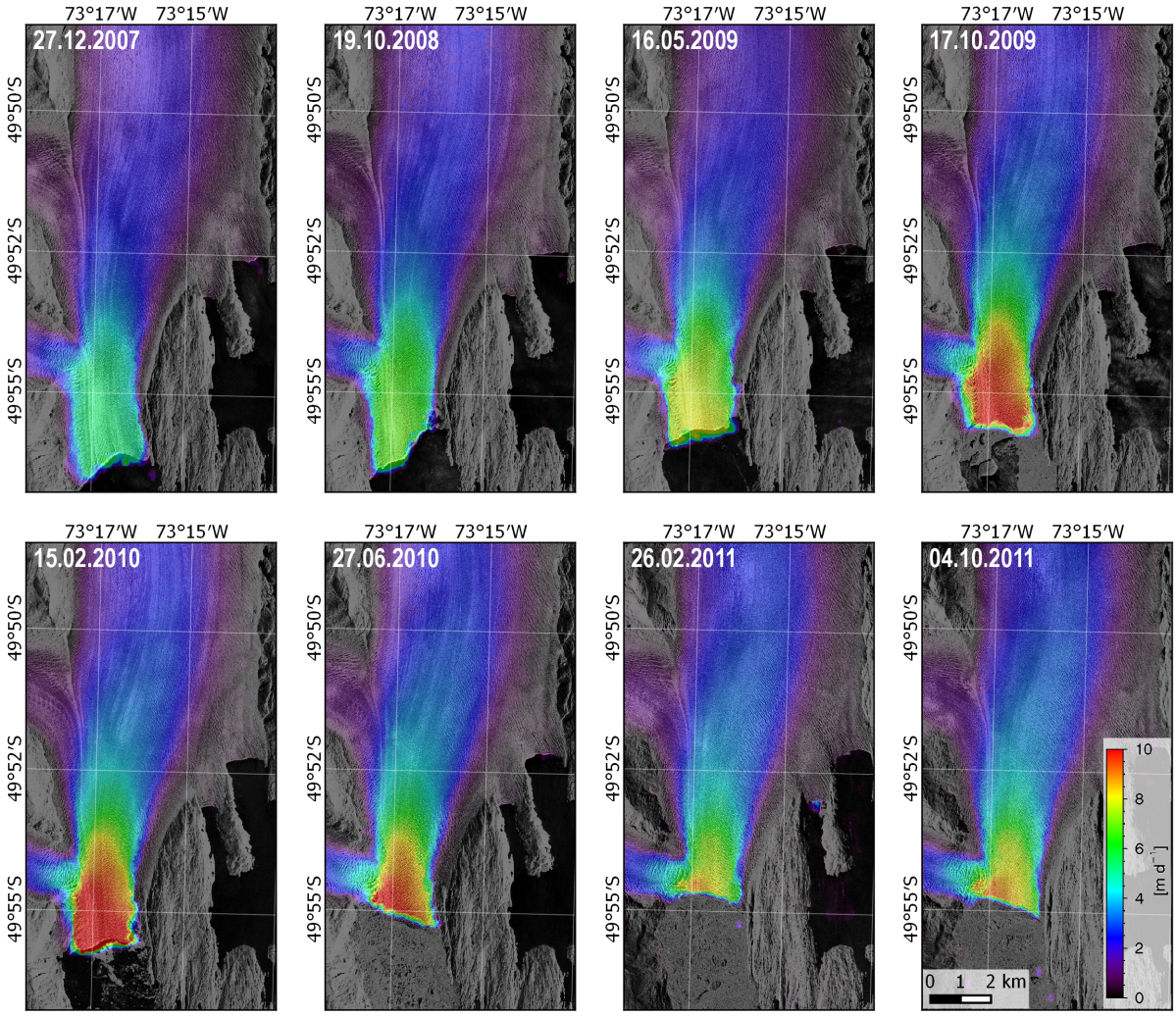

Figure 11.12 – Surface velocity of Upsala Glacier (SPI).

(ASAID) project and was obtained using a combination of Landsat-7 and ICESat laser altimetry mainly collected between 1999 and 2003 (Bindschadler *et al.*, 2011). The outlines of the active subglacial lakes (marked in red) have been derived by Smith *et al.* (2009) using ICESat laser altimetry data.

11.5.2.1 Drygalski Glacier

The Drygalski Glacier is located in the northern section of the Antarctic Peninsula, it is about 32 km long and 24 km wide at its head, calving on the east coast of the Graham land into the Weddell Sea at the Solari Bay. The glacier was the largest discharging into the Larsen A Ice Shelf, which collapsed in January 1995. Drygalski Glacier, as well as the other glaciers previously draining into the ice shelf, started to accelerate due to stress perturbation at the front after the ice shelf disintegrated. The analysis of ERS tandem InSAR data showed that in 1999 the signal of acceleration reached far upstream, with maximum acceleration near the calving front (Rott *et al.*, 2002). Here the glacier velocity was 2.6 $\mathrm{m\,d^{-1}}$ in November 1995, 7.1 $\mathrm{m\,d^{-1}}$ in 1999, 5.7 $\mathrm{m\,d^{-1}}$ in 2008, 5.5 $\mathrm{m\,d^{-1}}$ in 2010 and 7.4 $\mathrm{m\,d^{-1}}$ in 2013 (Rott *et al.*, 2011, 2014b).

A one year long time series starting October 2007 and composed by 29 Stripmap TerraSAR-X images and three additional pairs acquired two years later (cf. Table 11.5) were used to retrieve the surface velocity with a very high temporal and spatial resolution (Eineder *et al.*, 2011a).

The velocity matrices in output to the processing chain (thus after outlier elimination) are analysed along the temporal axis. The mean velocity field of the the 29+3 image pairs is shown in Figure 11.13, where the velocity in front of the glacier has been masked out for clarity although displaying

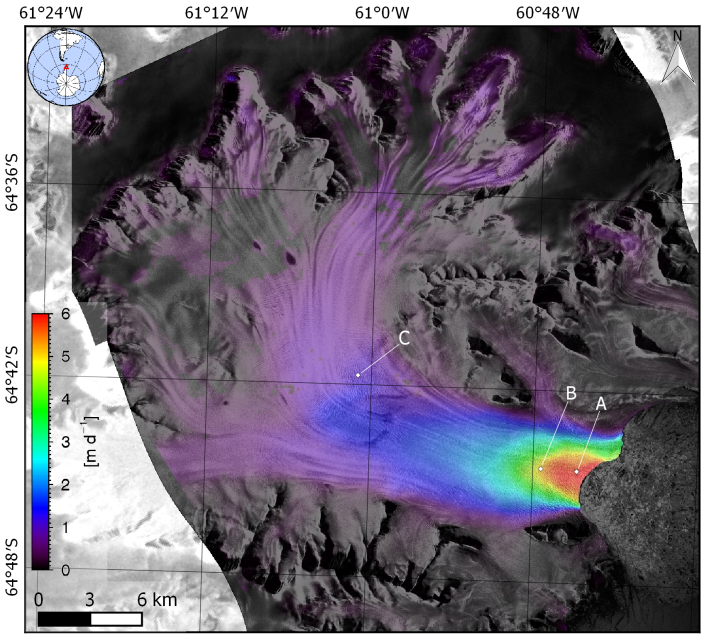

Figure 11.13 – Mean surface velocity of Drygalski Glacier over the period 2007 - 2010.

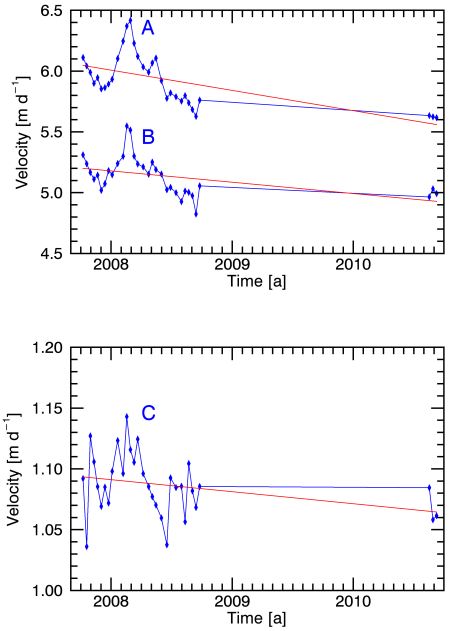

Figure 11.14 – Temporal velocity behaviour and linear fit at points A, B, C.

Table 11.5 – Processing parameters for Drygalski Glacier.

No. of image pairs	29 + 3 (time series)
Acquisition date range (master)	08.10.2007 - 24.09.2008 18.08.2010 - 09.09.2010
Δt [days]	11 (28), 22 (4)
Beam	strip_010
Orbit / look direction	ascending / right
Polarization	HH
Patch size / overlap [m] (side)	320 / 160
$B_\perp$ [m]	8.98 - 247.29

relatively good coherence due to the continuous calving of icebergs. The mean correlation coefficient (not shown) is higher on the glacier where a rougher surface pattern is present, particularly at the snout (where points A and B are selected) and in the middle of the glacier (where point C is selected). A linear fit is performed on each measurement patch, both on the one-year time series (29 pairs) and on the entire time series (29+3 pairs). The coefficient of each fitted line is assumed as acceleration value obtaining two acceleration images, one for 2007 - 2008 and one for 2007 - 2010 (not shown here, see Eineder *et al.* (2011a)).

The temporal behaviour of the velocity measurements for three patches located at points A, B and C is plotted in blue in Figure 11.14. Here the line fitted to the entire 2007 - 2010 series is shown in red, corresponding to a negative acceleration trend of $-45.59 \cdot 10^{-5}$ m d^{-2}, $-25.48 \cdot 10^{-5}$ m d^{-2} and $-2.71 \cdot 10^{-5}$ m d^{-2} for points A, B and C, respectively. A certain seasonal variation pattern is detectable, particularly at points A and B. At point C the measurement error has a larger impact given the lower amplitude of the shifts.

The TerraSAR-X analysis shows that the fast flow reported in Rott *et al.* (2002) and Rott *et al.* (2011) was maintained in 2010 at a similar level as in 1999, pointing out that the glacier is still far from an equilibrium state. In fact Rott *et al.* (2014b) reported further acceleration also in 2013. The consideration of mass continuity requires significant dynamic thinning along the glacier terminus over the years, which is still ongoing. The estimates of mass deficit imply that at least the lower section

of the terminus is floating. The temporal variation of velocity in 2007/2008 near the front shows a maximum in late summer (Figure 11.13). This could be due to different levels of stability of the ice melange floating in the bay. A similar seasonal behaviour has been observed by Rott *et al.* (2011) for Larsen-B outlet glaciers. The weak trend of velocity decrease measured near the front (points A, B) may be the response to a minor decrease in driving stress associated with thinning.

11.5.2.2 Nimrod and Byrd glaciers

Nimrod and Byrd are two main outlet glaciers located in the central Transantarctic Mountains (at the Shackleton and Hillary Coasts) draining ice from the East Antarctic Ice Sheet into the Ross Ice Shelf. The behaviour of these outlet glaciers and their neighbours is influenced by the upstream catchment area, by shearing across the rocky walls and along the glacier bed, where lubrication by subglacial water is possible, and the reaction of the floating ice shelf to the intrusion of upstream ice. The dynamical behaviour of these glaciers has been relatively steady over the past thousand of years, as evidenced by consistency between the modern ice shelf velocity field and flow stripes originating at the mouth of these outlet glaciers (Jezek, 1984). However important upstream changes in glacier flow of Byrd Glacier have been recently attributed to changes in subglacial water flow (Stearns *et al.*, 2008), leading to a 10% increase in ice discharge between December 2005 and February 2007 (Van Der Veen *et al.*, 2014) and highlighting the importance of up-to-date surface velocity measurements in this region. Consequently a vast acquisition plan of TerraSAR-X data in left looking direction was set up at DLR - IMF in order to cover interferometrically most of the outlet glaciers flowing into the Ross Ice Shelf.

The Byrd Glacier is one of the largest glaciers in East Antarctica (catchment basin area $1.07 \cdot 10^6$ km^2) with an estimated ice discharge into the Ross Ice Shelf is about 21 Gt a^{-1} (Rignot & Thomas, 2002), while Nimrod Glacier has a discharge of only 0.88 Gt a^{-1} (Stearns, 2011). The flow velocity of the Nimrod and Byrd glaciers were previously derived from ASTER imagery in Stearns & Hamilton (2005); Stearns *et al.* (2008); Stearns (2011) and by means of InSAR in Rignot *et al.* (2011a).

Two mosaics of surface velocity fields were obtained from TerraSAR-X Stripmap repeat pass pairs acquired in October 2009 for Nimrod Glacier (cf. Table 11.6) and between November 2010 and January 2011 for Byrd Glacier (cf. Table 11.7) and are shown in Figure 11.15 and 11.17, respectively (see also Jezek *et al.* (2011)). In order to support the analysis of the velocity fields, some transverse and longitudinal profiles have been extracted. The transverse profiles allow to determine the type of flow at a certain location, more specifically the prevalent driving force (whether basal motion or internal deformation) and resisting forces (e.g. basal or lateral drag). These concepts are explained in more detail in Section 3.4. The longitudinal velocity profile, retrieved along the flow direction approximately at the centreline of the glacier allows the estimation of the longitudinal strain rate. This is obtained according to (Forster *et al.*, 1999):

$$\dot{\varepsilon}_l = \frac{\Delta v_l}{\Delta d_l} \tag{11.17}$$

where Δv_l is the velocity variation between two points on the longitudinal profile and Δd_l is their distance. The strain rate expresses the degree of compression and extension the ice is subject to along a specific direction. Positive values correspond to expansion with the possibility of crevasse formation while negative values correspond to compression. The transverse and longitudinal velocity profiles and the longitudinal strain rate extracted are shown in Figure 11.16 and 11.18 for Nimrod and Byrd glaciers, respectively.

The velocity of Nimrod Glacier increases slowly upstream of the Kon-Tiki Nunatak where the strain rate plot shows an equilibrium status. As the nunatak approaches, the flow becomes constrained and increases in velocity, here strain rates around 0.02 a^{-1} are recorded. As the two channels merge again the velocity displays a peak of about 2.2 m d^{-1} and a strain rate of 0.1 a^{-1} is recorded, furthermore crevasses appear in this area. It must be noted that the position of the grounding line shown in Figure 11.15 (pink line) does not agree with other sources. The grounding line position was recently obtained by means of D-InSAR applied to TerraSAR-X data in Floricioiu *et al.* (2012), who place it further downstream, slightly above the transverse profile T. The transverse velocity profile T shows a central

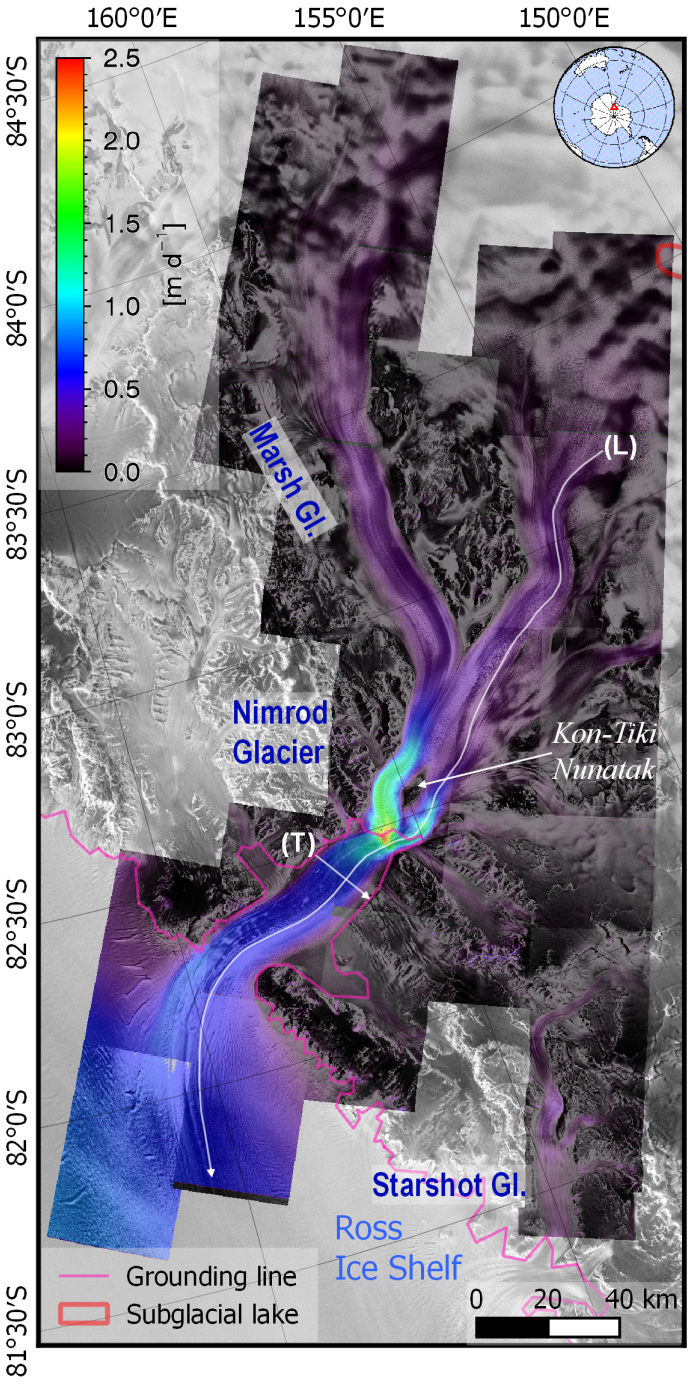

Figure 11.15 – Surface velocity of Nimrod Glacier.

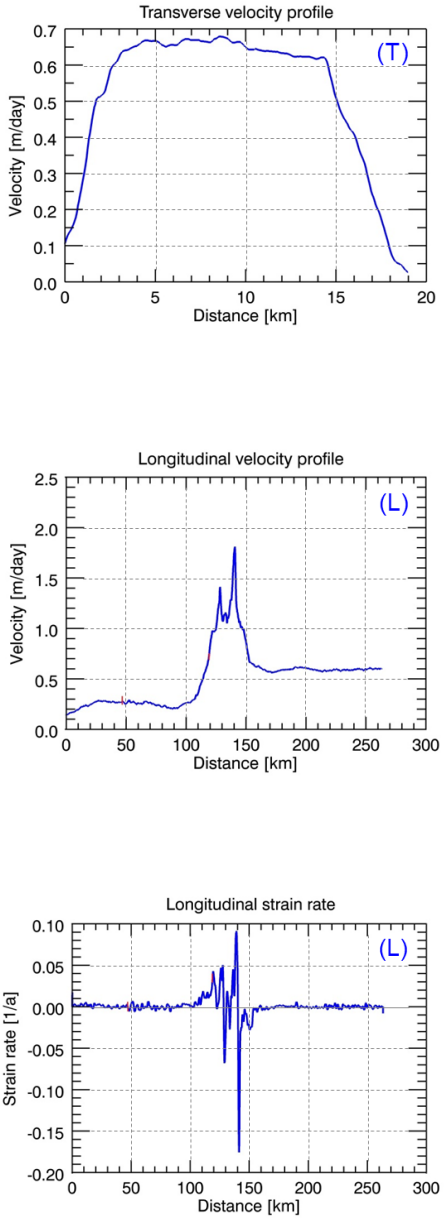

Figure 11.16 – Velocity profiles and longitudinal strain rate.

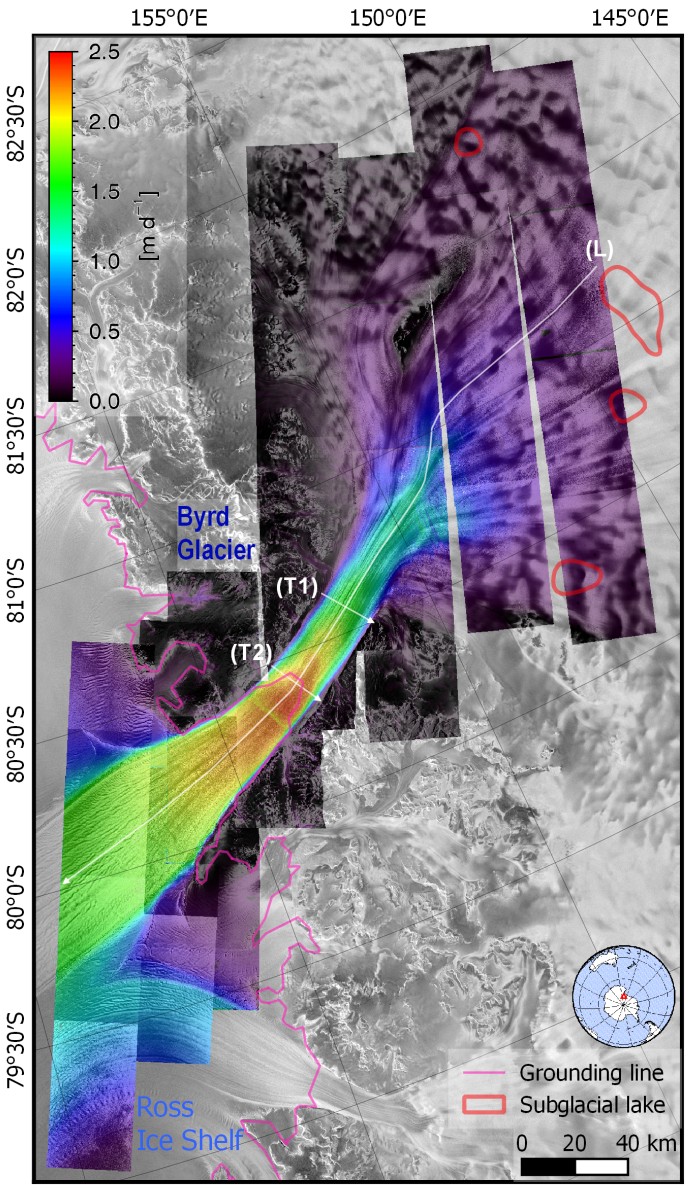

Figure 11.17 – Surface velocity of Byrd Glacier.

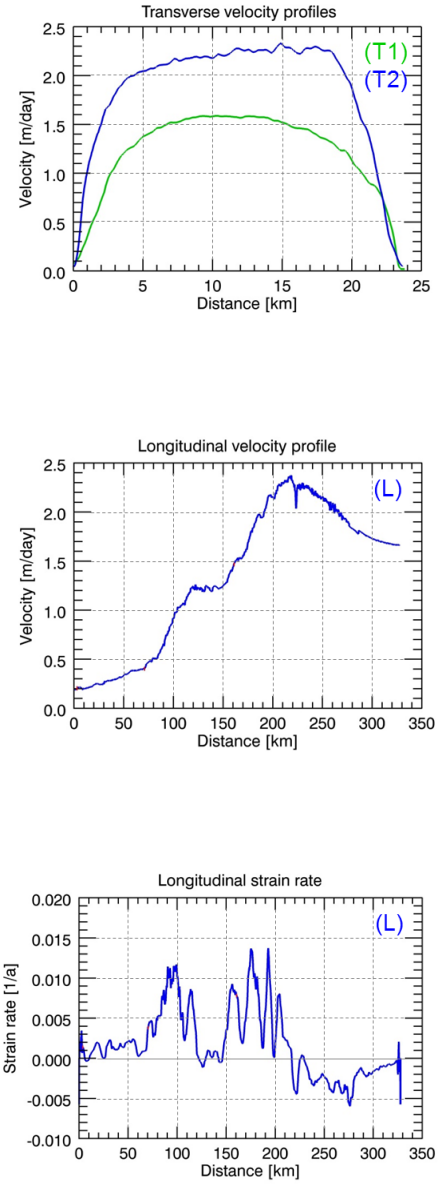

Figure 11.18 – Velocity profiles and longitudinal strain rate.

Table 11.6 – Processing parameters for Nimrod Glacier.

No. of image pairs	23
Acquisition date range (master)	06.10.2009 - 18.10.2009
Δt [days]	11
Beam	strip_014
Orbit / look direction	descending / left
Polarization	HH
Patch size / overlap [m] (side)	320 / 160
$B_\perp$ [m]	23.00 - 112.43

Table 11.7 – Processing parameters for Byrd Glacier.

No. of image pairs	29
Acquisition date range (master)	10.11.2010 - 22.01.2011
Δt [days]	11 (22), 22 (7)
Beam	strip_013 (6), 014 (23)
Orbit / look direction	descending / left
Polarization	HH
Patch size / overlap [m] (side)	320 / 160
$B_\perp$ [m]	16.01 - 109.06

band of approximately 12 km with nearly constant velocity of ~0.65 $m\,d^{-1}$ and lateral band with abrupt velocity reduction. This plug-like shape, coupled with shear at the margins suggests that the flow is mostly affected by side drag.

Byrd Glacier displays a different flow pattern than Nimrod Glacier as highlighted by the longitudinal profile in Figure 11.18. Flow velocity increases gradually as the ice starts to converge towards the narrow fjord (~ 22 km wide). The peak is reached approximately in correspondence of the grounding zone, afterwards the velocity decreases gradually as the ice streams into the Ross Ice Shelf. Here the position of the grounding line roughly agrees with the one found in Floricioiu *et al.* (2012), whose outline is defined with much higher precision and resolution. It must be noted that in Figure 11.17 and in the longitudinal profile, a thin transverse band of slower velocity is found downstream of the grounding zone. This artefact is caused by a jump in the DEM used to geocode the TerraSAR-X EEC images, likely caused by bad mosaicking of different sources in the GLOBE DEM. The longitudinal strain rate shows expansive behaviour (although with strong oscillations) up to the grounding line and it drops into compression zone as the velocity decreases.

An overall good agreement is found between the TerraSAR-X longitudinal profile and the profiles based on ASTER optical data from December 2005 to January 2008 published in Stearns *et al.* (2008). Two TerraSAR-X transverse velocity profiles are shown in Figure 11.18. The upstream profile T1 displays a parabolic shape indicating the prevalence of basal drag. The downstream profile T2, located in the grounding zone, starts to develop a plug-like shape suggesting a well lubricated bed and the prevalence of side drag. The transition from the upstream parabolic velocity profile to the plug-flow profile near the grounding line may be attributable to the weakening of the basal drag, causing the transfer of the flow resistance to side drag, and resulting in a transverse velocity profile similar to those observed on West Antarctic Ice streams by Stearns *et al.* (2005). Van Der Veen *et al.* (2014) apply force-balance calculations on the main trunk of Byrd Glacier. On a large scale they find that flow resistance is partitioned between ~80% of basal drag and ~20% of lateral drag. They further report that ice flow is mostly driven by basal sliding and concentrated vertical shear in the lower ice layers, indicating that the bed is at or close to pressure-melting temperature.

11.5.2.3 Glaciers of the Gould and Amundsen Coast

The surface velocity processing chain was used to map the glacier flow of many glaciers of the Central Transantarctic Mountains. The Beardmore Glacier is a large glacier south-west of the Nimrod Glacier, flowing into the Ross Ice Shelf at the Shackleton Coast. The glacier was covered with 17 repeat pass images (26.11.2009 - 16.12.2009). Its flow is fastest across the grounding line where it reaches approximately 0.95 $m\,d^{-1}$. The velocity map is not reported here but part of the doctoral thesis by Marsh (2013).

Surface velocities were derived for a vast area including the glaciers of the Central Transantarctic Mountains in correspondence of the Amundsen Coast (Liv, Amundsen, Scott, Leverett, Reedy) and for the wide ice streams flowing into the Ross Ice Shelf at the Gould Coast (Shimuzu, Horlick, Mercer, Van Der Veen, Whillans). The processing is based on 113 TerraSAR-X Stripmap image pairs (Table 11.8) and the resulting mosaic is shown in Figure 11.19. This result is part of the Master thesis by Amaro García (2012), where a detailed analysis is provided.

11.5.2.4 Thwaites Glacier

The Thwaites Glacier is located on the Walgreen Coast of Marie Byrd Land (West Antarctica) and flows into the Amundsen Sea at the Pine Island Bay. It is particularly broad and relatively fast. A mosaic of TerraSAR-X surface velocities was computed based on Stripmap data of late 2011 (Table 11.9) and is reported in Figure 11.20. The velocity fields and some TanDEM-X Raw DEM have been processed as a contribution to the DFG[4] project "The Antarctic ice sheet mass balance from satellite geodesy and modelling", which results are reported in Groh *et al.* (2014). Velocities up to ~9 $m\,d^{-1}$ are measured near the grounding line.

[4]Deutsche Forschungsgemeinschaft

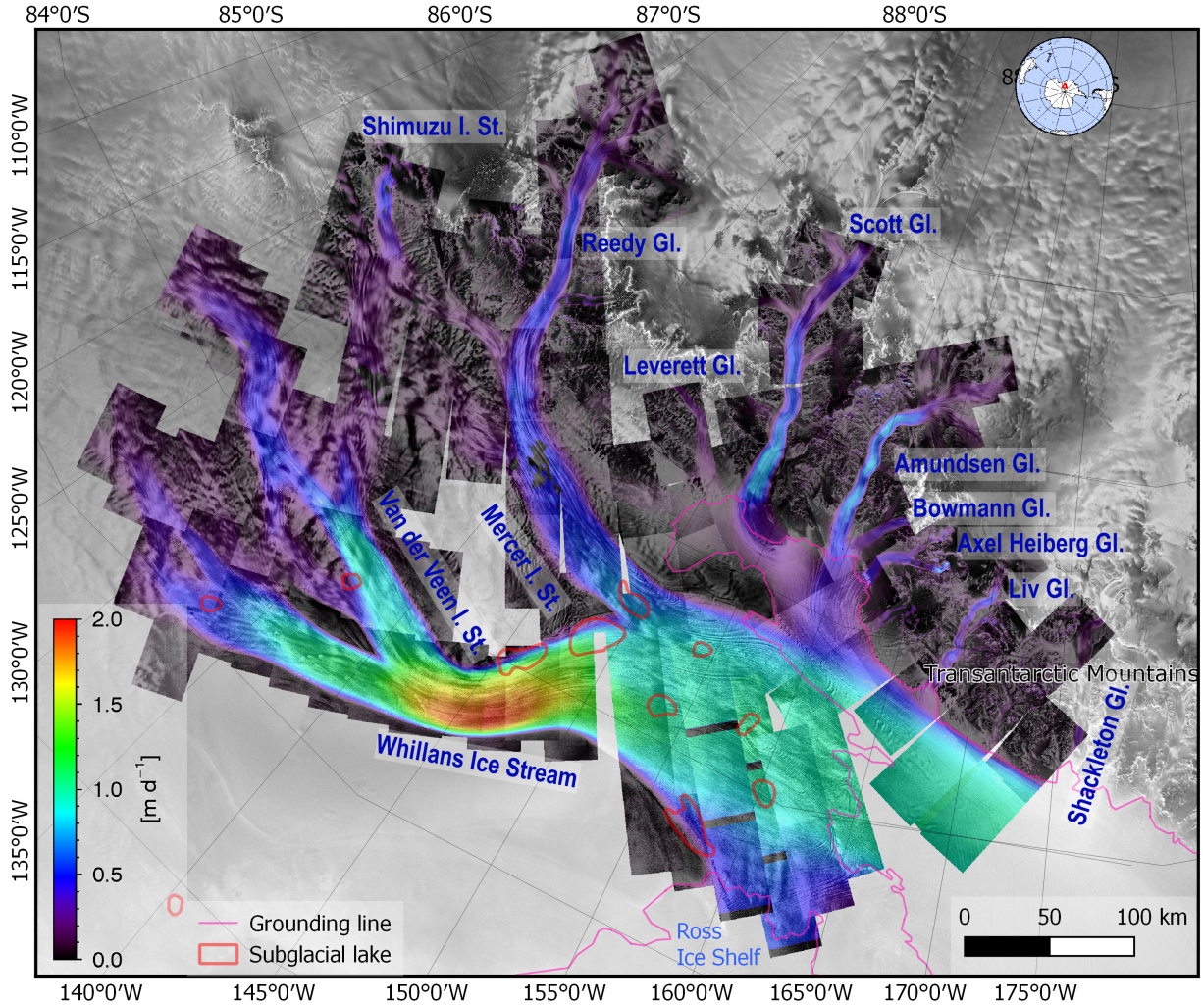

Figure 11.19 – Surface velocity of the Gould and Amundsen Coast glaciers.

Table 11.8 – Processing parameters for the Gould and Amundsen Coast glaciers.

No. of image pairs	113
Acquisition date range (master)	18.12.2009 - 05.12.2010
Δt [days]	11
Beam	strip_014
Orbit / look direction	ascending + descending / left
Polarization	HH
Patch size / overlap [m] (side)	320 / 160

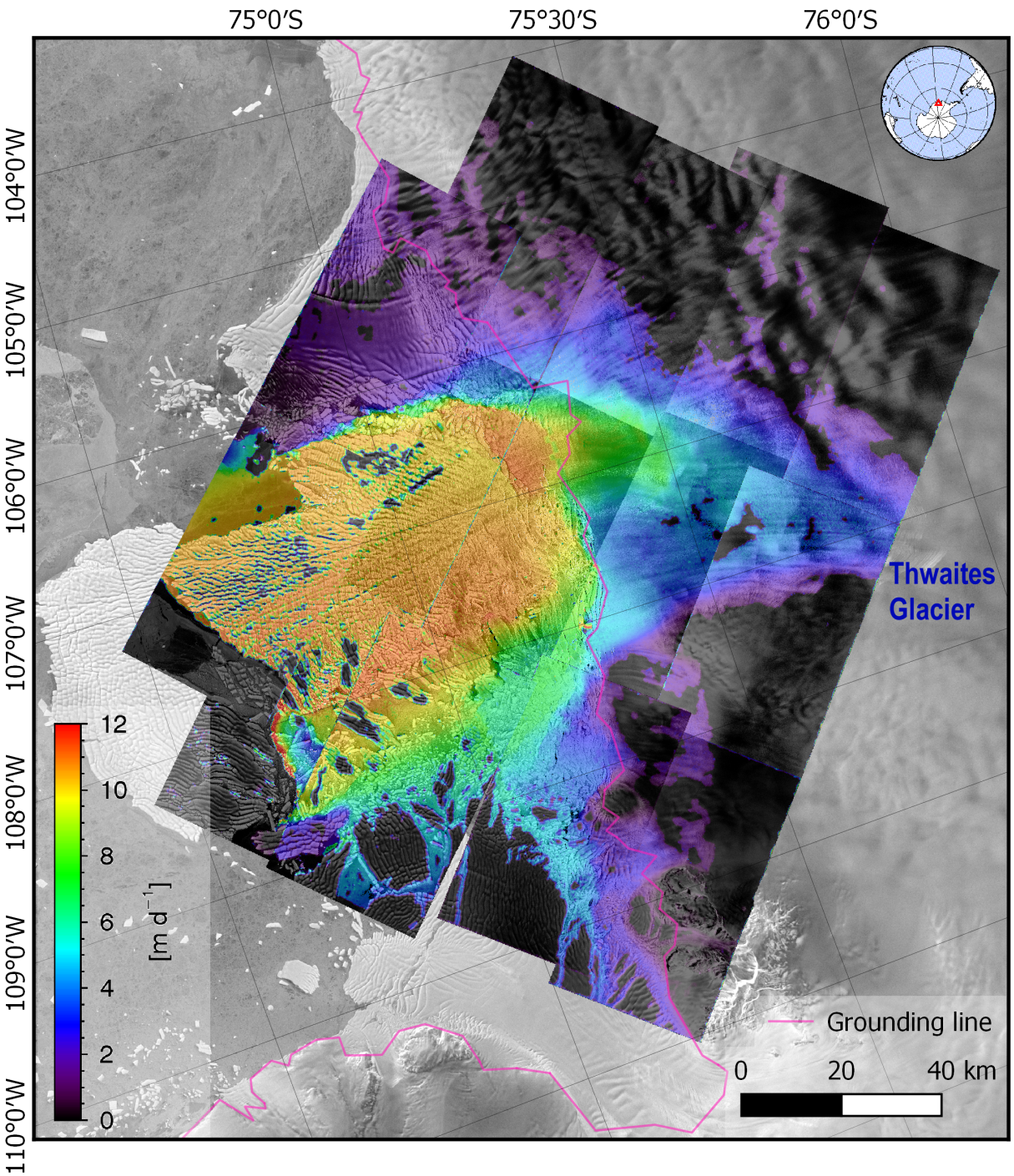

Figure 11.20 – Surface velocity of Thwaites Glacier.

Table 11.9 – Processing parameters for Thwaites Glacier.

No. of image pairs	14
Acquisition date range (master)	24.09.2011 - 18.11.2011
Δt [days]	11
Beam	strip_010, 011, 012
Orbit / look direction	ascending / right
Polarization	HH
Patch size / overlap [m] (side)	320 / 160
$B_\perp$ [m]	3.42 - 139.96

Table 11.10 – Processing parameters for the Recovery Glacier.

No. of image pairs	150
Acquisition date range (master)	30.10.2008 - 04.01.2009 (RAMP Gl.) 23.04.2011 - 05.02.2013 01.11.2013 - 20.11.2013 (Lakes A, B, C)
Δt [days]	11 (135), 22 (13), 33 (2)
Beam	strip_012, 013, 014
Orbit / look direction	ascending / left
Polarization	HH
Patch size / overlap [m] (side)	320 / 160

11.5.2.5 Recovery Glacier

The Recovery Glacier is located in Coates Land and flows west along the southern side of the Shackleton Range and ends into the Filchner Ice Shelf. The Recovery Glacier system is of considerable scientific interest because of its role in discharging ice from East Antarctica into the sea and because it has been subsequently learned that the flow of the glacier is likely controlled by the presence of subglacial lakes near the onset of faster glacier flow. A total of 150 Stripmap TerraSAR-X image pairs were processed to cover the main trunk and the two main tributaries, RAMP and Blackwall Glacier (Table 11.10). The resulting mosaic of surface velocity is reported in Figure 11.21, where the positions of the subglacial lakes are also marked (see also Floricioiu *et al.* (2014)). The surface velocity within the main trunk of Recovery as well as of the two tributaries increases slowly in the flow direction. In the upper part of the streams the ice speed is about 0.2 m d^{-1} for all three glaciers. The onset of faster flow at the heads of the two tributaries is remarkably abrupt. In the grounding zone the Recovery Glacier is confined in a narrow channel and maximum flow speeds of ~2.5 m d^{-1} are reached. General good agreement is found with the ice flow velocities provided by Rignot *et al.* (2011a). The result, along with a large mosaic of TanDEM-X Raw DEMs, contributed to the HGF[5] project “Remote Sensing and Earth System Dynamics”.

[5]Helmholtz-Gemeinschaft Deutscher Forschungszentren

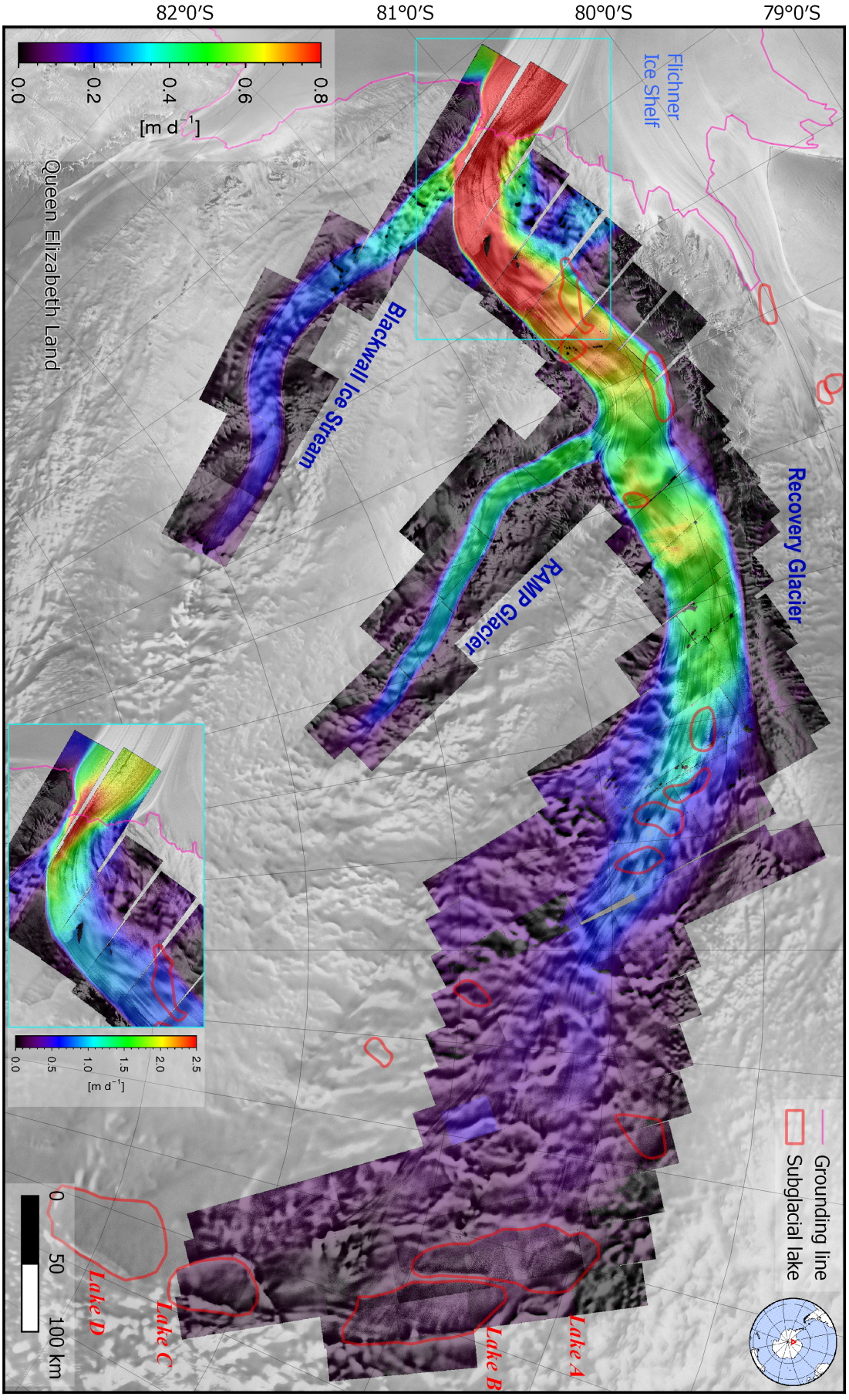

Figure 11.21 – Surface velocity of the Recovery Glacier.

Chapter 12

Conclusion

12.1 Discussion and conclusion

As mentioned in the introductory chapter of this thesis, all the elements of the cryosphere, and particularly glaciers and ice sheets, are fundamental components of the global climate system and are thus very sensitive to climate change. Detailed knowledge of the properties of land ice masses and precise observation of their temporal changes are hence pivotal scientific and societal priorities.

Traditional glaciology, based on *in situ* observations, has been revolutionised in the last decades by the advent of remote sensing, allowing to monitor the often inaccessible glaciers at a much larger spatial and temporal scale and at lower cost. Spaceborne and airborne synthetic aperture radar (SAR) imaging systems represent one of the most adequate remote sensing observation tools for glaciers, offering significant advantages over optical sensors, among which the ability to operate under any illumination and weather condition and to "perceive" features on and below the ice and snow surface otherwise invisible to optical systems. Since its introduction, the development of the SAR technology has been consistent and ongoing, nevertheless its potential for glaciological studies remains somehow underexploited. This dissertation aims at taking advantage of the data provided by multiple SAR systems, among which the recent high resolution products of DLR's TerraSAR-X and TanDEM-X missions and focuses on their applications in glaciology.

A significant and progressive ice mass loss trend has been registered worldwide in the last decades. To improve the currently uncertain global glacier loss projections, and consequently climate change models, a good understanding of the driving mechanisms governing mass balance and glacier flow are needed. To this end the improved estimation of both parameters based on high resolution SAR data is the general goal of this dissertation.

An up-to-date and accurate mass balance and its temporal trend for a wide pool of glaciers is hence fundamental, but of complex derivation. The traditional input-output method relies on field measurements and models to retrieve the surface mass balance. Furthermore to derive the loss due to glacier calving the cross-section and ice flow velocity at the calving gate are needed, and velocities are derivable on a large scale only by remote sensing. Since 2003 the GRACE satellite mission provides monthly gravity anomalies from which the mass balance of large ice covered areas can be monitored. The gravity field solutions offer coarse spatial resolution and necessitate models to isolate other mass change contributions leading to large uncertainty. The geodetic method is based on repeated measurements of glacier surface elevation and area allowing to retrieve volume changes which can be converted to mass changes if the ice density is known, but it cannot distinguish the contributions due to accumulation and ablation.

The geodetic mass balance has been applied by many authors relying on the most diverse elevation datasets. These can be inaccurate or incomplete: old cartographic maps obtained from aerial photographs and optical DEMs both suffer from the lack of features on smooth snow, laser and radar altimetry is more precise but lacks in spatial coverage. In this thesis the recent availability of TanDEM-X high resolution DEMs is exploited together with the proven reliability of the SRTM C-band DEM: these datasets acquired both by means of bistatic InSAR offer a considerable potential for the geodetic mass balance of glaciers with regards to spatial coverage, spatial resolution and height accuracy. The

combination of high resolution multitemporal TanDEM-X DEMs is also explored for the derivation of up-to-date elevation change maps and mass balances and the derivation of their temporal trends.

The geodetic mass balance results presented in the literature, partly because of the use of variegate and sometimes less accurate data, often lack a complete characterization of the error. Relevant aspects are neglected or summarily modelled, leading to both under and overestimation of the error. In this thesis a framework for the estimation of the uncertainty of the elevation change maps and the geodetic mass balance is defined by taking into account all relevant error sources, with particular regard to bistatic InSAR data.

Glacier surface velocities, besides being necessary to estimate the loss due to calving are important in assessing the stability of icefields and ice sheets and their responses to climate change. Detailed velocity maps are essential to ice dynamics, allowing to map the ice transport from accumulation to ablation regions and to estimate strain rates and other geophysical parameters. Taking advantage of large amounts of high resolution TerraSAR-X amplitude data to map surface velocity at a large spatial or temporal scale is one of the main goals of this dissertation.

The following are the main research contributions of this thesis:

- Detailed and extended elevation change maps (Figure 7.6 and 7.8) were derived over the vast Northern and Southern Patagonian icefields (area ~16700 km^2) by selecting and processing a large number of TanDEM-X Raw DEMs (from 2011/'12 for SPI and 2014 for NPI) which were precisely coregistered to the SRTM C-band DEM of 2000 before performing their subtraction. Despite the difficult topography a significant coverage of the icefields was obtained (NPI: 87% SPI: 93%), reducing the reliance on extrapolation. The results are dominated by significant thinning (up to $-26\ m\,a^{-1}$ on Jorge Montt Glacier) and display variable behaviour across the icefields. They are crucial for the glaciological community working on these very dynamic regions.

- The elevation change maps are used to derive the geodetic mass balance of NPI and SPI with a high degree of confidence (Table 9.7) and the elevation, volume and mass change rate with respect to altitude (Figures 9.16 and 9.17). Total mass change rates of $-3.96 \pm 0.14\ Gt\,a^{-1}$ and $-13.14 \pm 0.42\ Gt\,a^{-1}$ have been obtained for NPI (2000 - 2014) and SPI (2000 - 2011/'12), respectively (excluding subaqueous changes). The average thinning is found to be consistent between the two icefields. The total estimated mass loss of NPI and SPI amounts to $-17.1 \pm 0.44\ Gt\,a^{-1}$.

- Mass change rates of the region available in the literature were updated and corrected. The geodetic mass balance obtained for the same observation period by Willis *et al.* (2012a) appears to be higher, even significantly for SPI, they found a mass loss rate of $-4.9 \pm 0.3\ Gt\,a^{-1}$ and $-21.2 \pm 0.5\ Gt\,a^{-1}$ for NPI and SPI, respectively. The geodetic mass balance by Rignot *et al.* (2003) obtained for the period 1995 - 2000 also appears to be significantly overestimated. Gravimetric mass balances for NPI and SPI also overestimate significantly mass loss compared with the results found in this thesis. They report: $-25.1 \pm 9.9\ Gt\,a^{-1}$ (2001 - 2006) (Chen *et al.*, 2007), $-26 \pm 6\ Gt\,a^{-1}$ (2003 - 2009) (Ivins *et al.*, 2011) and $-23 \pm 9\ Gt\,a^{-1}$ (2003 - 2010) (Jacob *et al.*, 2012).

- A framework for the accuracy estimation of the geodetic mass balance has been developed. Relevant error sources, with particular focus on InSAR bistatic DEMs have been investigated and quantified. Among these are:

  - coregistration error acting as a systematic error on the elevation change rate samples;
  - uncertainty of the elevation difference sample: being of random nature it decreases with the square root of the number independent samples, which has been determined through a semivariogram analysis;
  - the variability of the interferometric error between glaciated and ice-free terrain has been assessed;

  - error due to seasonal elevation changes and SAR signal penetration into ice and snow;
  - crustal uplift due to glacial isostatic adjustment;
  - error of the glacier area;
  - error linked to the assumption of a certain ice density;
  - elevation bias due to different spatial resolution of the DEMs.

- A detailed analysis of the backscattering coefficient of both the SRTM (through recently released data) and the TanDEM-X has been performed through a review of the theory and published experiments regarding the backscattering of snow, a summary of which has been condensed in this dissertation (Chapter 4). The goal of such an analysis, which was also supported by meteorological data, was to assess the liquid water content of the snow and the consequent risk of signal penetration into snow and ice, a phenomenon producing an elevation bias in the InSAR DEM thus affecting the geodetic mass balance as a systematic height error on the interested areas.

- The disjoint geodetic mass balance of the Jorge Montt Glacier has been obtained for the observation period 2000 - 2011, when the glacier lost ice at an appalling rate of $-26\ \mathrm{m\,a^{-1}}$ at the snout and resulted in a mass balance of $-1.72\ \mathrm{Gt\,a^{-1}}$. To provide an updated value and to extract a temporal trend, a recent elevation change rate map and mass balance were obtained from two TanDEM-X Raw DEMs (2011 - 2014). Thinning rates up to $-33\ \mathrm{m\,a^{-1}}$ are found at the snout with a mass change rate of $-2.59\ \mathrm{Gt\,a^{-1}}$ (+50% compared to 2000 - 2011).

- A processing chain was developed for the derivation of glacier surface velocity maps from high resolution TerraSAR-X EEC SE amplitude images based on offset tracking based on the normalized cross-correlation function. It allows fast processing of a large number of data pairs with limited operator intervention providing reliable results under different glacier scenarios.

- The error sources and criticalities of the surface velocity estimation have been assessed.

- Spatially detailed surface velocity maps with wide coverage and multitemporal observations have been obtained for scientifically relevant glaciers worldwide (Section 11.5), with particular focus on remote regions such as the interior of Antarctica where measurements are still scarce (e.g. Recovery, Thwaites, Ross Ice Shelf glaciers). The results have been interpreted critically and additional parameters such as acceleration and strain rates have been derived.

12.2 Outlook

The approaches applied and the results obtained in this thesis for glaciology applications based on high resolution SAR data can be further improved, extended and used. Some recommendations for future work are the following:

- The elevation change results of NPI and SPI should be used to derive disjoint glacier parameters and mass balances for each glacier basin, following the procedure applied here for Jorge Montt Glacier.

- The presented approach for mass balance derivation can be applied on other glaciated regions of the Earth covered by the SRTM DEM (between 60°N and 56°S) or by other older DEMs.

- The TanDEM-X mission, initiated in June 2010, is still operating in bistatic mode at the time of writing. This mission provides to the glaciological community an invaluable elevation dataset based on bistatic InSAR with a temporal baseline up to at least 6.5 years. The TanDEM-X data should be exploited by applying the approaches and the guidelines proposed in this thesis for the derivation of updated elevation change maps, geodetic mass balances and the correspondent error budget as performed here on the Jorge Montt Glacier. This is potentially applicable on all

glaciers of the world where sufficient data has been acquired, but it is recommended on glaciers displaying strong variability, for instance the calving glaciers of Patagonia, Alaska, Greenland and the Antarctic Peninsula. In fact this is the goal of the recently started ESA Third Party Mission project “SAMBA - High Resolution SAR Algorithms for Mass Balance and Dynamics of Calving Glaciers”.

- The glacier surface velocity processing chain should be further exploited to cover vast regions in Antarctica and globally where TerraSAR-X data have been already acquired and archived and by acquiring new data taking advantage of the good state of health of the TSX-1 and TDX-1 satellites and their ability to cover latitudes south of 80°S by looking to the left of the flight path. These results are keenly requested by the glaciological community.

- The processing chain should be further developed in many aspects, including the use of Sentinel-1 data, the use of SSC products and the geocoding of the displacement measurements by means of the upcoming TanDEM-X global DEM (particularly in Antarctica), the correction of earth deformation and tropospheric effects, the estimation of the uncertainty of each displacement measurement, and a general improvement of the mosaicking and visualization algorithms.

- The glacier surface velocity results should be used as input to automated algorithms for the derivation of flow lines and calving flux and rates, parameters of crucial importance in glaciology, for instance for the derivation of mass balance of glaciers with the input-output method.

- For calving glaciers the calving flux derived from the glacier surface velocities (and the calving cross-section) can be subtracted from the net mass balance obtained with the geodetic method allowing a validation and a calibration of the surface mass balance (accumulation + ablation) estimates which feature a large uncertainty since they rely on climatic models. This is another objective of the SAMBA project.

Bibliography

ABDEL JABER, W., FLORICIOIU, D., ROTT, H., & EINEDER, M. 2012. Dynamics of fast glaciers in the Patagonia Icefields derived from TerraSAR-X and TanDEM-X data. *Pages 3226–3229 of: 2012 IEEE International Geoscience and Remote Sensing Symposium (IGARSS)*.

ABDEL JABER, W., FLORICIOIU, D., ROTT, H., & EINEDER, M. 2013. Surface elevation changes of glaciers derived from SRTM and TanDEM-X DEM differences. *Pages 1893–1896 of: 2013 IEEE International Geoscience and Remote Sensing Symposium (IGARSS)*.

ABDEL JABER, W., FLORICIOIU, D., & ROTT, H. 2014. Glacier dynamics of the Northern Patagonia Icefield derived from SRTM, TanDEM-X and TerraSAR-X data. *Pages 4018–4021 of: 2014 IEEE International Geoscience and Remote Sensing Symposium (IGARSS)*.

AMARO GARCÍA, D. F. 2012 (September). *Velocity estimation with speckle tracking based on TerraSAR-X. Application on glaciers and ice streams in the Ross Ice Shelf Sector, Antarctica*. M.Phil. thesis, Technische Universität München.

ANIYA, M. 1988. Glacier Inventory for the Northern Patagonia Icefield, Chile, and Variations 1944/45 to 1985/86. *Arctic and Alpine Research*, **20**(2), 179–187.

ANIYA, M. 1996. Holocene variations of Ameghino Glacier, southern Patagonia. *The Holocene*, **6**(2), 247–252.

ANIYA, M. 1999. Recent glacier variations of the Hielos Patagonicos, South America, and their contribution to sea-level change. *Arctic, Antarctic, and Alpine Research*, 165–173.

ANIYA, M. 2007. Glacier variations of Hielo Patagónico Norte, Chile, for 1944/45-2004/05. *Bulletin of glaciological research*, **24**, 59–70.

ANIYA, M., SATO, H., NARUSE, R., SKVARCA, P., & CASASSA, G. 1996. The use of satellite and airborne imagery to inventory outlet glaciers of the Southern Patagonia Icefield, South America. *Photogrammetric Engineering and Remote Sensing*, **62**(12), 1361–1369.

ANIYA, M., SATO, H., NARUSE, R., SKVARCA, P., & CASASSA, G. 1997. Recent glacier variations in the Southern Patagonia icefield, South America. *Arctic and Alpine Research*, 1–12.

ANTONY, J. W., HUESO GONZÁLEZ, J., SCHWERDT, M., BACHMANN, M., KRIEGER, G., & ZINK, M. 2013. Results of the TanDEM-X baseline calibration. *IEEE Journal of Selected Topics in Applied Earth Observations and Remote Sensing*, **6**(3), 1495–1501.

ARENDT, A., ECHELMEYER, K., HARRISON, W., LINGLE, C., ZIRNHELD, S., VALENTINE, V., RITCHIE, B., & DRUCKENMILLER, M. 2006. Updated estimates of glacier volume changes in the western Chugach Mountains, Alaska, and a comparison of regional extrapolation methods. *Journal of Geophysical Research: Earth Surface (2003–2012)*, **111**(F3).

ARENDT, A., BOLCH, T., COGLEY, J., GARDNER, A., HAGEN, J.-O., HOCK, R., KASER, G., PFEFFER, W., MOHOLDT, G., PAUL, F., *et al.* 2012. *Randolph Glacier Inventory [v2.0]: A Dataset of Global Glacier Outlines.* Digital Media.

ARENDT, A., , BLISS, A., BOLCH, T., COGLEY, J., GARDNER, A., HAGEN, J.-O., HOCK, R., HUSS, G., KASER, G., KIENHOLZ, C., PFEFFER, W., MOHOLDT, G., PAUL, F., *et al.* 2015. *Randolph Glacier Inventory - A Dataset of Global Glacier Outlines: version 5.0*. Digital Media.

ARENDT, A. A., ECHELMEYER, K. A., HARRISON, W. D., LINGLE, C. S., & VALENTINE, V. B. 2002. Rapid wastage of Alaska glaciers and their contribution to rising sea level. *Science*, **297**(5580), 382–386.

ARSLAN, A. N., HALLIKAINEN, M. T., & PULLIAINEN, J. T. 2005. Investigating of snow wetness parameter using a two-phase backscattering model. *IEEE Transactions on Geoscience and Remote Sensing*, **43**(8), 1827–1833.

BADER, H. 1954. Sorge's Law of densification of snow on high polar glaciers. *J. Glaciol*, **2**(15), 319–323.

BALSS, U., NIEDERMEIER, A., & BREIT, H. 2010. TanDEM-X Bistatic SAR Processing. *Pages 1–3 of: EUSAR 2010; 8th European Conference on Synthetic Aperture Radar*.

BALSS, U., BREIT, H., FRITZ, T., STEINBRECHER, U., GISINGER, C., & EINEDER, M. 2014a. Analysis of internal timings and clock rates of TerraSAR-X. *Pages 2671–2674 of: 2014 IEEE International Geoscience and Remote Sensing Symposium (IGARSS)*.

BALSS, U., GISINGER, C., CONG, X. Y., BRCIC, R., HACKEL, S., & EINEDER, M. 2014b. Precise measurements on the absolute localization accuracy of TerraSAR-X on the base of far-distributed test sites. *Pages 1–4 of: EUSAR 2014; 10th European Conference on Synthetic Aperture Radar*.

BAMBER, J. L., GOMEZ-DANS, J. L., & GRIGGS, J. A. 2009. A new 1 km digital elevation model of the Antarctic derived from combined satellite radar and laser data - Part 1: Data and methods. *The Cryosphere*, **3**(1), 101–111.

BAMBER, J. L., & RIVERA, A. 2007. A review of remote sensing methods for glacier mass balance determination. *Global and Planetary Change*, **59**(1), 138–148.

BAMLER, R. 2000. Interferometric stereo radargrammetry: absolute height determination from ERS-ENVISAT interferograms. *Pages 742–745 of: 2000 IEEE International Geoscience and Remote Sensing Symposium (IGARSS)*, vol. 2.

BAMLER, R., & EINEDER, M. 2005. Accuracy of differential shift estimation by correlation and split-bandwidth interferometry for wideband and delta-k SAR systems. *IEEE Geoscience and Remote Sensing Letters*, **2**(2), 151–155.

BAMLER, R., & HARTL, P. 1998. Synthetic aperture radar interferometry. *Inverse problems*, **14**(4), R1.

BAMLER, R., MEYER, F., & LIEBHART, W. 2007. Processing of bistatic SAR data from quasi-stationary configurations. *IEEE Transactions on Geoscience and Remote Sensing*, **45**(11), 3350–3358.

BARCAZA, G., ANIYA, M., MATSUMOTO, T., & AOKI, T. 2009. Satellite-derived equilibrium lines in Northern Patagonia Icefield, Chile, and their implications to glacier variations. *Arctic, Antarctic, and Alpine Research*, **41**(2), 174–182.

BARRAND, N. E., HINDMARSH, R. C. A., ARTHERN, R. J., WILLIAMS, C. R., MOUGINOT, J., SCHEUCHL, B., RIGNOT, E., LIGTENBERG, S. R. M., VAN DEN BROEKE, M. R., EDWARDS, T. L., *et al.* 2013. Computing the volume response of the Antarctic Peninsula ice sheet to warming scenarios to 2200. *Journal of Glaciology*, **59**(215), 397–409.

BECHOR, N. B. D., & ZEBKER, H. A. 2006. Measuring two-dimensional movements using a single InSAR pair. *Geophysical Research Letters*, **33**(16).

BERTHIER, E., VADON, H., BARATOUX, D., ARNAUD, Y., VINCENT, C., FEIGL, K. L., REMY, F., & LEGRESY, B. 2005. Surface motion of mountain glaciers derived from satellite optical imagery. *Remote Sensing of Environment*, **95**(1), 14–28.

BERTHIER, E., ARNAUD, Y., VINCENT, C., & REMY, F. 2006. Biases of SRTM in high-mountain areas: Implications for the monitoring of glacier volume changes. *Geophysical Research Letters*, **33**(8).

BERTHIER, E., ARNAUD, Y., KUMAR, R., AHMAD, S., WAGNON, P., & CHEVALLIER, P. 2007. Remote sensing estimates of glacier mass balances in the Himachal Pradesh (Western Himalaya, India). *Remote Sensing of Environment*, **108**(3), 327–338.

BERTHIER, E., SCHIEFER, E., CLARKE, G. K. C., MENOUNOS, B., & RÉMY, F. 2010. Contribution of Alaskan glaciers to sea-level rise derived from satellite imagery. *Nature Geoscience*, **3**(2), 92–95.

BINDSCHADLER, R., CHOI, H., WICHLACZ, A., BINGHAM, R., BOHLANDER, J., BRUNT, K., CORR, H., DREWS, R., FRICKER, H., HALL, M., HINDMARSH, R., KOHLER, J., PADMAN, L., RACK, W., ROTSCHKY, G., URBINI, S., VORNBERGER, P., & YOUNG, N. 2011. Getting around Antarctica: new high-resolution mappings of the grounded and freely-floating boundaries of the Antarctic ice sheet created for the International Polar Year. *The Cryosphere*, **5**(3), 569–588.

BINDSCHADLER, R. A., JEZEK, K. C., & CRAWFORD, J. 1987. Glaciological investigations using the synthetic aperture radar imaging system. *Annals of Glaciology*, **9**, 11–19.

BINDSCHADLER, R. 1998. Monitoring ice sheet behavior from space. *Reviews of Geophysics*, **36**(1), 79–104.

BINGHAM, A. W., & DRINKWATER, M. R. 2000. Recent changes in the microwave scattering properties of the Antarctic ice sheet. *IEEE Transactions on Geoscience and Remote Sensing*, **38**(4), 1810–1820.

BIPPUS, G. 2007. *Modelling mass balance and climate sensitivity of glaciers of the Southern Patagonia Icefield*. M.Phil. thesis, Institute of Meteorology and Geophysics, University of Innsbruck.

BOEX, J., FOGWILL, C., HARRISON, S., GLASSER, N., HEIN, A., SCHNABEL, C., & XU, S. 2013. Rapid thinning of the late Pleistocene Patagonian Ice Sheet followed migration of the Southern Westerlies. *Scientific Reports*, **3**.

BOLCH, T., PIECZONKA, T., & BENN, D. I. 2011. Multi-decadal mass loss of glaciers in the Everest area (Nepal Himalaya) derived from stereo imagery. *The Cryosphere*, **5**(2), 349–358.

BOLCH, T., SANDBERG SØRENSEN, L., SIMONSEN, S. B., MÖLG, N., MACHGUTH, H., RASTNER, P., & PAUL, F. 2013. Mass loss of Greenland's glaciers and ice caps 2003–2008 revealed from ICESat laser altimetry data. *Geophysical Research Letters*, **40**(5), 875–881.

BORLA TRIDON, D., BACHMANN, M., SCHULZE, D., ORTEGA-MÍGUEZ, C., POLIMENI, M. D., MARTONE, M., BÖER, J., & ZINK, M. 2013. TanDEM-X: DEM acquisition in the third year era. *International Journal of Space Science and Engineering*, **1**(4), 367–381.

BREIT, H., FRITZ, T., BALSS, U., NIEDERMEIER, A., EINEDER, M., YAGUE-MARTINEZ, N., & ROSSI, C. 2010a. Processing of bistatic TanDEM-X data. *Pages 2640–2643 of: 2010 IEEE International Geoscience and Remote Sensing Symposium (IGARSS)*.

BREIT, H., FRITZ, T., BALSS, U., LACHAISE, M., NIEDERMEIER, A., & VONAVKA, M. 2010b. TerraSAR-X SAR processing and products. *IEEE Transactions on Geoscience and Remote Sensing*, **48**(2), 727–740.

BREIT, H., YOUNIS, M., BALSS, U., NIEDERMEIER, A., GRIGOROV, C., HUESO GONZALEZ, J., KRIEGER, G., EINEDER, M., & FRITZ, T. 2011. Bistatic synchronization and processing of TanDEM-X data. *Pages 2424–2427 of: 2011 IEEE International Geoscience and Remote Sensing Symposium (IGARSS)*.

BREIT, H., LACHAISE, M., BALSS, U., ROSSI, C., FRITZ, T., & NIEDERMEIER, A. 2012. Bistatic and interferometric processing of TanDEM-X data. *Pages 93–96 of: EUSAR 2012; 9th European Conference on Synthetic Aperture Radar*.

BROWN, C. G., SARABANDI, K., & PIERCE, L. E. 2005. Validation of the shuttle radar topography mission height data. *IEEE Transactions on Geoscience and Remote Sensing*, **43**(8), 1707–1715.

BROWN, L. G. 1992. A survey of image registration techniques. *ACM Computing Surveys (CSUR)*, **24**(4), 325–376.

BUCKREUSS, S., & SCHÄTTLER, B. 2010. The TerraSAR-X ground segment. *IEEE Transactions on Geoscience and Remote Sensing*, **48**(2), 623–632.

CARABAJAL, C. C., & HARDING, D. J. 2006. SRTM C-band and ICESat laser altimetry elevation comparisons as a function of tree cover and relief. *Photogrammetric Engineering and Remote Sensing*, **72**(3), 287–298.

CARRASCO, J. F., CASASSA, G., & RIVERA, A. 2002. Meteorological and climatological aspects of the Southern Patagonia Icefield. *Pages 29–41 of:* CASASSA, G., SEPÚLVEDA, F. V., & SINCLAIR, R. M. (eds), *The Patagonian icefields: a unique natural laboratory for environmental and climate change studies*. Springer Science+Business Media.

CASASSA, G., BRECHER, H., RIVERA, A., & ANIYA, M. 1997. A century-long recession record of Glaciar O'Higgins Chilean Patagonia. *Annals of Glaciology*, **24**, 106–110.

CASASSA, G., RIVERA, A., ANIYA, M., & NARUSE, R. 2002. Current knowledge of the Southern Patagonia Icefield. *Pages 67–83 of:* CASASSA, G., SEPÚLVEDA, F. V., & SINCLAIR, R. M. (eds), *The Patagonian icefields: a unique natural laboratory for environmental and climate change studies*. Springer Science+Business Media.

CASASSA, G., RODRÍGUEZ, J. L., & LORIAUX, T. 2014. A new glacier inventory for the Southern Patagonia Icefield and areal changes 1986–2000. *Pages 639–660 of:* KARGEL, J. S., LEONARD, G. J., BISHOP, M. P., KAAB, A., & RAUP, B. H. (eds), *Global Land Ice Measurements from Space*. Springer.

CHEN, J. L., WILSON, C. R., TAPLEY, B. D., BLANKENSHIP, D. D., & IVINS, E. R. 2007. Patagonia icefield melting observed by gravity recovery and climate experiment (GRACE). *Geophysical Research Letters*, **34**(22).

CIAPPA, A., PIETRANERA, L., & BATTAZZA, F. 2010. Perito Moreno Glacier (Argentina) flow estimation by COSMO SkyMed sequence of high-resolution SAR-X imagery. *Remote Sensing of Environment*, **114**(9), 2088–2096.

CLARK, I. 1979. *Practical geostatistics*. Vol. 3. Applied Science Publishers London.

COGLEY, J. G., HOCK, R., RASMUSSEN, L. A., ARENDT, A. A., BAUDER, A., BRAITHWAITE, R. J., JANSSON, P., KASER, G., MÖLLER, M., NICHOLSON, L., *et al.* 2011. Glossary of glacier mass balance and related terms, IHP-VII technical documents in hydrology No. 86, IACS Contribution No. 2. *International Hydrological Program, UNESCO, Paris*.

COGLEY, J. G. 2009. Geodetic and direct mass-balance measurements: comparison and joint analysis. *Annals of Glaciology*, **50**(50), 96–100.

COLBECK, S. C. 1982. The geometry and permittivity of snow at high frequencies. *Journal of Applied Physics*, **53**(6), 4495–4500.

CONG, X. 2014. *SAR Interferometry for Volcano Monitoring: 3D-PSI Analysis and Mitigation of Atmospheric Refractivity*. Ph.D. thesis, Technische Universität München.

CONG, X., BALSS, U., EINEDER, M., & FRITZ, T. 2012. Imaging geodesy - Centimeter-level ranging accuracy with TerraSAR-X: An update. *IEEE Geoscience and Remote Sensing Letters*, **9**(5), 948–952.

COSTANTINI, M. 1998. A novel phase unwrapping method based on network programming. *IEEE Transactions on Geoscience and Remote Sensing*, **36**(3), 813–821.

COX, L. H., & MARCH, R. S. 2004. Comparison of geodetic and glaciological mass-balance techniques, Gulkana Glacier, Alaska, USA. *Journal of Glaciology*, **50**(170), 363–370.

CRESSIE, N. A. 1993. *Statistics for spatial data*. Wiley series in probability and mathematical statistics: Applied probability and statistics. J. Wiley.

CUFFEY, K. M., & PATERSON, W. S. B. 2010. *The physics of glaciers*. 4th edn. Academic Press.

CUMMING, I. G., & WONG, F. H.-C. 2005. *Digital processing of synthetic aperture radar data: algorithms and implementation*. Artech House.

CURLANDER, J. C., & MCDONOUGH, R. N. 1991. *Synthetic aperture radar*. John Wiley & Sons New York, NY, USA.

DALL, J. 2007. InSAR elevation bias caused by penetration into uniform volumes. *IEEE Transactions on Geoscience and Remote Sensing*, **45**(7), 2319–2324.

DALL, J., MADSEN, S. N., KELLER, K., & FORSBERG, R. 2001. Topography and penetration of the Greenland ice sheet measured with airborne SAR interferometry. *Geophysical Research Letters*, **28**(9), 1703–1706.

DAVIES, B. J., & GLASSER, N. F. 2012. Accelerating shrinkage of Patagonian glaciers from the Little Ice Age (˜AD 1870) to 2011. *Journal of Glaciology*, **58**(212), 1063–1084.

DAVIS, C. H. 1991. Remote sensing of the ice sheets. *IEEE Potentials*, **10**(2), 29–32.

DAVIS, C. H., POZNYAK, V., *et al.* 1993. The depth of penetration in Antarctic firn at 10 GHz. *IEEE Transactions on Geoscience and Remote Sensing*, **31**(5), 1107–1111.

DAVIS, C. H., LI, Y., MCCONNELL, J. R., FREY, M. M., & HANNA, E. 2005. Snowfall-driven growth in East Antarctic ice sheet mitigates recent sea-level rise. *Science*, **308**(5730), 1898–1901.

DE LANGE, R., LUCKMAN, A., & MURRAY, T. 2007. Improvement of Satellite Radar Feature Tracking for Ice Velocity Derivation by Spatial Frequency Filtering. *IEEE Transactions on Geoscience and Remote Sensing*, **45**(7), 2309–2318.

DE ZAN, F. 2014. Accuracy of Incoherent Speckle Tracking for Circular Gaussian Signals. *IEEE Geoscience and Remote Sensing Letters*, **11**(1), 264–267.

DE ZAN, F., KRIEGER, G., & LOPEZ-DEKKER, P. 2013. On Some Spectral Properties of TanDEM-X Interferograms Over Forested Areas. *IEEE Geoscience and Remote Sensing Letters*, **10**(1), 71–75.

DEBELLA-GILO, M., & KÄÄB, A. 2012. Measurement of surface displacement and deformation of mass movements using least squares matching of repeat high resolution satellite and aerial images. *Remote Sensing*, **4**(1), 43–67.

DEBYE, P. J. W. 1929. *Polar molecules*. Chemical Catalog Company, Incorporated.

DIETRICH, R., IVINS, E., CASASSA, G., LANGE, H., WENDT, J., & FRITSCHE, M. 2010. Rapid crustal uplift in Patagonia due to enhanced ice loss. *Earth and Planetary Science Letters*, **289**(1), 22–29.

DLR-CAF. 2010 (December). *TanDEM-X Ground Segment Raw DEM Specification (Project Internal)*. 1.1 edn. German Aerospace Center (DLR) - Cluster Applied Remote Sensing (CAF). TD-PGS-TN-3081.

DLR-CAF. 2013 (October). *TerraSAR-X Ground Segment Basic Product Specification Document*. 1.9 edn. German Aerospace Center (DLR) - Cluster Applied Remote Sensing (CAF). TX-GS-DD-3302.

DRINKWATER, M. R., LONG, D. G., & BINGHAM, A. W. 2001. Greenland snow accumulation estimates from satellite radar scatterometer data. *Journal of Geophysical Research: Atmospheres (1984–2012)*, **106**(D24), 33935–33950.

ECHELMEYER, K. A., HARRISON, W. D., LARSEN, C. F., SAPIANO, J., MITCHELL, J. E., DEMALLIE, J., RABUS, B., ADALGEIRSDOTTIR, G., & SOMBARDIER, L. 1996. Airborne surface profiling of glaciers: a case-study in Alaska. *Journal of Glaciology*, **42**(142), 538–547.

EINEDER, M. 2003. Ocillator clock drift compensation in bistatic interferometric SAR. *Pages 1449–1451 of: 2003 IEEE International Geoscience and Remote Sensing Symposium (IGARSS)*, vol. 3.

EINEDER, M., HUBIG, M., & MILCKE, B. 1998. Unwrapping large interferograms using the minimum cost flow algorithm. *Pages 83–87 of: 1998 IEEE International Geoscience and Remote Sensing Symposium (IGARSS)*, vol. 1.

EINEDER, M., ABDEL JABER, W., FLORICIOIU, D., ROTT, H., & YAGUE-MARTINEZ, N. 2011a. Glacier flow and topography measurements with TerraSAR-X and TanDEM-X. *Pages 3835–3838 of: 2011 IEEE International Geoscience and Remote Sensing Symposium (IGARSS)*.

EINEDER, M., MINET, C., STEIGENBERGER, P., CONG, X., & FRITZ, T. 2011b. Imaging geodesy - Toward centimeter-level ranging accuracy with TerraSAR-X. *IEEE Transactions on Geoscience and Remote Sensing*, **49**(2), 661–671.

ELSBERG, D. H., HARRISON, W. D., ECHELMEYER, K. A., & KRIMMEL, R. M. 2001. Quantifying the effects of climate and surface change on glacier mass balance. *Journal of Glaciology*, **47**(159), 649–658.

ERTEN, E. 2013. Glacier velocity estimation by means of a polarimetric similarity measure. *IEEE Transactions on Geoscience and Remote Sensing*, **51**(6), 3319–3327.

ERTEN, E., REIGBER, A., JAEGER, M., & HELLWICH, O. 2007. Robust measurement of glacier surface motion from multiscale speckle tracking using local constraints. *Pages 4237–4240 of: 2007 IEEE International Geoscience and Remote Sensing Symposium (IGARSS)*.

ERTEN, E., REIGBER, A., HELLWICH, O., & PRATS, P. 2009. Glacier velocity monitoring by maximum likelihood texture tracking. *IEEE Transactions on Geoscience and Remote Sensing*, **47**(2), 394–405.

ERTEN, E., REIGBER, A., & HELLWICH, O. 2010. Generation of three-dimensional deformation maps from InSAR data using spectral diversity techniques. *ISPRS Journal of Photogrammetry and Remote Sensing*, **65**(4), 388–394.

ESCOBAR, F. 1992. Water balance in the Patagonia Icefield. *Glaciological Researches in Patagonia, 1990*.

ETZELMÜLLER, B. 2000. On the quantification of surface changes using grid-based digital elevation models (DEMs). *Transactions in GIS*, **4**(2), 129–143.

EVANS, A. N. 2000. Glacier surface motion computation from digital image sequences. *IEEE Transactions on Geoscience and Remote Sensing*, **38**(2), 1064–1072.

EVANS, D. L., PLAUT, J. J., & STOFAN, E. R. 1997. Overview of the spaceborne imaging radar-C/X-band synthetic aperture radar (SIR-C/X-SAR) missions. *Remote Sensing of Environment*, **59**(2), 135–140.

EVANS, S. 1965. Dielectric properties of ice and snow–A review. *Journal of Glaciology*, **5**, 773–792.

FARR, T. G., ROSEN, P. A., CARO, E., CRIPPEN, R., DUREN, R., HENSLEY, S., KOBRICK, M., PALLER, M., RODRIGUEZ, E., ROTH, L., *et al.* 2007. The Shuttle Radar Topography Mission. *Reviews of Geophysics*, **45**(2).

FELBIER, A. 2009 (April). *Ausgleichung langwelliger Höhenfehler in SRTM mit Kugelflächenfunktionen auf Basis ausgewählter ICESat-Daten*. Diplomarbeit, Technische Universität München.

FERRETTI, A., PRATI, C., & ROCCA, F. 2000. Nonlinear subsidence rate estimation using permanent scatterers in differential SAR interferometry. *IEEE Transactions on Geoscience and Remote Sensing*, **38**(5), 2202–2212.

FLORICIOIU, D., & ROTT, H. 2001. Seasonal and short-term variability of multifrequency, polarimetric radar backscatter of alpine terrain from SIR-C/X-SAR and AIRSAR data. *IEEE Transactions on Geoscience and Remote Sensing*, **39**(12), 2634–2648.

FLORICIOIU, D., JEZEK, K., BAESSLER, M., & ABDEL JABER, W. 2012. Geophysical parameters estimation with TerraSAR-X of outlet glaciers in the Transantarctic Mountains. *Pages 1565–1568 of: 2012 IEEE International Geoscience and Remote Sensing Symposium (IGARSS)*.

FLORICIOIU, D., ABDEL JABER, W., & JEZEK, K. 2014. TerraSAR-X and TanDEM-X observations of the Recovery Glacier system, Antarctica. *Pages 4852–4855 of: 2014 IEEE International Geoscience and Remote Sensing Symposium (IGARSS)*.

FORSTER, R. R., RIGNOT, E., SACKS, B. L., & JEZEK, K. C. 1999. Interferometric radar observations of Glaciares Europa and Penguin, Hielo Patagonico Sur, Chile. *Journal of Glaciology*, **45**(150), 325–337.

FREEMAN, A. 1992. SAR calibration: An overview. *IEEE Transactions on Geoscience and Remote Sensing*, **30**(6), 1107–1121.

FRETWELL, P., PRITCHARD, H. D., VAUGHAN, D. G., BAMBER, J., BARRAND, N. E., BELL, R., BIANCHI, C., BINGHAM, R. G., BLANKENSHIP, D. D., CASASSA, G., *et al.* 2013. Bedmap2: improved ice bed, surface and thickness datasets for Antarctica. *The Cryosphere*, **7**(1).

FRICKER, H. A., COLEMAN, R., PADMAN, L., SCAMBOS, T. A., BOHLANDER, J., & BRUNT, K. M. 2009. Mapping the grounding zone of the Amery Ice Shelf, East Antarctica using InSAR, MODIS and ICESat. *Antarctic Science*, **21**(05), 515–532.

FRITZ, T., BREIT, H., ROSSI, C., BALSS, U., LACHAISE, M., & DUQUE, S. 2012. Interferometric processing and products of the TanDEM-X mission. *Pages 1904–1907 of: 2012 IEEE International Geoscience and Remote Sensing Symposium (IGARSS)*.

FRITZ, T., ROSSI, C., YAGUE-MARTINEZ, N., RODRIGUEZ-GONZALEZ, F., LACHAISE, M., & BREIT, H. 2011. Interferometric processing of TanDEM-X data. *Pages 2428–2431 of: 2011 IEEE International Geoscience and Remote Sensing Symposium (IGARSS)*.

GARDELLE, J., BERTHIER, E., ARNAUD, Y., *et al.* 2012. Impact of resolution and radar penetration on glacier elevation changes computed from DEM differencing. *Journal of Glaciology*, **58**(208), 419–422.

GARDNER, A., MOHOLDT, G., ARENDT, A., & WOUTERS, B. 2012. Accelerated contributions of Canada's Baffin and Bylot Island glaciers to sea level rise over the past half century. *The Cryosphere*, **6**(5), 1103–1125.

GARDNER, A. S., MOHOLDT, G., COGLEY, J. G., WOUTERS, B., ARENDT, A. A., WAHR, J., BERTHIER, E., HOCK, R., PFEFFER, W. T., KASER, G., *et al.* 2013. A reconciled estimate of glacier contributions to sea level rise: 2003 to 2009. *Science*, **340**(6134), 852–857.

GATELLI, F., MONTI GUARNIERI, A., PARIZZI, F., PASQUALI, P., PRATI, C., & ROCCA, F. 1994. The wavenumber shift in SAR interferometry. *IEEE Transactions on Geoscience and Remote Sensing*, **32**(4), 855–865.

GIESEN, R. H., & OERLEMANS, J. 2013. Climate-model induced differences in the 21st century global and regional glacier contributions to sea-level rise. *Climate Dynamics*, **41**(11-12), 3283–3300.

GILES, A. B., MASSOM, R. A., & WARNER, R. C. 2009. A method for sub-pixel scale feature-tracking using Radarsat images applied to the Mertz Glacier Tongue, East Antarctica. *Remote Sensing of Environment*, **113**(8), 1691–1699.

GLASSER, N. F., HARRISON, S., JANSSON, K. N., ANDERSON, K., & COWLEY, A. 2011. Global sea-level contribution from the Patagonian Icefields since the Little Ice Age maximum. *Nature Geoscience*, **4**(5), 303–307.

GOLDSTEIN, R. M., & ZEBKER, H. A. 1987. Interferometric radar measurement of ocean surface currents. *Nature*, **328**(August), 707–709.

GOLDSTEIN, R. M., ZEBKER, H. A., & WERNER, C. L. 1988. Satellite radar interferometry: Two-dimensional phase unwrapping. *Radio Science*, **23**(4), 713–720.

GOLDSTEIN, R. M., ENGELHARDT, H., KAMB, B., & FROLICH, R. M. 1993. Satellite radar interferometry for monitoring ice sheet motion: application to an Antarctic ice stream. *Science*, **262**, 1525–1525.

GOMBA, G., PARIZZI, A., DE ZAN, F., EINEDER, M., & BAMLER, R. 2016. Toward operational compensation of ionospheric effects in SAR interferograms: the split-spectrum method. *IEEE Transactions on Geoscience and Remote Sensing*, **54**(3), 1446–1461.

GOODMAN, J. W. 1976. Some fundamental properties of speckle. *Journal of the Optical Society of America*, **66**(11), 1145–1150.

GOODMAN, N. R. 1963. Statistical analysis based on a certain multivariate complex Gaussian distribution (an introduction). *The Annals of Mathematical Statistics*, **34**(1), 152–177.

GOURMELEN, N., KIM, S. W., SHEPHERD, A., PARK, J. W., SUNDAL, A. V., BJÖRNSSON, H., & PALSSON, F. 2011. Ice velocity determined using conventional and multiple-aperture InSAR. *Earth and Planetary Science Letters*, **307**(1), 156–160.

GRAY, A. L., SHORT, N., MATTAR, K. E., & JEZEK, K. C. 2001. Velocities and flux of the Filchner Ice Shelf and its tributaries determined from speckle tracking interferometry. *Canadian Journal of Remote Sensing*, **27**(3), 193–206.

GRAY, L., MATTAR, K., & SHORT, N. 1999. Speckle Tracking for 2-Dimensional Ice Motion Studies in Polar Regions: Influence of the Ionosphere. *In: Proceedings of the ESA Fringe '99 Workshop*.

GRIGGS, J. A., & BAMBER, J. L. 2009. A new 1 km digital elevation model of Antarctica derived from combined radar and laser data - Part 2: Validation and error estimates. *The Cryosphere*, **3**(1), 113–123.

GROH, A., EWERT, H., ROSENAU, R., FAGIOLINI, E., GRUBER, C., FLORICIOIU, D., ABDEL JABER, W., LINOW, S., FLECHTNER, F., EINEDER, M., DIERKING, W., & DIETRICH, R. 2014. Mass, volume and velocity of the Antarctic ice sheet: present-day changes and error effects. *Surveys in Geophysics*, **35**(6), 1481–1505.

GROHMAN, G., KROENUNG, G., & STREBECK, J. 2006. Filling SRTM voids: The delta surface fill method. *Photogrammetric Engineering and Remote Sensing*, **72**(3), 213–216.

GRUBER, A., WESSEL, B., HUBER, M., & ROTH, A. 2012. Operational TanDEM-X DEM calibration and first validation results. *ISPRS Journal of Photogrammetry and Remote Sensing*, **73**, 39–49.

HABERMEYER, M., MARSCHALK, U., & ROTH, A. 2009. W42 - a scalable spatial database system for holding Digital Elevation Models. *Pages 1–6 of: 2009 17th International Conference on Geoinformatics*.

HALLIKAINEN, M. T. 1989. Microwave radiometry of snow. *Advances in Space Research*, **9**(1), 267–275.

HALLIKAINEN, M. T., ULABY, F. T., & ABDELRAZIK, M. 1986. Dielectric properties of snow in the 3 to 37 GHz range. *IEEE Transactions on Antennas and Propagation*, **34**(11), 1329–1340.

HAMELIN, J. L., JACKSON, M. C., KIRCHWEY, C. B., & PILEGGI, R. A. 2002. STS-99 Shuttle Radar Topography Mission stability and control. *Advances in the Astronautical Sciences*.

HARRISON, S., & WINCHESTER, V. 1998. Historical fluctuations of the Gualas and Reicher Glaciers, North Patagonian Icefield, Chile. *The Holocene*, **8**(4), 481–485.

HARRISON, S., & WINCHESTER, V. 2000. Nineteenth- and twentieth-century glacier fluctuations and climatic implications in the Arco and Colonia valleys, Hielo Patagónico Norte, Chile. *Arctic, Antarctic, and Alpine Research*, 55–63.

HARRISON, S., GLASSER, N., WINCHESTER, V., HARESIGN, E., WARREN, C., DULLER, G. A., BAILEY, R., IVY-OCHS, S., JANSSON, K., & KUBIK, P. 2008. Glaciar León, Chilean Patagonia: Late-Holocene chronology and geomorphology. *The Holocene*, **18**(4), 643–652.

HASTINGS, D. A., & DUNBAR, P. K. 1999 (May). *Global Land One-kilometer Base Elevation (GLOBE)*. 34 edn. National Oceanic and Atmospheric Administration - National Geophysical Data Center, Boulder, Colorado.

HAUG, T., ROLSTAD, C., ELVEHØY, H., JACKSON, M., & MAALEN-JOHANSEN, I. 2009. Geodetic mass balance of the western Svartisen ice cap, Norway, in the periods 1968–1985 and 1985–2002. *Annals of Glaciology*, **50**(50), 119–125.

HELSEN, M. M., VAN DEN BROEKE, M. R., VAN DE WAL, R. S. W., VAN DE BERG, W. J., VAN MEIJGAARD, E., DAVIS, C. H., LI, Y., & GOODWIN, I. 2008. Elevation changes in Antarctica mainly determined by accumulation variability. *Science*, **320**(5883), 1626–1629.

HENSLEY, S., ROSEN, P. A., & GURROLA, E. 2000. Topographic map generation from the Shuttle Radar Topography Mission C-band SCANSAR interferometry. *Pages 179–189 of: Second International Asia-Pacific Symposium on Remote Sensing of the Atmosphere, Environment, and Space*. International Society for Optics and Photonics.

HERRON, M. M., & LANGWAY JR, C. C. 1980. Firn densification: an empirical model. *Journal of Glaciology*, **25**, 373–385.

HOFFMANN, J., & WALTER, D. 2006. How complementary are SRTM-X and -C band digital elevation models? *Photogrammetric Engineering & Remote Sensing*, **72**(3), 261–268.

HOLZNER, J., & BAMLER, R. 2002. Burst-mode and ScanSAR interferometry. *IEEE Transactions on Geoscience and Remote Sensing*, **40**(9), 1917–1934.

HOWAT, I. M., SMITH, B. E., JOUGHIN, I., & SCAMBOS, T. A. 2008. Rates of southeast Greenland ice volume loss from combined ICESat and ASTER observations. *Geophysical Research Letters*, **35**(17).

HUBER, M., WESSEL, B., KOSMANN, D., FELBIER, A., SCHWIEGER, V., HABERMEYER, M., WENDLEDER, A., & ROTH, A. 2009. Ensuring globally the TanDEM-X height accuracy: Analysis of the reference data sets ICESat, SRTM and KGPS-Tracks. *Pages 769–772 of: 2009 IEEE International Geoscience and Remote Sensing Symposium (IGARSS)*, vol. 2.

HUBER, M., GRUBER, A., WESSEL, B., BREUNIG, M., & WENDLEDER, A. 2010. Validation of tie-point concepts by the DEM adjustment approach of TanDEM-X. *Pages 2644–2647 of: 2010 IEEE International Geoscience and Remote Sensing Symposium (IGARSS)*.

HUESO GONZÁLEZ, J., BACHMANN, M., KRIEGER, G., & FIEDLER, H. 2010. Development of the TanDEM-X calibration concept: analysis of systematic errors. *IEEE Transactions on Geoscience and Remote Sensing*, **48**(2), 716–726.

HUESO GONZÁLEZ, J., ANTONY, J. M. W., BACHMANN, M., KRIEGER, G., ZINK, M., SCHRANK, D., & SCHWERDT, M. 2012. Bistatic system and baseline calibration in TanDEM-X to ensure the global digital elevation model quality. *ISPRS Journal of Photogrammetry and Remote Sensing*, **73**, 3–11.

HUSS, M. 2013. Density assumptions for converting geodetic glacier volume change to mass change. *The Cryosphere*, **7**(3).

IBARZABAL Y DONANGELO, T., HOFFMANN, J., & NARUSE, R. 1996. Recent climate changes in southern Patagonia. *Bulletin of Glacier Research*, 29–36.

IPCC. 2013. Summary for Policymakers. *Pages 1–30 of:* STOCKER, T. F., QIN, D., PLATTNER, G.-K., TIGNOR, M., ALLEN, S. K., BOSCHUNG, J., NAUELS, A., XIA, Y., BEX, V., & MIDGLEY, P. M. (eds), *Climate Change 2013: The Physical Science Basis. Contribution of Working Group I to the Fifth Assessment Report of the Intergovernmental Panel on Climate Change*. Cambridge University Press Cambridge, UK, and New York, NY, USA.

IVINS, E. R., & JAMES, T. S. 2004. Bedrock response to Llanquihue Holocene and present-day glaciation in southernmost South America. *Geophysical Research Letters*, **31**(24).

IVINS, E. R., WATKINS, M. M., YUAN, D.-N., DIETRICH, R., CASASSA, G., & RÜLKE, A. 2011. On-land ice loss and glacial isostatic adjustment at the Drake Passage: 2003-2009. *Journal of Geophysical Research: Solid Earth*, **116**(B2).

JACOB, T., WAHR, J., PFEFFER, W. T., & SWENSON, S. 2012. Recent contributions of glaciers and ice caps to sea level rise. *Nature*, **482**(7386), 514–518.

JEZEK, K., ABDEL JABER, W., & FLORICIOIU, D. 2011. TerraSAR-X observations of Antarctic outlet glaciers in the Ross Sea sector. *Pages 3855–3858 of: 2011 IEEE International Geoscience and Remote Sensing Symposium (IGARSS)*.

JEZEK, K. C. 1984. Recent changes in the dynamic condition of the Ross Ice Shelf, Antarctica. *Journal of Geophysical Research: Solid Earth*, **89**(B1), 409–416.

JISKOOT, H. 2011. Dynamics of Glaciers. *Pages 245–256 of: Encyclopedia of snow, ice and glaciers*. Springer.

JOSBERGER, E. G., BIDLAKE, W. R., MARCH, R. S., & KENNEDY, B. W. 2007. Glacier mass-balance fluctuations in the Pacific Northwest and Alaska, USA. *Annals of Glaciology*, **46**(1), 291–296.

JOUGHIN, I. 2002. Ice-sheet velocity mapping: a combined interferometric and speckle-tracking approach. *Annals of Glaciology*, **34**(1), 195–201.

JOUGHIN, I. R., WINEBRENNER, D. P., & FAHNESTOCK, M. A. 1995. Observations of ice-sheet motion in Greenland using satellite radar interferometry. *Geophysical Research Letters*, **22**(5), 571–574.

JOUGHIN, I. R., KWOK, R., & FAHNESTOCK, M. A. 1998. Interferometric estimation of three-dimensional ice-flow using ascending and descending passes. *IEEE Transactions on Geoscience and Remote Sensing*, **36**(1), 25–37.

JUNG, H.-S., WON, J.-S., & KIM, S.-W. 2009. An improvement of the performance of multiple-aperture SAR interferometry (MAI). *IEEE Transactions on Geoscience and Remote Sensing*, **47**(8), 2859–2869.

JUST, D., & BAMLER, R. 1994. Phase statistics of interferograms with applications to synthetic aperture radar. *Applied Optics*, **33**(20), 4361–4368.

KALNAY, E., KANAMITSU, M., KISTLER, R., COLLINS, W., DEAVEN, D., GANDIN, L., IREDELL, M., SAHA, S., WHITE, G., WOOLLEN, J., *et al.* 1996. The NCEP/NCAR 40-year reanalysis project. *Bulletin of the American Meteorological Society*, **77**(3), 437–471.

KAWANISHI, T., SEZAI, T., ITO, Y., IMAOKA, K., TAKESHIMA, T., ISHIDO, Y., SHIBATA, A., MIURA, M., INAHATA, H., & SPENCER, R. W. 2003. The Advanced Microwave Scanning Radiometer for the Earth Observing System (AMSR-E), NASDA's contribution to the EOS for global energy and water cycle studies. *IEEE Transactions on Geoscience and Remote Sensing*, **41**(2), 184–194.

KÄÄB, A. 2008. Glacier volume changes using ASTER satellite stereo and ICESat GLAS laser altimetry. A test study on Edgeøya, Eastern Svalbard. *IEEE Transactions on Geoscience and Remote Sensing*, **46**(10), 2823–2830.

KÄÄB, A., BERTHIER, E., NUTH, C., GARDELLE, J., & ARNAUD, Y. 2012. Contrasting patterns of early twenty-first-century glacier mass change in the Himalayas. *Nature*, **488**(7412), 495–498.

KENDRA, J. R., SARABANDI, K., & ULABY, F. T. 1998. Radar measurements of snow: Experiment and analysis. *IEEE Transactions on Geoscience and Remote Sensing*, **36**(3), 864–879.

KOBLET, T., GÄRTNER-ROER, I., ZEMP, M., JANSSON, P., THEE, P., HAEBERLI, W., & HOLMLUND, P. 2010. Reanalysis of multi-temporal aerial images of Storglaciären, Sweden (1959–99)–Part 1: Determination of length, area, and volume changes. *The Cryosphere*, **4**(3), 333–343.

KOPPES, M., CONWAY, H., RASMUSSEN, L., & CHERNOS, M. 2011. Deriving mass balance and calving variations from reanalysis data and sparse observations, Glaciar San Rafael, northern Patagonia, 1950–2005. *The Cryosphere*, **5**(3), 791–808.

KOVACS, A., GOW, A. J., & MOREY, R. M. 1995. The in-situ dielectric constant of polar firn revisited. *Cold Regions Science and Technology*, **23**(3), 245–256.

KRABILL, W., HANNA, E., HUYBRECHTS, P., ABDALATI, W., CAPPELEN, J., CSATHO, B., FREDERICK, E., MANIZADE, S., MARTIN, C., SONNTAG, J., *et al.* 2004. Greenland ice sheet: increased coastal thinning. *Geophysical Research Letters*, **31**(24).

KRIEGER, G., & DE ZAN, F. 2014. Relativistic Effects in Bistatic Synthetic Aperture Radar. *IEEE Transactions on Geoscience and Remote Sensing*, **52**(2), 1480–1488.

KRIEGER, G., & YOUNIS, M. 2006. Impact of oscillator noise in bistatic and multistatic SAR. *IEEE Geoscience and Remote Sensing Letters*, **3**(3), 424–428.

KRIEGER, G., MOREIRA, A., FIEDLER, H., HAJNSEK, I., WERNER, M., YOUNIS, M., & ZINK, M. 2007. TanDEM-X: A satellite formation for high-resolution SAR interferometry. *IEEE Transactions on Geoscience and Remote Sensing*, **45**(11), 3317–3341.

KWOK, R., & FAHNESTOCK, M. A. 1996. Ice sheet motion and topography from radar interferometry. *IEEE Transactions on Geoscience and Remote Sensing*, **34**(1), 189–200.

LACHAISE, M. 2015. *Phase Unwrapping of Multi-Channel Synthetic Aperture Radar Data: Application to the TanDEM-X Mission*. Ph.D. thesis, Technische Universität München.

LACHAISE, M., BALSS, U., FRITZ, T., & BREIT, H. 2012a. The dual-baseline interferometric processing chain for the TanDEM-X mission. *Pages 5562–5565 of: 2012 IEEE International Geoscience and Remote Sensing Symposium (IGARSS)*.

LACHAISE, M., FRITZ, T., BALSS, U., BAMLER, R., & EINEDER, M. 2012b. Phase unwrapping correction with dual-baseline data for the TanDEM-X mission. *Pages 5566–5569 of: 2012 IEEE International Geoscience and Remote Sensing Symposium (IGARSS)*.

LANG, O., RABUS, B. T., & DECH, S. W. 2004. Velocity map of the Thwaites glacier catchment, West Antarctica. *Journal of Glaciology*, **50**(168), 46–56.

LARSEN, C. F., MOTYKA, R. J., ARENDT, A. A., ECHELMEYER, K. A., & GEISSLER, P. E. 2007. Glacier changes in southeast Alaska and northwest British Columbia and contribution to sea level rise. *Journal of Geophysical Research: Earth Surface (2003–2012)*, **112**(F1).

LEE, J.-S., HOPPEL, K. W., MANGO, S. A., & MILLER, A. R. 1994. Intensity and phase statistics of multilook polarimetric and interferometric SAR imagery. *IEEE Transactions on Geoscience and Remote Sensing*, **32**(5), 1017–1028.

LEWIS, J. P. 1995. Fast normalized cross-correlation. *Pages 120–123 of: Vision Interface*, vol. 10.

LIU, H., ZHAO, Z., & JEZEK, K. C. 2007. Synergistic fusion of interferometric and speckle-tracking methods for deriving surface velocity from interferometric SAR data. *IEEE Geoscience and Remote Sensing Letters*, **4**(1), 102–106.

LIU, H., ZHAO, Z., YU, J., & JEZEK, K. 2008. Simultaneous least squares adjustment of multiframe velocities derived from interferometric and Speckle-Tracking methods. *IEEE Geoscience and Remote Sensing Letters*, **5**(2), 289–293.

LOPEZ, P., CHEVALLIER, P., FAVIER, V., POUYAUD, B., ORDENES, F., & OERLEMANS, J. 2010. A regional view of fluctuations in glacier length in southern South America. *Global and Planetary Change*, **71**(1), 85–108.

LUCKMAN, A., MURRAY, T., JISKOOT, H., PRITCHARD, H., & STROZZI, T. 2003. ERS SAR feature-tracking measurement of outlet glacier velocities on a regional scale in East Greenland. *Annals of Glaciology*, **36**(1), 129–134.

LUCKMAN, A., QUINCEY, D., & BEVAN, S. 2007. The potential of satellite radar interferometry and feature tracking for monitoring flow rates of Himalayan glaciers. *Remote Sensing of Environment*, **111**(2), 172–181.

MAKSYMIUK, O., MAYER, C., & STILLA, U. 2016. Velocity estimation of glaciers with physically-based spatial regularization - Experiments using satellite SAR intensity images. *Remote Sensing of Environment*, **172**, 190–204.

MARSH, O. J. 2013. *Ice dynamics and mass balance in the grounding zone of outlet glaciers in the Transantarctic Mountains*. Ph.D. thesis, University of Canterbury. Gateway Antarctica.

MARTONE, M., BRÄUTIGAM, B., RIZZOLI, P., GONZALEZ, C., BACHMANN, M., & KRIEGER, G. 2012. Coherence evaluation of TanDEM-X interferometric data. *ISPRS Journal of Photogrammetry and Remote Sensing*, **73**, 21–29.

MARTONE, M., RIZZOLI, P., BRÄUTIGAM, B., & KRIEGER, G. 2013. First 2 years of TanDEM-X mission: Interferometric performance overview. *Radio Science*, **48**(5), 617–627.

MATHERON, G. 1971. *The theory of regionalized variables and its applications*. Vol. 5. Ecole nationale supérieure des mines de Paris.

MATTAR, K. E., VACHON, P. W., GEUDTNER, D., GRAY, A. L., CUMMING, I. G., & BRUGMAN, M. 1998. Validation of alpine glacier velocity measurements using ERS tandem-mission SAR data. *IEEE Transactions on Geoscience and Remote Sensing*, **36**(3), 974–984.

MÄTZLER, C., STROZZI, T., WEISE, T., FLORICIOIU, D., & ROTT, H. 1997. Microwave snowpack studies made in the Austrian Alps during the SIR-C/X-SAR experiment. *International Journal of Remote Sensing*, **18**(12), 2505–2530.

MÄTZLER, C. 1987. Applications of the interaction of microwaves with the natural snow cover. *Remote Sensing Reviews*, **2**(2), 259–387.

MCGLONE, J. C. 2013. *Manual of photogrammetry*. American Soc. for Photogrammetry and Remote Sensing.

MCMILLAN, M., SHEPHERD, A., GOURMELEN, N., PARK, J.-W., NIENOW, P., RINNE, E., & LEESON, A. 2012. Mapping ice-shelf flow with interferometric synthetic aperture radar stacking. *Journal of Glaciology*, **58**(208), 265–277.

MEIER, M. F. 1984. Contribution of small glaciers to global sea level. *Science*, **226**(4681), 1418–1421.

MELKONIAN, A. K., WILLIS, M. J., PRITCHARD, M. E., RIVERA, A., BOWN, F., & BERNSTEIN, S. 2012. Satellite-Derived Volume Loss Rates and Glacier Speeds for the Cordillera Darwin Icefield, Chile. *The Cryosphere Discussions*, **6**, 3503–3538.

MICHEL, R., & RIGNOT, E. 1999. Flow of Glaciar Moreno, Argentina, from repeat-pass Shuttle Imaging Radar images: comparison of the phase correlation method with radar interferometry. *Journal of Glaciology*, **45**(149), 93–100.

MÖLLER, M., SCHNEIDER, C., & KILIAN, R. 2007. Glacier change and climate forcing in recent decades at Gran Campo Nevado, southernmost Patagonia. *Annals of Glaciology*, **46**(1), 136–144.

MÖLLER, M., & SCHNEIDER, C. 2010. Volume change at Gran Campo Nevado, Patagonia, 1984-2000: a reassessment based on new findings. *Journal of Glaciology*, **56**, 363–365.

MOHOLDT, G., NUTH, C., HAGEN, J. O., & KOHLER, J. 2010. Recent elevation changes of Svalbard glaciers derived from ICESat laser altimetry. *Remote Sensing of Environment*, **114**(11), 2756–2767.

MOHR, J. J., REEH, N., & MADSEN, S. N. 1998. Three-dimensional glacial flow and surface elevation measured with radar interferometry. *Nature*, **391**(6664), 273–276.

MONAHAN, P. A., & RAMAGE, J. 2010. AMSR-E melt patterns on the Southern Patagonia Icefield. *Journal of Glaciology*, **56**(198), 699–708.

MOREIRA, A., KRIEGER, G., HAJNSEK, I., HOUNAM, D., WERNER, M., RIEGGER, S., & SETTELMEYER, E. 2004. TanDEM-X: a TerraSAR-X add-on satellite for single-pass SAR interferometry. *Pages 1000–1003 of: 2004 IEEE International Geoscience and Remote Sensing Symposium (IGARSS)*, vol. 2.

MOUGINOT, J., & RIGNOT, E. 2015. Ice motion of the Patagonian Icefields of South America: 1984–2014. *Geophysical Research Letters*, **42**(5), 1441–1449.

MOUGINOT, J., SCHEUCHL, B., & RIGNOT, E. 2012. Mapping of ice motion in Antarctica using synthetic-aperture radar data. *Remote Sensing*, **4**(9), 2753–2767.

MÜLLER, K. 2011. *Microwave penetration in polar snow and ice: Implications for GPR and SAR*. Ph.D. thesis, University of Oslo.

NAGLER, T., & ROTT, H. 2000. Retrieval of wet snow by means of multitemporal SAR data. *IEEE Transactions on Geoscience and Remote Sensing*, **38**(2), 754–765.

NAGLER, T., ROTT, H., HETZENECKER, M., WUITE, J., & POTIN, P. 2015. The Sentinel-1 Mission: New opportunities for ice sheet observations. *Remote Sensing*, **7**(7), 9371–9389.

NARUSE, R., & SKVARCA, P. 2000. Dynamic features of thinning and retreating Glaciar Upsala, a lacustrine calving glacier in southern Patagonia. *Arctic, Antarctic, and Alpine Research*, 485–491.

NARUSE, R., SKVARCA, P., SATOW, K., TAKEUCHI, Y., & NISHIDA, K. 1995. Thickness change and short-term flow variation of Moreno Glacier, Patagonia. *Bulletin of Glacier Research*, 21–28.

NUTH, C., & KÄÄB, A. 2011. Co-registration and bias corrections of satellite elevation data sets for quantifying glacier thickness change. *The Cryosphere*, **5**(1), 271–290.

NUTH, C., KOHLER, J., AAS, H. F., BRANDT, O., & HAGEN, J. O. 2007. Glacier geometry and elevation changes on Svalbard (1936–90): a baseline dataset. *Annals of Glaciology*, **46**(1), 106–116.

NUTH, C., MOHOLDT, G., KOHLER, J., HAGEN, J. O., & KÄÄB, A. 2010. Svalbard glacier elevation changes and contribution to sea level rise. *Journal of Geophysical Research: Earth Surface (2003–2012)*, **115**(F1).

ORFANIDIS, S. J. 1999. *Electromagnetic waves and antennas*. Rutgers University New Brunswick, NJ.

PAUL, F. 2008. Calculation of glacier elevation changes with SRTM: is there an elevation-dependent bias? *Journal of Glaciology*, **54**(188), 945–946.

PAUL, F., & HAEBERLI, W. 2008. Spatial variability of glacier elevation changes in the Swiss Alps obtained from two digital elevation models. *Geophysical Research Letters*, **35**(21).

PAUL, F., BARRAND, N. E., BAUMANN, S., BERTHIER, E., BOLCH, T., CASEY, K., FREY, H., JOSHI, S. P., KONOVALOV, V., BRIS, R. L., *et al.* 2013. On the accuracy of glacier outlines derived from remote-sensing data. *Annals of Glaciology*, **54**(63), 171–182.

PFEFFER, W. T., ARENDT, A. A., BLISS, A., BOLCH, T., COGLEY, J. G., GARDNER, A. S., HAGEN, J.-O., HOCK, R., KASER, G., KIENHOLZ, C., *et al.* 2014. The Randolph Glacier Inventory: a globally complete inventory of glaciers. *Journal of Glaciology*, **60**(221), 537–552.

PRATS, P., SCHEIBER, R., REIGBER, A., ANDRES, C., & HORN, R. 2009. Estimation of the surface velocity field of the Aletsch glacier using multibaseline airborne SAR interferometry. *IEEE Transactions on Geoscience and Remote Sensing*, **47**(2), 419–430.

PRESS, W. H., TEUKOLSKY, S. A., VETTERLING, W. T., & FLANNERY, B. P. 1992. *Numerical recipes in C: the art of scientific computing (2nd Edition)*. Cambridge University Press.

PRITCHARD, H. D., ARTHERN, R. J., VAUGHAN, D. G., & EDWARDS, L. A. 2009. Extensive dynamic thinning on the margins of the Greenland and Antarctic ice sheets. *Nature*, **461**(7266), 971–975.

PROAKIS, J. G., & MANOLAKIS, D. G. 2007. *Digital Signal Processing*. Prentice Hall international editions. Pearson Prentice Hall.

RABUS, B., EINEDER, M., ROTH, A., & BAMLER, R. 2003. The shuttle radar topography mission - a new class of digital elevation models acquired by spaceborne radar. *ISPRS Journal of Photogrammetry and Remote Sensing*, **57**(4), 241–262.

RANEY, R. K., FREEMAN, T., HAWKINS, R. W., & BAMLER, R. 1994. A plea for radar brightness. *Pages 1090–1092 of: 1994 IEEE International Geoscience and Remote Sensing Symposium (IGARSS)*, vol. 2.

RANEY, R. K. 1971. Synthetic Aperture Imaging Radar and Moving Targets. *IEEE Transactions on Aerospace and Electronic Systems*, **7**(3), 499–505.

RASMUSSEN, L. A., CONWAY, H., & RAYMOND, C. F. 2007. Influence of upper air conditions on the Patagonia icefields. *Global and Planetary Change*, **59**(1), 203–216.

RAYMOND, C., NEUMAN, T., RIGNOT, E., RIVERA, A., & CASASSA, G. 2000. Retreat of Tyndall glacier, Patagonia, Chile. *EOS, Transactions American Geophysical Union*, **81**(48).

RAYMOND, C., NEUMANN, T. A., RIGNOT, E., ECHELMEYER, K., RIVERA, A., & CASASSA, G. 2005. Retreat of Glaciar Tyndall, Patagonia, over the last half-century. *Journal of Glaciology*, **51**(173), 239–247.

REEH, N. 2008. A nonsteady-state firn-densification model for the percolation zone of a glacier. *Journal of Geophysical Research: Earth Surface*, **113**(F3).

REES, W. G., & SQUIRE, V. A. 1989. Technological limitations to satellite glaciology. *Remote Sensing*, **10**(1), 7–22.

REES, W. G. 2005. *Remote sensing of snow and ice*. CRC press.

RIGNOT, E., & MOUGINOT, J. 2012. Ice flow in Greenland for the international polar year 2008–2009. *Geophysical Research Letters*, **39**(11).

RIGNOT, E., MOUGINOT, J., & SCHEUCHL, B. 2011a. Ice flow of the Antarctic ice sheet. *Science*, **333**(6048), 1427–1430.

RIGNOT, E. 2008. Changes in West Antarctic ice stream dynamics observed with ALOS PALSAR data. *Geophysical Research Letters*, **35**(12).

RIGNOT, E., & MACAYEAL, D. R. 1998. Ice-shelf dynamics near the front of the Filchner-Ronne Ice Shelf, Antarctica, revealed by SAR interferometry. *Journal of Glaciology*, **44**(147), 405–418.

RIGNOT, E., & THOMAS, R. H. 2002. Mass balance of polar ice sheets. *Science*, **297**(5586), 1502–1506.

RIGNOT, E., FORSTER, R., & ISACKS, B. 1996. Interferometric radar observations of Glaciar San Rafael, Chile. *Journal of Glaciology*, **42**(141), 279–291.

RIGNOT, E., ECHELMEYER, K., & KRABILL, W. 2001. Penetration depth of interferometric synthetic-aperture radar signals in snow and ice. *Geophysical Research Letters*, **28**(18), 3501–3504.

RIGNOT, E., RIVERA, A., & CASASSA, G. 2003. Contribution of the Patagonia Icefields of South America to sea level rise. *Science*, **302**(5644), 434–437.

RIGNOT, E., MOUGINOT, J., & SCHEUCHL, B. 2011b. Antarctic grounding line mapping from differential satellite radar interferometry. *Geophysical Research Letters*, **38**(10).

RIVERA, A., KOPPES, M., BRAVO, C., & ARAVENA, J. C. 2012. Little ice age advance and retreat of Glaciar Jorge Montt, Chilean Patagonia. *Climate of the Past*, **8**(2), 403–414.

RIVERA, A., & CASASSA, G. 1999. Volume changes on Pio XI glacier, Patagonia: 1975–1995. *Global and Planetary Change*, **22**(1), 233–244.

RIVERA, A., & CASASSA, G. 2004. Ice elevation, areal, and frontal changes of glaciers from national park Torres del Paine, Southern Patagonia Icefield. *Arctic, Antarctic, and Alpine Research*, **36**(4), 379–389.

RIVERA, A., LANGE, H., ARAVENA, J. C., & CASASSA, G. 1997. The 20th century and advance of Glaciar Pio XI, Chilean Patagonia. *Annals of Glaciology*, **24**, 66–71.

RIVERA, A., CASASSA, G., BAMBER, J., & KÄÄB, A. 2005. Ice-elevation changes of Glaciar Chico, southern Patagonia, using ASTER DEMs, aerial photographs and GPS data. *Journal of Glaciology*, **51**(172), 105–112.

RIVERA, A., BENHAM, T., CASASSA, G., BAMBER, J., & DOWDESWELL, J. A. 2007. Ice elevation and areal changes of glaciers from the Northern Patagonia Icefield, Chile. *Global and Planetary Change*, **59**(1), 126–137.

RIZZOLI, P., BRÄUTIGAM, B., KRAUS, T., MARTONE, M., & KRIEGER, G. 2012. Relative height error analysis of TanDEM-X elevation data. *ISPRS Journal of Photogrammetry and Remote Sensing*, **73**, 30–38.

RODRIGUEZ, E., MORRIS, C. S., BELZ, J. E., CHAPIN, E. C., MARTIN, J. M., DAFFER, W., & HENSLEY, S. 2005. *An assessment of the SRTM topographic products*. Tech. rept. D-31639. Jet Propulsion Laboratory.

RODRIGUEZ, E., MORRIS, C. S., & BELZ, J. E. 2006. A global assessment of the SRTM performance. *Photogrammetric Engineering and Remote Sensing*, **72**(3), 249–260.

ROLSTAD, C., HAUG, T., & DENBY, B. 2009. Spatially integrated geodetic glacier mass balance and its uncertainty based on geostatistical analysis: application to the western Svartisen ice cap, Norway. *Journal of Glaciology*, **55**(192), 666–680.

ROMSTAD, B., & ETZELMÜLLER, B. 2012. Mean-curvature watersheds: A simple method for segmentation of a digital elevation model into terrain units. *Geomorphology*, **139**, 293–302.

ROSEN, P. A., HENSLEY, S., JOUGHIN, I. R., LI, F. K., MADSEN, S. N., RODRIGUEZ, E., & GOLDSTEIN, R. M. 2000. Synthetic aperture radar interferometry. *Proceedings of the IEEE*, **88**(3), 333–382.

ROSENBLÜTH, B., FUENZALIDA, H. A., & ACEITUNO, P. 1997. Recent temperature variations in southern South America. *International Journal of Climatology*, **17**(1), 67–85.

ROSSI, C., EINEDER, M., FRITZ, T., & BREIT, H. 2010 (June). TanDEM-X Mission: Raw DEM Generation. *Pages 1–4 of: EUSAR 2010; 8th European Conference on Synthetic Aperture Radar*.

ROSSI, C., RODRIGUEZ-GONZALEZ, F., FRITZ, T., YAGUE-MARTINEZ, N., & EINEDER, M. 2012. TanDEM-X calibrated Raw DEM generation. *ISPRS Journal of Photogrammetry and Remote Sensing*, **73**, 12–20.

ROTT, H., MÜLLER, F., NAGLER, T., & FLORICIOIU, D. 2011. The imbalance of glaciers after disintegration of Larsen-B ice shelf, Antarctic Peninsula. *The Cryosphere*, **5**(1), 125–134.

ROTT, H. 1984. The analysis of backscattering properties from SAR data of mountain regions. *IEEE Journal of Oceanic Engineering*, **9**(5), 347–355.

ROTT, H., & DAVIS, R. E. 1993. Multifrequency and polarimetric SAR obervations on alpine glaciers. *Annals of Glaciology*, **17**, 98–104.

ROTT, H., & MÄTZLER, C. 1987. Possibilities and limits of synthetic aperture radar for snow and glacier surveying. *Annals of Glaciology*, **9**, 195–199.

ROTT, H., STUEFER, M., SIEGEL, A., SKVARCA, P., & ECKSTALLER, A. 1998. Mass fluxes and dynamics of Moreno glacier, southern Patagonia icefield. *Geophysical Research Letters*, **25**(9), 1407–1410.

ROTT, H., RACK, W., SKVARCA, P., & DE ANGELIS, H. 2002. Northern Larsen ice shelf, Antarctica: further retreat after collapse. *Annals of Glaciology*, **34**(1), 277–282.

ROTT, H., YUEH, S. H., CLINE, D. W., DUGUAY, C., ESSERY, R., HAAS, C., HELIERE, F., KERN, M., MACELLONI, G., MALNES, E., *et al.* 2010. Cold regions hydrology high-resolution observatory for snow and cold land processes. *Proceedings of the IEEE*, **98**(5), 752–765.

ROTT, H., NAGLER, T., RIPPER, E., VOGLMEIER, K., PRINZ, R., FROMM, R., COCCIA, A., META, A., DI LEO, D., & SCHUTTEMEYER, D. 2014a. KU-and X-band backscatter analysis and SWE retrieval for Alpine snow. *Pages 2407–2410 of: 2014 IEEE International Geoscience and Remote Sensing Symposium (IGARSS)*.

ROTT, H., FLORICIOIU, D., WUITE, J., SCHEIBLAUER, S., NAGLER, T., & KERN, M. 2014b. Mass changes of outlet glaciers along the Nordensjköld Coast, northern Antarctic Peninsula, based on TanDEM-X satellite measurements. *Geophysical Research Letters*, **41**(22), 8123–8129.

SAKAKIBARA, D., SUGIYAMA, S., SAWAGAKI, T., MARINSEK, S., & SKVARCA, P. 2013. Rapid retreat, acceleration and thinning of Glaciar Upsala, Southern Patagonia Icefield, initiated in 2008. *Annals of Glaciology*, **54**(63), 131–138.

SAPIANO, J. J., HARRISON, W. D., & ECHELMEYER, K. A. 1998. Elevation, volume and terminus changes of nine glaciers in North America. *Journal of Glaciology*, **44**(146), 119–135.

SCAMBOS, T. A., DUTKIEWICZ, M. J., WILSON, J. C., & BINDSCHADLER, R. A. 1992. Application of image cross-correlation to the measurement of glacier velocity using satellite image data. *Remote Sensing of Environment*, **42**(3), 177–186.

SCHAEFER, M., MACHGUTH, H., FALVEY, M., & CASASSA, G. 2013. Modeling past and future surface mass balance of the Northern Patagonia Icefield. *Journal of Geophysical Research: Earth Surface*, **118**(2), 571–588.

SCHAEFER, M., MACHGUTH, H., FALVEY, M., CASASSA, G., & RIGNOT, E. 2015. Quantifying mass balance processes on the Southern Patagonia Icefield. *The Cryosphere*, **9**(1), 25–35.

SCHÄTTLER, B., KAHLE, R., METZIG, R., STEINBRECHER, U., & ZINK, M. 2011. The joint TerraSAR-X/TanDEM-X ground segment. *Pages 2298–2301 of: 2011 IEEE International Geoscience and Remote Sensing Symposium (IGARSS)*.

SCHEIBER, R., & MOREIRA, A. 2000. Coregistration of interferometric SAR images using spectral diversity. *IEEE Transactions on Geoscience and Remote Sensing*, **38**(5), 2179–2191.

SCHERLER, D., LEPRINCE, S., & STRECKER, M. R. 2008. Glacier-surface velocities in alpine terrain from optical satellite imagery - Accuracy improvement and quality assessment. *Remote Sensing of Environment*, **112**(10), 3806–3819.

SCHIEFER, E., MENOUNOS, B., & WHEATE, R. 2007. Recent volume loss of British Columbian glaciers, Canada. *Geophysical Research Letters*, **34**(16).

SCHNEIDER, C., WUNDERLE, S., & FRIEDRICH, M. 1997. Snow cover investigations by means of ERS-SAR imagery on the Antarctic Peninsula. *EARSeL. Advances in Remote Sensing*, **5**, 71–81.

SCHUBERT, A., JEHLE, M., SMALL, D., & MEIER, E. 2012. Mitigation of atmospheric perturbations and solid Earth movements in a TerraSAR-X time-series. *Journal of Geodesy*, **86**(4), 257–270.

SCHUBERT, A., FAES, A., KÄÄB, A., & MEIER, E. 2013. Glacier surface velocity estimation using repeat TerraSAR-X images: Wavelet- vs. correlation-based image matching. *ISPRS Journal of Photogrammetry and Remote Sensing*, **82**, 49–62.

SCHULZE, D., BACHMANN, M., BRAEUTIGAM, B., BORLA-TRIDON, D., RIZZOLI, P., MARTONE, M., ZINK, M., & KRIEGER, G. 2014. Status of TanDEM-X DEM Acquisition, Calibration and Performance. *Pages 1–4 of: EUSAR 2014; 10th European Conference on Synthetic Aperture Radar*.

SCHWÄBISCH, M. 1998. A fast and efficient technique for SAR interferogram geocoding. *Pages 1100–1102 of: 1998 IEEE International Geoscience and Remote Sensing Symposium (IGARSS)*, vol. 2.

SEAL, D., & ROGEZ, F. 2000 (May). *SRTM As-Flown Mission Timeline*. Tech. rept. JPL NASA.

SHARMA, J. 2010. *Estimation of Glacier Ice Extinction Coefficients Using Long-wavelength Polarimetric Interferometric Synthetic Aperture Radar*. Ph.D. thesis, Karlsruhe Institute of Technology.

SHARY, P. A. 1995. Land surface in gravity points classification by a complete system of curvatures. *Mathematical Geology*, **27**(3), 373–390.

SHARY, P. A., SHARAYA, L. S., & MITUSOV, A. V. 2002. Fundamental quantitative methods of land surface analysis. *Geoderma*, **107**(1), 1–32.

SHEN, Y., SHAFFER, S. J., & JORDAN, R. L. 2000. Shuttle Radar Topography Mission (SRTM) flight system design and operations overview. *Pages 167–178 of: Second International Asia-Pacific Symposium on Remote Sensing of the Atmosphere, Environment, and Space*. International Society for Optics and Photonics.

SHEPHERD, A., IVINS, E. R., GERUO, A., BARLETTA, V. R., BENTLEY, M. J., BETTADPUR, S., BRIGGS, K. H., BROMWICH, D. H., FORSBERG, R., GALIN, N., *et al.* 2012. A reconciled estimate of ice-sheet mass balance. *Science*, **338**(6111), 1183–1189.

SHI, J., & DOZIER, J. 1995. Inferring snow wetness using C-band data from SIR-C's polarimetric synthetic aperture radar. *IEEE Transactions on Geoscience and Remote Sensing*, **33**(4), 905–914.

SHI, J., & DOZIER, J. 2000a. Estimation of snow water equivalence using SIR-C/X-SAR. I. Inferring snow density and subsurface properties. *IEEE Transactions on Geoscience and Remote Sensing*, **38**(6), 2465–2474.

SHI, J., & DOZIER, J. 2000b. Estimation of snow water equivalence using SIR-C/X-SAR. II. Inferring snow depth and particle size. *IEEE Transactions on Geoscience and Remote Sensing*, **38**(6), 2475–2488.

SHI, Z., & FUNG, K. B. 1994. A comparison of digital speckle filters. *In: 1994 IEEE International Geoscience and Remote Sensing Symposium (IGARSS)*, vol. 94.

SIHVOLA, A., NYFORS, E., & TIURI, M. 1985. Mixing formulae and experimental results for the dielectric constant of snow. *Journal of Glaciology*, **31**(108), 163–170.

SKVARCA, P., DE ANGELIS, H., NARUSE, R., WARREN, C., & ANIYA, M. 2002. Calving rates in fresh water: new data from southern Patagonia. *Annals of Glaciology*, **34**(1), 379–384.

SKVARCA, P., RAUP, B., & DE ANGELIS, H. 2003. Recent behaviour of Glaciar Upsala, a fast-flowing calving glacier in Lago Argentino, southern Patagonia. *Annals of Glaciology*, **36**(1), 184–188.

SLATER, J. A., GARVEY, G., JOHNSTON, C., HAASE, J., HEADY, B., KROENUNG, G., & LITTLE, J. 2006. The SRTM data 'finishing' process and products. *Photogrammetric Engineering & Remote Sensing*, **72**(3), 237–247.

SMITH, B. E., FRICKER, H. A., JOUGHIN, I. R., & TULACZYK, S. 2009. An inventory of active subglacial lakes in Antarctica detected by ICESat (2003–2008). *Journal of Glaciology*, **55**(192), 573–595.

SMITH, B., & SANDWELL, D. 2003. Accuracy and resolution of Shuttle Radar Topography Mission data. *Geophysical Research Letters*, **30**(9).

STEARNS, L. A. 2011. Dynamics and mass balance of four large East Antarctic outlet glaciers. *Annals of Glaciology*, **52**(59), 116–126.

STEARNS, L. A., & HAMILTON, G. S. 2005. A new velocity map for Byrd Glacier, East Antarctica, from sequential ASTER satellite imagery. *Annals of Glaciology*, **41**(1), 71–76.

STEARNS, L. A., JEZEK, K. C., & VAN DER VEEN, C. J. 2005. Decadal-scale variations in ice flow along Whillans Ice Stream and its tributaries, West Antarctica. *Journal of Glaciology*, **51**(172), 147–157.

STEARNS, L. A., SMITH, B. E., & HAMILTON, G. S. 2008. Increased flow speed on a large East Antarctic outlet glacier caused by subglacial floods. *Nature Geoscience*, **1**(12), 827–831.

STILES, W. H., & ULABY, F. T. 1981. *Dielectric properties of snow*. RSL Technical Report 527-1. University of Kansas Center for Research.

STILES, W. H., & ULABY, F. T. 1980. The active and passive microwave response to snow parameters: 1. Wetness. *Journal of Geophysical Research: Oceans*, **85**(C2), 1037–1044.

STROZZI, T., LUCKMAN, A., MURRAY, T., WEGMÜLLER, U., & WERNER, C. L. 2002. Glacier motion estimation using SAR offset-tracking procedures. *IEEE Transactions on Geoscience and Remote Sensing*, **40**(11), 2384–2391.

STROZZI, T., KOURAEV, A., WIESMANN, A., WEGMÜLLER, U., SHAROV, A., & WERNER, C. 2008. Estimation of Arctic glacier motion with satellite L-band SAR data. *Remote Sensing of Environment*, **112**(3), 636–645.

STUEFER, M. 1999. *Investigations on mass balance and dynamics of Moreno Glacier based on field measurements and satellite imagery*. Ph.D. thesis, University of Innsbruck, Austria.

STUEFER, M., ROTT, H., & SKVARCA, P. 2007. Glaciar Perito Moreno, Patagonia: climate sensitivities and glacier characteristics preceding the 2003/04 and 2005/06 damming events. *Journal of Glaciology*, **53**(180), 3–16.

SUCHANDT, S., & EINEDER, M. 2003. Experiences with SRTM/X-SAR phase unwrapping using the minimum cost flow method. *Pages 4380–4382 of: 2003 IEEE International Geoscience and Remote Sensing Symposium (IGARSS)*, vol. 7.

SURAZAKOV, A. B., & AIZEN, V. B. 2006. Estimating volume change of mountain glaciers using SRTM and map-based topographic data. *IEEE Transactions on Geoscience and Remote Sensing*, **44**(10), 2991–2995.

THOMAS, R., CSATHO, B., DAVIS, C., KIM, C., KRABILL, W., MANIZADE, S., MCCONNELL, J., & SONNTAG, J. 2001. Mass balance of higher-elevation parts of the Greenland ice sheet. *Journal of Geophysical Research: Atmospheres*, **106**(D24), 33707–33716.

TIURI, M. E., SIHVOLA, A. H., NYFORS, E. G., & HALLIKAIKEN, M. T. 1984. The complex dielectric constant of snow at microwave frequencies. *IEEE Journal of Oceanic Engineering*, **9**(5), 377–382.

TOUZI, R., LOPES, A., BRUNIQUEL, J., & VACHON, P. W. 1999. Coherence estimation for SAR imagery. *IEEE Transactions on Geoscience and Remote Sensing*, **37**(1), 135–149.

ULABY, F. T., STILES, W. H., FUNG, A. K., EOM, H. J., & ABDELRAZIK, M. 1982a. *Observations and modelling of the radar backscatter from snowpacks*. RSL Technical Report 527-4. University of Kansas Center for Research.

ULABY, F. T., & STILES, W. H. 1981. Microwave response of snow. *Advances in Space Research*, **1**(10), 131–149.

ULABY, F. T., & STILES, W. H. 1980. The active and passive microwave response to snow parameters: 2. Water equivalent of dry snow. *Journal of Geophysical Research: Oceans (1978–2012)*, **85**(C2), 1045–1049.

ULABY, F. T., MOORE, R. K., & FUNG, A. K. 1981. *Microwave Remote Sensing, Active and Passive, Volume I: Fundamentals and Radiometry*. Artech House, Inc.

ULABY, F. T., MOORE, R. K., & FUNG, A. K. 1982b. *Microwave Remote Sensing, Active and Passive, Volume II: Radar Remote Sensing and Surface Scattering and Emission Theory*. Artech House, Inc.

ULABY, F. T., STILES, W. H., & ABDELRAZIK, M. 1984. Snowcover influence on backscattering from terrain. *IEEE Transactions on Geoscience and Remote Sensing*, 126–133.

ULABY, F. T., MOORE, R. K., & FUNG, A. K. 1986. *Microwave Remote Sensing, Active and Passive, Volume II: From Theory to Applications*. Artech House, Inc.

ULANDER, L. M. H. 1996. Radiometric slope correction of synthetic-aperture radar images. *IEEE Transactions on Geoscience and Remote Sensing*, **34**(5), 1115–1122.

VAN DER VEEN, C. J. 2013. *Fundamentals of glacier dynamics*. CRC Press.

VAN DER VEEN, C. J., STEARNS, L. A., JOHNSON, J., & CSATHO, B. 2014. Flow dynamics of Byrd Glacier, East Antarctica. *Journal of Glaciology*, **60**(224), 1053–1064.

VAN ZYL, J. J., CHAPMAN, B. D., DUBOIS, P., & SHI, J. 1993. The effect of topography on SAR calibration. *IEEE Transactions on Geoscience and Remote Sensing*, **31**(5), 1036–1043.

VASILE, G., TROUVÉ, E., PETILLOT, I., BOLON, P., NICOLAS, J.-M., GAY, M., CHANUSSOT, J., LANDES, T., GRUSSENMEYER, P., BUZULOIU, V., *et al.* 2008. High-resolution SAR interferometry: Estimation of local frequencies in the context of Alpine glaciers. *IEEE Transactions on Geoscience and Remote Sensing*, **46**(4), 1079–1090.

VAUGHAN, D. G., COMISO, J. C., ALLISON, I., CARRASCO, J., KASER, G., KWOK, R., MOTE, P., MURRAY, T., PAUL, F., REN, J., RIGNOT, E., STEFFEN, K., & ZHANG, T. 2013. Observations: Cryosphere. *Chap. 4, pages 317–382 of:* STOCKER, T. F., QIN, D., PLATTNER, G.-K., TIGNOR, M., ALLEN, S. K., BOSCHUNG, J., NAUELS, A., XIA, Y., BEX, V., & MIDGLEY, P. M. (eds), *Climate Change 2013: The Physical Science Basis. Contribution of Working Group I to the Fifth Assessment Report of the Intergovernmental Panel on Climate Change*. Cambridge University Press Cambridge, UK, and New York, NY, USA.

VILLALBA, R., LARA, A., BONINSEGNA, J. A., MASIOKAS, M., DELGADO, S., ARAVENA, J. C., ROIG, F. A., SCHMELTER, A., WOLODARSKY, A., & RIPALTA, A. 2003. Large-scale temperature changes across the southern Andes: 20th-century variations in the context of the past 400 years. *Pages 177–232 of: Climate Variability and Change in High Elevation Regions: Past, Present & Future*. Springer.

VILLANO, M., & PAPATHANASSIOU, K. P. 2011. Differential shift estimation in the absence of coherence: performance analysis and benefits of polarimetry. *In: Proceedings of the ESA POLinSAR 2011 Workshop*.

WARREN, C., & ANIYA, M. 1999. The calving glaciers of southern South America. *Global and Planetary Change*, **22**(1), 59–77.

WARREN, C. R. 1993. Rapid recent fluctuations of the calving San Rafael glacier, Chilean Patagonia: climatic or non-climatic? *Geografiska Annaler. Series A. Physical Geography*, 111–125.

WARREN, C. R. 1994. Freshwater calving and anomalous glacier oscillations: recent behaviour of Moreno and Ameghino glaciers, Patagonia. *The Holocene*, **4**(4), 422–429.

WARREN, C. R., & SUGDEN, D. E. 1993. The Patagonian Icefields: a glaciological review. *Arctic and Alpine Research*, 316–331.

WARREN, S. G., & BRANDT, R. E. 2008. Optical constants of ice from the ultraviolet to the microwave: A revised compilation. *Journal of Geophysical Research: Atmospheres (1984–2012)*, **113**(D14).

WEBER HOEN, E., & ZEBKER, H. A. 2000. Penetration depths inferred from interferometric volume decorrelation observed over the Greenland Ice Sheet. *IEEE Transactions on Geoscience and Remote Sensing*, **38**(6), 2571–2583.

WEBSTER, R., & OLIVER, M. A. 2007. *Geostatistics for environmental scientists*. John Wiley & Sons.

WENDLEDER, A., FELBIER, A., WESSEL, B., HUBER, M., & ROTH, A. 2016. A Method to Estimate Long-Wave Height Errors of SRTM C-Band DEM. *IEEE Geoscience and Remote Sensing Letters*, **13**(5), 696–700.

WERNER, C., WEGMÜLLER, U., STROZZI, T., & WIESMANN, A. 2005. Precision estimation of local offsets between pairs of SAR SLCs and detected SAR images. *Pages 4803–4805 of: 2005 IEEE International Geoscience and Remote Sensing Symposium (IGARSS)*, vol. 7.

WILEY, C. A. 1954. *Pulsed doppler radar methods and apparatus*.

WILLIS, M. J., MELKONIAN, A. K., PRITCHARD, M. E., & RIVERA, A. 2012a. Ice loss from the Southern Patagonian Ice Field, South America, between 2000 and 2012. *Geophysical Research Letters*, **39**(17).

WILLIS, M. J., MELKONIAN, A. K., PRITCHARD, M. E., & RAMAGE, J. M. 2012b. Ice loss rates at the Northern Patagonian Icefield derived using a decade of satellite remote sensing. *Remote Sensing of Environment*, **117**, 184–198.

WINCHESTER, V., & HARRISON, S. 1996. Recent oscillations of the San Quintin and San Rafael glaciers, Patagonian Chile. *Geografiska Annaler. Series A. Physical Geography*, 35–49.

WISMANN, V. 2000. Monitoring of seasonal snowmelt on Greenland with ERS scatterometer data. *IEEE Transactions on Geoscience and Remote Sensing*, **38**(4), 1821–1826.

YAGUE-MARTINEZ, N., ROSSI, C., LACHAISE, M., RODRIGUEZ-GONZALEZ, F., FRITZ, T., & BREIT, H. 2010a. Interferometric processing algorithms of TanDEM-X data. *Pages 3518–3521 of: 2010 IEEE International Geoscience and Remote Sensing Symposium (IGARSS)*.

YAGUE-MARTINEZ, N., EINEDER, M., BRCIC, R., BREIT, H., & FRITZ, T. 2010b. TanDEM-X Mission: SAR Image Coregistration Aspects. *Pages 1–4 of: EUSAR 2010; 8th European Conference on Synthetic Aperture Radar*.

YOON, Y. T., EINEDER, M., YAGUE-MARTINEZ, N., & MONTENBRUCK, O. 2009. TerraSAR-X precise trajectory estimation and quality assessment. *IEEE Transactions on Geoscience and Remote Sensing*, **47**(6), 1859–1868.

ZEBKER, H. A., & CHEN, K. 2005. Accurate estimation of correlation in InSAR observations. *IEEE Geoscience and Remote Sensing Letters*, **2**(2), 124–127.

ZEBKER, H. A., & GOLDSTEIN, R. M. 1986. Topographic mapping from interferometric synthetic aperture radar observations. *Journal of Geophysical Research: Solid Earth*, **91**(B5), 4993–4999.

ZEBKER, H. A., & VILLASENOR, J. 1992. Decorrelation in interferometric radar echoes. *IEEE Transactions on Geoscience and Remote Sensing*, **30**(5), 950–959.

ZEBKER, H. A., WERNER, C. L., ROSEN, P. A., & HENSLEY, S. 1994. Accuracy of topographic maps derived from ERS-1 interferometric radar. *IEEE Transactions on Geoscience and Remote Sensing*, **32**(4), 823–836.

ZEMP, M., THIBERT, E., HUSS, M., STUMM, D., ROLSTAD DENBY, C., NUTH, C., NUSSBAUMER, S. U., MOHOLDT, G., MERCER, A., MAYER, C., *et al.* 2013. Reanalysing glacier mass balance measurement series. *The Cryosphere*, **7**(4), 1227–1245.

ZEMP, M., JANSSON, P., HOLMLUND, P., GÄRTNER-ROER, I., KOBLET, T., THEE, P., & HAEBERLI, W. 2010. Reanalysis of multi-temporal aerial images of Storglaciären, Sweden (1959–99)–Part 2: Comparison of glaciological and volumetric mass balances. *The Cryosphere*, **4**(3), 345–357.

ZEMP, M., FREY, H., GÄRTNER-ROER, I., NUSSBAUMER, S. U., HOELZLE, M., PAUL, F., HAEBERLI, W., DENZINGER, F., AHLSTRØM, A. P., ANDERSON, B., *et al.* 2015. Historically unprecedented global glacier decline in the early 21st century. *Journal of Glaciology*, **61**(228), 745–762.

ZITOVA, B., & FLUSSER, J. 2003. Image registration methods: a survey. *Image and Vision Computing*, **21**(11), 977–1000.

ZWALLY, H. J., SCHUTZ, B., ABDALATI, W., ABSHIRE, J., BENTLEY, C., BRENNER, A., BUFTON, J., DEZIO, J., HANCOCK, D., HARDING, D., *et al.* 2002. ICESat's laser measurements of polar ice, atmosphere, ocean, and land. *Journal of Geodynamics*, **34**(3), 405–445.

ZWALLY, H. J., & GIOVINETTO, M. B. 2011. Overview and assessment of Antarctic ice-sheet mass balance estimates: 1992–2009. *Surveys in Geophysics*, **32**(4-5), 351–376.

Acknowledgements

The journey culminating with this PhD thesis has been long and not always easy but it has certainly allowed me to grow personally and professionally. Many people have contributed to this growth and, directly or indirectly, to this thesis. I would like to briefly thank them here.

First of all I would like to express my sincere gratitude to Dr. Dana Floricioiu for the precious and continuous supervision, the useful discussions, the moral support and for carefully revising this rather long manuscript. Many thanks to Prof. Michael Eineder for offering me a position in the IMF SAR department and for the discussions on many aspect of SAR remote sensing. I am very grateful to Prof. Richard Bamler for his supervision and his valuable recommendations and for accepting me as a PhD candidate at the Technische Universität München and at the DLR IMF institute. Thanks to both of you for reviewing this thesis. A special thanks goes to Prof. Helmut Rott for accepting to be the external reviewer of this work. His willingness to share his vast knowledge of glaciology and remote sensing of the cryosphere is greatly appreciated. Thanks also to Dr. Manfred Gottwald for revising the German version of the abstract at short notice.

I would like to thank all the colleagues of the IMF SAR department for creating a very productive working environment and particularly Dr. Tomas Fritz and Dr. Helko Breit for the useful insight on TanDEM-X, TerraSAR-X and SRTM data. A big thank you goes to: Michael Bäßler, Daniele Cerra, Fabio Cian, Xiao Ying Cong, Francesco de Zan, Sergio Duque, Giorgio Gomba, Erling Johnson Gavilan, Lukas Krieger, Marie Lachaise, Alessandro Parizzi, Fernando Rodriguez-Gonzalez, Cristian Rossi, Paolo Sica and Nestor Yagüe-Martinez who offered a great contribution to this work and to my time at DLR IMF through invaluable discussion both on technical and non-technical topics. The friendship created with many of you has greatly helped me and this work.

I am grateful to all the teachers and professors who during many years have contributed with their commitment to my education. A kind thanks to Jutta Rieck for the perseverance in teaching the German language at DLR and for helping with the preparation of the Goethe Institut exam.

Living abroad especially while doing a PhD can be challenging. I want to heartily thank all the beautiful people who I met along the way and who contributed to making Munich feel more like home. Without you all this would not have been possible.

My unconditional gratitude goes to the people who love me, believe in me and support me whatever the geographical distance that separates us. Among these the most special of thank you goes to my parents and my brothers: your role in achieving this result is inestimable.

This work was carried out at the Deutsches Zentrum für Luft- und Raumfahrt e.V. (DLR) and supported by the projects “Remote Sensing and Earth System Dynamics” of the Helmoltz Alliance (HGF) and “The Antarctic ice sheet mass balance from satellite geodesy and modelling” of the Deutsche Forschungsgemeinschaft (DFG). TanDEM-X data were provided through the science proposal XTI GLAC 0495, TerraSAR-X data through the proposals HYD0396, HYD0438, HYD1303, HYD1451.

Oberpfaffenhofen, 3 July 2016